

Cumhuriyet Science Journal
Faculty of Science Cumhuriyet University 58140
Sivas-TURKEY
Phone: +90(346)2191010-1522
Fax: +90(346)2191186
e-mail: csj@cumhuriyet.edu.tr
http://dergipark.gov.tr/csj

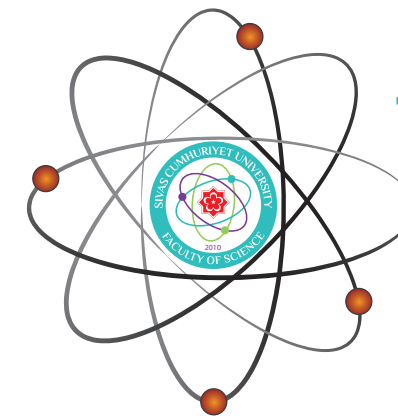
Cumhuriyet Science Journal Vol: 42 No: 3 Year: 2021



Sivas Cumhuriyet University

ISSN : 2587-2680
e-ISSN : 2587-246X

Cumhuriyet
Science
Journal



Volume: 42

Number: 3

Year: 2021



ISSN: 2587-2680
e-ISSN: 2587-246X
Period: Quarterly
Founded: 2002
Publisher: Sivas Cumhuriyet
University

Cumhuriyet Science Journal (CSJ)

Journal Previous Name: Cumhuriyet Üniversitesi Fen-Edebiyat Fakültesi Fen Bilimleri Dergisi

Old ISSN: 1300-1949

Owner on behalf of the Sivas Cumhuriyet University, Faculty of Science

Prof. Dr. İdris ZORLUTUNA (Sivas Cumhuriyet University)

Editor in Chief

Prof. Dr. İdris ZORLUTUNA (Sivas Cumhuriyet University)

Managing Editor

Assoc. Prof. Dr. Adil ELİK (Sivas Cumhuriyet University)

Editors

Prof. Dr. Baki KESKİN

bkeskin@cumhuriyet.edu.tr

Subjects: Mathematics and Statistics

Institution: Sivas Cumhuriyet University

Assoc. Prof. Dr. Adil ELİK

elik@cumhuriyet.edu.tr

Subjects: Chemistry and Chemical Engineering,
Environmental Sciences, Basic Sciences (General)

Institution: Sivas Cumhuriyet University

Prof. Dr. Nilüfer TOPSAKAL

ntopsakal@cumhuriyet.edu.tr

Subjects: Applied Mathematics

Institution: Sivas Cumhuriyet University

Prof. Dr. Serkan AKKOYUN

sakkoyun@cumhuriyet.edu.tr

Subjects: Physics and Physical Engineering

Institution: Sivas Cumhuriyet University

Prof. Dr. Hülya KURŞUN

hkursun@cumhuriyet.edu.tr

Subjects: Earth Sciences

Institution: Sivas Cumhuriyet University

Prof. Dr. Halil İbrahim ULUSOY

hiulusoy@cumhuriyet.edu.tr

Subjects: Chemistry, Analytical Chemistry, Drug Analysis, Pharmacy

Institution: Sivas Cumhuriyet University

Assoc. Prof. Dr. Nail ALTUNAY

naltunay@cumhuriyet.edu.tr

Subjects: Bioanalytical Chemistry, Chemometric Analysis

Institution: Sivas Cumhuriyet University

Section Editors

Prof. Dr. Natalia BONDARENKO

bondarenkonp@info.sgu.ru

Subjects: Applied Mathematics and Physics

Institution: Samara University

Prof. Dr. Muhammet BEKÇİ

mbekci@cumhuriyet.edu.tr

Subjects: Statistics

Institution: Sivas Cumhuriyet University

Prof. Dr. Marcello LOCATELLI

marcello.locatelli@unich.it

Subjects: Analytical Chemistry

Institution: University "G. d'Annunzio" of Chieti-Pescara

Prof. Dr. Konstantin P. KATIN

kpkatin@yandex.ru

Subjects: Theoretical Chemistry, Computational design of nanostructures, nanodevices and nanotechnologies

Institution: National Research Nuclear University

Assoc. Prof. Dr. Duran KARAKAŞ

dkarakas@cumhuriyet.edu.tr

Subjects: Inorganic Chemistry, Theoretical Chemistry

Institution: Sivas Cumhuriyet University

Assoc. Prof. Dr. Yaşar ÇAKMAK

ycakmak@cumhuriyet.edu.tr

Subjects: Applied Mathematics

Institution: Sivas Cumhuriyet University

Assoc. Prof. Dr. Sevgi DURNA DAŞTAN

sdurna@cumhuriyet.edu.tr

Subjects: Molecular Biology

Institution: Sivas Cumhuriyet University

Assist. Prof. Dr. Didem ALTUN

didemaltun@cumhuriyet.edu.tr

Subjects: Engineering sciences

Institution: Sivas Cumhuriyet University

Abstracted&Indexing

ULAKBİM TR-Dizin

Index Copernicus (ICI Journals Master List)

Clarivate Analytics Zoological Record

Crossref

Directory of Open Access Journals (DOAJ)

WorldCat

Akademik Dizin

Arastirmax Bilimsel Yayın İndeksi

Bielefeld Academic Search Engine (BASE)

Directory of Research Journal Indexing (DRJI)

Google Scholar

Research Gate

Idealonline

Editorial Board

Prof. Dr. Sezai ELAGÖZ (ASELSAN)
Prof. Dr. Mustafa SOYLAK (Erciyes University)
Prof. Dr. Chuan Fu Yang (Nanjing University of Science and Technology)
Prof. Dr. Münevver SÖKMEN (KGTU)
Prof. Dr. Hüseyin MERDAN (TOBB ETU)
Prof. Dr. Mehmet AKKURT (Erciyes University)
Prof. Dr. Mustafa KAVUTÇU (Gazi University)
Prof. Dr. Francois VOS (The University of Queensland)
Prof. Dr. Abuzar KABIR (International Forensic Research Institute)
Prof. Dr. Mustafa TÜZEN (GOP University)
Prof. Dr. Songül KAYA MERDAN (METU)
Prof. Dr. Jose Javier Valiente-Dobon (INFN-LNL, Padova University)
Prof. Dr. Yeşim SAĞ AÇIKEL (Hacettepe University)
Prof. Dr. Mehmet ŞİMŞİR (Sivas Cumhuriyet University)
Prof. Dr. Atalay SÖKMEN (KGTU)
Prof. Dr. Ricardo I. JELDRES (Universidad de Antofagasta)
Prof. Dr. Mustafa YILDIRIM (Sivas Cumhuriyet University)
Prof. Dr. Ali DELİCEOĞLU (Erciyes University)
Prof. Dr. Tuncay BAYRAM (Karadeniz Technical University)
Prof. Dr. Gökhan KOÇAK (Erciyes University)
Prof. Dr. Nadjet Laouet (Freres Mentouri Constantine-1 University)
Assoc. Prof. Dr. Savaş KAYA (Sivas Cumhuriyet University)

Layout Editors:

Assist. Prof. Dr. Merve Esra TÜRKAY
Lecturer Aykut HASBEK

Copyeditors:

Assist. Prof. Dr. Doğa Can SERTBAŞ
Assist. Prof. Dr. Hacı Ahmet KARADAŞ
Research Assistant Özgür İNCE

Proofreader:

Assist. Prof. Dr. Yener ÜNAL
Lecturer Aykut HASBEK

Publication Type. Peer Reviewed Journal

Cite Type: Cumhuriyet Sci. J.

Contact Information

Faculty of Science Cumhuriyet University
58140 Sivas- TURKEY
Phone: +90(346)2191010-1522
Fax: +90(346)2191186
e-mail: csj@cumhuriyet.edu.tr
<http://dergipark.gov.tr/csj>

CONTENTS

PAGES

Şifa TÜRKÖĞLU

Genotoxic effect of two commonly used textile dyes Reactive Blue 19 and Reactive Black 5 using Allium cepa L. as an indicator..... 515 - 525

Tuğcan KORAK, Fırat AŞIR, Esin IŞIK, Nur CENGİZ

Multiple sequence alignment quality comparison in T-Coffee, MUSCLE and M-Coffee based on different benchmarks... 526 - 535

Michael OSHO

Enzymatic degradation and fermentation of Corn Bran for Bioethanol production by Pseudomonas aeruginosa AU4738 and Saccharomyces cerevisiae using Co-culture technique..... 536 - 544

Deniz ŞAHİN

Effects of co-culturing Schizochytrium sp. and Escherichia coli cells on biomass and Docosahexaenoic acid (DHA) production..... 545 - 552

Parham TASLIMI, Yeliz DEMİR, Hatice Esra DURAN, Ümit Muhammet KOÇYİĞİT, Burak TÜZÜN, Osman Nuri ASLAN, Mustafa CEYLAN, İlhami GÜLÇİN

Some old 2-(4-(Aryl)-thiazole-2-yl)-3a,4,7,7a-tetrahydro-1H-4,7-tethanoisoindole-1,3(2H)-dione derivatives: Synthesis, inhibition effects and molecular docking studies on Aldose reductase and α -Glycosidase..... 553 - 564

Nuraniye ERUYGUR, Ümit Muhammet KOÇYİĞİT, Mehmet ATAŞ, Özge ÇEVİK, Faik GÖKALP, Parham TASLİMİ, İlhami GÜLÇİN

Composition characterization and biological activity study of Thymbra spicata l. var. spicata essential oil..... 565 - 575

Rebaz OMER, Pelin KOPARIR, Ibrahim Nazem QADER, Lana AHMED

Structure reactivity analysis for Phenylalanine and Tyrosine..... 576 - 585

Doğan KAYA

Structural analysis of pure PtCu₃ nanoparticles synthesized by modified Polyol process..... 586 - 592

Cem ERKMEN, Burçin BOZAL PALABIYIK, Bengi USLU

Sensitive electrochemical determination of Cefpirome in human urine using differential pulse voltammetry..... 593 - 601

Taner ERDOĞAN

DFT, molecular docking and molecular dynamics simulation studies on natural chromone derivatives from Cassia nomame for their possible antiviral activity against Coronavirus, SARS-CoV-2..... 602 - 615

Öznur GÜNGÖR

Determination of Salbutamol Sulfate in pharmaceutical formulation with differential pulse voltammetry using poly(Benzofuran-2-Boronic acid) modified platinum electrode..... 616 - 628

Songül ULUSOY

Synthesis of new solid phase sorbent for sensitive spectrophotometric determination of Quercetin..... 629 - 637

Aslı GÖÇENOĞLU SARIKAYA, Bilgen OSMAN

Tetracycline adsorption via dye-attached polymeric microbeads..... 638 - 648

Gülay AKYÜZ

Synthesis of Benzimidazole derivatives containing Schiff base exhibiting antiurease activities..... 649 - 655

Elvan ÜSTÜN, Neslihan ŞAHİN

Molecular docking studies of N-Heterocyclic Carbene molecules with Thioredoxin Reductase and DNA..... 656 - 662

Umar Muhammad ABUBAKAR, Muhammad Lawan KAURANGİNİ

New extension of beta, Gauss and confluent hypergeometric functions..... 663 - 676

Nuh DURNA, Mustafa YILDIRIM, Abbas KILIÇ

On the fine spectra of the Jacobi matrices on $c_{0,c,l,p}$ ($1 \leq p \leq \infty$) and $[[bv]]_p$ ($1 \leq p < \infty$)..... 677 - 687

Melisa SÖNMEZ, Sinan KUDAY <i>Measurement of out of field doses in brain proton therapy with GATE simulations.....</i>	688 - 693
Emre Bahadır AL <i>Effect of size modulation and donor position on intersubbands refractive index changes of a donor within a spherical core/shell/shell semiconductor quantum dot.....</i>	694 - 701
Ziyafer Gizem PORTAKAL UÇAR <i>Thermoluminescence characteristics and kinetic analysis of beta irradiated Ca₄LaO(BO₃)₃ phosphor.....</i>	702 - 714
Mustafa TOKAÇ <i>Magnetic phase transitions due to compositional variation across amorphous thin-films.....</i>	715 - 721
Sinan KUDAY, Yusuf ŞENGELEN <i>Projections for dual radioisotope applications in PET imaging.....</i>	722 - 727
Nilay BOSTAN <i>Preheating in radiatively corrected ϕ_4 inflation with non-minimal coupling in Palatini formulation.....</i>	728 - 734
Özlem YILMAZ, Sevda İLDAN ÖZMEN, Hülya METİN GÜBÜR <i>Effects of annealing on ZnS films produced by CBD method.....</i>	735 - 742
Ayfer Ezgi YILMAZ <i>How to use adjusted degree of distinguishability and inter-rater reliability simultaneously?.....</i>	743 - 750

Genotoxic effect of two commonly used textile dyes Reactive Blue 19 and Reactive Black 5 using *Allium cepa* L. as an indicator

Şifa TÜRKÖĞLU^{1, *} 

¹Sivas Cumhuriyet University, Faculty of Science, Department of Biology, Sivas/TURKEY

Abstract

In this study, the cytotoxic and genotoxic effects of Reactive Blue 19 and Reactive Black 5 were investigated using the *Allium* test and comet assay. These chemicals are fabric dyes used in textile industries in various parts of Turkey. Bulbs with roots of *Allium cepa* L. were treated with different concentrations (25, 50 and 100 ppm) of these textile dyes for 24 h. and 48 h. The root tips were processed for cytological studies by the aseto-orcein squash procedure. Distilled water and methyl methane sulfonate (MMS, 10 ppm) were used as a negative and positive control, respectively. Exposure of Reactive Blue 19 and Reactive Black 5 significantly decreased mitotic index values. Additionally, all treatments changed the frequency of mitotic phases when compared with the control groups. These dyes increased chromosome aberrations in test material. Among these abnormalities were anaphase bridges, c-mitosis, laggards, micronuclei and stickiness. A significant increase in DNA damage was also observed at all concentrations of both Reactive Blue 19 and Reactive Black 5 examined by comet assay.

Article info

History:

Received: 18.01.2021

Accepted: 26.08.2021

Keywords:

Reactive Blue 19,
Reactive Black 5,
Allium test,
Comet assay,
Genotoxicity.

1. Introduction

Since ancient times in history, coloring agents have had a place in human life. While the coloring agents that are as old as human history were formerly obtained from natural products, they were later replaced by synthetic colorants and the industrial revolution, the development of organic chemistry, and the textile and pharmaceutical industries.

Today there has been a growing interest in synthetic products because natural coloring agents are costly, their acquisition is rather challenging, and their color scale is narrow. Rapid developments in the textile industry have brought with them an uncontrollable growth, due to which the places that have suffered at most have doubtlessly been the seas, lakes, rivers, and drinking-water basins contaminated by the wastes of textile factories. The living organisms that live in these resources have been affected by this contamination with a great deal, and the substances being the causes of such contamination reach even humans through the food chain. The fact that some of these substances spreading uncontrollably around the environment may be mutagenic or carcinogenic has been a matter of discussion for years. These substances left in nature by humans by abandoning them to their fate lead to several diseases, including cardiac diseases, early aging, cataract, hereditary and developmental birth defects. Besides such diseases, the hypothesis that they

are the main cause of cancer is gaining strength by finding new supporters each passing day. The fact that the coloring agents used in the textile industry are emitted into the external environment through the factory wastes causes unhealthy conditions to occur. In particular, the wastewater into which the industrial water containing coloring agents are disposed of destroying the natural environment in terms of color, smell, and landscape, and thus, the natural flora and fauna existing within the environment are annihilated [1].

Al-Sabti [2], in a study he conducted by using a micronucleus test, reported that under the laboratory conditions, chlorotriazine Reactive Azo Red 120 textile dye, which is also found in the textile wastewater, posed a genotoxic effect by increasing the amount of micronucleus in the *Carassius auratus gibelio* erythrocytes. In another study conducted on *Clarias lazera*, the textile industrial wastewater was determined to increase the micronucleus formation [3].

Sumathi et al. [4], in a study they conducted by applying a comet test, reported that DNA damage occurred in the erythrocytes and liver cells of the fish belonging to *Cyprinus carpio* species exposed to the wastewater of textile dyes. It was also reported that the textile industrial wastewater given in different concentrations and at different periods had increased the amount of the micronucleus in the erythrocyte and

*Corresponding author. e-mail address: turkoglu@cumhuriyet.edu.tr
<http://dergipark.gov.tr/csj> ©2021 Faculty of Science, Sivas Cumhuriyet University

branchial cells of *O. niloticus* and enhanced the other nucleus anomalies [5].

In their study, Moawad et al. [6] researched the effects of different dyes applied on clover, lettuce, wheat, and tomato plants grown widely on the Nile Delta on seed germination, root elongation, and genotoxicity. As a result of the research, the germination rate in the seeds at increased dye concentrations decreased. Separately, a high level of dye concentrations was determined to have inhibited the shoot/offshoot formation. The elongation of the rootlet was also suppressed at high concentrations. It was observed that among the plants that were used, wheat had shown much more resistance to the toxic effect of the dye when compared to other plants.

In toxicology, the changes that have occurred in the genetic mutations, the number, and the structure of the chromosomes have been of great interest, and a wide variety of *in vivo* and *in vitro* test systems have been developed to determine any of these mutations. The genotoxicity tests used frequently are the Allium test, Ames test, micronucleus test, sister chromatid exchange (SCE) test, and the single-cell gel electrophoresis test (comet assay).

It is easier and more sensitive to perform genotoxicity with a plant bioassay because it is an efficient and cost-effective test system. High plants may be exposed to environmental pollutants directly in laboratories [7] or *in situ* [8-9]. *Allium cepa* L. (*A. cepa*) is used frequently to evaluate the potential of genotoxicity in pesticides, food additives, or other chemicals [10-13]. A good correlation has been determined between the Allium test results and the mammalian test systems [14]. The popularity of the Allium assay comes from its ability to evaluate chromosomal aberrations in cytogenetic tests in an efficient way [15].

On the other hand, comet assay is frequently used in finding the strand breaks in DNA of single cells because the comet assay is simple to use, sensitive, quick, cost-effective, and easy. In addition, it is a user-friendly application and requires a small number of cells compared with the other testing systems [16-17]. With the genotoxicity studies conducted in laboratories in the short term, a new system has been developed, and this is called the “the Micronucleus Formation Assay (MN)” and is used in detecting cytogenetic changes quickly and analyzes the dividing root meristems in *A. cepa* [18]. In the cell division, laggard chromosomes or acentric fragments are excluded from the nucleus, and therefore micronuclei are formed. These micronuclei are easy to detect in the subsequent interface.

In this study, to determine the possible genotoxic effects of the coloring agents, Reactive Blue 19 and Reactive Black 5 used in the textile industry, 25, 50, and 100 ppm – doses of these substances were applied into *A. cepa* root tip cells for the period of 24 and 48 hours, and their effects on the mitotic index, chromosome, and DNA structure were investigated through the Allium and comet tests.

2. Material-Method

2.1. Chemicals

The testing materials were bought from the Sigma-Aldrich Company (Turkey). Reactive Blue 19: Cas no: 2580-78-1, Molecular formula: $C_{22}H_{16}N_2Na_2O_{11}S_3$, Formula Weight: 626.54. Reactive Black 5: Cas no: 17095-24-8, Molecular formula: $C_{26}H_{21}N_5Na_4O_{19}S_6$, Formula Weight: 991.82. *Allium cepa* ($2n=16$) onion bulbs, 25-30 mm in diameter, non-treated, were bought from a supermarket in the city of Sivas. All the chemicals used in the comet assay were purchased from Sigma-Aldrich.

2.2. Allium test

The onions (*A. cepa*, $2n=16$) were determined according to whether they received the chemicals. They were transferred to test tubes containing pure water for 24 h. The root growth inhibition was determined via this method (% inhibition = changing in growth/total growth X 100). After one day, the EC_{50} values of Reactive Blue 19 and Reactive Black 5 were determined at room temperature with different concentrations. After a treatment period of 4 days, ten roots were obtained from each onion and took from measuring on them. EC_{50} concentration was determined as one of the concentrations decreasing the root growth by about 50 % compared with the control group. 25 ppm ($1/2x EC_{50}$), 50 ppm (EC_{50}), and 100 ppm ($2x EC_{50}$) concentrations of Reactive Blue 19 and Reactive Black 5 were determined and performed for the Allium test. Distilled water was used as the negative control. As the positive control group, Methyl methanesulfonate (MMS, 10 ppm) was used.

$1/2x EC_{50}$, EC_{50} , and $2x EC_{50}$ of concentrations were added into test tubes for 24 and 48 h when six onion bulbs germinate for 24 h. Tip of roots was collected from controls and treatment groups at the high level of maximum mitotic activity on sunny days and used Carnoy's fixative in ethanol: glacial acetic acid (3:1) for 24 h. 1 N HCL was used for hydrolyses at 60 °C for 7 mins. After aceto-orcein staining for cytogenetic analysis and destaining with 45% acetic acid, total and damaged cells were detected on six different slides with a 40x light microscope. Five slides per treatment were randomly coded and scored blindly. MI and CAs were calculated by using the following equations:

MI= (total number of dividing cells/total cell numbers) x 100

CA= (total number of abnormal cells/100 ana-telophase cells) x 100

2.3. Comet assay

The root meristem cells of *A. cepa* were exposed to concentrations similar to those used for cytogenetic analysis. The method used for comet assay was carried out as described by Tice et al. [19]. In brief, the root tips of *A. cepa* exposed to Reactive Blue 19 and Reactive Black 5 (25, 50, and 100 ppm) were placed in a watch glass which is kept in an ice base and gently sliced using a sharp razor blade to isolate the nuclei in Tris buffer pH 7.5. The microscope slides are pre-treated by 40 ml of 0.3% normal melting point (NMP, Cas no: 9012-36-6) agarose prepared in phosphate-buffered saline (PBS) evenly spread were air-dried. The suspension of nuclei (15 ml) mixed with 150 ml of low melting point (LMP, Cas no: 39346-81-1) agarose in PBS kept at 37 °C was pipetted over the slides. Slides were covered and left in a metal tray kept on ice. Nuclei were left for 1 h, and slides were rinsed in TAE buffer (40 mM Tris-acetate buffer, 1 mM EDTA, pH 8) to remove the salt. All operations were conducted under dimmed with yellow light. The slides were placed in a horizontal gel electrophoresis tank containing freshly prepared cold electrophoresis buffer (1 mM Na₂EDTA and 300 mM NaOH, pH 4,13). The nuclei were incubated for 10 min to facilitate DNA unwinding before the electrophoresis at 0.72Vcm₋₁ (26 V, 300 mA) for 25 min at 4 °C. Electrophoresed slides were stained with 80 ml ethidium bromide (20 mgml₋₁) for 5 min, dipped in ice-cold water to remove the excess ethidium bromide, and covered with a coverslip. For each slide, 25 randomly chosen nuclei

were analyzed using a fluorescence microscope with an excitation filter of BP 546/10 nm and a barrier filter of 590 nm. Three slides were evaluated for treatment, and each treatment was repeated at least twice. Each image was classified according to the intensity of the fluorescence in the comet tail and given a value of 0, 1, 2, 3, or 4 so that the total scores of the slide could be between 0 and 400 arbitrary units (AU microgel-1110) [20].

The Total Arbitrary Unit (AUT), which was used to express the extent of the DNA damage, may be calculated by using the equation below:

$$AU_T = N_0 \times 0 + N_1 \times 1 + N_2 \times 2 + N_3 \times 3 + N_4 \times 4$$

where N_i is the number of nuclei scored in each treatment.

2.4. Statistical analysis

The data of mitotic index, chromosomal aberrations and comet scores, expressed as percentages, and the levels of significance in the different treatment groups were analyzed. Least significance difference (LSD) test were performed by using one-way analysis of variance (ANOVA) on SPSS 23.0 version (at $p < 0.05$ levels). Windows-Microsoft Excel 2003 software was employed for data analysis and graphics.

3. Results

This study aims to determine the possible cytotoxic and genotoxic effects of the Reactive Blue 19 and Reactive Black 5; for this purpose, the Allium test and the comet assay were used.

Table 1. The effects of Reactive Blue 19 on mitotic index and mitotic phases in the root cells of *A. cepa*

Time	Doses	Total Cells Number	Mitotic index Mean±S.D.*	Prophase	Metaphase	Anaphase	Telophase
24 h	Control	5095	79.83±0,18 a	74,42	2,97	1,5	0,94
	MMS	5074	45.26±0,37 b	39,77	2,47	1,73	1,29
	25	5157	38.88±0,40 c	34,59	1,74	1,76	0,79
	50	5468	35.24±0,17 d	30,87	1,50	1,9	0,97
	100	5230	29.41±0,38 e	26,44	1,45	0,62	0,9
48 h	Control	5037	63.94±0,25 a	59,57	1,75	1,37	1,25
	MMS	5033	36.15±0,33 b	32,82	1,5	0,9	0,93
	25	5071	27.55±0,39 c	25,47	0,84	0,69	0,55
	50	5201	24.93±0,27 d	22,83	0,92	0,57	0,61
	100	5168	13.82±0,45 e	12,51	0,45	0,32	0,54

*: Means with same letter do not differ statistically at the level of 0.05

The effects of the Reactive Blue 19 on the MI and the mitotic phase in the root cells of the *A. cepa*, which received treatment for 24 hours and 48 hours, and the results show that the MI decreased in significant amounts in every Reactive Blue 19 concentration (Table 1).

The same is true for each time of exposure. For 24 hours, MI values of the Allium root tips, which were incubated in water (i.e., the negative control group), and which were also incubated in the 10 ppm Methyl Methane Sulfonate (i.e., the MMS, the positive control group), have been determined as being 79.83 ± 0.18 and 45.26 ± 0.37 , respectively. When the results were evaluated, it became clear that, as expected, the MMS treatment led to a decrease in the MI values in the root meristems compared with the control group. The 24-hour application of 25 ppm gave the highest MI values: 38.88 ± 0.40 . The percentage of the MI at the 24-hour

application, on the other hand, gave a lower result at 100 ppm: 29.41 ± 0.38 . At the 48-hours application, the important inhibition mitotic index was observed for all the dosages of the Reactive Blue 19, which was treated root meristem cells of *A. cepa*.

Table 2 gives the effects of various Reactive Black 5 concentrations on cytogenetic parameters (MI and mitotic phases). There appeared important differences between the bulbs which received MI of the control group and the Reactive Black 5 treated bulbs in every exposure period. The test concentrations inhibited the MI in a concentration-dependent manner. The control group gave the highest values at 24 hours and 48 hours (84.72 ± 2.01 and 78.01 ± 1.68 , respectively). The 100 ppm Reactive Black 5 gave the lowest values at 24 hours and 48 hours (34.69 ± 1.29 and 20.36 ± 1.20 , respectively).

Table 2. The effects of Reactive Black 5 on mitotic index and mitotic phases in the root cells of *A. cepa*

Time	Doses	Total Cells	Mitotic index	Prophase	Metaphase	Anaphase	Telophase
		Number	(Mean±S.D.)*				
24 h	Control	5344	$84,72 \pm 2,01$ a	66,48	8,17	3,96	6,11
	MMS	5320	$35,99 \pm 1,58$ bd	32,23	1,75	0,57	1,44
	25	5257	$42,31 \pm 1,01$ c	38,57	1,23	1,92	0,59
	50	5229	$36,81 \pm 0,77$ b	34,24	0,48	0,82	1,27
	100	5312	$34,69 \pm 1,29$ d	32,12	0,63	1,28	0,66
48 h	Control	5307	$78,01 \pm 1,68$ a	64	7,41	3,29	3,31
	MMS	5238	$54,61 \pm 2,01$ b	48,47	2,21	1,18	0,75
	25	5248	$40,63 \pm 2,27$ c	37,31	1,25	1,38	0,69
	50	5351	$33,19 \pm 1,98$ d	30,19	0,58	1,41	1,01
	100	5355	$20,36 \pm 1,20$ e	17,4	1,05	1,23	0,68

*: Means with same letter do not differ statistically at the level of 0.05.

Table 3. Genotoxicity testing of Reactive Blue 19 at 24 h and 48 h exposure in *A. cepa*.

Time	Doses	Counted cell numbers	Anaphase bridge	Stickiness	C-mitosis	Laggard	Micronuclei	Total abnormalities (Mean±S.E.)*
24 h	Control	500	0,00	0,00	0,00	0,00	0,00	0,00±0,00 a
	MMS	500	3,51	1,54	1,83	0,10	1,03	8,01±1,46 b
	25	500	5,24	1,39	7,38	0,00	0,82	14,83±1,03 c
	50	500	4,90	1,86	7,65	0,00	1,79	16,20±1,22 d
	100	500	6,39	2,93	8,17	0,00	1,53	19,02±1,38 e
48 h	Control	500	0,00	0,00	0,00	0,00	0,00	0,00±0,00 a
	MMS	500	3,75	1,59	2,19	0,00	1,74	9,27±1,31 b
	25	500	5,47	2,26	10,14	0,00	2,10	19,97±2,21 c
	50	500	7,63	2,91	13,92	0,00	2,57	27,03±1,18 d
	100	500	7,00	1,43	18,13	0,00	3,18	29,74±1,25 e

*: Means with same letter do not differ statistically at the level of 0.05

Table 4. Genotoxicity testing of Reactive Black 5 at 24 h and 48 h exposure in *A. cepa*.

Time	Doses	Counted cell numbers	Anaphase bridge	Stickiness	C-mitosis	Laggard	Micronuclei	Total abnormalities (Mean±S.D.)*
24 h	Control	500	0,00	0,00	0,00	0,00	0,00	0,00±0,00 a
	MMS	500	5,23	3,48	4,39	1,5	1,29	15,89±0,71 b
	25	500	6,41	4,59	9,14	3,18	2,87	26,19±1,55 c
	50	500	5,00	5,13	18,2	2,47	2,46	33,26±1,29 d
	100	500	8,11	7,71	20,04	1,38	4,04	41,28±1,20 e
48 h	Control	500	0,00	0,00	0,00	0,00	0,00	0,00±0,00 a
	MMS	500	4,43	2,21	3,51	1,14	1,51	12,80±1,68 b
	25	500	2,96	12,02	10,54	2,18	3,23	30,93±2,72 c
	50	500	8,74	12,72	18,41	3,97	3,56	47,40±1,04 d
	100	500	14,93	14,11	16,19	3,06	4,48	52,77±2,23 e

*: Means with same letter do not differ statistically at the level of 0.05

The types and frequencies of the chromosome aberrations in *A. cepa* meristem cells exposed to the Reactive Blue 19 and the Reactive Black 5 for 24 hours and 48 hours are given in Tables 3 and 4.

The dyes were reactive and showed an increase in a concentration-dependent manner in chromosome

aberrations frequency. Sticky and the anaphase bridge were the frequently observed chromosome aberrations. C-mitosis and micronucleus were also among the chromosome abnormalities. According to the results of our study, the number of the cells with anomaly was increased at an important level after 24-

hour and 48-hour applications with all dyes that were tested compared with the control group. Table 4 gives a summary of the comet assay results.

Table 5. Detection of DNA damage in nuclei of *A. cepa* root meristems exposure to Reactive Blue 19 and Reactive Black 5 using the Comet assay

Time	Doses	DNA Damages (Arbitrary Units±S.D.)*	
		Reactive Blue 19	Reactive Black 5
24 h	Control	35.40 ±3.92 a	39.18 ±1.57 a
	MMS	64.03 ±3.64 b	62.66 ±2.80 b
	25	42.58 ±2.17 c	56.32 ±3.12 c
	50	49.66 ±1.60 d	74.15 ±1.36 d
	100	65.43 ±2.39 b	82.42 ±0.83 e
48 h	Control	35.40 ±3.92 a	39.18 ±1.57 a
	MMS	64.03 ±3.64 b	62.66 ±2.80 b
	25	47.63 ±1.65 c	69.74 ±0.27 c
	50	59.98 ±1.19 d	83.98 ±2.61 d
	100	63.84 ±0.77 b	96.13 ±1.84 e

*: Means with same letter do not differ statistically at the level of 0.05.

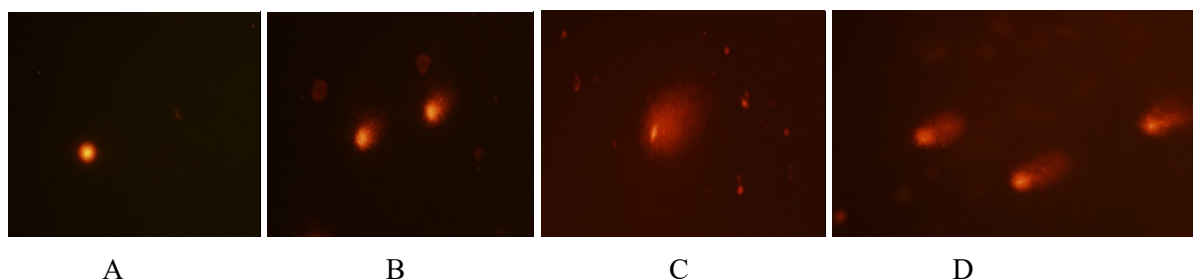


Figure 1. Assessment of genotoxicity DNA damage estimated by comet assay in root nuclei of *A. cepa*. A: control, B: 25 ppm, C: 50 ppm, D: 100 ppm

According to the results, the damages caused by the DNA are high at an important level in every concentration of the Reactive Blue 19 and the Reactive Black 5 when these values are compared with those of the control group ($p < 0.05$). The length of the comet's tail increased with the reactive dye concentrations, which also showed an increase after the prolonged exposure. The damage caused by the DNA in the Reactive Black 5 was determined as being higher than that of the Reactive Blue 19.

4. Discussion

Investigating the effects of the chemical materials used and spread around the environment unconsciously on the test organisms can be evaluated as an indicator of

possible toxic effects in humans and other living species.

The monitoring and screening of the genotoxic effects of the potentially toxic chemicals have a good indicator: High plants. The *A. cepa* is a high plant used commonly in evaluating the effects of the chemicals on genetic materials [21-22].

According to the findings of this study, the benefits of the *A. cepa* root meristem cells in textile dyes are obvious. The significant parameter in selecting the testing concentrations for the genotoxicity assays is the value of EC_{50} . In the tests conducted to reveal the inhibition of the *Allium* root growth, the important inhibition, dependent on the dosage, refers to the potential cytotoxicity of the chemical used for the

experiment. A reduction in the number of the dividing cells accompanies this inhibition of the root growth at all times [23], the cell elongation inhibition in the extension regions [24], and also the inhibition of the synthesis of the protein [25].

The mitotic index is a parameter allowing the prediction of the cellular division frequencies. These frequencies are beneficial in identifying the existence of cytotoxic chemicals [26]. The inhibition of DNA synthesis may reduce mitotic activity [27] or cause the S-phase synthesis of proteins [28]. According to the cell division ratio in the tips of the roots, the Reactive Blue 19 and Reactive Black 5 caused a reduction at an important level in the mitotic index when these values are compared with the control group and the MMS (Table 1 and 2). The decreased MI values were determined to be lower than the MMS after all the exposure values of the Reactive Blue 19 and the Reactive Black 5 (the only exception was determined at the 24-hour value). The MI inhibition (the important reduction on the prophase percentage at every concentration and treatment times used in the Reactive Blue 19, the Reactive Black 5, and the MMS) showed that the normal sequence of the cell division was interfered with by the treatment. Decreased cell division indices make us consider an inhibitory effect in the interphase level. The decrease in the DNA is observed together with this reduction and can happen because of the inhibition of DNA synthesis or the blocking in the cell cycle, G2 phase; this prevents the cell from entry to the mitosis [29].

Furthermore, the mitosis ratio has been determined as being related closely to the resulting level of ATP [30]. The mitotic indices in the treatments being lower and the decrease in the other stages make us consider that the treatments interfered with the respiratory pathway, leading to the lower levels of the ATP. In the current study, it was demonstrated that the Reactive Blue 19 and the Reactive Black 5 had a cytotoxic effect, and the reason for this was the decreasing level of the MI. In a substantially high number of studies conducted on *the A. cepa test in the literature*, the MI had similar influences [31-32].

Besides, there is the need for different test methods (e.g., flow cytometry) to determine how these chemical coloring agents impact the mitotic index and at what stage they affect the cell cycle.

Table 3 and Table 4 demonstrate the *A. cepa* chromosome aberration test, which was conducted to examine the genotoxic potential of the Reactive Blue 19, and the Reactive Black 5. The *A. cepa* root meristematic cells test was used in this testing. The following five forms of aberrations were determined in

the root-tip cells: anaphase bridge, sticky, c-mitosis, laggards, and micronucleus (the root cells received treatment with Reactive Blue 19, and the Reactive Black 5).

It has been demonstrated and proven that the *A. cepa* chromosomal aberration assay is a cost-effective, sensitive and effective test. It is used in testing the potential mutagens in the mitotic and meiotic cells [33]. The chromosomal aberrations are classified under two sub-groups as the clastogenic aberrations (chromosomal break and chromatin bridge); and the physiological aberrations (c-mitosis, sticky, laggard). The anaphase bridges show structural chromosomal mutation and can occur during the translocation of chromatid exchange which is unequal because of the following reasons: presence of disentric chromosomes, replication enzymes that are not much active, breakage and fusion of chromosomes and chromatids [34]. After the treatments with Reactive Blue 19, and the Reactive Black 5, the property of sticky of the chromosomes was determined. The sticky is an effect which is toxic at a higher level and its effects are irreversible and usually causes cell deaths. The sticky chromosomes are indicative of the fact that the textile dye affects the chromatin organization. These effects occur due to the balance which is broken between the quantity of the histones or the other proteins, which are responsible for proper structure control of the nuclear chromatin [35]. These results are in accordance with the results of many other studies conducted so far and which investigated the effects of various chemicals on different material types [36-37]. The most widespread chromosome aberration has been determined as being the c-mitosis. It was observed with the common c-mitosis cells that the textile dyes break the mitotic spindle and arrest the cell division in the early prophase and results in random scattering of the chromosomes which are condensed. The behavior of these dyes remind us of the colchicine. It is known that colchicine binds to the intermeric interface between α - β tubulin dimmers and inhibits microtubule polymerization that causes c-mitosis by blocking cells in prometaphase. According to the results of our study, it has been confirmed that the Reactive Blue 19, and the Reactive Black 5 cause the inhibition of the spindle formation which is similar to the effects of the colchicine. The clastogenic and aneugenic activities are estimated by the existence of the micronuclei, which can be formed from the acentric fragments, which is a consequence of a clastogenic action or the loss of an entire chromosome because of an aneugenic activity [38]. The spontaneous origination of the micronucleus is possible. On the other hand, the induction of them is used for determining the genetic damages which stem

from exposure to a mutagenic agent. Because of the abovementioned facts, and in the light of the induction of the micronuclei it can be concluded that the Reactive Blue 19, and the Reactive Black 5 may either be spindle inhibitors or clastogens. The dyes might enter the nucleus of the cell and then bind to the purine, pyrimidine bases, or to the proteins (i.e. spindle). These interactions might denature the spindles. It is also possible that they might lead to a delay in the chromosome-spindle complex formation, and this might lead to the formation of the MN.

According to the chromosomal analysis results obtained from this study, the reactive dyes used are believed to cause serious chromosomal abnormalities in *A. cepa* root meristems., which leads to decreases in the mitotic index.

The comet assay was performed to analyze the genotoxicity of the Reactive Blue 19 and the Reactive Black 5 in a single cell in *A. cepa* root tip. Table 6 gives a brief summary of the results which are obtained from the comet assay. According to the comet assay results, the DNA damage was higher at an important level in various concentrations of the Reactive Blue 19 and the Reactive Black 5 when they are compared with the negative control group. According to the chromosomal aberrations and mitotic index results, there is a good correlation with the comet assay. It is possible to explain the DNA damage with the increase in the activities of the free radicals and the reactive oxygen species in the treatments with reactive textile dyes. This situation leads to DNA strand break and DNA replication, repair, recombination, and transcription, which are irreversible [39].

In the comet analysis, when the increases in the injury rate observed in the DNA are evaluated, it can be stated that the textile dyes used in the study cause fractures in the DNA, due to which they may be considered as substances with clastogenic effect. Any organism can be affected by toxic chemicals in different ways. The damage rates may differ according to the amount and the type of the toxic material and its length of time to affect the organism. Tripathy and Patel [40] researched the effect of the coloring agent, reactive turquoise blue, on *A. cepa* root tip cells, and they stated at the end of the study that this substance had shown a genotoxic characteristic.

Studies with different biological tests have revealed that synthetic colorants may have genotoxic properties. In a study with *Vibrio fischeri*, a bioluminescent bacterium, the toxic property of Reactive Black 5 was revealed [41] (Gottlieb et al., 2003). In a study conducted by Şenel et al. [42], synthetic colorants Reactive Black 5, Reactive Blue 19, Reactive Red 74,

Reactive Red 141, Reactive Yellow 84 were investigated. As a result of the research, it was determined that Reactive Yellow 84, Reactive Black 5 had a mutagenic effect at a concentration of 400 µg/mL in the presence of S9 fraction and Reactive Black 5 at a concentration of 400 µg/mL in the absence of S9 fraction. Salas-Veizaga et al. [43] investigated the genotoxic effects of Reactive Black 5 and found that this substance did not cause any change in the mitotic index in *Vicia faba*; in other words, it did not cause a cytogenetic effect; on the contrary, it increased the formation of micronuclei and thus had a genotoxic effect. Leme et al., in a study they conducted in 2015, investigated the effects of textile dyes Reactive Blue 19 and Reactive Red 120 on aquatic organisms and humans using different test methods [44]. At the end of the study, it was determined that the damage caused by both colorants in DNA was not at a level that would threaten human health. In another study conducted by Leme et al. [45] with Reactive Green 19 disperse red 1 and Reactive Blue 2 dyes on human dermal cells, it was determined that eactive green 19, one of the textile dyes used, showed a genotoxic effect, while the other two dyes did not. Researchers stated that textile dyes might show different organ-specific genotoxic effects, and the genotoxic effect may change due to the cell culture media used.

5. Conclusion

Considering all the data obtained as the result of the study, it is seen that both Reactive Blue 19 and Reactive Black 5 textile coloring agents reduce the mitotic index compared to the control, increase the rate of damage in the chromosomes and lead to fractures in the DNA. The significant decreases in the mitotic index suggest that the dyes used have a cytotoxic effect. The chromosomal anomalies indicate that the dyes are genotoxic, which is also supported by the comet test. Separately, it is accepted that chromosomal anomalies or DNA injuries are also strongly associated with mutagenic and carcinogenic events.

In light of the results, it can be concluded that the Allium test may give more comprehensive data if it is performed in interaction with the comet assay. In our study, it has been determined that the Reactive Blue 19 and the Reactive Black 5 have a genotoxic effect, and this effect occurs due to chromosomal aberrations and DNA damage. Furthermore, it has also been determined that the textile dyes induce the inhibition of *A. cepa* root, the growth, and the mitodepressive effect on the division of the cells (the cytotoxic effect). On the other hand, detailed cytogenetic studies should deal with the clastogenicity and genotoxicity of the textile dyes and conduct more comprehensive genotoxicity

assessments in animal models. Such studies may reveal significant results for the welfare of human beings. In order to protect the future generation of humankind, eco-friendly dyes should be used and encouraged.

Acknowledgements

Author is thankful to Dr. Gülben Albayrak for fluorescence microscope.

Conflicts of interest

The authors state that did not have conflict of interests

References

- [1] Ekinci İ., Bir tekstil boyası olan poly r-478'in streptomisetler ile renk giderimi, Yüksek Lisans Tezi, Mersin Üniv., Fen Bilimleri Enstitüsü, Biyoloji Anabilim Dalı, Mersin, (2007).
- [2] Al-Sabti K., Chlorotriazine reactive azo red 120 textile dye induces micronuclei in fish, *Ecotoxicol. Environ. Saf.*, 47 (2000) 149-155.
- [3] Odeigah P.G.C., Osanyipeju A.O., Genotoxic effects of two industrial effluents and methyl methane sulfonate in *Clarias Lazera*, *Food Chem. Toxicol.*, 33 (1995) 501- 505.
- [4] Sumathi M., Kalaiselvi K., Palanivel M., Rajaguru P., Genotoxicity of textile dye effluent on fish (*Cyprinus carpio*) measured using the comet assay, *Bull. Environ. Contam. Toxicol.*, 66 (2001) 407- 414.
- [5] Çavaş T., Ergene- Gözükarar S., Micronuclei, nuclear lesions and interphase silver-stained nucleolar organizer regions (agnors) as cytogenotoxicity indicators in *Oreochromis niloticus* exposed to textile mill effluent, *Mutation Research.*, 538 (2003) 81-91.
- [6] Moawad H., Abd El-Rahim W.M., Khalafallah M.A., Evaluation of biotoxicity of textile dyes using two bioassay tests. *J. Basic Microbiol.*, 43 (3) (2003) 218- 229.
- [7] Fiskesjo G., The Allium test-an alternative in environmental studies: the relative toxicity of metal ions, *Mutat Res.*, 197 (1988) 243–260.
- [8] Liu T., Zhu L., Wang J., Wang J., Xie, H., The genotoxic and cytotoxic effects of 1-butyl-3-methylimidazolium chloride in soil on *Vicia faba* seedlings, *Journal of Hazardous Materials*, 285 (2015) 27–36.
- [9] Cui J., Zhang R., Wu G.L., Zhu H.M., Yang H., Salicylic acid reduces napropamide toxicity by preventing its accumulation in rapeseed (*Brassica napus* L.), *Arch. Environ. Contam. Toxicol.*, 59 (2010) 100–108.
- [10] Liman R., Ciğerci İ.H., Ozturk N.S., Determination of genotoxic effects of Imazethapyr herbicide in *Allium cepa* root cells by mitotic activity, chromosome aberration, and comet assay, *Pesticide Biochemistry and Physiology*, 118 (2015) 38-42.
- [11] Singh M., Das A., Singh D., Maiti P., Shabbir M., Das A., High genotoxicity of shipyard contaminants on *Allium cepa* and calf thymus DNA, *Environmental Chemistry Letters*, 12(2) (2014) 321-327.
- [12] Kwon J.Y., Lee S., Y. Koedrih P., Lee J. Y., Kim K. M., Oh J. M., Yang S. I., Kim M. K., Lee J. K., Jeong J., Maeng E. H., Lee B. J., Seo Y. R., Lack of genotoxic potential of ZnO nanoparticles in in vitro and in vivo tests, *Mutation research/Genetic Toxicology and Environmental Mutagenesis*, 761 (2014) 1-9.
- [13] Türkoğlu Ş., Genotoxicity of five food preservatives tested on root tips of *Allium cepa* L., *Mutation Research/Fundamental and Molecular Mechanisms of Mutagenesis*, 626 (1-2) (2007) 4-14.
- [14] Ma M., Tong Z., Wang Z., Zhu W., Acute Toxicity Bioassay Using the Freshwater Luminescent Bacterium *Vibrio-qinghaiensis* sp. Nov.—Q67, *Bull. Environ. Contam. Toxicol.*, 62 (1999) 247-253.
- [15] Fernandes T.C.C., Mazzeo D.E.C., Marin-Morales M.A., Mechanism of micronuclei formation in polyploidized cells of *Allium cepa* exposed to trifluralin herbicide, *Pestic. Biochem. Physiol.*, 88 (2007) 252–259.
- [16] Tice R.R., Agurell E., Anderson D., Burlinson B., Hartmann A., Kobayashi H., Miyamae Y., Rojas Y.F., Ryu E., Sasaki J.C., Single cell gel/comet assay: guidelines for in vitro and in vivo genetic toxicology testing, *Environ. Mol. Mutagen.*, 35 (2000) 206–221
- [17] Ciğerci İ.H., Liman R., Özgül E. and Konuk M., Genotoxicity of indium tin oxide by *Allium* and Comet tests, *Cytotechnology*, 67(1) (2013) 157–163.
- [18] Ma T. H., Xu Z. D., Xu C., The improved *Allium/Vicia* root tip micronucleus assay for clastogenicity of environmental pollutants, *Mutat Res.*, 334 (1995) 185–195.

- [19] Tice R.R., Agurell E., Anderson D., Burlinson B., Hartmann A., Kobayashi H., Sasaki Y.F., Single cell gel/comet assay: guidelines for in vitro and in vivo genetic toxicology testing, *Environ. Mol. Mutagen.*, 35 (3) (2000) 206-221.
- [20] Collins A. R., The comet assay for DNA damage and repair: principles applications and limitations, *Mol. Biotechnol.*, 26 (2004) 249–261.
- [21] Watanabe Y., Kubota Y., Fuma S., Kouichi M., Ichikawa S., Kubota M., Yoshida S., Cytokinesis block micronucleus assay in field plants for monitoring radiation-induced genotoxicity of the environment, *Mutation Research/Genetic Toxicology and Environmental Mutagenesis*, 774 (2014) 41-46.
- [22] Seregin I.V., Kozhevnikova A.D., Physiological role of nickel and its toxic effects on higher plants, *Russ. J. Plant Physiol.*, 53 (2006) 257–277.
- [23] Akinboro A., Bakare A.A., Cytotoxic and genotoxic effects of aqueous extracts of five medicinal plants on *Allium cepa* Linn., *Journal of Ethnopharmacology*, 112 (2007) 470-475.
- [24] Fusconi A., Repetto O., Bona E., Massa N., Gallo C., Dumas-Gaudot E., Berta G., Effects of cadmium on meristem activity and nucleus ploidy in roots of *Pisum sativum* L. cv. Frisson seedlings, *Environmental and Experimental Botany.*, 58 (2006) 253–260.
- [25] Seth C. S., Kumar C. P., Misra V., The role of phytochelatins and antioxidants in tolerance to Cd accumulation in *Brassica juncea* L., *Ecotoxicol Environ. Saf.*, 71(1) (2008) 76-85.
- [26] Fiskesjo G., The *Allium* test as a standart in environmental monitoring, *Hereditas*, 102 (1985) 99– 112.
- [27] Sudhakar R., Gowda N., Venu G., Mitotic abnormalities induced by silk Dyeing Industry Effluents in the cells of *Allium cepa*, *Cytologia*, 66 (2001) 235–239.
- [28] El-Ghamery A.A., El-Nahas A.I., Mansour M.M., The action of atrazine herbicide as an inhibitor of cell division on chromosomes and nucleic acids content in root meristems of *Allium cepa* and *Vicia faba*, *Cytologia*, 65 (2000) 277–287.
- [29] Olorunfemi D. I., Duru E., Okieimen F., Induction of chromosome aberrations in *Allium cepa* L. root tips on exposure to ballast water, *Caryologia: International Journal of Cytology, Cytosystematics and Cytogenetics*. 65(2) (2012) 147-151.
- [30] Abu N.E., Duru N.U., Cytological effects of oxytocic agents on mitotic chromosomes of *Allium cepa*, *Journal of Agriculture, Food, Environment and Extension.*, 5(2) (2006) 1-7.
- [31] Fındıklı Z., Türkoğlu Ş., The effects of Glyphos and DDVP on mitotic division and chromosomes in *Allium cepa* L., *Cumhuriyet Science Journal*, 31(2) (2010) 49-62.
- [32] Chukwujekwu J.C. Van Staden J., Cytotoxic and genotoxic effects of water extract of *Distephanus angulifolius* on *Allium cepa* Linn., *South African Journal of Botany*. 92 (2014) 147–150.
- [33] Namita K. and Sharma S., *Allium cepa* root chromosomal aberration assay: A Review, *Indian J. Pharm. Biol. Res.*, 1 (3) (2013) 105-119.
- [34] Khallef M., Liman R., Konuk M., Ciğerci İ.H., Benouareth D., Tabet M., Abda A., Genotoxicity of drinking water disinfection by-products (bromoform and chloroform) by using both *Allium anaphase-telophase* and comet tests, *Cytotechnology*, 67 (2) (2013) 207-213.
- [35] Radić S., Stipaničev D., Vujčić V., Rajčić M. M., Širac S., Pevalek-Kozlina B., The evaluation of surface and wastewater genotoxicity using the *Allium cepa* test, *Science of the Total Environment*, 408 (2010) 1228–1233.
- [36] Olorunfemi D.I., Olorunfemi O.P., Agbozu, I.E., Genotoxicity assessment of contaminated drinking water sources in a rural community in Edo State of Nigeria, *Journal of Geoscience and Environment Protection*. 2 (2014) 52-59.
- [37] Ping K.Y., Darah I., Yusuf U.K., Yeng C., Sasidharan S., Genotoxicity of *Euphorbia hirta*: An *Allium cepa* assay, *Molecules*, 17(7) (2012) 7782-7791.
- [38] Rodríguez Y.A., Christofolletti C., Pedro J., Bueno O.C., Malaspina O.R., Ferreira A.C., Fontanetti C.S., *Allium cepa* and *Tradescantia pallida* bioassays to evaluate effects of the insecticide imidacloprid, *Chemosphere*, 120 (2015) 438–442.
- [39] Yadav S.A., Sehrawat G., Evaluation of genetic damage in farmers exposed to pesticide mixtures, *Int. J. Hum. Genet.*, 11(2) (2011) 105-109.
- [40] Tripathy S.K., Patel S., Abnormal mitosis in root meristem cells of *Allium cepa* L. induced by a fabric dye reactive turquoise blue (Procion MX), *African Journal of Biotechnology*, 13 (38) (2014) 3881-3891.
- [41] Gottlieb A., Shaw C., Smith A., Wheatley A., Forsythe S., The toxicity of textile reactive azo

dyes after hydrolysis and decolourisation, *J. Biotechnol.*, 101(1) (2003) 49-56.

- [42] Şenel U., Sur H.İ., Demirtaş M., Investigation of mutagenic effects of some synthetic reactive dyes in textile industry by using umu-test, *Ekoloji*, 21(85) (2012) 49-56.
- [43] Salas-Veizaga D.M., Morales-Belpaire I., Terrazas-Siles E., Evaluation of the genotoxic potential of reactive black 5 solutions subjected to decolorizing treatments by three fungal strains, *Ecotoxicol Environ Saf.*, 89 (2013) 125-129.
- [44] Leme D.M., Oliveira G.A., Meireles G., Brito L.B., Rodrigues L. de B, Palma de Oliveira D., Eco- and genotoxicological assessments of two reactive textile dyes, *J. Toxicol Environ Health A.*, 78(5) (2015) 287-300.
- [45] Leme D.M., Primo F.L., Gobo G.G., da Costa C.R., Tedesco A.C., de Oliveira D.P., Genotoxicity assessment of reactive and disperse textile dyes using human dermal equivalent (3D cell culture system), *J. Toxicol Environ Health A.*, 78(7) (2015) 466-80.



Multiple sequence alignment quality comparison in T-Coffee, MUSCLE and M-Coffee based on different benchmarks

Tuğcan KORAK^{1,*} , Fırat AŞIR² , Esin IŞIK³ , Nur CENGİZ⁴ 

¹Kocaeli University, Department of Medical Biology, Faculty of Medicine, Kocaeli/ TURKEY

²Dicle University, Department of Histology and Embryology, Faculty of Medicine, Diyarbakır/ TURKEY

³University of Zurich, Institute of Molecular Cancer Research, Zurich/ SWITZERLAND

⁴University Hospital Cologne, Institute of Human Genetics, Köln/ GERMANY

Abstract

Multiple sequence alignment (MSA) is a fundamental process in the studies for determination of evolutionary, structural and functional relationships of biological sequences or organisms. There are various heuristic approaches comparing more than two sequences to generate MSA. However, each tool used for MSA is not suitable for every dataset. Considering the importance of MSA in wide range of relationship studies, we were interested in comparing the performance of different MSA tools for various datasets. In this study, we applied three different MSA tools, T-Coffee, MUSCLE and M-Coffee, on several datasets, BALiBase, SABmark, DIRMBASE, ProteinBali and DNABali. It was aimed to evaluate the differences in the performance of these tools based on the stated benchmarks regarding the % consistency, sum of pairs (SP) and column scores (CS) by using Suite MSA. We also calculated the average values of these scores for each tool to examine the results in comparative perspective. Eventually, we conclude that all three tools performed their best with the datasets from ProteinBali (average % consistency: 29.6, 32.3, 29.7; SP: 0.74, 0.73, 0.74; CS with gaps: 0.27, 0.27, 0.26 for T-Coffee, MUSCLE, M-Coffee, respectively), whereas the lowest performance was obtained in datasets from DIRMBASE (average % consistency: 1.8, 1.1, 4.3; SP: 0.05, 0.04, 0.04 CS with gaps: 0.01, 0, 0.008 for T-Coffee, MUSCLE, M-Coffee, respectively)

Article info

History:

Received: 17.12.2020

Accepted: 29.08.2021

Keywords:

Multiple sequence alignment, T-Coffee, MUSCLE, M-Coffee.

1. Introduction

Multiple sequence alignment (MSA) is a fundamental process in the studies for determination of evolutionary, structural and functional relationships [1-3]. It is generally used to predict the function and structure of proteins from biological sequences [4, 5]. While next generation sequencing methods have been developing, MSA plays a key role in function and structure comparison in this technology [6]. In addition, different MSA strategies can be developed and designed for specific targets. For instance, ODOTool, developed by Ugurel et al. (2020) [7] for bacterial single nucleotide polymorphism determination, is recently used for the analysis of mutations in genomes of SARS-CoV2 that causes COVID-19 pandemic. Also, various MSA algorithms have been developed and served as tools such as T-Coffee [8], MUSCLE [9], M-Coffee [10], CLUSTALW [11], Clustal Omega [12], Align-M [13], DIALIGN [14], Kalign [15], MAFFT [16, 17], ProbCons [18], PROMALS3D [19], 3DCoffee [20],

HALIGN [21], Espresso [22], PRANK [23, 24] and MUMMALS [25] etc.

T-Coffee (Tree-based Consistency Objective Function For alignment Evaluation) is one of the MSA methods that benefits from the progressive-alignment strategy [8, 10]. In this strategy, firstly a phylogenetic tree is constructed between sequences and then an alignment is established according to their order in the tree [26]. For the majority of cases, this approach is successful but its weak point is greediness. If errors occur in initial alignments, they cannot be corrected later, while the remaining sequences are added in [8, 10]. This is the first motivation for T-Coffee, which aims to minimize the greedy character of this algorithm and, hence, provides better use of information in the initial stages. Furthermore, global alignments which align entire sequences with each other do not assure to obtain optimal solutions. Besides, local alignments which

*Corresponding author. e-mail address: tugcankorak@gmail.com

align a part of sequence have great performance when net block of ungapped alignments found in each sequence. The combination of best features of these two alignments could form a powerful method to align multiple sequences and this is the second motivation to design a new method, T-Coffee [8].

Additionally, some tools follow iterative approach, in which progressive alignment in a group of sequences is repeated for certain times until reaching the best optimal alignment as seen in MUSCLE (Multiple Sequence Comparison by Log-Expectation) [26]. MUSCLE is an MSA tool which was developed by Robert C. Edgar in the beginning of 2000s. The algorithm of MUSCLE aims to decrease the time and computational costs with high throughput and accuracy, as most of the previous tools were unable to provide all of them at once. Four different benchmark datasets are used as a reference to test the algorithm by Robert C. Edgar. Those datasets are BALiBASE, SABmark, SMART and PREFAB. It was shown that 500 sequences with an average length of 350 amino acids are aligned only in seven minutes which is a significant improvement compared to the best MSA tools present in those times [9, 10].

The raise in the genomic, structural and functional knowledge and in the computing power resulted in a new approach named as meta-method, in which the requirement to arbitrarily pick a single method to perform MSA is eliminated. This method is called as M-Coffee, standing for Meta-Consistency Objective Function for Alignment Evaluation. It is a consistency-based meta-method, where results from diverse individual MSA tools are combined by T-Coffee to have a final single MSA [1, 3, 27, 28]. This is a major improvement in MSA approach, considering that there are no certain criteria to select the most proper method for every single study among the various approaches with their own advantages and disadvantages [1, 3, 27]. By using M-Coffee, it is possible to include the results from wide range of MSA tools and receive a final alignment incorporating all these tools [1, 3, 10].

The evaluation of a certain MSA tool regarding certain criteria, such as computational cost or accuracy, requires the comparison of the reference datasets obtained from multiple sequence alignment benchmarks. DIRMBASE is one of the various available systems providing benchmark datasets. It is set up by randomly putting highly conserved motifs created by random model of sequence evolution (ROSE) into the long DNA sequences that are unlikely to align [29]. Benchmark Alignment dataBASE (BALiBase) was the initially developed large scale benchmark tool applied in the assessment of MSA

quality. The reference alignments obtained from the BALiBase are constructed by considering three dimensional superposition of the alignments [30]. The Sequence Alignment Benchmark (SABmark) is another benchmark which supplies the alignments of proteins that are not close to each other regarding their homology [31]. The datasets in SABmark are divided into two sets which are Twilight Zone, with the alignments of low to low similarity, and Superfamilies, with the alignments of low to intermediate similarity [32].

Although MSA is used in wide range of bioinformatics, verification of an MSA reconstruction quality is impeded due to the deficiency of good reference MSAs [33, 34], and also MSA programs do not offer application to compare MSAs. Drawing inspiration from these, Suite MSA, which is a java-based execution, provides verification and rapid comparison of many MSAs by using alignment statistics. This comparison helps researchers to visually localize the regions where inconsistency occurs between an alternative MSA and a reference MSA. Beside these, Suite MSA contains graphical user interface (GUI) and phylogeny editor to make simulation of biological sequence evolution with determination of variable simulation parameters to generate reference MSAs. Also, the reference MSA can be acquired from a benchmark MSA database or can be manually created [33].

In this study, we applied and compared three different MSA tools, namely T-Coffee, MUSCLE and M-Coffee using different datasets. Suite MSA was run to evaluate the performances of the tools based on the reference datasets obtained from BALiBase, SABmark, DIRMBASE and the constructed ProteinBali and DNABali benchmarks.

2. Materials and Methods

The reference datasets were obtained from BALiBase (Version 3.0 R9), SABmark (Version 1.63), DIRMBASE (Version 1.0), and the constructed ProteinBali and DNABali benchmarks, that are all compatible with the three MSA tools (T-Coffee (Version 10.00.r1613), MUSCLE (Version 3.8.31) and M-Coffee (Version 10.00.r1613 mode mcoffee)), were used in this study. DIRMBASE dataset contains locally related DNA sequences including ROSE motifs and motifs of length 60 [29]. SABmark dataset provides MSA of protein sequences that have low similarity [31, 32]. BALiBase dataset designed specifically for MSA and offers high quality manually refined reference alignments by considering three dimensional superpositions. It provides simulation of

real problems that could be encountered during MSA and divided into reference datasets with different characteristics [30]. The reference data used in the current research were randomly selected from these datasets to be used in MSA tools. Box10, 22, 32 were selected from BALibase; d1a6m__d1ash, d1ash__d1dlwa, d1dlwa__d1ew6a, d1ew6a__d1gtea1, d1gtea1__d1gvha1 were selected from SABmark; dna-400-30-4-0, r1-dna-400-30-4-1, r1-dna-400-30-4-2 and r1-dna-400-30-4-3 were selected from DIRMBASE. ProteinBali was randomly constructed for protein sequences from a different subset of BALiBase benchmark and includes box001, 022, 034, 036, 046, 050, 054, 076, 0133, 0153. Finally, DNABali (Reference Protein-Coding DNA Alignments Databases: balibase_mdsa_all.tar.gz, <http://dna.cs.byu.edu/mdsas/download.shtml>) was randomly constructed for DNA sequences from BALiBase benchmark and includes RV61_sushi_ref6, RV64_kringle_1_ref6, RV65_zf_1_ref6, RV66_sushi_2_ref6 and RV70_photo_ref7.

The reference sequence from BALiBase was converted from “.msf” format into “.fasta” format using Jalview (<http://www.jalview.org/Download>), an MSA editor. Jalview enables researchers to carry out desired editing in MSA, to analyze the MSA and even to construct proper annotations [35]. Subsequently, the dashes in all reference datasets were deleted in order to obtain them in unaligned form that is required to upload them in MSA tools.

2.1. Processing through T-Coffee

Reference data in unaligned form from all datasets were uploaded to T-Coffee Multiple Sequence Alignment Server (<http://tcoffee.crg.cat/>). The output format was selected as fasta-aln and other parameters remained as default.

2.2. Processing through MUSCLE

The datasets in the unaligned form were uploaded to MUSCLE web server (<http://toolkit.tuebingen.mpg.de/muscle>). As an option “output sequences in input order” was marked and other parameters remained as default values which are “3” as maximum number of iteration and .fasta format as an output format.

2.3. Processing through M-Coffee

Since M-Coffee which is available from the web server (<http://tcoffee.crg.cat/apps/tcoffee/do:mcoffee>) was developed based on T-Coffee, their running procedure resembles to each other. In addition to all parameters selected for T-Coffee, as described above, a set of MSA tools was constructed by selecting Mpcma_msa, Mmafft_msa, Mclustalw_msa, Mdialigntx_msa,

Mpoa_msa, Mmuscle_msa, Mprobcons_msa and Mt_coffee_msa. Because M-Coffee is a consistency-based meta-method in which results from diverse individual MSA tools are combined by T-Coffee to have a final single MSA.

At the end, results of each tool were obtained from result folders by choosing fasta-aln. Next, this text file was converted to .fasta format by Jalview to become compatible with Suite MSA program. Then, Suite MSA was run to compare alignments with reference alignment. All these steps were repeated for each dataset.

2.4. Running suite MSA

Suite MSA has a wide range of applications. In this study, MSA Comparator was used for the comparison of the obtained alignment with the reference alignment. However, there was need to check whether the names, order and content of the aligned sequences except for the placement of the gaps in both reference and result files were exactly same. If not, they should be adjusted to have the identical names and sequences.

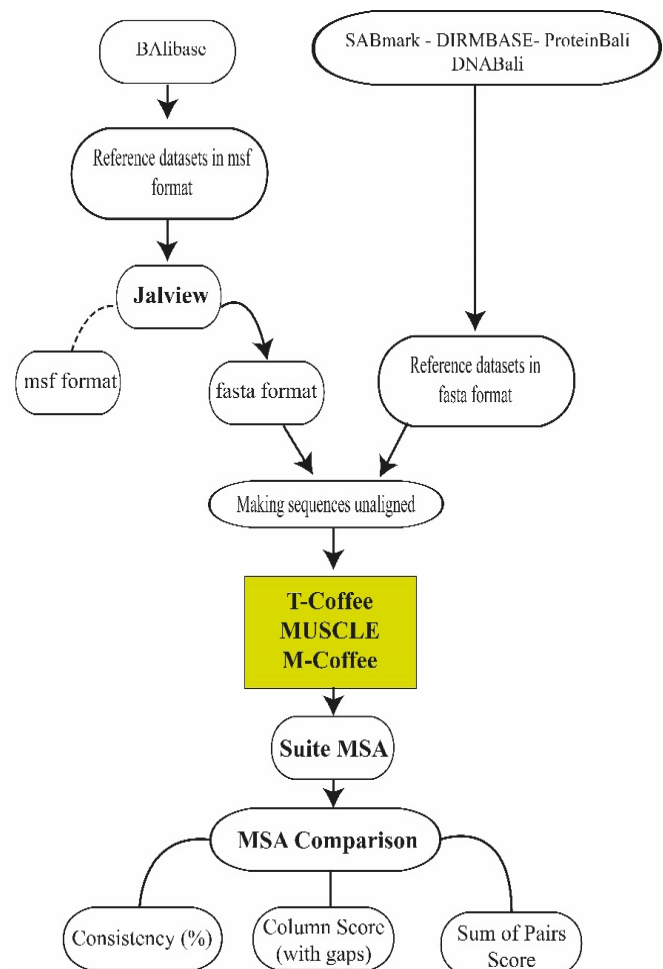


Figure 1. The workflow to evaluate the performance of MSA tools based on different benchmarks.

After ensuring these aspects, initially reference file and then result file were uploaded into the program. In the open window, there were several buttons for functions which would provide information about the compared files when selected. One of them was “Show sum of pairs” which informs about the % consistency, sum of pairs score (SP), column score (CS) without gaps and with gaps. These values were used to plot the graphs and bar charts providing the statistical analysis of the tools. All the steps above are summarized in Figure 1.

3. Results and Discussion

In our study, we used % consistency, SP score and CS score to evaluate the quality and reliability of three MSA tools. % consistency represents percentage of

columns in the obtained MSA which are 100% identical to the columns of reference MSA. SP score is calculated as a whole score of the alignment and a determinant parameter to understand how successful the tool in aligning. The SP score receives score 1 when the identical alignment is obtained from the comparison and score 0 refers to incorrect alignment. The greater SP score shows the greater number of correctly aligned sequences. However, in CS calculation for similarity, each column is scored independently from each other and then the total score is divided into number of columns analyzed. Therefore, SP score is used as the major indicator of quality, while other values are also analysed to support the result [30, 36].

Table 1. The acquired values for % consistency, sum of pairs score and column score

	T-Coffee			M-Coffee			MUSCLE		
		Cons.	SOP CS	Cons.	SOP CS	Cons.	SOP CS		
BaliBase	box10	8.581	0.53 0.069	9.008	0.546 0.072	8.031	0.496 0.064		
	box22	10015	0.486 0.051	12957	0.503 0.086	11623	0.464 0.044		
	box32	19225	0.472 0.221	20675	0.473 0.217	20966	0.468 0.216		
DIRMBASE	4-0	1603	0.032 0.009	2306	0.049 0.023	0.183	0.036 0		
	44200	2403	0.04 0.009	7143	0.064 0.011	30317	0.069 0		
	44231	1426	0.096 0.011	2936	0.024 0	2308	0.024 0		
	44259	1908	0.037 0.012	5137	0.032 0	0.182	0.035 0		
SABmark	1_2	31481	0.371 0.338	35669	0.419 0.369	30189	0.355 0.317		
	2_3	16456	0.075 0.067	33113	0.43 0.357	31013	0.28 0.248		
	3_4	8125	0.034 0.032	45261	0.046 0.035	20863	0.19 0.114		
	4_5	18132	0 0	17582	0 0	20968	0 0		
	5_6	18947	0 0	18717	0 0	25907	0 0		
DNABali	RV61	42805	0.031 0	37821	0.034 0	43492	0.038 0		
	RV64	0.566	0.112 0	2718	0.242 0	2773	0.2 0		
	RV65	9681	0.183 0	9538	0.356 0	41456	0.126 0		
	RV66	2463	0.134 0	6971	0.423 0	20852	0.187 0		
	RV70	5981	0.568 0.072	44420	0.647 0.133	9776	0.641 0.107		
ProteinBali	Box001	59366	0.837 0.635	59.24	0.835 0.622	59.97	0.822 0.623		
	Box022	16834	0.556 0.015	3887	0.567 0.03	5321	0.546 0.023		
	Box034	14575	0.798 0.145	16383	0.789 0.159	17863	0.779 0.145		
	Box036	62.08	0.925 0.679	62261	0.926 0.667	60938	0.929 0.628		
	Box046	2713	0.523 0	3948	0.534 0	4628	0.503 0		
	Box050	44348	0.815 0.428	32378	0.783 0.308	47.72	0.801 0.472		
	Box054	17477	0.606 0.209	20613	0.614 0.22	23922	0.594 0.244		
	Box076	1964	0.743 0	0.508	0.736 0	0.116	0.745 0		
	Box0133	69459	0.866 0.308	71662	0.876 0.368	70248	0.864 0.32		
	Box0153	44369	0.75 0.26	26039	0.753 0.278	32796	0.749 0.297		

Cons.: consistency (%), SOP: sum of pairs score, CS: column score.

As a consequence of performing Suite MSA on the alignments obtained from each tool for each datasets, a large quantity of data was generated. This data was organized in the Table 1 showing the values of % consistency, SP score and CS for each individual dataset. Then, these values were plotted as two different sets of graphs. The first graph set in Figure 2 and Figure 3 enables to compare the performance of

each tool on individual datasets in terms of % consistency, SP and CS values. The second graph set shown in Figure 4 shows general comparison of these three MSA tools by taking average % consistency, CS and SP scores into consideration. These average values obtained for each tool on different datasets from the given benchmark were plotted as bar charts.

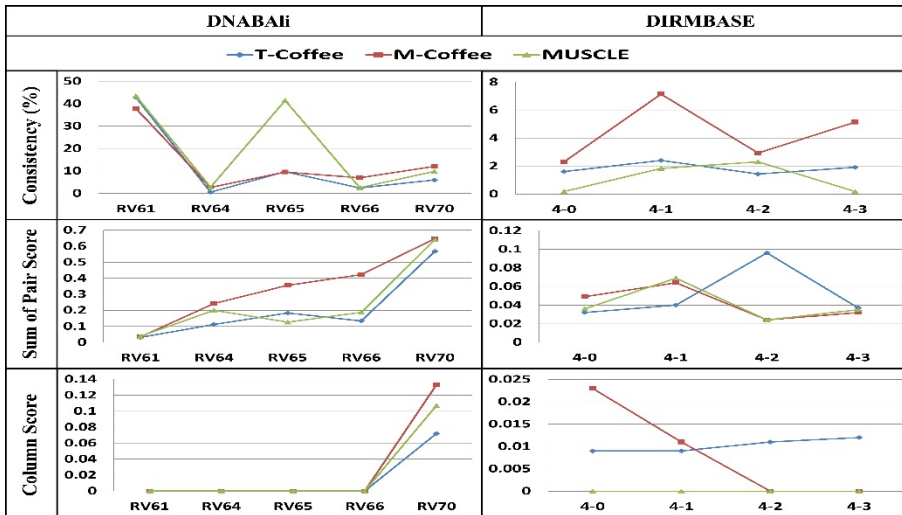


Figure 2. This figure indicates the results for the evaluation of the given tools based on the benchmark systems that provide nucleotide datasets. It consists of the graphs representing the results of the tools indicated by each column. The rows of the figure illustrates the acquired values for % consistency, sum of pairs score and column score. Each graph located in the cells of the figure shows the trend of the scores and accuracy over datasets. (For DNABali, RV61, RV64, RV65, RV66 and RV70 refer to RV61_sushi_ref6, RV64_kringle_1_ref6, RV65_zf_1_ref6, RV66_sushi_2_ref6 and RV70_photo_ref7, respectively. For DIRMBASE, 4-0, 4-1, 4-2, 4-3 refer to r1-dna-400-30-4-0, r1-dna-400-30-4-1, r1-dna-400-30-4-2 and r1-dna-400-30-4-3, respectively)

The scores acquired from DNABali (Figure 2) revealed that all of three tools perform similarly regarding their % consistency in each dataset, except for RV65 in which MUSCLE gave the highest percentage value. In contrast, RV65 had the lowest score for the SP with MUSCLE. M-Coffee gave the highest scores for SP in almost each dataset. Eventually, CS was obtained as 0 for datasets out of the RV70 dataset at which M-Coffee had the highest value.

Performance scores of the MSA tools compared in this study based on DIRMBASE datasets revealed the highest % consistency for M-Coffee for the whole dataset; while T-Coffee was more consistent than MUSCLE for datasets 4-0, 4-1 and 4-3. On the other hand, M-Coffee has a CS score equal to 0 in datasets of 4-2 and 4-3 while T-Coffee has relatively greater values. However, MUSCLE gave 0 for column scores in all datasets. Also, except for 4-2 and with superior value for T-Coffee, there is no distinctive difference in the SP scores of those three tools in all datasets of this

benchmark. Based on these, if higher consistency is desired, M-Coffee seems to be more convenient tool for the given datasets of DIRMBASE. However, CS and SP scores are either variable in each dataset for the tools or very close to each other's.

For ProteinBali represented in Figure 3.panel, overall % consistency, CS and SP scores are very similar for each datasets for each tool. However, MUSCLE has slightly higher consistency and CS for box050 and box054 datasets. SP scores do not show significant differences among the tools based on the tested dataset.

In Figure 3. panel representing graphs of BALiBase dataset, M-Coffee has given the overall highest scores for all statistical tests. % consistency and SP scores are very close to each other for all tools although M-Coffee is slightly higher than others. Similarly, column scores are also very close to each other but M-Coffee is significantly greater than others only for box22 in the given dataset.

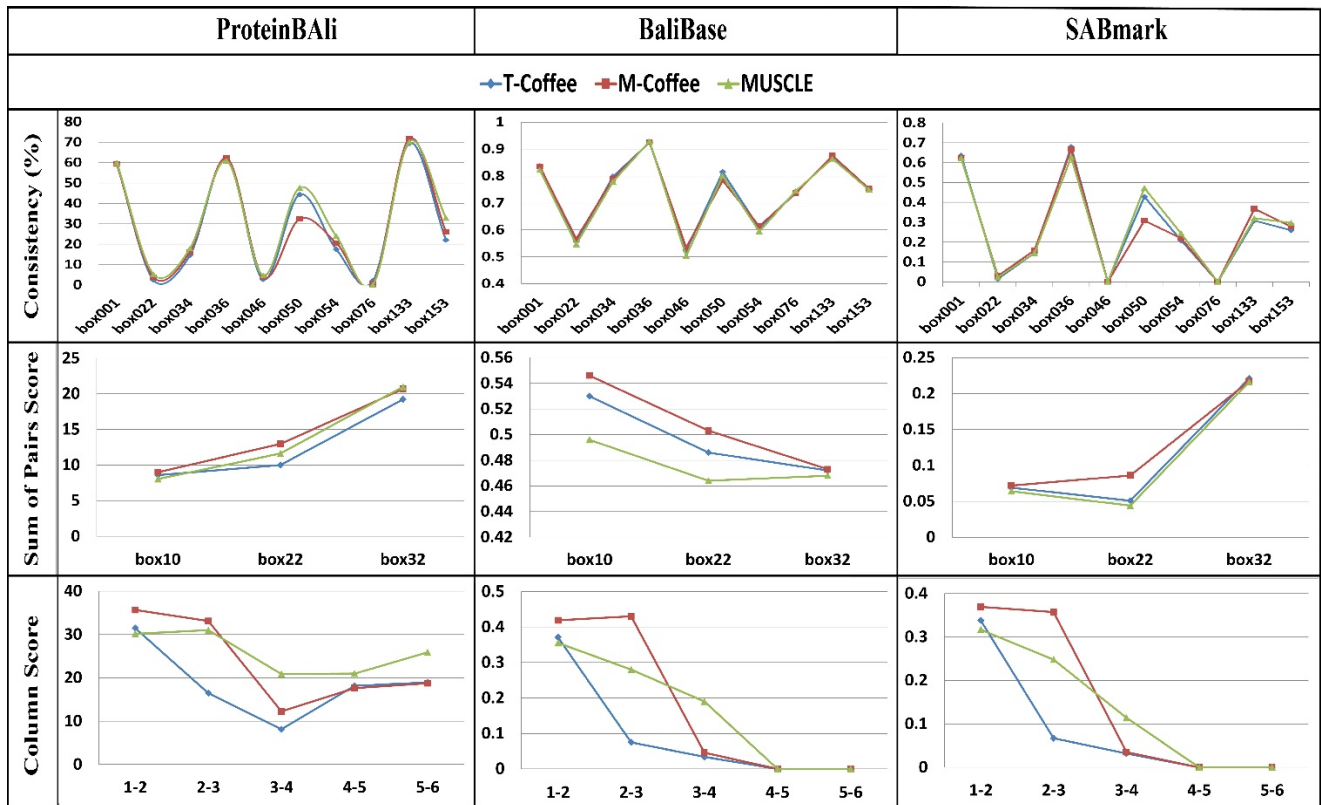


Figure 3. This figure indicates the results for the evaluation of the given tools based on the benchmark systems that provide amino acid datasets. It consists of the graphs representing the results of the tools indicated by each column. The rows of the figure illustrates the acquired values for % consistency, sum of pairs score and column score. Each graph located in the cells of the figure shows the trend of the scores and accuracy over datasets. (For SABmark, 1, 2, 3, 4, 5, 6 refer to d1a6m__, d1ash__, d1dlwa_, d1ew6a_, d1gtea1 and d1gvha1, respectively)

For 1-2 dataset of SABmark in Figure 3.panel, M-Coffee has the highest % consistency and others resulted in relatively similar values to each other. For 2-3 dataset, M-Coffee and MUSCLE had similar percentages and significantly higher than T-Coffee. For the remaining datasets, MUSCLE gave greater consistency than other tools having similar consistencies. When the CS is compared, all tools possess approximately same values for 1-2 datasets but T-Coffee has lower CS for 2-3 datasets than others. Next, 3-4 dataset shows very close CS in T-Coffee and M-Coffee but CS is slightly higher in MUSCLE. Additionally, CS is 0 for the other datasets in each tool. SP score is very close in T-Coffee and MUSCLE for 1-2 datasets but it is slightly higher in M-Coffee. For 2-3 dataset, there are noticeable differences among scores; M-Coffee has the greatest and T-Coffee has the lowest sum of pairs score. Next, for 3-4 datasets the highest SP score belongs to MUSCLE than other tools in

which scores are close to each other. The remaining datasets give 0 for SP score in each tool.

The information obtained from the bar charts illustrate that all tools have given the highest scores and % consistency with ProteinBali (Figure 4). The second highest scores are generated in SABmark and BaliBase datasets and their values are similar for % consistency and CS but BaliBase has greater results for the SP scores. Eventually, the lowest scores belong to DIRMBASE datasets. The % consistency values are in between 1% and 35% which is not high enough to mention about an acceptable consistency. SP scores varied between 0.04 and 0.75 and CS was between 0 and 0.27. SP scores (Figure 4) and CS indicate higher quality of tools for the given alignments if they are close to 1 and lower quality if they are close to 0. Our results clearly show that both SP and CS are very close to 0 for all tools and datasets except for scores for ProteinBali (Figure 4).

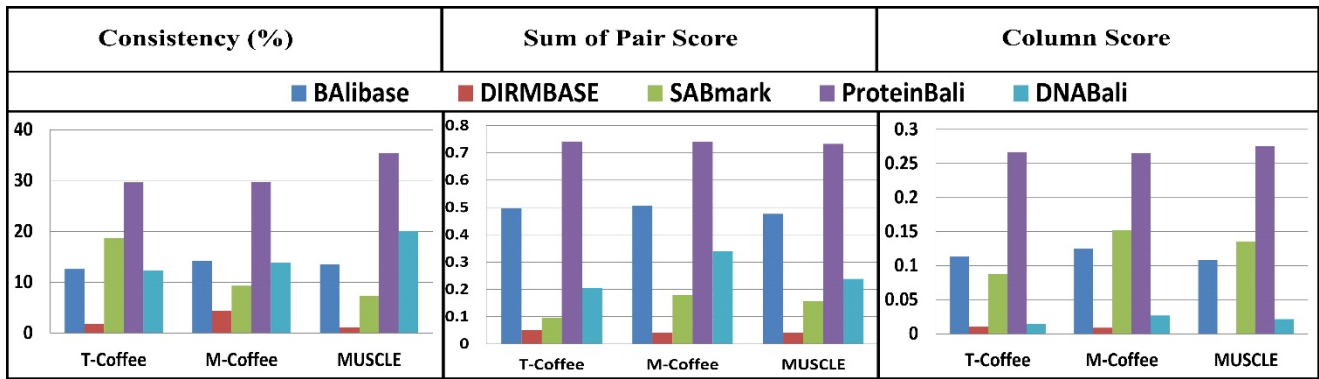


Figure 4. Bar chart graphs belonging to average % consistency, sum of pairs and column score values of the given tool for the given benchmark.

MSA is a process required in a wide range of bioinformatic studies (Bawono et al., 2017). There are numerous distinctive approaches for MSA, each of which possesses their own limitations and advantages. Despite the lack of certain criteria, aligners attempt to use the ones which provide high accuracy, take shorter computational time and do not cause problems with the computational memory. Therefore, the selection of the proper tool is not straightforward and requires consideration of several aspects based on the study and circumstance [10].

As expected, some of the tools perform better than the others on some datasets. Although there were various sequences in DNABali, some of them could be processed by all three tools due to some limitations. In addition to number of sequence limitation, which is at most 150 sequences for T-Coffee and M-Coffee, there is also number of character limitation in M-Coffee which cannot accept more than 2500 characters. Although MUSCLE was predicted to be more advantageous in terms of its ability to accept input with any length, it resulted in some outputs which were not applicable to Suite MSA. The reason of the error is because the residues within the sequence of RV62, RV63 and RV67 obtained from MUSCLE are not identical to their reference alignments. This seems to be caused by that several of the residues in the DNA sequences found in these datasets have been changed by MUSCLE into ambiguity codes. To use MSAcomparator, residues in each sequence have to be the same so the comparison scores cannot be obtained for these datasets of DNABali. Consequently, only 5 of the given datasets were processed by all three tools. The acquired scores from DNABali (Figure 2) revealed that MUSCLE seems to be advantageous for only one of the datasets to obtain higher % consistency and in the other datasets, the percentages are similar in three tools. However, M-Coffee seems to be preferable regarding with the other scores. For the scores of DIRMBASE datasets (Figure 2), if a higher consistency is desired, M-Coffee seems to be more

convenient tool for given datasets of DIRMBASE. However, CS and SP scores vary greatly among the tested MSA tools for some sub-datasets and similar for the others. Therefore, a general conclusion in terms of more preferable tool cannot be done based on these parameters.

From the ProteinBali scores (Figure 3), it can be deduced that since none of the tools has a score dominance to others, they are almost equally convenient for this datasets. For the BALibase dataset (Figure 3), even though M-Coffee had higher scores for the tested datasets, the values do not significantly outperform MUSCLE and T-Coffee. Scores of SABmark reveals that for the greater consistency, MUSCLE can be suitable for each given datasets of this benchmark. However, the general convenient tool cannot be determined for the other scores because obtained scores are variable in each given dataset. Additionally, CS and SP score is 0 for the all tools in 4-5 and 5-6 datasets even though % consistency different from 0 is obtained. These might be improved by alterations in the settings of the tools. Otherwise, these tools may not be preferred for the analysis of these datasets.

As seen from the above, the given datasets of benchmarks show differences in terms of % consistency, CS and SP score. Thus, it is difficult to deduce the proper tool for benchmarks. To approach more general and to distinct tool performances clearly, bar charts that represent average scores of each benchmark were plotted (Figure 4). It provides less detail about which tool performs higher scores on which benchmark. At a first glance, it is possible to see the tool and corresponding benchmark with greater scores. The information obtained from these bar charts illustrate that all tools have given the highest scores and % consistency with ProteinBali. Also, both SP and CS are very close to 0 for all tools and datasets except for scores for ProteinBali (Figure 4). Additionally, BALibase resulted in greater scores compared to

remaining tools. Relatively higher scores for BALiBase dataset can be related to relatively higher % consistency values and high % consistency values might be resulted from higher sequence similarity levels. Low scores for others mean that MUSCLE, M-Coffee and T-Coffee tools are not very reliable for the given datasets. This was unexpected; however, it can be due to small size of our datasets. Because, the evaluation of such tools are carried out with much larger datasets containing hundreds or thousands of sequences. It is also difficult to associate the results to the average length of the sequences as the measurements of the sequence similarity are not available. Additionally, more information should be taken into consideration for comprehensive analysis such as scoring matrices or gap penalties, minimum level of sequence similarities. Number of iterations, for MUSCLE, could be another factor that may be affecting the quality of the alignment as it can be manually controlled, also can be determined automatically.

Finally, % consistency, CS and SP are low for each tool in different benchmarks. The underlying reasons could be related to quality of the given data. Next, the aligned sequence lengths can affect the obtained scores because tools work better in proper length intervals and the given sequence lengths may be out of this interval. Furthermore, level of homology with the reference sequence is important in the performance of the tools. For example, some tools give greater scores as the percentage of homolog sequences increase. Beside these, the suitability of given dataset to the tools should be considered when the low scores are encountered. However, this is not the case for T-Coffee, M-Coffee and MUSCLE which can be used for protein, DNA and RNA datasets. Nevertheless, when the datasets used in this study are considered, it can be obviously seen that all three tools are much more appropriate for the amino acid datasets (Figure 4). This situation may change with different benchmarks or datasets. Additionally, the differences in the algorithms may also affect the scores. However, this is less probable according to our results (Figure 2 and 3), since there is no clear difference when T-Coffee and M-Coffee that has progressive algorithm is compared with MUSCLE having an iterative strategy in its algorithm.

M-Coffee is a meta-method combining results from various tools and then apply T-Coffee on the results for these tools to reach the ultimate MSA. As expected, M-Coffee took longer time compared to MUSCLE and T-Coffee because of this distinct processing scheme. M-Coffee was expected to be more reliable and to give better results than particularly T-Coffee due to its strategy. However, there are some datasets of which

values are greater with T-Coffee or MUSCLE than with M-Coffee. This can be resulted from again the similarity level of the sequences, as one of the limitations of this computationally intensive method is that it is not preferable when the distant sequences are attempted to align [1]. Consequently, these unexpected lower values for M-Coffee may be related to the percentages of sequence similarity.

This study has shown that the choice of the proper tool for MSA is not straightforward and several aspects such as the homology level or length of sequences should be taken into consideration. Although we carried out our study for only small size of data, our results are sufficient to support the idea that while the MSA tool is suitable for a dataset from a certain benchmark, it may be inappropriate for another dataset from the same benchmark system. This illustrates that there are still plenty of limitations to be eliminated in MSA tools. With the increasing information about the structure and function and also improvements in the computing power, it may lead to the development of the new strategies not only revealing more accurate alignments but also confirming and fixing the results acquired from previous studies.

All in all, available powerful MSA methods with the distinctive strategies like M-Coffee, T-Coffee and MUSCLE are fundamental steps through the further studies like three-dimensional structure determination. However, as seen in our results, the evaluation of them is dependent on the references from benchmark systems and is complicated process, since the tools are not suitable and reliable for all the datasets.

Acknowledgment

The authors acknowledge Prof.Dr. Jens Allmer for his guidance in the conceptualization of this study.

Conflicts of interest

All authors declare that they have no conflict of interest.

References

- [1] Notredame C., Recent evolutions of multiple sequence alignment algorithms, *PLoS Comput. Biol.*, 3(8) (2007) e123.
- [2] Edgar R.C., MUSCLE: multiple sequence alignment with high accuracy and high throughput, *Nucleic Acids Res.*, 32(5) (2004) 1792-1797.
- [3] Moretti S., Armougom F., Wallace I.M., Higgins D.G., Jongeneel C.V., Notredame C., The M-Coffee web server: a meta-method for computing multiple sequence alignments by combining alternative alignment methods, *Nucleic Acids Res.*, 35(Web Server issue) (2007) W645-648.
- [4] Wang Y., Wu H., Cai Y., A benchmark study of sequence alignment methods for protein clustering, *BMC Bioinformatics*, 19(Suppl 19) (2018) 529.
- [5] Maiolo M., Zhang X., Gil M., Anisimova M., Progressive multiple sequence alignment with indel evolution, *BMC Bioinformatics*, 19(1) (2018) 331.
- [6] Bawono P., Dijkstra M., Pirovano W., Feenstra A., Abeln S., Heringa J., Multiple Sequence Alignment, *Methods Mol. Biol.*, 1525 (2017) 167-189.
- [7] Ugurel O.M., Ata O., Turgut-Balik D., An updated analysis of variations in SARS-CoV-2 genome, *Turk. J. Biol.*, 44(3) (2020) 157-167.
- [8] Notredame C., Higgins D.G., Heringa J., T-Coffee: A novel method for fast and accurate multiple sequence alignment, *J. Mol. Biol.*, 302(1) (2000) 205-217.
- [9] Edgar R.C., MUSCLE: a multiple sequence alignment method with reduced time and space complexity, *BMC Bioinformatics*, 5 (2004) 113.
- [10] Edgar R.C., Batzoglou S., Multiple sequence alignment, *Current Opinion in Structural Biology*, 16(3) (2006) 368-373.
- [11] Thompson J.D., Higgins D.G., Gibson T.J., CLUSTAL W: improving the sensitivity of progressive multiple sequence alignment through sequence weighting, position-specific gap penalties and weight matrix choice, *Nucleic Acids Res.*, 22(22) (1994) 4673-4680.
- [12] Sievers F., Wilm A., Dineen D., Gibson T.J., Karplus K., Li W., Lopez R., McWilliam H., Remmert M., Söding J., Thompson J.D., Higgins D.G., Fast, scalable generation of high-quality protein multiple sequence alignments using Clustal Omega, *Mol. Syst. Biol.*, 7 (2011) 539.
- [13] Van Walle I., Lasters I., Wyns L., Align-m--a new algorithm for multiple alignment of highly divergent sequences, *Bioinformatics*, 20(9) (2004) 1428-1435.
- [14] Morgenstern B., Frech K., Dress A., Werner T., DIALIGN: finding local similarities by multiple sequence alignment, *Bioinformatics*, 14(3) (1998) 290-294.
- [15] Lassmann T., Sonnhammer E.L.L., Kalign – an accurate and fast multiple sequence alignment algorithm, *BMC Bioinformatics*, 6(1) (2005) 298.
- [16] Katoh K., Misawa K., Kuma K., Miyata T., MAFFT: a novel method for rapid multiple sequence alignment based on fast Fourier transform, *Nucleic Acids Res.*, 30(14) (2002) 3059-3066.
- [17] Katoh K., Standley D.M., MAFFT Multiple Sequence Alignment Software Version 7: Improvements in Performance and Usability, *Molecular Biology and Evolution*, 30(4) (2013) 772-780.
- [18] Do C.B., Mahabhashyam M.S., Brudno M., Batzoglou S., ProbCons: Probabilistic consistency-based multiple sequence alignment, *Genome Res.*, 15(2) (2005) 330-40.
- [19] Pei J., Kim B.H., Grishin N.V., PROMALS3D: a tool for multiple protein sequence and structure alignments, *Nucleic Acids Res.*, 36(7) (2008) 2295-2300.
- [20] O'Sullivan O., Suhre K., Abergel C., Higgins D.G., Notredame C., 3DCoffee: Combining Protein Sequences and Structures within Multiple Sequence Alignments, *Journal of Molecular Biology*, 340(2) (2004) 385-395.
- [21] Zou Q., Hu Q., Guo M., Wang G., HAlign: Fast multiple similar DNA/RNA sequence alignment based on the centre star strategy, *Bioinformatics*, 31(15) (2015) 2475-2481.
- [22] Armougom F., Moretti S., Poirot O., Audic S., Dumas P., Schaeli B., Keduas V., Notredame C., Espresso: automatic incorporation of structural information in multiple sequence alignments using 3D-Coffee, *Nucleic acids research*, 34(Web Server issue) (2006) W604-W608.
- [23] Löytynoja A., Goldman N., An algorithm for progressive multiple alignment of sequences with insertions, *Proc. Natl. Acad. Sci. U S A*, 102(30) (2005) 10557-10562.

- [24] Löytynoja A., Goldman N., Phylogeny-aware gap placement prevents errors in sequence alignment and evolutionary analysis, *Science*, 320(5883) (2008) 1632-1635.
- [25] Pei J., Grishin N.V., MUMMALS: multiple sequence alignment improved by using hidden Markov models with local structural information, *Nucleic Acids Research*, 34(16) (2006) 4364-4374.
- [26] Kemena C., Notredame C., Upcoming challenges for multiple sequence alignment methods in the high-throughput era, *Bioinformatics*, 25(19) (2009) 2455-2465.
- [27] Wallace I.M., O'Sullivan O., Higgins D.G., Notredame C., M-Coffee: combining multiple sequence alignment methods with T-Coffee, *Nucleic Acids Research*, 34(6) (2006) 1692-1699.
- [28] Rosenberg M.S., Sequence alignment: Methods, models, concepts, and strategies, In: Rosenberg M.S., (Ed) California: University of California Press, (2009).
- [29] Subramanian A.R., Kaufmann M., Morgenstern B., DIALIGN-TX: greedy and progressive approaches for segment-based multiple sequence alignment, *Algorithms for molecular biology:AMB*, 3 (2008) 6.
- [30] Pais F.S., Ruy P.C.,Oliveira G., Coimbra R.S., Assessing the efficiency of multiple sequence alignment programs, *Algorithms Mol. Biol.*, 9(1) (2014) 4.
- [31] Menke M., Berger B., Cowen L., Matt: local flexibility aids protein multiple structure alignment, *PLoS Comput. Biol.*, 4(1) (2008) e10.
- [32] Van Walle I., Lasters I., Wyns L., SABmark--a benchmark for sequence alignment that covers the entire known fold space, *Bioinformatics*, 21(7) (2005) 1267-1268.
- [33] Anderson C.L., SuiteMSA User's Manual. Nebraska, USA: University of Nebraska–Lincoln, (2011).
- [34] Saeed F., Perez-Rathke A., Gwarnicki J., Berger-Wolf T., Khokhar A., A high performance multiple sequence alignment system for pyrosequencing reads from multiple reference genomes, *Journal of Parallel and Distributed Computing*, 72(1) (2012) 83-93.
- [35] Waterhouse A.M., Procter J.B., Martin D.M., Clamp M., Barton G.J., Jalview Version 2--a multiple sequence alignment editor and analysis workbench, *Bioinformatics*, 25(9) (2009) 1189-1191.
- [36] Anderson C.L., Strope C.L., Moriyama E.N., SuiteMSA: visual tools for multiple sequence alignment comparison and molecular sequence simulation, *BMC Bioinformatics*, 12(1) (2011) 184.



Enzymatic degradation and fermentation of Corn Bran for Bioethanol production by *Pseudomonas aeruginosa* AU4738 and *Saccharomyces cerevisiae* using Co-culture technique

Michael Bamitale OSHO^{1,*}

¹ McPherson University, College of Natural and Applied Sciences, Department of Biological Sciences, , Seriki Sotayo, P.M.B. 2094, Sapon, Abeokuta, Ogun State, NIGERIA

Abstract

Ethanol is one of the bioenergy sources with low environmental and high efficiency impact. The aim of this study was to screen for the bacterial isolate capable of degrading starch, investigate the enzymatic hydrolysis and fermentation of corn bran through submerged fermentation using co-culture technique for bioethanol production. The isolate was identified using 16S rRNA sequence technique as *Pseudomonas aeruginosa* AU4738. Corn bran was used as substrates with and without garlic powder (*Allium sativum* L.) as activator and subsequently optimized for production of bioethanol. Reducing sugar from the hydrolysate and ethanol concentration of the distillate were analyzed using spectrophotometry and gas chromatography mass spectrometry techniques respectively. There was an increase in glucose concentration (23.8% and 17.8%) in the culture medium with and without activator at 48 h respectively but steadily decreased from 72 h to 168 h. Maximum ethanol concentration obtained in substrate culture with activator was 35% higher compared with that without activator at 120 h fermentation time. Thus a cheap, renewable and readily available agricultural waste has been effectively utilized as substrate for bioethanol production and incorporation of activator also had significant effect on the viability of fermenting organisms thus subjugating the intolerance of alcohol concentration.

Article info

History:

Received: 04.12.2020

Accepted: 07.09.2021

Keywords:

Corn bran,
Bioethanol,
Pseudomonas aeruginosa AU4738,
Saccharomyces cerevisiae,
Co-culture technique.

1. Introduction

Sources of biofuel have become more salient as economical substitute to declining and much exorbitant fossil fuels [1]. Bioethanol is the only liquid fuels that do not contribute to the greenhouse gas effect [2]. Due to fluctuating prices and dwindling oil reserves at global market, fermentation processes have attracted great demand in comparison to conventional production of bioethanol [3]. Thus high cost has resulted to energy catastrophe in african countries that are oil contingent. It has been delineated that in many part of the world biofuel remains censorious energy development target if petroleum prices be a cut above US \$ 60

per barrel [4]. Brazil is the world prime biofuel producer and Nigeria has joined the confederation of biofuel users from sugarcane and cassava sources [5]. Cassava, yam, and sweet potato are main starches that serve as staple foods for people throughout the world's humid and hot regions [6]. However, potatoes are high starchy value crops which do not require complex

pretreatment. Waste byproducts from sweet potato cultivation could be utilized for bioethanol production [7, 8]. The use of these staple starchy crops poses threat to food surveillance in the face of growing ethanol fuel demand. Imaginably, the divergence of food resource to bio-fuel production may to a large extent cause food crises worldwide [9]. As a result it becomes exigent that spotlight be turned to the use of non-food starchy piece for bioethanol production.

Saccharomyces cerevisiae (baker's yeast) is one of the most significant microbes in the fermentation of sugar to bioethanol due to its high tolerance to ethanol concentration, high fermentation rate, high ethanol yield, high selectivity, good tolerance to substrate concentrations, low accumulation of by-products, and lower pH value [10, 11]. Several researchers, Abouzied and Reddy, [12], Oyeleke *et al.*, [13] Duhan *et al.*, [1] George *et al.*, [14] combined *Saccharomyces cerevisiae* with other group of saccharifying fungi such as *Aspergillus* sp., *Kluyveromyces* sp., *Zymomonas*

*Corresponding author. e-mail address: mikebamoshogmail.com

mobilis, *Gloeophyllum sepiarium*, *Trichoderma* sp. and *Pleurotus ostreatus* to improve bioethanol production. This research was aimed at assessing the appropriateness of using the corn bran through two-step processes: saccharification and fermentation using co-culture method for bioethanol production by *Pseudomonas aeruginosa* AU4738 and *Saccharomyces cerevisiae*. Evaluation of the substrate pre-treatment processes for transformation of starch into fermentable sugar and successive use of the spice from garlic as activator was conducted to alleviate product inhibition potency of microorganism in the production of ethanol.

2. Materials and Methods

2.1. Materials

The bacterial isolate was obtained from Culture Collection Centre, Department of Biological Sciences, McPherson University, Seriki Sotayo, Nigeria and was characterized using 16S rDNA sequencing technique while the baker's yeast was purchased from Apongbo Market, Lagos Island Local Government, Lagos. Corn bran, soya beans and garlic were purchased from Awolowo Market, Sagamu, Remo North Local Government, Ogun State, Nigeria. Nutrient agar (NA) (Accumix, Diagnostic, Ltd., India), Yeast Extract Agar (YEA) (LOBA Chemie Pvt. Ltd. India). Iodine, 3,5-Dinitrosalicylic acid (DNS) (Baker Inc., USA), sodium potassium tartrate (Klincent Laboratories, Mumbai, India) and Tetraoxosulphate (VI) acid were of analar grade.

2.2 Methods

Screening of starch hydrolyzing bacteria

Pure culture of the bacterial isolate was inoculated into nutrient agar containing 1 g soluble starch and stay for 5 min and visualized for hydrolytic activity. Clear zones which appeared around growing bacteria indicate hydrolysis of starch [15].

Determination of hydrolysis rate of the isolate

Ability of the bacterial isolates to degrade starch was described by the starch degrading index (SDI). The isolate was re-plated on starch agar and their halo diameter (Z) and colony diameter (C) was determined after 24 h incubation at 35 °C. The formula $Z - C / C \times 100$ was employed to calculate the percentage hydrolysis efficiency according to the method of Sreedevi and Reddy [16].

Molecular identification of gene sequences of the bacterial isolate

The total genomic DNA extraction, Polymerase Chain Reaction (PCR) and DNA sequencing according to the

standard protocols were carried out. The isolate which demonstrated starch degrading ability was subjected to extraction of total genomic DNA according to the procedures of Zymo Research Bacterial DNA MiniPrep™ instruction manual and kit.

In determining the phylogenetic grouping of sample genomic DNA, this was amplified using standard PCR. The genomic DNA extract was amplified using PCR reaction and completed within 36 cycles under conditions of initial denaturation (94 °C for 5 min); denaturation (94 °C for 30 s); annealing (56 °C for 30 s); extension (72 °C for 45 s); final extension step (72 °C for 7 min); and indefinitely final holding at 10 °C. Thus, this protocol helped to amplify the 16S rRNA gene of interest.

A 5 µl sample of PCR product reaction mixture was analyzed by 1.5% agarose gel electrophoresis in 1 x Tris Acetic EDTA buffer. It was run at 80 V and 107 mA for 45 min. A staining medium ethidium bromide was applied on the gel and visualization of bands under UV illumination was evidence. The 16S rRNA sequences were determined by fluorescently labeled 16s RNA products analysis generated by PCR cocktail mix on a DNA sequencer AB 373a Stretch (short gun). Primers (27F:AGAGTTTGATCMTGGCTCAG and 1525R: AAGGAGGTGWTCARCCGCA) were used in all sequencing reactions. The 16S rRNA sequences obtained were aligned with the non-reductant nucleotide database at Genbank using the BLAST program (<http://www.ncbi.nlm.nih.gov>). A phylogenetic tree was constructed by the neighbour-joining method using MEGA 7 package [17].

Preparation and pretreatment of substrates

Corn bran and soya bean were blended into powdery form using the electric grinder (Marlex, Electrolin) and stored in an air tight container prior to use. Garlic was peeled, dried at 40 °C, blended and stored in an air tight container for subsequent use [18].

Preparation of inocula

The bacterial inoculum was prepared in 50 ml broth containing nutrient broth (0.65 g), corn bran (1 g) and soya bean (0.5 g). The medium was adjusted to pH 6.5 solutions autoclaved and cooled at room temperature. It was inoculated with 100 µl *Pseudomonas aeruginosa* AU4738 (2.3×10^4 cfu) and incubated for 24 h at 35 °C.

Saccharomyces cerevisiae inoculum was prepared in 100 ml yeast extract broth (0.75 g), adjusted to pH 6.5 autoclaved, cooled at room temperature and inoculated with baker's yeast (1 g). It was then incubated at 120 rpm for 24 h (30 °C) [19].

Preparation of production medium and substrate treatments

Pretreatment slurry of substrate was prepared by adding 20 g corn bran powder and 2 g soya bean powder to 250 ml distilled water (w/v) with and without 1 g garlic as activator respectively [20]. Production media were prepared in duplicate and adjusted to pH 6.5 and thereafter autoclaved at 121 °C for 30 min. Co-culture technique involved simultaneous addition of both starch hydrolytic and fermentation microorganisms. Optimized protocol with very little modification was adopted [20]. The adjustment includes fermentation conditions such as ethanol production parameters (pH 6.5; temperature 37 °C; incubation period 72 h). They were inoculated with *P. aeruginosa* AU4738 (5 ml) and Baker's yeast (12.5 mL) at the same time and incubated at 37 °C for 144 h. All the treatments were manually mixed at 24 h interval to promote uniform utilization of substrate. pH was checked and also recorded each day.

Generation of glucose standard curve

Standard glucose stock solution was prepared by dissolving 0.25 g glucose in 100 mL distilled water. Working standard solution was also prepared by adding up 10 ml stock solution to the 100 mL.

Glucose standard solution ranging from 0.1 – 1.0 µmol/mL was transferred into clean, dry test tubes, 1 mL DNS reagent was added to each tube and cotton plugged. A blank was prepared with 1 mL DNS added, the test tubes were boiled in water bath for 5 min cooled at room temperature and 9 mL distilled water was added. Absorbance at 540 nm using a spectrophotometer (GS-UV11, General Scientific) was read against the blank.

Determination of reducing sugar from the fermented broth

Fermented broth (10 mL) was centrifuge at 3000 rpm for 15 min to obtain supernatant for each sample with duplicates. One (1) mL supernatant was dispensed into a test tube, followed by another 1 ml prepared DNS reagent. The resulting mixture was boiled at 100 °C for 5 min, cooled and 10 mL distilled water was added and absorbance reading was taken at 540 nm. Thus, concentration values were interpolated from the glucose standard curve [18].

Distillation process

Distillation was carried out using distillation apparatus after fermentation process. Top fermented broth (15 mL) was transferred into round-bottom flask with an enclosed distillation apparatus of a running tap water

flask in a heating mantle and fixed to the other end of distillation column for the collection of distillate at 78 °C (standard temperature for ethanol production).

Determination of Ethanol concentration

The ethanol concentration was determined by spectrophotometric method [22]. Distillate (0.5 mL) was measured into a conical flask containing 15 mL distilled water, and 12.5 mL K₂CrO₇ solution was added. The resulting mixture (20 mL) was transferred into a test tube and incubated at 60 °C for 20 min in a water bath and then cooled at room temperature. Five (5) mL was taken and diluted with 5 mL distilled water and absorbance was determined at 600 nm using spectrophotometer. The ethanol concentration was calculated from absolute ethanol standard curve, while the ethanol yield was determined using Yoswathana and Phuriphat [23] procedure as shown below:

$$\text{Ethanol Yield} = \frac{\text{Ethanol measure in Sample}}{\text{Amount of initial sugar content} \times 0.5}$$

Gas chromatography mass spectrometry (gcms) analysis of bioethanol

Gas Chromatography Mass Spectrometer (Shimadzu QP 2010 Ultra, Japan) equipped with Mass Spectrometer Detection 5975C (VLMSSD) and injector (Auto) 7683B series) was used for the analysis. Absolute ethanol GC grade was used as internal standard in Gas Chromatography measurements. An aliquot (1 µl) reaction medium was measured and diluted in absolute ethanol (GC grade). The column temperature was kept at 40 °C, held for 1 min, raised to 290 °C at the rate of 3 °C /min, and then maintained at this temperature for 1.65 min. The final run time was 54.2 min. The detector and injector temperatures were set at 240 and 230 °C respectively. GC measurements were taken in triplicate.

3. Results and Discussion

Screening of microorganisms capable of hydrolyzing starch and hydrolysis efficiency

Screening of bacterial isolates for ability to hydrolyze starch depends on clear zone exhibition around their colonies. Zone of inhibition obtained from the screened bacterium showed appreciable differences in ability to hydrolyze starch (Figure 1). Hennessy *et al.* [24] described series of methods for the isolation, screening, and selection of glycoalkaloids (GA)-degrading bacteria. The screening of bacterial crude extracts for the ability to hydrolyze GAs was performed using a combination of thin layer chromatography (TLC), high performance liquid

chromatography (HPLC), and liquid chromatography mass spectrometry (LC-MS). These revealed the principal monomer of sugar constituents available for microorganisms' consumption for hydrolysis.

However, the bacterium in question was selected based on exhibition of halo zone diameter (19 mm) with calculated hydrolysis efficiency of 63.3%. Occurrence of isolate producing such large diameter of zone of inhibition was an indication that this substrate could serve as potential amylase producing bacterial medium [16, 20]. The starch hydrolysis was otherwise described by Gudeta (25) as starch degrading index (SDI).

Though the procedures carried out by the extracellularly secreted commercial α -amylase from bacteria could be very expensive for large scale production. The zone of inhibition exhibited by the bacterial isolate was an indication that it is more efficient on starch hydrolysis for monomeric sugars production. Furthermore, starch molecules are too large to enter bacterial cells, hence their transportation after hydrolysis into the cell and are thereafter used for metabolism reactions. These exoenzymes viz α -amylase and oligo-1,6-glucosidase are able to

hydrolyze starch (amylase test) into dextrin, maltose, or glucose subunits using the starch agar as differential nutritive medium [26].

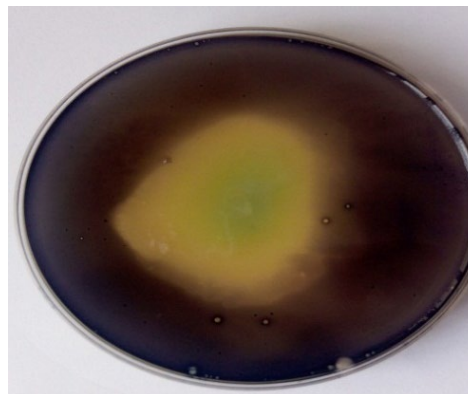


Figure 1. *Pseudomonas aeruginosa* showing Zone of Clearance on Starch Agar plate

Identification of the PCR amplified 16S rRNA

The isolate with NCBI Accession number HQ1481651.1 was identified as *Pseudomonas aeruginosa* AU4738. The maximum percentage identity was 93 % as shown in Figure 2.

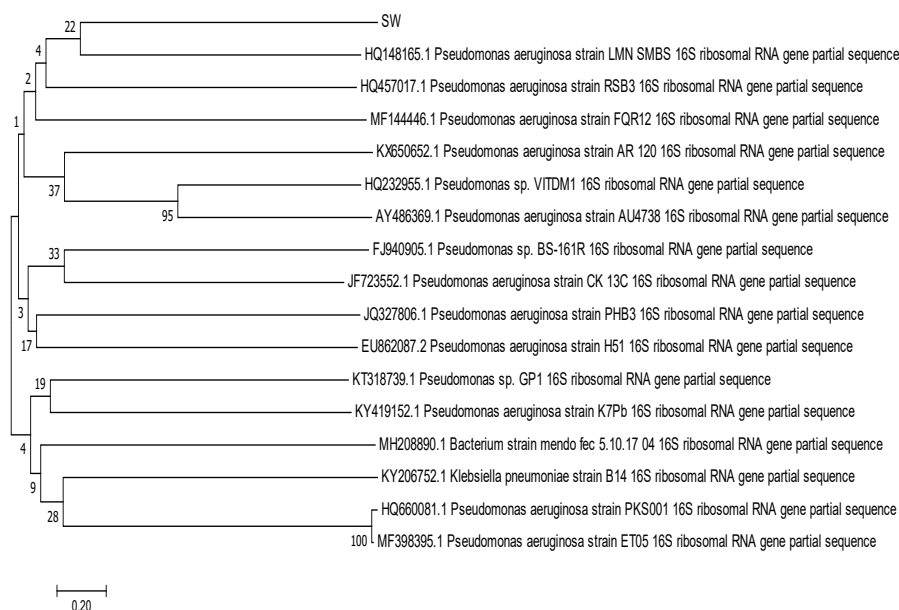


Figure 2. Phylogenetic Tree based on relationship of *Pseudomonas aeruginosa* strain AU4738

Optimization of the Glucose and Bio-Ethanol from the Corn bran substrate

There was an increase in activity of the starch degrading enzyme for glucose production by 23.8 and 17.8% at 48 h in culture with and without activator respectively and a steady decrease at 72 h to 168 h (Figure 3). This revealed fast starch-degrading enzyme produced by *P. aeruginosa* AU4738. According to

Zakpa *et al.*, [27] the reducing sugar concentration retention may be directly proportional to the initial starch concentration available in corn bran. Incomplete hydrolysis of starch at a given saccharification time possibly resulted in reduction of reducing sugar that could have been converted even after addition of baker's yeast. This was in conformity with the results of Bekele *et al.* [28] when they produced bioethanol from potato waste peels.

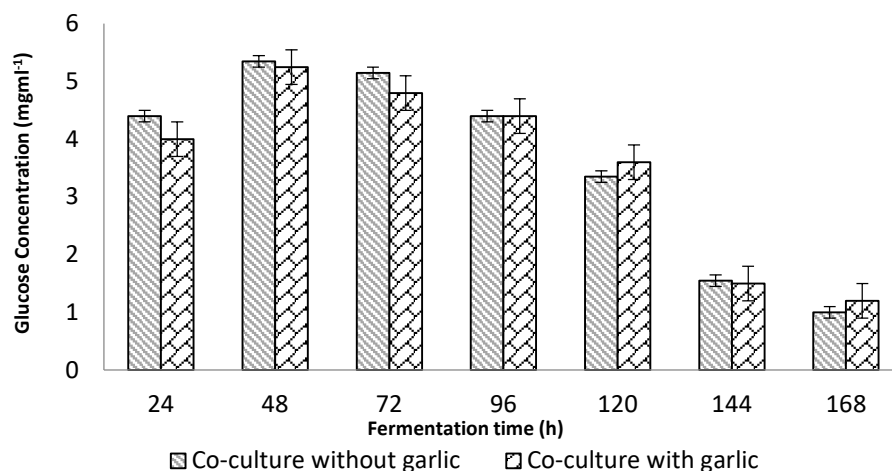


Figure 3. Effect of Culture Techniques on Glucose Production during the Fermentation of Corn Bran with or without Activator

In studying the effect of garlic powder on bioethanol synthesis, activated corn bran has maximum ethanol concentration of 18.25% v/v which was 35% higher than its counterpart without activator that recorded 11.86 % v/v at 120 h fermentation time (Figure 4). Subsequent fermentation process time drastically reduced the concentration. The procedure could be

assumed as an alternative cost-efficiency in the trailing of fuel ethanol production protocol. Moreover, the incorporation of activator in the medium had significant effect on the bioethanol yield. Consequently the intolerance alcohol concentration posed to the viability of fermenting microorganisms was subdued.

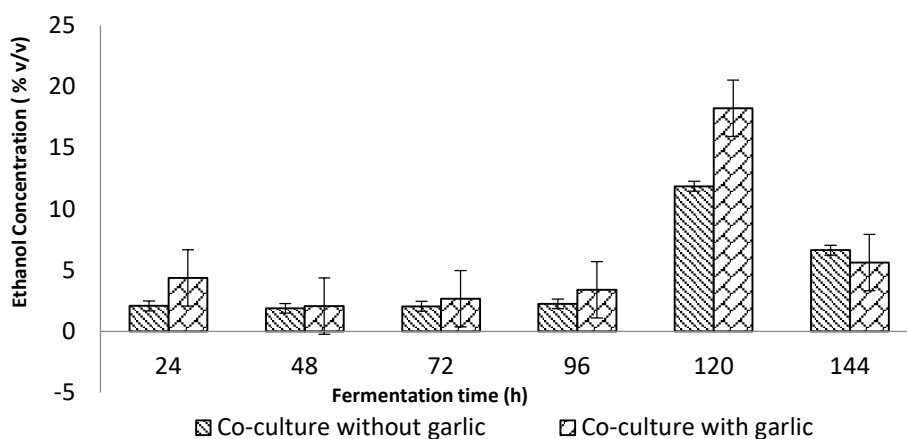


Figure 4. Effect of Culture Technique on Ethanol Production during the Fermentation of Corn bran with or without Activator

Garlic extract has been reportedly used to prevent acetaldehyde synthesis from ethanol by inhibiting the alcohol dehydrogenase [29]. Teixeira *et al.* [30] noted that the discrimination of alcohol concentration greater than 10% (v/v) will pose difficulty on the adequacy of fermenting microbes if it has potential to produce ethanol concentrations $\geq 17\%$ (v/v). There was a report on reduction in the levels of acetaldehyde and acetate,

after the introduction of garlic to investigation animals with significant increase in ethanol concentration [31]. In a work conducted by Abouzied and Reddy, [12] when *Aspergillus niger* and *Saccharomyces cerevisiae* were co-cultured for bioethanol production, the barrier of the intolerance of the yeast to alcohol concentration was supposedly a concern. The activator circumvented this obstacle which also might be due to its phenolic

constituent. Garlic has been contemplated as one of the richest vegetable origin for total phenolic compounds [32]. As a result, most researchers now look plant origin for phytochemicals that could specifically target and prevent enzyme synthesis of these fermentation inhibitors distinctively acetate.

Pseudomonas aeruginosa AU4738 and baker's yeast concomitantly employed in this study enhanced the bioethanol synthesis. This was also in agreement with Igbokwe *et al.*, [33] that reported a keen increase in the percentage ethanol yield from 120 to 216 h incubation. Moreover, from glucose and lignocellulosic biomass hydrolysate substrates according to Joshi *et al.* [34], ethanol was efficiently and effectively produced by a coalescence of *S. cerevisiae* CDBT2 and *W. anomalous* CDBT7 yeast strains and indicated almost complete utilization of reducing sugars. Contrariwise, there was no improvement in ethanol production obtained after inoculation with *S. stipitis* in the sequential co-culture of *S. cerevisiae* and *S. stipitis* but lower ethanol was recovered with simultaneous co-culture in the consumption of xylose and glucose substrates. Moreover, *S. cerevisiae* fermentation of Kraft pulp hydrolysate in fermenter resulted in a slightly lower ethanol productivity and yield [35].

It has been told of that final ethanol concentration acquired differ either in the type of substrate concentration, pre-treatment given to substrate, mode of operation, substrate detoxification procedure, temperature, or fermentation strain [36]. Consequently ethanol from amylolytic fungus hydrolysates was

lower than ethanol from acid hydrolysate of various substrates [37].

Identification test for Bio-Ethanol

A conventional method for determination of reducing sugars and total alcohols in raw fermentation broths has been developed and widely employed. The fermented broth culture is often pretreated to remove polysaccharides, proteins, glycerol and organic acids. The colorimetric change from total alcohols and reducing sugars were measured by potassium permanganate oxidation and determined by DNS test and subtracted. The remaining portion of colorimetric change was then used to calculate the total alcohol concentration in the sample. However, ethanol concentration can also be determined using ethanol oxidase or ethanol dehydrogenase, but the results are easily disturbed by the presence of various enzymes in the fermentation broth [38]. In this study, the GC analysis revealed 5.73% w/v and 3.6% w/v total component of ethanol from corn bran with and without activator using co-culture respectively as presented in Figures 5 and 6 respectively. However, the ethanol concentration determination by spectrophotometric method was estimated by percentage whereas the GC analysis revealed the component base on proportion, hence the disparity in quantification. Though there are some disadvantages in using this method. Potassium permanganate being unstable as it react with water at low pH and complicate the test results. To mitigate this setback, potassium permanganate solution was prepared right before it is used and kept in dark.

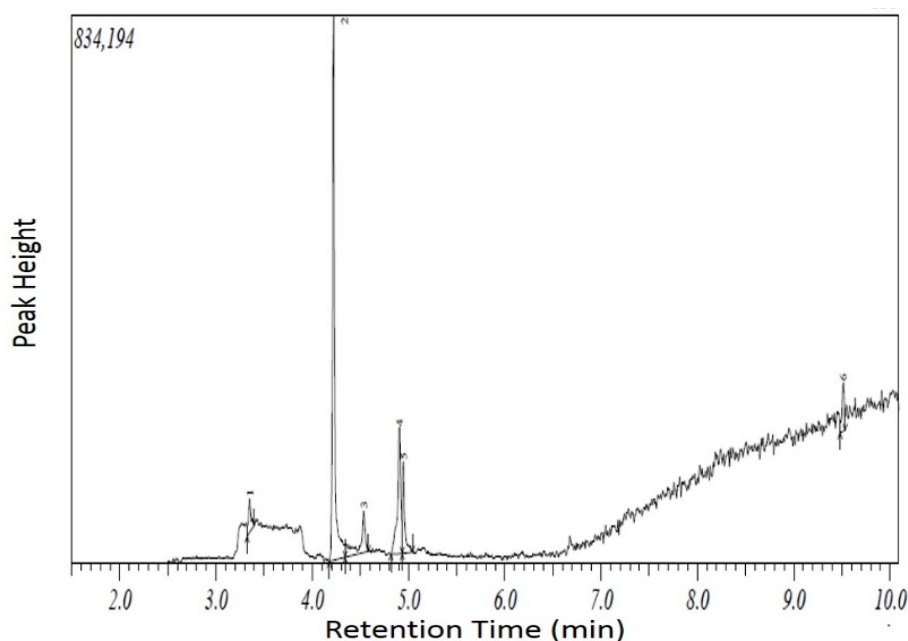


Figure 5. Gas Chromatogram of Ethanol concentration from Corn bran with activator

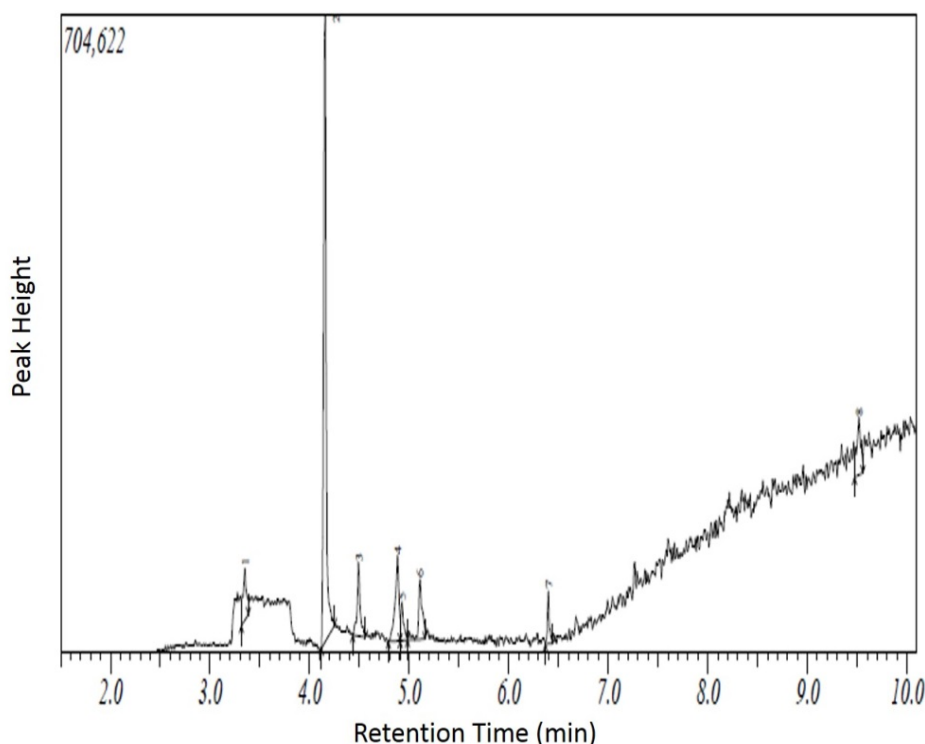


Figure 6. Gas Chromatogram of Ethanol Concentration from Corn Bran without Activator

Acknowledgment

I would like to acknowledge the Messrs. David Adesida and Kola Kusimo, Laboratory Staff of the Department of Biological Sciences for their technical assistance.

Conflicts of interest

The author simply declares there is no conflict of interest.

References

- [1] Duhan J.S., Kumar A., Tanwar S.K., Bio-ethanol production from starchy part of tuberous plant (potato) using *Saccharomyces cerevisiae* MTCC-170, *African Journal of Microbiology Research*, 7(46) (2013) 5253-5260.
- [2] Anuj K.C., Ravinder R., Lakshmi M.N., Rao V., Ravindra P., Economic and environmental impact of bio-ethanol production technology, *Biotechnology and Molecular Biology Review*, 2(1) (2007) 14-32.
- [3] Brook A.A., Ethanol potential of local yeast strains isolated from ripe banana peels, *African Journal of Biotechnology*, 7(20) (2008) 3749 – 3752.
- [4] Naylor R.L., Liska A., Burke M., Falcon W.P., Gaskell J., Razello S., Cassaman K., The effect: Biofuel, food security and the environment, *Environmental Microbiology*, 49(9) (2007) 30-43.
- [5] Aisien F.A., Aguye M.D., Aisien E.T., Blending of ethanol produced from cassava waste water with gasoline as source of automobile fuel, *Electronic Journal of Environment, Agriculture and Food Chemistry*, 9(5) (2010) 946-950.
- [6] Klass D.L., Biomass for renewable energy fuels and chemicals, London: Academic Press, (1998) 544.
- [7] Limatainen H., Kuokkanen T., Kaariainen J., Development of bio-ethanol production from waste potatoes. In: Pongracz, E., (ed.) Proceedings of the Waste Minimization and Resources Use Optimization Conference, Finland, Oulu: Oulu University Press, (2004) 123-129.
- [8] Adarsha R., Asha D.L. Balaji R.R., Production of bio-ethanol from *Pectobacterium carotovorum* induced soft rotten potatoes, *African Journal of Microbiology Research*, 4(12) (2010) 1340-1342.

- [9] Srinorakutara T., Kaewvimol L., Saengow I., Approach of cassava waste water pre-treatment for fuel ethanol production in Thailand, *Journal of Science Research*, 31(1) (2008) 77-84.
- [10] Muhamud F. Bin I., Production of Bio-ethanol from Tapioca Starch using *Saccharomyces cerevisiae*, PD thesis, University of Malaysia Pahang, (2009).
- [11] Lee W., Jin Y., Evaluation of ethanol production activity by engineered *Saccharomyces cerevisiae* fermenting cellobiose through the phosphorolytic pathway in simultaneous saccharification and fermentation of cellulose, *Journal of Microbiology and Biotechnology*, 27(9) (2017) 1649–1656.
- [12] Abouzied M.M., Reddy C.A., Direct fermentation of potato starch to ethanol by co-culture of *Aspergillus niger* and *Saccharomyces cerevisiae*, *Applied and Environmental Microbiology*, 52(5) (1986) 1055-1059.
- [13] Oyeleke S.B., Dauda B., Oyewole O.A., Okoliegbe I.N., Ojebode T., Production of Bio-ethanol from cassava and sweet potato peels, *Advances in Environmental Biology*, 6(1) (2012) 241-245.
- [14] George P., Aggelos G., Aikaterini K., Styliani K., Dimitris K., Diomi M., Bioethanol Production from Food Waste Applying the Multienzyme System Produced On-Site by *Fusarium oxysporum* F3 and Mixed Microbial Cultures, *Fermentation*, 6 (2020) 39.
- [15] Farias D.F., Carvalho A.F.U., Oliveira C.C., Sousa N.M., Rocha-Bezerra L.C.B., Ferreira P.M.P., Hissa D.C., Alternative method for quantification of alpha-amylase activity, *Brazilians Journal of Biology*, 70(2) (2010) 405-407.
- [16] Sreedevi S., Reddy B.B.N., Isolation, screening and optimization of phytase production from newly isolated *Bacillus sp.* C43, *International Journal of Pharmacy and Biological Science*, 2(2) (2012) 218-231.
- [17] Kumar S., Stecher G., Tamura K., MEGA7: Molecular Evolutionary Genetics Analysis Version 7.0 for Bigger Datasets, *Molecular Biology Evolution*, 33(7) (2016) 1870-1874.
- [18] Amadi P.U., Ifeanacho M.O., Impact of changes in fermentation time, volume of yeast, and mass of plantain pseudo-stem substrate on the simultaneous saccharification and fermentation potentials of African land snail digestive juice and yeast, *Journal of Genetic Engineering and Biotechnology*, 14(2) (2016) 289-297.
- [19] Akponah E., Akpomie O.O., Analysis of the suitability of yam, potato and cassava root peels for bioethanol production using *Saccharomyces cerevisiae*, *International Research Journal of Microbiology*, 2(10) (2011) 393-398.
- [20] Swain M.R., Mishra J., Thatoi H., Bio-ethanol Production from Sweet Potato (*Ipomoea batatas* L.) Flour using Co-Culture of *Trichoderma sp.* and *Saccharomyces cerevisiae* in Solid-State Fermentation, *Brazil Archive of Biology Technology*, 56 (2) (2013) 171-179.
- [21] Amadi B.A., Agomuo E.N., Ibegbulan CO. Research Methods in Biochemistry, Owerri-Nigeria: Supreme Publishers, (2004); 93-99.
- [22] Caputi A., Ueda M., Brown T., *American Journal of Enology and Viticulture*, 19 (1968) 160–165.
- [23] Yoswathana N., Phuriphapat P., Bioethanol Production from Rice Straw, *Energy Research Journal*, 11 (2010) 26–31.
- [24] Hennessy R.C., Jørgensen N.O.G., Scavenius C., Enghild J.J., Greve-Poulsen M., Sørensen O.B., Stougaard P.A., Screening Method for the Isolation of Bacteria Capable of Degrading Toxic Steroidal Glycoalkaloids Present in Potato, *Frontier Microbiology*, 9 (2018) 2648.
- [25] Gudeta D., Isolation and characterization of starch degrading rhizobacteria from soil of Jimma University Main Campus, Ethiopia, *African Journal of Microbiology Research*, 12(32) (2018) 788-795.
- [26] Rijal N., Starch Hydrolysis Test: Principle, Procedure, Results. In *Mucormycosis: Pathogenesis, Clinical Manifestations and Treatment*. Available at: <https://microbeonline.com/starch-hydrolysis-test/>. Retrieved September, 2021.
- [27] Zakpa H.D., Mak-Mensah E.E., Johnson F.S., Production of ethanol from corncobs using *Aspergillus niger* and *Saccharomyces cerevisiae* in simultaneous saccharification and fermentation, *African Journal of Biotechnology*, 8(13) (2009) 3018-3022.
- [28] Bekele A., Fite A., Alemu S., Sewhunegn T., Bogele E., Simachew M., Debele T., Production of bio-ethanol from waste potato peel collected from University of Gondar, student’s cafeteria, *Global Journal of Biochemistry and Biotechnology*, 3(3) (2015) 132-140.

- [29] Rabinkov A., Miron T., Konstantinovski L., Wilchek M., Mirelman D., Weiner L., The mode of action of alliin: trapping of radicals and interaction with thiol containing proteins, *Biochemical and Biophysical Acta.*, 1379 (1998) 233–244.
- [30] Teixeira M.C., Godinho C.P., Cabrito T.R., Mira N.P., Sa'Correia I., Increased expression of the yeast multidrug resistance ABC transporter Pdr18 leads to increased ethanol tolerance and ethanol production in high gravity alcoholic fermentation, *Microbial Cell Facts*, 11(1) (2012) 98.
- [31] Kishimoto J., Ehama R., Wu L., Jiang S., Jiang N., Burgeson R.E., Re-Selective activation of versican promoter by epithelial-mesenchymal interactions during hair follicle development, *Proceedings of National Academy of Science (USA)*, 96 (1999) 7336-7341.
- [32] Martins N., Petropoulos S., Ferreira C.F.R., Chemical composition and bioactive compounds of garlic (*Allium sativum* L.) as affected by pre- and post-harvest conditions: A review, *Food Chemistry*, 211 (2016) 41-50.
- [33] Igbokwe P.K., Idogwu C.N., Nwabanne J.T., Enzymatic Hydrolysis and Fermentation of Plantain Peels: Optimization and Kinetic Studies, *Advances in Chemical Engineering and Science*, 6 (2016) 216-235.
- [34] Joshi J., Dhungana P., Prajapati B., Maharjan R., Poudyal P., Yadav M., Mainali M., Yadav A.P., Bhattarai T., Sreerama L., Enhancement of Ethanol Production in Electrochemical Cell by *Saccharomyces cerevisiae* (CDBT2) and *Wickerhamomyces anomalus* (CDBT7), *Frontier Energy Research*, 7 (2019) 70.
- [35] Rita H.R.B., Mariana S.T.A., Luísa S.S., Ana MRBX. Ethanol Production from Hydrolyzed Kraft Pulp by Mono- and Co-Cultures of Yeasts: The Challenge of C6 and C5 Sugars Consumption, *Energies*, 13(3) (2020) 744.
- [36] Olofssen K., Bertilsson M., Liden G., A short review on SSF – an interesting process option for ethanol production from lignocellulose feedstocks, *Biotechnology for Biofuels*, 1(7) (2008) 1-14.
- [37] Arotupin D.J., Evaluation of microorganisms from cassava waste for production of amylase and cellulase, *Resource Journal of Microbiology*, 2(5) (2007) 475-480.
- [38] Zhang P., Hai H., Sun D., Yuan W., Liu W., Ding R., Teng M., Ma L., Tian J., Chen C., A high throughput method for total alcohol determination in fermentation broths, *BMC Biotechnology*, 19 (2019) 30.

Effects of co-culturing *Schizochytrium* sp. and *Escherichia coli* cells on biomass and Docosaehaenoic acid (DHA) production

Deniz ŞAHİN^{1,*} 

¹Istanbul Technical University, Faculty of Science and Letters, Department of Molecular Biology and Genetics, Istanbul/TURKEY

Abstract

Heterotrophic marine microalga *Schizochytrium* sp. is one of the most studied microorganisms for docosaehaenoic acid (DHA) production. Several strategies were reported to enhance DHA production, including co-culturing algal cells with different microorganisms. In this study, *Schizochytrium* sp. and *Escherichia coli* were co-cultured to examine the effect of bacterial cells on the algal growth and DHA production. The cells were incubated for 168 h and recovered to analyze biomass production, lipid content and DHA yield in the mixed culture medium. Cultivation of algal and bacterial species together decreased the biomass production (g/L), total lipid concentration (ml/L), DHA yield (g/L) and DHA percentage in lipid content about 4.1, 1.7, 3.8 and 2.2 folds, respectively, compared to algal monoculture. The only increasing amount was obtained with DHA yield per biomass (mg/gCDW) which was about 1.1 fold higher in the mixed culture. The results showed that presence of *Escherichia coli* cells in the medium affected the growth of *Schizochytrium* sp. cells and DHA production negatively. It was estimated that the interaction between algal and bacterial cells were competition instead of mutualistic interaction in which bacterial cells outcompeted the algal cells and limited the cell density increase of algal cells in the mixed culture.

Article info

History:

Received: 01.05.2021

Accepted: 15.09.2021

Keywords:

Docosaehaenoic acid, Omega-3, *Schizochytrium* sp., *Escherichia coli*, Cocultivation.

1. Introduction

Docosaehaenoic acid (DHA) is one of the most important omega-3 fatty acids with their beneficial effects on human development and health [1, 2]. Although the most widely used source for DHA is cold water fish, increasing human population and consumption and decreasing fish stocks make development of alternative sources inevitable [3, 4].

Schizochytrium is a genus of heterotrophic marine microalgae and one of the most studied microorganism for DHA production. Obtained strains of *Schizochytrium* genus may be used to produce high amount of DHA (~100 g/L biomass production, 50-70% of cell dry weight as fatty acid and 30-70 % of lipids as DHA) [5]. Several studies were reported to enhance DHA production in *Schizochytrium* sp. including optimization of growth medium [6-8] using different carbon and nitrogen sources and co-culturing algal cells with different organisms [9-11].

Co-culturing microalgal cells with different organisms including other algal cells, yeast cells and bacterial cells is a promising strategy to increase biomass production and DHA yield. The interaction between

each pair of organisms needs to be studied carefully to analyze the outcome of co-culturing [10, 11]. Moreover, bacterial contamination is also an unintentionally formed co-cultured environment which needs to be analyzed in terms of effect on the DHA production. Although using organic-rich media may increase algal growth rate and lipid content, heterotrophic bacteria may proliferate quickly which may affect the growth of algae and production of lipid and DHA [12, 13].

In this study, *Schizochytrium* sp. and *Escherichia coli* cells were co-cultured to investigate the effect of microalgae-bacteria co-cultivation on algal growth and production yield of omega-3 fatty acids. Microalgal and bacterial cells were cultured together for 168 h of incubation. pH change of the growth medium, cell densities and biomass production for each cell type were recorded. Lipid production, fatty acid composition and DHA yield were calculated at the end of incubation period. The results indicated that co-cultivation of algal and bacterial species decreased the biomass production (g/L), total lipid concentration (ml/L), DHA yield (g/L) and DHA percentage in lipid content about 4.1, 1.7, 3.8 and 2.2 folds, respectively.

*Corresponding author. e-mail address: sahinden@itu.edu.tr

<http://dergipark.gov.tr/csj> ©2021 Faculty of Science, Sivas Cumhuriyet University

DHA yield (mg/gCDW) increased about 1.1 fold in the mixed culture compared to algal monoculture. The interaction between algal and bacterial cells were estimated as competition instead of mutualistic interaction in which bacterial cells outcompeted the algal cells and limited the cell density increase of algal cells in the mixed culture.

2. Materials and Methods

2.1. Algae and bacteria cells and growth conditions

Schizochytrium sp. S31 and *Escherichia coli* K12 strains were obtained from American Type Culture Collection (ATCC® 20888™ and ATCC® 10798™, respectively). The growth medium (Complex medium-CM) including glucose (40 g/L), yeast extract (5 g/L), peptone (8 g/L), NaCl (25 g/L) and MOPS (21 g/L) was used for the cultivation of the cells at 28°C on a shaker (200 rpm) [6]. pH of the starting medium was adjusted to 6.0. The samples were scaled up to 500 ml flasks containing 100 ml of CM (pH:6.0) with initial OD₆₀₀ and OD₆₀₀ for bacterial and algal cells, respectively, at 0.01 as starting cell concentration for monoculture and co-culture samples.

2.2. Measuring biomass production and growth rates

Microalgal and bacterial monocultures and the co-culture were incubated for 168 h at 28°C on a shaker (200 rpm). Samples were taken every 24 h to measure cell dry weight (CDW) and cell densities at OD₆₀₀ and OD₆₀₀ for *Escherichia coli* and *Schizochytrium* sp., respectively. Growth curves were formed for algal and bacterial monocultures and co-culture sample. Cell densities and daily biomass production were given in Figure 1. The change in pH values for algal and bacterial monocultures and the co-culture sample during incubation period were recorded and given in Figure 2.

2.3. Fatty acid composition analysis by Gas Chromatography

After 168 h of incubation, the cultures were centrifuged for 15 minutes at 3000xg (Optima MAX Ultracentrifuge) to precipitate the cells. Freeze-drying was applied on the precipitated cells (Christ-Alpha 1-2 LDplus) for 48 h to measure CDW. Following protocol was used for the lipid extraction process [6]. Briefly, n-hexane (FisherScientific) was mixed with culture

samples in 6:1 ratio (v/CDW) and sonicated for disruption of the cells (three bursts of 20 s). Disrupted cells were put on an orbital shaker (150 rpm) and incubated for 6 h at 27°C. Then, the cells were centrifuged at 3000g for 10 minutes to obtain supernatants. The supernatant samples were kept under fume hood until a viscous liquid was left the bottom of the tubes.

For the fatty acid composition determination, the extracted lipids from each sample were analyzed using GC-FID (Agilent Technologies 6890N), gas chromatography with flame ionization detector. The protocol which was used in our previous study was followed to prepare fatty acid methyl esters, cold esterification method and the conditions for the GC analysis [6].

3. Results and Discussion

3.1. Growth curves for *Schizochytrium* sp. and *Escherichia coli* monocultures and microalgae-bacteria co-culture

OD₆₀₀ and OD₆₀₀ absorbance values for *Schizochytrium* sp. and *Escherichia coli*, respectively, were measured every 24 h to plot growth curves for monoculture and co-culture samples. Figure 1 indicates both cell densities and cell dry weight measurements during the incubation period. Initial cell densities for each monoculture were arranged to OD value of 0.01. The co-culture sample was initiated with the same cell densities from both microalgae and bacteria cells, each having final OD value of 0.01.

At 24 h, algal monoculture had the lowest OD₆₀₀ value, around 0.13. On the other hand, cell densities in bacterial monoculture and co-culture increased quickly to OD 2.24 and 1.89, respectively. The growth in the co-culture was slower than the growth in the bacterial monoculture. The cell density increase in the co-culture sample was mainly due to bacterial cells which outcompeted the microalgal cells. After 24 h, cell density for algal monoculture started to increase and reached OD₆₀₀ of 2.03 at 48 h and kept increasing steadily till the end of the 168 h to OD₆₀₀ of 4.41. For the bacterial monoculture, cell density entered relatively a stationary phase after the 24 h and increased slowly to OD₆₀₀ value of 2.9 at the 168 h. Similar cell density trend was observed for the co-culture sample after the 24 h which increased slowly from 2.09 to 2.69 (OD₆₀₀ values) and 1.89 to 2.4 (OD₆₀₀ values).

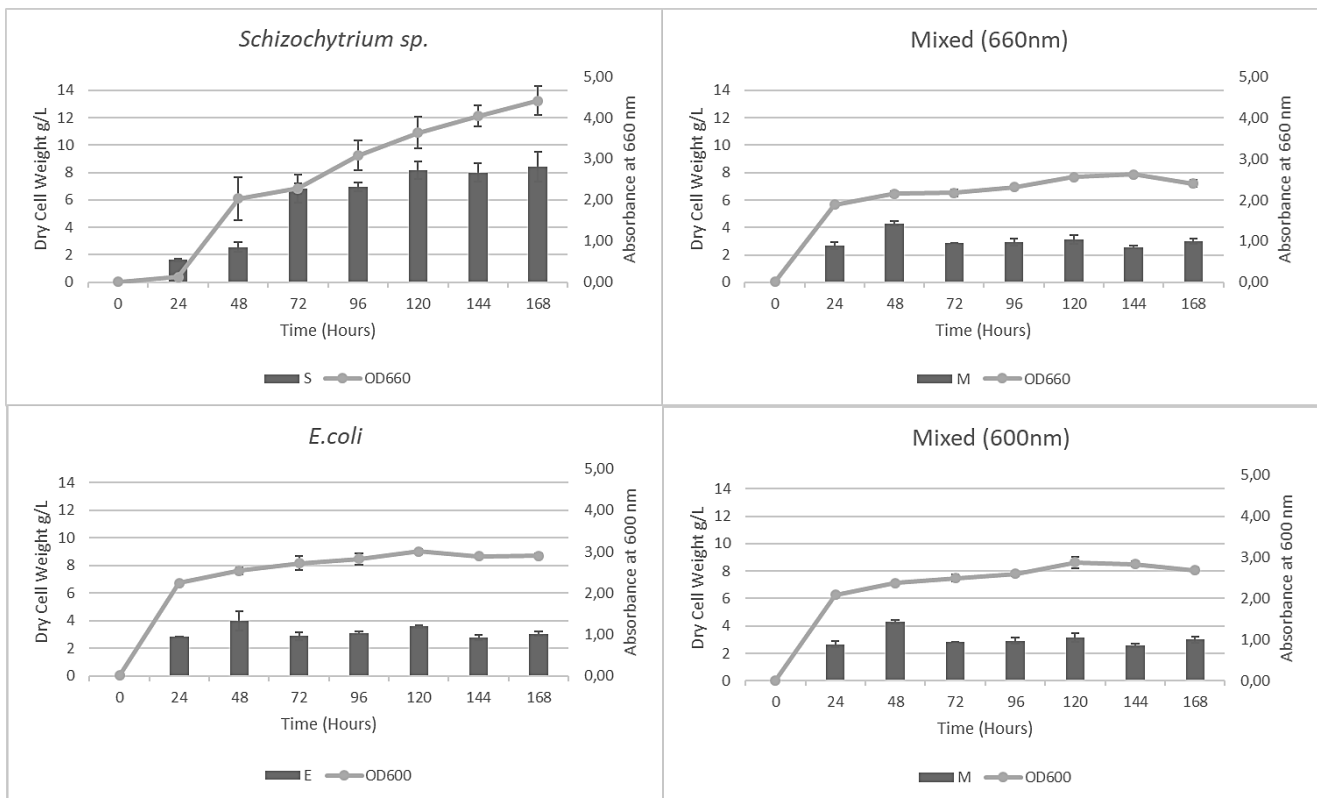


Figure 1. Cell densities (OD) and cell dry weights (CDW) for algal and bacterial monocultures and mixed co-culture sample. *Schizochytrium sp.* and *Escherichia coli* monocultures and co-culture sample were grown for 168 h at 28°C on a shaker (200 rpm). To measure cell density and cell dry weight for each culture, samples were collected from each flask every 24 h. OD₆₆₀ and OD₆₀₀ values were recorded for algal and bacterial cells, respectively. For the mixed culture, OD values (600-660 nm) were recorded.

For the algal monoculture, cell dry weight was measured as 1.62 g/L and 2.55 g/L at 24 and 48 h, respectively. After 48 h, CDW increased quickly to 6.82 g/L and entered relatively a stationary phase reaching 8.42 at the end of the 168 h. For the bacterial monoculture, CDW increased from 2.83 g/L at 24 h to 4 g/L at 48 h and then fluctuated between 2 and 4 g/L and ending with 3.05 g/L at 168 h. The maximum CDW was obtained at 48 h. Similar CDW pattern was observed for the co-culture sample, in which CDW increased from 2.68 g/L at 24 h to 4.30 g/L at 48 h which was the maximum for the co-culture sample. CDW for the co-culture was almost same with CDW of bacterial monoculture but less than CDW of algal monoculture.

Several studies in literature reports the effect of co-culturing the microalgae cells with different cell types on DHA production. The nature of the interaction between the cells in the mixed culture will determine the outcome of the growing environment. In our previous study [9], we co-cultured *Schizochytrium sp.* cells with *Rhodotorula glutinis* yeast cells and enhanced biomass, DHA and β -carotene production by ~2.6, ~1.18 and 1.76 fold, respectively. In that study, unlike the current study, the increase in biomass was high for both cell types, which was confirmed by

microscope examination. After all, we suggested that the interaction between these two heterotrophic species could be mainly competition between cells instead of the mutualistic interaction and the stress conditions due to quick increase in bacterial cell density caused an increase in DHA production by algal cells. Chierslip *et al.* (2011) and Dong and Zhao (2004) suggested that when photosynthetic algae and heterotrophic yeast were mixed, the algae could take a role of an oxygen generator while the yeast provides CO₂ to the algae. The increase in the growth of both cells may be due to the exchange of oxygen and carbon dioxide. We do not expect such an exchange-based cooperation here and in our previous work.

Microalgae and bacteria share same environments in nature and play crucial roles in ecosystem. Bacteria may affect the algal growth under autotrophic conditions either positively or negatively [15-19]. Bacterial cells promote growth of algae cells by reducing dissolved oxygen concentration and consuming the organic materials excreted by algae [20] and secreting biotin, cobalt amine and thiamine [21]. In return, algal cells provide oxygen and extracellular compounds which promotes the bacterial cells [15, 16]. This can be considered as a mutualistic relationship

between algal and bacterial cells based on mutual exchange of materials.

Higgins et al. (2014) co-cultured photosynthetic microalgae *Chlorella minutissima* with *Escherichia coli* under mixotrophic conditions to assess the effects of bacterial contamination on algal biofuel production. It was estimated that *E. coli* would dominate the microalgae cells for the nutrient sources. However, microalgal cells grew more rapidly than bacterial cells in co-cultured environment which was explained by symbiotic relationship between organisms. In a review by Subashchandrabose et al. (2013), mixotrophic cyanobacteria and microalgae co-culture was presented as bioremediation agents. The cells form a symbiotic interaction and cell densities of the both cell types increase. In our current study, the opposite was observed, with bacterial cells dominating, restricting the growth of algal cells.

In heterotrophic cultures, the species may primarily compete for the resources instead of forming a mutualistic interaction which may increase CDW and lipid production [23]. Cheirslip et al. (2011) suggests that increase in lipid production comes with increase in biomass. In the co-culture, first the cells increase in number in log phase benefiting from the rich medium [12, 24]. When one of the nutrients, particularly nitrogen, is limited, lipid production will initiate indicating that the cells are in stress. The change in pH due to growth and depletion of medium, will cause a decrease in O₂ levels, increase in CO₂ levels and decrease in cell growth in algae causing for lipid production.

Here, the aim of the study is to investigate the effects of co-culturing *Schizochytrium sp.* and *Escherichia coli* cells on the biomass and DHA production. Growth curves and CDW values indicate that bacterial cells outcompete the microalgal cells in the mixed culture. Indeed, observation of the mixed culture under microscopy verified that about 10-fold more surface coverage of bacterial cells than microalgal cells was observed. Although most of the biomass production in the mixed culture was due to the bacterial cell density, there was still a slow increase in cell density of microalgae cells. Bacterial cells were also affected negatively from the microalgal cells in the mixed environment which was observed from relatively lower OD₆₀₀ values. Although both cells were affected by the co-culture medium, algal cells were more affected. The result of the co-culture environment can be directly observed in the slowdown in the growth of algae cells.

3.2. Analysis of total biomass and total fatty acid production

After 168 h of incubation, the cells were collected by centrifugation, disrupted by sonication and finally freeze dried to obtain the cell dry weight. The samples were subjected to hexane extraction protocol to extract the fatty acid content of the cells for the gas chromatography analysis. Total biomass, total lipid concentration, and DHA yield after 168 h of incubation are listed in Table 1.

Table 1: Biomass production, lipid concentration and DHA yields for *Schizochytrium sp.* and *Escherichia coli* monocultures and the mixed culture. Co-culturing algal and bacterial species together decreased the biomass production (g/L), total lipid concentration (ml/L) and DHA yield (g/L) about 4.1, 1.7 and 3.8 folds, respectively, compared to algal monoculture. The only increasing amount was obtained with DHA yield per biomass (mg/gCDW) which was about 1.1 fold higher in the mixed culture.

	Total Biomass (g / L)	Total Lipid concentration (ml / L)	DHA Yield (g / L)	DHA Yield (mg / gCDW)
Schizochytrium sp. (S)	7.74 ± 1.207	0.92	0.249	32.27
E.coli (E)	2.74 ± 1.61	0.51	0.055	20.19
Co-cultivation (S+E)	1.89 ± 0.26	0.53	0.066	35.05

The highest biomass production was observed in algal monoculture at 7.74 g/L CDW which was about three times more than that of bacterial monoculture at 2.74 g/L CDW. Mixed co-culture sample had the lowest biomass production at 1.89 g/L. Both species in the

mixed culture sample were affected negatively by the presence of the other species.

Total lipid production for algal monoculture was 0.92 ml/L which was higher than bacterial and mixed cultures at 0.51 ml/L and 0.53 ml/L, respectively. On the other hand, lipid production per CDW for the

mixed culture was more than algal and bacterial monocultures. CDW values indicate that co-culturing *Schizochytrium sp.* and *E. coli* cells did not enhance the total biomass production. The bacterial density increased rapidly and dominated the algal cells. Therefore, the biomass contribution of algal cells was constrained. In our previous study [9], we achieved the maximum biomass production in *Schizochytrium sp.* and *Rhodotorula glutinis* co-cultured medium, although total lipid production was lower in co-cultured medium than that of algal monoculture.

In mixed culture, each cell type will contribute to total lipid production at different rates. Densities of algal and bacterial cells and the lipid production from each cell type will determine the contribution of algal and bacterial cells in the final lipid production. Here, we had about 4.1-fold more biomass production in algal monoculture than the mixed culture, yet the lipid production in algal monoculture was just about 1.8-fold more than both bacterial monoculture and the mixed culture. Even though 1.45 fold less biomass production was observed in the mixed culture than bacterial monoculture, lipid productions were almost same which shows the contribution of algal cells on the lipid content in the mixed sample. Several parameters such as culture medium, pH and temperature of the medium and the nature of each cell type will be effective on the lipid accumulation. A balanced environment is needed for the maximum biomass production and final lipid content otherwise one of the species in the co-cultured medium could predominate the system and affect the growth of others negatively [9].

3.3. Fatty acid composition analysis and DHA yield determination

Fatty acid composition analysis for algal and bacterial monocultures and the mixed culture at the end of 168 h of incubation was shown in Table 2. The table includes omega-3, omega-6 and other fatty acids. Among the omega-3 fatty acids, DHA amounts (% w/v) were 27.15%, 10.85% and 12.50% for algal monoculture, bacterial monoculture and the co-culture samples, respectively. The highest DHA content was achieved with algal monoculture. On the other hand, there was about 2.17-fold decrease in DHA content in the mixed culture than algal monoculture.

Other omega-3 fatty acids, Eicosapentaenoic acid, α -Linolenic acid and Eicosatrienoic acid, were also produced in smaller amounts compared to DHA production. In algal monoculture, EPA production was 1.92% which decreased about 2.5 fold in the mixed culture. α -Linolenic acid production increased in mixed culture which was not detected in algal monoculture.

Schizochytrium sp. is known as a high DHA producer species [6]. Here, DHA content in total extracted fatty acid was 27.15% (%w/v) in the algal monoculture medium which can be enhanced by different medium conditions [6]. Although total lipid production in bacterial monoculture and mixed co-culture samples are almost same, the percentage of DHA in the total fatty acid content is higher in co-culture sample possibly due to contribution of slowly growing algal cells in the medium.

In our previous study [9], DHA production was enhanced in *Schizochytrium sp.* and yeast *Rhodotorula glutinis* mixture. The interaction was possibly competition instead of mutualism which put the algal cells in stress. On the other hand, algal cells kept increasing their density which was not observed here. The increase in algal density in the mixed co-culture was very slow in the current study. In our previous study, both of the cells increased their numbers and kept producing DHA under stress conditions. On the contrary, the algal cells in the mixed culture here was in stress conditions contributing DHA production but cell density increase was limited.

DHA yield (g/L) decreased about 4 fold in the mixed culture which was about 1.25 fold more than bacterial culture (Table 1). On the other hand, DHA yield (mg/gCDW) in the mixed culture was about 1.75 fold higher than that of bacterial monoculture indicating that *E. coli* cells in the mixed culture contribute to the fatty acid production but DHA production is due to algal contribution.

Altogether, growing algal cells with bacterial cells caused a decrease in cell density, biomass production and DHA percentage in lipid content. On the other hand, DHA yield was enhanced per CDW indicating higher fatty acid production in a decreasing biomass.

Table 2: Fatty acid composition (%: w/v) of oil extracts from *Schizochytrium sp.* (S), *Escherichia coli* (E) and the co-culture (S+E) samples according to Gas chromatography-FID analysis. DHA content for S+E sample decreased ~2.2 fold compared to S sample. (ND: Not detected)

	S	E	S+E
Omega-3			
Docosahexaenoic acid (C22:6 n-3)	27.15	10.85	12.5
Eicosapentaenoic acid (C20:5 n-3)	1.92	ND	0.77
α -Linolenic acid (C18:3 n-3)	0.05	0.41	0.69
Eicosatrienoic acid (C20:3n-3)	0.47	ND	ND
Omega-6			
γ -linolenic acid (C18:3 n-6)	0.21	ND	0.11
Others			
Palmitic acid (C16:0)	39.05	25	26.55
Myristic acid (C14:0)	15.35	6.8	8.42
Palmitoleic acid (C16:1)	3.68	1.59	1.98
Oleic acid (C18:1n+9c)	3.59	2.42	3.08
Stearic acid (C18:0)	2.82	27.16	14.58
Pentadecanoic acid (C15:0)	2.62	0.96	1.33
Lauric acid (C12:0)	0.75	1.27	1.42
Margaric acid (C17:0)	0.57	18.46	24.58
Erucic acid C22 1n-9	0.56	0.3	0.27
Tridecanoic acid (C13:0)	0.24	0.16	0.99
Behenic acid (C22:0)	0.22	0.11	0.16
Lignoceric acid (C24:0)	0.2	0.22	0.35
Nervonic acid (C24:1)	0.19	0.59	ND
Arachidic acid (C20:0)	0.09	0.71	0.32
Myristoleic acid (C14:1)	0.08	0.15	0.19
Heptadecenoic acid (C17:1)	ND	2.48	ND
γ -linoleic acid (C18:2n+6c)	ND	0.23	1.14
Heleicosanoic acid (C21:0)	ND	0.11	0.17
Eicosenoic acid (C20:1)	ND	ND	0.25
Eicosadienoic (C20:2)	ND	ND	0.17

3.4 pH variations

pH values for algal and bacterial monocultures and the mixed culture during 168 h of incubation period were given in Figure 2. pH value for the algal monoculture remained between 5.4 and 6.0 which was higher than pH values of bacterial monoculture and the mixed culture samples. For both of the bacterial monoculture and the mixed culture, pH of the media decreased quickly below 5.0 after 24 h of incubation and then fluctuated between pH 4.2 and 5.0, following a similar pattern during incubation period.

Initial decrease in pH in all of the samples can be explained with the initial increase in cell density in all monoculture and mixed culture species. Wu et al. (2005) suggested that reduction in pH was due to the secretion of organic acids such as succinic acid, pyruvic acid, and malic acid. Here, we observed a quick increase in cell densities of bacterial cells in monoculture and mixed co-culture which may cause an increase in CO₂ concentration decreasing pH of the

medium. Increase in pH between 24 and 72 h in all mediums, specifically algal medium, indicates that CO₂ was used for lipid production metabolism [26]. Addition of bacterial cells to the growth medium after 24 h of algal incubation may change the nature of the interaction between the cells and in this way different pH and lipid production can be observed.

Here, the aim of the study was to investigate the effects of co-culturing *Schizochytrium sp.* and *Escherichia coli* cells on the growth and biomass production of algal cells and DHA yield. The results indicated that algal and bacterial cells did not form a mutualistic interaction and the presence of bacterial cells affected the algal cells negatively. The density of the bacterial cells increased quickly which caused a decrease in the pH of the medium and growth and biomass production of algal cells. DHA yield per liter of culturing medium also decreased in the mixed culture compared to algal monoculture.

For further studies, bacterial cells can be added to the growth medium after algal cells have passed the lag phase and reached a certain cell density. Similarly, starting cell density of the algal cells can be increased in the co-culture medium. For both conditions, the interaction between bacterial and algal cells may be

affected by different cell densities of each cell type, resulting in different amounts of lipid and DHA production. Additionally, using different growth medium conditions as we reported in our previous studies may affect CDW and lipid production and DHA content.

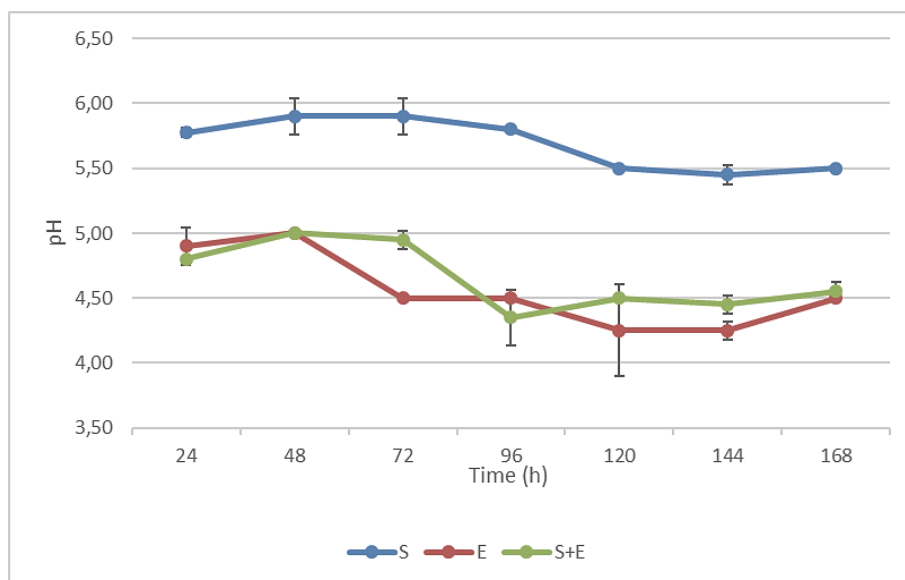


Figure 2.: pH change of the incubation mediums with time. pH values for *Schizochytrium* sp. (S), *Escherichia coli* (E) monocultures and the mixed culture sample (S+E) were measured every 24 h. pH for each medium was arranged to 6.0 at t=0 h. pH of the S medium was between 5.4 and 6, while for E and S+E mediums, pH values decreased quickly in the first 24 h and fluctuated between 4.2 and 5.0 values till the end of 168 h of incubation.

Conflicts of interest

The author declares that there is no conflict of interest.

References

- [1] Connor W.E., Importance of n-3 fatty acids in health and disease, *Am. J. Clin. Nutr.*, 71 (2000) 171-175.
- [2] Simopoulos A.P., Omega-3 fatty acids in inflammation and autoimmune diseases, *J. Am. Coll. Nutr.*, 21(6) (2002) 495-505.
- [3] Leite G.B., Abdelaziz A.E.M., Hallenbeck P.C., Algal biofuels: Challenges and opportunities, *Bioresour. Technol.*, 145 (2013) 134-141.
- [4] Ochsenreither K., Gluck C., Stressler T., Fischer L., Syldatk C., Production Strategies and Applications of Microbial Single Cell Oils, *Front Microbiol*, 7 (2016) 1539.
- [5] Aasen I.M., Ertesvåg H., Heggeset T.M., Liu B., Brautaset T., Vadstein O., Ellingsen T.E., Thraustochytrids as production organisms for docosahexaenoic acid (DHA), squalene, and carotenoids, *Appl. Microbiol. Biotechnol.*, 100(10) (2016) 4309-21.
- [6] Sahin D., Tas E., Altindag U.H., Enhancement of docosahexaenoic acid (DHA) production from *Schizochytrium* sp. S31 using different growth medium conditions, *AMB Express.*, 8(7) (2018).
- [7] Chatdumrong, W., Yongmanitchai W., Limtong S., Worawattanamatekul S., Optimization of docosahexaenoic acid (DHA) production and improvement of astaxanthin content in a mutant *Schizochytrium limacinum* isolated from mangrove forest in Thailand, *Nat. Sci.*, 41 (2007) 324-334.
- [8] Patil K.P., Gogate P.R., Improved synthesis of docosahexaenoic acid (DHA) using *Schizochytrium limacinum* SR21 and sustainable media, *J. Chem. Eng.*, 268 (2015) 187-196.
- [9] Sahin D., Altindag U.H., Tas E., Enhancement of

- docosahexaenoic acid (DHA) and beta-carotene production in *Schizochytrium* sp. using symbiotic relationship with *Rhodotorula glutinis*, *Process Biochemistry*, 75 (2018) 10-15.
- [10] Cheirsilp B, Suwannarat W, Niyomdecha R, Mixed culture of oleaginous yeast *Rhodotorula glutinis* and microalga *Chlorella vulgaris* for lipids production from industrial wastes and its use as biodiesel feedstock, *N. Biotechnol.*, 28(4) (2011) 362-368.
- [11] Santos C.A., Reis A., Microalgal symbiosis in biotechnology, *Appl. Microbiol. Biotechnol.*, 98(13) (2014) 5839-5846.
- [12] Zhang Y., Su H., Zhong Y., Zhang C., Shen Z., Sang W., Yan G., Zhou X., The effect of bacterial contamination on the heterotrophic cultivation of *Chlorella pyrenoidosa* in wastewater from the production of soybean products, *Water Research*, 46(17) (2012) 5509-5516.
- [13] Han J., Zhang L., Wang S., Yang G., Zhao L., Pan K., Co-culturing bacteria and microalgae in organic carbon containing medium, *J. Biol. Res. (Thessalon)*. 23 (2016) s40709.
- [14] Dong Q.L., Zhao X.M., In situ carbon dioxide fixation in the process of natural astaxanthin production by a mixed culture of *Haematococcus pluvialis* and *Phaffa rhodozyma*. *Catal. Today*, 98(4) (2004) 537-544.
- [15] de-Bashan L.E., Bashan Y., Moreno M., Lebsky V.K., Bustillos J.J., Increased pigment and lipid content, lipid variety, and cell and population size of the microalgae *Chlorella* spp. When coimmobilized in alginate beads with the microalgae growth promoting bacterium *Azospirillum brasilense*, *Can. J. Microbiol.*, 48 (2002) 514-21.
- [16] Ethier S., Woisard K., Vaughan D., Wen Z., Continuous culture of the microalgae *Schizochytrium limacinum* on biodiesel-derived crude glycerol for producing docosahexaenoic acid, *Bioresour Technol.* 102 (2011) 88–93.
- [17] Lorincz Z., Preininger E., Kósa A., Pónyi T., Nyitrai T., Sarkadi L., Artificial tripartite symbiosis involving a green alga (*Chlamydomonas*), a bacterium (*Azotobacter*) and a fungus (*Alternaria*): morphological and physiological characterization, *Folia Microbiol. (Praha)*, 55 (2010) 393–400.
- [18] Ortiz-Marquez J.C., Do Nascimento M., Dublan Mde L., Curatti L., Association with an ammonium-excreting bacterium allows diazotrophic culture of oil-rich eukaryotic microalgae, *Appl. Environ. Microbiol.*, 78 (2012) 2345–52.
- [19] Subashchandrabose S.R., Ramakrishnan B., Megharaj M., Venkateswarlu K., Naidu R., Mixotrophic cyanobacteria and microalgae as distinctive biological agents for organic pollutant degradation, *Environ. Int.*, 51 (2013) 59-72.
- [20] Mouget J.L., Dakhama A., Lavoie M.C., de la Noüe J., Algal growth enhancement by bacteria: is consumption of photosynthetic oxygen involved?, *FEMS Microbiol. Ecol.*, 18 (1995) 35–43.
- [21] Croft M.T., Lawrence A.D., Raux-Deery E., Warren M.J., Smith A.G., Algae acquire vitamin B12 through a symbiotic relationship with bacteria, *Nature*, 438 (2005) 90–3.
- [22] Higgins B.T., VanderGheynst J.S., Effects of *Escherichia coli* on mixotrophic growth of *Chlorella minutissima* and production of biofuel precursors, *PLoS One*, 9(5) (2014) e96807.
- [23] Perez-Garcia O., Escalante F.M.E., de-Bashan L.E., Bashan Y., Heterotrophic cultures of microalgae: Metabolism and potential products, *Water Res.*, 45(1) (2011) 11-36.
- [24] Kot A.M., Blazejak S., Kurcz A., Gientka I., Kieliszek M., *Rhodotorula glutinis*-potential source of lipids, carotenoids, and enzymes for use in industries, *Appl. Microbiol. Biotechnol.*, 100(14) (2016) 6103-6117.
- [25] Wu S.T., Yu S.T., Lin L.P., Effect of culture conditions on docosahexaenoic acid production by *Schizochytrium* sp S31, *Process Biochem.*, 40(9) (2005) 3103-3108.
- [26] Magdouli S., Brar S.K., Blais J.F., Co-culture for lipid production: Advances and challenges, *Biomass Bioenergy*, 92 (2016) 20-30.



Some old 2-(4-(Aryl)- thiazole-2-yl)-3a,4,7,7a-tetrahydro-1H-4,7-tethanoisoindole-1,3(2H)-dione derivatives: Synthesis, inhibition effects and molecular docking studies on Aldose reductase and α -Glycosidase

Parham TASLİMİ¹ , Yeliz DEMİR² , Hatice Esra DURAN³ , Ü.Muhammet KOÇYİĞİT⁴
Burak TUZUN^{5,*} , Osman Nuri ASLAN⁶ , Mustafa CEYLAN⁶ , İlhami GÜLÇİN⁷

¹ Bartın University, Faculty of Science, Department of Biotechnology, Bartın 74100, TURKEY

² Ardahan University, Nihat Delibalta Göle Vocational High School, Department of Pharmacy Services, Ardahan, TURKEY

³ Kafkas University, Faculty of Medicine, Department of Medical Biochemistry, 36100, Kars, TURKEY

⁴ Sivas Cumhuriyet University, Faculty of Pharmacy, Department of Basic Pharmaceutical Sciences, Division of Biochemistry, 58140 Sivas, TURKEY

⁵ Sivas Cumhuriyet University, Sivas Vocational School of Technical Sciences, Department of Organic Agriculture, Department of Crop and Animal Production, 58140-Sivas, TURKEY

⁶ Gaziosmanpasa University, Faculty of Arts and Sciences, Department of Chemistry, Tokat, TURKEY

⁷ Atatürk University, Faculty of Science, Department of Chemistry, 25240 Erzurum, TURKEY

Abstract

Utilizing the simple chromatic techniques, Aldose reductase (AR) was derived from sheep liver. In addition, α -glycosidase from *Saccharomyces cerevisiae* was used as the enzyme. It was determined the interactions between compounds and the enzymes. Molecular docking method used to compare biological activity values of molecules against enzymes.

In the current study, the inhibition effect of synthetic isoindol-substitute thiazole derivatives (**3a-f**) on AR, and α -glycosidase enzymes was studied. In the thiazole series, compound **3b** (K_i : $9.70 \pm 4.72 \mu\text{M}$) showed a maximum inhibitory impact towards AR while compound **3f** (K_i : $44.40 \pm 17.18 \mu\text{M}$) showed a lowest inhibitory impact towards AR. It was investigated potent inhibition profiles with K_i values in the range of 24.54 ± 6.92 – $44.25 \pm 10.34 \mu\text{M}$ against α -glycosidase. Theoretical results were found consistent with experimental results.

Acting as antidiabetic agents, these compounds have the potential to be the selective inhibitor of α -glycosidase and AR enzymes. The biological activities of the studied molecules against AR and α -glycosidase enzymes will be compared with molecular docking method. ADME analysis of the molecules will be done.

Article info

History:

Received: 16.03.2021

Accepted: 20.09.2021

Keywords:

Asymmetric synthesis, Enzyme inhibition, Aldose reductase, α -Glycosidase, Molecular docking.

1. Introduction

In general, naturally occurring, isoindole-1,3-dione is important for sustaining a desired life quality. Extracts of isoindole-1,3-dione have long been the focus for their antifungal, antibacterial, antimicrobial [1], hypoglycemic [2], anti-tumor [3], anti-inflammatory [4], anticovulsants [5], and anti-inflammatory [6]. High blood sugar resulting from the complete or partial deficiency in the secretion of insulin is one of the characteristics of diabetes mellitus. Long-term

complications of diabetes are found to be tightly linked with the chronic hyperglycemia of diabetes. Cataracts of both eyes, cardiovascular complications, retinopathy, nephropathy and neuropathy are among the major complications [7].

Under hyperglycemic conditions, various biochemical pathways are activated. The polyol pathway comprises the most promising and the most widely studied one. The polyol pathway is functional in the metabolization of excessive glucose. Through polyol pathway, glucose is transformed to sorbitol by aldose reductase (AR) [8].

*Corresponding author. e-mail address: btuzun@cumhuriyet.edu.tr

Some studies have displayed the connection between glucose metabolism and long-term complications of diabetes via the polyol pathway. Within the polyol pathway, AR is the crucial enzyme that gives rise to diabetic complications [9]. In the prevention and attenuation of diabetic complications, AR inhibition plays a crucial factor. As a result, the synthesis of new and useful AR inhibitors (ARIs) having antioxidant properties is of great importance [10].

In the small intestine, α -glycosidase hydrolyzes polysaccharide and oligosaccharides to such monosaccharide units as fructose and glucose [8]. α -glycosidase inhibitors (α -GIs) possess key role in keeping human hyperglycemia and type-2 diabetes mellitus (T2DM) under control. α -GIs can repress T2DM and postprandial hyperglycemia and reduce the absorption of carbohydrates through diet. Hence, these types of α -GIs have a sugar molecule that competes with oligosaccharides in binding with the active site of the enzyme, thus efficiently decreasing the amounts of postprandial glucose in T2DM [11].

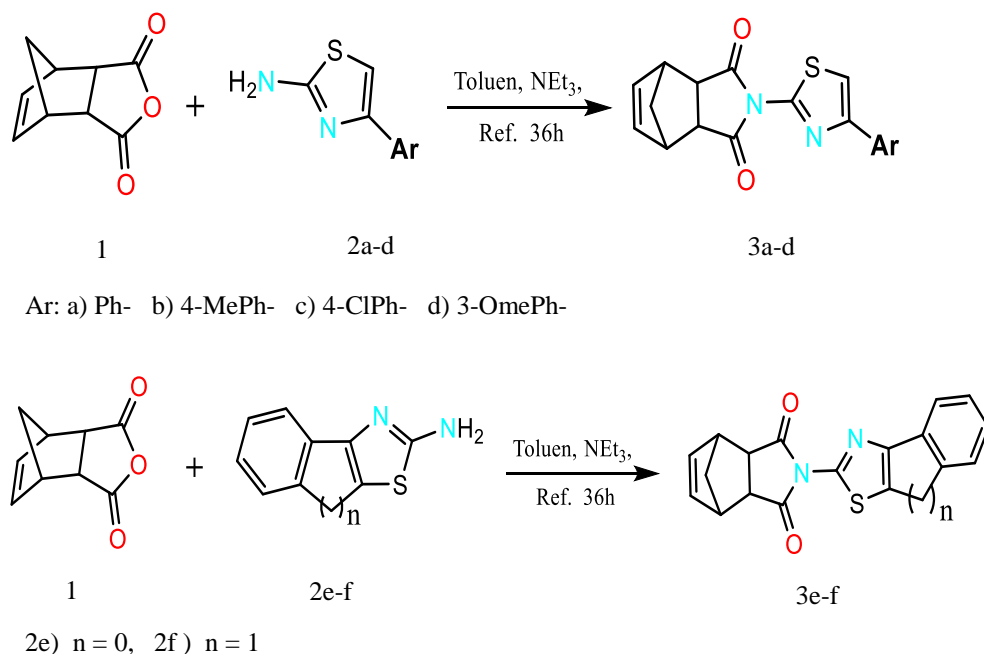
There are many experimental and theoretical methods to calculate the numerical values of the activities of molecules in studies conducted today. Because of both

time and money, theoretical methods have developed too much. Molecular docking is also one of these methods. It should be well known that molecular docking is a common method used to evaluate the molecular level biological activity against certain enzymes [12-13]. In this study, thiazole derivatives (3a-f) against enzymes, which are AR whose ID is 3V36, and α -glycosidase whose ID is 1XSI, were compared for their biological activities. In the present paper, the in vitro inhibition impacts of isoindole-1,3(2H)-dione derivatives (3a-f) on AR and α -glycosidase as metabolic enzymes were studied, and the molecular docking properties were determined.

2. Material and Methods

2.1. Chemistry

From the isoindol-substitute thiazole derivatives, a synthesis (3a-f) was carried out in line with to the steps explained in our previous study [14]. From the reaction of thiazole derivatives (2a-f) with dicarboxylic anhydride (1) in the presence of NEt_3 , the compounds 3a-f were synthesized. The spectral data of all compounds are in agreement with the data reported previously [14].



Scheme 1. Synthesis route of investigated compounds in this study

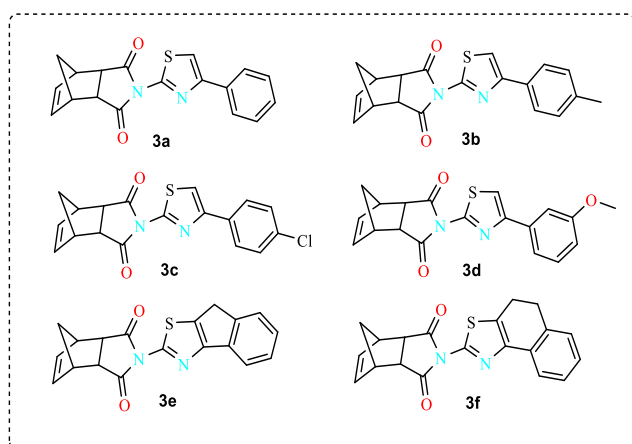


Figure 1. The tested compounds in this study

2.2. Biological studies

2.2.1. α -Glycosidase enzyme assay

α -Glycosidase enzyme was assayed according to previous study [15].

2.2.2. The analysis of AR activity

The analysis of AR activity was conducted the decrease of NADPH as 340 nm spectrophotometrically [16].

2.2.3. Purification of AR

AR enzyme was purified using, DE-52 cellulose, Sephadex G-100 and 2'5'-ADP-Sepharose-4B affinity from sheep liver [17]. Quantitative amounts of AR enzyme were determined in line with the Bradford procedure at 595 nm, spectrophotometrically [18]. The purity level of the enzyme was determined in line with the Laemmli's method [28] as explained previously [19-21].

2.2.4. Enzyme inhibition analysis

In order for determining the effect of isoindol-substitute thiazole derivatives on α -glycosidase, and AR, various concentrations of them were included into the reaction medium. The IC_{50} values were calculated from activity (%) versus some isoindol-substitute thiazole concentration plots. The K_i values were determined by Lineweaver and Burk's curves [22].

2.2.5. Docking studies

Nowadays there are many methods to calculate the molecular activities [23]. One of the most common methods is molecular docking. For molecular docking calculations, optimized structures of molecules are calculated by using the Gaussian Package program [24]. The optimized structures of the molecules were calculated by the Gaussian software program. The structures of the optimized molecules are obtained from *.pdb files.

Molecular docking calculations of the studied molecules were done using Maestro Molecular Modeling platform (version 12.2) by Schrödinger, LLC [25]. Crystal structures of enzyme proteins have been downloaded from the Protein Data Bank (PDB) site. The enzymes studied are AR that is ID: 3V36 [26], and α -glycosidase that is ID: 1XSI [27], respectively. The pH 7.0 ± 2.0 range was used in all calculations for the interaction of isoindol-substitute thiazole derivatives with enzymes. Enzymes that interact with molecules are made up of many proteins. Studied proteins were prepared for calculations using the protein preparation module [28], for calculations.

Later, the proteins in the active regions of the studied proteins were prepared for interactions. The preparation process of the molecules was started. Optimized structures of isoindol-substitute thiazole derivatives were obtained from the Gaussian software program [24]. The drawn structures were prepared for molecular docking calculations using LigPrep module [29]. 3D structures of isoindol-substitute thiazole derivatives were obtained. The Glide ligand docking module [30] was used for the interaction of isoindol-substitute thiazole derivatives with enzymes.

Following, ADME analysis was performed to examine the use of isoindol-substituted thiazole derivatives as drugs in future experimental studies. The Qik-prop module of Schrödinger software [31] was used to perform this analysis. many parameters are calculated using this module. With these parameters, information is obtained about the properties of the molecules.

3. Results and Discussion

AR has been linked to diabetes complications such as nephropathy, cataractogenesis, retinopathy and neuropathy. Hence, ARIs are used the therapeutic approach in the treatment complications of the diabetic. The development of reliable and novel ARIs is necessary to enhance the quality of life for patients with diabetic [32].

In the present study, synthetic isoindol-substitute thiazole derivatives (3a-f) were studied for their potential to inhibit the AR enzyme. In order for this, AR was the purified from sheep liver. The enzyme was obtained with a specific activity of 1.48 EU/mg protein and 113.85-fold purification (Table 1). SDS-PAGE was done following the purification of the AR enzyme. (Figure 2). The molecular weight of AR was determined as about 38 kDa. There is a growing demand for new and potent ARIs. The primary objective of this study was to recognize extremely useful and potent inhibitors for AR and α -glycosidase.

The inhibitory effect results of studied isoindole-substitute thiazole derivatives are displayed in Table 2.

In the related literature, there are some research about the inhibitory effect of AR. For instance, Stefek et al. [33] investigated 15 different compounds, which display an indole-1-acetic acid moiety inhibit AR. Fatmawati et al. [34] isolated prenylated xanthenes from *Garcinia mangostana* Linn. They found that 3-isomangostin showed a better inhibitory effect against AR, with an IC_{50} of 3.48 μ M. In another study, Ali et al. [35] synthesized and evaluated iminothiazolidin-4-one acetate derivatives were as AR inhibitors. The highest AR inhibitory potency in the series was evaluated for 2k with IC_{50} values 2.54 mM, respectively. In another study, Taslimi et al. [36] studied the inhibitory impact of bromophenols, diarylmethanes, and diarylmethanones on AR. In that study, it was found that 2d showed the best inhibition effect for AR. Demir et al. [10] displayed the effects of diarylmethanones and bromophenols on α -glycosidase and AR. They reported that 2d showed the best inhibition effect for α -glycosidase and 1f for AR.

The synthetic isoindol-substitute thiazole derivatives (3a-f) displayed a potent inhibition towards AR. K_i values order of compounds exhibiting inhibitory potency was 3b (9.70 \pm 4.72 μ M) > 3a (10.03 \pm 0.51 μ M) > 3e (19.82 \pm 1.99 μ M) > 3d (21.22 \pm 3.33 μ M) > 3c (26.62 \pm 2.63 μ M) > 3f (44.40 \pm 17.18 μ M) against purified AR. In the thiazole series, compound 3b exhibited a maximum inhibitory impact against AR while compound 3f showed a lowest inhibitory effect against AR. When an internal comparison is conducted between the compounds 3a and 3b, the addition of the methyl group in the aromatic ring on 3b has shown better inhibitory activity. Replacement of methyl group in 3b with chloro ion (3c) exhibited lower inhibitory activity. Adding methoxy group to 3a decreased to inhibitory effect. (3d K_i : 21.22 \pm 3.33 μ M). In this series

derivatives, the methyl group may be more a in AR inhibition according to our results.

α -Glycosidase hydrolyzes to polysaccharide and oligosaccharides to such monosaccharides as fructose and glucose. It also hydrolyzes the final stage in the digestive activity of carbohydrates [37,38] α -glycosidase inhibitors have the potential of preventing complications resulting from diabetic conditions [39].

In addition, the α -glycosidase enzyme was studied in the current paper. Studied compounds (3a-f) were determined for their inhibition impacts towards α -glycosidase enzyme, which displayed a significant inhibition commonly. The results of this research can be seen from Table 2. For this enzyme, the compounds had IC_{50} values in 19.75-30.25 range and K_i values in 24.54 \pm 6.92-44.25 \pm 10.34 μ M range (Table 2). The results displayed that all studied compounds had a rather parent α -glycosidase inhibitory effects in comparison to that of acarbose (IC_{50} : 22800 nM) as the standard α -glycosidase inhibitor. The order of compounds with K_i values exhibiting inhibition effect was 3c (24.54 \pm 6.92 μ M) > 3f (27.94 \pm 03.44 μ M) > 3e (29.16 \pm 4.51 μ M) > 3a (30.85 \pm 5.82 μ M) > 3b (37.03 \pm 3.05 μ M) > 3d (44.25 \pm 10.34 μ M) against α -glycosidase. In the thiazole series, compound 3c displayed a maximum inhibitory impact towards α -glycosidase while compound 3d showed a lowest inhibitory impact towards α -glycosidase (Figure 3 and 4). When the 3a and 3b compounds are evaluated among themselves, the addition of the methyl group in the aromatic ring on 3b has shown lower inhibitory activity by contrast with AR enzyme. Replacement of methyl group in 3b with chloro ion (3c) exhibited better inhibitory activity. Adding methoxy group to 3a decreased to inhibitory effect. (3d K_i : 44.25 \pm 10.34 μ M).

Table 1. Purification steps of AR from sheep liver

Purification Steps	Activity (EU/mL)	Total volume (mL)	Protein (mg/mL)	Total protein (mg)	Total activity (EU)	Specific activity (EU/mg)	Yield (%)	Purification fold
Homogenate	0.30	20	23.43	468.60	6.00	0.013	100	1
Ammonium sulfate precipitation and dialysis	0.33	16	19.15	306.40	5.28	0.017	88.00	1.31
DE-52 Cellulose anion exchange chromatography	0.17	10	5.43	54.30	1.70	0.031	28.33	2.38
Sephadex G-100 gel filtration chromatography	0.095	6	0.84	5.04	0.57	0.113	9.50	8.69
Affinity chromatography	0.013	3	0.009	0.027	0.040	1.48	0.67	113.85

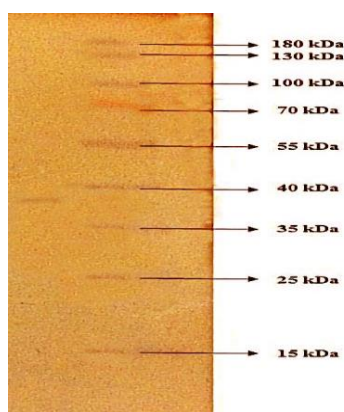


Figure 2. SDS–PAGE analysis of purified AR which obtained single band

Table 2. Inhibition effects of some isoindole- 1,3(2H)-dione derivatives on α -glycosidase and purified AR from sheep liver

Chemical names	STRUCTURES of MOLECULES	AR		α -Glycosidase	
		K_i (μ M)	IC_{50}	K_i (μ M)	IC_{50}
(3aR,4S,7R,7aS)-2-(4-phenylthiazol-2-yl)-3a,4,7,7a-tetrahydro-1H-4,7-methanoisoindole-1,3(2H)-dione (3a)		10.03±0.51	12.16	30.85±5.82	24.54
(3aR,4S,7R,7aS)-2-(4-(p-tolyl)thiazol-2-yl)-3a,4,7,7a-tetrahydro-1H-4,7-methanoisoindole-1,3(2H)-dione (3b)		9.70±4.72	10.83	37.03±3.05	28.17
(3aR,4S,7R,7aS)-2-(4-(4-chlorophenyl)thiazol-2-yl)-3a,4,7,7a-tetrahydro-1H-4,7-methanoisoindole-1,3(2H)-dione (3c)		26.62±2.63	28.88	24.54±6.92	19.75
(3aR,4S,7R,7aS)-2-(4-(3-methoxyphenyl)thiazol-2-yl)-3a,4,7,7a-tetrahydro-1H-4,7-methanoisoindole-1,3(2H)-dione (3d)		21.22±3.33	17.77	44.25±10.34	30.25
(3aR,4S,7R,7aS)-2-(8H-indeno[1,2-d]thiazol-2-yl)-3a,4,7,7a-tetrahydro-1H-4,7-methanoisoindole-1,3(2H)-dione (3e)		19.82±1.99	16.50	29.16±4.51	23.11
(3aR,4S,7R,7aS)-2-(4,5-dihydronaphtho[1,2-d]thiazol-2-yl)-3a,4,7,7a-tetrahydro-1H-4,7-methanoisoindole-1,3(2H)-dione (3f)		44.40±17.19	36.48	27.94±3.44	20.83
ACR*		-	-	12600±780	2800

* Acarbose (ACR) was used as positive control for α -glycosidase enzyme

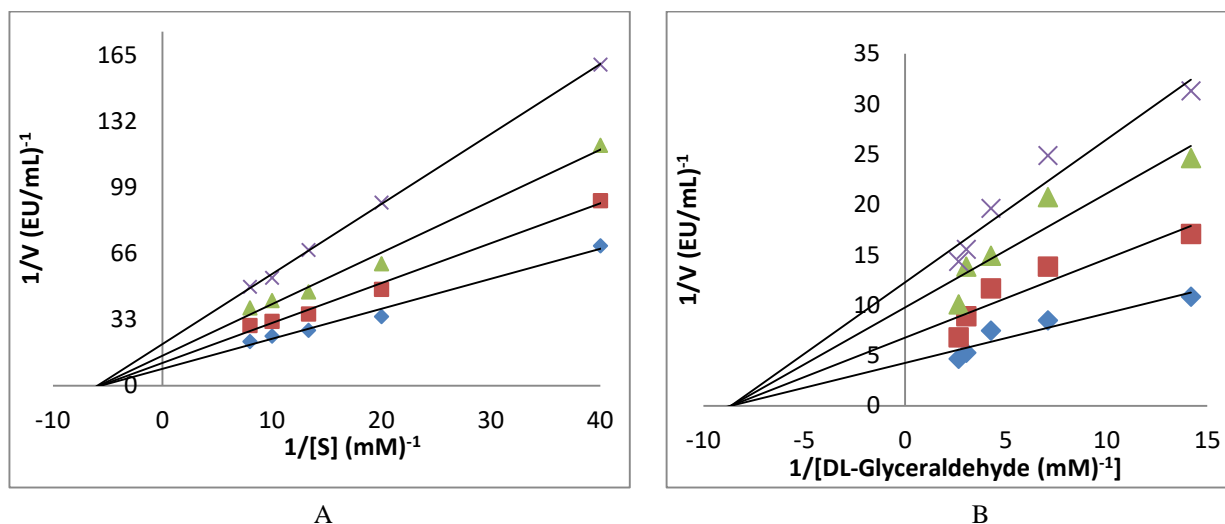


Figure 3. Determination of Lineweaver-Burk graphs for excellent inhibitors of α -Gly (3c) compounds (A) and AR (3b) (B)

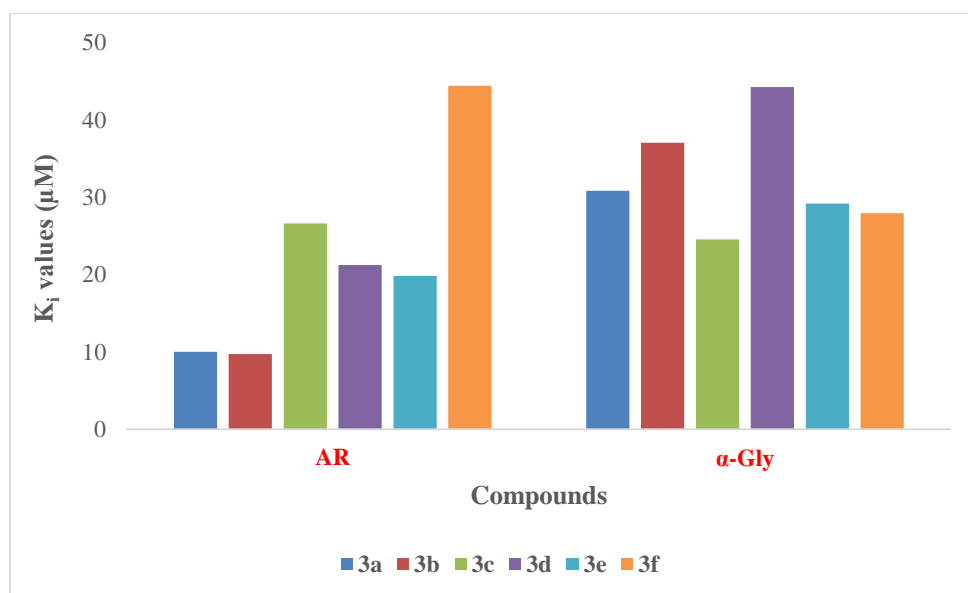


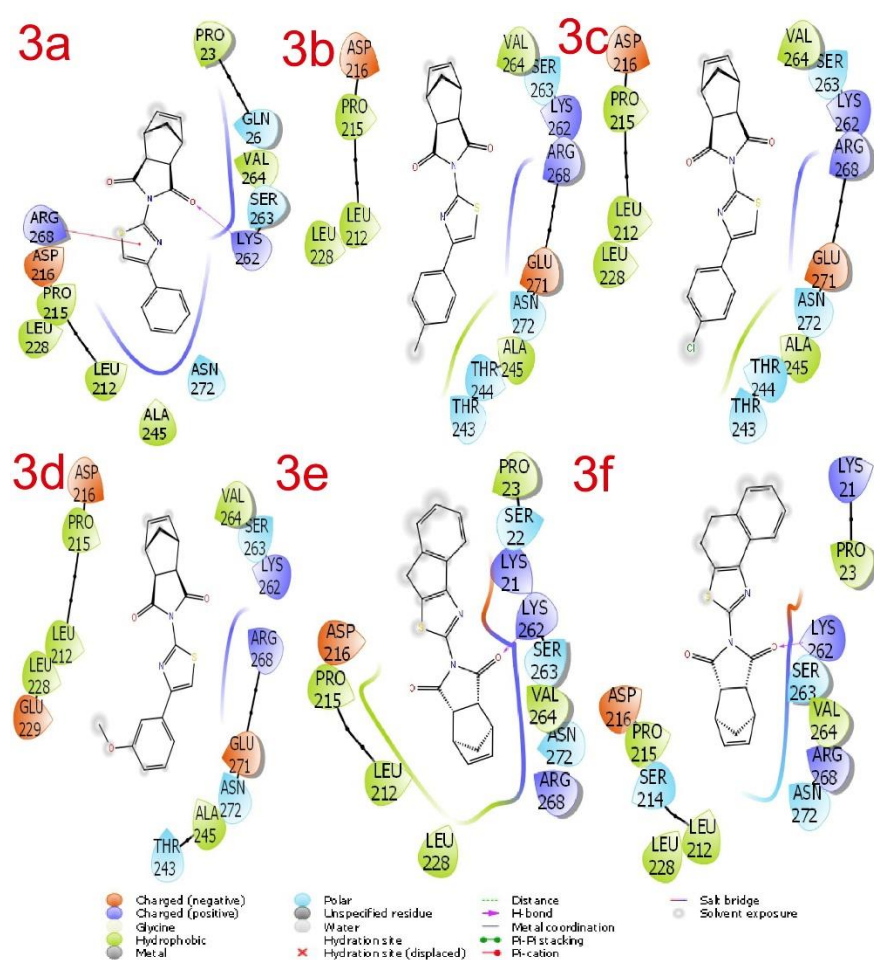
Figure 4. K_i values of studied enzymes

The isoindol-substituted thiazole derivatives were interacted with enzymes and their biological activities were compared. Molecular docking calculations were made with enzymes of isoindol-substituted thiazole derivatives. Biological activity comparison of isoindol-substituted thiazole derivatives can be made by using the numerical value of these parameters. It is thought that the biological activity value of the molecule with the lowest numerical value of this

parameter is high [40]. As a result, the biological activities of compounds are listed according to the numerical value of this parameter. Other parameters obtained are used to explain the interactions of molecules with enzymes. As a result of docking studies, the interactions of isoindol-substituted thiazole derivatives with enzymes are given in Figure 5 and 6. The numerical value of the parameters obtained as a result of these interactions are given in Table 3.

Table 3. Numerical values of the parameters obtained from interaction of enzymes studied with enzymes

		3a	3b	3c	3d	3e	3f
α -Gly	Docking Score	-3.6	-3.3	-3.8	-3.3	-3.7	-3.6
	Glide hbond	-0.15	0.00	0.00	0.00	-0.16	-0.15
	Glide emodel	-31.6	-34.8	-38.2	-35.8	-33.4	-33.4
	Glide ligand efficiency	-0.15	-0.14	-0.14	-0.13	-0.15	-0.14
Ald. red.	Docking Score	-3.5	-3.9	-3.1	-3.7	-3.8	-3.0
	Glide hbond	0.00	0.00	0.00	0.00	0.00	0.00
	Glide emodel	-34.9	-34.2	-37.6	-36.9	36.7	-34.0
	Glide ligand efficiency	-0.15	-0.14	-0.13	-0.15	-0.15	-0.12

**Figure 5.** Interaction of molecules against AR enzyme

Docking calculations have shown that as the interactions of isoindol-substituted thiazole derivatives with enzymes increase, the biological activity values of

isoindol-substituted thiazole derivatives increase. Interactions between molecules and enzymes are very significant and showed in Figure 7.

Table 4. ADME properties of molecules

	3a	3b	3c	3d	3e	3f	Referance Range
mol MW	322	336	357	352	334	348	130-725
dipole	2.1	1.6	4.4	3.1	2.0	1.9	1.0-12.5
SASA	564	597	588	596	575	592	300-1000
FOSA	139	227	139	226	192	235	0-750
FISA	89	89	89	85	97	91	7-330
PISA	299	243	251	241	250	234	0-450
WPSA	37	37	109	44	35	32	0-175
volume	984	1045	1028	1060	1005	1048	500-2000
donorHB	0	0	0	0	0	0	0.0-6.0
accptHB	4.5	4.5	4.5	5.25	4.5	4.5	2.0-20.0
glob	0.8	0.8	0.8	0.8	0.8	0.8	0.75-0.95
QPpolrz	36.1	38.0	37.4	37.9	36.4	38.0	13.0-70.0
QPlogPC16	10.3	10.5	10.9	10.7	10.2	10.5	4.0-18.0
QPlogPoct	14.5	15.1	15.5	15.5	14.6	15.1	8.0-35.0
QPlogPw	8.2	7.9	7.9	8.3	7.9	7.8	4.0-45.0
QPlogPo/w	3.4	3.7	3.9	3.5	3.4	3.7	-2.0-6.5
QPlogS	-4.7	-5.3	-5.5	-4.8	-4.9	-5.2	-6.5-0.5
CIQPlogS	-4.8	-5.1	-5.5	-5.1	-5.0	-5.3	-6.5-0.5
QPlogHERG	-5.4	-5.4	-5.4	-5.2	-5.2	-5.2	*
QPPCaco	1412	1412	1412	1554	1180	1353	**
QPlogBB	-0.2	-0.2	0.0	-0.2	-0.3	-0.2	-3.0-1.2
QPPMDCK	1149	1150	2833	1380	917	1022	**
QPlogKp	-2.1	-2.3	-2.3	-2.1	-2.4	-2.4	Kp in cm/hr
IP(eV)	9.3	9.1	9.2	9.1	9.2	9.1	7.9-10.5
EA(eV)	1.2	1.2	1.3	1.2	1.1	1.1	-0.9-1.7
#metab	5	6	5	6	6	7	1-8
QPlogKhsa	0.3	0.4	0.4	0.2	0.3	0.5	-1.5-1.5
HumanOralAbsorption	3	3	3	3	3	3	-
PercentHumanOralAbsorption	100	100	100	100	100	100	***
PSA	67	67	67	75	69	68	7-200
RuleOfFive	0	0	0	0	0	0	Maximum is 4
RuleOfThree	0	0	0	0	0	1	Maximum is 3
Jm	0.0	0.0	0.0	0.0	0.0	0.0	-

* concern below -5, **<25 is poor and >500 is great.

*** <25% is poor and >80% is high.

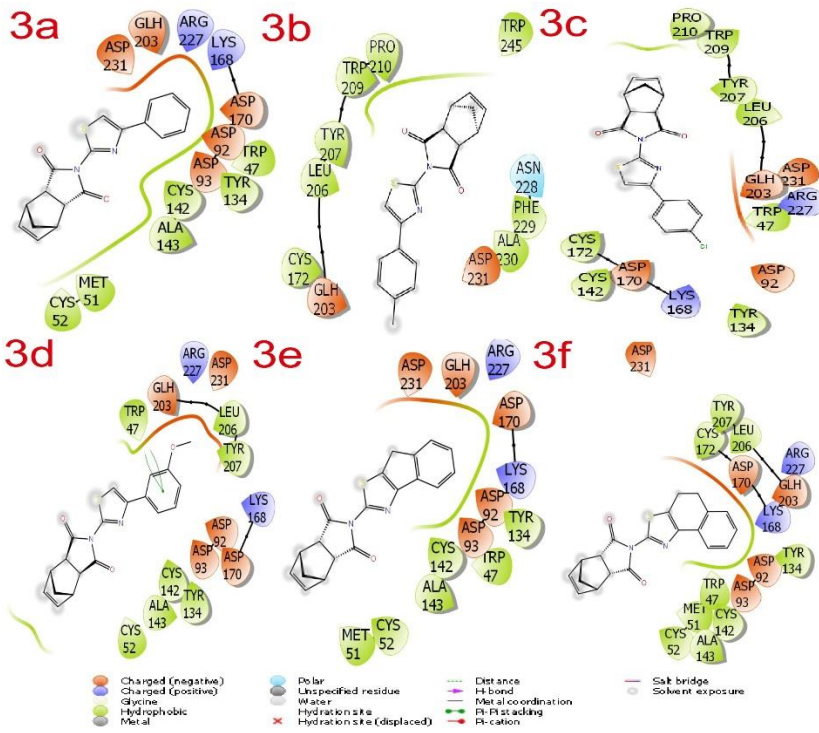


Figure 6. Interaction of molecules against α -Glycosidase enzyme

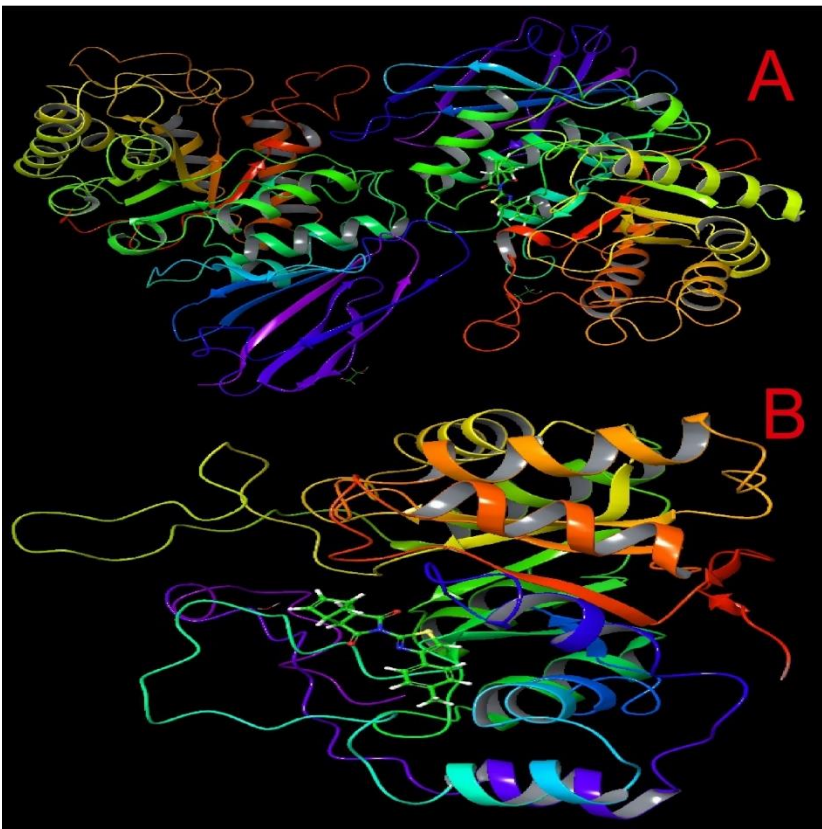


Figure 7. A. Interaction of molecule 3b with proteins of AR enzyme B. Interaction of molecule 3c with proteins of α -Glycosidase enzyme

After molecular docking calculations, it provides us to comment on whether the molecules can be used as medicines in the future with ADME analysis of isoindol-substituted thiazole derivatives. Many parameters were obtained by using Qik-prop module for ADME analysis of molecules. If the numerical values of these parameters are in a certain range, it is thought to be used as a medicine in the future.

The parameters obtained for the ADME properties of the molecules are given in table 4. Many parameters for molecules are calculated in this table. Considering the results given table, Solute as Donor-Hydrogen Bonds is number of hydrogen bond donors [12], Solute as Acceptor-Hydrogen Bonds is number of hydrogen bond acceptors, QP log p for octanol/water is octanol/water partition coefficient, Apparent MDCK Permeability is cell permeability in nm/s, QP log BB for brain/blood is Predicted brain/blood partition coefficient for orally delivered drugs, etc [11]. The numerical values of these parameters give researchers a lot of information [13]. At the end of ADME analysis of molecules, it can be seen that the molecules can be used as a drug in the future.

Conclusions

In the current paper, studied compounds showed strong inhibition profiles towards α -glycosidase and AR enzymes. Micromolar levels of IC₅₀ values were obtained for all derivatives on AR and α -glycosidase enzymes, these compounds can be a selective inhibitor of α -glycosidase and AR enzymes as antidiabetic. Molecular docking scores were in agreement with the experimental results. The biological activity of molecule 3b was found to be highest against AR enzyme. however, the biological activity of molecule 3c is highest against α -Glycosidase.

Acknowledgments

This work is supported by the Scientific Research Project Fund of Sivas Cumhuriyet University under the project number RGD-020 and ECZ-079. This research was made possible by TUBITAK ULAKBIM, High Performance and Grid Computing Center (TR-Grid e-Infrastructure).

Conflict of Interest

The authors declare that there are no conflicts of interest.

References

- [1] Abdel-Hafez A. A. M., Synthesis and anticonvulsant evaluation of N-substituted-isoindolinedione derivatives, *Archives of Pharmacal Research*, 27(5) (2004) 495-501.
- [2] Hassanzadeh F., Rabbani M., Fasihi A., Hakimelah, G. H., Mohajeri M., Synthesis of phthalimide derivatives and evaluation of their anxiolytic activity, *Research in Pharmaceutical Sciences*, 2(1) (2008) 35-41.
- [3] Wang J. J., Liu T. Y., Yin P. H., Wu C. W., Chern, Y. T., & Chi, C. W., Adamantyl maleimide induced changes in adhesion molecules and ROS are involved in apoptosis of human gastric cancer cells, *Anticancer Research*, 20(5A) (2000) 3067-3073.
- [4] Ali I.A., Fathalla W., Synthesis of N-substituted-3, 4, 5, 6-tetrachlorophthalimide using trichloroacetimidate CC bond formation method, *Arkivoc*, 13 (2009) 193-199.
- [5] Kant P., Saksena R. K., Synthesis and antimicrobial activity of some new 2-phenyl-3-p-(2'-methyl-3'-aryl-4'-oxo-thiazolin-2'-yl) phenyl quinazolin-4-ones and 2-phenyl-3-p-(1'-aryl-3-phthalimido-4'-methylazetidin-2'-one-2'-yl) phenyl-quinazolin-4-ones, *Indian Journal Of Heterocyclic Chemistry*, 12(4) (2003) 315-318.
- [6] Kim J. N., Breaker R. R., Purine sensing by riboswitches, *Biology of the Cell*, 100(1) (2008) 1-11.
- [7] Demir Y., Isık M., Gulcin I., Beydemir S., Phenolic compounds inhibit the aldose reductase enzyme from the sheep kidney, *J. Biochem. Mol. Toxicol.*, 31(9) (2017) e21935.
- [8] Demir Y., Taslimi P., Ozaslan M. S., Oztaskin N., Çetinkaya Y., Gulçin İ., Goksu S., Antidiabetic potential: in vitro inhibition effects of bromophenol and diarylmethanones derivatives on metabolic enzymes, *Archiv der Pharmazie*, 351(12) (2018) 1800263.
- [9] Türkeş C., Demir Y., Beydemir Ş., Anti-diabetic properties of calcium channel blockers: inhibition effects on aldose reductase enzyme activity, *Applied Biochemistry and Biotechnology*, 189(1) (2019) 318-329.
- [10] Demir Y.; Ozaslan M.S.; Duran H.E.; Küfrevioğlu O.I.; Beydemir S., Inhibition effects of quinones on aldose reductase: antidiabetic

- properties, *Environmental Toxicology and Pharmacology*, 70 (2019) 103195.
- [11] Aktaş A., Barut Celepci D., Kaya R., Taslimi P., Gök Y., Aygün M., İ. Gulçin İ., Novel morpholine liganded Pd-based N-heterocyclic carbene complexes: Synthesis, characterization, crystal structure, antidiabetic and anticholinergic properties, *Polyhedron*, 159 (2019) 345-354.
- [12] Gedikli M.A., Tüzün B., Aktaş A., Sayin K., Ataseven H., Do clarithromycin, azithromycin and their analogues effective in the treatment of COVID19?, *Bratislavske Lekarske Listy*, 122 (2021).
- [13] Akta A., Tüzün B., Aslan R., Sayin K., Ataseven, H., New anti-viral drugs for the treatment of COVID-19 instead of favipiravir, *Journal of Biomolecular Structure and Dynamics*, (2020) 1-11.
- [14] Kocyigit, U. M., Aslan, O. N., Gulcin, I., Temel, Y., & Ceylan, M., Synthesis and Carbonic Anhydrase Inhibition of Novel 2-(4-(Aryl)thiazole-2-yl)-3a,4,7,7a-tetrahydro-1H-4,7-methanoisindole-1,3(2H)-dione Derivatives, *Arch Pharm Chem Life Sci*, 349 (2016) 955–963.
- [15] Tao, Y.; Zhang, Y.; Cheng, Y.; Wang, Y. Rapid screening and identification of α -glucosidase inhibitors from mulberry leaves using enzyme-immobilized magnetic beads coupled with HPLC/MS and NMR, *Biomed Chromatogr.*, 27 (2017) 148-155.
- [16] Cerelli, M.J.; Curtis, D.L.; Dunn, J.P.; Nelson, P.H.; Peak, T.M.; Waterbury, LD., Antiinflammatory and aldose reductase inhibitory activity of some tricyclic arylacetic acids, *J Med Chem.*, 29 (1986) 2347–51.
- [17] Aslan, H.E.; Beydemir, S., Phenolic compounds: The inhibition effect on polyol pathway enzymes, *Chem. Biol. Interact.*, 266 (2017) 47-55.
- [18] Bradford, M.M., A rapid and sensitive method for the quantitation of microgram quantities of protein utilizing the principle of protein-dye binding, *Anal. Biochem.*, 72 (1976) 248–254.
- [19] Laemmli, U.K., Cleavage of structural proteins during the assembly of the head of bacteriophage T4, *Nature*, 227 (1970) 680–685.
- [20] Demir, Y.; Beydemir, S., Purification, refolding, and characterization of recombinant human paraoxonase-1, *Turk. J. Chem.*, 39 (2015) 764–776.
- [21] Ceylan, H., Demir, Y., & Beydemir, Ş. Inhibitory effects of usnic and carnosic acid on some metabolic enzymes: an in vitro study, *Protein and Peptide Letters*, 26(5) (2019) 364-370.
- [22] Lineweaver H., Burk D., The determination of enzyme dissociation constants, *J. Am. Chem. Soc.*, 56 (1934) 658–666.
- [23] Tüzün B., Examination of anti-oxidant properties and molecular docking parameters of some compounds in human body, *Turkish Computational and Theoretical Chemistry*, 4(2) (2020) 76-87.
- [24] Frisch M.J., Trucks G.W., Schlegel H.B., Scuseria G.E., Robb M.A., Cheeseman J.R., Scalmani G., Barone V., Mennucci B., Petersson G.A., Nakatsuji H., Caricato H., Li X., Hratchian H.P., Izmaylov A.F., Bloino J., Zheng G., Sonnenberg J.L., Hada M., Ehara M., Toyota K., Fukuda R., Hasegawa J., Ishida M., Nakajima T., Honda Y., Kitao O., Nakai H., Vreven T., Montgomery J.A., Peralta J.E., Ogliaro F., Bearpark M., Heyd J.J., Brothers E., Kudin K.N., Staroverov V.N., Kobayashi R., Normand J., Raghavachari K., Rendell A., Burant J.C., Iyengar S.S., Tomasi J., Cossi M., Nega R., Millam J.M., Klene M., Knox J.E., Cross J.B., Bakken V., Adamo C., Jaramillo J., Gomperts R., Stratmann R.E., Yazyev O., Austin A.J., Cammi R., Pomelli C., Ochterski J.W., Martin R.L., Morokuma K., Zakrzewski V.G., Voth G.A., Salvador P., Dannenberg J.J., Daprigh S., Daniels A.D., Farkas A, Foreaman JB, Ortiz JV, Cioslowski J, Fox DJ., Gaussian 09, Revision D.01, Gaussian Inc., Wallingford CT, (2009).
- [25] Schrödinger L., Small-Molecule Drug Discovery Suite (2019-4).
- [26] Zheng X., Zhang L., Chen W., Chen Y., Xie W., Hu X., *Chem.Med.Chem.*, 7(11) (2012) 1921-1923.
- [27] Lovering A.L., Lee S.S., Kim Y.W., Withers S.G., Strynadka, N.C., Mechanistic and structural analysis of a family 31 α -glycosidase and its glycosyl-enzyme intermediate, *Journal of Biological Chemistry*, 280(3) (2005) 2105-2115.
- [28] Schrödinger Release 2019-4: Protein Preparation Wizard; Epik, Schrödinger, LLC, York, NY, 2016; Impact, Schrödinger, LLC, New York, NY, 2016; Prime, Schrödinger, LLC, New York, NY, 2019.
- [29] Schrödinger Release 2019-4: LigPrep, Schrödinger, LLC, New York, NY, 2019.

- [30] Taslimi P., Turhan K., Türkan F., Karaman H. S., Turgut Z., Gulcin İ., Cholinesterases, α -glycosidase, and carbonic anhydrase inhibition properties of 1H-pyrazolo [1, 2-b] phthalazine-5, 10-dione derivatives: Synthetic analogues for the treatment of Alzheimer's disease and diabetes mellitus, *Bioorganic Chemistry*, 97 (2020) 103647.
- [31] Schrödinger Release 2020-1: QikProp, Schrödinger, LLC, New York, NY, 2020.
- [32] Patil K.K., Gacche R.N., Inhibition of glycation and aldose reductase activity using dietary flavonoids: A lens organ culture studies, *Int. J. Biol. Macromol.*, 98 (2017) 730-738.
- [33] Stefek M.; Snirc V., Djoubissie P.O., Majekova M., Demopoulos V., Rackova L., Bezakova Z., Karasu C., Carbone V., El-Kabbani O., Carboxymethylated pyridoindole antioxidants as aldose reductase inhibitors: Synthesis, activity, partitioning, and molecular modeling, *Bioorg Med Chem.*, 16 (2018) 4908-4920.
- [34] Fatmawati S., Ersam T., Shimizu K., The inhibitory activity of aldose reductase in vitro by constituents of *Garcinia mangostana* Linn, *Phytomedicine*, 22 (2015) 49-51.
- [35] Ali S., Saeed A., Abbas N., Shahid M., Bolte M., Iqbal, J., Design, synthesis and molecular modelling of novel methyl[4-oxo-2-(aroylimino)-3-(substituted phenyl)thiazolidin-5-ylidene]acetates as potent and selective aldose reductase inhibitors, *Med. Chem. Commun.*, 3 (2012) 1428.
- [36] Taslimi P., Aslan H.E., Demir Y., Oztaskin N., Maraş A., Gulçin İ., Beydemir S., Goksu S., Diarylmethanon, bromophenol and diarylmethane compounds: Discovery of potent aldose reductase, α -amylase and α -glycosidase inhibitors as new therapeutic approach in diabetes and functional hyperglycemia, *Int. J. Biol. Macromol.*, 119 (2018) 857-863.
- [37] Gulçin İ., Taslimi P., Aygün A., Sadeghian N., Bastem E., Kufrevioglu O.I., Turkan F., Şen F., Antidiabetic and antiparasitic potentials: Inhibition effects of some natural antioxidant compounds on α -glycosidase, α -amylase and human glutathione S-transferase enzymes, *Int. J. Biol. Macromol.*, 119 (2018) 741-746.
- [38] Chun H.S., Chang H.B., Kwon YI., Yang H.C., Characterization of an α -glucosidase inhibitor produced by *Streptomyces* sp. CK-4416, *J. Microbiol. Biotechnol.*, 11 (2001) 389-393.
- [39] Taslimi P., Akıncıoğlu H., Gulçin I., Synephrine and phenylephrine act as α -amylase, α -glycosidase, acetylcholinesterase, butyrylcholinesterase and carbonic anhydrase enzymes inhibitors, *J. Biochem. Mol. Toxicol.*, 31(11) (2017) e21973.
- [40] Koçyiğit Ü. M., Taslim P., Tüzün, B., Yakan H., Muğlu H., Güzel E., 1, 2, 3-Triazole substituted phthalocyanine metal complexes as potential inhibitors for anticholinesterase and antidiabetic enzymes with molecular docking studies, *Journal of Biomolecular Structure and Dynamics*, (2020) 1-11.



Composition characterization and biological activity study of *Thymbra spicata* L. var. *spicata* essential oil

Nuraniye ERUYGUR¹ , Umit M. KOCYIGIT² , Mehmet ATAS³ , Ozge CEVIK⁴ , Faik GÖKALP^{5,*} , Parham TASLİMİ⁶ , İlhami GULCİN⁷

¹ Department of Pharmacognosy, Selcuk University Faculty of Pharmacy Konya / Turkey

² Vocational School of Health Services, Cumhuriyet University, Sivas / Turkey

³ Department of Pharmaceutical microbiology, Cumhuriyet University Faculty of Pharmacy, Sivas / Turkey

⁴ Department of Biochemistry, Cumhuriyet University Faculty of Pharmacy, Sivas / Turkey

⁵ Department of Mathematics and Science Education, Kırıkkale University Faculty of Education, Kırıkkale / Turkey

⁶ Department of Biotechnology, Faculty of Science, Bartın University, Bartın / Turkey

⁷ Department of Chemistry, Ataturk University Faculty of Sciences, Erzurum / Turkey

Abstract

The current research aimed to determine and report in vitro antioxidant, antimicrobial, antibiofilm, cytotoxic, anti-cholinesterase, and anti-diabetic properties and the stability of the major component of basic oil of *Thymbra spicata* var. *spicata* through different phases as theoretically. Essential oil exhibits potential biological activities because of the multiple components it contains. In the current research, the evaluation of *Thymbra spicata* essential oil antioxidant properties was conducted utilizing 1,1-diphenyl-2-picrylhydrazyl (DPPH) and 2,2-azinobis[3-ethylbenzthiazoline]-6-sulfonic acid (ABTS) radical scavenging activity. Antimicrobial activity was assessed from minimum inhibition concentration (MIC) using the technique of microdilution and cytotoxicity activity was evaluated by MTT assay through MCF-7 and PC3 human cancer cell lines. Consequently, Cytotoxic activity was evaluated by means of MTT assay utilized. The essential oil was detected to have 340 µg/mL inhibiting influence on the growth of PC3 prostate cancer cells with IC50 value. Also, the *T. spicata* plant was observed to significantly repress the enzymes, namely acetylcholinesterase (AChE), butyrylcholinesterase (BChE), α-glycosidase. IC50 values of enzymes were obtained 0.23 µg/mL for AChE, 1.64 µg/mL for BChE, 7.78 µg/mL for α-glycosidase. It was concluded that this plant may be used for Alzheimer's and diabetes disease.

Article info

History:

Received: 08.04.2021

Accepted: 07.09.2021

Keywords:

Thymbra spicata,
Antioxidant activity,
Antimicrobial activity,
Cytotoxicity,
Enzyme activity.

1. Introduction

Essential oil exhibits potential biological activities because of the multiple components it contains. Recently, the number of biological activity studies on volatile oils has increased rapidly, resulting in brilliant results. The interest in the use of essential oil as natural antioxidants are growing rapidly due to many essential oils has antioxidant properties [1].

The genus *Thymbra* L. (Lamiaceae), is known by Turkish local people as 'kekik or zahter'. It is not only important for its economic significance, but also important in commonly utilized in Turkish cuisine as edible ingredients of salad, condiment or herbal teas.

The genus is also important for its chemical constituents such as carvacrol and thymol as main components [2], exhibiting many biological activities [3]. Therefore, the leaves and essential oil of the genus uses for various purposes in flavoring, perfume, food and pharmaceutical industries.

T. spicata stands out with its significant medicinal effects in mainly Mediterranean countries where it is mostly used as in spice form and for purpose of preserving other food products [4]. Located within the Mediterranean and also in semi-arid climatic conditions, it mostly sprouts on calcareous soils located on hillsides with ample sunlight [5]. Also, the dried plant of *T. spicata* is used for curing asthma, colic, and bronchitis and coughs [6]. In this context,

*Corresponding author. e-mail address: akgokalp@gmail.com

characterization of chemical composition and revealing of its biological activities is important to establish the basis for the uses of these plant raw materials and essential oil.

AD is characterized by neurofibrillary tangles and amyloid plaques. The AChEIs such as galanthamine, donepezil, rivastigmine, and tacrine are currently accessible as drugs for universal clinical therapy of AD [7]. In addition to red blood cells, synapses and neuromuscular connections in the brain generally contain cholinergic AChE in high concentrations [8]. Additionally, a non-special kind of ChE enzyme butyrylcholinesterase (BChE), commonly existing throughout the body, most significantly, in the blood, liver, the central nervous system and pancreas of humans, hydrolyzes various kinds of choline esters and [9]. BuChE has a common association with endothelial and glial cells in the brain [10].

Diabetes mellitus (DM) is a well-known metabolic disorder, which is characterized as an unusual postprandial enhance of blood glucose amount [11,12]. The control of postprandial hyperglycemia is known to be significant in the therapy of DM [13]. α -Glycosidase exists in intestinal chorionic epithelium which is accountable for the depreciation of carbohydrates [14]. α -Glycosidase inhibitors (AGIs) fall under the third class of oral hypoglycemic factors [15]. Diverse AGIs, such as voglibose and acarbose obtained from plant sources, can impressively control blood glucose amounts after food intake and thus in clinical use in the treatment of DM [16].

The present research aimed to characterize the basic oil contents and also to determine the biological activity such as antioxidant, antimicrobial, cytotoxicity, antidiabetic and anti-cholinesterase activity.

2. Materials and Methods

2.1.Plant materials

The plant content was purchased in a market in Hatay, Turkey, following it was identified by a plant specialist Dr. Mehmet Tekin of Trakya University, Faculty of Pharmacy, Department of Pharmaceutical Botany.

2.2.Essential oil preparat

In order to obtain the essential oil, flowers and leaves of *T. spicata* were exposed to a hydrodistillation process through a Clevenger type apparatus for about 3 hours. The resulting oil yield accounted for 3.87 %.

2.3.GC-MS analysis

GS-MS analysis was conducted in the plant, drug and scientific research center of Anadolu University. Qualification of the essential oil was performed using

an Agilent 5977B Mass Spectrometer coupled with an Agilent GC-7890B series (Agilent Technologies, USA). The GC was equipped with HP-Innowax capillary column (60 m \times 250 μ m \times 0.25 μ m film thickness) with helium (He) utilized as the transport agent with 0.7 mL/min rate of flow. GC oven temperature program was as follows: 60oC for 10 min, up to 240oC at 1oC/min and then kept at 220oC for 20 min, a total of 80 min. The injection temperature was 250oC. In EI mode at 70 eV of the mass spectrometer, 1 μ L of the oils were injected into the column. The components of the oil were detected through a comparison between relative retentive indices, mass spectra and pure original sample indices.

2.4.Antioxidant activities

2.4.1.DPPH radical scavenging process

DPPH assay is in wide use for assessment of antioxidant process due to the reliance of its mechanism on measuring hydrogen atom or electron donating process. The assessment of (DPPH)-free radical scavenging activity of the stable 1, 1-diphenyl-2-picrylhydrazyl was conducted through the Sannigrahi approach [17]. Sample solution at different concentrations prepared in 80% methanol in a 1:3 volume to volume ratio in separate test tubes in triplicates was blended with 1 ml of 0.1mM of DPPH in methanol. After 30 min standing in dark, decreased DPPH• was determined as 517 nm. Decreases in solution absorbance of DPPH resulted in increases in DPPH radical scavenging activity. Methanol with DPPH solution (without sample) functioned as a control. Through linear regression analysis of dose-response curve plotting between % inhibition and concentrations, 50% (IC50 value) DPPH• plant extracts scavenging processes were attained. The % inhibition calculation is as the equation below:

$$\% \text{ inhibition} = (\text{Absorbance of control} - \text{Absorbance of the sample}) / \text{Absorbance of control} \times 100$$

2.4.2Decolorisation assay of ABTS radical cation

As described previously, Re et. al., [18] method was utilized in the determination of ABTS free radical scavenging process [19]. Through 2.45 mM potassium persulphate and 7 mM aqueous ABTS stock solutions at a volume of 1:1 ratio, following ABTS radical cations production, the cations were left for incubation for attaining the reaction at 25°C for 16 hours in the dark. Dilution of the stock solutions with ethanol in order to give 0.70 ± 0.02 absorbance at 734 nm and equilibrated at 30°C yielded ABTS•+ working solution. Trolox, which is a vitamin E analog soluble in water, constituted the norm. At alternating concentrations as 0, 50, 100, 150, 200, 250, and 500

μM , a standard curve for calibration for Trolox is formed. In test tubes, 1 mL of each sample was mixed with radical cation solution, 1 mL of fresh ABTS⁺, and their absorbances are detected (at 734 nm) following a 7 min incubation period in the environment in the absence of light.

2.5. Antimicrobial activity

The antimicrobial features of basic oil of *T. spicata* was determined by micro-well dilution assay according to standard procedures against 5 bacterial and fungal traits, namely as Grampositive (*Staphylococcus aureus* (ATCC 29213) and *Enterococcus faecalis* (ATCC 29212)), Gram-negative (*Pseudomonas aeruginosa* (ATCC 27853) and *Escherichia coli* (ATCC 25922)) and fungal trait (*Candida albicans* (ATCC 10231)). The essential oil was dissolved in 8% DMSO to prepared 20 mg/ml of stock solution. Serial two-fold dilutions of the essential oil stock were done with distilled water to provide final concentration between 5.0 and 0.02 mg mL⁻¹. Final size of inoculum was 5 x10⁵ CFU/mL at bacteria and 0.5-2.5 x10³ CFU/mL at *Candida* in each well. The inoculated plates were incubated at 37 °C for bacteria and 35 °C for *Candida* for a period of 16 to 24 hours under anaerobic conditions. Following, 10 μL of a sterile 0.5 % aqueous solution of 2, 3, 5-Triphenyltetrazolium chloride (TTC) (Merck, Germany) was mixed with each well to confirm microbial development. This experiment was performed in duplicate. The microplates were left to re-incubate at 37 °C for a period of 2 hours. Reducing the TTC by succinate dehydrogenase in viable cells led to the formation of formazan and the color changed from yellow to red, was determined as MIC value [20].

2.6. Cytotoxicity assay

Colorimetric MTT assay conducted in vitro cytotoxic activity of essential oil by using cell lines of two different cancers as human breast cancer MCF-7 and prostate cancer cell PC-3 lines [21]. The culture was carried out in 25 cm² flasks in RPMI-1640 culture medium supplemented with 10% fetal bovine serum, 100 U/mL Penicillin, and 100 $\mu\text{g}/\text{mL}$ Streptomycin in a humidified atmosphere including 5% CO₂, at 37°C. Exponential growing was inoculated in 96-well microplates at a density of 5 × 10³ cells per well in 100 μL of 10% FBS included the following trypsinization with 1x trypsin - EDTA and were allowed to 24 h of incubation before treatment. The essential oil concentrations in increasing amounts (1–1000 $\mu\text{g}/\text{mL}$) were then added in methanol. These cells were left to re-incubation for an additional 24 h with or without essential oil. Following this process, 10 μL of MTT solution was mixed with the content of each well. After incubation for 4h, the color changes were determined

at 570 nm using a microplate reader (Epoch, USA). These applications were conducted in triplicate. The essential oil cytotoxicity, IC₅₀ value, was determined the concentration resulting in the inhibition of 50% of the cells.

2.7. Determination of Apoptosis

Such staining methods as acridine orange and ethidium bromide (AO/EB) were used for investigating the effects of essential oil on inducing apoptosis for cell lines of two different cancers like breast cancer MCF-7 and prostate cancer PC-3. Cell lines were inoculated into 12-well plate at a density of 2×10⁵ cells/well in triplets and treated by *T. spicata* essential oil at a final concentration of 100 $\mu\text{g}/\text{mL}$ in a growth medium without antibiotics for 24h. After incubation, each well was stained by 1 $\mu\text{g}/\text{mL}$ AO/EB solution and the fluorescence intensities were screened by microscopy (Zeiss). Living cells clustered as green fluorescence and apoptotic cells clustered as red fluorescence.

2.8. Enzyme inhibition activity

2.8.1. AChE/BChE inhibitory activity determination

The determination of *T. spicata* inhibition efficacy on AChE/BChE activities was conducted in line with the spectrophotometric procedure recommended by Ellman et. al., [22] as described previously [7]. In both reactions, the substrates utilized were acetylthiocholine iodide and butyrylthiocholine iodide (AChI/BChI) [23].

2.9. Theoretical stability calculation of the major component

In this study, theoretical calculations of the stability of Carvacrol, the major component of *T. spicata. var. spicata*, were done in the ethanol, methanol and water phase. For the dielectric constant for ethanol, methanol and water dielectric EPS = 24.55, 32.63 and 78.39 values of the constants have been entered [24]. DFT procedure was used as the calculation method. 6-31G containing polarizing functions (d, p) basis set was used [25,26]. The calculations are carried out in Gaussian 09W program [40] supported by Kırıkkale University.

3. Results and Discussion

Theoretical results of component

As can be seen from Fig 1., the oil of *T. spicata. var. spicata* was dominated by carvacrol (63.4%), p-cymene (12.1%), γ -terpinene (11.9%) and thymol (3.0%) as a major component.

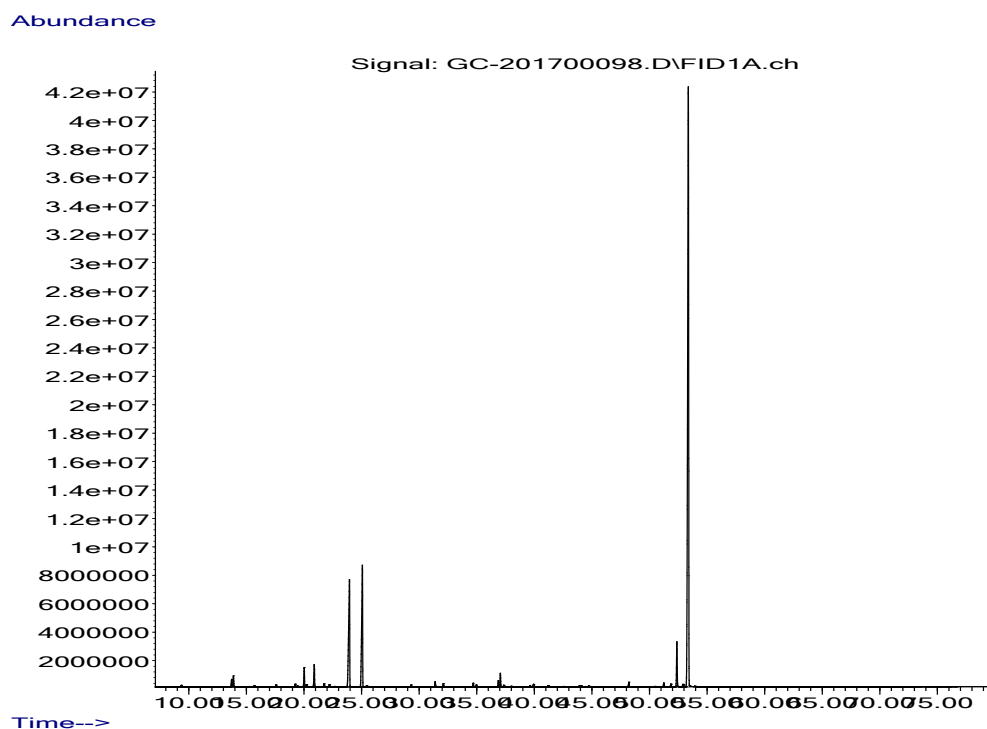


Figure 1. GC-MS chromatogram of *T. spicata* var. *spicata* essential oils

Carvacrol is the major component of *T. spicata* var. *spicata* and the theoretical calculation of it by using density functional theory (DFT) in different phases is given in Table 1.

Table 1. Carvacro’s values of ΔG , HOMO, LUMO, Δ (HOMO-LUMO) and Dipol Moment by using DFT

Carvacrol in different phases (gas, ethanol, methanol and water)	ΔG Free Energy (Hartree)	HOMO (eV)	LUMO (eV)	Δ (HOMO-LUMO) (eV)	Dipole Moment (Debye)
Gas	-464.590955	-0.22108	-0.00907	0.21201	1.3559
Ethanol	-464.597174	-0.22538	-0.01223	0.21315	1.8493
Methanol	-464.597291	-0.22550	-0.01232	0.21318	1.8597
Water	-464.597504	-0.22572	-0.01249	0.21323	1.8788

According to data from Table1; Stability; (HOMO-LUMO difference) Carvacrol in water > Carvacrol in methanol > Carvacrol in ethanol > Carvacrol in gas

Polarity: (Dipol moment) Carvacrol in water > Carvacrol in methanol > Carvacrol in ethanol > Carvacrol in gas

Gibbs's free energy (ΔG) Carvacrol in water > Carvacrol in methanol > Carvacrol in ethanol > Carvacrol in gas

Our theoretical results show that the stability of Carvacrol in water is more than the others phases and Carvacrol in water has a large dipole moment so it has a good resolution in water.

The 3D structures of the two target enzymes as AChE and BChE had been downloaded from the protein databank (PDB) and determined PDB id: 1ACL and 1POP, respectively [27,28]. (Table 2.) The inhibition effect of them on AChE and BChE related to AD was indicated by using the docking [40] program.

Table 2. The inhibition of binding energy score of some active compounds on AChE and BChE

Active compounds/Enzymes (inhibition of binding energy score)	AChE (1ACL)	BChE (1POP)
Carvacrol	-1145.75	362.31
Tacrine	-893.15	179.30

When we look at the table; We see that Carvacrol's AChE binding energy is relatively low compared to the Tacrine. As a result, AChE inhibiting effect is higher from Tacrine, which is the positive control group of the experimental study, therefore the docking scores define in which step the active substance in the plant we use in this inhibiting mechanism is more effective.

Antioxidant activity

Minimum one benzene ring with a hydroxyl functional group, which are usually called phenolic compounds, exists in the structure of the majority of natural molecules, especially those of plant origin. Due to the properties of donating hydrogen or single electron, this group usually has significant effects on the plant extracts or essential oils antioxidant activity [29]. In this study, the two most widely used antioxidant assays, DPPH and ABTS radical scavenging activity tests were employed for the assessment of antioxidant activity of essential oil from *T. spicata*. As can be inferred from antioxidant activity results and GC-MS analysis, the basic oil exhibited stronger activity in terms of free radical scavenging, which might be resulting from the higher amounts of phenolic components such as thymol and carvacrol (Figure 2 and 3).

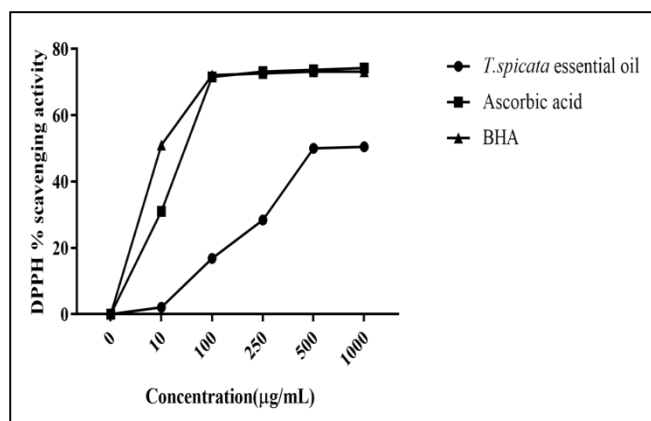
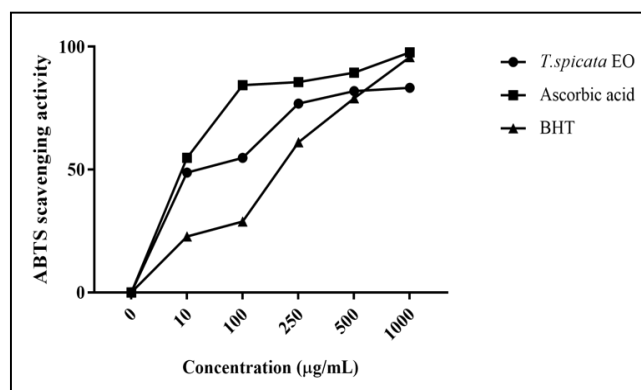
**Figure 2.** DPPH free radical scavenging activity of *T. spicata* var. *spicata* essential oil**Figure 3.** ABTS radical scavenging activity of *T. spicata* essential oil

Figure 3 demonstrated extract ABTS radical scavenging activity. Extract solubility and stereoselectivity of radicals were reported to have an effect on the extract's capacity in various test settings [30]. In the present study, ethanol extracts of *T. spicata* demonstrated potent scavenging activities for ABTS radicals. In comparison with DPPH, the extract, even in lower concentrations, has yielded potent ABTS radical scavenging activity. This high potential of the extract is likely to be resulting from its polar constituent known to be more potent in comparison to DPPH in yielding radical scavenging activity for ABTS, which might result from the water-soluble characteristics of ABTS; whereas DPPH does not have this trait [31].

Antimicrobial activity

Broth microdilution assay was utilized as the medium detecting MIC values of the essential of *T. spicata*. Essential oil demonstrated various antimicrobial activity with microorganisms tested in the study (Table 3).

Table 3. Minimum inhibitory concentrations of essential oil obtained from *T. spicata* herbs

S/No.	Essential oil of <i>T. spicata</i> L. var. Microorganisms	mg/mL
1	<i>E. coli</i>	1.25
2	<i>S. aureus</i>	1.25
3	<i>P. aeruginosa</i>	5.0
4	<i>E. faecalis</i>	5.0
5	<i>C. albicans</i>	1.25

1.25 - 5.0 mg/mL was determined as the range of the extracts MIC values. According to the results, *E. faecalis* and *P. aeruginosa* were less affected by the essential oil of *T. spicata* than other microorganisms with the lowest MIC values 5.0 mg/mL, while the MIC value against other microorganisms is 1.25 mg/mL.

Cytotoxicity assay

3-(4, 5-dimethylthiazol-2-yl)-2,5-diphenyltetrazolium bromide (MTT) assay was the medium of evaluation of essential oil proliferative effect on cellular development. The transition of tetrazolium bromide (MTT) from yellow to purple formazan through mitochondrial enzyme succinate dehydrogenase activity in viable cells constitutes colorimetric assay. The findings clearly demonstrate that for MCF-7 cancer cells, PC-3 cancer cells, basic oil possesses a significant antiproliferative activity, with IC₅₀ of 88.63 µg/mL and with IC₅₀ of 79.25 µg/mL, respectively.

Enzymes inhibitory activity

The utilizing these plant origin materials as supplementary medicines in dementia treatment, shows variations in line with the expectations of that specific society ("Alzheimer's Association). In

comparison to the ones in the Far East countries such as China with the exception of the limited number of plants like Ginkgo biloba, whose major contents, the ginkgolides, are shown to have neuroprotective, antioxidant, and cholinergic activities related to AD mechanisms, in traditional Western medicine, memory enhancing plants or pharmacological properties of traditional cognitive have not been extensively evaluated in the context of prevalent models of AD [32]. Placebo-controlled clinical trials reported similar therapeutic effects of Ginkgo biloba extracts in AD currently prescribed drugs such as donepezil or tacrine and, importantly, undesirable side effects of Ginkgo biloba are minimal [33].

In the Alzheimer's -afflicted brain, the cells that utilize ACh are destroyed or harmed, leading to lower amounts of the chemical messenger [34, 35]. A ChEI is designed to reduce AChE activity, thereby slowing ACh separation. By memorizing levels of ACh, the drug can help compensate for the detriment of functioning brain cells. In the present study, *T. spicata* plant efficiently managed to inhibit AChE, BChE, and α-glycosidase enzymes (Table 4).

Table 4. The enzyme inhibition results of essential oil of *Thymbra spicata* L. var. *spicata* against AChE, BChE, and α-glycosidase enzymes.

Extract or Reference Compounds	α-glycosidase		AChE		BChE	
	IC ₅₀ (µg/mL)	R ²	IC ₅₀ (µg/mL)	R ²	IC ₅₀ (µg/mL)	R ²
<i>Thymbra spicata</i> L.	7.78	0.971	0.23	0.992	1.64	0.989
Tacrine*	-	-	12.36	0.958	19.11	0.981
Acarbose**	22.8	-	-	-	-	-

*Tacrine was used as positive control for AChE and BChE enzymes and determined as µM levels.

**Acarbose was used as positive control for α-amylase and α-glycosidase enzymes and determined as µM levels, which given in references (Noh et al., 2011).

TAC (9-amino-1, 2, 3, 4-tetrahydroacridine), the initial drug to be legally accepted for placative treatment in AD, acts as an agent reversibly inhibiting BChE and AChE. These enzymes IC₅₀ values were obtained 0.23 µg/mL for AChE, 1.64 µg/mL for BChE, 7.78 µg/mL. Moreover, Tacrine (TAC), utilized as BChE and AChE inhibition positive standard, yielded IC₅₀ values 19.11 µmol/L and 12.36 µmol/L, respectively. In terms of their safety requirements and therapeutic implications, edible plant materials in food supplement form and various herbs of natural origin which are in use as medicinal agents in medicine have witnessed an accumulating surge of scientific interest in the treatment of diabetic disease. Considering the fact that the majority of the drugs provided by modern Western medicine on the counters are, to a certain extent, obtained from plant materials, this trend is far from being scientifically predicted [36].

Natural α-amylase and α-glucosidase inhibitors are being evaluated as novel candidates to control hyperglycemia in diabetic patients [37]. For instance, the traditional Arabic medicine is still determined and may create efficient novel compounds for treating diabetes disease and other diseases, as the 69 plant species that are introduced in a review about diabetes treatment in Jordan [38]. Some of these plants have been shown to inhibit glucosidase and amylase activities in vivo and in vitro, including *Varthemia iphionoides*, *Geranium graveolens*, *Sarcopoterium spinosum*, *Pistacia atlantica*, and *Rheum ribes* [39].

The interactions of active ingredients in *T. spicata* essential oil with cancer cells are given in Figures 4, 5, 6 and 7.

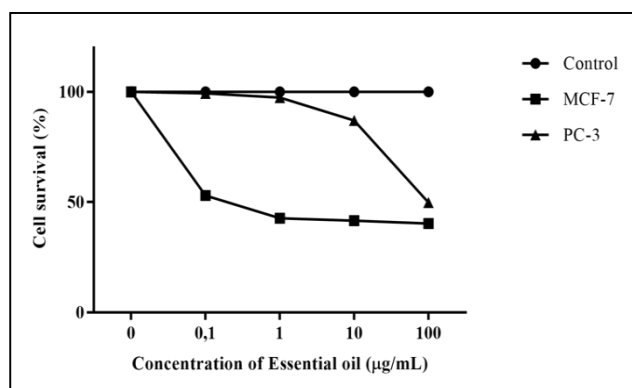


Figure 4. Cell proliferation assay of MCF-7 and PC-3 cell lines in the presence of the essential oil of *T. spicata* with different concentrations for 24 h.

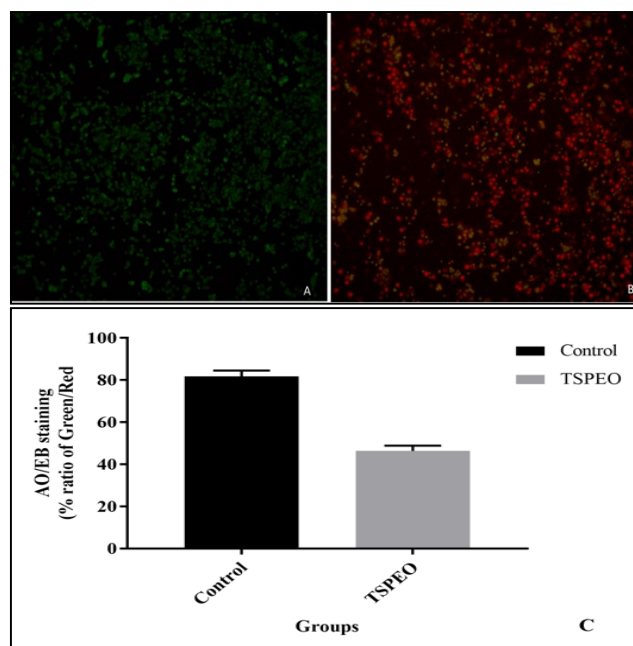


Figure 5. AO/EB staining of MCF-7 cancer cell lines with the concentration of 100 µg/mL for the incubation period of 24h. A: Fluorescence images of control MCF-7 cells; B: Fluorescence images of treated MCF-7 cells with *T. spicata* essential oil after staining, C: ratios of AO/EB staining in MCF-7 cell line at 100 µg/mL concentrations of *T. spicata* essential oil for 24h.

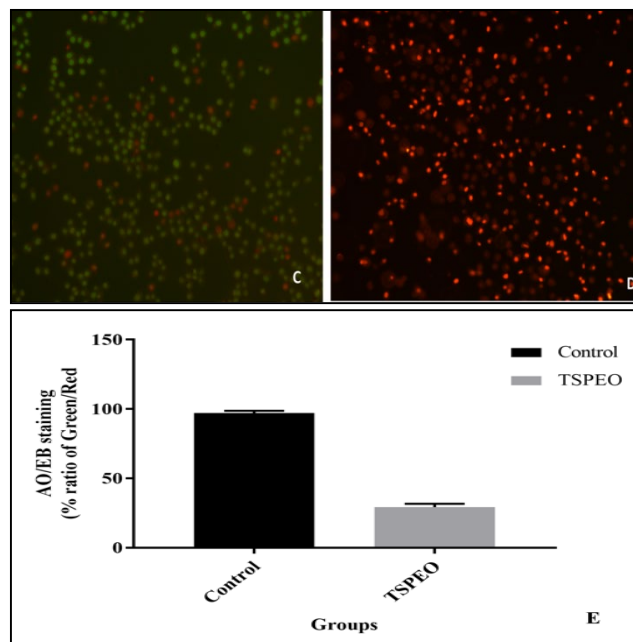
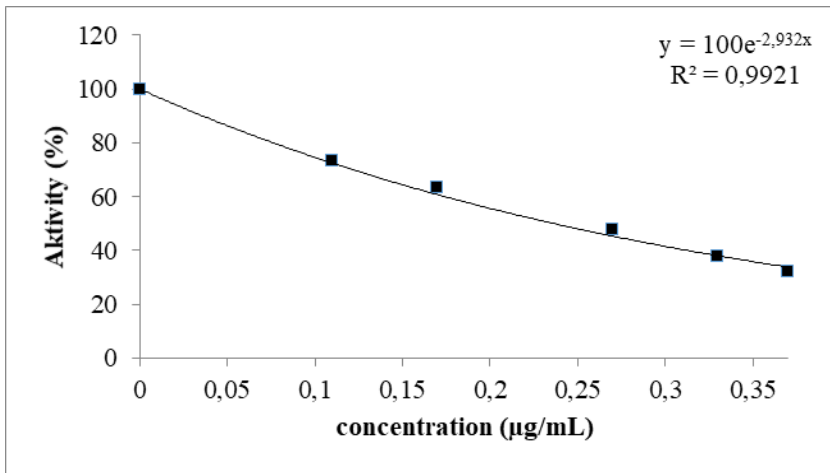
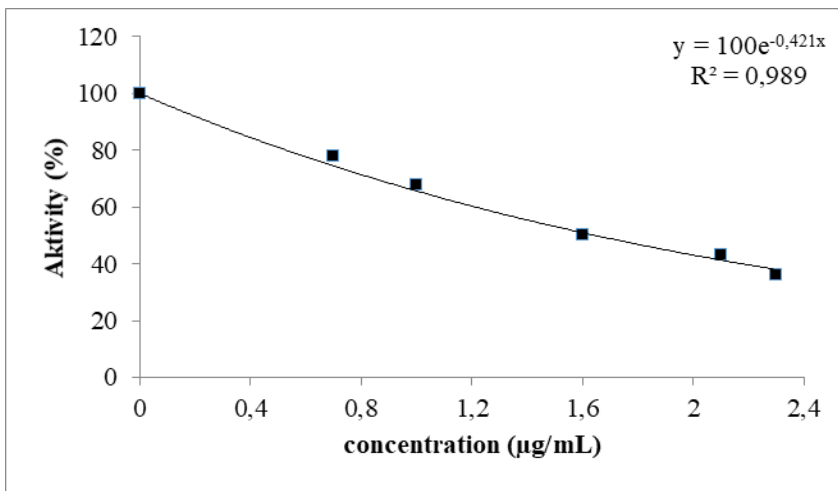


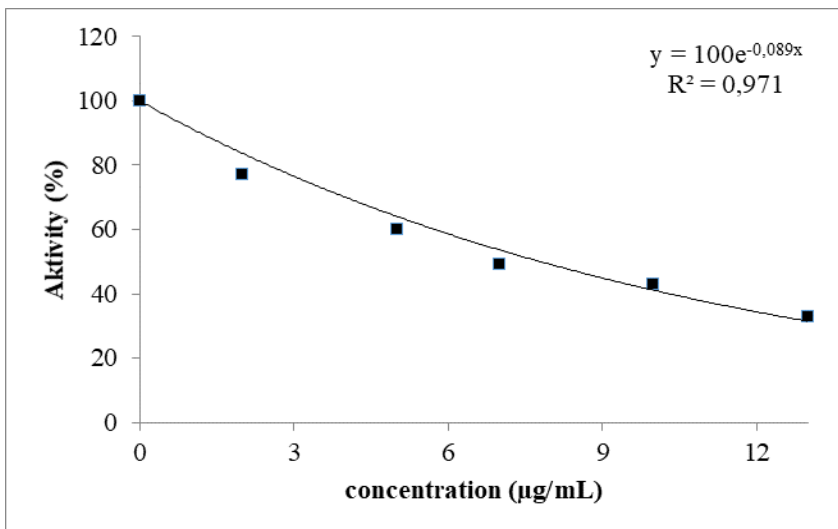
Figure 6. AO/EB staining of PC-3 cancer cell lines with the concentration of 100 µg/mL for the incubation period of 24h. C: Fluorescence images of control PC-3 cells; D: Fluorescence images of treated PC-3 cells with *T. spicata* essential oil after staining; E: ratios of AO/EB staining in PC-3 cell line at 100 µg/mL concentrations of *T. spicata* essential oil for 24h.



A



B



C

Figure 7. The IC₅₀ graphs of *Thymbra spicata* L. var. *spicata* essential oil against A) AChE, B) BChE, C) α-glycosidase enzymes.

Conclusion

The current research demonstrates that the essential oil of *T. spicata* is a good source of potent and natural antioxidants as well as a good α -glycosidase, BChE, and AChE inhibitors. The activities mentioned above may have a relation with high levels of phenolic content existing within such essential oil. The plant materials have demonstrated a satisfactory inhibitory effect on the enzymes mentioned above. AChE, BChE inhibition has significant potential not only in the development of drugs but also in other fields such as toxicology and medicine. Moreover, the main component of *T. spicata*, Carvacrol, in water has low chemical reactivity and high kinetic stability. On the other hand, this plant can be a drug candidate as antidiabetic, anticholinergic and food additive.

Conflicts of Interest

The study has been performed in accordance with ethical standards. All authors read and approved the manuscript. The authors have no conflict of interest. All authors read and approved the manuscript. The research has not human participants and/or animals.

References

- [1] Chaieb K., Zmantar T., Ksouri R., Hajlaoui H., Mahdouani K., Abdelly C., Bakhrouf A., Antioxidant properties of the essential oil of *Eugenia caryophyllata* and its antifungal activity against a large number of clinical *Candida* species, *Mycoses*, 50(5) (2007) 403-406.
- [2] Kokkini S.V.D., Carvacrol-rich plants in Greece, *J. Flavour Fragr.*, 4 (1989) 1-7.
- [3] Juven B. J., Kanner J., Schved F., Weisslowicz H., Factors that interact with the antibacterial action of thyme essential oil and its active constituents, *J. Appl. Bacteriol.*, 76 (1994) 626-631.
- [4] Kızıl S., Toncer O., Dıraz E., Variation of agronomical characteristics and essential oil components of zahter (*Thymbra spicata* L. var. *spicata*) populations in semi-arid climatic conditions, *Turkish J. F. Crop.*, 20 (2015) 242-251.
- [5] Kızıl S., Determination of essential oil variations of *Thymbra spicata* var. *spicata* L. naturally growing in the wild flora of East Mediterranean and Southeastern Anatolia regions of Turkey, *Ind. Crops Prod.*, 32 (2010) 593-600.
- [6] İnan M, Kırpık M, Kaya DA, K.S., Effect of harvest time on essential oil composition of *Thymbra spicata* L. growing in flora of Adıyaman, *Advanced Environ. Biol*, 5 (2011) 356-358.
- [7] Bayrak C, Taslimi P, Gulcin İ, M.A., The first synthesis of 4-phenylbutenone derivative bromophenols including natural products and their inhibition profiles for carbonic anhydrase, acetylcholinesterase and butyrylcholinesterase enzymes, *Bioorg Chem.*, 72 (2017) 359-366.
- [8] Caglayan C., Demir Y., Kucukler S., Taslimi P., Kandemir F.M., Gulçin İ., The effects of hesperidin on sodium arsenite-induced different organ toxicity in rats on metabolic enzymes as antidiabetic and anticholinergics potentials: A biochemical approach, *J. Food Biochem.*, 43(2) (2019b) e12720.
- [9] Kocyigit U.M., Taşkıran A.Ş., Taslimi P., Yokuş A., Temel Y., Gulcin İ., Inhibitory effects of oxytocin and oxytocin receptor antagonist atosiban on the activities of carbonic anhydrase and acetylcholinesterase enzymes in the liver and kidney tissues of rats, *J. Biochem. Mol. Toxicol.* (2017b) e21972.
- [10] Gul H.I. A., Demirtas G., Ucar P.T., Gulcin İ., Synthesis of Mannich bases by two different methods and evaluation of their acetylcholine esterase and carbonic anhydrase inhibitory activities, *Lett. Drug Des. Discov.*, 14(10) (2016) 573-580.
- [11] Taslimi P., Aslan H.E., Demir Y., Oztaskin N., Maraş A., Gulçin İ., Beydemir S., Goksu S., Diarylmethanon, bromophenol and diarylmethane compounds: Discovery of potent aldose reductase, α -amylase and α -glycosidase inhibitors as new therapeutic approach in diabetes and functional

- hyperglycemia, *Int. J. Biol. Macromol.*, 119 (2018) 857-863.
- [12] Demir Y., Taslimi P., Ozaslan M.S., Oztaskin N., Çetinkaya Y., Gulçin İ., Beydemir Ş., Goksu S., Antidiabetic potential: In vitro inhibition effects of bromophenol and diarylmethanones derivatives on metabolic enzymes, *Arch. Pharm. (Weinheim)*, 351(12) (2018) e1800263.
- [13] Demir Y., Özaslan M.S., Duran H.E., Küfrevioğlu Ö.İ., Beydemir Ş., Inhibition effects of quinones on aldose reductase: Antidiabetic properties, *Environ. Toxicol. Pharmacol.*, 70 (2019) 103195.
- [14] Demir Y., Durmaz L., Taslimi P., Gulçin İ., Antidiabetic properties of dietary phenolic compounds: Inhibition effects on α -amylase, aldose reductase, and α -glucosidase, *Biotechnol. Appl. Biochem.*, 66(5) (2019) 781-786.
- [15] Demir Y., Duran H.E., Durmaz L., Taslimi P., Beydemir Ş., Gulçin İ., The Influence of Some Nonsteroidal Anti-inflammatory Drugs on Metabolic Enzymes of Aldose Reductase, Sorbitol Dehydrogenase, and α -Glucosidase: a Perspective for Metabolic Disorders, *Appl. Biochem. Biotechnol.*, 190(2) (2020) 437-447.
- [16] Kang W., Song Y., Gu X., α -glucosidase inhibitory *in vitro* and antidiabetic activity *in vivo* of *Osmanthus fragrans*, *J. Med. Plants Res.*, 6 (2012) 2850-2856.
- [17] Sannigrahi S., Mazuder U.K., Pal D.K., Parida S., Jain S., Antioxidant potential of crude extract and different fractions of *Enhydra fluctuans* Lour, Iran. *J. Pharm. Res.*, 9 (2010) 75-82.
- [18] Re R., Pellegrini N., Proteggente A., Pannalaa A., MinYang, Rice-Evans C., Rice-Evans, Antioxidant activity applying an improved ABTS radical cation decolorization assay, *Free Radic. Biol. Med.*, 26 (1999) 1231-1237.
- [19] Topal F., Topal M., Gocer H., Kalın P., Kocyigit U.M., Gulcin İ., Alwasel S.H., Antioxidant activity of taxifolin: An activity-structure relationship, *Journal of Enzyme Inhibition and Medicinal Chemistry*, 31(4) (2016) 674-683.
- [20] Tao Y., Zhang Y., Cheng Y., Wang Y., Rapid screening and identification of α -glucosidase inhibitors from mulberry leaves using enzyme-immobilized magnetic beads coupled with HPLC/MS and NMR, *Biomed. Chromatogr.*, 27 (2013) 148-155.
- [21] Trojan-Rodrigues M., Alves T.L.S., Soares G.L.G., Ritter M.R., Plants used as antidiabetics in popular medicine in Rio Grande do Sul, southern, Brazil, *J. Ethnopharmacol.*, 139 (2012) 155-163.
- [22] Athar M., Back J.H., Tang X., Kim K.H., Kopelovich L., Bickers D.R., Kim A.L., . Resveratrol: A review of preclinical studies for human cancer prevention, *Toxicol. Appl. Pharmacol.*, 224 (2007) 274-283.
- [23] Noh J.S., Park C.H., Yokozawa T., Treatment with oligonol, a low-molecular polyphenol derived from lychee fruit, attenuates diabetes-induced hepatic damage through regulation of oxidative stress and lipid metabolism, *Br. J. Nutr.*, 106 (2011) 1013-1022.
- [24] Varmaghan Z., Monajjemi M., Mollaamin F. Ab Initio Study of Vinblastine- Tubulin Anticancer Complex, *Biomacromolecular Journal*, 1(1) (2015) 46- 51.
- [25] Gökalp F., The chemical activity of Juglone in different phases as a protective agent, *Journal of Fluorine Chemistry*, 42 (2021) 109701.
- [26] Gökalp F., An investigation of the olive phenols activity as a natural medicine, *Journal of Food and Drug Analysis*, 26(2) (2018) 657-661.
- [27] Ritchie D.W., Recent progress and future directions in protein-protein docking, *Curr. Protein Pept. Sci.*, 9(1) (2008) 1-15.
- [28] Ahmad H., Ahmad S., Shah S.A.A., Latif A., Ali M., Khan F.A., Tahir M.N., Shaheen F., Wadood A., Ahmad M., Antioxidant and anticholinesterase potential of diterpenoid alkaloids from *Aconitum heterophyllum*, *Bioorg. Med. Chem.*, 25(13) (2017) 3368-3376.
- [29] Gülçin İ., Antioxidant activity of eugenol: a structure-activity relationship study, *J. Med.*

Food, 14(9) (2011)975-85.

- [30] Yu L., Haley S., Perret J., Harris M., Wilson J., Qian M., Free radical scavenging properties of wheat extracts, *J. Agric. Food Chem.*, 50 (2002)1619–1624.
- [31] Gulcin İ., Antioxidant activity of food constituents-An overview, *Archives of Toxicology*, 86(3) (2012) 345-391.
- [32] Herring A., Ambrée O., Tomm M., Habermann H., Sachser N., Paulus W., Keyvani K., Environmental enrichment enhances cellular plasticity in transgenic mice with Alzheimer-like pathology, *Exp. Neurol.*, 216 (2009) 184–192.
- [33] Francis P.T., Palmer A.M., Snape M., Wilcock G.K., The cholinergic hypothesis of Alzheimer's disease: a review of progress, *J. Neurol. Neurosurg Psychiatry*, 66 (1999) 137–147.
- [34] Kocyigit U.M., Budak Y., Gurdere M.B., Erturk F., Yencilek B., Taslimi P., Gulcin İ., Ceylan M., Synthesis of chalcone-imide derivatives and investigation of their anticancer and antimicrobial activities, carbonic anhydrase and acetylcholinesterase enzymes inhibition profiles. *Arch. Physiol. Biochem.*, (2017) 3455.
- [35] Kocyigit U.M., Taslimi P., Gezegen H., Gulcin İ., Ceylan M., Evaluation of acetylcholinesterase and carbonic anhydrase inhibition profiles of 1, 2, 3, 4, 6-pentastituted-4-hydroxy-cyclohexanes, *J. Biochem. Mol. Toxicol*, 31(9) (2017) 21938
- [36] Sy G.Y., Cissé A., Nongonierma R.B., Sarr M., Mbodj N.A., Faye B., Hypoglycaemic and antidiabetic activity of acetonic extract of *Vernonia colorata* leaves in normoglycaemic and alloxan-induced diabetic rats, *J. Ethnopharmacol.*, 98 (2005) 171–175.
- [37] Jung M., Park M., Lee H.C., Kang Y.H., Kang E.S., Antidiabetic agents from medicinal plants, *Curr. Med. Chem.*, 13 (2006) 1203–1218.
- [38] Malviya N., Jain S., Malviya S., Antidiabetic potential of medicinal plants, *Acta Pol. Pharm. - Drug Res.*, 67 (2010) 113–118.
- [39] Grover J.K., Yadav S., Vats V., Medicinal plants of India with anti-diabetic potential, *J. Ethnopharmacol.*, 81 (2002) 81–100.
- [40] Frisch M.J., Trucks G.W., Schlegel H.B., Scuseria G.E., Robb M.A., Cheeseman J.R., G. Scalmani, V. Barone, B. Mennucci, G.A. Petersson, H. Nakatsuji, M. Caricato, X. Li, H.P. Hratchian, A.F. Izmaylov, J. Bloino, G. Zheng, J.L. Sonnenberg, M. Hada, M. Ehara, K. Toyota, R. Fukuda, J. Hasegawa, M. Ishida, T. Nakajima, Y. Honda, O. Kitao, H. Nakai, T. Vreven, J.A. Montgomery Jr., J.E. Peralta, F. Ogliaro, M. Bearpark, J.J. Heyd, E. Brothers, K.N. Kudin, V.N. Staroverov, R. Kobayashi, J. Normand, K. Raghavachari, A. Rendell, J.C. Burant, S.S. Iyengar, J. Tomasi, M. Cossi, N. Rega, J. M. Millam, M. Klene, J.E. Knox, J.B. Cross, V. Bakken, C. Adamo, J. Jaramillo, R. Gomperts, R.E. Stratmann, O. Yazyev, A.J. Austin, R. Cammi, C. Pomelli, J.W. Ochterski, R.L. Martin, K. Morokuma, V.G. Zakrzewski, G.A. Voth, P. Salvador, J.J. Dannenberg, S. Dapprich, A.D. Daniels, O. Farkas, J.B. Foresman, J.V. Ortiz, J. Cioslowski, D.J. Fox, Gaussian, Inc., Wallingford CT, (2009).

Structure reactivity analysis for Phenylalanine and Tyrosine

Rebaz Anwar OMER^{1,5*} , Pelin KOPARIR² , Ibrahim Nazem QADER^{3,6} ,
Lana Omer AHMED⁴ 

¹Koya University, Faculty of Science & Health Chemistry Department, Koya, Iraq

²Institute of Forensics, Malatya, TURKEY

³University of Raparin, College of Science, Department of Physics, Sulaymanyah, Iraq

⁴Koya University, Faculty of Science & Health Physics Department, Koya, Iraq

⁵Firat University, Faculty of Science, Department of Chemistry, 23169 Elazig, Turkey

⁶Firat University, Faculty of Science, Department of Physics, 23169 Elazig, Turkey

Abstract

Phenylalanine (Phe) is one of the amino acids that cannot be produced in the body and must be ingested through diet. Tyrosine (Tyr) is also a non-essential amino acid and can be produced by Phe hydroxylation in the liver when the dietary intake of Tyr is low. Structure analysis is very important to know the correct synthesis and the reactivity of the molecule. In this study, the characterization of Phe and Tyr molecules were investigated using quantum chemical calculations. The molecular geometry for both molecules was determined using density functional theory (B3LYP) by handling the 6-311++G(d,p) basis set. The method of TD-DFT which is based on the B3LYP/6-311++G(d,p) level, was utilized in ethanol solvent to find the electronic absorption spectra. In addition, frontier molecular orbitals, electrostatic potential and molecular charge distributions analysis were carried out by B3LYP/6-311++G(d,p) theory. The energy differences between HOMO and LUMO for Phe were obtained as 0.19851 eV, which have a good argument with the reactivity compared with tyrosine, and energy band gap was 0.20501 eV.

Article info

History:

Received: 18.01.2021

Accepted: 26.08.2021

Keywords:

Phenylalanine,
Tyrosine,
DFT,
HOMO,
LUMO.

1. Introduction

The kinetics of Phe and Tyr were studied in humans [1]. The amino acids have been studied, to determine their biological and chemical properties. Additionally, in optoelectronic, they have a wide range of applications [2, 3]. In biology, Phe and Tyr are two organic compounds that have some fundamental differences in their structures. Both molecules have an NH₂ group (amino), a COOH group (carboxylic acid), and a radical group (R-group) [4]. Generally, the amino acids family has been classified as polar and nonpolar, whereby Phe and Tyr belong to the nonpolar and the polar groups, respectively [5]. Tyr has one more hydroxide bonded with a phenyl ring compared to a Phe molecule Figure 1. In addition, they have some isomers with the same composition, but different geometry.

L-Phe is an isomer of Phe molecules that can be naturally found, while, D -Phe is an artificial product.

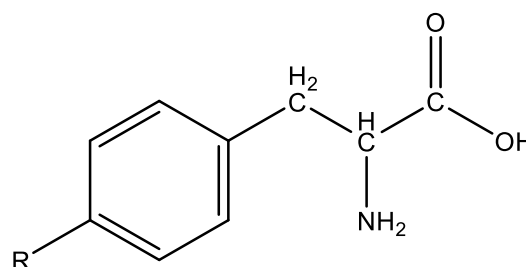


Figure 1. The chemical structure of phenylalanine (when R represents H) and Tyrosine (when R represents OH)

Similarly, Tyr has also L and D chemical structures. Amino acids are nonlinear optical biomolecules that can change the direction of electromagnetic radiation. Theoretical and experimental measurements, such as deuterium NMR [6], FT-IR, and Raman spectrometry [4, 7] have been carried out to determine structurally and some other properties of L-Phe and L-Tyr. Freire et al. [4] studied the vibrational behavior of all kinds of amino acids, includes L-Phe and L-Tyr, through the Raman spectrum.

*Corresponding author. e-mail address: rebazanward@gmail.com

Density functional theory (DFT) is commonly used to study the electronic properties of organic compounds, molecular structure, chemical reactivity, and hydrogen bonding [8-11]. Among all of the approaches, the energy correlation is the main advantage in the DFT; accordingly, the estimated exchange nature energy coordination has a direct effect on the confidence. The DFT methods are creative exchange energy management, therefore, in many theoretical kinds of research DFT methods were used regularly [12, 13]. There are rare or no studies in which extensively make comparisons between L-Phe and L-Tyr molecules. Therefore, this study can cover these two amino acids from many points of view and it can make many contributions to the literature.

In this study, a theoretical computation based on the DFT technique has been carried out for Phe and molecules using the Gaussian 09W. The geometrical, charge distribution, and vibrational properties of these biomolecules have been compared in their ground states and the same conditions. The results have been compared to experimental results in the literature.

2. Computational Methods

Gaussian 09W software package was used for computations based on DFT with a B3LYP hybrid functional and 6-311++G(d,p) basis set [14, 15]. The conformational and molecular energy profile was found by used B3LYP/6-311++(d,p) [16]. The molecular electrostatic potentials were assessed using the B3LYP/6-311++G(d,p) method to examine the reactive sites of our compounds. Also, frontier

molecular orbitals parameters were performed for both compounds on the basis set of B3LYP/6-311++G(d,p).

3. Results and Discussion

3.1. Molecular geometry

The B3LYP/6-311++G(d,p) system acquires the best study for optimal geometry. Figure 2 shows the scheme of chemical composition and geometry of the L-Phe and L-Tyr molecules. Several molecular properties such as the dipole moment and spectroscopic transitions can be utilized by molecular symmetry. Both Phe and Tyr are aromatic due to the delocalization of the continued electrons in the benzene ring. The bond length for C-C and C=C in a benzene ring is equal to 1.54 and 1.40 Å, respectively, while the bond length for C=C (from ethylene) is equal to 1.34 Å [17]. For the DFT calculation using B3LYP/6-311++G(d,p), the bond length for C-C and C=C (in benzene ring) for our compounds was 1.51 and 1.39 Å, respectively. The bond length for C-N in both structures was 1.45 Å, which is consistent with the previous studies [18].

The C=O bond length for was equal to 1.231622 Å which is a little be smaller than C=O in Tyr equal to 1.233 Å. The bond length for C-O for both compounds is equal to 1.378 Å. It can be seen that in the geometrical structure in Figure 2. The result showed they are very different in the rotation of the atoms in a molecule, which means the bond angle and the dihedral were very different for both Phe and tyrosine. The values for the calculated geometric parameters are shown in Table 1.

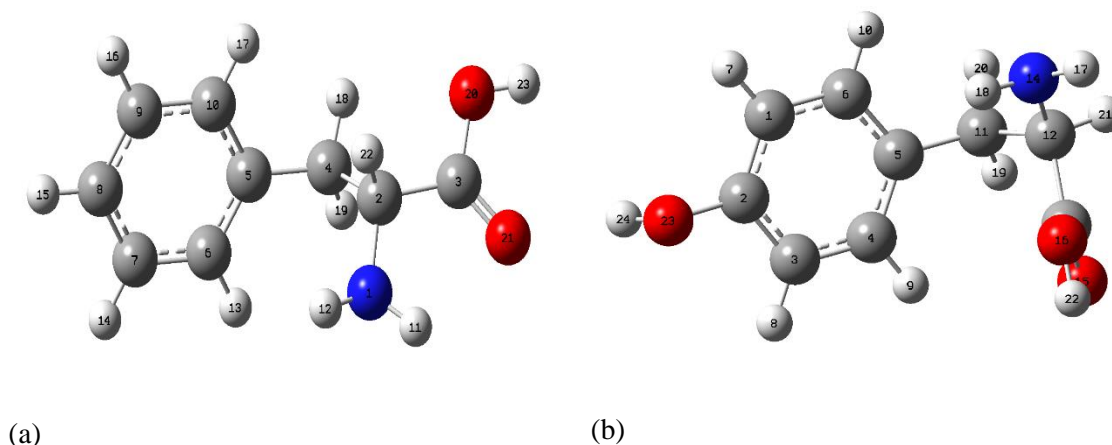


Figure 2. The theoretical geometrical structure of a) the phenylalanine and b) the Tyrosine with B3LYP/6-311++G(d,p).

Table 1. Geometrical parameters of Phenylalanine and Tyrosine by B3LYP/6-311++G(d,p).

phenylalanine		Tyrosine	
Parameters	6-311++G(d,p)	Parameters	6-311++G(d,p)
Bond Length		Bond Length	
N(1)-C(2)	145.487	C(1)-C(2)	139.381
C(2)-C(3)	151.182	C(2)-C(3)	139.418
C(2)-C(4)	156.092	C(3)-C(4)	139.676
C(4)-C(5)	151.385	C(4)-C(5)	140.584
C(5)-C(6)	140.397	C(1)-C(6)	139.746
C(6)-C(7)	139.847	C(5)-C(11)	151.573
C(7)-C(8)	139.779	C(11)-C(12)	155.857
C(8)-C(9)	139.854	C(12)-(13)	152.950
C(9)-C(10)	139.726	C12-N(14)	145.516
C(3)-O(20)	137.844	C(13)-O(15)	123.369
C(3)-O(21)	123.162	C(13)-O(16)	137.802
C(2)-O(23)		C92)-O(23)	141.725
Bond Angles (°)		Bond Angles (°)	
N(1)-C(2)-C(3)	10.871.990	C(1)-C(2)-C(3)	12.053.109
N(1)-C(2)-C(4)	11.171.210	C(2)-C(3)-C(4)	11.958.521
C(2)-C(4)-C(5)	11.211.240	C(3)-C(4)-C(5)	12.102.014
C(4)-C(5)-C(6)	12.112.410	C(2)-C(1)-C(6)	11.953.222
C(5)-C(6)-C(7)	12.078.110	C(4)-C(5)-C(11)	12.093.766
C(6)-C(7)-C(8)	12.021.650	C(5)-C(11)-C(12)	11.430.130
C(7)-C(8)-C(9)	11.957.120	C11-C12-C13	10.953.644
C(8)-C(9)-C(10)	12.008.260	C11-C12-N14	11.131.945
C(2)-C(3)-O(20)	11.223.110	C12-C13-O15	12.460.178
C(2)-C(3)-O(21)	12.577.080	C12-C13-O16	11.358.959
		C1-C2-O23	11.966.523
Dihedral Angles (°)		Dihedral Angles (°)	
C(3)-C(2)-C(4)-C(5)	6.387.876	C4-C5-C11-C12	-8.988.074
C(2)-C(4)-C(5)-C(6)	-9.329.010	C11-C12-C13-C16	12.689.600

3.2. Frontier molecular orbitals

The principle characterizing of the molecular orbital is the relationship between HOMO and LUMO with HOMO-1 and LUMO+1. In quantum chemistry, the frontier molecular orbital theory is critical [19]. The maximum straight-forward of such interactions, which helps to identify molecular qualities, is the one linked to the discrepancy between a natural system's highest occupied molecular orbital (HOMO) and the lowest unoccupied molecular orbital (LUMO) [20, 21].

The LUMO energy is associated with the affinity of the electrons and defines how sensitive the molecule to the nucleophilic attack. The HOMO energy is linked to the

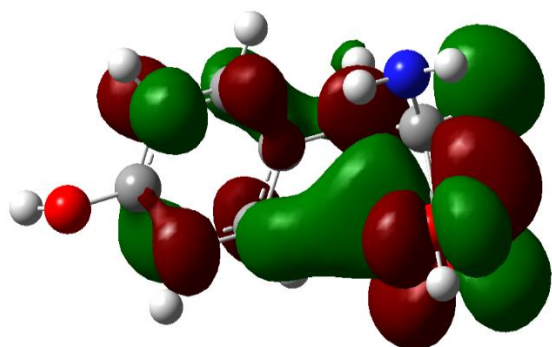
potential for ionization and defines how sensitive the molecule is to an electrophilic attacked [22, 23]. The chemical activity of the compound is generally indicated by the HOMO and LUMO energy values and the potential differences between them.

The small energy difference between HOMO and LUMO denotes a robust interaction and rapid reaction. Figure 3 shows the arrangement and energy levels of orbitals, including HOMO-1, HOMO, LUMO, and LUMO+1, which determined by a B3LYP/6-311++G(d,p) level for Phe and tyrosine. The results show that the higher energy level between HOMO and LUMO was appeared in Tyr molecule compared with

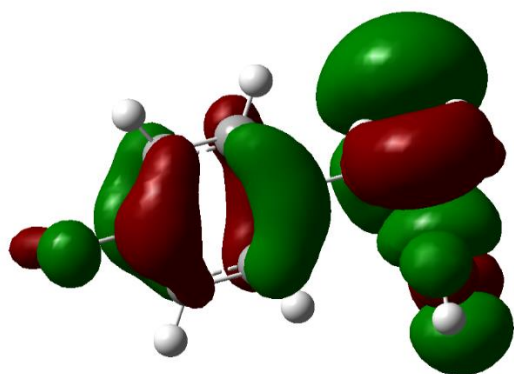
Phenylalanine, while the energy level between HOMO-1 and LUMO+1 for both compounds are closed to each other. The energy gap for Phe and Tyr

are 0.19851eV and 0.20501 eV, which indicates that Phe molecule has more reactivity compared to Tyr molecule this is due to lower energy bandgap.

(a)



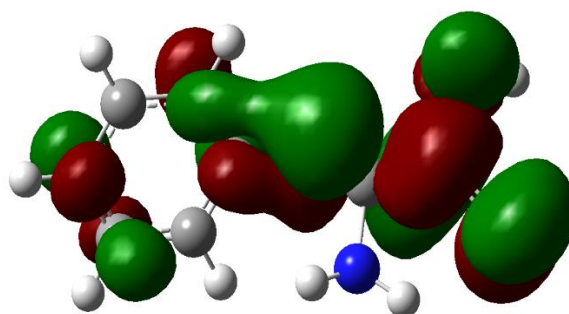
LUMO = - 0.03716



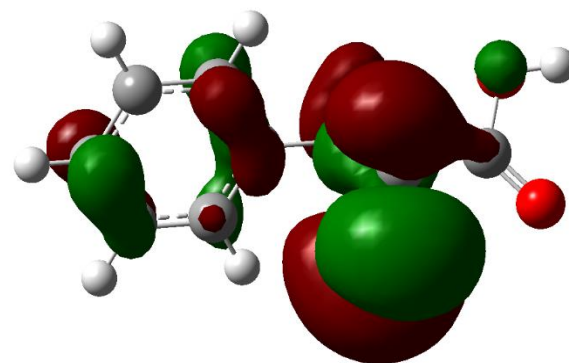
HOMO = - 0.24217

$\Delta E = - 0.20501$

(b)



LUMO = - 0.03836



HOMO = - 0.23687

$\Delta E = 0.19851$

Figure 3. Molecular orbital surfaces and energy levels for the HOMO and LUMO analysis by B3LYP/6-311++G(d,p) a) Tyrosine b) phenylalanine

Various molecular parameters can be calculated based on the HOMO and LUMO energy values [24]. The minimum amount of energy required to eliminate an electron in a gaseous state from the atom or molecule is known as the ionization potential which is expressed as $I = -E_{HOMO}$, also the amount of energy expelled as a result of one electron being added to a gaseous molecule is called electron affinity ($A = -E_{LUMO}$) [25,

26]. The predilection of a nuclear to draw electrons is known as electronegativity (X) [27]. The prevention of weight transfer in a molecule is denoted by chemical hardness (η) [28]. Table 2 shows the electronic structure parameters, which determined using the B3LYP/6-311++G(d,p) technique. The results show that the hardness of Phe less than Tyr molecule.

Table 2. Electronic parameters for both Phe and Tyr.

In a Basis Set	B3LYP/6-311++G(d,p)	Equations	Result of phenylalanine	Result of Tyrosine
$E_{\text{LOMO}+1}$ (eV)		$E_{\text{LOMO}+1}$ (eV)	-0.02107	-0.02444
E_{LOMO} (eV)		E_{LOMO} (eV)	-0.03836	-0.03716
E_{HOMO} (eV)		E_{HOMO} (eV)	-0.23687	-0.24217
$E_{\text{HOMO}-1}$ (eV)		$E_{\text{HOMO}-1}$ (eV)	0.25743	0.25444
$\Delta E = E_{\text{HOMO}} - E_{\text{LOMO}}$ (eV)		HOMO - LOMO	-0.19851	-0.20501
$\Delta E = E_{\text{HOMO}-1} - E_{\text{LOMO}+1}$ (eV)		(HOMO-1) – (LOMO+1)	-0.23636	-0.23000
I (eV)		$I = -E_{\text{HOMO}}$	0.23687	0.24217
A (eV)		$A = -E_{\text{LUMO}}$	0.03836	0.03716
X (eV)		$X = I + A/2$	0.51918	0.51858
n (eV)		$n = I - A/2$	0.48082	0.48142
S (eV)		$S = 1/2n$	1.03989	1.03859
μ_{total}			0.68230	1.73720
μ_x			-0.09750	0.79250
μ_y			0.63660	1.37380
μ_z			-0.22530	-0.70900

3.3. UV–Vis spectral studies

The electronic absorption is primarily defined by one electron excitation from HOMO to LUMO, which is equivalent to the transition from ground to the first excited state. Typically, the categorization of electronic transitions is based on the orbitals involved or certain sections of the molecule concerned [29, 30]. The most frequent electronic transfer occurred in organic molecules from π (donor) – π^* (acceptor). The source of the absorption in organic compounds causes the vibration of the electrons from the ground state to excited state [31, 32]. According to the Franck Condon principle, the maximum absorption peak was

equivalent to the vertical excitation. Figure 4 reveals the UV spectrum measurement in ethanol. It was found that the first electron transition of Phe occurred at 276 nm with oscillator strength 0.0332 corresponding to H-1/L, the second transition occurred at 238 nm with 0.0046 oscillator strength, and the third on at 235 nm with 0.05 oscillator strength, corresponding to H-2/L. Figure 4b shows three electronic transitions of Tyrosine, which located at 274, 242, and 233 nm with oscillator strength 0.02, 0.0032, and 0.0079, respectively. The results approve that Tyr is a more stable compound because it has a less excitation energy compared by phenylalanine.

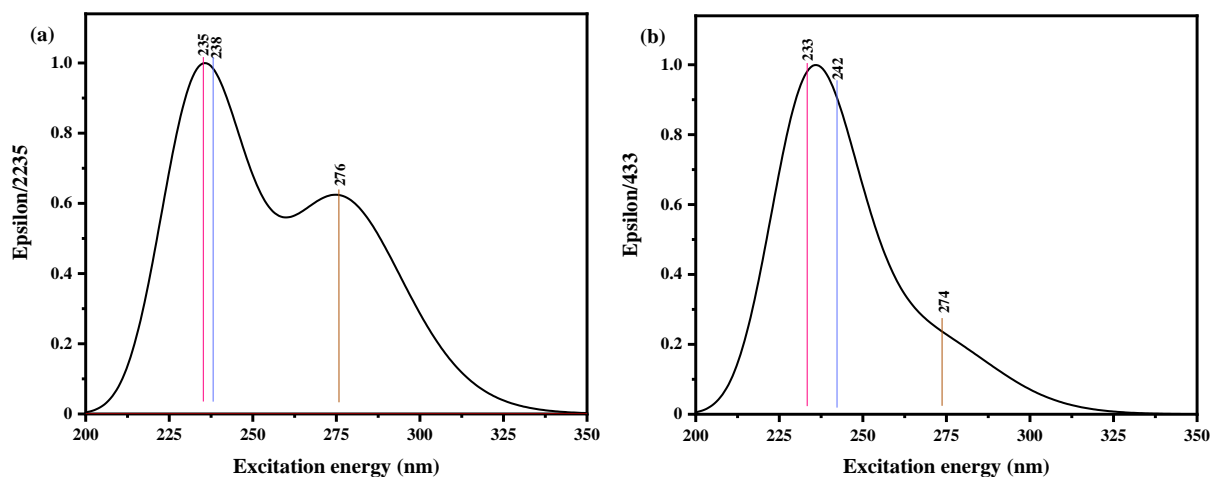


Figure 4. UV spectrum on the TD-DFT//B3LYP/6-311++G(d,p) level in ethanol a) Phenylalanine b) Tyrosine

3.4. Molecular electrostatic potential

Electrostatic potential map (EPM) shows the 3D charge distributions of molecules, which is known as electrostatic potential energy map, therefore the load differences can be found in the various areas of the molecule. If the distributions of charges are known, the essence of the interaction between the molecules can be elucidated. Besides, the analysis and anticipation of a molecule's reactive behavior can be effectively carried out using the EMP. The space surrounding the nuclei and electrons in a molecule is considered as the generate charge distributions[33, 34]. Various colors denote different electrostatic potential values, where

red indicates the most negative value and blue represents the most positive value. In accordance with the color spectrum, colors allocate the intermediate potentials, such that: red < orange < yellow < green < blue. The red areas on the map represents the maximum electrons abundance; while the blue areas exposes the lowest electron concentration [35, 36]. For the compound, the MEP map's color code ranged from -0.06074 a.u. (Extreme red) to 0.06074 a.u. (Extreme blue) are the strongest attraction and the strongest repulsion, respectively.

-6.074e-2  6.074e-2

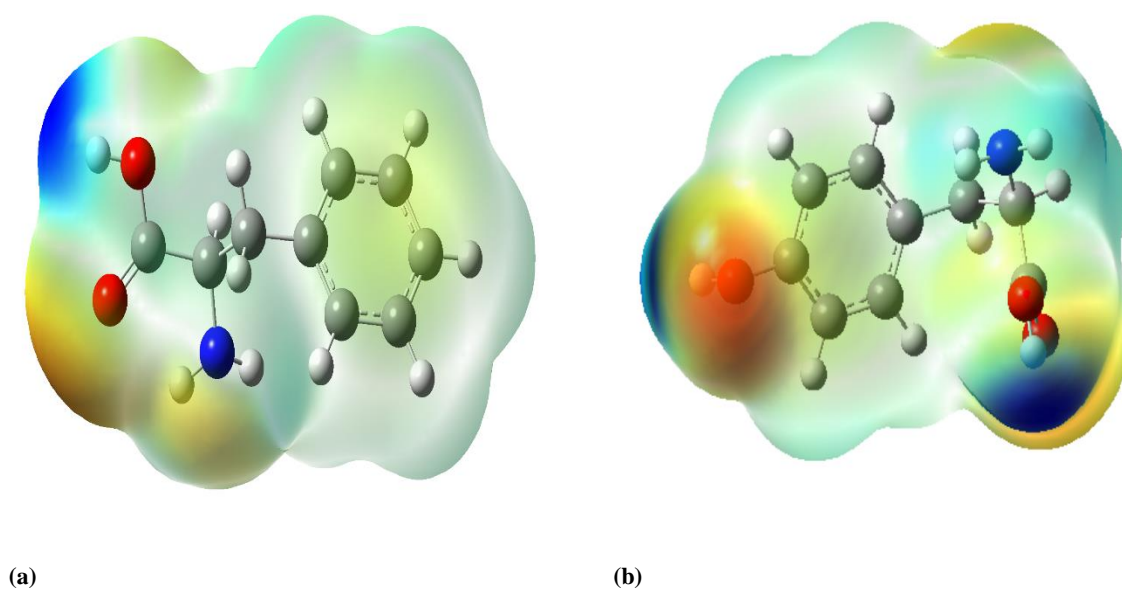


Figure 5. Molecular electrostatic potential calculated at B3LYP/6-31++G(d,p) level. a) Phenylalanine b) Tyrosine.

Figure 5 shows the mapping of the potentially electrostatic surface for the Phe and Tyr compounds. Red and blue signify the greatest repulsion and greatest attraction, respectively. The result shows that the light red color (negative) has appeared on the (C=O) groups and the blue color (positive) was appeared on the hydrogen of the (OH) group in Phe molecule, while the deep red color in Tyr molecule has appeared on the hydroxyl group of the phenyl and the blue color appeared on the hydrogen of the (OH) groups. Also, the overall results confirm that the Tyr molecule are more attractive with electrophiles than phenylalanine, which is due to the OH group in the Tyr molecule.

3.5. Atomic Charge Distributions

The distributions of charges over the atoms suggest the creation of donor and acceptor pairs that require the transfer of charges within the molecule. Table 3 displays the Mulliken atomic charges of our compounds for carbon and oxygen atoms, calculated at the level of B3LYP/6-311++G(d,p) with the molecule in the gas phase.

Table 3. Atomic charges distribution (e) of the Phenylalanine and Tyrosine title compound in gas phase.

phenylalanine		Tyrosine	
Atom	Charge	Atom	Charge
N1	-0.43012	C1	-0.05399
C2	-113.456	C2	-105.566
C3	0.23728	C3	-0.18587
C4	-0.70471	C4	-0.25410
C5	103.836	C5	108.035
C6	-0.44246	C6	-0.15452
C7	-0.47620	H7	0.33801
C8	-0.40982	H8	0.33893
C9	-0.27919	H9	0.33047
C10	-0.25798	H10	0.32079
H11	0.35185	C11	-0.89210
H12	0.33987	C12	-0.51829
H13	0.33599	C13	-0.22598
H14	0.28690	N14	-0.47708
H15	0.26519	O15	-0.28066
H16	0.28381	O16	-0.21678
H17	0.29835	H17	0.37870
H18	0.32553	H18	0.37350
H19	0.24924	H19	0.31678
O20	-0.28971	H20	0.31174
O21	-0.32614	H21	0.31293
H22	0.34637	H22	0.38406
H23	0.39217	O23	-0.55498
		H24	0.38374

Mulliken method imposes that the negative atomic charges of the oxygen in the hydroxyl groups of the phenyl in Tyr molecule, which is not in the Phe this is the big difference between to molecule. The oxygen of the carboxylic acid in Phe was a greater negative charge compared with the carboxyl group in tyrosine.

Mulliken charge distribution is very popular to determine dipole moments, atomic charge effects, molecular polarization, electronic structures, and other properties of a molecule [37, 38].

4. Conclusion

Structural analysis and electronic investigation for both Phe and Tyr have been carried out using DFT/B3LYP methods with basis set 6-311++G(d,p). Bond length, bond angle, and dihedral angle were calculated by B3LYP on the basis set 6-311++G(d,p) to find the geometrical structures for both compounds. The reactivity and structure properties of the molecules were determined throughout the energy bandgaps between HOMO and LUMO, which were calculated by B3LYP/6-311++G(d,p). The band gap between HOMO and LUMO for Phe was equal to 0.19851 eV, which has a good argument with its reactivity compared to tyrosine with energy band gap of 0.20501 eV. For the phenylalanine, the maximum excitation energy was obtained by TD/DFT, which show that the molecule is more reactive than tyrosine. Molecular electrostatic potential maps and charge distribution showed that the OH of the carboxylic groups has positive potential sites around in both Phe and tyrosine. Also, a deep negative potential site was found around the OH of the phenyl groups in Tyr molecule which was not observed in the phenylalanine.

Conflict of interest

The authors declare that they have no conflict of interest.

References

- [1] Matthews D. E., An overview of phenylalanine and tyrosine kinetics in humans, *The Journal of Nutrition*, 6(137) (2007) 1549-1555.
- [2] Selvarani K., Mahalakshmi R., A Review on Physical and Chemical Properties of L-Phenylalanine Family of NLO Single Crystals, *Journal of Chem. Tech. Research*, 1(9) (2016) 113.
- [3] Omar R., Koparir P., Koparir M., Synthesis of 1, 3-Thiazole derivatives, *Indian Drugs*; 1(58) (2021) 1.
- [4] Freire P. T., Barboza F. M., Lima J. A., Melo F. E., Mendes Filho J., Raman spectroscopy of amino acid crystals, *Raman Spectroscopy and Applications*, (2017) 201.
- [5] Kumar K., Analysis of Tryptophan and Tyrosine in the Presence of Other Bioactive Molecules Using Generalized Rank Annihilation Method on Excitation-emission Fluorescence Spectroscopic Data Sets, *Journal of Fluorescence*, (2020) 1-6.
- [6] Kinsey R. A., Kintanar A., Oldfield E., Dynamics of amino acid side chains in membrane proteins by high field solid state deuterium nuclear magnetic resonance spectroscopy. Phenylalanine, tyrosine, and tryptophan, *Journal of Biological Chemistry*, 17(256) (1981) 9028-9036.
- [7] Moreno J. R. A., Moreno M. d. M. Q., Ureña F. P., González J. J. L., Conformational preference of short aromatic amino acids from the FT-IR, FT-Raman and Far-IR spectroscopies, and quantum chemical calculations: l-phenylalanine and l-tyrosine, *Tetrahedron: Asymmetry*, 14(23) (2012) 1084-1092.
- [8] Palafox M. A., Rastogi V., Tanwar R., Mittal L., Vibrational frequencies and structure of 2-thiouracil by Hartree-Fock, post-Hartree-Fock and density functional methods, *Spectrochimica Acta Part A: Molecular and Biomolecular Spectroscopy*; 11(59) (2003) 2473-2486.
- [9] Mohan S., Sundaraganesan N., Mink J., FTIR and Raman studies on benzimidazole, *Spectrochimica Acta Part A: Molecular Spectroscopy*, 8(47) (1991) 1111-1115.
- [10] Ten G., Nechaev V., Pankratov A., Berezin V., Baranov V., Effect of hydrogen bonding on the structure and vibrational spectra of the complementary pairs of nucleic acid bases. II. adenine-thymine, *Journal of Structural Chemistry*, 5(51) (2010) 854-861.
- [11] Qader I. N., Mohammad A., Azeez Y. H., Agid R. S., Hassan H. S., Al-Nabawi S. H. M., Chemical Structural and Vibrational Analysis of Potassium Acetate: A Density Function Theory Study, *Journal of Physical Chemistry and Functional Materials*, 1(2) 22-24.
- [12] Cansız A., Orek C., Koparir M., Koparir P., Cetin A., 4-Allyl-5-pyridin-4-yl-2, 4-dihydro-3H-1, 2, 4-triazole-3-thione: Synthesis, experimental and theoretical characterization, *Spectrochimica Acta Part A: Molecular and Biomolecular Spectroscopy*, (91) (2012) 136-145.
- [13] Koparir P., Sarac K., Orek C., Koparir M., Molecular structure, spectroscopic properties and quantum chemical calculations of 8-t-butyl-4-methyl-2H-chromen-2-one, *Journal of Molecular Structure*, (1123) (2016) 407-415.
- [14] Frisch M., Trucks G., Schlegel H. B., Scuseria G., Robb M., Cheeseman J., Scalmani G., Barone V., Mennucci B., Petersson G., GAUSSIAN 09. Revision D. 01. Gaussian Inc. Wallingford, CT, USA; (2009).
- [15] Lee C., Yang W., Parr R. G., Development of the Colle-Salvetti correlation-energy formula into a functional of the electron density, *Physical review B*, 2(37) (1988) 785.
- [16] Beck A. D., Density-functional thermochemistry. III. The role of exact exchange, *J. Chem. Phys.*, 7(98) (1993) 5648-6.
- [17] Fortenberry R. C., Novak C. M., Lee T. J., Bera P. P., Rice J. E., Identifying Molecular Structural Aromaticity for Hydrocarbon Classification, *ACS omega*, 11(3) (2018) 16035-16039.

- [18] Ahmed L., Omer R., Kebiroglu H., A theoretical study on Dopamine molecule, *Journal of Physical Chemistry and Functional Materials*, 2(2) (2019) 66-72.
- [19] Celikezen, F., Orek C., Parlak A., Sarac K., Turkez H., Tozlu Ö. Ö., Synthesis, structure, cytotoxic and antioxidant properties of 6-ethoxy-4-methylcoumarin, *Journal of Molecular Structure*, (1205) (2020) 127577.
- [20] Amalanathan M., Rastogi V., Joe I. H., Palafox M., Tomar R., Density functional theory calculations and vibrational spectral analysis of 3, 5-(dinitrobenzoic acid), *Spectrochimica Acta Part A: Molecular and Biomolecular Spectroscopy*, 5(78) (2011) 1437-1444.
- [21] Rebaz O., Koparir P., Ahmed L., Koparir M., Computational determination the reactivity of salbutamol and propranolol drugs, *Turkish Computational and Theoretical Chemistry*, 2(4) (2020) 67-75.
- [22] Koparir M., Orek C., Alayunt N., Parlak A. E., Koparir, P., Sarac K., Dastan S. D., Cankaya N., Synthesis, Structure Investigation, Spectral Characteristics and Biological Activitie of 4-Benzyl-3-(2-Hydroxyphenyl)-1H-1, 2, 4-Triazole-5 (4H)-Thione, *Communications in Computational Chemistry*, 3(1) (2013) 244-268.
- [23] Omer R. A., Ahmed L. O., Koparir M., Koparir P., Theoretical analysis of the reactivity of chloroquine and hydroxychloroquine, *Indian Journal of Chemistry-Section A (IJCA)*, 12(59) (2020) 1828-1834.
- [24] Perdew J. P., Levy M., Physical content of the exact Kohn-Sham orbital energies: band gaps and derivative discontinuities, *Physical Review Letters*, 20(51) (1983) 1884.
- [25] Janak J. F., Proof that $\partial E \partial n_i = \epsilon_i$ in density-functional theory, *Physical Review B*, 12(18) (1978) 7165.
- [26] Koopmans T., Ordering of wave functions and eigenenergies to the individual electrons of an atom, *Physica*, 1 (1933) 104-113.
- [27] Parr R. G., Pearson R. G., Absolute hardness: companion parameter to absolute electronegativity, *Journal of the American chemical society*, 26(105) (1983) 7512-7516.
- [28] Pearson R. G., Absolute electronegativity and hardness correlated with molecular orbital theory, *Proceedings of the National Academy of Sciences*, 22(83) (1986) 8440-8441.
- [29] Adamo C., Jacquemin D., The calculations of excited-state properties with Time-Dependent Density Functional Theory, *Chemical Society Reviews*, 3(42) (2013) 845-856.
- [30] Scuseria R., a. GE, An efficient implementation of time-dependent density-functional theory for the calculation of excitation energies of large molecules, *J. Chem. Phys.*, 19(109) (1998) 8218-8224.
- [31] Arjunan V., Sakiladevi S., Marchewka M., Mohan S., FTIR, FT-Raman, FT-NMR and quantum chemical investigations of 3-acetylcoumarin, *Spectrochimica Acta Part A: Molecular and Biomolecular Spectroscopy*, 109 (2013) 79-89.
- [32] Joseph L., Sajan D., Reshmy R., Sasi B. A., Erdogdu Y., Thomas K. K., Vibrational spectra, structural conformations, scaled quantum chemical calculations and NBO analysis of 3-acetyl-7-methoxycoumarin, *Spectrochimica Acta Part A: Molecular and Biomolecular Spectroscopy*, 99 (2012) 234-247.
- [33] Palafox, M. A., Bhat, D., Goyal, Y., Ahmad, S., Joe, I. H., and Rastogi, V., FT-IR and FT-Raman spectra, MEP and HOMO–LUMO of 2, 5-dichlorobenzonitrile: DFT study. *Spectrochimica Acta Part A: Molecular and Biomolecular Spectroscopy*; 136 (2015) 464-472.
- [34] Ahmed L., Rebaz O., Spectroscopic properties of Vitamin C: A theoretical work, *Cumhuriyet Science Journal*, 41(4) (2020) 916-928.
- [35] Jeyavijayan S., Arivazhagan, M., Vibrational spectral investigation, NBO, first hyperpolarizability and UV–Vis spectral analysis of 3, 5-dichlorobenzonitrile and m-bromobenzonitrile by ab initio and density

functional theory methods, *Spectrochimica Acta Part A: Molecular and Biomolecular Spectroscopy*; 136 (2015) 234-246.

- [36] Omer, L. A., Rebaz O., Computational Study on Paracetamol Drug, *Journal of Physical Chemistry and Functional Materials*, 1(3) 9-13.
- [37] Reed A. E., Weinstock R. B., Weinhold F., Natural population analysis, *The Journal of Chemical Physics*, 2(83) (1985) 735-746.
- [38] Mulliken R. S., Electronic population analysis on LCAO–MO molecular wave functions I., *The Journal of Chemical Physics*, 10(23) (1955) 1833-1840.



Structural analysis of pure PtCu₃ nanoparticles synthesized by modified Polyol process

Doğan KAYA^{1,*}

¹ Çukurova University, Vocational School of Adana, Department of Electronics and Automation, 01160, Adana / TURKEY

Abstract

The development of effective multi-functional Pt-based nanoparticles (NPs) with enhanced activity, stability, and reduced cost for advanced applications still remains a challenge. In this study, Pt(acac)₂ and Cu(OAc)₂ metal precursors were reduced to form Pt-Cu NPs at 140 °C in ethylene glycol and sodium borohydride that is a secondary reducing agent in the modified polyol method. The x-ray diffraction (XRD) and Rietveld refinement analyses confirmed the face-centered cubic PtCu₃ structure with the space groups of $Fm\bar{3}m$ and a lattice constant of $a=b=c=3.6829$ Å. The average crystal size was found to be 2.76 nm by Scherrer's formula. Scanning electron microscopy (SEM) images confirm the formation of monodisperse PtCu₃ NPs with an average size of 8.04 nm within a narrow range of 5-13 nm. While energy-dispersive x-ray spectroscopy (EDS) analysis confirmed that the composition is formed of 26% Pt and 74% Cu atoms and XRD and EDS analyses were confirmed impurity, by-products, and oxidation free NPs formation.

Article info

History:

Received: 13.12.2020
Accepted: 24.06.2021

Keywords:

PtCu₃ NP,
Modified polyol
process,
Structural properties

1. Introduction

Platinum group metals (PGM), that are Pt, Pd, Rh, Ir, Ru, and Os, have attracted enormous interests due to their wide range of applications in catalysis [1], fuel cells and metal winning electrodes [2], dental alloys [3], and even semiconductors [4]. Among these groups, commercially available Pt NPs provided enhanced structural and catalytic activities for catalytic converters in automobiles and fuel cell production methods due to their low environmental pollution, low operating temperatures, and high energy conversion factor [5-7]. Today's biggest problems of Pt catalysis are high cost, mining difficulties, and running out of resources. So there should be an immediate solution to reduce the cost of Pt-based highly active catalytic materials. Recent studies showed that loading Pt metal with other non-precious metals such as Fe, Co, Ni, Cu, etc. enhanced electronic and electro-catalytic properties [8, 9] for oxygen reduction reaction (ORR), ethanol oxidation reactions (EOR), and hydrogenation reactions for fuel cells [10-13]. Reduction of Pt and Cu precursors to form Pt-Cu NPs via chemical synthesis process usually results in three different compositions that are Pt₃Cu, PtCu, and PtCu₃ [14, 15]. These results also showed that increasing Cu content results in a decrease unit volume so that a more dense crystal structure is formed. The results of the structural

analysis showed that Pt₃Cu phase: $Fm\bar{3}m$; $a=3.852$ Å (ICDD # 04-017-6718), PtCu phase: $Fm\bar{3}m$; $a=3.7960$ Å (JCPDS #48-1549), and PtCu₃ phase: $Pm\bar{3}m$; $a=3.692$ Å (ICDD #03-065-3247). Additionally comparing methanol oxidation catalytic activities of Pt₃Cu, PtCu, and PtCu₃ NPs (5.43, 6.96, and 8.65 mA/cm², respectively) with commercial Pt NPs (1.14 mA/cm²) indicated that increasing Cu ratio in Pt-Cu alloy enhanced electro-oxidation ability [14]. Therefore, PtCu₃ alloy becomes a more interesting material to investigate and study the structural and morphological properties for catalytic applications.

Preparing desired pure Pt and Pt-based materials are possible with various methods, such as magnetron sputtering, sol-gel process, polyol process, reverse micelles, thermal decomposition, hydrothermal routes [16-22]. Although all these methods provide a well-controlled composition, size, and shape, the polyol process has been a versatile process to synthesis pure, alloyed, core-shell Pt-based NPs with small sizes [23]. To achieve the desired composition, size, and shape in this process, chemical ingredients, such as surfactants, reducing, and capping agents are highly crucial to form chemically stable and oxidation-free NPs. In the literature, there are plenty of studies on the synthesis

*Corresponding author. e-mail address: dogankaya@cu.edu.tr

and structural analysis of PtCu-based alloys [24]. Choosing precursor, surfactant, solvent, reducing agent, additive, annealing temperature and time controls the morphological properties, such as particle size, shape, and crystalline structure. There are different PtCu nanoalloys structures, such as nanoframes, nanowires, spherical, triangular, hexapod, octahedral, hollow nanocages, hierarchical dendrites branched, nanodendrites, etc. with size varies from 2.4 nm to 109 nm [24]. Among these synthesis methods and structures, the nanoalloy size is mostly over 10 nm and there are a few studies, which are mostly for nanowires, reduced the nanoalloy size between 2.4 nm to 5 nm [25, 26]. For example, stabilizing the pH level of the mixture around 9.5-10 with strong bases, such as NaOH or KOH, results in a decrease in the particle size below 7 nm [27, 28]. On the other hand, sodium borohydride (NaBH_4) is a secondary reducing agent which was provided successful results for the polyol process of Cu, Ni, Co NPs in ethylene glycol (EG) by slow addition of NaBH_4 produced fairly monodisperse isotropic NPs [23]. Capping agent such as oleylamine, oleic acid, or PVP protects the NP from oxidation and provide long term chemical durability in time and led to form cubic, or spherical particle formation, respectively [29-31].

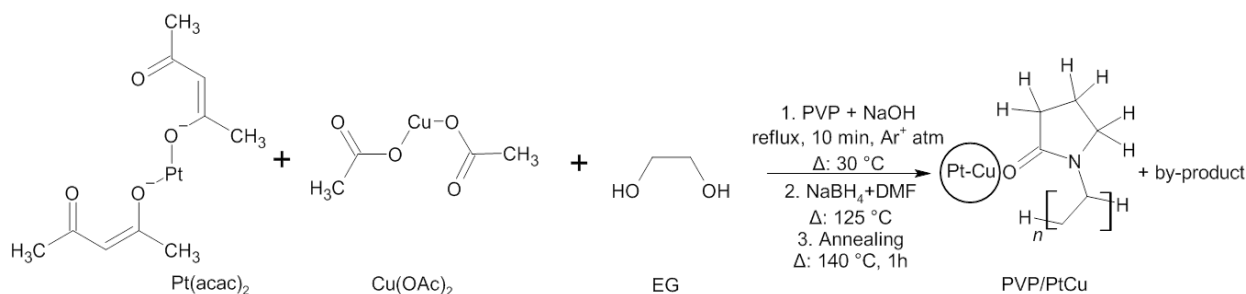


Figure 1. Proposed Pt-Cu NP formation mechanism showing reducing $\text{Pt}(\text{acac})_2$ and $\text{Cu}(\text{OAc})_2$ metal salts with ethylene glycol. The process followed by adding PVP+NaOH at 30°C under Ar gas flow and NaBH_4 at 125°C , and annealing at 140°C for 1 h.

2.2. Synthesis of Pt-Cu NPs

The proposed Pt-Cu NP formation mechanism was given in Figure 1, 0.77 mmol (0.3041 g) $\text{Pt}(\text{acac})_2$ and 0.77 mmol (0.1404 g) $\text{Cu}(\text{OAc})_2$ were dissolved in a 50 ml ethylene glycol (EG) and 30 ml DMF under magnetic stirring. The mixture color was bright turquoise. Ingredients were simultaneously added 3.09 mmol (0.1237 g) PVP as a surface agent and 23.19 mmol (0.9279 g) NaOH to stabilize the pH level in the composition (light blue color). Ar gas was bubbled in the fitted condenser during preparation to prevent CuO formation. The mixture temperature started to rise and at 125°C (green-black color) NaBH_4 , which was diluted in 50 ml DMF, was slowly injected into the

The Pt-Cu NPs were synthesized using a modified polyol process that has been previously employed for various Pt alloys. In this work, low cost, structurally stable, and oxidation-free Pt-Cu NPs was synthesized by controlling amount of solvents, reducing agents, and surfactants which modify the particle size, structure, and morphology. Choosing suitable and optimized additives ratios resulted in the formation of PtCu_3 NPs. Following, the structural and morphological properties of as-prepared Pt-Cu NPs were determined by x-ray diffraction (XRD), scanning electron microscopy (SEM), energy-dispersive x-ray spectroscopy (EDS), and Rietveld refinement analyses. The structural analysis showed that the size of PtCu_3 NPs was below 10 nm and free from the possible by-products such as impurities and oxidations.

2. Experimental Method

2.1. Materials

The metal precursors of Platinum(II) acetylacetonate ($\text{Pt}(\text{acac})_2$, $\geq 97.0\%$) and Copper(II) acetate ($\text{Cu}(\text{OAc})_2$, $\geq 98.0\%$), ethylene glycol ($\geq 99.8\%$), sodium borohydride (NaBH_4 $\geq 98\%$), Polyvinylpyrrolidone (PVP, M_{av} 40 000), N,N-Dimethylformamide (DMF $\geq 99.8\%$), and sodium hydroxide (NaOH $\geq 98\%$), were purchased from Sigma-Aldrich. All chemicals were of analytical grade and used without further purification.

solution. To complete the synthesis, the mixture was annealed at 140°C for 1 h. The mixture color turned to black which indicates all particles were reduced and then the system cooled down to room temperature via passing tap water around the three-necked bottom flask. Finally, the particles were washed with ethanol and dichloromethane and centrifuged at 9000 rpm for 10 min. The product was dried in an oven at 55°C for 24 h and used as-prepared before the structural analysis.

2.3. Structural characterizations

The phase structure of Pt-Cu NP was determined by a PANalytical XRD system with $\text{Cu-K}\alpha$ radiation ($\lambda=1.54 \text{ \AA}$). To determine the structural parameters

FullProf suite was used for Rietveld refinement analysis. SEM images were collected at different places to find average particle size and NP morphology. Collecting EDS data were provided average composition to determine the stoichiometric ratio of Pt-Cu NP.

3. Results and Discussions

The structural analysis of the as-prepared Pt-Cu NP was determined by XRD and Rietveld refinement analysis and presented in Figure 2a. Four major diffraction peaks of face-centered-cubic (fcc) of PtCu₃ structure (blue circles) match well with that of the standard PtCu₃ alloy with the space groups of $Fm\bar{3}m$ (JCPDS No. 35-1358). The peaks at $2\theta=42.58^\circ$, 49.58° , 72.74° , and 88.11° were assigned to the (111), (200), (220), and (311) reflections planes, respectively [14, 32]. Using FullProf suite crystal structure, space group, reflection plane, d -space, lattice parameters, and angle of PtCu₃ NP structure were obtained by Rietveld refinement analysis and were summarized in Table 1. The simulation patterns (black line), the difference (green line), and Bragg positions (red bars) were presented in Figure 2a. The refinement analysis confirmed the space groups of $Fm\bar{3}m$ of fcc structure and reflection planes for the PtCu₃ structure. Figure 2b shows an atomic ball model of the fcc structure of PtCu₃ NP obtained by Rietveld refinement analysis. Here the representation of Pt and Cu atoms colored in grey and blue, respectively. The d -spaces were found to be 2.12, 1.84, 1.30, and 1.11 Å for the reflection planes of (111), (200), (220), and (311), respectively. The lattice constants and the unit-cell volume were

calculated as $a=b=c=3.6829$ Å and 49.9539 Å³ which are similar to earlier findings [14]. The crystallite size can be calculated by Scherrer's formula $D_p=K\lambda/(B\cos\theta)$. Here, D_p is the average crystallite size (nm), K is Scherrer constant and varies from 0.68 to 2.08. $K=0.94$ for spherical crystallites with cubic symmetry. λ is the wavelength of X-rays, $\text{Cu-K}\alpha=1.54178$ Å. B is Full Width at Half Maximum (FWHM) of XRD peak. θ is Bragg's angle. The average crystal size was calculated to be 2.76 nm for the PtCu₃ structure [33]. This XRD analysis showed that PtCu₃ NPs successfully synthesized with small crystal size and free from the possible by-products such as impurities and oxidations.

In this study, 50% Pt and 50% Cu precursors were aimed as an entry, however, the PtCu₃ structure was obtained via XRD and Rietveld refinement analysis. The chemical synthesis root of NP requires more parameters to control the particle properties such as annealing temperature, annealing time, pH level, precursors, reducing agents, or capping agents. The metal salts were mixed with EG and DMF with a mole ratio of 350 and 100, respectively. Following, PVP and NaOH were added at 30 °C with a mole ratio of 2 and 15, respectively. Finally, NaBH₄ was slowly injected with a mole ratio of 24 at 125 °C in 10 min in the mixture under Ar gas atm. The reason for the formation of PtCu₃ NP is due to the earlier reduction stage of Cu during the synthesis process. The formation of pure Cu and Pt NPs dissolved in EG and used PVP and NaBH₄ during the modified polyol process is mostly developed above 100 °C and 140 °C, respectively [23].

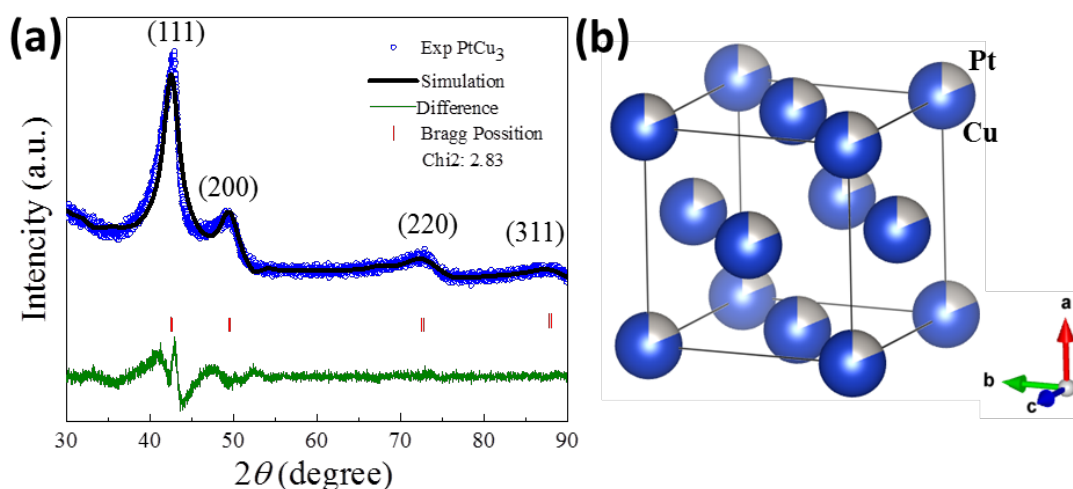


Figure 2. (a) X-ray diffraction profiles of PtCu₃ NP (blue circles) show the major peaks of [110], [100], and [111] directions. Rietveld refinement analysis: calculated patterns (black line), the difference plot (green line), and Bragg positions (red bars). (b) Atomic ball model of fcc structure of PtCu₃ NP obtained by Rietveld refinement analysis.

Table 1. Crystal structure, Space group, Reflection plane, d -space, Lattice parameter, and Angle of PtCu₃ NP structure obtained by Rietveld refinement analysis.

Crystal Structure	Space Group	Reflection plane	d -space (Å)	Lattice Parameter (Å)	Angle (°)
fcc	$Fm\bar{3}m$	(111), (200), (220), (311)	2.12, 1.84, 1.30, 1.11	$a=b=c=3.6829$	$\alpha=\beta=\gamma=90^\circ$

The morphology and surface structure of the as-prepared PtCu₃ NP were characterized by SEM. Figure 3a and b shows a typical surface image of the NPs with a magnification of x200000 and x400000, respectively. Uniform particle distribution is obtained without aggregation on the surfaces. The average particle size was determined by SEM images and binned in 0.5 nm as seen in Figure 3c. The average size of the NPs was found to be $d_0=8.04 \pm 0.08$ nm by fitting the histogram as a function of particle size with the log-normal distribution (blue line) in Figure 3d. Here, δ is the log standard deviation and d_0 is the median diameter of PtCu₃ NPs. In literature, the smallest sizes of 4.8 nm was obtained for spherical PtCu nanoparticles with using H₂PtCl₆ and Cu(NO₃)₂ precursors,

Ndimethylformamide, oleylamine, and hexadecyltrimethyl ammonium bromide agents and annealed at 170 °C for 24 min [34]. In this study, monodisperse ~8 nm of PtCu nanoalloy synthesis was achieved. Crystallite size can be determined by the peak of XRD which corresponds to the single crystal within a polycrystalline nanoparticle or the size of the grains of a powder sample [35]. Therefore, the crystalline size is expected to be lower than the average particle size of nanoparticles. In this study, we calculated the crystal size to be 2.76 nm which is three times smaller than the average particle size of 8.04 nm. It can be said that there are multicrystalline formation in an average particle.

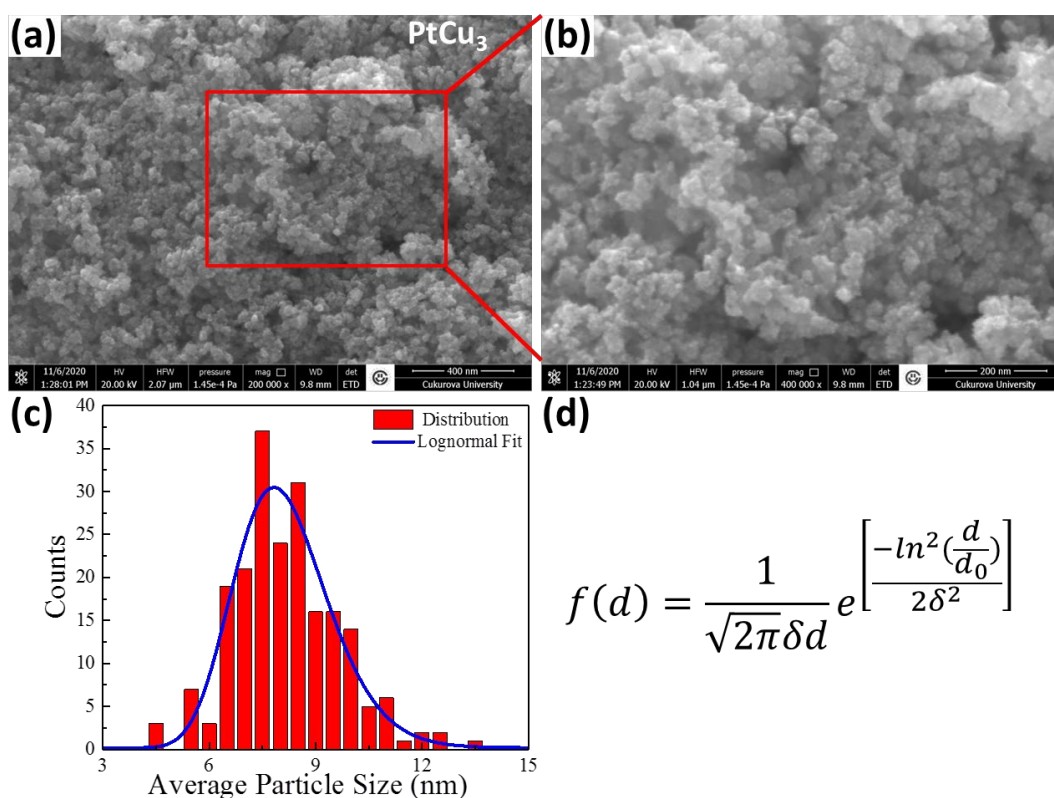


Figure 3. SEM images analysis of PtCu₃ NP. (a) The surface morphology of the particles with a magnification of 200000. (b) A selected area from (b). (c) The size distribution of PtCu₃ NPs (red bar) with the log-normal fit (blue line) and (d) formula.

To determine atomic composition of as-prepared Pt-Cu NPs, EDS analysis was performed on different areas and collected the average atomic composition percentage. Figure 4a and b show intensity as a function of energy plot and selected point where the EDS data collected. The major Cu and Pt peaks observed in the spectra as well as C and O peaks which are mostly arise from carbon tape used to stabilize particles and surface agents used during preparation. The inset table collected the average atomic composition of detected atoms in Figure 4a. The

structure composition ratio was found to be 1:2.8 for Pt:Cu via stoichiometric calculation. This PtCu_{2.8} ratio is quite similar with findings by Rietveld refinement analysis results. The reason of the formation of PtCu₃ NPs, reducing Pt²⁺ and Cu²⁺ ions in the mixture EG was used and the Cu²⁺ ions reduce much faster than Pt²⁺ ions and Pt atoms surrounded by Cu atoms instead of binding with other Cu²⁺ ions. For this structure there are 12 Cu atom enclose a Pt atom and 4 Pt atoms bind with a Cu atom [14].

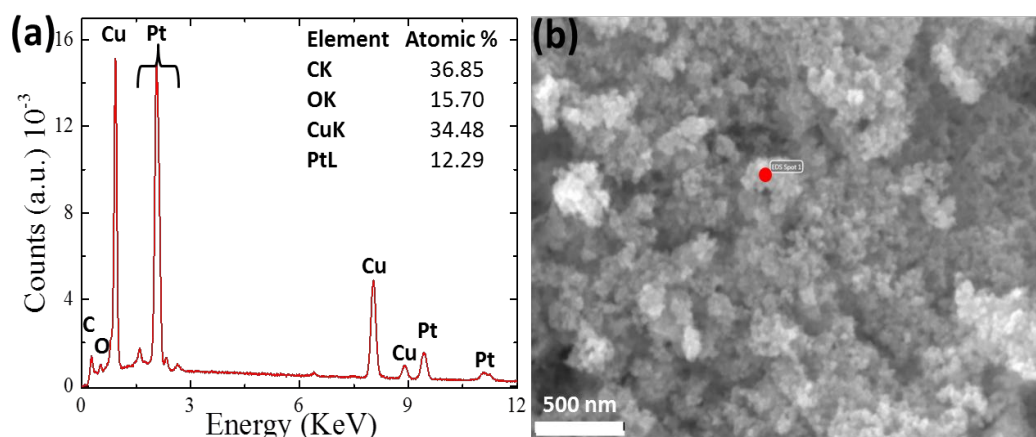


Figure 4. (a) EDS analysis of as-prepared PtCu₃ NPs with major Cu and Pt as well as C and O peaks. The inset table collected the average atomic composition of detected atoms. (b) SEM image of EDS spot on the surface.

4. Conclusion

In conclusion, bimetallic PtCu₃ NP was synthesized via the modified polyol process in which EG and NaBH₄ used initial and secondary reducing agents, respectively. The particles were reduced to 140 °C under an Argon gas environment to prevent unwanted oxidation formation. Using PVP as a surface capping agent also vastly improved the particle protection from oxidation and provides chemical stability. The structural formation of PtCu₃ NPs was first determined by XRD and Rietveld refinement analysis in that were confirmed the *Fm* $\bar{3}$ *m* space group with a lattice constant of $a=b=c=3.6829$ Å. The crystal size of PtCu₃ NPs was determined by FWHM of the XRD peaks and calculated as 2.76 nm using Scherrer's formula. Following the average size of PtCu₃ was 8.04 nm via SEM images. The structural composition was found to be 1:2.8 for Pt:Cu confirmed by EDS with oxidation and impurity-free compositions.

Acknowledgement

I would like to thank Prof.Dr. Faruk Karadag and Assoc.Prof. Ahmet Ekicibil for valuable discussions.

Conflict of interest

The authors declare that they have no conflict of interests.

References

- [1] Wang X.X., Swihart M.T., Wu G., Achievements, challenges and perspectives on cathode catalysts in proton exchange membrane fuel cells for transportation, *Nat. Catal.*, 2(7) (2019) 578-589.
- [2] Pivovar B., Catalysts for fuel cell transportation and hydrogen related uses, *Nat. Catal.*, 2(7) (2019) 562-565.
- [3] Colic M., Stamenkovic D., Anzel I., Lojen G., Rudolf R., The influence of the microstructure of high noble gold-platinum dental alloys on their corrosion and biocompatibility in vitro, *Gold Bull.*, 42(1) (2009) 34-47.
- [4] Ben Saber N., Mezni A., Alrooqi A., Altalhi T., A review of ternary nanostructures based noble metal/semiconductor for environmental and renewable energy applications, *J. Mater. Res. Technol.*, 9(6) (2020) 15233-15262.
- [5] Xia B.Y., Wu H.B., Yan Y., Lou X.W., Wang X., Ultrathin and Ultralong Single-Crystal Platinum Nanowire Assemblies with Highly Stable Electrocatalytic Activity, *J. Am. Chem. Soc.*, 135(25) (2013) 9480-9485.
- [6] Wang J., Barriers of scaling-up fuel cells: Cost, durability and reliability, *Energy*, 80 (2015) 509-521.
- [7] Chen Y., Zhang G., Ma J., Zhou Y., Tang Y., Lu T., Electro-oxidation of methanol at the different carbon materials supported Pt nano-particles, *Int. J. Hydrogen Energy*, 35(19) (2010) 10109-10117.
- [8] Zaleska-Medynska A., Marchelek M., Diak M., Grabowska E., Noble metal-based bimetallic nanoparticles: the effect of the structure on the optical, catalytic and photocatalytic properties, *Adv. Colloid Interface Sci.*, 229 (2016) 80-107.
- [9] Srinoi P., Chen Y.-T., Vittur V., Marquez M., Lee T., Bimetallic Nanoparticles: Enhanced Magnetic and Optical Properties for Emerging Biological Applications, *Appl. Sci.*, 8 (2018) 1106.
- [10] Li C.-H., Li M.-C., Liu S.-P., Jamison A.C., Lee D., Lee T.R., Lee T.-C., Plasmonically Enhanced Photocatalytic Hydrogen Production from Water: The Critical Role of Tunable Surface Plasmon Resonance from Gold-Silver Nanoshells, *ACS Appl. Mater. Interfaces*, 8(14) (2016) 9152-9161.
- [11] Hien Pham T.T., Cao C., Sim S.J., Application of citrate-stabilized gold-coated ferric oxide composite nanoparticles for biological separations, *J. Magn. Magn. Mater.*, 320(15) (2008) 2049-2055.
- [12] Li X., Liu H., Liu S., Zhang J., Chen W., Huang C., Mao L., Effect of Pt-Pd hybrid nano-particle on CdS's activity for water splitting under visible light, *Int. J. Hydrogen Energy*, 41(48) (2016) 23015-23021.
- [13] Farahmandjou M., Effect of Oleic Acid and Oleylamine Surfactants on the Size of FePt Nanoparticles, *J. Supercond. Novel Magn.*, 25(6) (2012) 2075-2079.
- [14] Jia Y., Cao Z., Chen Q., Jiang Y., Xie Z., Zheng L., Synthesis of composition-tunable octahedral Pt-Cu alloy nanocrystals by controlling reduction kinetics of metal precursors, *Sci. Bull.*, 60 (2015).
- [15] Saravanan G., Khobragade R., Chand Nagar L., Labhsetwar N., Ordered intermetallic Pt-Cu nanoparticles for the catalytic CO oxidation reaction, *RSC Adv.*, 6(88) (2016) 85634-85642.
- [16] Vernieres J., Steinhauer S., Zhao J., Chapelle A., Menini P., Dufour N., Diaz R.E., Nordlund K., Djurabekova F., Grammatikopoulos P., Sowwan M., Gas Phase Synthesis of Multifunctional Fe-Based Nanocubes, *Adv. Funct. Mater.*, 27(11) (2017) 1605328.
- [17] Salavati-Niasari M., Davar F., Mazaheri M., Shaterian M., Preparation of cobalt nanoparticles from [bis(salicylidene)cobalt(II)]-oleylamine complex by thermal decomposition, *J. Magn. Magn. Mater.*, 320(3) (2008) 575-578.
- [18] Gul I.H., Maqsood A., Structural, magnetic and electrical properties of cobalt ferrites prepared by the sol-gel route, *J. Alloys Compd.*, 465(1) (2008) 227-231.
- [19] Shemer G., Tirosh E., Livneh T., Markovich G., Tuning a Colloidal Synthesis to Control Co²⁺ Doping in Ferrite Nanocrystals, *J. Phys. Chem. C.*, 111(39) (2007) 14334-14338.
- [20] Millot N., Le Gallet S., Aymes D., Bernard F., Grin Y., Spark plasma sintering of cobalt ferrite nanopowders prepared by coprecipitation and hydrothermal synthesis, *J. Eur. Ceram. Soc.*, 27(2) (2007) 921-926.
- [21] Lisiecki I., Pileni M.P., Synthesis of Well-Defined and Low Size Distribution Cobalt Nanocrystals: The Limited Influence of Reverse Micelles, *Langmuir*, 19(22) (2003) 9486-9489.
- [22] Meng Q., Zhang Y., Dong P., Use of electrochemical cathode-reduction method for leaching of cobalt from spent lithium-ion batteries, *J. Clean. Prod.*, 180 (2018) 64-70.

- [23] Fiévet F., Ammar-Merah S., Brayner R., Chau F., Giraud M., Mammeri F., Peron J., Piquemal J.Y., Sicard L., Viau G., The polyol process: a unique method for easy access to metal nanoparticles with tailored sizes, shapes and compositions, *Chem. Soc. Rev.*, 47(14) (2018) 5187-5233.
- [24] Yan W., Zhang D., Zhang Q., Sun Y., Zhang S., Du F., Jin X., Synthesis of PtCu-based nanocatalysts: Fundamentals and emerging challenges in energy conversion, *J. Energy Chem.*, 64 (2022) 583-606.
- [25] Fang D., Wan L., Jiang Q., Zhang H., Tang X., Qin X., Shao Z., Wei Z., Wavy PtCu alloy nanowire networks with abundant surface defects enhanced oxygen reduction reaction, *Nano Res.*, 12(11) (2019) 2766-2773.
- [26] Liao Y., Yu G., Zhang Y., Guo T., Chang F., Zhong C.-J., Composition-Tunable PtCu Alloy Nanowires and Electrocatalytic Synergy for Methanol Oxidation Reaction, *J. Phys. Chem. C.*, 120(19) (2016) 10476-10484.
- [27] Huang K.-C., Ehrman S.H., Synthesis of Iron Nanoparticles via Chemical Reduction with Palladium Ion Seeds, *Langmuir*, 23(3) (2007) 1419-1426.
- [28] Li N., Tang S., Meng X., Reduced Graphene Oxide Supported Bimetallic Cobalt-Palladium Nanoparticles with High Catalytic Activity towards Formic Acid Electro-oxidation, *J Mater Sci Technol.*, 31(1) (2015) 30-36.
- [29] Arán-Ais R.M., Vidal-Iglesias F.J., Solla-Gullón J., Herrero E., Feliu J.M., Electrochemical Characterization of Clean Shape-Controlled Pt Nanoparticles Prepared in Presence of Oleylamine/Oleic Acid, *Electroanalysis*, 27(4) (2015) 945-956.
- [30] Tong Y.Y., Polyvinylpyrrolidone (pvp) for enhancing the activity and stability of platinum-based electrocatalysts, *Google Patents*, 2015.
- [31] Cao Y., Yang Y., Shan Y., Huang Z., One-Pot and Facile Fabrication of Hierarchical Branched Pt-Cu Nanoparticles as Excellent Electrocatalysts for Direct Methanol Fuel Cells, *ACS Appl. Mater. Interfaces*, 8(9) (2016) 5998-6003.
- [32] Wu F., Niu W., Lai J., Zhang W., Luque R., Xu G., Highly Excavated Octahedral Nanostructures Integrated from Ultrathin Mesoporous PtCu₃ Nanosheets: Construction of Three-Dimensional Open Surfaces for Enhanced Electrocatalysis, *Small*, 15(10) (2019) 1804407.
- [33] Papa F., Negrila C., Miyazaki A., Balint I., Morphology and chemical state of PVP-protected Pt, Pt-Cu, and Pt-Ag nanoparticles prepared by alkaline polyol method, *J. Nanopart. Res.*, 13(10) (2011) 5057.
- [34] Du X., Luo S., Du H., Tang M., Huang X., Shen P.K., Monodisperse and self-assembled Pt-Cu nanoparticles as an efficient electrocatalyst for the methanol oxidation reaction, *J. Mater. Chem. A.*, 4(5) (2016) 1579-1585.
- [35] Bishnoi A., Kumar S., Joshi N., Chapter 9 - Wide-Angle X-ray Diffraction (WXRd): Technique for Characterization of Nanomaterials and Polymer Nanocomposites, in: S. Thomas, R. Thomas, A.K. Zachariah, R.K. Mishra (Eds.), Amsterdam: Elsevier, (2017) 313-337.

Sensitive electrochemical determination of Cefpirome in human urine using differential pulse voltammetry

Cem ERKMEN¹ , Burcin BOZAL PALABIYIK¹ , Bengi USLU^{1,*} 

¹ Ankara University, Faculty of Pharmacy, Department of Analytical Chemistry, 06560, Ankara / TURKEY

Abstract

Cefpirome, which is a fourth-generation cephalosporin, was analyzed for the first time at a glassy carbon electrode using differential pulse voltammetry in this novel method. Different experimental conditions were optimized, such as pH and electrolyte type, to achieve a high peak current. Under the optimum conditions, the oxidation of cefpirome exhibited diffusion-controlled process depending on pH. Cefpirome was electrochemically determined at the linear range between 2-200 μM , and the detection limit was found as 0.167 μM in pH 4.7 acetate buffer solution. Analysis results showed that the proposed electrochemical method could be used for the determination of cefpirome in human urine samples. A linear relationship has been obtained in the concentration range of 2-10 μM . At the same time, the detection limit was found as 0.101 μM for cefpirome in human urine. Moreover, to check the selectivity of the proposed method, the effect of some interference species, including ascorbic acid, uric acid, dopamine, glucose, Na^+ , K^+ , Ca^{+2} , NO_3^- , have also been investigated. As a result, a simple, sensitive, reproducible, no time-consuming, and more environmentally friendly method was developed when compared to the literature studies.

Article info

History:

Received: 21.03.2021
Accepted: 04.07.2021

Keywords:

Cefpirome,
Differential pulse
Voltammetry,
Electrochemistry,
Human urine,
Validation.

1. Introduction

Since the discovery of penicillin in 1928, numerous antibiotics have been investigated and introduced for the treatment of various bacterial and fungal infections in humans or livestock. Cephalosporins are classified as one of the semisynthetic antibiotics. They are produced from the side-chain of cephalosporin C, and cephalosporin C exhibits resistance to degradation caused by β -lactamases [1,2]. Cefpirome (Figure 1) is a fourth-generation cephalosporin, and it is generally used parenterally. In the chemical structure of cefpirome, there is a 2-amino-thiazolymethoxyimino group in the side chain at position 7 and a cyclopentapyridine group at position 3, which are responsible for the side effect of antibacterial activity of cefpirome [3,4]. Moreover, the high level of resistance to β -lactamases stems from these elements present in the structure of cefpirome. Cefpirome is highly active against Gram-negative bacteria, including *Pseudomonas aeruginosa*, and Gram-positive bacteria such as *Staphylococcus aureus*. Furthermore, cefpirome can effectively treat infections of skin and soft tissue, lower respiratory tract, and upper or lower urinary tract [4].

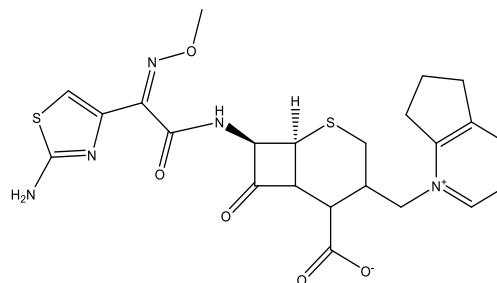


Figure 1. Chemical structure of cefpirome.

Previous studies demonstrate different analytical methods for the detection and determination of cefpirome in bulk form and from biological fluids such as serum, urine, milk, and muscle. These methods include liquid chromatography-tandem mass spectrometry (LC-MS/MS) [5,6], high-performance liquid chromatography (HPLC) [7-10] and reversed phase thin-layer chromatography [10], and electrochemical methods including differential pulse voltammetry (DPV) and square wave voltammetry (SWV) [4]. In their study, Jain and Vikas used multiwalled carbon nanotube modified glassy carbon electrode (GCE) for the determination of cefpirome in bulk form and pharmaceutical formulation. The linear range of 200–600 $\mu\text{g mL}^{-1}$ was obtained by using both SWV and DPV. They found the detection limit as

*Corresponding author. e-mail address: buslu@pharmacy.ankara.edu.tr
<http://dergipark.gov.tr/csj> ©2021 Faculty of Science, Sivas Cumhuriyet University

0.647 $\mu\text{g mL}^{-1}$ via SWV method and 5.540 $\mu\text{g mL}^{-1}$ via DPV method [4]. Although chromatographic methods are widely used for the determination of several compounds, these methods can be costly due to the necessity of sample separation and pretreatment steps. Also, chromatographic methods require a large amount of organic solvents and generate considerable amount of waste, leading to environmental degradation. Moreover, the major drawback of chromatographic methods is inability to achieve sensitive results [11-13]. Electrochemical methods are the most popular methods due to their advantages such as simplicity, rapidity, high sensitivity, low cost, and easy integration. These methods are more eco-friendly than other methods since they require low amounts of analytes and solvents. Moreover, lower detection limits, good repeatability, and reproducibility resulted in a growing interest in electrochemical methods [14-17].

A GCE is an excellent electrode for different applications as a conventional electrode material. It has excellent mechanical and electrical properties. Also, it provides the opportunity to work at a wide operating potential range. GCE is also significant for its low reactivity (high corrosion resistance) compared to the other electrodes. Its most important properties are high temperature resistance, extreme resistance to chemical attack, and impermeability to gases and liquids [18,19].

In this study, a DPV method was developed and validated according to ICH guidelines [20] at GCE for the sensitive detection and determination of cefpirome from bulk form. Since 80% of cefpirome is excreted unchanged from urine [21], its determination from human urine samples was also applied. Furthermore, to check the selectivity of the proposed method, the influence of potential foreign compounds on the determination of cefpirome in the optimum conditions was investigated. The developed method exhibited high sensitive results and good reproducibility for cefpirome detection in bulk form and human urine samples. Moreover, the advantages of the proposed method were compared to previously published studies.

2. Materials and Methods

2.1. Apparatus and reagents

In this study, an AUTOLAB-PGSTAT204 electrochemical and electroanalytical device was used to obtain cyclic and differential pulse voltammograms (Eco Chemie, Utrecht, The Netherlands). NOVA 2.1 software was used for data processing. GCE was used as a working electrode (BASi; ϕ : 3 mm, diameter).

Ag/AgCl (BASi; 3 M KCl) and a platinum wire (BASi) were used as a reference electrode and an auxiliary electrode, respectively. A Mettler Toledo MA 235 pH meter that includes a glass electrode-reference electrode was used for all pH measurements (Mettler Toledo TR Olcum Aletleri Tic. Satis ve Servis Hizm. A.S. Istanbul, Turkey).

Cefpirome was purchased from CHEMOS GmbH (Regenstauf, Germany). A stock solution of cefpirome (1×10^{-3} M) was prepared in bi-distilled water and kept in a refrigerator. Working solutions of cefpirome were prepared by diluting the stock solution with desired buffer solutions for voltammetric measurements. In this study, 0.1 M H_2SO_4 solution, 0.5 M H_2SO_4 solution, phosphate buffer solution (PBS) for pH 2.0, 3.0 and 6.0-8.0, acetate buffer solution (ABS) for pH 3.7-5.7, Britton-Robinson buffer solution (BRB) for pH 2.0-12.0 were used as supporting electrolytes. To prepare supporting electrolytes, CH_3COOH and H_2SO_4 were purchased from Merck. H_3PO_4 and analytical grade of $\text{NaH}_2\text{PO}_4 \cdot 2\text{H}_2\text{O}$, Na_2HPO_4 , NaOH , and H_3BO_3 were purchased from Riedel-de Haen.

2.2. Assay procedure for cefpirome

An adequate amount of cefpirome powder was carefully weighed, dissolved in bi-distilled water, and sonicated to prepare the stock solution (1.0×10^{-3} M). Working solutions were prepared by diluting with pH 4.7 ABS. Before each measurement, the GCE surface cleaning process was carried out mechanically on a polishing pad using alumina slurry. Then, it was rinsed with bi-distilled water and allowed to dry in the air. DPV conditions were as follows; 0.005 V as a step potential; 0.025 V as a modulation amplitude; 0.05 s as a modulation time; 0.40 s as an interval time, and DP voltammograms were recorded using GCE to prepare the calibration graph. Furthermore, the proposed DPV method for the determination of cefpirome was validated through assessment of linearity, precision, the limit of detection (LOD), and the limit of quantification (LOQ).

2.3. Determination of cefpirome in human urine sample

Drug-free human urine samples were supplied from healthy volunteers. To prepare cefpirome stock solution in urine samples, 3.6 mL urine sample and 5.4 mL acetonitrile for protein precipitation were added into a 10.0 mL centrifuge tube. Then 1.0 mL 1.0×10^{-3} M stock cefpirome solution was added into this tube to obtain a final concentration of 1.0×10^{-4} M cefpirome. The same procedure was used for drug-free urine as a blank solution. Firstly, the prepared solution was sonicated for 15 min in the ultrasonic bath. Then, this

sample was centrifuged for 15 min at 5000 rpm to obtain the supernatant. Required volumes of clear supernatant were diluted up with pH 4.7 ABS. The working concentrations of cefpirome were prepared in the range of 2-10 μM in human urine samples. The calibration graph was obtained using peak currents corresponding to cefpirome concentrations. Moreover, the recovery results were investigated using a calibration graph in urine samples.

3. Results and Discussion

3.1. Influence of the pH on the peak currents

The electrooxidation behavior of cefpirome was investigated over a pH range of 0.3–12.0 various

supporting electrolytes such as 0.1 M and 0.5 M H_2SO_4 solutions and buffer solutions, including ABS, PBS, and BRB. The cyclic voltammograms of cefpirome at GCE in 0.1 M H_2SO_4 , pH 2.0 BRB, pH 4.7 ABS and pH 7.0 PBS were shown in Figure 2A, B, C and D, respectively. As can be seen, no peak was observed in the reverse scan suggesting that the oxidation of cefpirome at GCE is irreversible. Cefpirome peak currents decreased by the second and consecutive cycles as a result of the consumption of adsorbed cefpirome on the electrode surface.

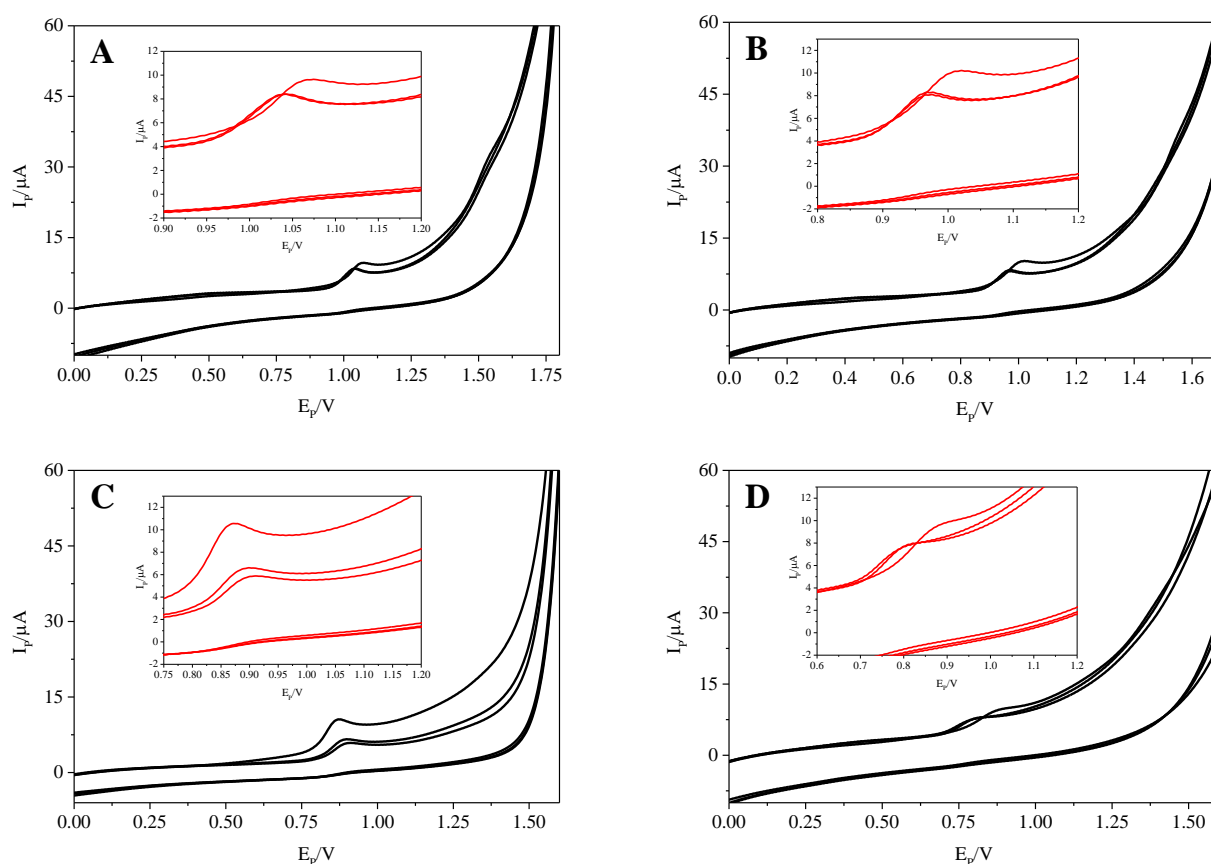


Figure 2. Cyclic voltammograms of 2.0×10^{-4} M cefpirome with GCE in 0.1 M H_2SO_4 (A), pH 2 BRB (B), pH 4.7 ABS (C) and pH 7.0 PBS (D).

To investigate the effect of pH on peak current (I_p) and peak potential (E_p) were constructed using the related data of pH measurements in the presence of 2.0×10^{-4} M cefpirome (Figure 3A). According to the pH study results, E_p of cefpirome shifted to less positive values with increasing pH. The curve of E_p vs. pH (Figure 3B) exhibited a good linear relationship with the following equation

$$E_p(\text{V}) = -0.054 \text{ pH} + 1.074; r = 0.9945$$

The slope of this equation (54 mV per pH) showed that equal numbers of protons and electrons are involved in the redox behavior of cefpirome on GCE.

Moreover, the best peak shape, the highest current value, and good repeatability were obtained at pH 4.7 ABS. Therefore, pH 4.7 ABS was chosen as the optimum supporting electrolyte and used for further analytical applications.

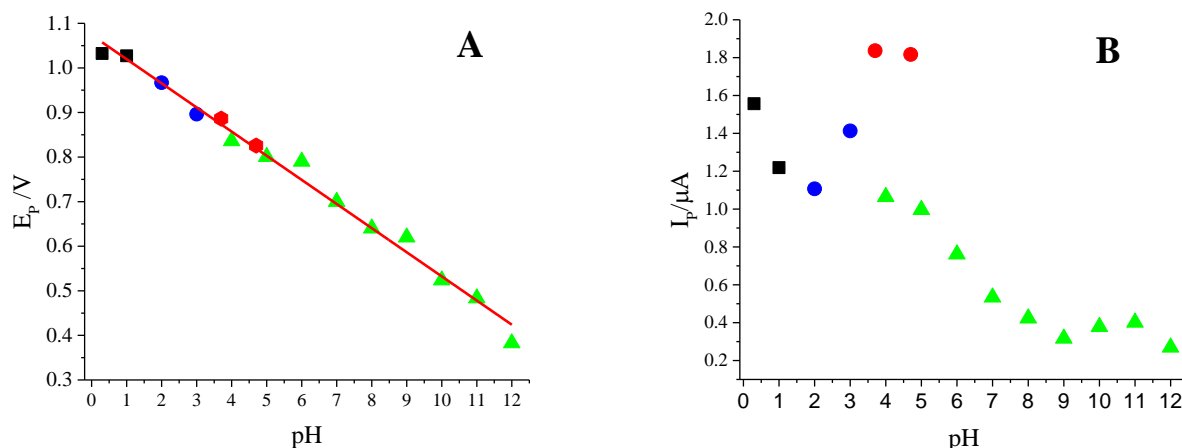


Figure 3. Plots of E_p vs pH (A) and I_p vs pH (B) obtained in 2.0×10^{-4} M cefpirome using DPV; (\blacktriangle): BRB, (\bullet): ABS, (\blacksquare): H₂SO₄, (\circ): PBS.

3.1. Influence of scan rate on GCE

In this study, the information about the electrochemical behavior of cefpirome was investigated by CV using the relationship between peak current and scan rate. The scan rate was changed in the range between 5 and 1000 mV s^{-1} . This study was performed to understand whether the oxidation process is diffusion or adsorption-controlled in 2.0×10^{-4} M cefpirome on GCE. When the relationship between I_p and $v^{1/2}$ was investigated (Figure 4A), a linear relationship was found with the equation below:

$$I_p(\mu\text{A}) = 0.266 v^{1/2}(\text{mV s}^{-1}) + 0.16; r = 0.9966$$

Therefore, it can be said that the oxidation process of cefpirome is controlled by diffusion on GCE. In addition, the curve of $\log I_p$ vs $\log v$ (Figure 4B) exhibited a linear relationship with the regression equation below;

$$\log I_p(\mu\text{A}) = 0.442 \log v (\text{mV s}^{-1}) - 0.432; \\ r = 0.9968$$

For diffusion controlled process in an ideal reaction, the slope value of curve of $\log I_p$ vs $\log v$ is 0.5 [22]. From the obtained data, the slope value of this plot was found as 0.442, and this value was nearer to that of the desired value. This result also supported that oxidation of cefpirome was diffusion controlled.

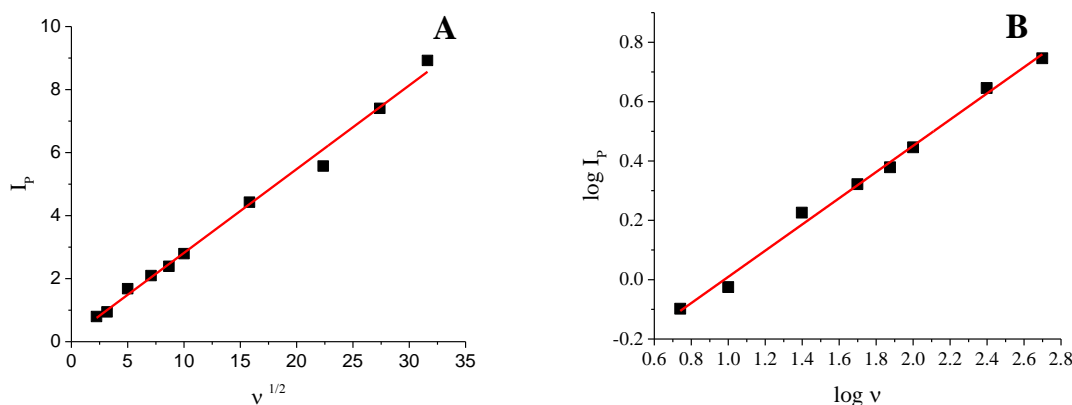


Figure 4. Curves of I_p vs $v^{1/2}$ (A) and $\log I_p$ vs $\log v$ (B).

3.3. Validation of the method and determination of cefpirome in spiked human urine samples

In this novel electrochemical method, a linear correlation between I_p values and increasing cefpirome concentrations was obtained for the determination of cefpirome under the optimum conditions. Some of the

DP voltammograms from the linear range between 2-200 μM cefpirome in bulk form and 2-10 μM cefpirome in human urine were shown in Figure 5A and Figure 5B. Also, the linearity of cefpirome for the DPV method was measured (Figure 5C and Figure 5D) with the following equations;

$$I_p(\mu\text{A}) = 0.0089 C (\mu\text{M}) + 0.0367; r = 0.9975 \text{ for bulk form}$$

$$I_p(\mu\text{A}) = 0.021 C (\mu\text{M}) - 0.0094; r = 0.9979 \text{ for human urine}$$

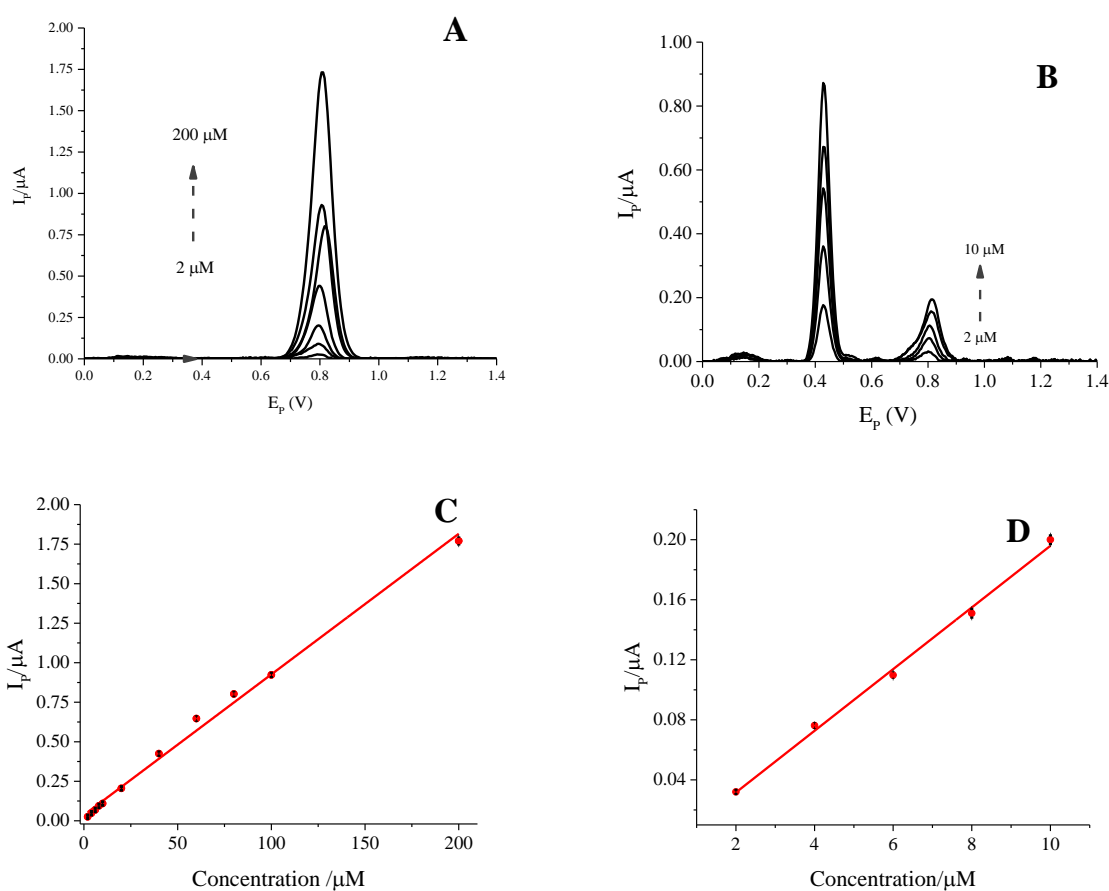


Figure 5. DP voltammograms obtained from increasing concentrations of cefpirome for bulk form (A) and for human urine (B) in pH 4.7 ABS. Calibration curves of cefpirome for bulk form (C) and for human urine (D) in pH 4.7 ABS.

As a part of the validation of the proposed DPV method for the determination of cefpirome, LOD and LOQ values were evaluated in bulk form and human urine. LOD and LOQ values were calculated according to the following equations:

$$\text{LOD} = 3 s/m$$

$$\text{LOQ} = 10 s/m$$

In these equations, m is the slope of calibration plots, and s is the standard deviation of peak current [23]. LOD values for bulk form and human urine were calculated using the calibration curve and found as 0.167 μM and 0.101 μM , respectively. For the developed method, some characteristics of the validation results were presented in Table 1.

Table 1. Regression data of the calibration lines of cefpirome by DPV in bulk form and in human urine.

Parameters	Bulk form	Human urine
Measured Potential (V)	0.80	0.80
Linearity range (μM)	2-200	2-10
Slope ($\mu\text{A } \mu\text{M}^{-1}$)	0.0089	0.021
Intercept (μA)	0.0367	-0.0094
Correlation coefficient	0.9975	0.9979
SE of slope	2.08×10^{-4}	7.05×10^{-4}
SE of intercept	0.016	0.004
LOD (μM)	0.17	0.10
LOQ (μM)	0.50	0.34
Within-day precision of peak current (%RSD)*	0.34	2.19
Between-days precision of peak current (%RSD)*	1.16	2.51

* Obtained from five experiments.

The repeatability of the developed method was studied by conducting five repetitive measurements for bulk form and human urine at fixed cefpirome concentrations (20 μM for bulk form and 6.0 μM for human urine). For within-day precision, the relative standard deviation (RSD %) values of peak current were calculated as 0.34 and 2.19 for bulk form and human urine, respectively. Moreover, between-days precision was investigated by conducting five repetitive measurements at the same cefpirome concentrations. The RSD % values of peak current were found as 1.16 and 2.51 for bulk form and human urine, respectively. Therefore, it can be clearly said that the method is precise based on obtained results.

Moreover, recovery studies were performed by the standard addition method. The recovery % and Bias % were presented in Table 2, and they were all in acceptable ranges. So, the results of recovery studies showed that the developed method is accurate.

Table 2. Results obtained for cefpirome determination from spiked human urine samples.

Parameters	Human urine
Reference concentration (μM)	6.00
Observed concentration (μM)	6.18
Number of experiments	5
Average recovery %	103.09
RSD % of recovery	1.42
Bias %	-3.09

To sum up, when the developed method is compared to literature studies (Table 3), it can be said that a more sensitive DPV method was developed with a 0.101 μM (0.06 $\mu\text{g mL}^{-1}$) detection limit. In addition, this method is both low-cost and more environmentally friendly as there was very simple preparation procedure, which is one of the requirements of chromatographic methods, and this method did not require organic solvent consumption.

Table 3. Comparison of major characteristics in literature studies for determination of cefpirome.

Method	Linear range	LOD	Applications	Ref.
LC-MS/MS	0.7–100 $\mu\text{g mL}^{-1}$	0.30 $\mu\text{g mL}^{-1}$	Pork muscle	[6]
HPLC	20-30 $\mu\text{g mL}^{-1}$	2.38 $\mu\text{g mL}^{-1}$	Bulk form	[7]
HPLC	0.5–200 $\mu\text{g mL}^{-1}$	0.1 $\mu\text{g mL}^{-1}$	Human serum	[8]
HPLC	up to 500 $\mu\text{g mL}^{-1}$	0.6 $\mu\text{g mL}^{-1}$	Human milk and urine	[9]
HPLC	5.0–50 $\mu\text{g mL}^{-1}$	1.45 $\mu\text{g mL}^{-1}$	Bulk form	[10]
DPV	100–600 $\mu\text{g mL}^{-1}$	5.54 $\mu\text{g mL}^{-1}$	Bulk form	[4]
SWV		0.647 $\mu\text{g mL}^{-1}$		
DPV	1.03–41.17 $\mu\text{g mL}^{-1}$	0.09 $\mu\text{g mL}^{-1}$	Bulk form	Proposed method
	1.03–5.15 $\mu\text{g mL}^{-1}$	0.06 $\mu\text{g mL}^{-1}$	Human urine	

DPV: Differential pulse voltammetry, HPLC: High-performance liquid chromatography, LC-MS/MS: Liquid chromatography–tandem mass spectrometry, SWV: Square wave voltammetry

3.4. Interference effects in the determination of cefpirome

Selectivity is one of the most important validation parameters of developed analytical methods. It is not desirable for different species to interfere with the compound to be analyzed [24]. To demonstrate the selectivity of the developed method, cefpirome determination was performed in the presence of some organic species, including ascorbic acid, uric acid, dopamine, glucose, and Na⁺, K⁺, Ca⁺² and NO₃⁻ ions. In the presence of 1:1, 1:10, and 1:100 molar ratio of the

interfering species, recovery (%) values were determined. For this purpose, the peak current of 10 μM cefpirome in the standard solution was compared to the peak currents of cefpirome in the presence of interfering species (Table 4). While 10 μM cefpirome was also determined in the presence of 1:1 and 1:10 molar ratios of ascorbic acid, uric acid, Na⁺, K⁺, Ca⁺² and NO₃⁻ within the 10% tolerance limit, interference effect was observed in the presence of dopamine and glucose. Moreover, cefpirome current did not change more than 10 % in the presence of 1:100 molar ratio of ascorbic acid, Na⁺, K⁺, Ca⁺² and NO₃⁻.

Table 4. 10 μM cefpirome assayed in the presence of some interfering species

Interfering species	Recovery (%) by DPV		
	1:1 (M/M)	1:10 (M/M)	1:100 (M/M)
Ascorbic acid	102.69 ± 0.003	104.41 ± 0.02	110.57 ± 0.01
Uric acid	108.77 ± 0.02	106.67 ± 0.02	116.49 ± 0.01
Dopamine	87.35 ± 0.02	-	-
Glucose	88.14 ± 0.02	-	-
Na ⁺	95.44 ± 0.01	94.74 ± 0.01	95.26 ± 0.02
K ⁺	94.21 ± 0.01	96.14 ± 0.005	92.28 ± 0.01
Ca ⁺²	96.32 ± 0.01	92.63 ± 0.02	90.35 ± 0.02
NO ₃ ⁻	96.67 ± 0.01	96.91 ± 0.01	95.23 ± 0.003

4. Conclusions

In the novel proposed method, the electrochemical behavior of cefpirome was investigated by DPV using GCE. The effect of the type and pH of supporting electrolytes and scan rate in optimum supporting electrolyte were optimized. The developed electrochemical method provided a simple low cost and fast analysis for the determination of cefpirome from bulk form and human urine samples. Especially, the proposed method is suitable for screening purposes, compared to other analytical methods. The proposed method was also validated in accordance with ICH guidelines. In this study, a lower detection limit was obtained than the reported LC-MS/MS, HPLC, DPV, and SWV methods.

In this study, the sample preparation procedure is very simple for determination from human urine samples. The sample preparation procedure has a simple and convenient one-step precipitation method. Therefore, this DPV method is more feasible than other methods for cefpirome detection in human urine samples. Moreover, satisfactory results were obtained in the

determination of cefpirome in spiked human urine samples. So, it can be said that the proposed method is applicable for real sample analysis. In addition, the novel developed method can be adopted for pharmacokinetic studies, clinical applications, or quality control laboratories.

Acknowledgment

The authors would like to thank the Ankara University Scientific Research Projects Commission for financial support (Project No: 18B0237001).

Conflicts of interest

The authors state that did not have conflict of interests.

References

- [1] Nawaz M., Arayne M. S., Sultana N., Abbas H. F., Investigation of interaction studies of Cefpirome with ACE-Inhibitors in various buffers, *Spectrochim. Acta - Part A Mol. Biomol. Spectrosc.*, 137 (2015) 1050–1054.
- [2] Kong X. X., Jiang J. L., Qiao B., Liu H., Cheng J. S., Yuan Y. J., The biodegradation of Cefuroxime, Cefotaxime and Cefpirome by the Synthetic Consortium with Probiotic *Bacillus Clausii* and investigation of their potential biodegradation pathways, *Sci. Total Environ.*, 651 (2019) 271–280.
- [3] Zalewski P., Skibiński R., Szymanowska-Powalowska D., Piotrowska H., Kozak M., Pietralik Z., Bednarski W., Cielecka-Piontek J., The Radiolytic Studies of Cefpirome Sulfate in the solid state, *J. Pharm. Biomed. Anal.*, 118 (2016) 410–416.
- [4] Jain R., Vikas, Voltammetric Determination of Cefpirome at Multiwalled Carbon Nanotube modified Glassy Carbon Sensor based electrode in bulk form and Pharmaceutical formulation, *Colloids Surfaces B. Biointerfaces*, 87(2) (2011) 423–426.
- [5] Hong Y. H., Xu X. L., Li W. Q., Xu B. Z., Wu H. Q., Cheng Y., Chen H., Zhang B. S., Zhang F., A high-accuracy screening method of 44 Cephalosporins in meat using liquid Chromatography Quadrupole-Orbitrap hybrid mass spectrometry, *Anal. Methods*, 9(46) (2017) 6534–6548
- [6] Li W., Shen H., Hong Y., Zhang Y., Yuan F., Zhang F., Simultaneous determination of 22 Cephalosporins drug residues in Pork Muscle using liquid Chromatography-Tandem mass spectrometry, *J. Chromatogr. B. Anal. Technol. Biomed. Life Sci.*, 1022 (2016) 298–307.
- [7] Zalewski, P., Skibiński R., Cielecka-Piontek J., Bednarek-Rajewska K., Development and validation of stability-indicating HPLC method for determination of Cefpirome Sulfate, *Acta Pol. Pharm.*, 71(5) (2014) 731–736.
- [8] Breilh D., Lavallee C., Fratta A., Ducint D., Cony-Makhoul P., Saux M. C., Determination of Cefepime and Cefpirome in human serum by high-performance liquid Chromatography using an ultrafiltration for antibiotics serum extraction, *J. Chromatogr. B Biomed. Sci. Appl.*, 734(1) (1999) 121–127.
- [9] Kearns G.L., Johnson V.A., Hendry I.R., Wells T.G., Microanalytical high-performance liquid Chromatographic assay for Cefpirome in human milk and Urine, *J. Chromatogr.*, 574(2) (1992) 356-60.
- [10] Elghobashy M. R., Bebawy L. I., Abbas S. S., and Shokry R. F., Stability-indicating HPLC and RP-TLC determination of Cefpirome Sulfate with kinetic study, *Chromatographia*, 76 (17–18) (2013) 1141–1151.
- [11] Watanabe E., Review of Sample Preparation Methods for Chromatographic analysis of Neonicotinoids in agricultural and environmental matrices: from classical to state-of-the-art methods, *J. Chromatogr. A.*, 462042 (2021).
- [12] Mattrey F. T., Makarov A. A., Regalado E. L., Bernardoni F., Figus M., Hicks M. B., Zheng J., Wang L., Schafer W., Antonucci V., Hamilton S., Zawatzky K., and Welch C.J., Current challenges and future prospects in Chromatographic method development for pharmaceutical research, *TrAC - Trends Analyt Chem*, 95 (2017) 36–46.
- [13] Tobiszewski M., Namieśnik J., Direct Chromatographic methods in the context of green analytical chemistry, *TrAC - Trends Analyt. Chem.*, 35 (2012) 67–73.
- [14] Ganjali M. R., Gupta V. K., Faridbod F., Norouzi P., Electrochemical Determination of Lanthanides Series., In: Ganjali M. R., Gupta V. K., Faridbod F., Norouzi P., (Eds). In *Lanthanides Series Determination by Various Analytical Methods.*, Amsterdam: Elsevier, (2016).
- [15] Glasscott M. W., Vannoy K. J., Iresh Fernando P.U.A., Kosgei G. K., Moores L. C., Dick J. E., Electrochemical sensors for the detection of Fentanyl and its analogs:

- foundations and recent advances, *TrAC - Trends Analyt. Chem.*, 132 (2020) 16037.
- [16] Meenakshi S., Rama R., Pandian K., Gopinath S.C.B., Modified electrodes for electrochemical determination of Metronidazole in drug formulations and biological samples: An overview, *Microchem. J.*, 165 (2021) 106151.
- [17] Boumya W., Taoufik N., Achak M., Bessbousse H., Elhalil A., Barka N., Electrochemical sensors and biosensors for the determination of diclofenac in pharmaceutical, biological and water samples, *Talanta*, 3 (2021) 100026.
- [18] Boumya W., Taoufik N., Achak M., Barka N. Chemically modified carbon-based electrodes for the determination of Paracetamol in drugs and biological samples, *J. Pharm. Anal.*, 11(2) (2020) 138-154.
- [19] Li T., Xu J., Zhao L., Shen S., Yuan M., Liu W., Tu Q., Yu R., Wang J., Au nanoparticles/poly(caffeic acid) composite modified glassy carbon electrode for voltammetric determination of Acetaminophen, *Talanta*, 159 (2016) 356–364.
- [20] ICH Expert Working Group, ICH guideline Q1A(R2) stability testing of new drug substances and products, *Int. Conf. Harmon.*, 24 (2003).
- [21] Strenkoski L.C., Nix D.E., Cefpirome clinical pharmacokinetics, *Clin Pharmacokinet.*, 25(1993) 263-273.
- [22] Deepa S., Swamy B. E. K., Pai K. V. A., Surfactant SDS modified carbon paste electrode as an enhanced and effective electrochemical sensor for the determination of Doxorubicin and Dacarbazine its applications: a voltammetric study, *J. Electroanal. Chem.*, 879 (2020) 114748.
- [23] Kurbanoglu S., Uslu B., Ozkan S.A., Validation of Analytical Methods for the Assessment of Hazards in Food., In: Grumezescu A. M., Holban A. M., (Eds). Food Safety and Preservation, Modern Biological Approaches to Improving Consumer Health., London: Academic Press, 2018.
- [24] Dogan-Topal B., Uslu B., Ozkan S. A., Voltammetric studies on the hiv-1 inhibitory drug efavirenz: the interaction between DsDNA and drug using electrochemical DNA biosensor and adsorptive stripping voltammetric determination on disposable pencil graphite electrode, *Biosens. Bioelectron.*, 24(8) (2009) 2358–2364.



DFT, molecular docking and molecular dynamics simulation studies on natural chromone derivatives from *Cassia nomame* for their possible antiviral activity against Coronavirus, SARS-CoV-2

Taner ERDOGAN^{1,*}

¹ Kocaeli University, Kocaeli Vocational School, Department of Chemistry and Chemical Processing Technologies, Kocaeli / TURKEY

Abstract

In this study, two naturally occurred chromone derivatives obtained from *Cassia nomame* which are recently entered the literature, have been investigated computationally for their potential antiviral activity against SARS-CoV-2. In the first part of the study, DFT calculations were performed on the investigated compounds. In this part, geometry optimizations, frequency analyses, molecular electrostatic potential map calculations, frontier molecular orbital calculations and NMR spectral studies have been performed. In the second part of the study, molecular docking calculations were performed. SARS-CoV-2 main protease (SARS-CoV-2 M^{pro}) was selected as receptor for molecular docking calculations. In the third part of the study, molecular dynamics simulation studies were performed on the top scoring SARS-CoV-2 M^{pro} – ligand complexes. In this part, binding free energy calculations were also performed on the SARS-CoV-2 M^{pro} – ligand complexes with the use of molecular mechanics with Poisson-Boltzmann surface area (MM-PBSA) method. Results showed that, two naturally occurred chromone derivatives, 5-(isobutyryl)-2-(2-oxopropyl)-7-methoxy-4*H*-chromen-4-one and 5-(isobutyryl)-2-(2-oxopropyl)-6-methoxy-4*H*-chromen-4-one, showed quite high binding affinity to SARS-CoV-2 M^{pro} and remained stable during the molecular dynamics simulations. Additionally, in the last part of the study, drug-likeness analyses were performed on the investigated compounds with the use of Lipinski's rule of five and no violation was observed.

Article info

History:

Received: 16.05.2020

Accepted: 14.07.2021

Keywords:

COVID-19,
Chromone derivatives,
Cassia nomame,
Molecular docking,
Molecular dynamics
simulation.

1. Introduction

Since its first appearance in China in December 2019, SARS-CoV-2 has been causing human pulmonary infections and despite all the measures taken, it continues to spread all over the world very quickly. Currently, vaccination is the only effective way to treat COVID-19, and unfortunately, a specific drug treatment has not been developed yet, and it is a critical issue to propound specific drug treatment options today and in near future.

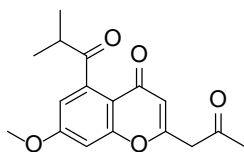
Drug treatment investigations for SARS-CoV-2 infections can be divided into two groups: (1) To use the drugs currently used in SARS and MERS treatments due to the similarity between the target proteins and (2) to develop new specific drugs. Currently, intensive studies are being conducted on whether drugs used in the treatment of SARS and MERS can be used against SARS-CoV-2 such as favipiravir, ribavirin, remdesivir, galidesivir,

disulfiram, lopinavir, ritonavir etc. and other synthesized or isolated compounds found in databases are being investigated against SARS-CoV-2. [1–8] Since it has an important role in viral replication and transcription, SARS-CoV-2 M^{pro} is a commonly selected target in drug repurposing and new drug development studies for the treatment of COVID-19. [9,10]

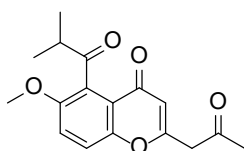
In this study, two novel natural products which were isolated by Liao et al. [11] from *Cassia nomame* have been investigated computationally for their possible antiviral activity against SARS-CoV-2 via performing molecular docking calculations and molecular dynamics simulations. The structures of these natural chromone derivatives are given in Figure 1.

*Corresponding author. e-mail address: taner.erdogan@kocaeli.edu.tr
<http://dergipark.gov.tr/csj> ©2021 Faculty of Science, Sivas Cumhuriyet University

In the first part of the study, density functional theory calculations were performed on the investigated compounds.



5-(isobutyryl)-2-(2-oxopropyl)-7-methoxy-4H-chromen-4-one
Comp.1



5-(isobutyryl)-2-(2-oxopropyl)-6-methoxy-4H-chromen-4-one
Comp.2

Figure 1. Chemical structures of Comp. 1 and 2.

Geometry optimizations, frequency analyses, MEP (molecular electrostatic potential) map calculations, frontier molecular orbital (FMO) calculations and NMR spectral studies were carried out. In the second part, molecular docking calculations were performed, and then molecular dynamics simulations were carried out on the top-scoring enzyme – ligand complexes, and binding free energies were determined. Finally, drug-likeness analyses were performed on the investigated compounds.

2. Materials and Methods

2.1. DFT calculations

In this part, the title compounds have been investigated computationally and geometry optimizations, frequency analyses, MEP map calculations, FMO calculations and NMR spectral analyses were performed. In DFT calculations, Gaussian 09 Rev.D.01 [12], GaussView 5 [13], VeraChem VConf [14] and Avogadro 1.1.1 [15] software packages were used. All calculations were performed with the use of DFT B3LYP method and various basis sets including 6-31+G(d), 6-31+G(d,p), 6-311+G(d,p) and 6-311+G(2d,p). Geometry optimizations were performed in gas phase. Prior to geometry optimizations, a conformational search was performed for each structure and frequency analyses were also performed to confirm that each optimized geometry corresponds to a global minimum.

2.2. Molecular docking calculations and molecular dynamics simulations

Geometry optimized structures of Comp. 1 and 2 were used for molecular docking calculations. In molecular docking calculations AutoDock Tools [16] and

AutoDock Vina were used and Discovery Studio Visualizer [17] was used for the representation of the docking results. 3D structure of SARS-CoV-2 M^{pro} was obtained from RCSB Protein Data Bank [18,19] (PDB ID:5R80). Prior to molecular docking, water molecules and the bound ligands in the structure of the enzyme were removed, hydrogen atoms and Gasteiger charges were added, and docking calculations were performed with the use of Lamarckian genetic algorithm. After performing molecular docking calculations, top-scoring ligand-enzyme complexes were subjected to 30 ns molecular dynamics simulations. In molecular dynamics simulations, GROMACS [20] program package, AMBER [21] force field and TIP3P water model were used. Acypc Server [22] was used in the preparation of ligand topologies. After energy minimizations, 200 ps NVT and NPT ensemble equilibrations, molecular dynamics simulations were performed for 30 ns at 1 bar and 300 K reference pressure and temperature. After performing molecular dynamics simulations, binding free energies were calculated with the use of MM-PBSA method for the last 20 ns of the MD simulations. In MM-PBSA calculations, g_mmpbsa tool [23,24] was used.

2.3. Drug-likeness analyses

Lipinski's rule of five [25,26] was used to evaluate drug-likeness of the investigated compounds. Drug-likeness of the investigated compounds were tested with the use of DruLiTo software package [27].

3. Results and Discussion

3.1. DFT calculations

Optimized structures of the investigated natural compounds obtained from DFT calculations with the use of 6-311+G(2d,p) basis set are given in Figure 2. A frequency analysis was performed for each structure to confirm that the optimized structures correspond to global minima and results showed that geometry optimized structures correspond to global minima.

To obtain information about the electron deficient and the electron rich regions of the compounds under investigation, MEP map calculations were performed at the same level of theory.

MEP maps of the compounds obtained with the use of 6-311+G(2d,p) basis set are given in Figure 3. It was observed that negative charge was mainly localized on the carbonyl oxygens of both compounds 1 and 2, while positive charge as located generally on the alkyl hydrogens. Molecular docking and molecular dynamics simulation results showed that these negative and positive centers took part in the interactions between investigated compounds and SARS-CoV-2 M^{pro}.

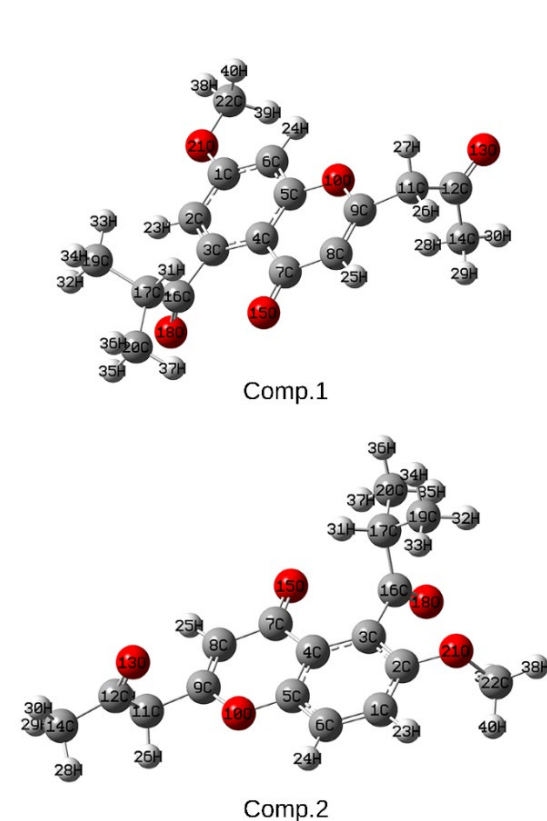


Figure 2. Optimized geometries of Comp. 1 and 2.

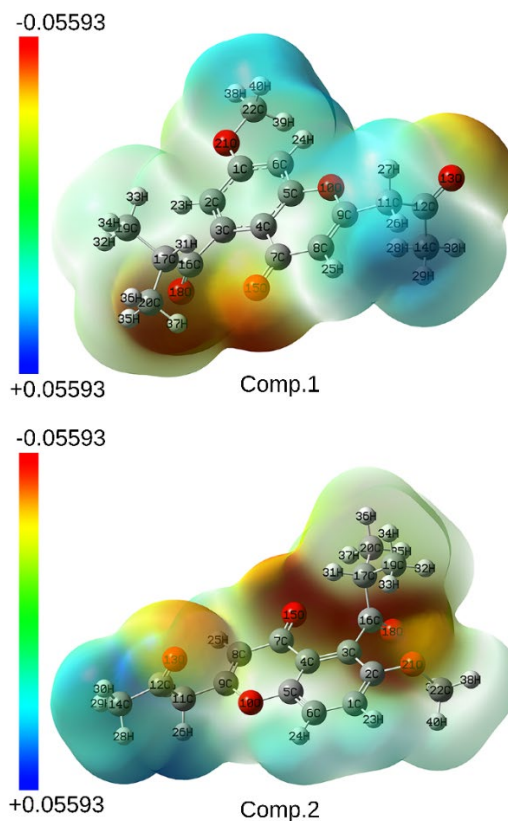


Figure 3. MEP maps of Comp. 1 and 2

FMOs and FMO energies of the investigated compounds have also been determined and are given in Figure 4. It was observed that HOMO-LUMO gap of compound 1 is slightly greater than that of compound 2. HOMO-LUMO gap is thought to be useful parameter for examining the kinetic stability. Since compound 1 has larger HOMO-LUMO gap value, it can be said that compound 1 is more stable than compound 2. HOMO-LUMO energies and HOMO-LUMO gaps of the investigated compounds calculated with the use of 6-31+G(d), 6-31+G(d,p), 6-311+G(d,p) and 6-311+G(2d,p) basis sets are given in Table 1. All values in Table 1 are given in eV.

Nuclear magnetic shield tensors for the compounds were performed at the same level of theory with the use of GIAO method. In this part, 6-31+G(d), 6-31+G(d,p), 6-311+G(d,p) and 6-311+G(2d,p) basis sets were used. In NMR calculations IEFPCM solvation model was used and CDCl_3 was selected as solvent.

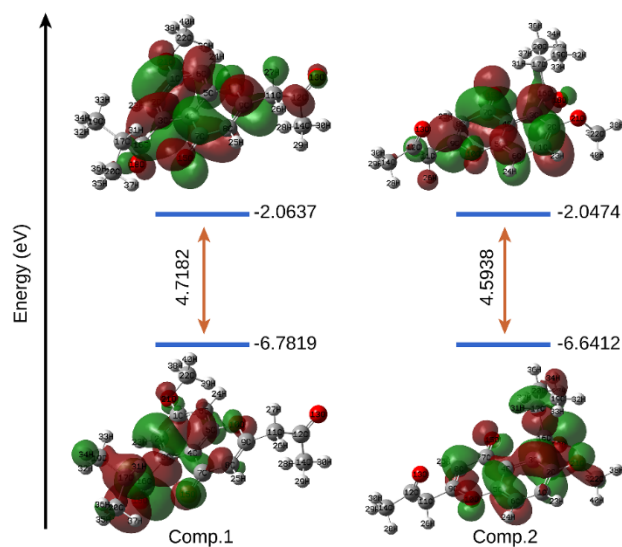


Figure 4. FMOs of Comp. 1 and 2

Calculated and experimental NMR chemical shifts reference to TMS are given in Tables 2, 3, 4 and 5.

Table 1. Calculated FMO energies and HOMO-LUMO gaps of investigated compounds.

Atom	6-31+G(d)	6-31+G(d,p)	6-311+G(d,p)	6-311+G(2d,p)
Comp. 1				
LUMO	-1.7565	-1.7228	-2.0814	-2.0637
HOMO	-6.2488	-6.3928	-6.7735	-6.7819
Gap	4.4923	4.6700	4.6921	4.7182
Comp. 2				
LUMO	-1.7451	-1.6885	-2.0819	-2.0474
HOMO	-6.2390	-6.2864	-6.6682	-6.6412
Gap	4.4939	4.5979	4.5863	4.5938

It was observed that except some certain types of hydrogen and carbon, smaller basis sets gave more satisfactory results than larger basis sets and there is no need to use larger basis sets.

Table 2. Experimental and calculated ¹H-NMR data for Comp. 1

Atom	Exp. [11]	6-31+G(d)	6-31+G(d,p)	6-311+G(d,p)	6-311+G(2d,p)
23-H	7.42	6.72	6.96	6.97	7.08
24-H	7.12	6.74	7.04	7.12	7.23
25-H	6.32	5.95	6.22	6.27	6.37
26-H	3.55	3.56	3.63	3.74	3.83
27-H	3.55	3.56	3.63	3.74	3.83
28-H	2.17	2.17	2.26	2.36	2.40
29-H	2.17	2.17	2.26	2.36	2.40
30-H	2.17	2.17	2.26	2.36	2.40
31-H	4.25	3.05	3.07	3.09	3.22
32-H	1.23	1.03	1.04	1.13	1.13
33-H	1.23	1.03	1.04	1.13	1.13
34-H	1.23	1.03	1.04	1.13	1.13
35-H	1.23	1.46	1.48	1.58	1.56
36-H	1.23	1.46	1.48	1.58	1.56
37-H	1.23	1.46	1.48	1.58	1.56
38-H	3.82	3.92	3.99	4.04	4.06
39-H	3.82	3.92	3.99	4.04	4.06
40-H	3.82	3.92	3.99	4.04	4.06

Table 3. Experimental and calculated ^{13}C -NMR data for Comp. 1

Atom	Exp. [11]	6-31+G(d)	6-31+G(d,p)	6-311+G(d,p)	6-311+G(2d,p)
1-C	166.8	157.8	160.0	172.6	172.6
2-C	106.2	108.8	109.8	119.1	118.7
3-C	136.8	142.8	144.8	154.2	153.9
4-C	114.8	113.0	114.8	123.2	123.2
5-C	155.4	153.9	155.8	166.5	166.8
6-C	110.2	99.5	100.5	108.3	107.7
7-C	181.4	169.8	171.6	183.1	183.8
8-C	112.8	110.7	111.8	120.3	119.9
9-C	158.2	159.5	161.4	172.2	172.5
11-C	48.3	51.0	51.9	55.3	54.9
12-C	203.1	200.1	201.6	215.6	215.6
14-C	30.4	29.9	30.3	32.7	32.4
16-C	208.5	209.4	211.2	226.4	226.0
17-C	38.3	46.2	47.0	49.6	50.0
19-C	18.6	21.3	21.6	21.9	21.5
20-C	18.6	21.3	21.6	21.9	21.5
22-C	56.2	55.0	55.2	58.2	58.1

Table 4. Experimental and calculated ^1H -NMR data for Comp. 2

Atom	Exp. [11]	6-31+G(d)	6-31+G(d,p)	6-311+G(d,p)	6-311+G(2d,p)
23-H	6.93	7.49	7.71	7.74	7.82
24-H	7.10	7.50	7.73	7.79	7.86
25-H	6.35	5.99	6.25	6.31	6.37
26-H	3.56	3.55	3.63	3.76	3.82
27-H	3.56	3.55	3.63	3.76	3.82
28-H	2.17	2.18	2.26	2.38	2.40
29-H	2.17	2.18	2.26	2.38	2.40
30-H	2.17	2.18	2.26	2.38	2.40
31-H	4.27	3.03	3.05	3.09	3.16
32-H	1.26	1.30	1.31	1.42	1.37
33-H	1.26	1.30	1.31	1.42	1.37
34-H	1.26	1.30	1.31	1.42	1.37
35-H	1.26	1.30	1.31	1.42	1.37
36-H	1.26	1.30	1.31	1.42	1.37
37-H	1.26	1.30	1.31	1.42	1.37
38-H	3.84	3.82	3.91	3.97	4.02
39-H	3.84	3.82	3.91	3.97	4.02
40-H	3.84	3.82	3.91	3.97	4.02

Table 5. Experimental and calculated ^{13}C -NMR data for Comp. 2

Atom	Exp. [11]	6-31+G(d)	6-31+G(d,p)	6-311+G(d,p)	6-311+G(2d,p)
1-C	120.2	126.2	127.3	137.6	137.1
2-C	156.4	150.6	152.6	164.3	164.0
3-C	121.4	135.2	137.0	146.6	146.4
4-C	118.5	120.0	121.8	130.7	130.9
5-C	150.4	149.4	151.4	161.6	161.8
6-C	122.9	116.1	117.3	126.7	126.1
7-C	181.8	170.5	172.3	183.8	184.5
8-C	110.9	109.9	111.0	119.6	119.2
9-C	159.9	159.9	161.8	172.4	172.9
11-C	48.1	51.7	52.5	56.0	55.6
12-C	203.4	199.9	201.4	215.1	215.1
14-C	30.2	29.8	30.1	32.6	32.2
16-C	208.4	208.4	210.2	224	223.7
17-C	38.2	47.6	48.4	50.6	50.8
19-C	18.6	21.0	21.3	21.6	21.2
20-C	18.6	21.0	21.3	21.6	21.2
22-C	56.2	66.2	66.6	69.1	69.4

3.2. Molecular docking calculations and molecular dynamics simulation studies

After performing molecular docking calculations, 30 ns molecular dynamics simulations were carried out.

The structures of the SARS-CoV-2 M^{pro} – Comp. 1 complex obtained from the trajectory for every 5 ns of the 30 ns molecular dynamics simulation are given in Figure 5.

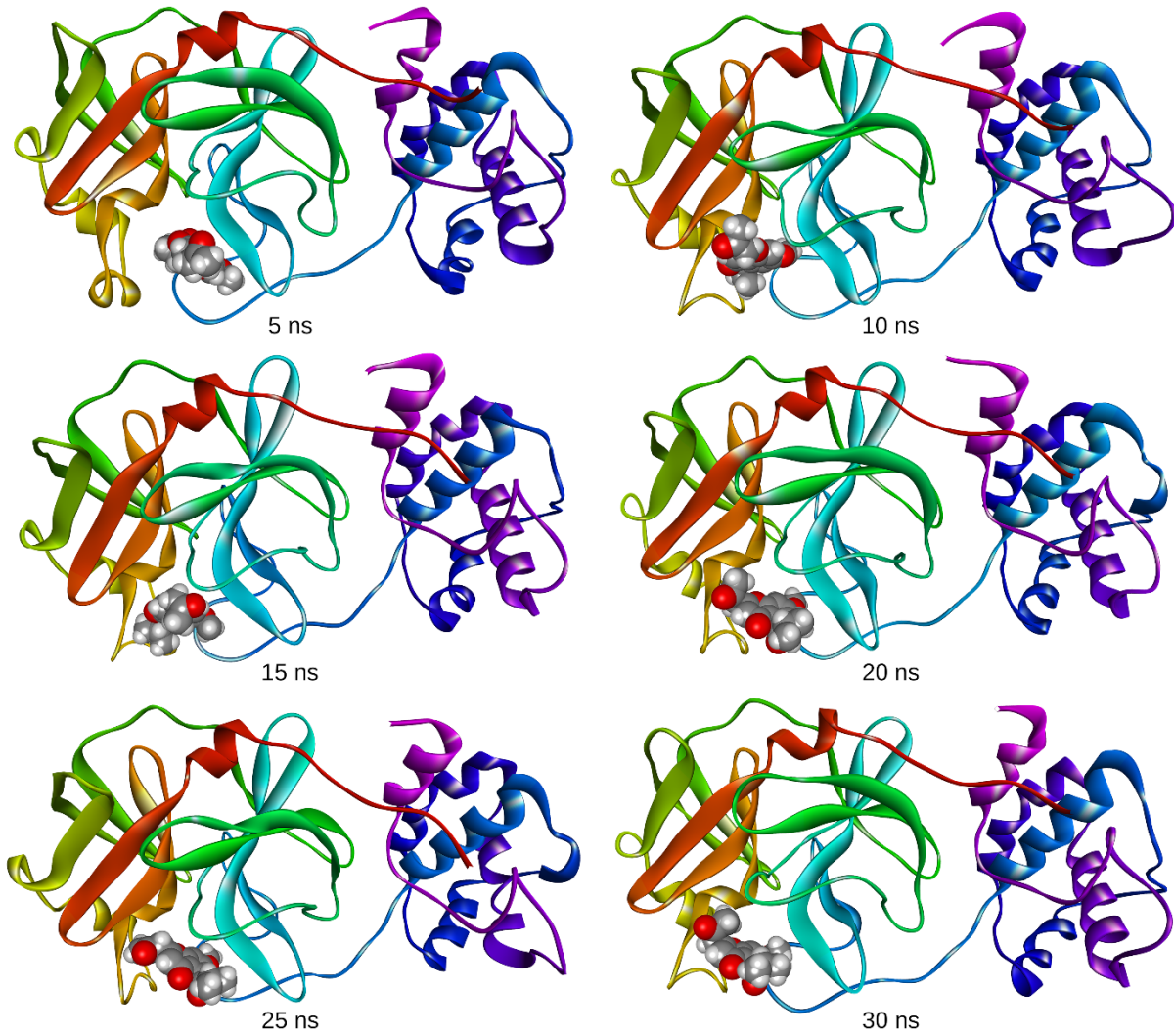


Figure 5. The structures of enzyme – Comp. 1 complex extracted from the trajectory of MD simulation.

Results showed that Comp. 1 bound to the active site of SARS-CoV-2 M^{pro} and held its position throughout the entire simulation. The structures of the SARS-CoV-2 M^{pro} – Comp. 2 complex obtained from the trajectory for every 5 ns of the 30 ns molecular

dynamics simulation are given in Figure 6 and it was observed that Comp. 2 also bound to the active site of the enzyme and held its position throughout the entire simulation.

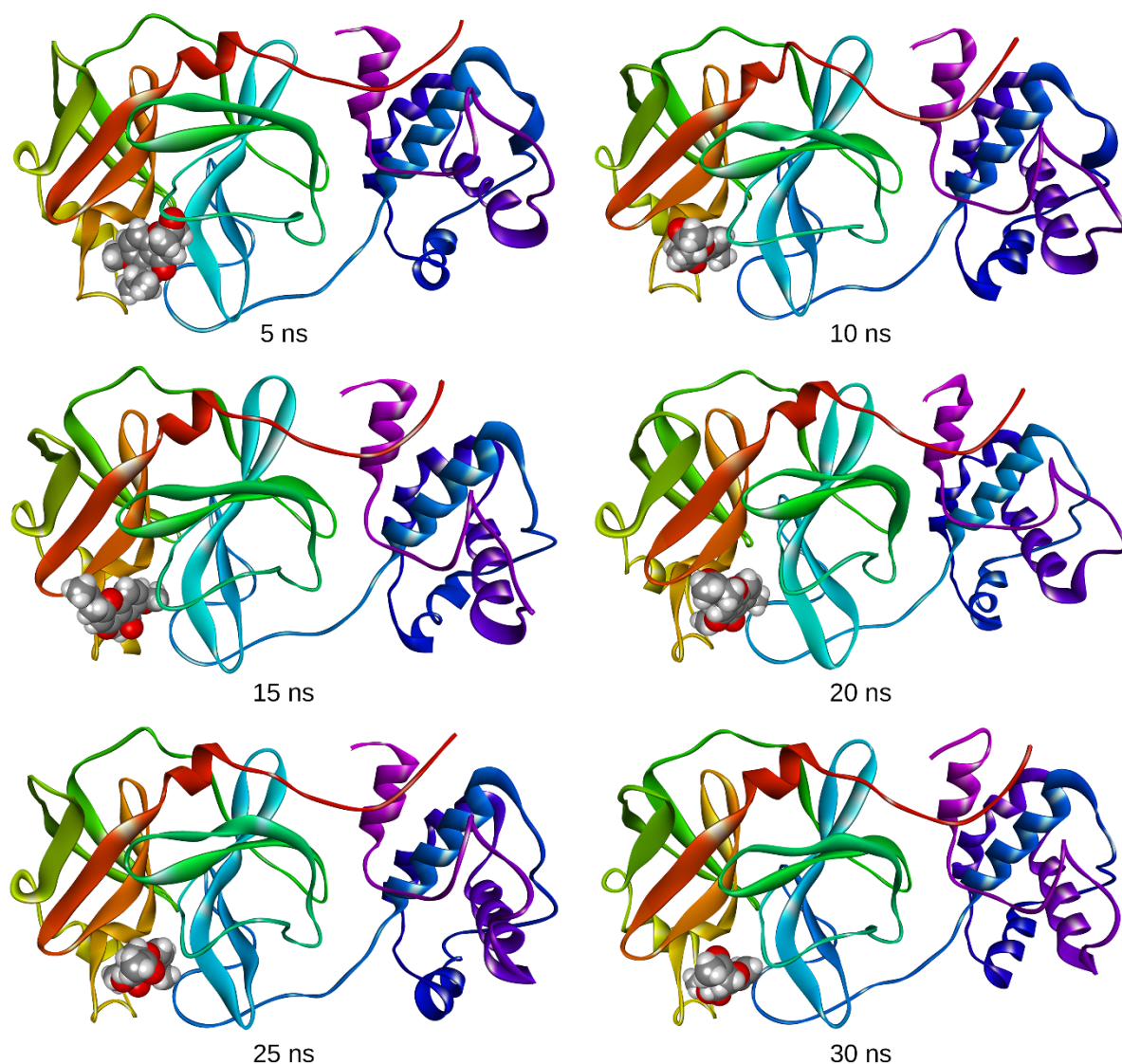


Figure 6. The structures of enzyme – Comp. 2 complex extracted from the trajectory of MD simulation.

In Figure 7, 3D and 2D interactions between investigated compounds and SARS-CoV-2 M^{pro} at the end of molecular dynamics simulations are illustrated. Results showed that, Comp. 1 interacted with HIS41, MET49, MET165, VAL186 and GLN189 amino acids of SARS-CoV-2 M^{pro}. Hydrogen bonds, alkyl, π -alkyl

and π -sulfur interactions took part in the stabilization of the enzyme – Comp. 1 complex. On the other hand, Comp. 2 interacted with HIS41, MET49, GLY143, CYS145 and SER46. Hydrogen bonds, alkyl and π -alkyl interactions took part in the stabilization of enzyme – Comp. 2 complex.

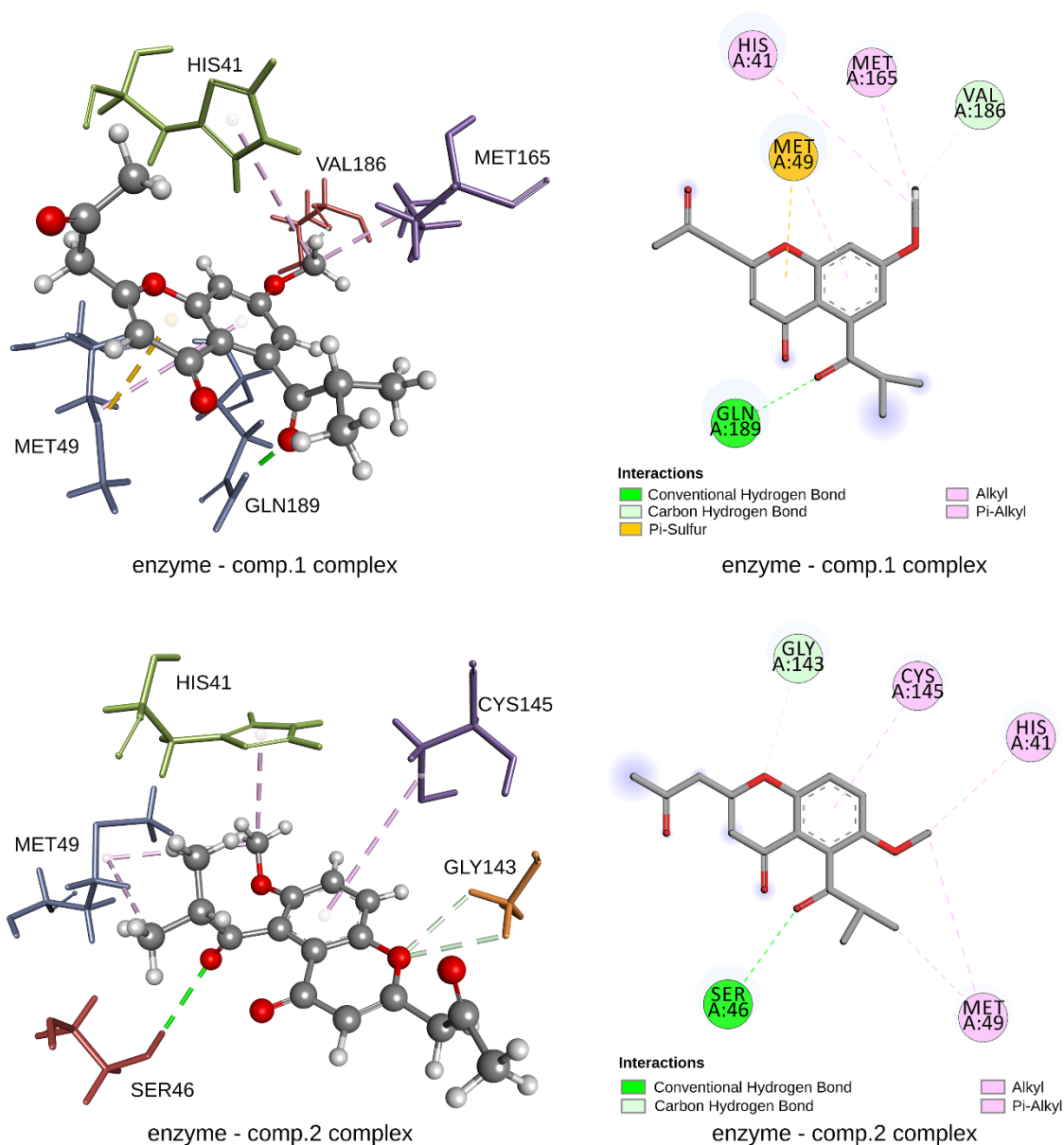


Figure 7. Interactions between ligands and enzyme after MD simulation.

Molecular dynamics simulation results for enzyme – Comp. 1 complex are illustrated in Figure 8. Root mean square deviation (RMSD) and radius of gyration (RG) of protein are useful tools for determining the stability of a ligand-protein complex. Results showed that enzyme – Comp. 1 complex remained stable during the MD simulation (Figure 8b and 8c). Average RMSD of backbone after least square fit to backbone was found to be 0.189 ± 0.021 nm and average RG of protein was found to be 2.224 ± 0.014 nm. It was observed that there is a noticeable change in the

position of Comp. 1 around 7 ns and then, a slight change around 18 ns. Results showed that ligand reached its equilibrium position at the 18th ns of the simulation and held its position for the remaining time of the simulation (Figure 8a). Average RMSD of Comp. 1 after least square fit to protein was found to be 0.499 ± 0.152 nm. Number of hydrogen bonds was also monitored during the MD simulation (Figure 8d). Results showed that at least one hydrogen bond was formed between the ligand and the enzyme in nearly one third of the simulation time.

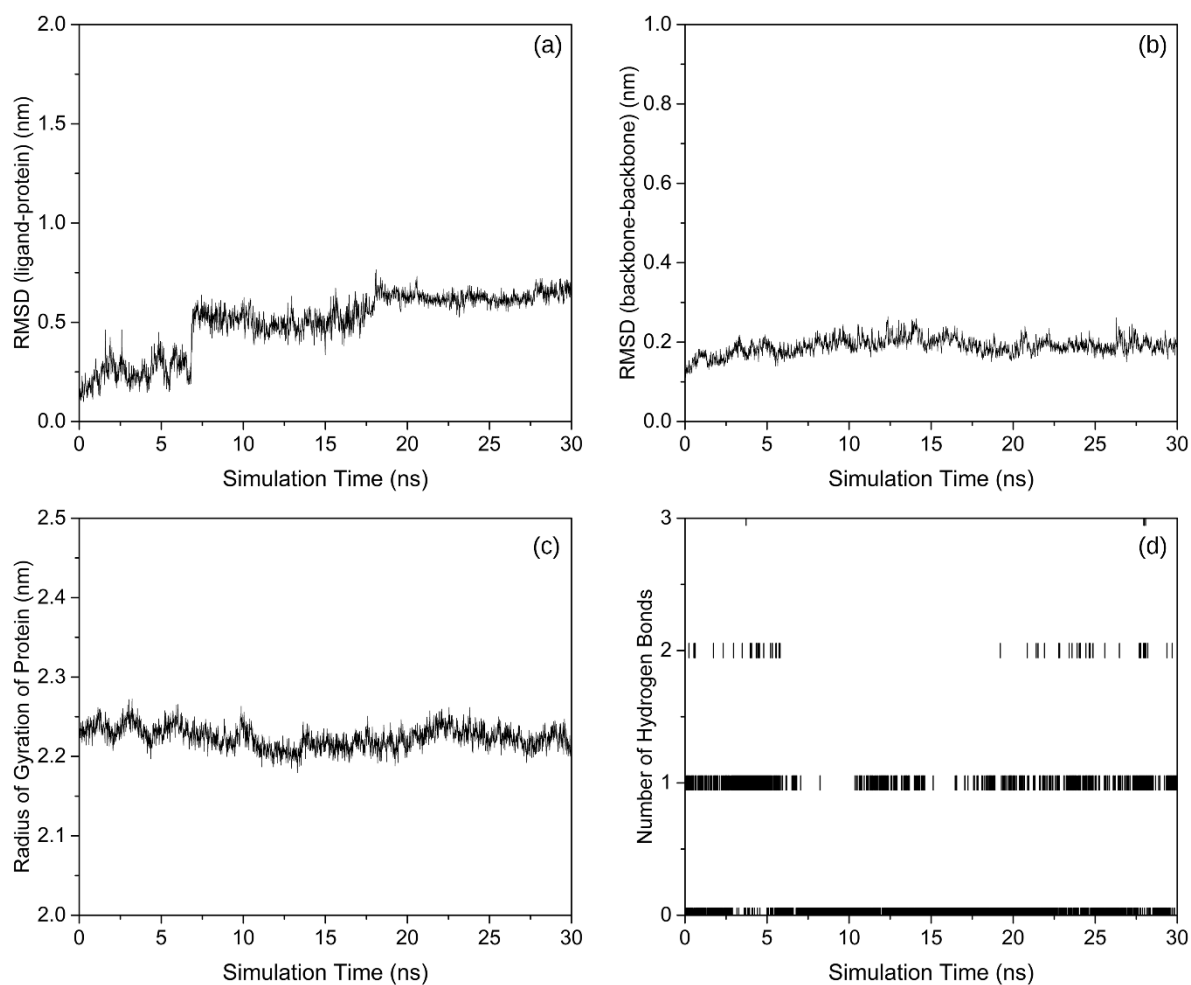


Figure 8. MD simulation results (a) RMSD of ligand after least square fit to protein, (b) RMSD of backbone after least square fit to backbone, (c) Radius of gyration of protein and (d) number of hydrogen bonds between protein and Comp. 1.

Molecular dynamics simulation results for enzyme – Comp. 2 complex are illustrated in Figure 9. Results showed that enzyme remained stable during the MD simulation (Figure 9b and 9c). Average RMSD of backbone after least square fit to backbone was found to be 0.219 ± 0.031 nm and average RG of protein was found to be 2.212 ± 0.010 nm. It was observed that RMSD of ligand after least square fit to protein

increased until 17th ns, and then it decreased gradually and reached its equilibrium position at the 24th ns of the MD simulation (Figure 9a). Average RMSD of Comp. 2 after least square fit to protein was found to be 0.612 ± 0.173 nm. Results showed that at least one hydrogen bond was formed between Comp. 2 and the enzyme in nearly half of the simulation time.

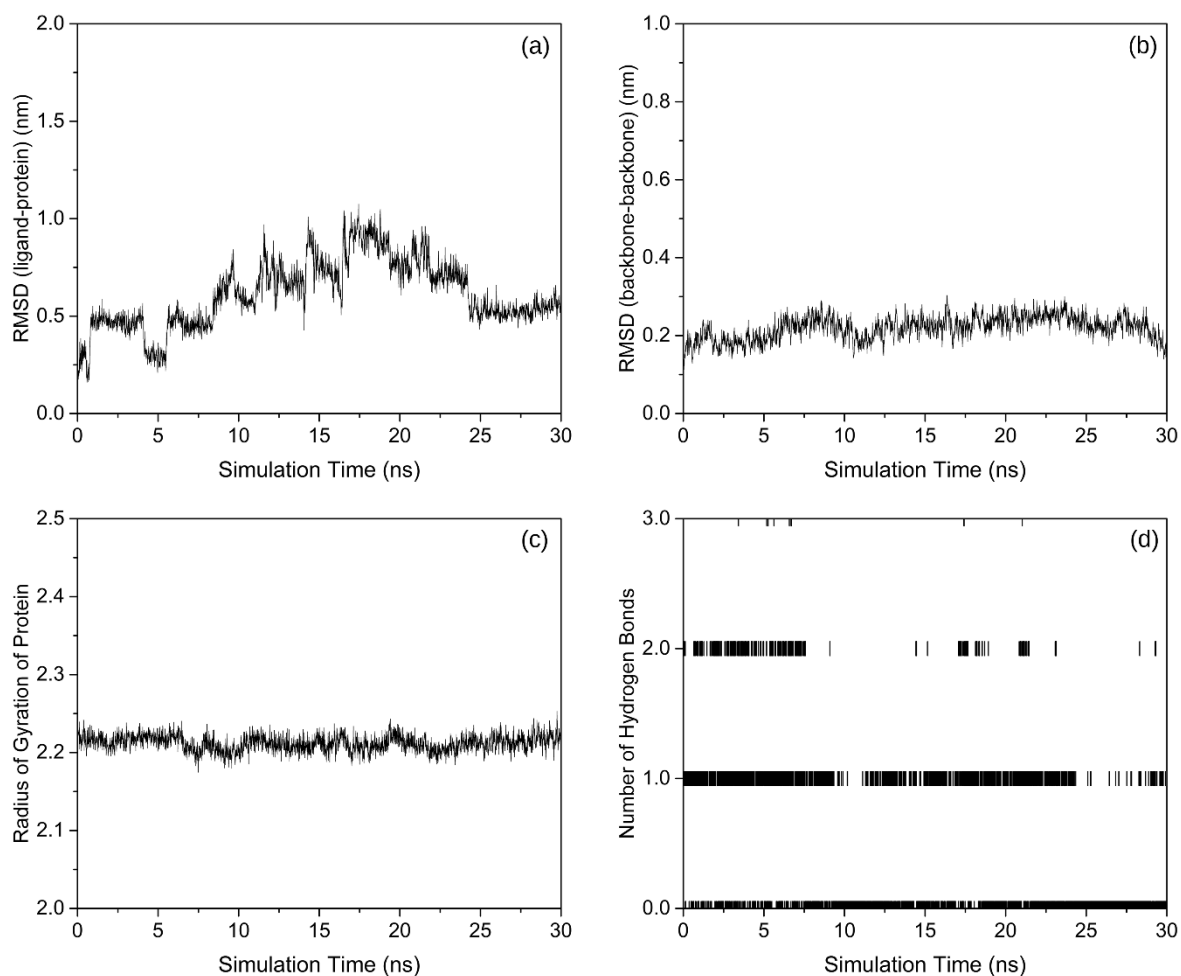


Figure 9. MD simulation results (a) RMSD of ligand after least square fit to protein, (b) RMSD of backbone after least square fit to backbone, (c) Radius of gyration of protein and (d) number of hydrogen bonds between protein and Comp. 2.

Binding free energies were calculated with the use of MM-PBSA method (Figure 10). Binding free energies of the reference drugs are literature values which were determined in our previous work. [8] Results showed that binding affinities of the investigated compounds

are quite high. It was observed that although the binding affinity of Comp. 1 is lower than those of lopinavir and hydroxychloroquine, it was higher than that of remdesivir.

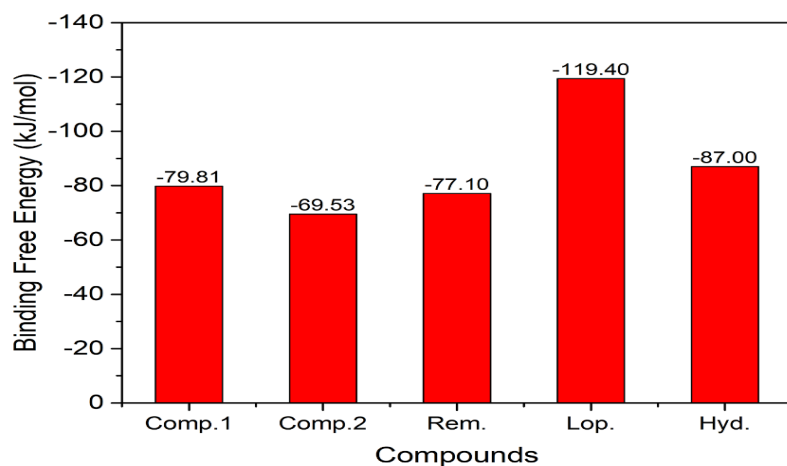


Figure 10. Binding free energies belong to investigated compounds and reference drugs obtained from MM-PBSA calculations [8] (Rem.: Remdesivir, Lop.:Lopinavir and Hyd.: Hydroxychloroquine).

3.3. Drug-likeness analysis

Lipinski's rule of five [25,26] was used to evaluate drug-likeness of the investigated compounds. Drug-likeness of the investigated compounds were tested with the use of DruLiTo software package [27]. As known, Lipinski's rule describes the molecular properties which are important for a drug's pharmacokinetics, including absorption, distribution, metabolism, and excretion. According to Lipinski's rule a potential drug molecule has no more than one violation of the following criteria:

- A molecular mass less than 500 daltons
- An octanol-water partition coefficient (logP) that doesn't exceed 5
- No more than 5 HBD (hydrogen bond donors)
- No more than 10 HBA (hydrogen bond acceptors)

For the investigated molecules (both Comp. 1 and 2), molecular weight, logP, HBD and HBA values were found to be 302.12, 0.999, 0 and 5, respectively (Table 6). Results showed that there is no violation of the criteria of Lipinski's rule.

Table 6. Results of drug-likeness analyses.

Parameter	Criteria	Calculated Value	
		Comp. 1	Comp. 2
MW	< 500	302.12	302.12
logP	< 5	0.999	0.999
HBD	< 5	0	0
HBA	< 10	5	5

4. Conclusion

In the present study, two newly introduced chromone derivatives have been investigated for their possible antiviral activity against SARS-CoV-2 with the assistance of computational methods including DFT calculations, molecular docking calculations and molecular dynamics simulations. In the study, MM-PBSA calculations and drug-likeness analyses were also carried out. Results showed that investigated compounds efficiently bound to SARS-CoV-2 M^{Pro} and held their positions throughout the entire molecular dynamics simulations. Binding affinities of the investigated compounds were found to be quite high and comparable to the reference drugs. Especially binding affinity of Comp. 1 is higher than that of Comp. 2 and reference drug remdesivir. However, it was found that the binding affinities of the investigated

compounds are lower than those of lopinavir and hydroxychloroquine. Additionally, it was observed that both compounds obey Lipinski's rule of five and no violation was observed. In the study it was concluded that these natural chromone derivatives can be promising structures in the treatment of SARS-CoV-2 infections and worth for further research.

Acknowledgements

The computational studies reported in this paper were partially performed at TUBITAK ULAKBIM, High Performance and Grid Computing Center (TRUBA resources) and Kocaeli University.

Conflict of interest

The authors declare that they have no conflict of interests.

References

- [1] Cheng C.Y., Lee Y.L., Chen C.P., Lin Y.C., Liu C.E., Liao C.H., Cheng S.H., Lopinavir/ritonavir did not shorten the duration of SARS CoV-2 shedding in patients with mild pneumonia in Taiwan, *Journal of Microbiology, Immunology and Infection*, 53 (2020) 488–492.
- [2] Lin M.H., Moses D.C., Hsieh C.H., Cheng S.C., Chen Y.H., Sun C.Y., Chou C.Y., Disulfiram can inhibit MERS and SARS coronavirus papain-like proteases via different modes, *Antiviral Research*, 150 (2018) 155–163.
- [3] Yu R., Chen L., Lan R., Shen R., Li P., Computational screening of antagonists against the SARS-CoV-2 (COVID-19) coronavirus by molecular docking, *International Journal of Antimicrobial Agents*, 56(2) (2020) 106012.
- [4] Elfiky A.A., Ribavirin, Remdesivir, Sofosbuvir, Galidesivir and Tenofovir against SARS-CoV-2 RNA dependent RNA polymerase (RdRp): A molecular docking study, *Life Sciences*, 253 (2020).
- [5] Cai Q., Yang M., Liu D., Chen J., Shu D., Xia J., Liao X., Gu Y., Cai Q., Yang Y., Shen C., Li X., Peng L., Huang D., Zhang J., Zhang S., Wang F., Liu J., Chen L., Chen S., Wang Z., Zhang Z., Cao R., Zhong W., Liu Y., Liu L., Experimental Treatment with Favipiravir for COVID-19: An Open-Label Control Study, *Engineering*, 6 (2020) 1192–1198.

- [6] Choy K.T., Wong A.Y.L., Kaewpreedee P., Sia S.F., Chen D., Hui K.P.Y., Chu D.K.W., Chan M.C.W., Cheung P.P.H., Huang X., Peiris M., Yen H.L., Remdesivir, lopinavir, emetine, and homoharringtonine inhibit SARS-CoV-2 replication in vitro, *Antiviral Research*, 178 (2020) 104786.
- [7] McKee D.L., Sternberg A., Stange U., Laufer S., Naujokat C., Candidate drugs against SARS-CoV-2 and COVID-19, *Pharmacological Research*, 157 (2020) 104859.
- [8] Erdogan T., DFT, molecular docking and molecular dynamics simulation studies on some newly introduced natural products for their potential use against SARS-CoV-2, *Journal of Molecular Structure*, 1242 (2021) 130733.
- [9] Liu X., Wang X.J., Potential inhibitors against 2019-nCoV coronavirus M protease from clinically approved medicines, *Journal of Genetics and Genomics*, 47 (2020) 119–121.
- [10] Xu Z., Peng C., Shi Y., Zhu Z., Mu K., Wang X., Zhu W., Nelfinavir was predicted to be a potential inhibitor of 2019-nCov main protease by an integrative approach combining homology modelling, molecular docking and binding free energy calculation, *BioRxiv*, (2020) 2020.01.27.921627.
- [11] Liao L.M., Sun Y.Q., Li J., Kong W.S., Liu X., Xu Y., Huang H.T., Zeng W.L., Mi Q.L., Yang G.Y., Hu Q.F., Li Y.K., Two New Chromone Derivatives from Cassia nomame and their Anti-Tobacco Mosaic Virus Activity, *Chemistry of Natural Compounds*, 56 (2020) 58–61.
- [12] Frisch M.J., Trucks G.W., Schlegel H.B., Scuseria G.E., Robb M.A., Cheeseman J.R., Scalmani G., Barone V., Mennucci B., Petersson G.A., Nakatsuji H., Caricato M., Li X., Hratchian H.P., Izmaylov A.F., Bloino J., Zheng G., Sonnenberg J.L., Hada M., Ehara M., Toyota K., Fukuda R., Hasegawa J., Ishida M., Nakajima T., Honda Y., Kitao O., Nakai H., Vreven T., Montgomery J. A., Peralta J.E., Ogliaro F., Bearpark M., Heyd J.J., Brothers E., Kudin K.N., Staroverov V.N., Keith T., Kobayashi R., Normand J., Raghavachari K., Rendell A., Burant J.C., Iyengar S.S., Tomasi J., Cossi M., Rega N., Millam J.M., Klene M., Knox J.E., Cross J.B., Bakken V., Adamo C., Jaramillo J., Gomperts R., Stratmann R.E., Yazyev O., Austin A.J., Cammi R., Pomelli C., Ochterski J.W., Martin R.L., Morokuma K., Zakrzewski V.G., Voth G.A., Salvador P., Dannenberg J.J., Dapprich S., Daniels A.D., Farkas O., Foresman J.B., Ortiz J. V, Cioslowski J., Fox D.J., Gaussian 09, (2013).
- [13] Dennington, R., T. Keith, J. Millam, GaussView, Version 5, (2009).
- [14] Chang C. E. Gilson M.K., Tork: Conformational analysis method for molecules and complexes, *Journal of Computational Chemistry*, 24 (2003) 1987–1998.
- [15] Hanwell M.D., Curtis D.E., Lonie D.C., Vandermeersch T., Zurek E., Hutchison G.R., Avogadro: an advanced semantic chemical editor, visualization, and analysis platform, *Journal of Cheminformatics*, 4 (2012) 17.
- [16] Morris G.M., Huey R., Lindstrom W., Sanner M.F., Belew R.K., Goodsell D.S., Olson A.J., AutoDock4 and AutoDockTools4: Automated docking with selective receptor flexibility, *J Comput. Chem.*, 30 (2009) 2785–2791.
- [17] BIOVIA, D.S., Discovery Studio Visualizer, v20.1.0.19295, (2016).
- [18] RCSB PDB, Available at: <https://www.rcsb.org/>, Retrieved May, 2021.
- [19] Berman H.M., Westbrook J., Feng Z., Gilliland G., Bhat T.N., Weissig H., Shindyalov I.N., Bourne P.E., The Protein Data Bank, *Nucleic Acids Research*, 28 (2000) 235–242.
- [20] Lindahl, Abraham, Hess, van der Spoel, GROMACS 2020 Source code, (2020).
- [21] Ponder J.W., Case D.A., Force fields for protein simulations, *Advances in Protein Chemistry*, 66 (2003) 27–85.
- [22] Sousa Da Silva A.W., Vranken W.F., ACPYPE - AnteChamber PYthon Parser interfacE, *BMC Research Notes*, 5 (2012) 367.
- [23] Kumari R., Kumar R., Lynn A., G-mmpbsa -A GROMACS tool for high-throughput MM-PBSA calculations, *Journal of Chemical Information and Modeling*, 54 (2014) 1951–1962.
- [24] Baker N.A., Sept D., Joseph S., Holst M.J., McCammon J.A., Electrostatics of nanosystems: Application to microtubules and the ribosome, *Proceedings of the National Academy of Sciences of the United States of America*, 98 (2001) 10037–10041.
- [25] Lipinski C.A., Lombardo F., Dominy B.W., Feeney P.J., Experimental and computational approaches to estimate solubility and permeability in drug discovery and development settings, *Advanced Drug Delivery Reviews*, 46 (2001) 3–

26.

- [26] Lipinski C.A., Lombardo F., Dominy B.W., Feeney P.J., Experimental and computational approaches to estimate solubility and permeability in drug discovery and development settings, *Advanced Drug Delivery Reviews*, 23 (1997) 3–25.
- [27] Drug Likeness Tool (DruLiTo), Available at: http://www.niper.gov.in/pi_dev_tools/DruLiToWeb/DruLiTo_index.html, Retrieved May, 2020.

Determination of Salbutamol Sulfate in pharmaceutical formulation with differential pulse voltammetry using poly(Benzofuran-2-Boronic acid) modified platinum electrode

Öznur GÜNGÖR^{1*} 

¹Department of Chemistry, Faculty of Arts and Sciences, İnönü University, 44280, Malatya / TURKEY

Abstract

In this study, determination of salbutamol sulfate (SBS) was carried out using poly(benzofuran-2-boronic acid)/platinum electrode (BF2BA/PtE). Polymerization of BF2BA was conducted in acetonitrile (AcN) containing 0.1 M sodium perchlorate (NaClO₄) on bare PtE by cyclic voltammetry (CV) method. The electrochemical properties of the prepared polymer electrode were investigated by CV and electrochemical impedance spectroscopy (EIS) techniques in ferricyanide/KNO₃ solution. Then, prepared poly(BF2BA/PtE) was used for detection of the SBS. Monomer type, concentration, the number of cycles and scan rate were worked using differential pulse voltammetry (DPV) in citrate-phosphate buffer containing 1.15 mM SBS. The effects of parameters such as electrolyte type, pH effect on SBS DPV responses were studied. The SBS responses of the modified electrodes were also investigated by square wave voltammetry (SWV). The oxidative current peak stem from SBS concentration showed at 0.65V potential and a linear calibration curve was obtained in the range from 50 to 2000 μM SBS concentration. Limit of detection (LOD), and limit of quantitation (LOQ), was calculated as 49.14 μM and 163.80 μM, respectively. The recovery efficiency for synthetic urine samples was obtained from 91.47 to 110.43% by using BF2BA/PtE.

Article info

History:

Received: 24.04.2021

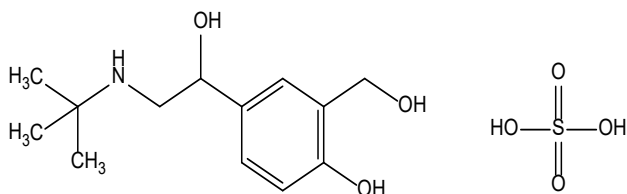
Accepted: 27.07.2021

Keywords:

Benzofuran-2-boronic acid,
Salbutamol sulfate,
Square wave voltammetry,
Platinum electrode,
Sensor.

1. Introduction

Salbutamol (SBS) is a selective beta-2 adrenergic agonist and its IUPAC name is 2-(tert-butylamino)-1-(4-hydroxy-3-hydroxymethyl) phenylethanol. The structure of SBS is shown in scheme 1. This agonist is used in the treatment of the distinctive feature of chronic obstructive pulmonary disease (COPD) and bronchial asthma [1].



Scheme 1. Structural formula of salbutamol sulfate (SBS)

SBS, marketed as Ventolin, is usually considered the drug of choice as relief medication for symptoms of bronchospasm. It is an agonist of β₂ receptors which are present in the bronchioles of lungs of the human body. Athletes using β₂-agonists, usually inhale them

prophylaxis prior to competition or training [2]. Especially during an asthma attack, since its effect starts quickly preferable. Apart from its metabolic side effects, many side effects can be seen in skeletal muscles, central nervous system and cardiovascular system [3]. For these potential side effects, detection of the SBS in body fluids and urine is very important. Spectrophotometric techniques [4-8], gas chromatography-mass spectrometry [9,10], high performance liquid chromatography [11,12], liquid chromatography-mass spectrometry [13-15], capillary electrophoresis [16-20] and chemiluminescence [21,22] are used for the determination of salbutamol in different samples. These techniques need costly equipment, competent personnel and require complex sample pretreatment procedure.

Electrochemical methods as an alternative to the above-mentioned methods for the determination of SBS and other biologically important molecules have not been studied sufficiently [23-25]. Simple set up,

*Corresponding author. e-mail address: oznur.gungor@inonu.edu.tr

<http://dergipark.gov.tr/csj> ©2021 Faculty of Science, Sivas Cumhuriyet University

high sensitivity and do not require intensive sample preparation step as an alternative method. Determination of salbutamol in biological fluids by electrochemical methods is limited in the literature [26-29]. Amare et al. Determined SBS using the DPV method with poly 4-amino-3-hydroxynaphthalene sulfonic acid (AHNSA) / GCE [26]. Goyal et al. showed that SBS determination can be made by using SWV method with nano gold particles modified indium tin oxide (NGITO) electrode [27]. In another study by Goyal et al., determination was made with C60-modified glassy carbon electrode using SWV method [28]. Li et al. Showed that SBS determination can be made using the MIP method with Ag / N-doped reduced graphene oxide and showed the importance of SBS determination [29]. In this study, poly(benzofuran-2-boronic acid film modified Pt electrode was used for SBS determination. The reason for choosing this film structure is that it provides strong H-bonding with the -N-H and -OH groups on the SBS surface, allowing the SBS to be cumulated on the electrode surface and provide electrode affinity. With this poly(benzofuran-2-boronic acid film coated on the electrode surface, the electrode surface area and the electrode efficiency increased.

The aim of the study is to develop a new type of electrode that can be prepared effectively and easily in addition to the existing studies in the literature. Both DPV and SWV methods were used together in the study. EIS and Nyquist plots of the bare PtE and the BF2BA/ PtE were monitored. A new electrochemical sensor has been developed for the determination of SBS using the CV method for electropolymerization on the electrode surface, the DPV method for optimizing the polymer and the SWV methods for the determination of salbutamol. The recovery study of the developed sensor was carried out by real sample application on the synthetic urine sample.

As a result, it has been shown that the developed electrochemical method has a very good recovery (91.47 to 110.43%) with selectivity, stability, good reproducibility for SBS compared to other methods, making it a suitable method for the rapid determination of SBS in pharmaceutical samples.

2. Materials and Methods

2.1. Apparatus and reagents

All voltammetric analyzes were performed with the Ivium Vertex One brand potentiostat. The potentiostat device is controlled by Ivium Soft™ software, which is used for both data collection and data analysis and includes different electrochemical techniques. The analyses were performed by DPV, CV and SWV

techniques. The bare and BF2BA/PtE were also characterized by EIS. Electroanalytical measurements were made in an electrochemical cell (BASi C3 Cell Stand) with a three-electrode system. In the three-electrode system consisting of platinum electrode (BASi®-MF-2113) as working electrode, platinum wire electrode (BASi®-MW-1032) as auxiliary electrode and Ag/AgCl (BASi®-MF 2052) reference electrode as comparison electrode were used. Before each measurement in the voltammetric cell, nitrogen gas was passed for about 5 minutes to remove oxygen from the solution inside the cell.

3-Furan boronic acid (3FBA), benzofuran-2-carboxylic acid (BF2CA), aniline-2-sulfonic acid (An2SA) and benzofuran-2-boronic acid (BF2BA) and citric acid were obtained from Sigma-Aldrich Chemical Company. Potassium ferricyanide ($K_3[Fe(CN)_6]$), potassium dihydrogen phosphate (KH_2PO_4), sodium monohydrogen phosphate (Na_2HPO_4), potassium chloride (KCl) were also purchased from Sigma-Aldrich. Sodium acetate (CH_3COONa), acetic acid (CH_3COOH) were purchased from Across Organics Company. Acetonitrile (AcN), Sodium hydroxide, sodium perchlorate ($NaClO_4$), nitric acid (HNO_3) were supplied from Merck (Darmstadt, Germany). "Ronkotol" is a liquid drug. It was purchased from the pharmacy and, was used as a source of SBS.

2.2. Construction of the modified sensor (BF2BA/PtE)

Firstly, monomer solutions were prepared 3-furan boronic acid (3FBA), benzofuran-2-carboxylic acid (BF2CA), aniline-2-sulfonic acid (An2SA) and benzofuran-2-boronic acid (BF2BA) in Water:AcN (1:1) mixture containing 0.1 M $NaClO_4$. Platinum electrode surface was modified with each of the mentioned monomers by electrochemical method and SBS voltammetric responses of these electrodes were obtained. The best answer for SBS was obtained on the surface of modified PtE, which was produced by BF2BA (4 mM, 4 cycle, 50 mV/s).

2.3. Electrochemical procedures

Electrochemical analyzes were performed using three different techniques such as CV, DPV and SWV techniques. CV and EIS techniques were also used to obtain information on the surface properties of the bare PtE and BF2BA / PtE. For CV analysis, scanning speed 50 mV s⁻¹ and equilibrium time 2 s were used as measurement parameters in the potential range of -0.6 - 1.2 V. DPV analysis was performed after two seconds of equilibration time in the potential range 0.0 to 1.2 V. For DPV analysis were applied as pulse amplitude 10

mV and pulse time 10 ms. As in the DPV analysis, SWV analysis was performed after two seconds of equilibration time in the potential range 0.0 to 1.2 V. For SWV analysis was applied under optimum conditions (pulse amplitude; 20 mV, frequency; 80 Hz). The standard SBS solution was prepared by citrate-phosphate buffer. Then, before making electrochemical measurements, the prepared SBS was taken from the standard solution and diluted with electrolyte solutions. The calibration curve was obtained by plotting the voltammetry oxidation peak current values on the BF2BA / PtE against increasing SBS concentrations. The limit of detection (LOD) and limit of quantification (LOQ) were calculated according to “ $3 S/m$ ” and “ $10 S/m$ ”, respectively [30,31]. “S” in these equations is the standard deviation of the oxidation peak currents, “m” is the slope of the calibration curve. In order to test the applicability of the prepared BF2BA/PtE, electroanalytical detection study and recovery studies were performed in synthetic urine samples.

3. Results and Discussion

3.1. Calculation of effective surface area

CV technique was used to calculate the electroactive surface areas of the electrodes. CV measurements taken with increasing scan rates were used to calculate the electroactive surface areas of the bare PtE and BF2BA/PtE. These CV results were shown in Figure 1. For calculate of the electroactive surface areas was used Randles Sevcik equation. According to Randles Sevcik equation, the square root ($v^{1/2}$) of increasing scanning rates against current (I_p) values was plotted. The effective surface area of the electrode was calculated from the slope values of this curve. The peak current of a reversible electrode reaction at 25 °C is indicated by the following Randles Sevcik equation (Eq. 1).

$$I_p = 2.69 \times 10^5 n^{3/2} A D^{1/2} v^{1/2} C \quad [1]$$

In the Randles Sevcik equation, I_p indicates oxidation peak current (Ampere), n is the number of electrons transferred, A is the surface area of the electrode (cm^2), D is the diffusion coefficient ($\text{cm}^2 \text{s}^{-1}$), v is the scanning rate (V s^{-1}) and C (mol cm^{-3}) is the concentration of ferricyanide in potassium chloride electrolyte as redox probe. D is $6.67 \times 10^{-6} \text{ cm}^2 \text{ s}^{-1}$ at constant pressure and temperature, n is 1, and C is 6 mM for oxidation and reduction of potassium ferricyanide [32,33].

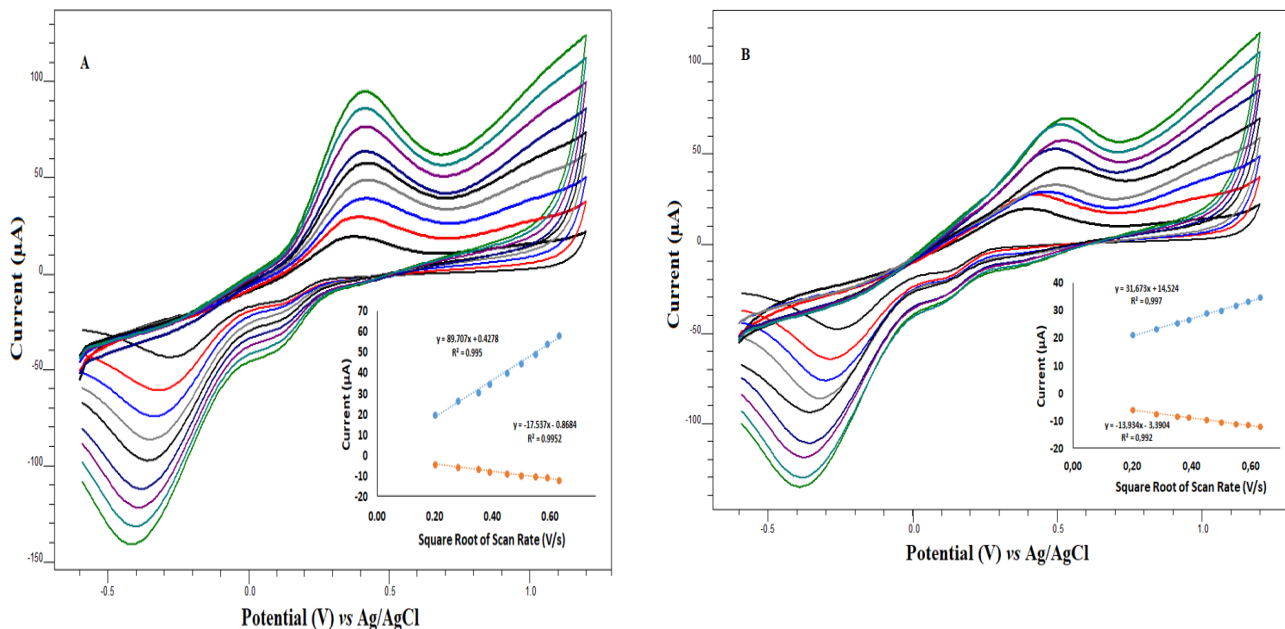


Figure 1. The CVs of 6.0 mM ferricyanide in 0.1 M KNO_3 of bare PtE (A) and BF2BA modified electrode (B) at different scan rates (40, 80, 120, 160, 200, 250, 300, 350 and 400 $\text{mV}\cdot\text{s}^{-1}$)(inset:peak current-square root of scan rate graphs of the bare and the modified electrode)

As seen in the voltammograms from Figure 1A and Figure 1B, increases in the oxidation peak are due to electrochemical stimulation. The shift of the reduction peak potential to negative and the oxidation peak potential to positive can be explained by the increase in the electron transfer rate as a result of the increase in the effective surface area of the electrode. According to the calculated results, the surface area for the bare PtE was found to be 0.0215 cm^2 and the surface area after electrochemical stimulation of the prepared BF2BA / PtE was found to be 0.0076 cm^2 .

The electrochemical impedance spectroscopy (EIS) was employed for investigate the modification effect

of the BF2BA/PtE. Impedance spectra were fitted to equivalent circuits (Figure 2) using ivium software. In the Nyquist curves, the increase in the diameter of the semicircle recorded at high frequencies indicates that the electron transfer speed on the electrode surface is slow, and the decrease in the diameter indicates that the electron transfer speed on the surface is high. Nyquist plots of the modified electrode represent a larger semicircle in the high frequency region than that observed for the bare electrode. From this change can be concluded that the surface resistance is greater and consequently the conductivity is lower. This change also confirms the film structure on the modified electrode surface.

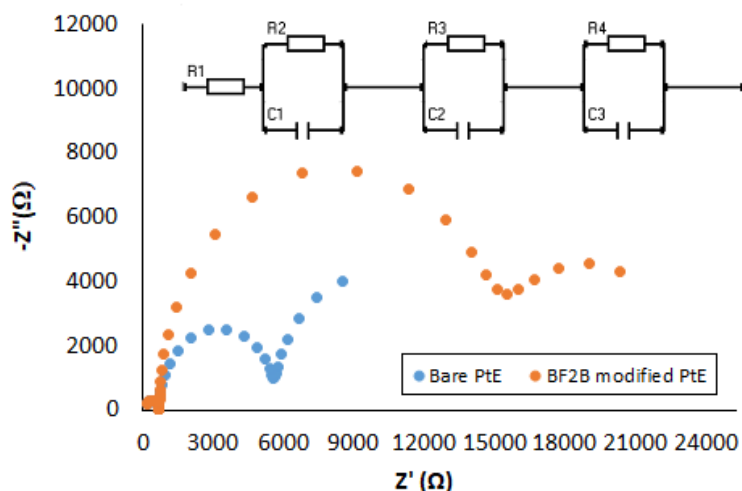


Figure 2. Impedance spectra of bare PtE and BF2BA/PtE.

3.2. The effect of monomer type, concentration, film thickness and scan rate on the SBS response

In order to examine the electrochemical behavior of SBS, firstly, it is necessary to determine of the monomer type to be used for optimum film structure was carried out by using different monomer structures. For this purpose; 3FBA, BF2CA, An2SA and BF2BA were electropolymerized on the PtE and the resulting electrodes were used for SBS determination with DPV technique. According to Figure 3, the prepare electrode with using BF2BA, was given high peak current for

1.15 mM SBS. Thus, BF2B/PtE was chosed the optimum electrode for SBS deduction.

The voltammograms obtained in the determination of SBS by DPV method are given in Figure 3(A). The highest peak current corresponds to PtE modified with BF2BA. The effect of BF2BA concentration (2; 3; 4; 6 and 8 mM) in electrode modification on SBS oxidation peak current was investigated and the optimum monomer concentration was found to be 4 mM (Figure 3(B)).

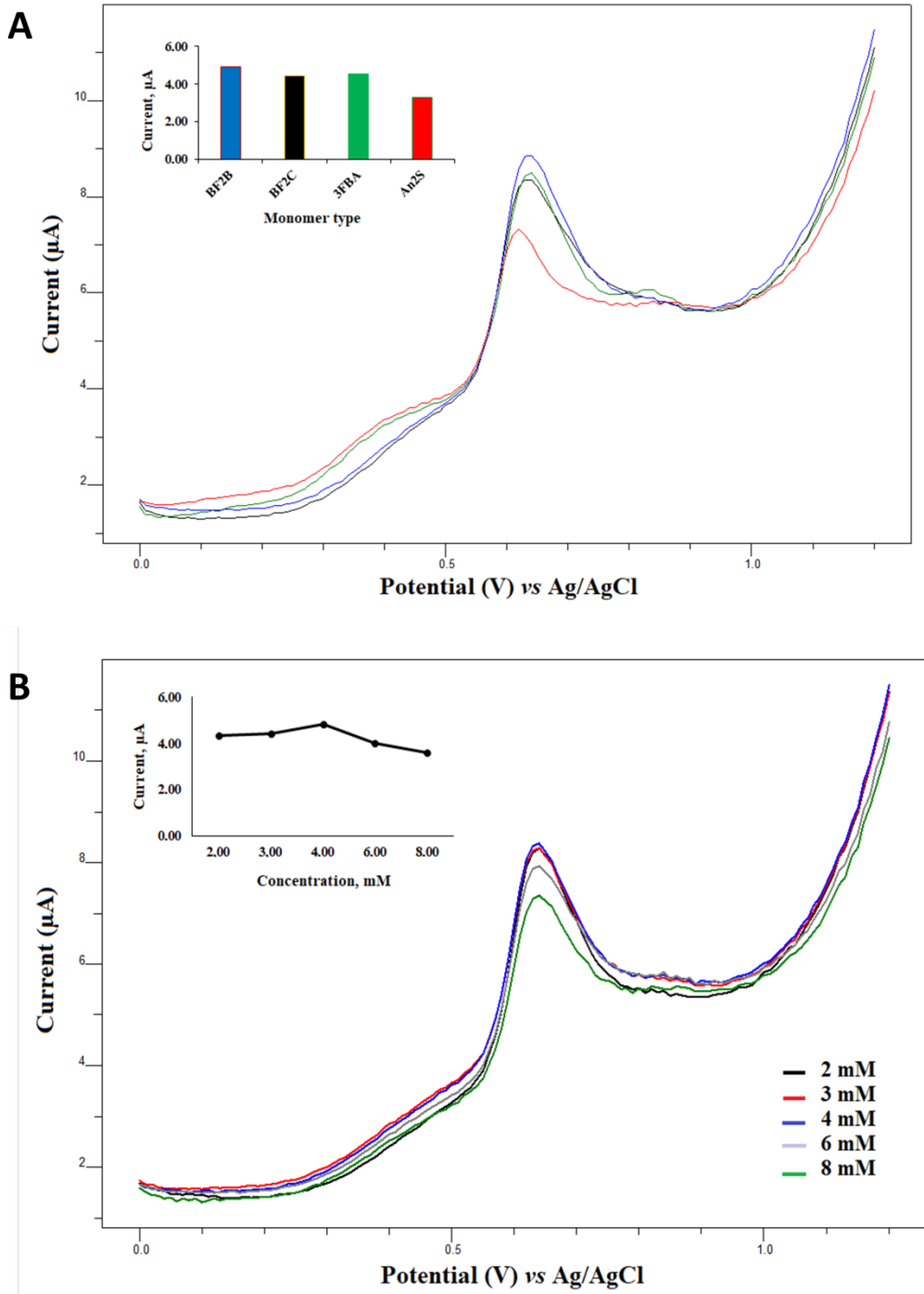


Figure 3. A; Effect of monomer type on DPV responses for 1.15 mM SBS. B; Effect of BF2BA concentration on DPV responses for 1.15 mM SBS.

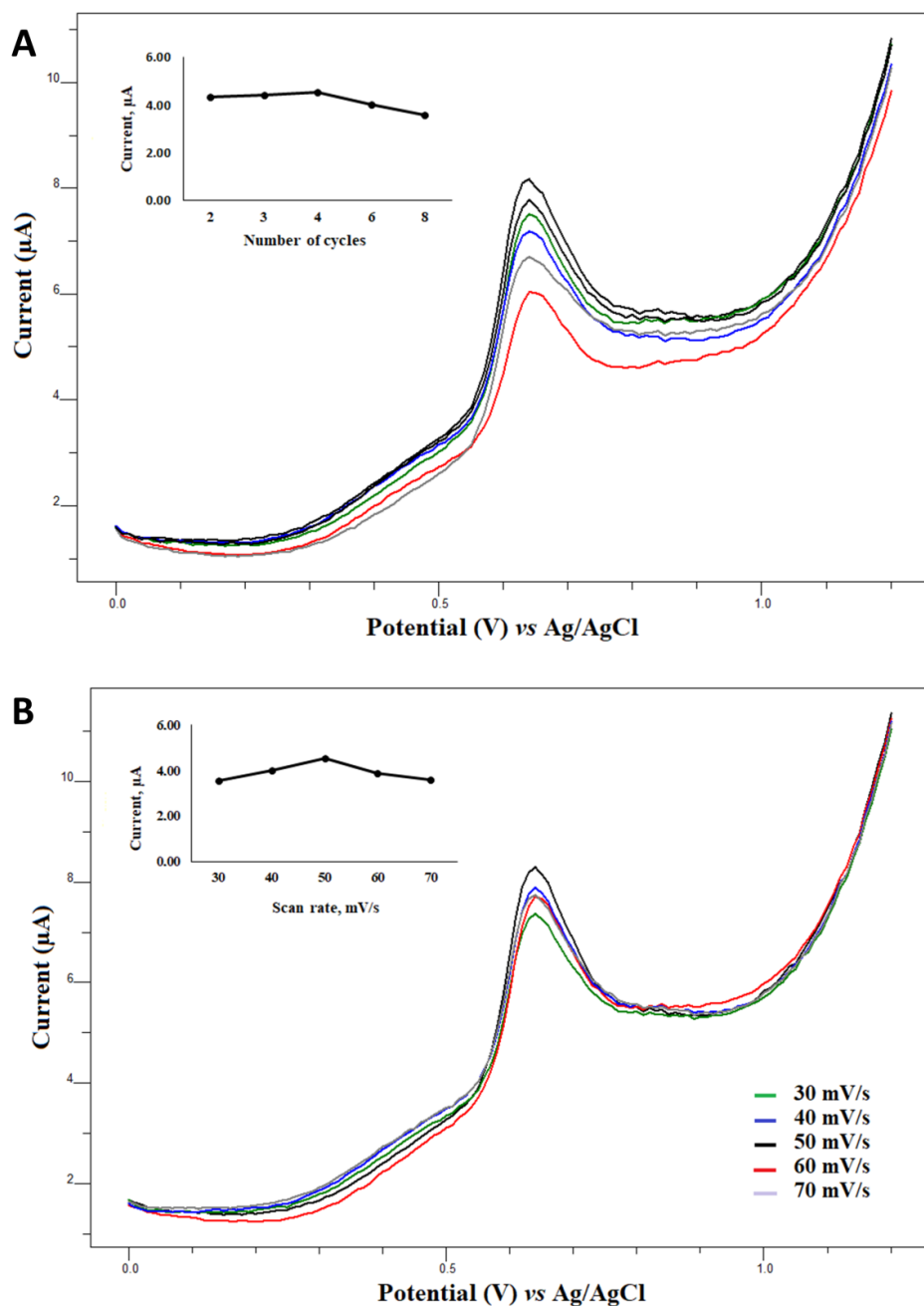


Figure 4. A; Effect of coating thickness on DPV responses for 1.15 mM SBS. B; Effect of scan rate on DPV responses for 1.15 mM SBS.

In this study, the thick of the polymer film was determined by studying cycle number with CV method during electropolymerization process. As shown in Figure 4(A), film thickness of 4 cycles in polymerization cycles increased the current response of SBS. As the number of cycles increased further, thicker films were formed and SBS responses decreased. From these results, it was understood that the optimum film thickness was obtained with 4 cycles, and in subsequent studies, the film thickness was used as 4 cycles. The effect of scan rate during the electropolymerization process was investigated in the

range of 30 - 70 mV/s. As can be seen in Figure 4(B), it is clear that the DPV response of the electrode modified with a scanning speed of 50 mV/s was the best.

3.3. Influence of electrolyte type, and pH on SBS peak Current

After selecting the monomer type, the best electrolyte solution for the analyte and the pH value of this electrolyte solution were determined. To determine the optimum electrolyte type for the determination of SBS, citrate buffer (CB), acetate buffer (AB), phosphate

buffer (PB), Britton Robinson buffer (BRB) and citrate-phosphate buffer (C-PB) were used. The results obtained for DPV technique on modified electrode surface at different electrolyte for SBS are shown in Figure 5(A). In accordance with results, maximum and best peak currents for SBS were obtained in 0.15 M C-PB solutions. The effect of pH value of the C-PB on the SBS response of the BF₂BA/PtE was investigated

with using 6.0, 6.5, 7.0, 7.5 and 8.0 pH values C-PB solutions by DPV technique. The results obtained from DPV technique on modified electrode surface at different pH values for SBS are given in Figure 5(B). In accordance with results, maximum and best peak currents for SBS were obtained in 0.15 M C-PB at pH 7.5.

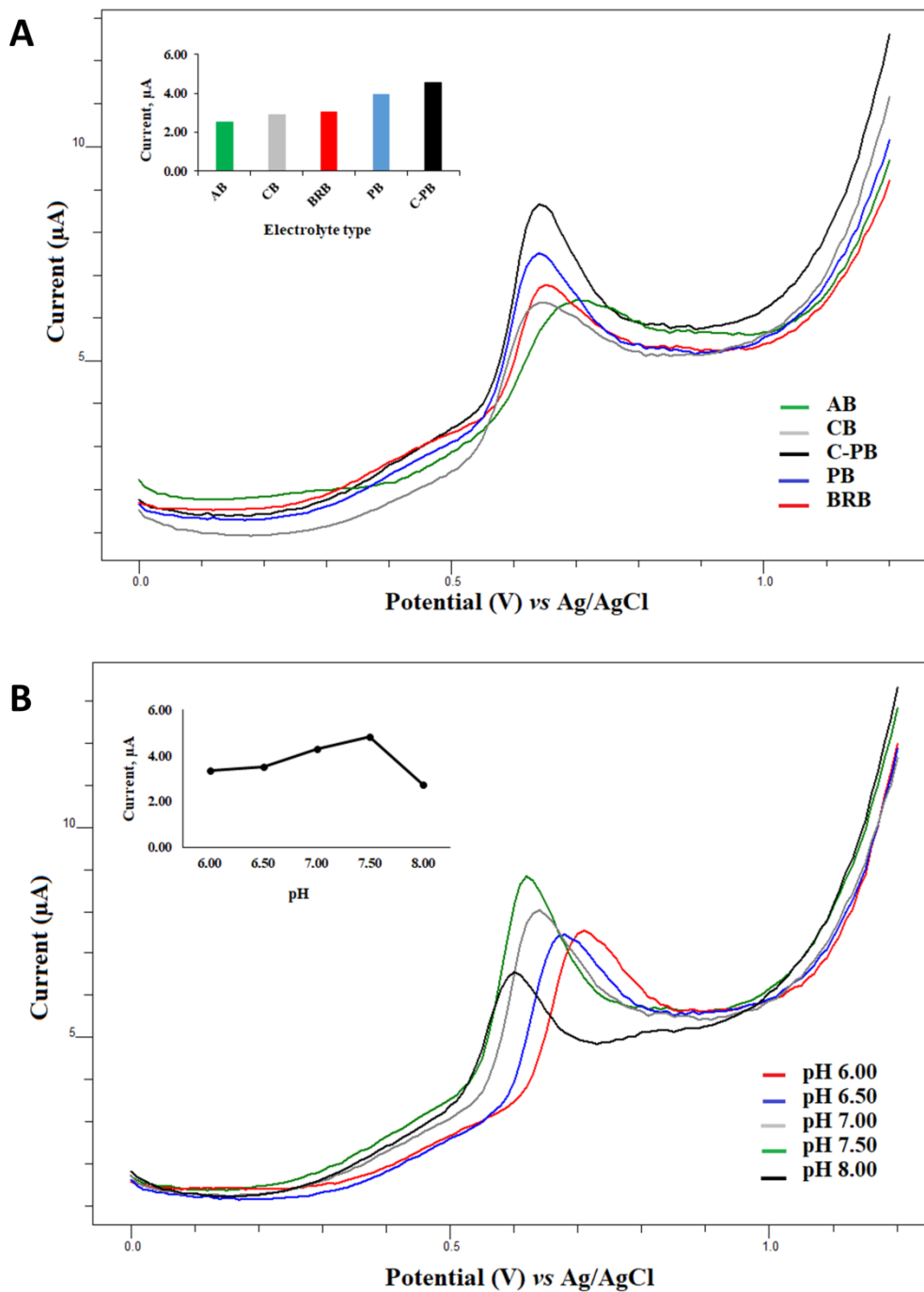


Figure 5. A; Effect of electrolyte type on DPV responses of prepared BF₂BA/PtE for 1.15 mM SBS. B; Effect of pH value on DPV responses of prepared BF₂BA/PtE for 1.15 mM SBS.

3.4. Optimizations of the SWV technique (Accumulation potential and pccumulation time)

The SWV technique was more sensitive and is a more suitable technique for analyzing low concentration analytes than the DPV technique. Therefore, SWV technique was used in quantitative studies of SBS. The effect of the accumulation potential to the SBS peak

current for 10 s and 300 rpm in 0.15 M pH 7.50 citrate-phosphate buffer was investigated by SWV in the range 0.25 to 0.45 V (Figure 6(A)). The results showed that optimum accumulation potential increased up to 0.35 V and then decreased. Therefore, it was decided to operate at a potential of 0.35 V in subsequent studies.

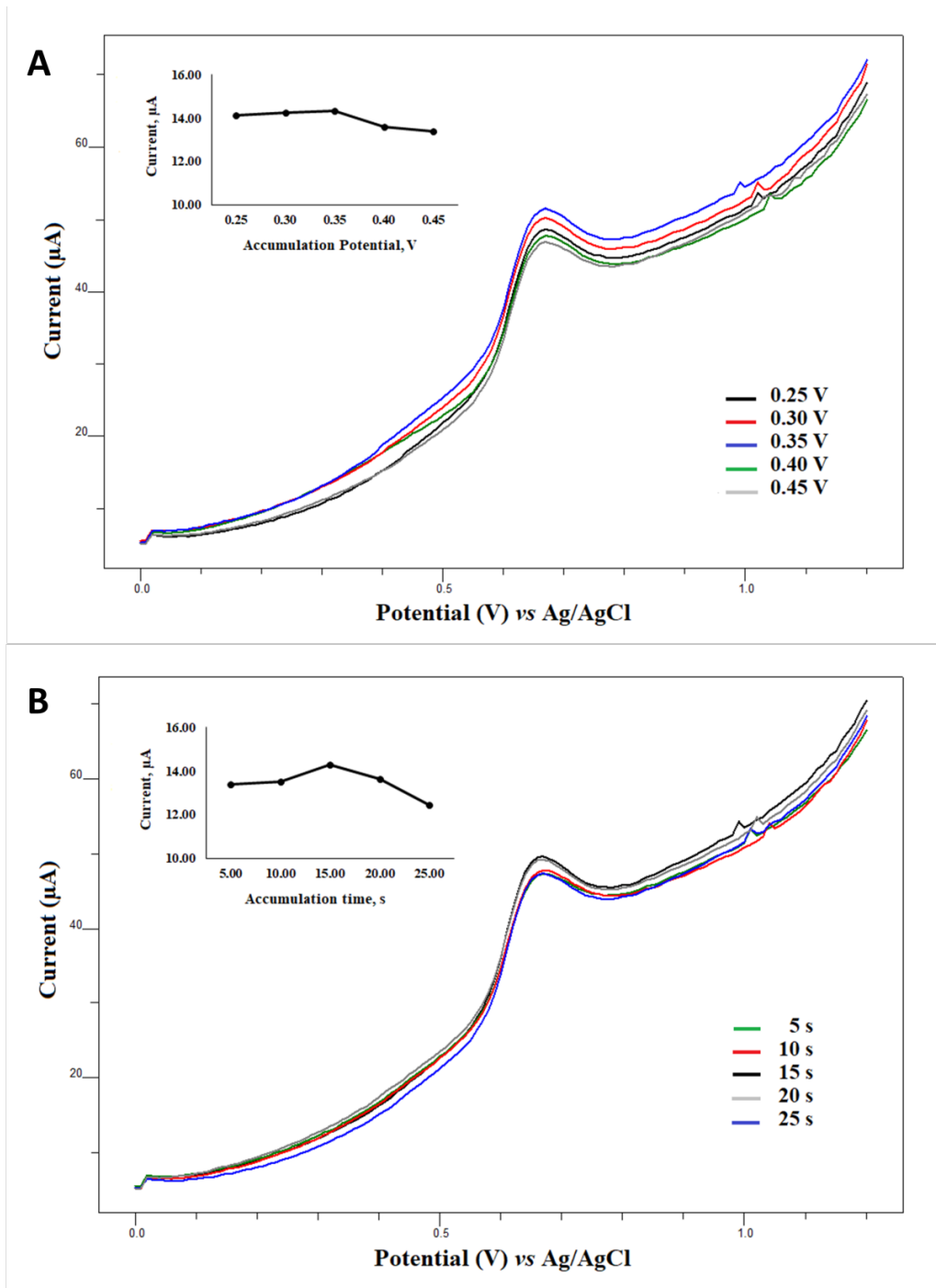


Figure 6. A; Effect of accumulation potential on 1.15 mM SBS SWV peak current in 0.15 M C-PB, pH 7.50. B; Effect of accumulation time on 1.15 mM SBS SWV peak current in 0.15 M C-PB, pH 7.50.

In order to determine the effect of the accumulation time on the SBS voltammetric response, it was studied in the range of 5-25 s and the voltammograms obtained were examined. According to these results, the optimum accumulation time was 15 s (Figure 6(B)).

3.5. Analytical parameters of the prepared modified electrode

SWV measurements were carried out with BF2BA/PtE at increasing SBS concentrations under optimal experimental conditions. SWV responses obtained at increasing SBS concentrations are given in Figure 7. Peak currents increased linearly with increasing SBS concentration. According to SWV measurement

results from Figure 3 to Figure 6, the electrochemical performance and SBS selectivity of the modified electrode were determined. With the developed sensor, it has ensured the sensitive and selective determination of SBS in a wide linear range of 50-2000 μM and the obtained calibration curve given in Figure 7 (inset). With the calibration curve obtained, LOD value for the modified electrode was determined. The LOD value of the modified electrode was calculated with the equation $\text{LOD} = 3S/m$ (S standard deviation; m is the slope of the calibration curve) and was determined as 49.14 μM . The LOQ value of the modified electrode was calculated with the equation $\text{LOQ} = 10S/m$ and was determined as 163.80 μM .

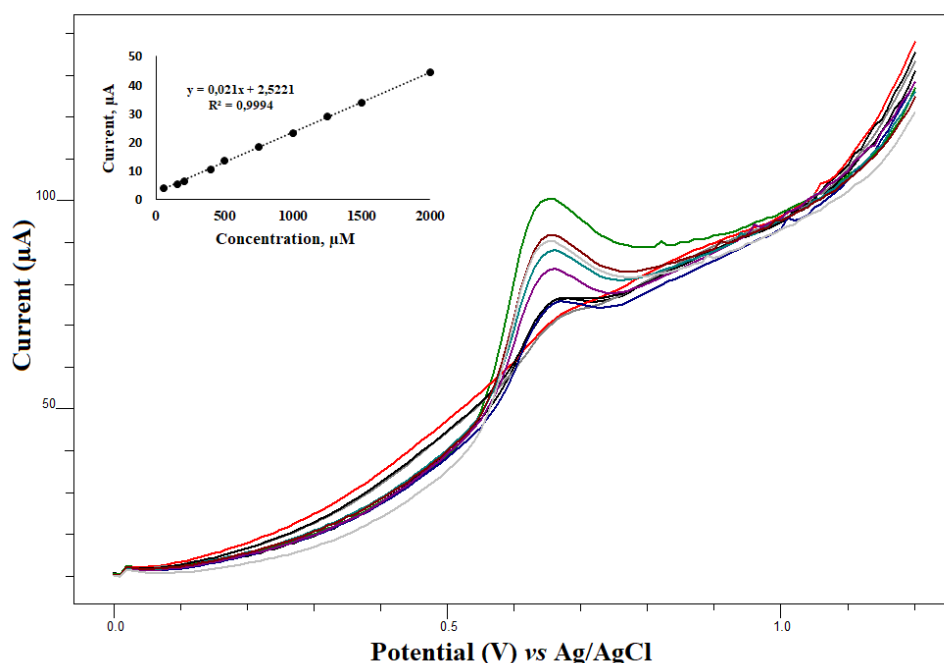


Figure 7. SWV responses of BF2BA modified electrode at 50, 150, 200, 400, 500, 750, 1000, 1250, 1500 and 2000 μM SBS concentrations. Calibration curve for increasing SBS concentrations (inset).

3.6. Reproducibility results of the prepared modified electrode

To test the reproducibility of the prepared electrodes, SWV responses were received of 500 μM SBS solutions in 0.15 M C-PB (pH 7.50) on BF2BA/PtE. The voltammograms obtained for reproducibility results of modified electrode are given in Figure 8. The reproducibility of the voltammetric responses obtained with ten measurements using the modified electrode

indicates that the stability of the present method is very good. According to the voltammograms obtained, SBS peak currents are given as bar graphs in Figure 8(inset graph). The standard deviation and the % relative standard deviation (% RSD) of modified electrode calculated 0.14 and 1.11 respectively, from the bar graph in Figure 8. As a result, the reproducible, highly stable and extremely sensitive (98.89%) of prepared sensor and SBS determination method proved.

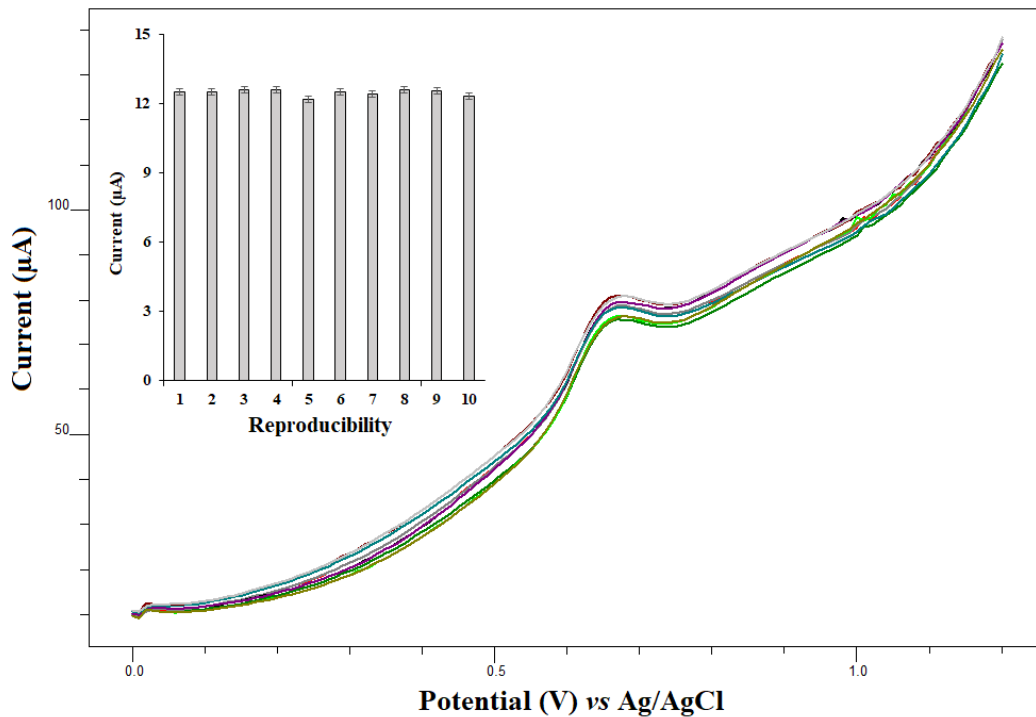


Figure 8. The reproducibility of BF2BA/PtE in C-PB for 500 μM SBS (pH 7.50) ($n = 10$). Inset graph; reproducibility bar graph of BF2BA/PtE.

3.7. Interference effect on the SBS determination

In order to evaluate the selectivity of the modified electrode, some biological molecules (dopamine (DA), uric acid (UA) and glucose (GC)) were tested under optimized conditions. The interferent study was carried out in the presence of 50 μM concentration of various

non-target agents. No interference in the voltammograms was observed as shown in Figure 9, which confirmed excellent specificity of the electrode. Therefore, the designed modified electrode has good selectivity for the determination of low levels of analytes.

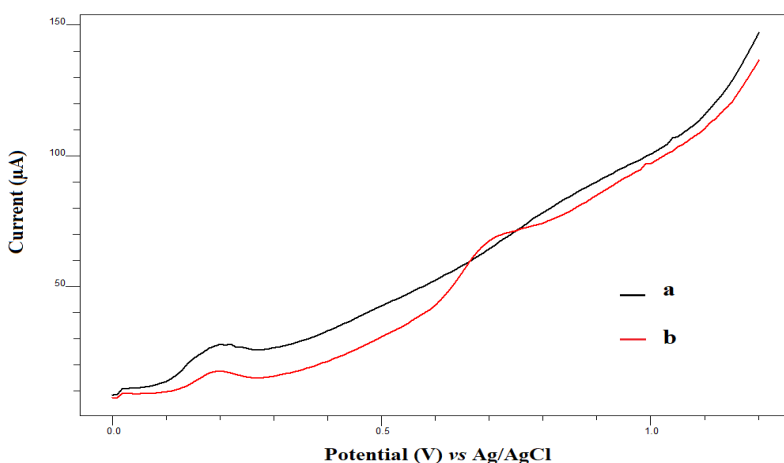


Figure 9. SWV Curves of BF2BA/PtE in C-PB a) in the presence of 50 μM DA, UA and GC, b) in the presence of 50 μM UA, DA and GC with 500 μM SBS.

3.8. Real sample analysis

In order to test the applicability of the produced BF2BA / PtE, the SWV technique was used to

determine the amount of SBS in synthetic urine samples.

Table 1. Analysis of synthetic urine sample added to SBS standard solution using SWV technique.

Sample	Original found in sample (μmolL^{-1})	Standard added (μmolL^{-1})	Total Found (μmolL^{-1}) ^a	RSD ^b (%)	R (%)
Synthetic urine	Not detected	50.00	50.84 \pm 0.010	0.386	101.68
Synthetic urine	Not detected	150.00	153.32 \pm 0.003	0.064	102.22
Synthetic urine	Not detected	200.00	220.86 \pm 0.012	0.171	110.43

a) Average of three measurements. b) RSD is three replicate of found concentration.

High peak current values, which are oxidized at the same potentials, are acquired with the SWV technique. Three consecutive concentrations were added to the synthetic urine sample to determine the SBS in the flacon samples with the electrodes obtained with the BF2BA modification of Pt. The recovery results obtained were given in Table 1. As can be seen from

the table, detection of SBS content in the range 101.68 to 110.43% of the labeled value showed good agreement. According to the results obtained, it is consistent with the amount of SBS of the proposed method with recovery value for determining the amount of SBS in flacon samples.

Table 2. The comparison of SBS detection methods with the literature

Methods	Electrode/ Modifier sensors	Linear range, M	LOD, M	Ref
DPV	GCE/ AHNSA	0.2 x 10 ⁻⁶ ~ 8.0 x 10 ⁻⁶	6.8 x 10 ⁻⁸	[26]
SWV	NGITO	2.09 x 10 ⁻¹¹ ~ 9.5 x 10 ⁻¹²	3.13 x 10 ⁻¹¹	[27]
MIP	Ag-N-RGO	0.03 x 10 ⁻⁶ ~ 20.0 x 10 ⁻⁶	7.0 x 10 ⁻⁹	[29]
	GCE/ NiFe ₂ O ₄	2.0 x 10 ⁻⁶ ~ 60.0 x 10 ⁻⁶	1.0 x 10 ⁻⁶	[34]
SWV	GCE/MWNT	8.0 x 10 ⁻⁷ ~ 1.0 x 10 ⁻⁵	2.0 x 10 ⁻⁷	[35]
SWV	PtE/ BF2BA	50.0 x 10 ⁻⁶ ~ 2000 x 10 ⁻⁶	49.14 x 10 ⁻⁶	This study

GCE/ AHNSA : glassy carbon electrode/ 4-amino-3- hydroxynaphthalene sulfonic acid

NGITO : nanogold modified indium tin oxide electrode

MIP : molecularly imprinted polymer

GCE/ NiFe₂O₄ : glassy carbon electrode /NiFe₂O₄ nanoparticles

GCE/MWNT : glassy carbon electrode/ multicarbon nanotubes

PtE/ BF2BA : platinum electrode / benzofuran-2-boronic acid

The comparison of SBS detection methods with the literature was given in Table 2. According to Table 2, prepare electrode has short response time, easy preparation advantage and high reproducibility. Thus, prepared BF2BA/PtE has the potential to be used in biomedical applications and in the medical field.

4. Conclusions

In this study, firstly, the modification of Pt with BF2BA electrode was successfully produced by electropolymerization. Then, electroanalytical SBS responses of prepared BF2BA/PtE were investigated in C-PB (pH 7.50) solution by Cyclic Voltammetry,

Differential Pulse Voltammetry and Square Wave Voltammetry techniques. The electrochemical performance of the BF2BA/PtE was also confirmed by CV and EIS experiments. The low LOD and LOQ values were obtained with the prepared modified electrode for the determination of SBS. The developed method was applied with 91.47 %-110.43 %recovery of SBS in the flacon sample. The applications of the BF2BA/PtE have proven to show excellent reproducibility and stability. As a result, synthetic urine sample applications have confirmed that the method has been applied successfully. Thus, it has been proved that SBS in real samples can easily detect with the developed novel BF2BA/PtE and this BF2BA/PtE has the potential to be used in biomedical applications and in the medical field.

Conflicts of interest

The author simply declares there is no conflict of interest.

References

- [1] Barisione G., Baroffio M., Crimi E., Brusasco V., Beta-Adrenergic Agonists, *Pharmaceuticals*, 3 (2010) 1016–1044.
- [2] Shihab A. I., Al-Sabha N. T., Application of Cloud Point Method for Spectrophotometric Determination of Salbutamol Sulphate and Methyl dopa, *Pak. J. Anal. Environ. Chem.*, 21 (1) (2020) 10-18.
- [3] Balanag V.M., Yunus F., Yang P.C., Jorup C., Efficacy and safety of budesonide formoterol compared with salbutamol in the treatment of acute asthma, *Pulm. Pharmacol. Ther.*, 19 (2) (2006) 139–147.
- [4] El-Enany N., Belal F., Rizk M., A simple kinetic spectrophotometric method for the determination of salbutamol in dosage forms, *Chem. Anal. (Warsaw, Poland)* 49 (4) (2004) 587-599.
- [5] Habib I.H.I., Hassouna M.E.M., Zaki G.A., Simultaneous Spectrophotometric Determination of Salbutamol and Bromhexine in Tablets, *Il Farmaco*, 60 (3) (2005) 249-254.
- [6] Kalyani L., Chava V.N. Rao, Simultaneous spectrophotometric estimation of Salbutamol, Theophylline and Ambroxol three component tablet formulation using simultaneous equation methods, *Karbala International Journal of Modern Science*, 4(1) (2018) 171-179.
- [7] Ayad M. M., Abdellatef H. E., Hosny M. M., Abdel-Sattar Kabil N., Spectrophotometric Determination of Etilerfrine HCl, Salbutamol Sulphate and Tiemonium Methyl Sulphate Using Surface Plasmon Resonance Band of Gold Nanoparticles, *Nano Biomed. Eng.*, 10(1) (2018) 16-24.
- [8] R'afat M. N., Mahmoud M. I., Mozer H. AL-K., Akila A. S., Alaa A. S., Raluca van S. I. S., Hassan Y. A.-E., Development and validation of kinetic and atomic absorption spectrophotometric methods for the determination of salbutamol sulfate, *RSC Advances*, 5(70) (2015) 57164–57170.
- [9] Gabiola C., Garcia-Calonge M.A., Portillo M.P., Martinez J.A., del Barrio A.S., Validation of a method for the determination of salbutamol in animal urine by gas chromatography-mass spectrometry and its application to treated lamb samples, *J. Microcol.*, 8(5) (1996) 361-364.
- [10] Liu H., Gan N., Chen Y., Ding Q., Huang J., Lin S., Cao Y., Li T., Novel method for the rapid and specific extraction of multiple β -agonist residues in food by tailor-made monolith-MIPs extraction disks and detection by gas chromatography with mass spectrometry, *J Sep Sci.*, 39(18) (2016) 3578–3585
- [11] Sutariya V.B., Mashru R.C., Sankalia M.G., Sankalia J.M., Liquid chromatographic determination and pharmacokinetics study of salbutamol sulphate in rabbit plasma, *ArsPharm.*, 47(2) (2006) 185-197.
- [12] Kulikovskii AV, Lisitsyn AB, Gorlov IF, Slozhenkina MI, Savchuk SA. Determination of growth hormones (β -agonists) in muscle tissue by HPLC with mass spectrometric detection, *J Anal Chem.*, 71(10) (2016) 1052–1056.
- [13] Chang K.-C., Chang Y.-T., Tsai C.-E., Determination of ractopamine and salbutamol in pig hair by liquid chromatography tandem mass spectrometry, *Journal of Food and Drug Analysis*, 26(2) (2018) 725-730.
- [14] Zhang L.Y., Chang B.Y., Dong T., He P.L., Yang W.J., Wang Z.Y., Simultaneous Determination of Salbutamol, Ractopamine, and Clenbuterol in Animal Feeds by SPE and LC–MS, *Journal of Chromatographic Science*, 47(4) (2009) 324-328.
- [15] Chan S.H., Lee W., Asmawi M.Z., Tan S.C., Chiral liquid chromatography-mass spectrometry (LC-MS/MS) method development for the detection of salbutamol in urine samples, *J. Chromatogr. B.*, 1025 (2016) 83–91.

- [16] Changguo C., Hong L., Yujing F., Determination of salbutamol sulfate in medicaments by capillary electrophoresis with contactless conductivity detection, *Chin. J. Chromatogr.*, 29(2) (2011) 137–140.
- [17] Sirichai S., Khanatharana P., Rapid analysis of clenbuterol, salbutamol, procaterol, and fenoterol in pharmaceuticals and human urine by capillary electrophoresis, *Talanta*, 76(5) (2008) 1194–1198.
- [18] Nguyen T.A.H., Pham T.N.M., Doan T.T., Ta T.T., Saiz J., Nguyen T.Q.H., Hauser P.C., Mai T.D., Simple semi-automated portable capillary electrophoresis instrument with contactless conductivity detection for the determination of beta-agonists in pharmaceutical and pig-feed samples, *J. Chromatogr. A.*, 1360 (2014) 305–311.
- [19] Lodén H., Pettersson C., Arvidsson T., Amini A., Quantitative determination of salbutamol in tablets by multiple-injection capillary zone electrophoresis, *J. Chromatogr. A.*, 1207 (1-2) (2008) 181–185.
- [20] Chen Q., Fan L.-Y., Zhang W., Cao C.-X., Separation and determination of abused drugs clenbuterol and salbutamol from complex extractants in swine feed by capillary zone electrophoresis with simple pretreatment, *Talanta*, 76(2) (2008) 282–287.
- [21] Lindino C.A., Bulhões L.O.S., Determination of fenoterol and salbutamol in pharmaceutical formulations by electrogenerated Chemiluminescence, *Talanta*, 72(5) (2007) 1746–1751.
- [22] Barnett N. W., Hindson B. J., Lewis S. W., Determination of Ranitidine and Salbutamol by Flow Injection Analysis with Chemiluminescence Detection, *Analytica Chimica*, 384(2) (1999) 151–158.
- [23] Demir E., İnam O., İnam R., Determination of ophthalmic drug proparacaine using multi-walled carbon nanotube paste electrode by square wave stripping voltammetry, *Analytical Sciences*, 34 (2018) 771–776.
- [24] İnam O., Demir E., Uslu B., Voltammetric Pathways for the Analysis of Ophthalmic Drugs, *Current Pharmaceutical Analysis*, 16 (2020) 367–391.
- [25] Güngör Ö., Kılıç B., Karasürmeli T.S., Özcan İ., Köytepe S., Voltammetric determination of alpha lipoic acid using chitosan-based polyurethane membrane electrode, *Measurement*, 182 (2021) 109752.
- [26] Amare M., Menkir G., Differential pulse voltammetric determination of salbutamol sulfate in syrup pharmaceutical formulation using poly(4-amino-3-hydroxynaphthalene sulfonic acid) modified glassy carbon electrode, *Heliyon*, 3(10) (2017) e00417.
- [27] Goyal R.N., Oyama M., Singh S.P., Fast determination of salbutamol, abused by athletes for doping, in pharmaceuticals and human biological fluids by square wave voltammetry, *J. Electroanal. Chem.*, 611(1-2) (2007) 140–148.
- [28] Goyal R.N., Kaur D., Singh S.P., Pandey A.K., Effect of graphite and metallic impurities of C60 fullerene on determination of salbutamol in biological fluids, *Talanta*, 75(1) (2008) 63–69.
- [29] Li J., Xu Z., Liu M., Deng P., Tang S., Jiang J., Feng H., Qian D., He L., Ag/N-doped reduced graphene oxide incorporated with molecularly imprinted polymer: An advanced electrochemical sensing platform for salbutamol determination, *Biosensors and Bioelectronics*, 90 (2017) 210–216.
- [30] Miller J.C., Miller J.N., *Statistics for Analytical Chemistry*, New York: Halsted Press, (1984).
- [31] Riley M., Rosanske T.W., *Development and validation of analytical methods*, New York: Elsevier Science Ltd., (1996).
- [32] Bard A.J., Faulkner L.R., *Electrochemical Methods (2nd edition)*, New York: John Wiley & Sons, Inc., (2001), 166.
- [33] Huang T.-Y., Kung C.-W., Wei H.-Y., Boopathi K.M., Chu C.-W., Ho K.-C., A High Performance Electrochemical Sensor for Acetaminophen Based on a rGO-PEDOT Nanotube Composite Modified Electrode, *J. Mater. Chem. A*, 2 (2014) 7229–7237.
- [34] Luo S.X., Wu Y.H., Gou H., Liu Y., A Novel Electrochemical Sensor for the Analysis of Salbutamol in Pork Samples by Using NiFe₂O₄ Nanoparticles Modified Glassy Carbon Electrode, *Advanced Materials Research*, 850–851 (2014) 1279–1282.
- [35] Wei Y., Zhang Q., Shao C., Li C., Zhang L., Li X., Voltammetric Determination of Salbutamol on a Glassy Carbon Electrode Coated with a Nanomaterial Thin Film, *Journal of Analytical Chemistry*, 65(4) (2010) 398–403

Synthesis of new solid phase sorbent for sensitive spectrophotometric determination of Quercetin

Songül ULUSOY^{1,*} 

¹ Cumhuriyet University, Department of Pharmacy, Vocational School of Health Service, Sivas 58140, TURKEY

Abstract

Sensitive and easy applicable analysis of Quercetin molecules was executed whereby solid phase extraction (SPE) and molecular spectrophotometric determination. For the determination of quercetin, an accurate, economical, time-saving and a new environmentally friendly method has been developed with a simple spectrophotometer device available in every laboratory. As a solid-phase sorbent, a new polymer nanocomposite has been synthesized and characterized by Fourier Transform Infrared Spectroscopy (FT-IR) and Scanned Electron Microscopy (SEM). Experimental solid phase extraction variables have been investigated and optimized step by step, such as pH, adsorption time and desorption conditions, etc. According to optimization results, desorption of quercetin molecules was carried out by 2-propanol solvent and absorbance of eluent solutions were measured as systematic at 255 nm and at 370 nm. However, the best results were obtained at 370 nm wavelength. Therefore, all measurements were made at 370 nm. (LOD) means that the detection limit and (LOQ), the quantitation limit values for quercetin were calculated as 5.97 ng mL⁻¹ and 17.91 ng mL⁻¹, respectively. Standard addition and recovery experiments were performed as an indicator of the accuracy of the method. The method developed was effectively conducted to model solutions.

Article info

History:

Received: 15.05.2021

Accepted: 07.09.2021

Keywords:

Quercetin,
Solid phase extraction,
Polymeric adsorbent,
Analytical method
development.

1. Introduction

Flavonoid molecules in food samples have a long history of natural sources of antioxidants. The determination of such molecules in real samples attracts much attention in many countries. Main properties of these compounds can be displayed such as anti-carcinogenic, anti-allergic, anti-inflammatory, and antiviral action[1]. Quercetin, which is systematically named as (3,5,7,3', 4'-pentahydroxyflavone) by IUPAC, is in the flavonoid class of bioflavonoids. Molecular formula of quercetin was given in Figure 1.

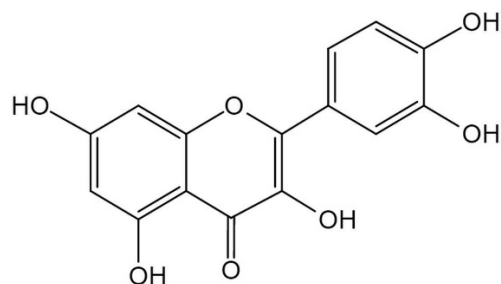


Figure 1. Molecular structure of quercetin

Quercetin is mostly existed in various samples such as, coffee, tea, vegetables, seeds, fruits, fern and natural dyes. Flavonoids are actually bioflavonoids that are composed of more than 6000 different species found in every plant. It gives plants bright yellow, orange and red colors that dazzle our eyes. Most flavonoids act as antioxidants in the human body. With these functions, they prevent the cells from being damaged by neutralizing the excessively reactive molecules containing oxygen. They show a 2-phenyl benzopyron structure (C6-C3-C6) with 15 C atoms. They are considered as polyphenolic compounds due to their structure. Since their skeletal structures are different, they have derivatives such as flavone, flavonol, flavonone, biflavonoid, chalcone. Flavonoids have been reported to have other properties than antioxidant properties. These properties can be summarized as follows; antitumor effect, antiviral effect, antithrombotic effect, anti-inflammatory effect, anti-allergic effect, protection effect from atherosclerosis and coronary heart diseases[2,3].

Flavonoids constitute one of the most characteristic classes of compounds found in most plant species. The vast majority of flavonoids are easily recognized as

*Corresponding author. e-mail address: sonulusoy@yahoo.com

<http://dergipark.gov.tr/csj> ©2021 Faculty of Science, Sivas Cumhuriyet University

flower pigments in the flowering plant family but are not always floral pigments. Analysis of flavonoids has interested much attention by many researchers from different and interdisciplinary so like that chemistry, pharmacy, medicine, biology area etc. Quercetin, a polyphenol belonging to the class of flavonoids, is categorized as flavanol, one of the subclasses of flavonoid compounds.[4]. Thanks to its superior chemical and biological properties, quercetin has proven to have an important role in the treatment of many diseases such as ulcers, allergies, diabetes, cancer, cardiovascular and inflammatory diseases. [5,6]. Quercetin molecules acts as a free-radical scavenger and shows a useful antioxidant properties for human health [7]. Various analytical methods are used for analysis of quercetin molecules in real samples such as spectrophotometric [2], chromatographically [8] and electroanalytical methods [9]. Mostly, a pre-concentration method is combined with these technical[10]. Simple and reliable separation and pre-concentration methods are generally preferred for the sensitive determination of naturally occurring biomolecules in samples. The primary challenge of this type of analysis is to assess the success of the pretreatment method. Solid phase extraction approaches are mostly preferred owing to easy applicable properties. The major advantages of combining this approach with the conventional analytical method are the ability to determine the trace analyte without the use of complicated or expensive tools. The richest food sources of natural antioxidant quercetin are broccoli , grapes, apples, citrus fruits ,strawberries, cherries, onions ,capers, buckwheat, green leafy vegetables, hazelnuts and black tea[11]. By cause of the complex matrix and the trace amount of quercetin in real samples, a good sample preparation and method development is needed to identify target molecules. The main challenge in this procedure is to do the preconcentration method correctly. The better this step, the more successful the enrichment process. Magnetic solid phase extraction is preferred as a simple method to concentrate target molecules prior to the detection step. [12]. For this, it is applied by interacting with target molecules using magnetic solid phase extraction, which is one of the sample preparation techniques, before the determination process. [13]. Newly, more and more of these utilizations have given the use of hybrid nanoparticles for the selective extraction of trace species from a complex matrix environment[14–16]. The major advantage of combining this approach with the conventional method of analysis is the ability to determine the trace analyte without the use of complicated or costly tools[17].

In the light of the information described above, as part of current study, a method for the adsorption and enrichment of quercetin in model solutions with a newly developed polymeric material was developed with the help of UV-VIS spectrophotometer. The developed method is applied to model solutions. A method has been developed for the separation and enrichment of quercetin in model solution and its determination by UV-VIS spectrophotometer. In this method, a new polymeric material was synthesized and characterization studies were carried out. By optimizing the necessary analytical parameters (pH, adsorption time, extraction solvent volume, etc.), recovery studies were carried out for the quantitative analysis of quercetin.

2. Materials and Methods

2.1. Apparatus

A spectrophotometer (Shimadzu, UV-Visible 1800, Japan) equipped with a 1 cm quartz cell was used for absorbance measurements. This spectrophotometer has in the wavelength range of 190–1100 nm. A pH meter with a glass electrode (Hanna, Germany) was used to measure the pH values. A centrifuge (Elektromag centrifuge, Turkey) was used to accelerate the phase separation. Orbital shaker (Elektromag) was used to achieve homogenization between the analyte and the synthesized material. FT-IR analysis of developed material was carried out by using the FT-IR spectrophotometer (Bruker) for checking of functional groups in the range of 400–4000 cm^{-1} . The surface morphology of solid phase material was observed with a scanning electron microscope (TESCAN MIRA3 XMU, FEG-SEM, Brno, Czechia).

2.2. Reagents

Ultrapure Milli-Q water (18.2 $\text{M}\Omega$ cm, Millipore Corporation, Turkey) was used in all of the experiments. A 500 $\mu\text{g mL}^{-1}$ of Quercetin solution (Sigma, St. Louis, MO, USA) was prepared by dissolving quercetin in isopropanol 0.02 M Britton-Robinson (BR) buffer solution was used to work at required pH values. Acryl amide(AA), N,N'-methylenebisacrylamide , ammonium persulphate, and fuchsin acid (FA) were also used at analytical grade. The chemicals contained in this buffer are as follows. 0.024 M H_3BO_3 (Merck), 0.02 M H_3PO_4 (Merck) and 0.02 M CH_3COOH (Merck) that has been set to the wanted pH with 0.1 M NaOH.

2.3. Synthesis of solid phase material

A new adsorbent was synthesized for using as solid phase sorbent(PAA@FA). It is widely known polymeric material with some minor modifications.

PAA@FA was prepared by a chemical reaction by means of adding fuchsin acid (FA) during poly acryl amide (PAA) formation. It is well known grafting procedure for this type [18,19] materials. Briefly, 200 mg of FA were dissolved completely in the solution including 5 g of acrylamide and 0.5 g of cross-linker (N,N'-methylenebisacrylamide) in 10 mL of water. Then, the mixture was kept in ultrasonic water bath for 10 min and mixture at 500 rpm on a magnetic stirrer. For starting of polymerization reaction, 0.2 g of ammonium persulphate was transferred to this solution immediately. After the polymerization reaction was sustained by adding 100 μL of N,N,N',N'-tetramethylethylenediamine (TEMED) at room temperature. PAA@FA was washed with ultra-pure water for five times and ethanol for 2 times in order to remove non-grafted reagents. The collected composite was dried at 40 $^{\circ}\text{C}$ in a vacuum oven.

2.4. The solid phase extraction procedure

10 ml of fractional sample containing Quercetin (within 10- 1200 ng mL^{-1}) was located in a falcon tube. Then 1.0 mL of pH: 4.00 buffer, 50 mg of adsorbent (PAA@FA) were supplemented and completed to 10 mL with ultra-pure water. The latest solution was retained on an orbital shaker at 100 revolutions per minute for 40 minutes. At the end of this period, the adsorbent was isolated from the aqueous medium by

centrifugation at 4000 revolutions per minute for 5 minutes. The watery phase was ejected with the help of an injector and the adsorbent phase was gathered at the base of the tube. And then, 400 μL of 2-propanol was joined later, stripping adsorbed quercetin molecules using a wormhole for 30 s prior to spectrophotometric detection at 370 nm. Another blank solution was subjected to the same process. Finally, the quantity of Quercetin was determined using either the calibration curve obtained directly from the spectrophotometer or the standard addition method.

2.5. Application to model solutions

The suggested method was practiced to model solutions including quercetin at various concentrations. The prepared model solutions were filtered through Whatman grade No. 40 filter paper. 20 mL of this solution was treated under the developed method.

3. Results and Discussion

3.1. Selection of working wavelength

Figure 2 exhibits the absorption spectra of Quercetin after SPE for five different concentration levels. The obtained results showed that maximum absorbance occurs at 255 and 370 nm. As is shown, the absorbance of target molecules increased progressively with concentration at both wavelengths.

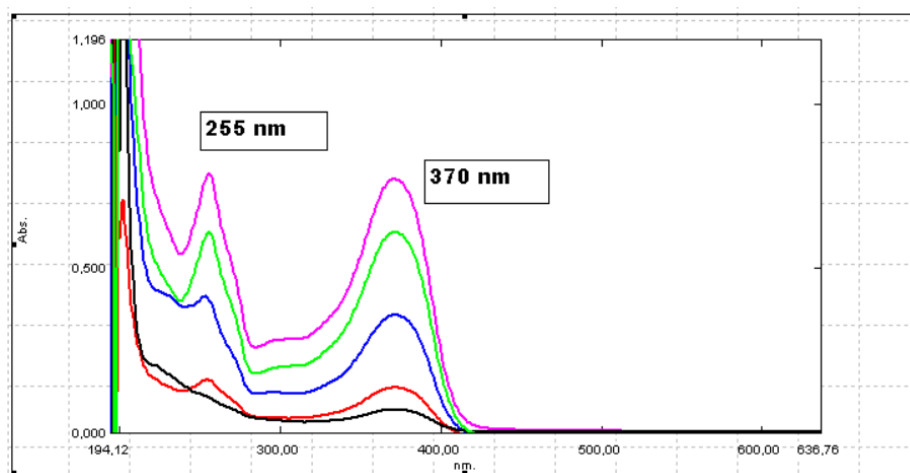


Figure 2. Absorption spectrum of Quercetin solutions in different concentrations after SPE

3.2. Characterization of synthesized material

The FT-IR spectra of the used polymeric material (PAA@FA) was illustrated in Figure 3. The spectrum of PAA showed a broad band of NH_2 at 3300 cm^{-1} , peaks of carboxyl and amide groups (CONH_2) at 1600--

1700 cm^{-1} , and a C-N stretch at $1000\text{--}1200\text{ cm}^{-1}$ [20]. There was no significant difference between PAA and FA because the concentration of the grafted molecules was very low. Only, the grafting procedure can be provided by increasing peak at 2800 cm^{-1} .

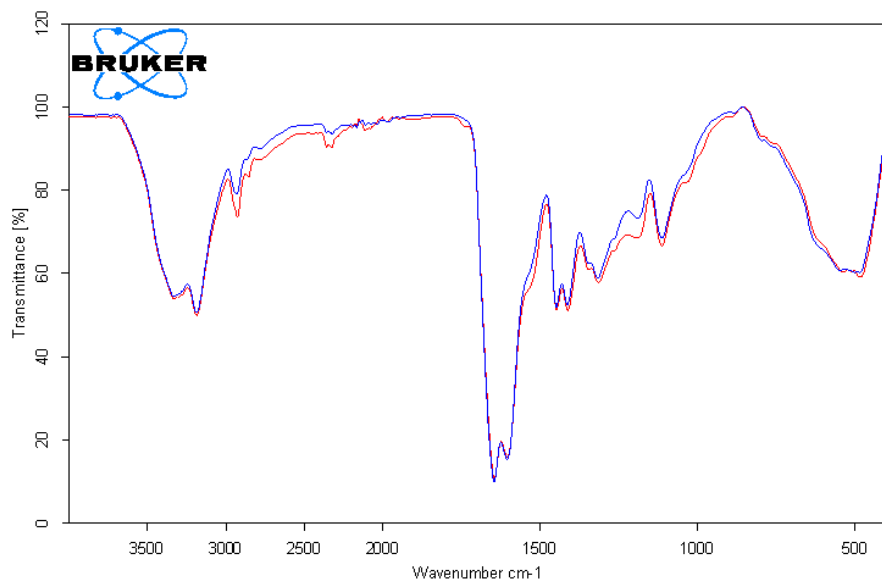


Figure 3. FTIR spectrum of new developed polymeric material (Red: PAA, Blue: PAA@FA)

SEM images of PAA@FA was shown in Fig. 4. The surface morphology of PAA@FA is clearly seen in this figure with different focusing centers. The image of PAA@FA demonstrates a porous and bittie surface

structure, while it displays an in-order surface and smoother structure. Adsorbent surface morphology is suitable for adsorption of target molecules.

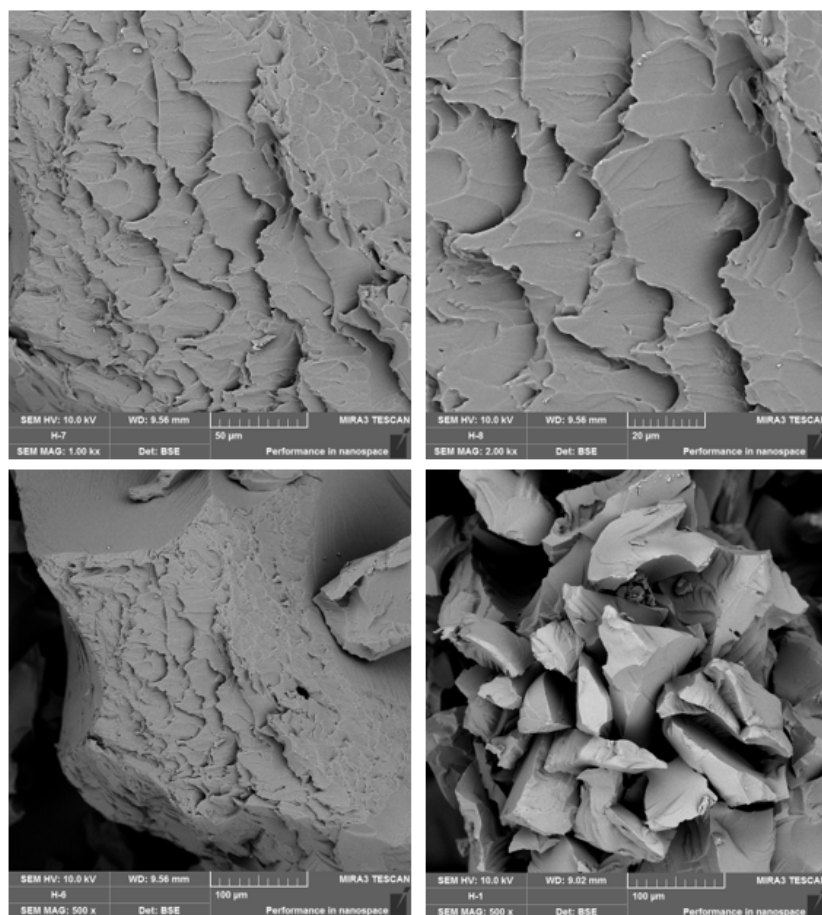


Figure 4. SEM image of new developed polymeric material

3.3. Effect of pH

Considering the pH of the sample solution on both adsorption and enrichment factor, it is of great importance to study this parameter. The effect of pH on extraction efficiency was studied by changing the pH of the sample solution from 2 to 10. The results were shown in Figure 5. The signals of Quercetine increased until pH 4.0 and decreased beyond this pH. Possibly, an increase in pH resulted in a decrease in the transfer of Quercetin molecules. The pKa value of the quercetin is 6.38 [21]. Beyond this value, hydrogen ion separate from quercetine and the molecule turns into ionized negative charged form. And, this change decrease the extraction efficiency. Then, the next studies were continued by using pH 4.0 buffer. After suitable pH were selected, the concentration of buffer (0.1 M) was studied within the framework 0-2 mL by means of changing volume of buffer. According to experimental results as illustrated Figure 5, better signals were achieved using 1 mL buffer solution.

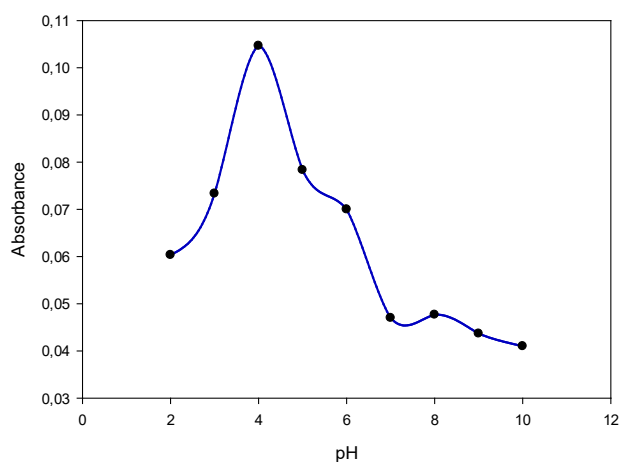


Figure 5. The effect of pH on developed method

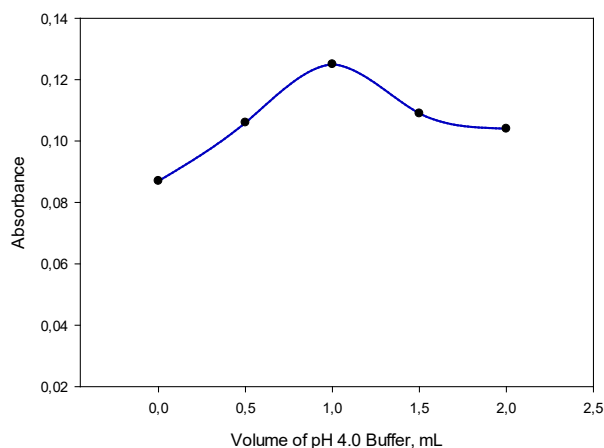


Figure 6. The volume effect of pH on developed method

3.4. Eluent(desorption) type and its volume

The suitable solvent should be chosen for desorption process which directly effects success of pre-concentration method. Therefore, one of the most important steps in SPE experiments is to determine the most ideal solvent for the elution process. In addition, when choosing the eluent, its suitability to the detection system should also be considered. The change of analytical signals by different solvent types on desorbing of Quercetin out of PAA@FA were studied and the results were presented in Figure 7. As shown in the Figure, the best signals of Quercetin after SPE were acquired through isopropanol (2-propanol). In our study, the volume of elution solvent is one of the important parameters to obtain a high preconcentration factor (PF). Because PF decrease while the volume increases due to dilution effect. For this reason, the affect of eluent volume on pre-concentration of Quercetin was examined in the scope of 300-1500 μ L. As reflected from Figure 7 the best signal values were acquired with 600 μ L 2-propanol. Consequently, next steps were pursued utilizing this value.

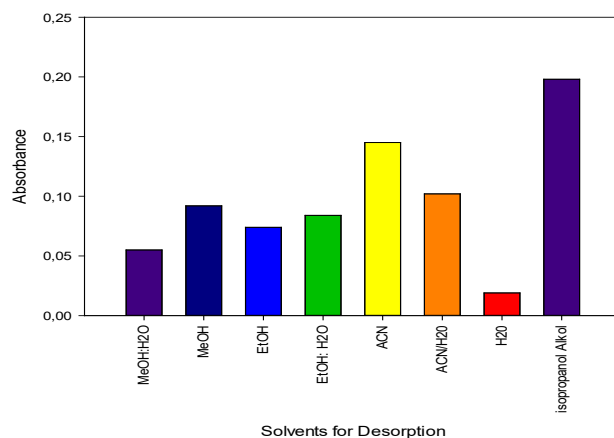


Figure 7. The effect of desorption solvent

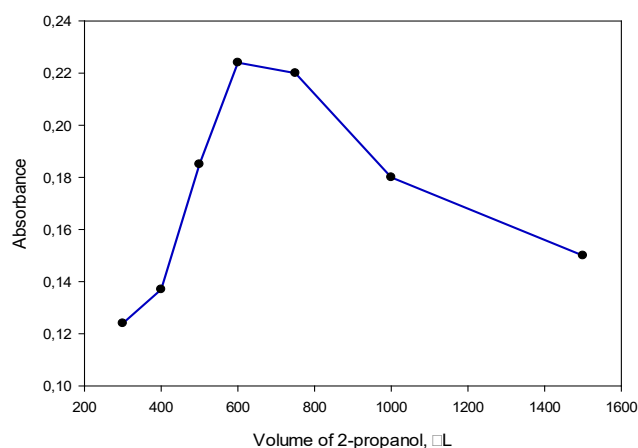


Figure 8. Volume optimization of desorption solvent

3.5. Optimization of adsorption and elution time

Our goal in this optimization step is to ensure that the experimental procedure is completed as soon as possible. The developed method includes two main steps: pre-concentration and determination. As is known, the determination step is a routine spectrophotometric analysis and there is nothing that can be done to shorten this step. For this reason, solid phase extraction experiments, which the enrichment step, were studied and evaluated in terms of time. SPE procedures include adsorption and desorption steps. The adsorption step of SPE was carried out using orbital shaker at room temperature. Secondly, the desorption step of SPE was performed by vortexing at 100 rpm. Time optimization for the adsorption step was investigated in the range of 0 to 100 minutes using 200 ng mL⁻¹ Quercetin model solutions. Desorption time was optimized using model solutions in the range of 5-60 s. As seen in Figure 9, 40 minutes is sufficient for complete adsorption of quercetin molecules at a shaking speed of 100 rpm. In addition, 30 seconds of vortexing is sufficient for all of the analyte to pass into the elution solution.

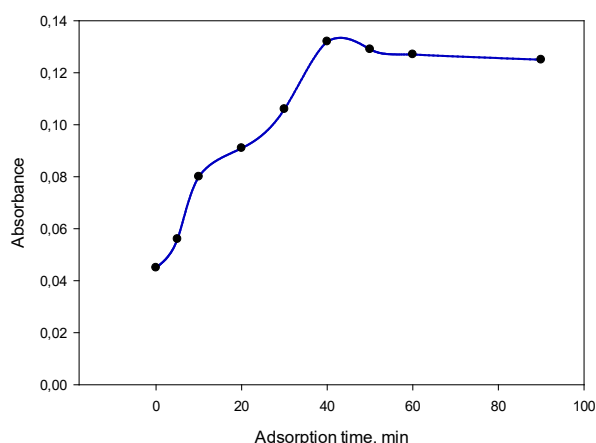


Figure 9. Optimization of adsorption time on the developed method

Table 1. Analytical qualities of the presented method .

Parameters	The Values	
	Before SPE	After SPE
Linear range	0.8–5.0 µg mL ⁻¹	20–800 ng mL ⁻¹
Slope	0.009	0.324
Correlation coefficient (r ²)	0.9928	0.9915
RSD (%)	3.5 (for 1.00 µg L ⁻¹ , n: 5)	2.8 (for 200 ng mL ⁻¹ , n: 5)
LOD	0.24 µg L ⁻¹	5.97 ng mL ⁻¹
LOQ	0.72 µg L ⁻¹	17.91 ng mL ⁻¹
Preconcentration factor ^a	-	16.7
Enrichment factor ^b	-	36

3.6. Reusability properties of material

One of the most important properties of a new developed material is reusability studies. The analysis cost of a new method is directly affected of new material. In a solid phase extraction method, if sorbent phase can be applied once more, the cost of the analysis decreases. The measure of the reusability of a material shows the robustness of that material.

For this study, the new polymeric material was weighed and run the optimized extraction conditions. After every use, the amount of adsorbed quercetin molecules was compared previous one. The experiments were kept to obtain 5.0 % a change in measured amount of quercetin. It was noticed that there isn't significant change in the signal after 10 times use. Then for each experiment, polymeric material was washed with 2.0 mL isopropanol twice after each use.

3.7. Analytical characteristics

The analytical frameworks of the proposed method were studied step by step that is, LOD and LOQ, linear range ,repeatability ,regression equation and pre-concentration factor. The linearity of method was observed in the range of 20-800 ng mL⁻¹.

LOD and LOQ values were calculated as 5.97 and 17.91 ng mL⁻¹, respectively. The preconcentration factor was determined as a factor of 16.7 because SPE experiment started with 10 mL and final volume of solution was 0.6 mL after SPE. Moreover, the enrichment factor was also found as 36 by calculating the ration between slopes of the calibration plots before and after SPE.

3.8. Determination of Quercetin in Model Solutions

Application of the submitted method was tested via model solutions. Repeatability, and accuracy values was evaluated by relative standard deviations and recovery values, respectively. Every sample was analyzed for 5 replicate. The results were

demonstrated in Table 2. Recovery studies were performed too after having been enriched with samples of known quercetin concentrations of 50 and 100 ng mL⁻¹. RSD % values were calculated as indicator of repeatability of method by considering intraday and interday analysis results.

Table 2. Determination of Quercetin in model solutions (N=5)

Sample	Added Quercetin ng mL ⁻¹	Found Quercetin ng mL ⁻¹	Recovery %	intraday interday	
				RSD%	RSD%
	-	--	-	-	-
Model Solution	50.00	50.78 ± 1.45	101.6	2.85	3.65
	100.00	102.93 ± 2.52	102.9	2.45	3.52

3. Conclusions

In this presented study, a new polymeric adsorbent material was firstly synthesized for the enrichment and determination of Quercetin molecules. Solid phase extraction experiments and all necessary optimization processes were performed with this original material. The data obtained as a result of all these optimization processes; A new, economical, very simple and environmentally friendly analytical method has been developed for the separation and enrichment of quercetin molecules in model solutions by UV-

spectrophotometric determination. An effective and easily method for determination of Quercetin molecules by means of the SPE. The method offers significant green advantages very little the use of organic solvents in the extracting process. The proposed methodology consists of a simple experimental procedure. The required experimental equipment can simply be provided by each analytical laboratory. A comparison table was shown in table 3. As can be seen, the proposed method has similiar and comparable properties with literature.

Table 3. Comparison of the developed method with other existing methods.

Pre-treatment Procedure	Determination Method	Limit of detection	Pre-concentration factor (PF)or Enrichment factor(EF)	Ref.
Deep eutectic solvent in ultrasound-assisted emulsification microextraction	UV-VIS	18.8 µg L ⁻¹	15 (PF)	[2]
Amine-based liquid phase microextraction	UV-VIS	70 µg L ⁻¹	26.7 (PF)	[21]
Ultrasonic-assisted restricted access supramolecular solvent-based liquid phase microextraction	UV-VIS	9.93 µg L ⁻¹	30 (PF)	[16]
Magnetic solid phase extraction	HPLC-DAD	1.46 ng mL ⁻¹	125 (PF) 103.7 (EF)	[14]
Solid Phase Extraction (SPE)	UV-VIS	5.97 ng mL ⁻¹	16.7 (PF) 36 (EF)	The Developed Method

The number of methods used in the literature for analysis of quercetin molecules is generally used chromatographically approaches. But, it is well known, every laboratory does not have this facilities. Spectrophotometric methods and the used equipment are available in almost research laboratory. For this reason, the important of developed method can be understood better.

Conflicts of interest

There is no conflict of interest: The author state that did not have conflict of interests

References

- [1] Kurzawa M., Determination of quercetin and rutin in selected herbs and pharmaceutical preparations, *Anal. Lett.*, 43 (2010) 993–1002.
- [2] Kanberoglu G.S., Yilmaz E., Soylak M., Application of deep eutectic solvent in ultrasound-assisted emulsification microextraction of quercetin from some fruits and vegetables, *J. Mol. Liq.*, 279 (2019) 571–577.
- [3] Zhiltsova E.P., Ibatullina M.R., Lukashenko S.S., Kuttyreva M.P., Zakharov L.Y., Spectrophotometric study of quercetin in metallomicellar solutions of 1-hexadecyl-4-aza-1-azoniabicyclo[2.2.2] octane bromide complex with copper dibromide, *J. Mol. Liq.*, 249 (2018) 716–722.
- [4] Ranjbar Banforuzi S., Hadjmohammadi M.R., Two-phase hollow fiber-liquid microextraction based on reverse micelle for the determination of quercetin in human plasma and vegetables samples, *Talanta*, 173 (2017) 14–21.
- A. Murakami H., Ashida J., Terao, Multitargeted cancer prevention by quercetin, *Cancer Lett.*, 269 (2008) 315–325.
- [5] Boots A.W., Haenen G.R.M.M., Bast A., Health effects of quercetin: From antioxidant to nutraceutical, *Eur. J. Pharmacol.*, 585 (2008) 325–337.
- [6] Lobo V., Patil A., Phatak A., Chandra N., Free radicals, antioxidants and functional foods: Impact on human health, *Pharmacogn. Rev.*, 4 (2010) 118.
- [7] Jiang H., Engelhardt U.H., Thräne C., Maiwald B., Stark J., Determination of flavonol glycosides in green tea, oolong tea and black tea by UHPLC compared to HPLC, *Food Chem.*, 183 (2015) 30–35.
- [8] Xiao P., Zhao F., Zeng B., Voltammetric determination of quercetin at a multi-walled carbon nanotubes paste electrode, *Microchem. J.*, 85 (2007) 244–249.
- [9] Chafer A., Pascual M.C., Salvador A., Berna A., Supercritical fluid extraction and HPLC determination of relevant polyphenolic compounds in grape skin, *J. Sep. Sci.*, 28 (2005) 2050–2056.
- [10] Wu H., Chen M., Fan Y., Elsebaei F., Zhu Y., Determination of rutin and quercetin in Chinese herbal medicine by ionic liquid-based pressurized liquid extraction-liquid chromatography-chemiluminescence detection, *Talanta*, 88 (2012) 222–229.
- [11] Ranjbari E., Biparva P., Hadjmohammadi M.R., Utilization of inverted dispersive liquid-liquid microextraction followed by HPLC-UV as a sensitive and efficient method for the extraction and determination of quercetin in honey and biological samples, *Talanta*, 89 (2012) 117–123.
- [12] Ulusoy H.İ., Applications of magnetic nanoparticles for the selective extraction of trace species from a complex matrix, 1st ed., New York: Nova Scientific Publishers, (2017).
- [13] Ulusoy S., Yilmaz E., Erbas Z., Ulusoy H.İ., Soylak M., Trace analysis of quercetin in tea samples by HPLC-DAD system by means of a new nanocomposite including magnetic core-shell, *Sep. Sci. Technol.*, (2019).
- [14] Şenol Z.M., Şimşek S., Ulusoy H.İ., Mahmood A., Kaya S., Insight from adsorption properties of Xylidyl Blue embedded hydrogel for effective removal of uranyl: Experimental and theoretical approaches, *Polym. Test.*, (2020).
- [15] Memon Z.M., Yilmaz E., Soylak M., Multivariate statistical design optimization for ultrasonic-assisted restricted access supramolecular solvent-based liquid phase microextraction of quercetin in food samples, *J. Iran. Chem. Soc.*, 14 (2017) 2521–2528.
- [16] Karaca E., Ulusoy S., Morgül U., Ulusoy H.İ., Development of Analytical Method for Sensitive Determination of Streptozotocin based on Solid Phase Extraction, *Cumhur. Sci. J.*, 41 (2020) 826–831.
- [17] Ulusoy H.İ., Şimşek S., Removal of uranyl ions in aquatic mediums by using a new material: Galloxyanine grafted hydrogel, *J. Hazard. Mater.*, 255 (2013) 397–405.
- [18] Şimşek S., Şenol Z.M., Ulusoy H.İ., Synthesis and characterization of a composite polymeric material including chelating agent for adsorption of uranyl ions, *J. Hazard. Mater.*, 338 (2017) 437–446.

- [19] Ulusoy H.T., Şimşek S., Removal of uranyl ions in aquatic mediums by using a new material: Galloctyanine grafted hydrogel, *J. Hazard. Mater.* 254–255 (2013) 397-405.
- [20] Soylak M., Ozdemir B., Yilmaz E., An environmentally friendly and novel amine-based liquid phase microextraction of quercetin in food samples prior to its determination by UV–vis spectrophotometry, *Spectrochim. Acta - Part A Mol. Biomol. Spectrosc.*, 243 (2020) 118806.

Tetracycline adsorption via dye-attached polymeric microbeads

Aslı GÖÇENOĞLU SARIKAYA¹ , Bilgen OSMAN^{1,*} 

¹Bursa Uludağ University, Faculty of Science and Art, Department of Chemistry, Bursa / TURKEY

Abstract

In this study, the adsorption of tetracycline (TC) onto polymeric microbeads was investigated. For this purpose, suspension polymerization was used to synthesize poly(2-hydroxyethyl methacrylate) [poly(HEMA)] microbeads. Cibacron Blue F3GA (CB) was covalently attached to poly(HEMA) microbeads and the microbeads were tested as an adsorbent for subsequent TC adsorption. The effects of various parameters, such as pH value, initial TC concentration, temperature, and contact time, were investigated. The maximum adsorption capacity (Q) of microbeads was found to be 9.63 mg g⁻¹ at pH 7.0. The results showed that the adsorption process was fast and occurred spontaneously within the first 5 minute. The adsorption process was fitted to the Freundlich isotherm model. The thermodynamic parameters of the adsorption, the enthalpy (ΔH°) and entropy (ΔS°), were calculated as 69.26 kJ mol⁻¹ and 0.290 kJ mol⁻¹ K⁻¹, respectively. The Gibbs free energy (ΔG°) was also calculated in the range of -11.069 kJ mol⁻¹ to -17.159 kJ mol⁻¹ with increase in temperature from 277 K to 298 K indicating that the TC adsorption process was spontaneous and endothermic. The results revealed that the poly(HEMA) microbeads could be effectively used to adsorption of TC from aqueous solution.

Article info

History:

Received: 28.05.2020

Accepted: 14.09.2021

Keywords:

Adsorption,
Cibacron Blue F3GA,
Microbeads,
Poly(HEMA),
Tetracycline.

1. Introduction

Antibiotics are widely used to cure pathogenic or bacterial diseases in animals and humans [1]. Besides, they are also used as feed additives in aquaculture and the poultry industry to promote animal growth [2]. Since most antibiotics are difficult to metabolize, a large fraction of ingested antibiotics is excreted in feces or urine into the environment [3] and pollutes soil [4] and water sources [5].

Tetracyclines (TCs), which comprise oxytetracycline (OTC), chlortetracycline (CTC), and tetracycline (TC), are commonly used antibiotics worldwide [6]. TC is an aromatic polyketide product of the biosynthetic pathway with poor absorption, low metabolism and overexploitation. Thus, the environmental pollution by TC residues affects human health and aquatic ecosystems [7].

At present, there are various technologies to remove TC from water, like coagulation [8], photocatalytic degradation [9], electrochemical processes [10], ion exchange [11], filtration [12], biological processes [13], sedimentation [14], ozonation [15], and adsorption [16]. Among these, adsorption is an attractive and effective process [17] due to its removal efficiency, safety, low-cost adsorbents, and easy

operation [18]. Furthermore, various adsorbents, such as biological sludge [19], cryogels [20], activated carbons [21], metal oxides [22], chitosan [23], and polymers [24], are used to remove TCs.

Reactive dyes are often used as affinity ligands for the adsorption or separation of proteins, enzymes and heavy metals. In addition, they are effective and can easily be attached to the carrier matrix. Cibacron Blue F3GA (CB) is a monochlorotriazine dye containing four amino and three sulfonate groups and has been used as an affinity ligand in various biotechnological studies [25].

In the present study, poly(2-hydroxyethyl methacrylate) [poly(HEMA)] microbeads were synthesized via suspension polymerization, and CB was covalently attached onto microbeads. Poly(HEMA)-CB microbeads were characterized by Fourier transform-infrared spectroscopy (FT-IR), elemental analysis, and scanning electron microscopy (SEM). Then, the effects of pH, initial TC concentration, temperature, and contact time on the TC adsorption onto poly(HEMA)-CB microbeads were examined. Furthermore, the adsorption mechanism, adsorption isotherms and kinetic parameters of TC adsorption were evaluated, and the thermodynamic parameters were also calculated and discussed.

*Corresponding author. e-mail address: bilgeno@uludag.edu.tr
<http://dergipark.gov.tr/csj> ©2021 Faculty of Science, Sivas Cumhuriyet University

2. Materials and Methods

2.1. Materials

2-hydroxyethyl methacrylate (HEMA) and ethylene glycol dimethacrylate (EGDMA) were obtained from Fluka. 2,2'-azobisisobutyronitrile (AIBN), toluene,

NaOH and ethylene glycol were obtained from Merck. Cibacron Blue F3GA (CB), tetracycline (TC), poly(vinyl alcohol) (PVA), CH₃COOH, CH₃COONa, NaH₂PO₄, Na₂HPO₄ and KNO₃ were purchased from Sigma. The chemical structures of TC and CB were given in Figure 1.

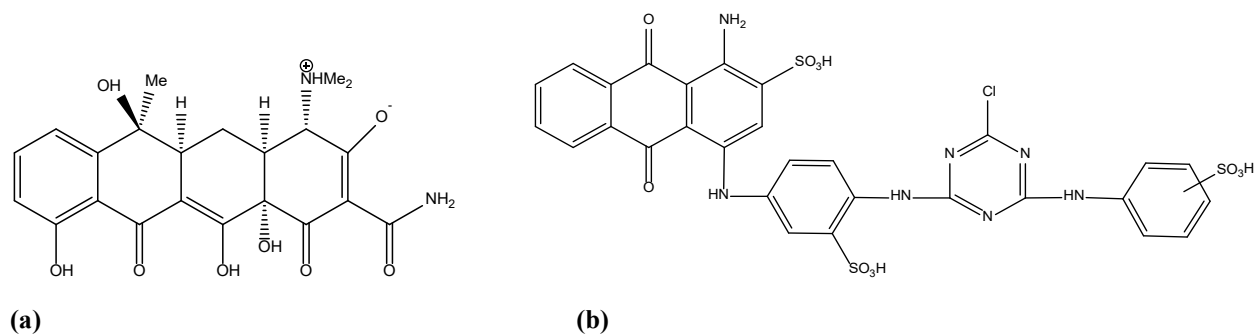


Figure 1. The chemical structures of (a) TC and (b) CB

2.2. Preparation of poly(HEMA) microbeads

Poly(HEMA) microbeads were prepared by suspension polymerization in aqueous media [26]. Ethylene glycol dimethacrylate (EGDMA, 4 mL) and 2-hydroxyethyl methacrylate (HEMA, 4 mL) were used as comonomers and mixed with toluene (4 mL) to prepare the organic phase. First, 0.2 g poly(vinyl alcohol) (PVA) was dissolved in 50 mL distilled water to prepare the dispersion medium. Then, 0.1 g of 2,2'-azobisisobutyronitrile (AIBN) was dissolved in the monomer phase which was used as the polymerization initiator. The mixture was poured into a glass polymerization reactor (100 mL) and then, stirred magnetically at 400 rpm. The polymerization was performed at 65 °C for 4 h and at 80 °C for 2 h. After polymerization, the poly(HEMA) microbeads were washed with distilled water and ethanol several times to remove residuals.

2.3. Cibacron Blue F3GA attachment to poly(HEMA) microbeads

Poly(HEMA) microbeads (3.0 g) were magnetically stirred (400 rpm) with CB aqueous solution (3.5 mg/mL, 100 mL) which was containing NaOH (4.0 g) at 80 °C for 4 h [26]. After incubation, CB-attached microbeads were filtered and for removing unattached CB, washed with ethanol and distilled water several times.

2.4. Characterization studies

To identify the morphology of the microbeads SEM (ZEISS EVO 40, Carl Zeiss AG, Germany) was used. FTIR spectrophotometer was used to characterized the poly(HEMA) microbeads, CB and CB-modified

poly(HEMA) (poly(HEMA)-CB) microbeads (Perkin Elmer, Spectrum 100, USA).

Elemental analysis was performed to determine the amount of CB attached to the poly(HEMA) microbeads (Leco Elemental Analyzer, CHNS-932, St. Joseph, MI).

The size distribution and average size of the microbeads were detected by screen analysis performed with Tyler standard sieves (Retsch Gmb & Co., KG, Haan, Germany).

2.5. Adsorption studies

Adsorption studies were performed in a batch system containing 20 mL of TC solution and 0.02 g poly(HEMA)-CB microbeads. To detect the effect of the pH of the medium on the adsorption capacity (Q) of the poly(HEMA)-CB microbeads, TC solutions with various pH values (in the range of 3.0 to 9.0, 10 mg L⁻¹, 20 mL) were prepared using acetate or phosphate buffer (0.1 M). The microbeads were stirred magnetically at 200 rpm at 25 °C. In the concentration range of 1.0 mg L⁻¹ to 50.0 mg L⁻¹, the TC solutions were prepared at pH 7.0 to investigate the effect of the initial TC concentration on the Q of the poly(HEMA)-CB microbeads at 4 °C, 12 °C and 25 °C (20 mL, 200 rpm). After the adsorption of TC onto poly(HEMA)-CB microbeads, the suspensions were centrifuged (Allegra 64R, Beckman Coulter) at 10,000 rpm for 10 min. The concentrations of the initial and final TC solutions were measured spectrophotometrically at 358 nm (Shimadzu-2100 UV-vis spectrophotometer). All batch studies were performed in triplicate. The amount of adsorbed TC was calculated as follows:

$$Q = \frac{(C_0 - C_e)V}{m} \quad (1)$$

where Q (mg g^{-1}) is the adsorption capacity, C_0 and C_e (mg L^{-1}) are the initial and final concentrations of the solution, respectively, V (L) is the volume of the initial solution, and m (g) is the adsorbent weight.

2.6. Desorption and repeated studies

To specify the performance of the adsorbent, adsorption-desorption cycles were performed five times by using the same microbeads. The initial TC concentration of the solution was 5 mg L^{-1} and the final volume was 20 mL at 25°C . KNO_3 (1 M) solution, ethylene glycol (10 %, w/w %) solution and KNO_3 :ethylene glycol (1:1; 1 M:10 %) mixture were used as desorption agents. The total volume of the

desorption agents was 20 mL and was stirred magnetically (200 rpm) at 25°C . The final TC solutions were measured spectrophotometrically. The desorption ratio was calculated as follows:

$$\text{Desorption Ratio} = \frac{\text{amount of TC desorbed}}{\text{amount of TC adsorbed}} \times 100 \quad (2)$$

3. Results and Discussion

3.1. Characterization of the poly(HEMA)-CB microbeads

The surface morphology was determined by SEM analyses (Figure 2). The SEM images reveal that the beads were homogeneous and spherical with a rough surface and a diameter in the range of 106 to $300 \mu\text{m}$.

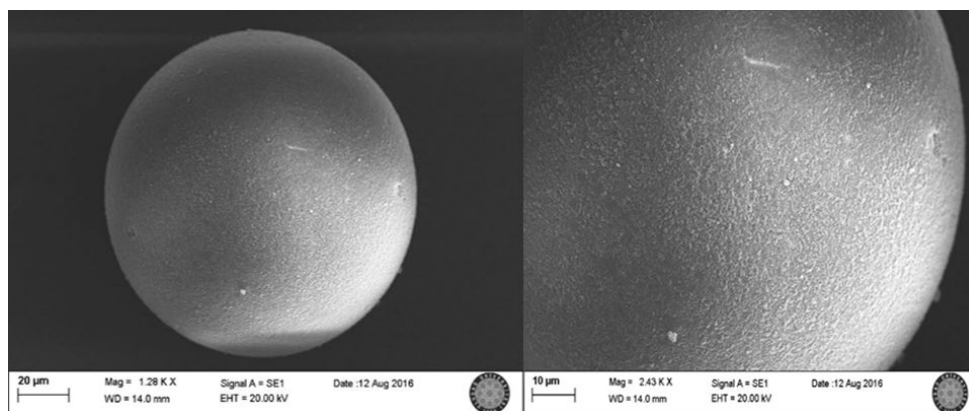


Figure 2. SEM images of poly(HEMA) microbeads

According to the nitrogen stoichiometry determined by elemental analysis, the amount of attached CB to poly(HEMA) microbeads was 10.44 mg CB/g microbeads [26].

To examine the interaction between the poly(HEMA) microbeads and CB, the FTIR spectra of poly(HEMA) microbeads, CB and poly(HEMA)-CB microbeads were achieved (Figure 3). The FTIR spectrum of poly(HEMA) microbeads exhibited a characteristic O-H stretching vibration band at $3200\text{-}3600 \text{ cm}^{-1}$. The C-H stretching band of CH_3 , the C=O stretching band, and the C-O ester stretching vibration band were observed at 2948 cm^{-1} , 1716 cm^{-1} , and 1247 cm^{-1} , respectively. The C-Cl stretching band at 1087 cm^{-1} and the S-O stretching vibration band at 1042 cm^{-1} and 1022 cm^{-1} , respectively, appeared in the FTIR

spectrum of CB. In the FTIR spectrum of poly(HEMA)-CB microbeads, the characteristic O-H stretching vibration band appeared as a broad peak at $3200\text{-}3600 \text{ cm}^{-1}$. Due to the dye attachment to the polymer, some additional absorption bands that differed from poly(HEMA) microbeads were observed in the spectrum of poly(HEMA)-CB microbeads. The bands at 1022 cm^{-1} , 1073 cm^{-1} , and 1154 cm^{-1} can be attributed to the stretching vibration of S-O, the symmetric stretching of S=O, and the asymmetric stretching of S=O, respectively, and are a result of the CB attachment to poly(HEMA) microbeads. Additionally, vibrations of the primary and secondary amine groups of CB were observed at 849 cm^{-1} and 897 cm^{-1} . At 1534 cm^{-1} , N-H bending was determined as a broad band. This result shows that CB was successfully attached to poly(HEMA) microbeads [26-28].

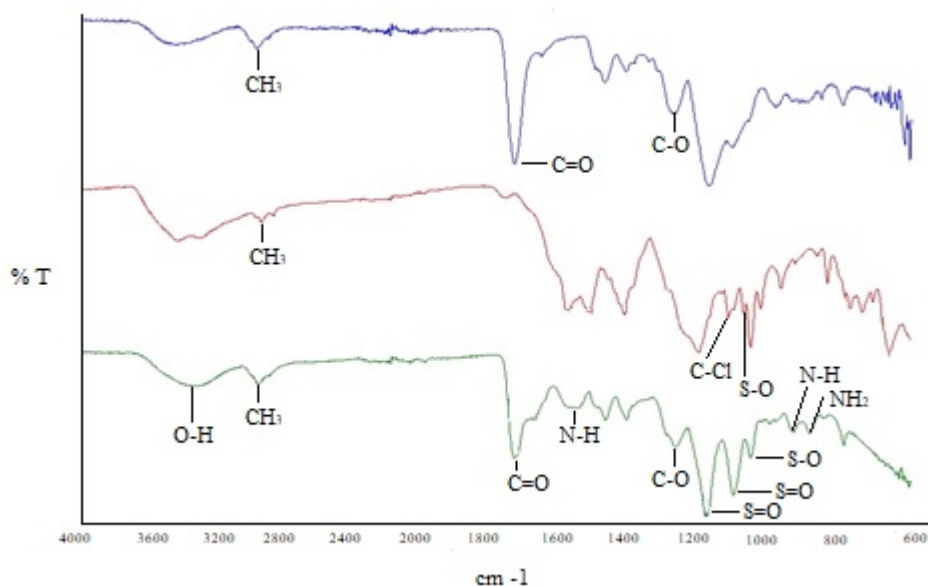


Figure 3. FTIR spectra of poly(HEMA)-CB (green), CB (red), and poly(HEMA) (blue)

3.2. Effect of pH value on TC adsorption

One of the most important parameter in an adsorption processes is the initial pH value of the solution. To identify the effect of the pH on the TC adsorption on poly(HEMA)-CB microbeads, 10 mg L⁻¹ TC solution was prepared at various pH values ranging from 3.0 to 9.0 (Figure 4). TC exhibits ionizable and polar groups such as amino, phenol, ketone, carboxyl and alcohol groups. It has three dissociation constants, and under acidic, partially acidic to neutral, and alkaline conditions, it appears as cationic species (pK_a = 3.3), zwitterionic species (pK_a = 7.68) and anionic species (pK_a = 9.7), respectively [29]. Due to the amphoteric character of TC, the initial pH value of the aqueous solution can easily affect both the protonation of the TC molecule and the physicochemical properties of the adsorbent [30]. CB (pK_a = 0.78), a monochlorotriazine

dye, contains four basic primary and secondary amino groups and three sulfonic acid groups that affect ionic and hydrophobic interactions. CB dye molecules were covalently attached to the poly(HEMA) microbeads via the hydroxyl groups of the polymer and the reactive triazine ring of the dye [31]. The adsorption capacity of poly(HEMA)-CB for TC increased in the pH ranging from 4.0 to 7.0 and dramatically decreased for pH values higher than 8.0. These results could be caused by repulsive electrostatic forces between TC and the CB dye. *Q* was observed as 1.17 mg g⁻¹ at pH 7.0. Specific interactions, such as hydrogen bonding and electrostatic and hydrophobic interactions between poly(HEMA)-CB microbeads and TC, may result from the ionization states of the dye (i.e., sulfonic acid and amino) and TC (i.e., amino) at pH 7.0. In Figure 5, possible interactions between poly(HEMA)-CB and TC are also given.

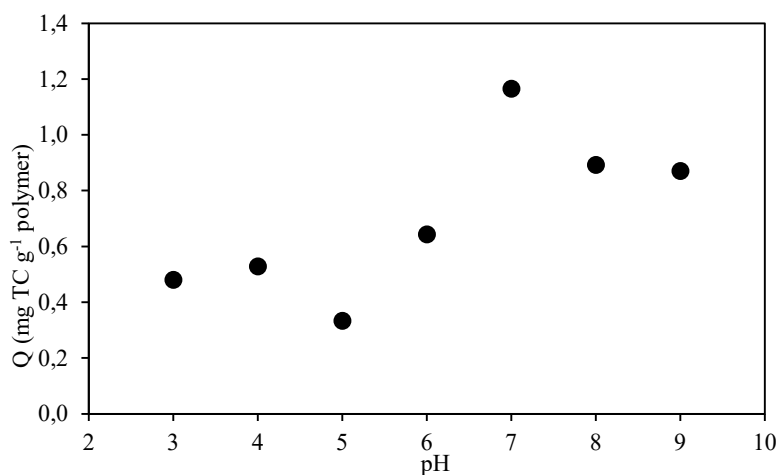


Figure 4. Effect of the pH on TC adsorption ($C_{TC} = 10$ mg/L; $T = 25$ °C; $m_{\text{poly(HEMA)-CB}} = 0.02$ g; $V = 20$ mL)

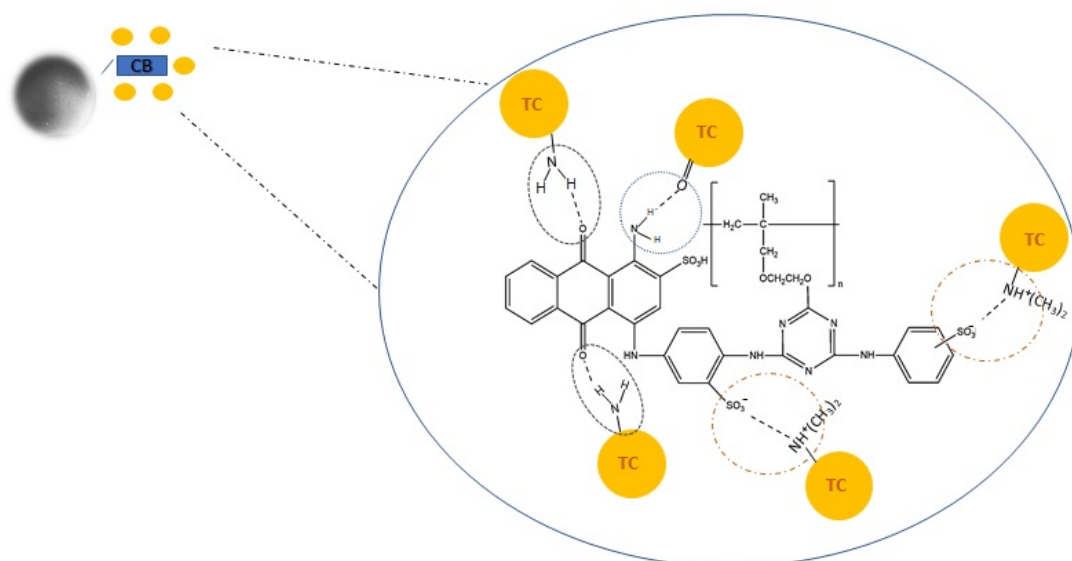


Figure 5. Schematic representation of possible interactions between poly(HEMA)-CB and TC

3.3. Effects of initial concentration and contact time on TC adsorption

Figure 6 shows the effect of the initial TC concentration on the adsorption at various temperatures (4 °C, 12 °C and 25 °C). The adsorption

process was carried out for 24 hours. The adsorption capacity increased from 0.121 mg g⁻¹ to 5.159 mg g⁻¹ and from 0.686 mg g⁻¹ to 9.627 mg g⁻¹ after increasing the initial TC concentration from 1 mg L⁻¹ to 50 mg L⁻¹ at 12 °C and 25 °C, respectively. The maximum adsorption capacity did not change dramatically at 4 °C.

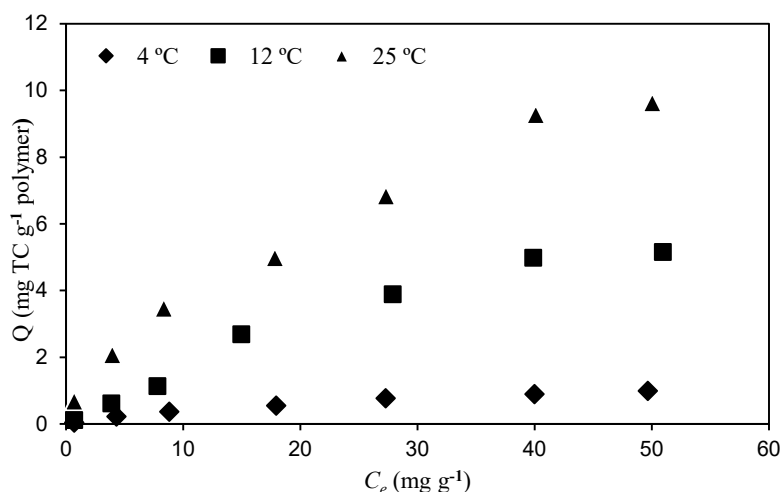


Figure 6. Effect of the initial TC concentration on adsorption at different temperatures ($C_{TC} = 1-50 \text{ mg/L}$; $m_{\text{poly(HEMA)-CB}} = 0.02 \text{ g}$; $V = 20 \text{ mL}$)

To develop an effective and applicable adsorption process, it should be performed in a short time [32]. To determine the TC adsorption performance over time, the adsorption process was performed at different contact times ranging from 5 min to 60 min at various temperatures (4 °C, 12 °C and 25 °C). TC adsorption occurred quickly within the first 5 min and continued for 60 min with no remarkable change after 60 min.

The adsorption capacities for 10 mg L⁻¹ initial concentration of TC were calculated as 1.323 mg g⁻¹, 1.985 mg g⁻¹ and 3.415 mg g⁻¹ at 4 °C, 12 °C and 25 °C, respectively (Figure 7). The adsorption of TC onto poly(HEMA)-CB microbeads occurred at a fast rate; therefore, the kinetic parameters could not be calculated.

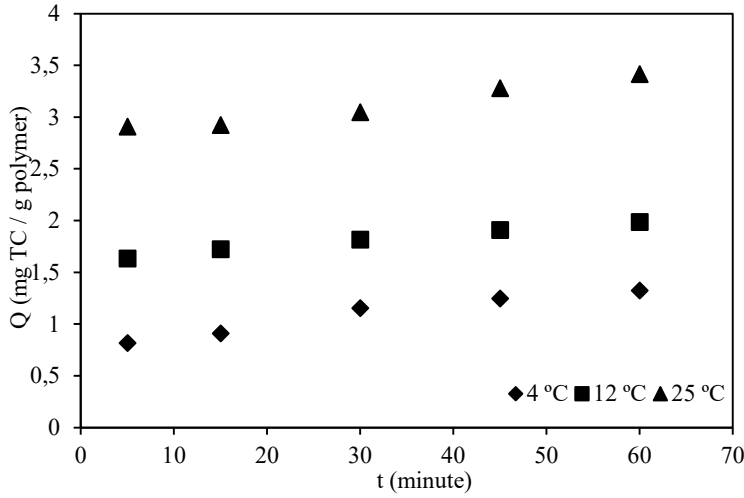


Figure 7. Effect of contact time on TC adsorption ($C_{TC} = 10 \text{ mg/L}$; $m_{\text{poly(HEMA)-CB}} = 0.02 \text{ g}$; $V = 20 \text{ mL}$)

3.4. Adsorption isotherms

Isothermal analysis was also performed to investigate the adsorption capacity of poly(HEMA)-CB microbeads for TC. The Langmuir (Eq. 3), Freundlich (Eq. 4) and Dubinin-Radushkevich (D-R) (Eq. 4) isotherm models were applied to analyze the adsorption process of poly(HEMA)-CB microbeads at 277, 285 and 298 K (Figure SI 1-Figure SI 9).

The Langmuir isotherm model is defined as follows:

$$\frac{C_e}{q_e} = \frac{1}{Q_L K_L} + \frac{C_e}{Q_L} \quad (3)$$

where $C_e \text{ (mg L}^{-1}\text{)}$ is the concentration of the adsorbate in solution at equilibrium, $Q_L \text{ (mg g}^{-1}\text{)}$ is the maximum adsorbate uptake, $q_e \text{ (mg g}^{-1}\text{)}$ is the adsorbate uptake at equilibrium, and $K_L \text{ (L mg}^{-1}\text{)}$ is the Langmuir adsorption equilibrium constant [33].

The Freundlich isotherm model is defined as follows:

$$\ln q_e = \ln K_F + \frac{1}{n} \ln C_e \quad (4)$$

where $C_e \text{ (mg L}^{-1}\text{)}$ is the concentration of the adsorbate in solution at equilibrium, $K_F \text{ (mg g}^{-1}\text{)}$ is the Freundlich adsorption equilibrium constant, n is the Freundlich linearity index, and $q_e \text{ (mg g}^{-1}\text{)}$ is the adsorbate uptake at equilibrium [34].

The Langmuir and Freundlich parameters were determined by the MATLAB package program. The adjusted R^2 (R^2_{adj}) and standard deviation (SD) of the obtained models were calculated. The adsorption

isotherms of TC for various temperatures are given in Table 1.

The Dubinin-Radushkevich isotherm model is defined as follows:

$$\ln Q_e = \ln Q_{D-R} - K_{D-R} \varepsilon^2 \quad (5)$$

where $Q_e \text{ (mg g}^{-1}\text{)}$ is the amount of adsorbed solute, $K_{D-R} \text{ (mol}^2 \text{ J}^{-2}\text{)}$ is the D-R constant, and $Q_{D-R} \text{ (mg g}^{-1}\text{)}$ is the maximum adsorption capacity. ε is the Polanyi potential (J mol^{-1}) and can be defined as:

$$\varepsilon = RT \ln \left(1 + \frac{1}{C_e} \right) \quad (6)$$

where $R \text{ (J mol}^{-1} \text{ K}^{-1}\text{)}$ is the gas constant, $C_e \text{ (mg L}^{-1}\text{)}$ is the equilibrium concentration of the adsorbate, and $T \text{ (K)}$ is the temperature [35]. K_{D-R} values were used to calculate the free energy of adsorption (E_{fe}) (Eq. 7):

$$E_{fe} = \frac{1}{\sqrt{-2K_{D-R}}} \quad (7)$$

The Langmuir, Freundlich and Dubinin-Radushkevich isotherm models were used to fit the experimental data. The Langmuir isotherm model describes adsorption processes on a homogeneous surface. The Freundlich model can be applied to multilayer adsorption with a nonuniform distribution over a heterogeneous surface [34]. In the present study, the Freundlich model ($R^2 > 0.9647$, $R^2_{adj} > 0.9576$) and the Langmuir model ($R^2 > 0.9823$, $R^2_{adj} > 0.9787$) were fitted to adsorption data with high correlation coefficients (Table 1).

Table 1. Parameters of adsorption isotherms of TC onto poly(HEMA)-CB at different temperatures

Isotherm Model	Parameter	Temperature (K)		
		277	285	298
Langmuir	Q_{exp} (mg g ⁻¹)	0.989	5.158	9.620
	Q_L (mg g ⁻¹)	1.565	9.676	16.880
	$K_L \times 10^3$ (L mg ⁻¹)	33.830	24.400	27.090
	R^2	0.9965	0.9823	0.9848
	R^2_{adj}	0.9958	0.9787	0.9818
Freundlich	SD	0.0229	0.3049	0.4675
	K_F (mg g ⁻¹) (L mg ⁻¹) ^{1/n}	0.1013	0.3897	0.899
	N	1.693	1.478	1.626
	R^2	0.9931	0.9647	0.9906
	R^2_{adj}	0.9917	0.9576	0.9906
D-R	SD	0.0323	0.4303	0.3356
	Q_{exp} (mg g ⁻¹)	0.989	5.158	9.620
	Q_{D-R} (mg g ⁻¹)	0.536	4.230	7.120
	K_{D-R} (mol ² J ⁻²)	6.13×10^{-7}	7.14×10^{-6}	2.01×10^{-5}
	E (kJ mol ⁻¹)	0.902	0.264	0.160
	R^2	0.8239	0.8004	0.8903

In Langmuir model in spite of high values of R^2 and R^2_{adj} , Q_{exp} values are not close to Q_L values at all studied temperatures. According to the results, $1/n < 1$, where $1/n$ is a heterogeneity parameter, fit the Freundlich isotherm model.

The Dubinin-Radushkevich isotherm model, which is a pore-filling model, is generally applied to explain the adsorption mechanism onto a heterogeneous surface with a Gaussian energy distribution, and it is temperature-dependent [35]. The values of the free energy of adsorption (E_{fe}) were 0.902 kJ mol⁻¹, 0.264 kJ mol⁻¹ and 0.160 kJ mol⁻¹ for 277 K, 285 K and 298 K, respectively. D-R model is used to determine the nature of the adsorption processes as whether chemical ($8 < E_{fe} < 16$ kJ mol⁻¹) or physical (< 8 kJ mol⁻¹). The

results show that the adsorption of TC onto poly(HEMA)-CB microbeads was a physical process.

Numerous adsorbents were used for TC adsorption, and the comparative results of some adsorption capacities for different adsorbents are shown in Table 2. The adsorption capacity of poly(HEMA)-CB is comparable with other adsorbents which have been used in TC removal from aqueous solutions. As can be seen in Table 2, poly(HEMA)-CB has the second best performance. The size and shape of adsorbents also have an important role in adsorption process. It affects the adsorption capacity. Also, the physical composition of adsorbent can be easily controlled in the polymerization compared to given methods used to prepare biochars.

Table 2. Comparative results of different adsorbents for TC adsorption.

Adsorbent	pH	q_e (mg g ⁻¹)	Time (min)	Adsorption isotherm	Reference
Magnetic chitosan	6.0	14.34	120	Freundlich	[36]
Rice husk ash	5.0	8.37	600	Langmuir	[37]
Biochar	6.0	5.26	1440	Freundlich	[38]
Microplastics	-	0.12	1440	Linear	[39]
Poly(HEMA)-CB microbeads	7.0	9.63	1440	Freundlich	This study

3.5. Thermodynamic parameters

Thermodynamic parameters play an important role in predicting the adsorption mechanism, whether it is a chemical or physical process. Thermodynamic parameters (i.e., enthalpy (ΔH°), the Gibbs free energy (ΔG°), and entropy (ΔS°)) explain the spontaneity and feasibility of an adsorption process, and are directly dependent on the equilibrium constant between two phases. Generally, the van't Hoff equation is used to determine the thermodynamic parameters:

$$\ln K = -\frac{\Delta H^\circ}{RT} + \frac{\Delta S^\circ}{R} \quad (8)$$

where R ($8.314 \text{ J mol}^{-1} \text{ K}^{-1}$) is the universal gas constant, and K is the equilibrium constant, and T (K) is the temperature.

The values of ΔG° (kJ mol^{-1}) were calculated from the K values for each temperature, and the values of ΔS° ($\text{kJ mol}^{-1} \text{ K}^{-1}$) and ΔH° (kJ mol^{-1}) were calculated from the intercept and slope of the plot of $\ln K$ versus $1/T$, respectively. ΔG° can be calculated as:

$$\Delta G^\circ = \Delta H^\circ - T\Delta S^\circ \quad (9)$$

From Eq. 9, ΔG° was calculated as $-11.069 \text{ kJ mol}^{-1}$, $-13.389 \text{ kJ mol}^{-1}$ and $-17.159 \text{ kJ mol}^{-1}$ at 277 K, 285 K and 298 K, respectively. The negative value of ΔG° indicates a spontaneous adsorption process. In addition, more negative values of ΔG° with increasing temperature suggest that the adsorption is more favorable at higher temperatures [40]. From the van't Hoff equation, ΔS° and ΔH° were calculated as $0.290 \text{ kJ mol}^{-1} \text{ K}^{-1}$ and $69.26 \text{ kJ mol}^{-1}$, respectively. These results indicate that the reaction is endothermic with an increased randomness of the adsorbent-liquid interface

during TC adsorption onto the active sites of poly(HEMA)-CB microbeads and that this adsorption process is possible and occurs spontaneously.

3.6. Desorption studies

Desorption studies indicate that KNO_3 :ethylene glycol (1:1; 1 M:10 %) mixture was more efficient than KNO_3 (1 M) solution or ethylene glycol (10 %, w/w %) solution in desorbing TC. The desorption efficiency of KNO_3 :ethylene glycol mixture, KNO_3 solution and ethylene glycol solution was calculated as 94.87 %, 78.38 %, and 55.55 %, respectively. To examine the reusability of the microbeads, five adsorption-desorption cycles were conducted, and it was found that the Q decreased from 9.63 mg g^{-1} to 8.97 mg g^{-1} (6.85 %) during an adsorption-desorption cycle. The results showed that the adsorbent can be used repeatedly without losing efficiency.

3.7. Comparison of poly(HEMA) and poly(HEMA)-CB microbeads

To examine the efficiency of TC adsorption onto CB-attached poly(HEMA) microbeads, TC adsorption experiments were performed with both of the microbeads. TC adsorption was performed for 24 h at 25°C with a total solution volume of 20 mL. According to the results, for a 50 mg L^{-1} initial TC concentration, the maximum adsorption capacities of TC on poly(HEMA) and poly(HEMA)-CB were calculated as 2.02 mg g^{-1} and 9.63 mg g^{-1} , respectively (Figure 8). Thus, the TC adsorption onto poly(HEMA)-CB is higher than the adsorption onto poly(HEMA). The higher adsorption of TC onto poly(HEMA)-CB can be based on the increased number of binding sites due to covalently attached CB.

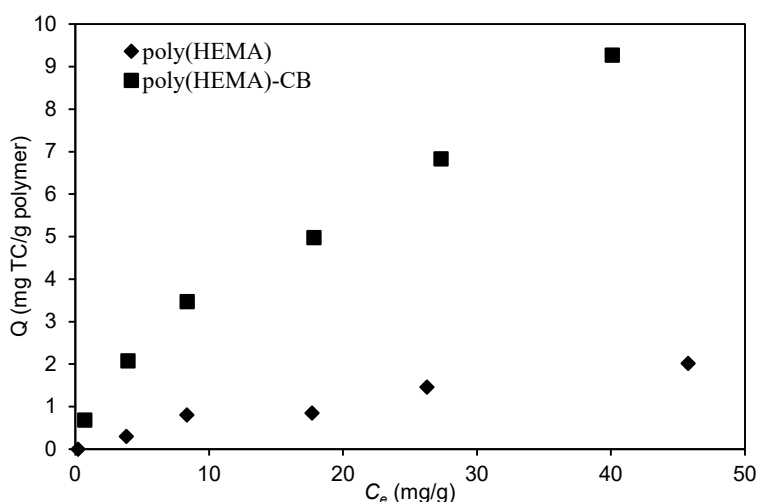


Figure 8. TC adsorption onto poly(HEMA) and poly(HEMA)-CB ($C_{\text{TC}} = 10 \text{ mg/L}$; $T = 25^\circ \text{C}$; $m_{\text{poly(HEMA)-CB}} = 0.02 \text{ g}$; $V = 20 \text{ mL}$)

4. Conclusion

Tetracycline is an important endocrine-disrupting chemical (EDC) and can be effectively removed from aquatic solutions or waste waters. Adsorption is an easy, low cost and attractive method for water treatment. The main goal of this study is to prepare an effective adsorbent for TC removal from aqueous solutions. Dye attached poly(HEMA) microbeads have good adsorption capacity for TC and they can be used repeatedly for five times without losing their efficiencies.

In this study, Cibacron Blue G3FA-attached poly(HEMA) microbeads were synthesized, characterized, and used as adsorbent for tetracycline adsorption from aqueous solution. The optimum pH value and temperature for the adsorption of TC were determined to be 7.0 and 25 °C, respectively. All adsorption experiments were performed at this optimum pH value and temperature. The maximum adsorption capacity (Q) of the poly(HEMA)-CB was determined to be 9.63 mg g⁻¹ at 25 °C. In addition, decreasing the temperature from 12 °C to 4 °C decreased Q by 5.16 mg g⁻¹ to 0.99 mg g⁻¹. Isotherm models such as Langmuir, Freundlich, and D-R models were used to represent the adsorption process. The mean values of the thermodynamic parameters of the standard entropy ($\Delta S^\circ = 0.29$ kJ mol⁻¹ K⁻¹), standard enthalpy ($\Delta H^\circ = 69.26$ kJ mol⁻¹) and standard free energy of the adsorption were determined. In conclusion, the CB-attached poly(HEMA) microbeads were used as adsorbents for TC, and the nature of the adsorption process was discussed.

Conflicts of interest

The authors state that they have no conflict of interests.

References

- [1] Li J., Han M., Guo Y., Wang F., Meng L., Mao D., Ding S., Sun C., Hydrothermal synthesis of novel flower-like BiVO₄/Bi₂Ti₂O₇ with superior photocatalytic activity toward tetracycline removal, *Appl. Catal. A-Gen.*, 524 (2016) 105-114.
- [2] Wang H., Yao H., Sun P., Pei J., Li D., Huang C., Oxidation of tetracycline antibiotics induced by Fe(III) ions without light irradiation, *Chemosphere.*, 119 (2015) 1255-1261.
- [3] Leng Y., Bao J., Chang G., Zheng H., Li X., Du J., Snow D., Li X., Biotransformation of tetracycline by a novel bacterial strain *Stenotrophomonas maltophilia* DT1, *J. Hazard. Mater.*, 318 (2016) 125-133.
- [4] Hu X., Zhou Q., Luo Y., Occurrence and source analysis of typical veterinary antibiotics in manure, soil, vegetables and groundwater from organic vegetable bases, northern China, *Environ. Pollut.*, 158 (2010) 2992-2998.
- [5] Li M.F., Liu Y.G., Zeng G.M., Liu S.B., Hu X.J., Shu D., Jiang L., Tan X., Cai X., Yan Z., Tetracycline absorbed onto nitrilotriacetic acid-functionalized magnetic graphene oxide: influencing factors and uptake mechanism, *J. Colloid Interface Sci.*, 485 (2017) 269-279.
- [6] Dong H., Jiang Z., Zhang C., Deng J., Hou K., Cheng Y., Zhang L., Zeng G., Removal of tetracycline by Fe/Ni bimetallic nanoparticles in aqueous solution, *J. Colloid Interface Sci.*, 513(1) (2018) 17-125.
- [7] Cetecioglu Z., Ince B., Gros M., Rodriguez-Mozaz S., Barcelo D., Orhon D., Ince O., Chronic impact of tetracycline on the biodegradation of an organic substrate mixture under anaerobic conditions, *Water Res.*, 47 (2013) 2959-2969.
- [8] Saitoh T., Shibata K., Fujimori K., Ohtani Y., Rapid removal of tetracycline antibiotics from water by coagulation-flotation of sodium dodecyl sulfate and poly(allylamine hydrochloride) in the presence of Al(III) ions, *Sep. Purif. Technol.*, 187 (2017) 76-83.
- [9] Belhouchet N., Hamdi B., Chenchouni H., Bessekhoud Y., Photocatalytic degradation of tetracycline antibiotic using new calcite/titania nanocomposites, *J. Photochem. Photobiol. A.*, 372 (2019) 196-205.
- [10] Wang J., Zhi D., Zhou H., He X., Zhang D., Evaluating tetracycline degradation pathway and intermediate toxicity during the electrochemical oxidation over a Ti/Ti₄O₇ anode, *Water Res.*, 137 (2018) 324-334.

- [11] Lv J., Ma Y., Chang X., Fan S., Removal and removing mechanism of tetracycline residue from aqueous solution by using Cu-13X, *Chem. Eng. J.*, 273 (2015) 247-25.
- [12] Liu M., Liu Y., Bao D., Zhu G., Yang G., Geng J., Li H., Effective removal of tetracycline antibiotics from water using hybrid carbon membranes, *Sci. Rep.*, 7 (2017) 43717.
- [13] Benavides J., Barrias P., Piro N., Arenas A., Orrego A., Pino E., Villegas L., Dorta E., Aspee A., Lopez-Alarcon C., Reaction of tetracycline with biologically relevant chloramines, *Spectrochim. Acta A Mol. Biomol. Spectrosc.*, 178 (2017) 171-180.
- [14] Saitoh T., Shibata K., Hiraide M., Rapid removal and photodegradation of tetracycline in water by surfactant-assisted coagulation-sedimentation method, *J. Environ. Chem. Eng.*, 2 (2014) 1852-1858.
- [15] Sun Q., Lu J., Wu J., Zhu G., Catalytic ozonation of sulfonamide, fluoroquinolone, and tetracycline antibiotics using nano-magnesium hydroxide from natural bischofite, *Water Air Soil Pollut.*, 230 (2019) 55-70.
- [16] Yu B., Bai Y., Ming Z., Yang H., Chen L., Hu X., Feng S., Yang S., Adsorption behaviors of tetracycline on magnetic graphene oxide sponge, *Mater. Chem. Phys.*, 198 (2017) 283-290.
- [17] Zhou Y., Zhang F., Tang L., Zhang J., Zeng G., Luo L., Simultaneous removal of atrazine and copper using polyacrylic acid-functionalized magnetic ordered mesoporous carbon from water: adsorption mechanism, *Sci. Rep.*, 7 (2017) 43831.
- [18] Yu Z., Zhang C., Zheng Z., Hu L., Li X., Yang Z., Ma C., Zeng G., Enhancing phosphate adsorption capacity of SDS-based magnetite by surface modification of citric acid, *App. Surf. Sci.*, 403 (2017) 413-425.
- [19] Yang X., Xu G., Yu H., Zhang Z., Preparation of ferric-activated sludge-based adsorbent from biological sludge for tetracycline removal, *Bioresour. Technol.*, 211 (2016) 566-573.
- [20] Ersan M., Bagda E., Bagda E., Investigation of kinetic and thermodynamic characteristics of removal of tetracycline with sponge like, tannin based cryogels, *Colloids Surf. B Biointerfaces.*, 104 (2013) 75-82.
- [21] Marzbali M.H., Esmaili M., Abolghasemi H., Marzbali M.H., Tetracycline adsorption by H₃PO₄-activated carbon produced from apricot nut shells: A batch study, *Process Saf. Environ.*, 102 (2016) 700.
- [22] Tian N., Tian X., Nie Y., Yang C., Zhou Z., Li Y., Biogenic manganese oxide: An efficient peroxymonosulfate activation catalyst for tetracycline and phenol degradation in water, *Chem. Eng. J.*, 352 (2018) 469-476.
- [23] Jia S., Yang Z., Yang W., Zhang T., Zhang S., Yang X., Dong Y., Wu J., Wang Y., Removal of Cu(II) and tetracycline using an aromatic rings-functionalized chitosan-based flocculant: Enhanced interaction between the flocculant and the antibiotic, *Chem. Eng. J.*, 283 (2016) 495-503.
- [24] Zhu J., Tian S., Polyacrylamide worked as adsorbents for tetracycline-polluted water treatment, *J. Nanoelectron. Optoelectron.*, 12 (2017) 1364-1368.
- [25] Percin I., Sener G., Demircelik A.H., Bereli N., Denizli A., Comparison of two different dye immobilized poly(hydroxyethyl methacrylate) cryogel discs for purification of lysozyme, *Appl. Biochem. Biotechnol.*, 175 (2015) 2795-2805.
- [26] Osman B., Cansev A., Cibacron Blue F3GA ile modifiye polimerik mikroküreler ile RuBisCO adsorpsiyonu, *BAUN Fen Bil. Enst. Dergisi.*, 23(2) (2021) 685-702.
- [27] Arica M.Y., Denizli A., Salih B., Pişkin E., Hasırcı V., Catalase adsorption onto Cibacron Blue F3GA and Fe(III) derivatized poly(hydroxyethyl methacrylate) membranes and application to a continuous system, *J. Membr. Sci.*, 129 (1997) 65-76.
- [28] Doğan A., Özkara S., Sarı M.M., Uzun L., Denizli A., Evaluation of human interferon adsorption performance of Cibacron Blue F3GA attached cryogels and interferon

- purification by using FPLC system, *J. Chromatogr. B.*, 893-894 (2012) 69-76.
- [29] Gu C., Karthikeyan K.G., Sibley S.D., Pedersen J.A., Complexation of the antibiotic tetracycline with humic acid, *Chemosphere.*, 66 (2007) 1494-1501.
- [30] Yu F., Ma J., Han S., Adsorption of tetracycline from aqueous solutions onto multi-walled carbon nanotubes with different oxygen contents, *Sci. Rep.*, 4 (2014) 1-8.
- [31] Kocakulak M., Denizli A., Rad A.Y., Pişkin E., New sorbent for bilirubin removal from human plasma: Cibacron Blue F3GA-immobilized poly(EGDMA-HEMA) microbeads, *J. Chromatogr. B Biomed. Sci. Appl.*, 693 (1997) 271-276.
- [32] Okoli C.P., Ofomaja A.E., Degree of time dependency of kinetic coefficient as a function of adsorbate concentration; new insights from adsorption of tetracycline onto monodispersed starch-stabilized magnetic nanocomposite, *J. Environ. Manage.*, 218 (2018) 139-147.
- [33] Langmuir I., The constitution and fundamental properties of solids and liquids, *J. Franklin Inst.*, 183 (1917) 102-105.
- [34] Freundlich H. Over the adsorption in solution, *J. Phys. Chem.*, A 57 (1906) 385-471.
- [35] Dubinin M.M., Radushkevich L.V. The equation of the characteristic curve of activated charcoal, *Dokl. Akad. Nauk. SSSR.*, 55 (1947) 331.
- [36] Oladoja N.A., Adelagun R.O.A., Ahmad A.L., Unuabonah E.I., Bello H.A., Preparation of magnetic, macro-reticulated cross-linked chitosan for tetracycline removal from aquatic systems, *Colloids Surf. B.*, 117 (2014) 51-59.
- [37] Chen Y., Wang F., Duan L., Yang H., Gao J., Tetracycline adsorption onto rice husk ash, an agricultural waste: Its kinetic and thermodynamic studies, *J. Mol. Liq.*, 222 (2016) 487-494.
- [38] Zhang P., Li Y., Cao Y., Han L., Characteristics of tetracycline adsorption by cow manure biochar prepared at different pyrolysis temperatures, *Bioresour. Technol.*, 285 (2019) 121348.
- [39] Yu F., Yang C., Huang G., Zhou T., Zhao Y., Ma J., Interfacial interaction between diverse microplastics and tetracycline by adsorption in an aqueous solution, *Sci. Total Environ.*, 721 (2020) 137729.
- [40] Umar Isah A., Abdulraheem G., Bala S., Muhammad S., Abdullahi M., Kinetics, equilibrium and thermodynamics studies of C.I. Reactive Blue 19 dye adsorption on coconut shell based activated carbon, *Int. Biodeterior. Biodegradation.*, 102 (2015) 265-273.

Synthesis of Benzimidazole derivatives containing Schiff base exhibiting antiurease activities

Gülay AKYÜZ^{1,*} 

¹ Recep Tayyip Erdoğan University, Faculty of Arts and Sciences, Department of Chemistry, Rize, TURKEY

Abstract

In this study some novel Schiff bases derivatives of benzimidazole containing thiophene ring were designed and synthesized by using various aldehydes. Seven different aromatic aldehydes with various side groups were used for synthesized. ¹H-NMR, ¹³C-NMR spectra and LC-MS were used to identify all of the compounds. All synthesized compounds anti urease activities were calculated according to phenol-hypochlorite method by Weatherburn. The results indicated that all compounds have anti urease activity between 12.70±0.11 µg/mL and 14.00±0.08 µg/mL IC₅₀ values. Especially the compound N'-[(1E)-2-furylmethylene]-2-[5,6-dimethyl-2-(2-thienylmethyl)-1H-benzimidazol-1-yl]acetohydrazide (5g) has very close IC₅₀ value (12.70±0.11 µg/mL) to thiourea (12.60±0.10 µg/mL) that is the standard inhibitor. 5g bearing furan ring at the N-3 position on the benzimidazole nucleus has the smallest volume of side group than others.

Article info

History:

Received: 25.01.2021

Accepted: 20.09.2021

Keywords:

Benzimidazole,
Schiff bases,
Antiurease,
Thiophene,
Weatherburn.

1. Introduction

Enzyme inhibition studies, which are important areas of pharmaceutical research, have already led to the discovery of wide variety of drugs useful in a number of diseases. Urease inhibitors are important to control the damaging effects of ureolytic bacterial infections in humans such as urinary stone formation, peptic ulcer and hepatic coma. Also, urease inhibitors have been regarded as targets for new antiulcer drugs [1,2]. Urease inhibitors have received special attention over the past few years because of their potential uses besides of using medicine. Controlling hydrolysis of urea in soil is crucial situation. Urease inhibitors protect soil from pH elevation [3]. These inhibitors, which are generally divided into two classes, substrate structural analogs like hydroxamic acid and those which affect the mechanism of the reaction like phosphoramidat, lansoprazole, omeprazole, thiol-compounds, quinines and Schiff base derivatives are reported as potent urease inhibitors [4]. In our recent studies we have investigated Schiff base derivatives, which were most active inhibitors of Jack bean urease [5,6].

Benzimidazoles are significant heterocyclic compounds because of their structurally similarity to purine and its derivatives, proteins inside the bacterial

cell wall and it is the basic part of the structure of vitamin B₁₂. [7] Also, benzimidazoles have a wide range of biological activities including antioxidant [8], anticancer, antimicrobial [9], antihistaminic, antiinflammatory [10], enzyme inhibitions [11,12] and they have an important role in the field of medicine. A condensation reaction between aldehydes or ketones with primary amines in alcoholic conditions form Schiff bases. Aromatic-based Schiff bases have many advantages and show more potential in biological applications as a result of the free electron delocalization with the ring structure. They are very significant class of organic compounds that show interest in industrial sectors with many biological and pharmaceutical applications [13]. The heterocyclic compounds such as imidazole and benzimidazole and also thiophene ring have most predominant heteroatoms which are mainly nitrogen, oxygen, and sulfur (N, O, S). Also, they are important class of pharmacophores and they are well known as drugs [14,15].

The present study covers the synthesis of novel benzimidazoles containing thiophene ring linked with Schiff base and their evaluation as urease inhibitors.

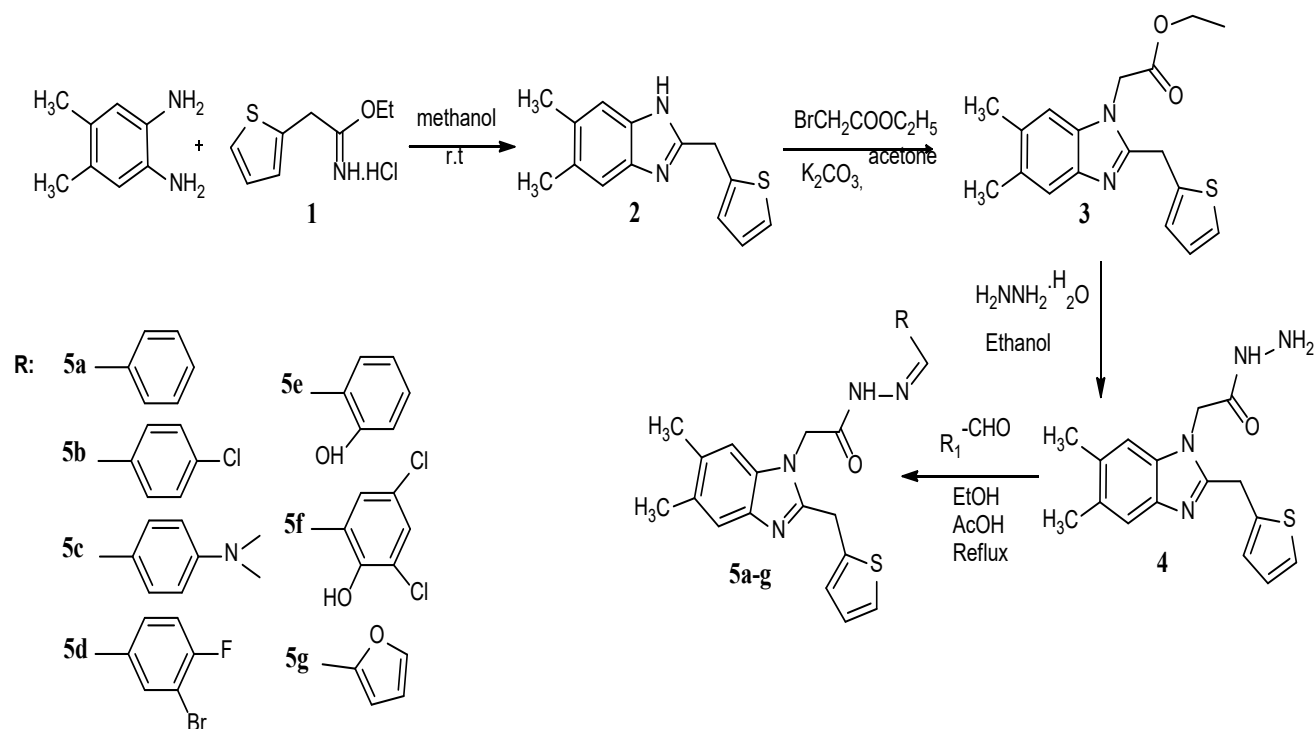
*Corresponding author. e-mail address: gulay.candan@erdogan.edu.tr
<http://dergipark.gov.tr/csj> ©2021 Faculty of Science, Sivas Cumhuriyet University

2. Results and Discussion

2.1. Chemistry

I have synthesized seven new Schiff bases based of benzimidazole. Synthesis scheme of all target compounds is shown in Scheme 1. Firstly, iminoester

hydrochloride (**1**) was prepared according to the procedure [16]. Compound **1** was added to the solution of 4,5-dimethyl-1,2-phenylenediamine in methanol and refluxed. The starting benzimidazole (**2**) was reacted with ethyl bromoacetate in acetone with K_2CO_3 to synthesize ethyl[5,6-dimethyl-2-(thiophen-2-ylmethyl)-1H-benzimidazol-1-yl]acetate (**3**).



Scheme 1. The synthetic way of the target compounds

Ethyl [5,6-dimethyl-2-(thiophen-2-ylmethyl)-1H-benzimidazol-1-yl]acetate (**3**) reacted with hydrazine hydrate in pure ethanol gave benzimidazole derivative of hydrazide compound **4**. After this stage, hydrazide (**4**) was treated with seven different aromatic aldehydes catalysed with AcOH in ethanol to synthesize Schiff bases (**5a-g**). The structures of all these compounds were identified by Infrared (IR), Proton and Carbon Nuclear Magnetic Resonance data and Mass spectra. All data of compounds are compatible with each other. IR spectra gave NH bands from benzimidazoles of these compounds between 3187 and 3407 cm^{-1} , C=O band between 1656 and 1706 cm^{-1} and C=N band between 1521 and 1600 cm^{-1} . Proton NMR spectra of Schiff bases (**5a-f**) gave the correct signals with proposed structures. NH signals are appeared at about 11.43 - 11.86 ppm with different cis/trans conformer ratios. NCH_2 signals are between 5.14 and 5.44 ppm.

There are two $-CH_3$ signals in spectrum from benzimidazole ring. C=N signals of benzimidazoles are at about 152.64 ppm in carbon NMR spectra for all compounds. The imine carbon atoms from Schiff bases (**5a-g**) are resonated at 149.11 (for **5a**), 150.32 (for **5b**), 149.06 (for **5c**), 152.79 ppm (for **5d**), 151.26 (for **5f**), 149.41 (for **5g**) in the ^{13}C -NMR spectrum.

2.2. Urease inhibitory assay

Urease inhibition studies of new compounds were calculated according to Phenol-hypochlorite method by Weatherburn (1967) [17]. All of the compounds and thiourea were dissolved in DMSO and screened at $20\text{ }\mu\text{g/mL}$ final concentration. Schiff bases showed inhibitor activity at low final concentrations. Thiourea was used as positive control. In this study lower IC_{50} values of compounds display higher enzyme inhibitory effectiveness.

Table 1: The new Schiff Bases Chemical Structures and IC₅₀ values

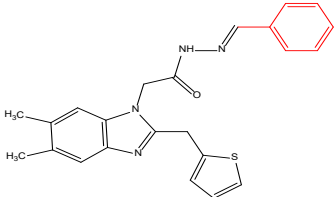
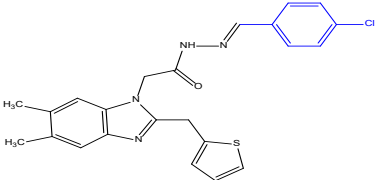
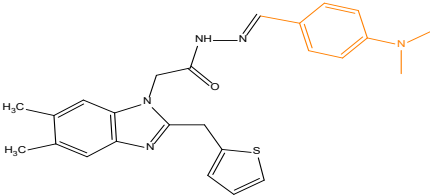
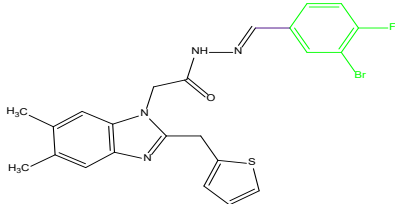
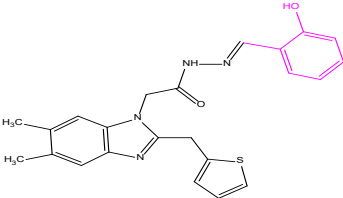
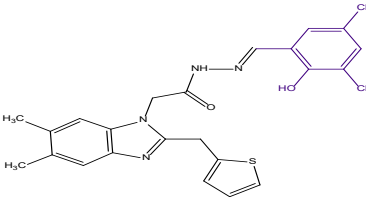
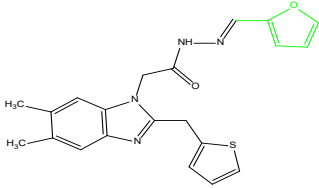
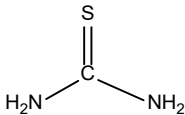
Compounds	Chemical Structure	IC ₅₀ (µg/mL)
5a		12.79±0.10 µg/mL
5b		12.80±0.08 µg/mL
5c		13.50±0.12 µg/mL
5d		14.00±0.08 µg/mL
5e		13.12±0.09 µg/mL
5f		13.60±0.06 µg/mL
5g		12.70±0.11 µg/mL
Thiourea		12.60±0.10 µg/mL

Table 1 shows IC₅₀ values of compounds and the standard at 20 µg/mL final concentrations. All Schiff bases have anti urease activity between 12.70±0.11 and 14.00±0.08 µg/mL values. **5g** has the best inhibition activity with IC₅₀: 12.70±0.11 µg/mL. **5g** bearing furan ring at the N-3 position on the benzimidazole nucleus. The results show that antiurease activity decreases with increased volume of side groups.

3. Experimental

3.1. Synthesis of compound 2

0.2 g (0.010 mol) iminoester hydrochloride (1) was added to the solution of 0.13 g 4,5-dimethyl-1,2-phenylenediamine (1 mmol) in 40 ml dry methanol. The mixture was stirred about an hour and then refluxed at about 2h. When the reaction completed controlled by TLC, the balloon was cooled until room temperature. Water was added to the mixture to precipitate the product. White compound was filtrated and recrystallized from ethanol.

3.1.1. 5,6-Dimethyl -2- (thiophen-2-ylmethyl) -1H-benzimidazole (2)

Yield 83%, mp: 147-149°C, IR (ν_{\max} , cm⁻¹): 3250 (NH), 1500 (C=N). ¹H-NMR (400 MHz, DMSO-d₆): 1.17 (t, J= 6.8 Hz, 3H, CH₃), 4.40 (s, 2H, CH₂), 6.80–7.45 (m, 5H, ArH) and 12.08 (s, 1H, NH). ¹³C-NMR (100 MHz, DMSO-d₆): 20.36 (CH₃), 29.77 (CH₂), 125.32, 126.62, 126.40, 127.32, 130.07, 140.17 (Ar-C) and 152.11 (C=N). LC-MS, m/z: 242.98 [M+H]⁺.

3.2. Synthesis of compound 3

2.42 g compound 1 (0.010 mol) in 10 mL of acetone and 3.45 g K₂CO₃ (0.025 mol) was stirred at room temperature for 1h in a balloon. Ethyl bromoacetate (0.011 mol) was added into the mixture and stirred at room temperature for further 8h. The mixture was poured into water and the white solid was filtered off and recrystallized from a solution of ethanol:water (1:3).

3.2.1. Ethyl [5,6-dimethyl-2-(thiophen-2-ylmethyl)-1H-benzimidazol-1-yl]acetate (3): Yield 90%, mp: 114-116 °C, IR (ν_{\max} , cm⁻¹): 1738 (C=O), 1515 (C=N). ¹H-NMR (400 MHz, DMSO-d₆): 1.12 (t, 3H, J= 7.2 Hz, CH₃), 4.02 (m, 2H, OCH₂), 4.41 (s, 2H, CH₂), 5.08 (s, 2H, NCH₂), 6.92 (t, J= 7.2 Hz, 3H, ArH), 7.19 (s, 1H, ArH), 7.35 (d, J=7.2 Hz 1H, ArH). ¹³C-NMR (100 MHz, DMSO-d₆): 14.38 (CH₃), 20.27 (CH₃), 20.51 (CH₃), 28.03 (CH₂), 44.92 (NCH₂), 61.55 (OCH₂), ArC [110.65, 119.30, 125.69, 126.65, 130.31, 131.07, 134.60, 139.15, 140.99], 152.39 (C=N) and 168.24 (C=O). LC-MS, m/z: 328.94 [M+H]⁺.

3.3. Synthesis of compound 4

To a solution of compound 2 (3.28 g, 0.010 mol) in 10 mL of ethanol, hydrazine monohydrate (0.035 mol) was added and the mixture was stirred for 4h. The reaction was scanned by TLC (ethanol:ethyl acetate, 3:1). The mixture was filtered off, dried and recrystallized.

3.3.1. 2-[5,6-Dimethyl-2-(thiophen-2-ylmethyl)-1H-benzimidazol-1-yl]acetohydrazide (4)

Yield 85%, mp: 237-239 °C. IR (ν_{\max} , cm⁻¹): 3379-3165 (NH-NH₂), 1663 (C=O), 1518 (CN). ¹H-NMR (400 MHz, DMSO-d₆): 9.45 (s, 1H, NH), 7.86 (m, 2H, ArH), 7.17 (s, 1H, ArH), 6.94 (m, 3H, ArH), 4.72 (s, 2H, NCH₂), 4.42 (s, 2H, NH₂), 4.02 (s, 2H, CH₂). ¹³C-NMR (100 MHz, DMSO-d₆): 20.29, 20.57 (CH₃), 28.15 (CH₂), 44.86 (NCH₂), ArC [110.59, 119.27, 125.55, 126.61, 127.18, 130.13, 134.52, 139.34, 141.08], 152.71 (C=N), 166.41 (C=O), 170.59 (C-S). LC-MS, m/z: 314.94 [M+H]⁺.

3.4. Synthesis of compounds 5a–g.

About ten mmol of aromatic aldehyde was added to the solution of compound 3 (3.14 g, 10 mmol) in 15 mL dry ethanol and containing 0.5 mL of glacial acetic acid. The mixture was then refluxed for 5h and the reaction was viewed by TLC. Then, the mixture was cooled to room temperature, and a white solid was precipitated. The product was filtrated, washed with water, and recrystallized from ethanol to obtain pure compounds **5a–g**.

3.4.1. 2-[5,6-Dimethyl-2-(2-thienylmethyl)-1H-benzimidazol-1-yl]-N'-[(1E)-phenylmethylene]acetohydrazide (5a)

Yield: 90%, mp: 217–219°C. IR (ν_{\max} , cm⁻¹): 3187 (NH), 1700 (C=O), 1521 (C=N) cm⁻¹. ¹H-NMR (400 MHz, DMSO-d₆): 1.10 (3H, t, J=8.0 Hz, CH₃), 4.46 (2H, s, CH₂), 5.44 (2H, s, NCH₂), 6.94 (1H, s, ArH), 7.27 (1H, s, ArH), 7.36–7.52 (3H, m, ArH), 7.79 (2H, d, J=8.0 Hz, ArH), 8.31 (1H, s, CH), 11.85 (1H, s, NH). ¹³C-NMR (100 MHz, DMSO-d₆): 20.28, 20.44 (CH₃), 27.83 (CH₂), 44.88 (NCH₂), ArC:[111.12, 118.51, 125.79, 126.87, 127.21, 129.13, 129.20, 129.33, 133.41, 134.92, 138.64, 143.29, 146.67], 149.11 (C=N, Schiff base), 152.64 (C=N, benzimidazole), 168.34 (C=O). LC-MS, m/z: 242.98 [M+H]⁺. LC-MS, m/z: 403.05 [M+H]⁺. Cal: 402.51 [M⁺].

3.4.2. *N'*-[(1*E*)-(4-chlorophenyl)methylene]-2-[5,6-dimethyl-2-(2-thienylmethyl)-1*H*-benzimidazol-1-yl]acetohydrazide (5b)

Yield: 90%, mp: 114–116 °C. IR (ν_{\max} , cm^{-1}): 3207 (NH), 1697 (C=O), 1608 (C=N). $^1\text{H-NMR}$ (400 MHz, DMSO- d_6): 1.12 (3H, t, $J=8.2$ Hz, CH_3), 4.48 (2H, s, CH_2), 5.44 (2H, s, NCH_2), 6.92–7.27 (3H, m, ArH), 7.37 (1H, s, ArH), 7.52 (1H, d, $J=8.0$ Hz, ArH), 7.71 (2H, d, $J=8.0$ Hz, ArH), 7.78 (1H, d, $J=8.0$ Hz, ArH), 8.32 (1H, s, CH), 11.85 (1H, s, NH). $^{13}\text{C-NMR}$ (100 MHz, DMSO- d_6): 20.28, 20.43 (CH_3), 27.82 (CH_2), 44.87 (NCH_2), ArC: [111.10, 118.49, 125.79, 126.87, 127.21, 129.13, 129.32, 130.85, 131.50, 134.40, 134.92, 135.08, 138.86, 143.31, 146.68], 150.32 (C=N, Schiff base), 152.63 (C=N, benzimidazole), 168.32 (C=O). LC-MS, m/z : 437.00 [$\text{M}+\text{H}$] $^+$. Cal: 436.96 [M^+].

3.4.3. *N'*-[(1*E*)-4-(dimethylamino) phenyl methylene] -2-[5,6-dimethyl -2-(2-thienylmethyl) -1*H*- benzimidazol-1-yl]acetohydrazide (5c)

Yield: 92%, mp: 199–200 °C. IR (ν_{\max} , cm^{-1}): 3190 (NH), 3024 (ArCH), 1656 (C=O), 1597 (C=N) cm^{-1} . $^1\text{H-NMR}$ (400 MHz, DMSO- d_6): 1.18 (3H, t, $J=8$ Hz, CH_3), 4.44 (2H, s, CH_2) and 5.31 (2H, s, NCH_2), 6.70 (2H, t, $J=8$ Hz, ArH), 6.92 (1H, s, ArH), 7.19 (1H, s, ArH), 7.25 (1H, s, ArH), 7.34 (1H, s, ArH), 7.49–7.52 (2H, m, ArH), 7.93 (1H, s, CH), 11.43 (1H, s, NH). $^{13}\text{C-NMR}$ (100 MHz, DMSO- d_6): 20.25, 20.41, 20.48 (CH_3), 40.19 (N-CH_3), 44.65 (CH_2) and 45.28 (NCH_2), ArC: [110.91, 112.16, 118.76, 121.61, 125.70, 126.74, 127.27, 128.79, 129.02, 130.70, 131.37, 134.34, 134.68, 138.96, 140.25, 145.74], 149.06 (C=N, Schiff base), 152.05 (C=N, benzimidazole), 167.70 (C=O). LC-MS, m/z : 446.10 [$\text{M}+\text{H}$] $^+$. Cal: 445.58 [M^+].

3.4.4. *N'*- [(1*E*) - (3-bromo - 4- fluorophenyl) methylene] -2- [5,6-dimethyl -2- (2-thienylmethyl) -1*H*- benzimidazol -1 -yl]acetohydrazide (5d)

Yield: 93%, mp: 258–260 °C. IR (ν_{\max} , cm^{-1}): 3407 (NH), 3094 (ArCH), 1707 (C=O), 1609, 1540 (C=N) cm^{-1} . $^1\text{H-NMR}$ (400 MHz, DMSO- d_6), δ , ppm: 1.05 (3H, s, CH_3), 4.40 (2H, s, CH_2), 5.42 (2H, s, NCH_2), 6.93 (s, 2H, ArH), 7.20–7.45 (3H, m, Ar-H), 7.79 (1H, s, Ar-H), 8.01 (1H, s, N=CH), 8.14 (1H, s, ArH), 11.81 (1H, s, NH). $^{13}\text{C-NMR}$ (100 MHz, DMSO- d_6): 20.29, 28.18 (CH_3), 44.68 (CH_2), 45.75 (NCH_2), ArC: [109.37, 110.79, 117.48, 119.18, 125.55, 126.60, 127.10, 129.06, 129.98, 130.75, 131.87, 132.82, 135.03, 139.32, 141.11, 141.86], 152.79 (C=N, Schiff base), 158.18 (Benzimidazole, C=N), 160.66 (C-F, d, $J_{\text{CF}} = 247$ Hz), 168.76 (C=O). LC-MS, m/z : 500.00 [$\text{M}+\text{H}$] $^+$. Cal M^+ : 499.40 [M^+].

3.4.5. *N'*-[(1*E*)-(2-hydroxyphenyl)methylene]-2-[5,6-dimethyl-2-(2-thienylmethyl)-1*H*-benzimidazol-1-yl]acetohydrazide (5e):

Yield: 89%, mp: 200–202 °C. IR (ν_{\max} , cm^{-1}): 3397 (NH), 1698 (C=O), 1606, 1548 (C=N) cm^{-1} . $^1\text{H-NMR}$ (400 MHz, DMSO- d_6): 1.20 (3H, t, $J=7.2$ Hz, CH_3), 4.34 (2H, s, CH_2), 5.14 (2H, s, NCH_2), 6.91 (s, 2H, ArH), 7.20–7.34 (3H, m, Ar-H), 7.75 (1H, s, Ar-H), 8.36 (1H, s, N=CH), 8.56 (1H, s, ArH), 10.23 (1H, s, OH), 11.71 (1H, s, NH). $^{13}\text{C-NMR}$ (100 MHz, DMSO- d_6): 21.29, 30.18 (CH_3), 44.62 (CH_2), 45.75 (NCH_2), ArC: [110.62, 119.36, 122.05, 124.40, 126.66, 127.68, 128.07, 128.76, 129.16, 130.32, 130.75, 131.04, 134.66, 135.02, 139.30, 141.07], 147.19, 151.26 (C=N, Schiff base), 152.72 (Benzimidazole, C=N), 164.01, 168.50 (C=O). LC-MS, m/z : 418.94 [$\text{M}+\text{H}$] $^+$. Cal: 418.51 [M^+].

3.4.6. *N'*-[(1*E*) - (3,5-dichloro-2-hydroxyphenyl) methylene]-2-[5,6-dimethyl-2-(2-thienylmethyl)-1*H*-benzimidazol-1-yl]acetohydrazide (5f)

Yield: 95%, mp: 278–280 °C. IR (ν_{\max} , cm^{-1}): 3076 (NH), 1706 (C=O), 1479 (C=N) cm^{-1} . $^1\text{H-NMR}$ (400 MHz, DMSO- d_6): 1.12 (3H, t, $J=8.0$ Hz, CH_3), 4.44 (2H, s, CH_2), 5.44 (2H, s, NCH_2), 6.90–6.98 (m, 2H, ArH), 7.35 (1H, d, $J=8.0$ Hz, ArH), 7.23 (1H, d, $J=8.0$ Hz, ArH), 7.79 (1H, s, Ar-H), 8.29 (1H, s, N=CH), 8.39 (1H, s, ArH), 10.33 (1H, s, OH), 11.86 (1H, s, NH). $^{13}\text{C-NMR}$ (100 MHz, DMSO- d_6): 20.29, 28.18 (CH_3), 44.68 (CH_2), 45.75 (NCH_2), ArC: [110.62, 119.34, 123.05, 124.40, 125.54, 126.68, 127.07, 128.76, 130.00, 130.32, 130.75, 131.04, 134.66, 135.02, 139.30, 141.07], 147.19, 151.26 (C=N, Schiff base), 152.72 (Benzimidazole, C=N), 164.01, 168.50 (C=O). LC-MS, m/z : 486.98 [$\text{M}+\text{H}$] $^+$. 487.40 [M^+].

3.4.7. *N'*-[(1*E*) -2-furylmethylene] -2- [5,6-dimethyl -2- (2-thienylmethyl) - 1*H* - benzimidazol -1- yl] acetohydrazide (5g)

Yield: 82%, mp: 208–210 °C. IR (ν_{\max} , cm^{-1}): 3087 (NH), 1702 (C=O), 1509 (C=N) cm^{-1} . $^1\text{H-NMR}$ (400 MHz, DMSO- d_6): 1.04, (3H, s, CH_3), 4.40 (2H, s, CH_2), 5.28 (2H, s, NCH_2), 6.61–6.93 (m, 3H, ArH), 7.19, (1H, s, ArH), 7.34 (1H, s, ArH), 7.92 (2H, t, ArH), 8.11(1H, s, ArH), 11.66 (1H, s, NH). $^{13}\text{C-NMR}$ (100 MHz, DMSO- d_6): 19.00, 20.27 (CH_3), 44.56 (CH_2), 56.47 (NCH_2), ArC: [110.62, 112.64, 114.37, 119.15, 125.56, 126.57, 127.12, 130.05, 130.86, 134.67, 134.93, 137.79, 139.33, 141.05, 145.59], 149.41 (C=N, Schiff base), 152.79 (Benzimidazole, C=N), 163.57, 168.26 (C=O). LC-MS, m/z : 392.97 [$\text{M}+\text{H}$] $^+$. Cal: 392.47 [M^+].

3.5. Antiurease activity assay

Urease enzyme inhibition studies were performed according to the method developed by Weatherburn (1967) in the literature [17]. Phenol-hypochlorite method based on enzyme substrat interaction resulting ammonium ion. Reaction mixtures including 400 μ L of buffer at pH 8.2 (100 mM urea, 0.01 M K_2HPO_4 , 1 mM EDTA and 0.01 M LiCl), 200 μ L of Jack Bean Urease and 100 μ L of the test compound solution in DMSO were incubated at room temperature for 15 min. 650 μ L phenol reagent (1% w/v phenol and 0.005% w/v sodium nitroprusside) and 650 μ L alkali reagent (0.5% w/v sodium hydroxide and 0.1% v/v NaOCl) were added to each tube and the increasing absorbance at 625 nm with blue-navy colour was measured after 50 min, using a UV/vis spectrophotometer. Jack bean urease was used as model enzyme. Thiourea was used as positive control. Different concentrations of inhibitory compounds were used and IC_{50} values were calculated.

The percentage inhibition was calculated using the following equation $100 - \frac{OD_{test}}{OD_{control}} \times 100$.

4. Conclusions

I designed and synthesized new Schiff bases containing thiophene ring and derivatives of benzimidazoles. I used seven different aromatic aldehydes with several side groups. Schiff bases synthesized with high efficiency and their chemical structures were confirmed by spectral methods. Their urease inhibition activities were evaluated using Phenol-hypochlorite method by Weatherburn and compared to the standard inhibitor thiourea. Results indicate that all synthesized Schiff bases have antiurease activity and especially compound N'-[(1E)-2-furylmethylene]-2-[5,6-dimethyl-2-(2-thienylmethyl)-1H-benzimidazol-1-yl]acetohydrazide has the best IC_{50} value that is bearing furan ring at the N-3 position on the benzimidazole nucleus, which has the smallest volume of side group than others.

Conflicts of interest

The authors state that did not have conflict of interests

References:

- [1] Akyüz G., Mentese E., Emirik M., Baltaş N., Synthesis and molecular docking study of some novel 2,3-disubstituted quinazolin-4(3H)-one derivatives as potent inhibitors of urease, *Bioorganic Chemistry*, 80 (2018) 121-128.
- [2] Amtul A.Z., Rahman A., Siddiqui R.A., Choudhary M.I., Chemistry and mechanism of urease inhibition, *Curr. Med. Chem.*, 9 (2002) 1323-1348.
- [3] Upadhyay L.S.B., Urease Inhibitors: A review, *Indian Journal of Biotechnology*, 11 (2012) 381-388.
- [4] Mumtaz A., Arshad J., Saeed A., Nawaz M., Iqbal J., Synthesis, characterization and urease inhibition studies of transition metal complexes of thioureas bearing ibuprofen moiety, *J. Chil. Chem. Soc.*, 63(2) (2018) 3934-3940.
- [5] Akyüz G., Mentese E., Emirik M., Baltaş N., Synthesis and molecular docking study of some novel 2,3-disubstituted quinazolin-4(3H)-one derivatives as potent inhibitors of urease, *Bioorganic Chemistry*, 80 (2018) 121-128.
- [6] Mentese E., Akyüz G., Yılmaz F., Baltaş N., Emirik M., Synthesis of some novel quinazolin-4(3H)-one hybrid molecules as potent urease inhibitors, *Arch pharm.*, 351(12) (2018)180-182.
- [7] Mentese E., Yılmaz F., Emirik M., Ülker S., Kahveci B. Synthesis, molecular docking and biological evaluation of some benzimidazole derivatives as potent pancreatic lipase inhibitors, *Bioorganic Chemistry*, 76 (2018) 478-486.
- [8] Usta A., Yılmaz F., Kapucu G., Baltaş N., Mentese E., Synthesis of some new benzimidazole derivatives with their antioxidant activities, *Letters in Organic Chemistry*, 12 (4) (2015) 227-232.
- [9] Palit R., Kumar R., Saraswat N., Wal A., Upadhyaya K., Benzimidazole: an overview, *Int. J. Res. Ayurveda Pharm.*, 7(6) (2016) 68-73.
- [10] Mentese E., Yılmaz F., Mutlu F., Kahveci B., Synthesis of new coumarin containing benzimidazole derivatives, *Journal of Chemical Research*, (39) (2015) 645-648.
- [11] Mentese E., Yılmaz F., Emirik M., Ulker S., Kahveci B., Synthesis, molecular docking and biological evaluation of some benzimidazole derivatives as potent pancreatic lipase inhibitors, *Bioorganic Chemistry*, 76 (2018) 478-486.

- [12] Baltas N., Yılmaz F., Mentese E., Synthesis, antioxidant, xanthine oxidase and urease inhibitory activities of some chlorine containing benzimidazoles, *J. Biol. Chem.*, 44 (3) (2016) 293-305.
- [13] Kajal A., Bala S., Kamboj S., Schiff bases: a versatile pharmacophore, *J. Catal.*, (2013) 1–14.
- [14] Fonkui T.Y., Ikhile M.I., Njobech P.B., Ndintech D.T., Benzimidazole Schiff base derivatives: synthesis, characterization and antimicrobial activity, *BMC Chemistry*, 13 (2019) 127.
- [15] Mentese E., Yılmaz F., Baltaş N., Bekircan O., Kahveci B., Synthesis and antioxidant activities of some new triheterocyclic compounds containing benzimidazole, thiophene, and 1,2,4-triazole rings, *J. Enzyme Inhib. Med. Chem.*, 30(3) (2015) 435-41.
- [16] Pinner A., Die Imidoäther und ihre Derivate, 1 Auflage, Oppenheim: Berlin, (1892).
- [17] M.W. Weatherburn. Phenol-hypochlorite reaction for determination of ammonia, *Anal. Chem.*, 39 (1967) 971- 974.



Molecular docking studies of N-Heterocyclic Carbene molecules with Thioredoxin Reductase and DNA

Elvan ÜSTÜN^{1,*} , Neslihan ŞAHİN²

¹ Ordu University, Faculty of Art and Science, Department of Chemistry, 52200, Ordu, TURKEY

² Cumhuriyet University, Faculty of Education, Department of Basic Education, 58140, Sivas, TURKEY

Abstract

Thioredoxin which is induced by thioredoxin reductase causes the proliferation of cancerous cells and metastasis due to its effects on cell growth, besides its regulatory effects on the amount of reactive oxygen species. One of the procedures recently used in cancer treatment is thioredoxin reductase inhibition. Different types of bioactivities of NHC and metal-NHC complexes have been studied and anti-cancer is one of these activities. In addition to in-vitro anticancer activity, molecular docking methods are also one of the important methods used in drug design. This method achieves foresight about future studies and the mechanisms that are difficult to analyze experimentally. In this study, previously synthesized and characterized [1-(2-methyl-2-propenyl)-3-(4-methylbenzyl) benzimidazolium]⁺ (1a) and [1-(2-methyl-2-propenyl)-3-(4-isopropylbenzyl) benzimidazolium]⁺ (1b) molecules and their Ag(I)-NHC complexes (2a and 2b) were investigated using molecular docking method for thioredoxin reductase. In addition, the interaction of these molecules with DNA was evaluated. 2b has the best binding energy of -8.95 kcal/mol with the region that comprised Ile10, Phe254, Ala38, Val41 of thioredoxin reductase. Also, ligands interacted with Cyt11, Gua10, Cyt9, and Thy8 while complexes interacted with Ade5, Ade6, Thy7, and Thy8 part of DNA.

Article info

History:

Received: 23.03.2021

Accepted: 06.09.2021

Keywords:

Molecular Docking,
N-Heterocyclic
Carbene,
TrxR.

1. Introduction

Cancer is one of the highly fatal diseases in the world [1]. One of the most important causes of cancer is oxidative stress [2]. It is known that cellular metabolisms produce Reactive Oxygen Species (ROS). The amount of ROS is important in many cellular processes such as gene expression and cell proliferation [3]. High ROS level lead degradation in some components such as proteins, lipids, nucleic acids, and even cell death in later stages. The formation of ROS and their scavenging by intracellular antioxidant systems must be in balanced for healthy cells. In cancerous cells, a ROS level increment is observed due to abrupt proliferation and high metabolic rate [4]. The conditions in which the ROS level increases dramatically is called oxidative stress [5].

The Thioredoxin (Trx) system contains the redox-active protein Thioredoxin, Thioredoxin Reductase (TrxR) enzyme, and NADPH [6]. The Trx system plays an important role in many cellular functions such as redox control of transcription factors, synthesis of deoxyribonucleotides, cell growth, and protection

against oxidative stress [7]. Trxs are small proteins conserved in all species, from bacteria to humans. All Trxs contain redox-active sites that reduce disulfides in proteins and peptides [8]. Reduced Trx catalyzes the reduction of ROS in many intracellular and extracellular proteins and oxidizes in this process. TrxR is required for oxidation of Trx [9]. Since cancer cells generally lead to high oxidative stress, the expression of antioxidant proteins such as Trx is increased [10]. It has been noted that Trx expression increases in many cancer types such as lung, pancreatic, colorectal, and breast cancer [11]. However, overexpression of thioredoxin due to oxidative stress gives rise to the growth of cancer cells, metastasis, and resistance to chemotherapeutic agents [12]. So Trx can be considered a potential target in cancer and the inhibition of TrxR could be a good strategy for treatment. Because Trx system can be regulated by the inhibition of TrxR, some synthetic TrxR inhibitors have reached the clinical test stage while some of them have received FDA approval for cancer treatment. For example, arsenic trioxide is used in the treatment of leukemia. This molecule irreversibly inhibits TrxR, and it is also recorded that

*Corresponding author. e-mail address: elvanustun77@gmail.com

this inhibition is efficient in MCF-7 breast cancer [13]. Curcumin is a recent well-known anti-cancer agent, and it has been determined that the detected activity of this molecule is emerged from TrxR inhibition [14]. Further studies are still needed to resolve the effects of the thioredoxin system and TrxR inhibition in cancer treatment. The studies must be focused on both elucidating the thioredoxin system and synthesizing more effective TrxR inhibitors [15].

NHCs are known as easily synthesized and modified molecules [16]. These molecules which are known for their catalytic activity have remarkable results in many bioactivity researches [17]. Many metal-NHC complexes have been synthesized and analyzed after the usage of metal complexes in treatment procedures

[18]. Besides the many known activities of metal-NHC complexes, good results have been obtained from anticancer studies especially for Au-NHC and also Ag-NHC [19,20]. Therefore, evaluation of the interaction of Ag(I)-NHC complexes with TrxR for analysis of the anticancer activity seems as a reasonable strategy. In this study, previously synthesized and characterized [1-(2-methyl-2-propenyl)-3-(4-methylbenzyl)benzimidazolium]⁺ (**1a**) and [1-(2-methyl-2-propenyl)-3-(4-isopropylbenzyl)benzimidazolium]⁺ (**1b**) molecules [21] and their Ag(I) complexes (**2a** and **2b**) (Figure 1) were investigated using molecular docking method for TrxR. In addition, the interaction of these molecules with DNA was evaluated.

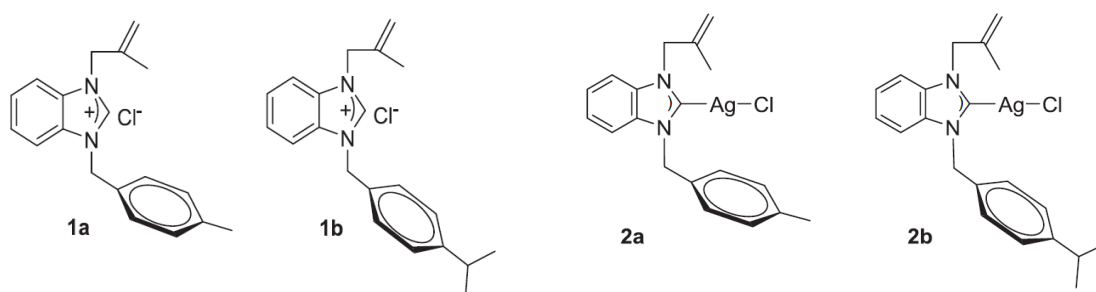


Figure 1. Alkyl substituted allyl benzimidazolium molecules and their Ag(I)-NHC complexes

2. DFT Optimization and Molecular Docking Method

Before the molecular docking process, molecules are optimized with ORCA package program. ORCA version 2.8 using the BP86 functional were used for DFT-based calculations, with a def2-SVP def2-SVP/j basis set for ligand and complexes. Also, grid4, and tightscf options were used for geometry optimizations [22,23]. Molecular docking was performed using AutoDock 4.2. with the crystal structure of thioredoxin reductase (PDB id: 4CBQ) [24] and DNA dodecamer (PDB id: 1BNA) [25] from RCSB protein data bank [26]. Water in the proteins was removed and polar hydrogen atoms and Kollman charges were evaluated for target molecules in the docking process. Gasteiger charges, randomized starting positions, optimizations, and torsions have been evaluated for ligand molecules. The genetic algorithm population was used as 150 while applying Lamarkian genetic algorithms [27]. The spacing values of the **1a** and **2a** were used as 0.375 and npts are 68-58-54 against for TrxR docking. Additionally, the molecular dockings were performed

with 0.375 spacing and 46-46-54 npts values for **2a** and **2b**. In DNA docking performance all the crystal structure were scanned.

3. Results and Discussion

In a healthy person, the body has a perfect balance, and the disease could actually be considered as an imbalance in the body. The type of imbalance determines the type of the disease. The body has mechanisms that work to reconstruct the balance [28-30]. Cancer is still one of the most fatal diseases in the world. The most important cause of cancer is the imperfection of the balance of ROS in the body [31]. The increasing amount of ROS leads to decay of basic components such as lipids, proteins. Various mechanisms are induced in order to rearrange the deteriorated ROS balance. Trx system is one of the systems that works for the regulation of ROS balance as well as having important functions in many processes such as cell growth and synthesis of deoxyribonucleotides [32]. Cancer increases ROS levels in the body and Trx system is induced. This causes overexpression of Trx, and this overexpression

also causes cancer cell growth, metastasis, and resistance to the chemotherapeutic agent [33]. Trx system consists of Trx, TrxR, and NADPH and TrxR

induces Trx. Inhibition of TrxR for restriction of Trx over-expression is considered as a possible cancer treatment procedure.

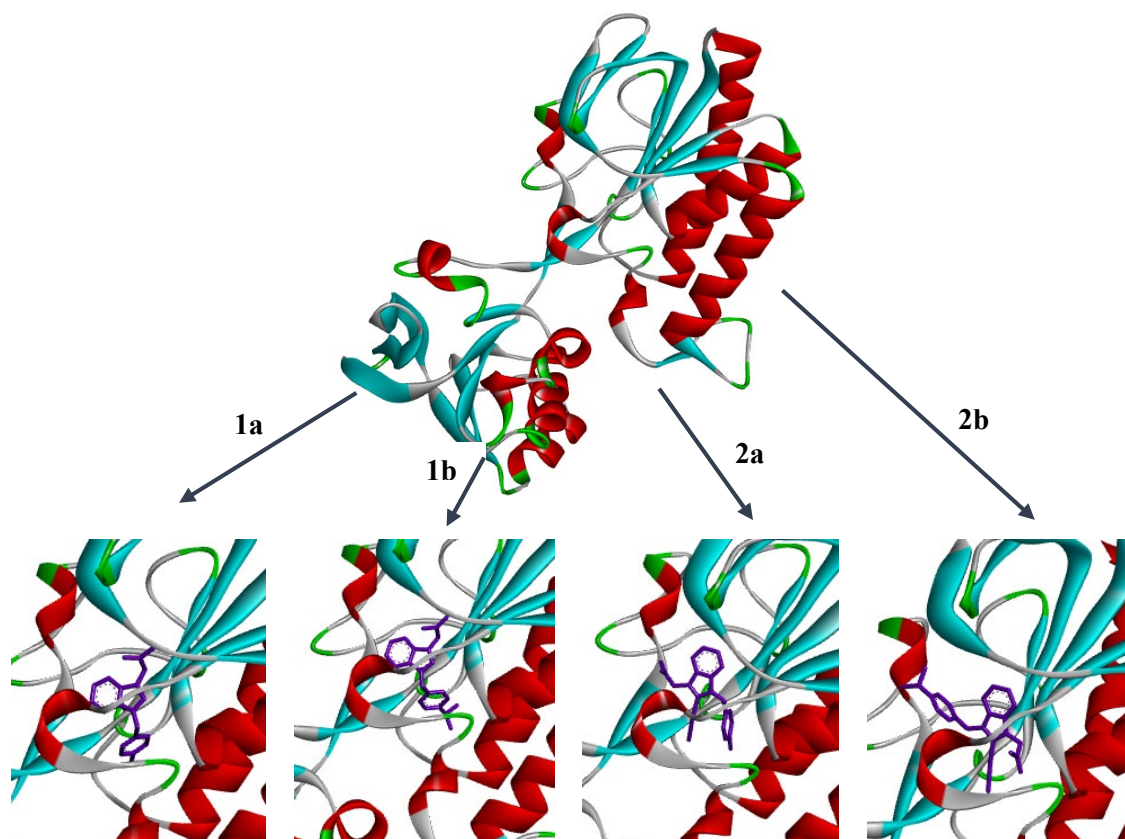


Figure 2. Ribbon style crystallographic structure of thioredoxin reductase (upper). Docked residues of the molecules in thioredoxin reductase (down)

The basic principle in standard in vitro anticancer studies is to examine the effect of molecules on specific cancer cells [34,35]. It is clear that the in vitro analysis of the effects is important. However, it is very difficult (sometimes impossible) to examine the mechanism of action of molecules in treatment. Therefore, molecular docking methods have recently become an essential tool in activity and drug design studies. Many experimental studies are supported by molecular docking studies with suitable target molecules [36-38]. In this study, the interactions of NHC ligands and their Ag(I) complexes were investigated by molecular docking with TrxR (Figure 2 and Figure 3) and DNA (Figure 4).

1a interacted with the region which comprised Ala38, Ile88, Ile10, Gly35, Glu34, Thr117, Gly11, Ser12, and Val41 in TrxR with -7.13 kcal/mol binding energy. Van der Waals interactions occur most intensely, and amino acids in these interactions can be analyzed in

Figure 3. The molecule made alkyl and pi-alkyl interactions with Ile88, Ile10, Val41, and Ala38. Ala38 also shows pi-sigma interactions with the conjugate electrons of the benzimidazole ring of the molecule. Carbon hydrogen bonding with Glu34 and Ser12 also contribute to the binding energy. 2a, the Ag(I) complex of 1a, has a binding energy of -7.37 kcal/mol with approximately the same region of TrxR. Van der Waals interactions are more remarkable in 2a, like 1a. Pi-sigma interaction with Thr117, and the alkyl/pi-alkyl interactions with Val41, Phe254, and Ala38 also are also noteworthy. 1b was docked in a region where Ala38, Ile10, Ile88, Pro14, Thr117 were located in TrxR. Pi-sigma interaction between Ala38 and benzimidazole, alkyl interactions with Ile10, Ile88, and Pro14, and many van der Waals interactions contribute to the binding energy of -8.58 kcal/mol. 2b, the Ag(I) complex of 1b, was docked with a binding energy of -8.95 kcal/mol to approximately the same region as the

other molecules. In this molecule, van der Waals interactions are conspicuous, and the amino acids that make up these interactions can be studied in Figure 3.

Pi-sigma interaction with Ile10 and the alkyl/pi-alkyl interactions with Phe254, Ala38, Val41 are also noteworthy.

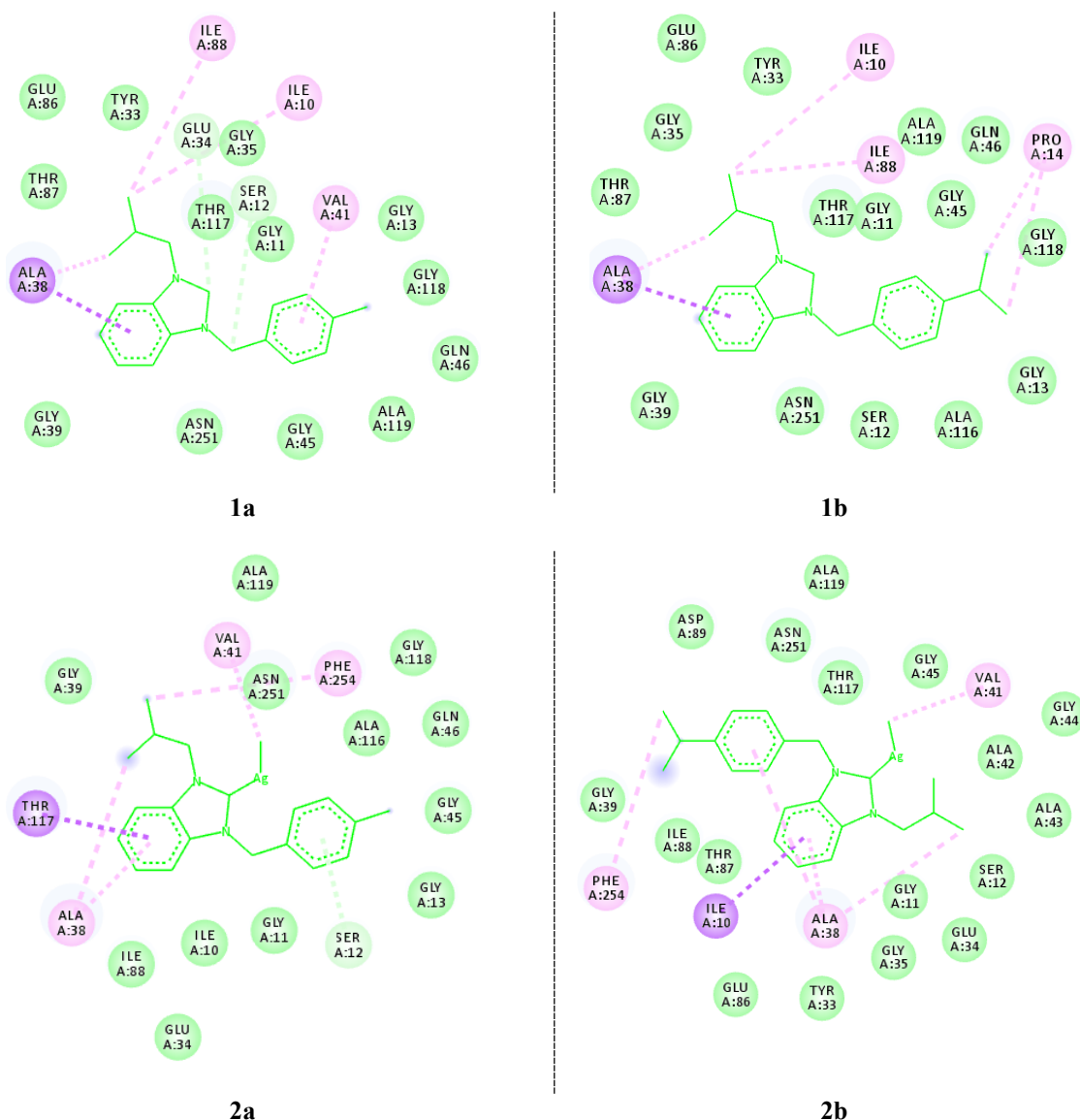


Figure 3. Graphical illustration of the interactions between TrxR and the molecules

In previous anti-cancer studies of the molecules [21] analyzed in this study, it has been determined that complex molecules have higher anti-cancer activity than ligand molecules. In addition, it had been stated that the isopropyl substituted molecule had higher anti-cancer activity than the methyl-substituted molecule. In molecular docking studies, the binding energy is accepted as a suitable criterion for comparing the activity. Accordingly, the binding energies obtained within this study are in accordance with the experimental results.

It is important to get information about the interaction between molecules and DNA in many activity studies, especially in anti-cancer studies. The obtained results will also be important in new drug design studies. For this reason, the interactions of the molecules in this study with DNA were made by using DNA dodecamer (pdb id: 1BNA). **1a** and **1b** ligands interacted with Cyt11, Gua10, Cyt9, and Thy8 (Figure 4). However, **2a** and **2b** complexes interacted with Ade5, Ade6, Thy7, and Thy8. The interactions are mostly pi-pi (pink) and pi-alkyl (purple) interactions (Figure 4).

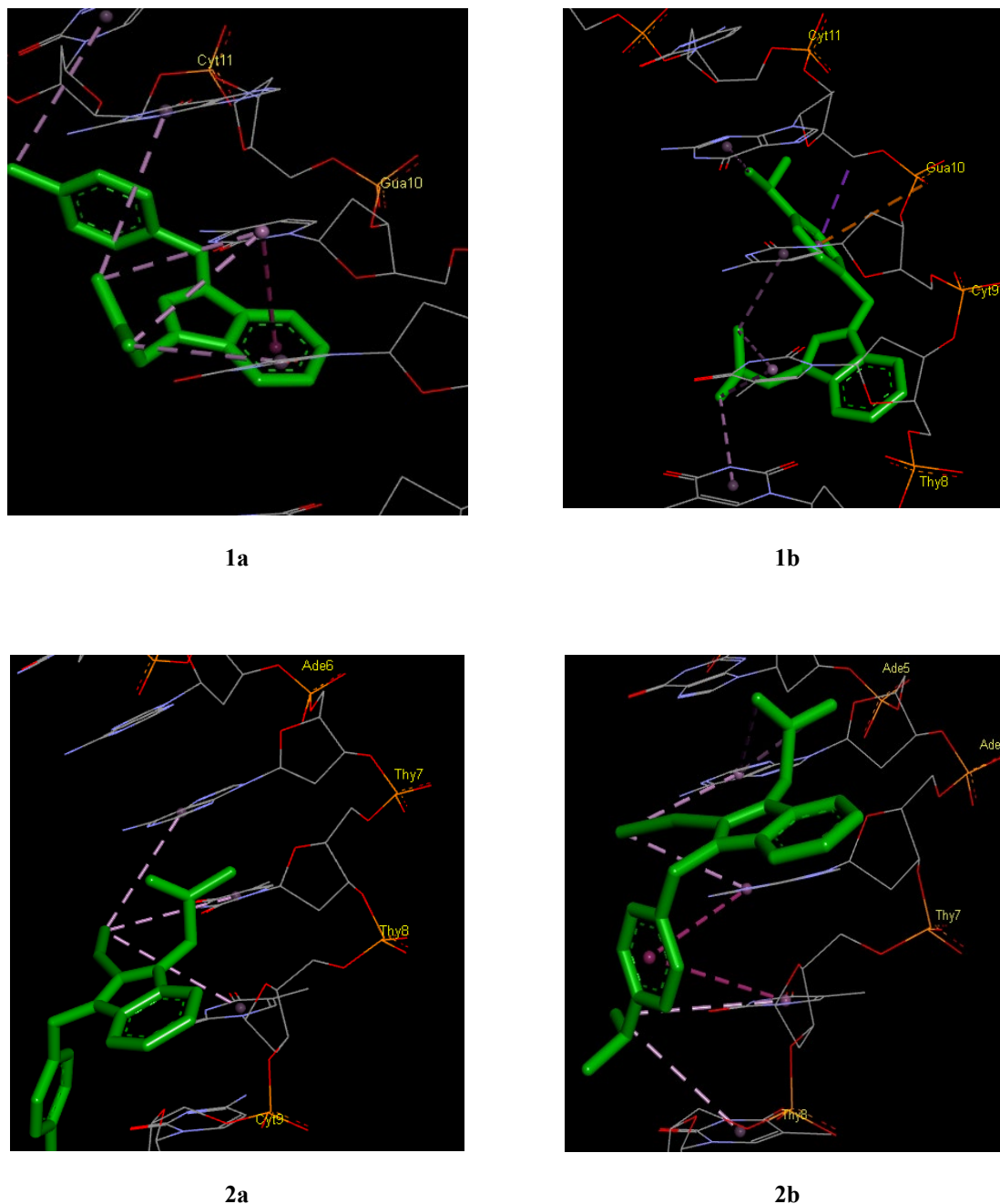


Figure 4. Graphical illustration of the interactions between DNA dodecamer and the molecules

4. Conclusion

New developments have been provided in cancer research in every day. Since the disease is wide in terms of diversity and mechanism of action, unfortunately, the studies have not been able to catch up with the pace of the disease. In addition to in vitro anti-cancer studies, all kinds of methods to understand the mechanism of action are important in these studies. The Trx system is one of the mechanisms examined in recent cancer studies. The studies about the synthesis and analysis of molecules for restricting Trx

expression by TrxR inhibition are continuing. However, due to the difficulty of conducting these studies, it is reasonable to carry out these studies in silico. In silico studies both give an idea about the mechanism of action of the molecule and provide foresight in designing new studies. In this study, the interactions of molecules with thioredoxin reductase were examined and the binding energy results obtained with TrxR agree with the experimental results, but it is clear that much more studies must be done. In the next

studies, it is planned to diversify the studies with different substituted ligands and molecules.

Conflicts of interest

There is no conflict of interest between the authors.

References

- [1] Siegel R.L., Miller K.D., Jemal A., Cancer statistics, 2019, *CA: A Cancer Journal For Clinicians*, 69(1) (2019) 7-34.
- [2] Hayes J.D., Dinkova-Kostova A.T., Tew K.D., Oxidative stress in cancer, *Cancer Cell*, 38(2) (2020) 67-197.
- [3] Milkovic L., Cipak Gasparovic A., Cindric M., Mouthuy P.A., Zarkovic N., Short overview of ROS as cell function regulators and their implications in therapy concepts, *Cells*, 8(8) (2019) 793.
- [4] Zhu J., Thompson C.B., Metabolic regulation of cell growth and proliferation, *Nat. Rev. Mol. Cell Bio.*, 20(7) (2019) 436-450.
- [5] Sies H., In *Oxidative stress and vascular disease*, Boston: Springer, (2000) 1-8.
- [6] Arnér E.S., Holmgren A., Physiological functions of thioredoxin and thioredoxin reductase, *Eur.J. Biochem.*, 267(20) (2000) 6102-6109.
- [7] Lu J., Holmgren A., Thioredoxin system in cell death progression, *Antioxid. Redox Signal.*, 17(12) (2012) 1738-1747.
- [8] Gromer S., Urig S., Becker K., The thioredoxin system from science to clinic, *Med. Res. Rev.*, 24(1) (2004) 40-89.
- [9] Koharyova M., Kolarova M., Oxidative stress and thioredoxin system, *Gen. Physiol. Biophys.*, 27(2) (2008) 71-84.
- [10] Tonissen K.F., Di Trapani G., Thioredoxin system inhibitors as mediators of apoptosis for cancer therapy, *Mol. Nutri. Food Res.*, 53(1) (2009) 87-103.
- [11] Holmgren A., Lu J., Thioredoxin and thioredoxin reductase: current research with special reference to human disease, *Biochem. Biophys. Res. Commun.*, 396(1) (2010) 120-124.
- [12] Zhang J., Li X., Han X., Liu R., Fang J., Targeting the thioredoxin system for cancer therapy, *Trends Pharmacol. Sci.*, 38(9) (2017) 794-808.
- [13] Lu J., Chew E.H., Holmgren A., Targeting thioredoxin reductase is a basis for cancer therapy by arsenic trioxide, *Proceedings of the National Academy of Sciences*, 104(30) (2007) 12288-12293.
- [14] Qiu X., Liu Z., Shao W.Y., Liu X., Jing D.P., Yu Y.J., Gu L.Q., Synthesis and evaluation of curcumin analogues as potential thioredoxin reductase inhibitors, *Bioorg. Med. Chem.*, 16(17) (2008) 8035-8041.
- [15] Urig S., Becker K., On the potential of thioredoxin reductase inhibitors for cancer therapy, In *Seminars in cancer biology*, Elsevier, 16(6) (2006) 452-465.
- [16] Saturnino C., Barone I., Iacopetta D., Mariconda A., Sinicropi M. S., Rosano C., Andò S., N-heterocyclic carbene complexes of silver and gold as novel tools against breast cancer progression, *Future Med. Chem.*, 8(18) (2016) 2213-2229.
- [17] Oehninger L., Rubbiani R., Ott I., N-Heterocyclic carbene metal complexes in medicinal chemistry, *Dalton Trans.*, 42(10) (2013) 3269-3284.
- [18] Jalal M., Hammouti B., Touzani R., Aouniti A., Ozdemir I., Metal-NHC heterocycle complexes in catalysis and biological applications: Systematic review, *Materials Today: Proceedings*, 31 (2020) 122-129.
- [19] Vellé A., Maguire R. C., Kavanagh K., Sanz Miguel, P., Montagner, D., Steroid-Au(I)-NHC Complexes: Synthesis and Antibacterial Activity, *ChemMedChem.*, 12(11) (2017) 841-844.
- [20] Slimani I., Mansour L., Abutaha N., Harrath A. H., Al-Tamimi J., Gürbüz N., Özdemir İ., Hamdi N., Synthesis, structural characterization of silver(I)-NHC complexes and their antimicrobial, antioxidant and antitumor activities, *J. King Saud Univ. Sci.*, 32(2) (2020) 1544-1554.
- [21] Şahin-Bölükbaşı S., Şahin N., Novel Silver-NHC complexes: Synthesis and anticancer properties, *J. Organomet.Chem.*, 891 (2019) 78-84.
- [22] Neese F., Wennmohs F., Becker U., Riplinger C. The ORCA quantum chemistry program package, *The J. Chem. Phys.*, 152(22) (2020) 224108.

- [23] Neese F., Software update: the ORCA program system, version 4.0., *Wiley Interdisciplinary Reviews: Comput. Mol. Sci.*, 8(1) (2018) e1327.
- [24] Parsonage D., Sheng F., Hirata K., Debnath A., Mckerrow J.H., Reed S.L., Abagyan R., Poole L.B., Podust L.M., X-Ray Structures of Thioredoxin and Thioredoxin Reductase from *Entamoeba Histolytica* and Prevailing Hypothesis of the Mechanism of Auranofin Action, *J. Struct. Biol.*, 194 (2016) 180.
- [25] Drew H.R., Wing R.M., Takano T., Broka C., Tanaka S., Itakura K., Dickerson R.E., Structure of a B-DNA dodecamer: conformation and dynamics, *Proc. Natl. Acad. Sci., USA*, 78 (1981) 2179-2183
- [26] Protein Data Bank (PDB), Available at: <https://www.rcsb.org/>. Retrieved September 2021.
- [27] Gaillard T., Evaluation of AutoDock and AutoDock Vina on the CASF-2013 benchmark, *J. Chem. Info. Model.*, 58(8) (2018) 1697-1706.
- [28] Nogueira V., Hay N., Molecular pathways: reactive oxygen species homeostasis in cancer cells and implications for cancer therapy, *Clinic. Cancer Res.*, 19(16) (2013) 4309-4314.
- [29] Valko M., Rhodes C.J., Moncol J., Izakovic M., Mazur M., Free radicals, metals and antioxidants in oxidative stress-induced cancer, *Chem. Biol. Interact.*, 160 (2006) 1-40.
- [30] Wells, P.G., McCallum G.P., Chen C.S., Henderson J.T., Lee C.J., Perstin J., Preston T.J., Wiley M.J., Wong A.W., Oxidative stress in developmental origins of disease: teratogenesis, neurodevelopmental deficits, and cancer, *Toxicol Sci.*, 108 (2009) 4-18.
- [31] Sosa V., Moliné T., Somoza R., Paciucci R., Kondoh H., LLeonart M., EOxidative stress and cancer: an overview, *Age. Res. Rev.*, 12 (1) (2013) 376-390.
- [32] Muri J., Heer S., Matsushita M., Pohlmeier L., Tortola L., Fuhrer T., Kopf M., The thioredoxin-1 system is essential for fueling DNA synthesis during T-cell metabolic reprogramming and proliferation, *Nat. Commun.*, 9(1) (2018), 1-16.
- [33] Patenaude A., Murthy M.V., Mirault M.E., Mitochondrial thioredoxin system: effects of TrxR2 overexpression on redox balance, cell growth, and apoptosis, *J. Bio. Chem.*, 279(26) (2004) 27302-27314.
- [34] Knopf K.M., Murphy B.L., MacMillan S.N., Baskin J.M., Barr M.P., Boros E., Wilson J.J., In vitro anticancer activity and in vivo biodistribution of rhenium(I) tricarbonyl aqua complexes, *J. Am. Chem. Soc.*, 139(40) (2017), 14302-14314.
- [35] N. E. A. El-Naggar M. H., Hussein A., A. El-Sawah, Bio-fabrication of silver nanoparticles by phycocyanin, characterization, in vitro anticancer activity against breast cancer cell line and in vivo cytotoxicity, *Sci. Rep.*, 7 (2017) 10844.
- [36] De Ruyck J., Brysbaert G., Blossey R., Lensink M. F., Molecular docking as a popular tool in drug design, an in silico travel, *Advances and Applications in Bioinformatics and Chemistry, AABC*, 9 (2016) 1.
- [37] Torres P. H., Sodero A. C., Jofily P., Silva-Jr F. P., Key topics in molecular docking for drug design, *Int. J. Mol. Sci.*, 20(18) (2019) 4574.
- [38] Nakano S., Megro S. I., Hase T., Suzuki T., Isemura M., Nakamura Y., Ito S., Computational molecular docking and X-ray crystallographic studies of catechins in new drug design strategies, *Molecules*, 23(8) (2018) 2020.



New extension of beta, Gauss and confluent hypergeometric functions

Umar Muhammad ABUBAKAR^{1,*}  Muhammad Lawan KAURANGINI² 

^{1,2}Kano University of Science and Technology, Wudil, Department of Mathematics, Kano State/ NIGERIA

Abstract

There are many extensions and generalizations of Gamma and Beta functions in the literature. However, a new extension of the extended Beta function $B_{\zeta, \alpha_1}^{\alpha_2; m_1, m_2}(a_1, a_2)$ was introduced and presented here because of its important properties. The new extended Beta function has symmetric property, integral representations, Mellin transform, inverse Mellin transform and statistical properties like Beta distribution, mean, variance, moment and cumulative distribution which were also presented. Finally, the new extended Gauss and Confluent Hypergeometric functions with their properties were introduced and presented.

Article info

History:
Received: 14.12.2020
Accepted: 27.05.2021

Keywords:
Gamma function,
Beta function,
Beta distribution,
Pochhammer symbol,
Mellin transform.

1. Introduction

Functions like factorial and others attracted the attention of Mathematicians for a long period of time. For example, in 1729 a Swiss Mathematician, Leonard Euler generalized factorial function from the domain of natural numbers to the domain over the positive complex plane. Also, in 1811, French Mathematician Adrien-Marie Legendre decomposed Euler's Gamma function into incomplete gamma functions and later in 1814 he introduced the notation of Γ for gamma function. In 1730, Euler also introduced beta function, $B(a_1, a_2)$ for a pair of complex numbers a_1 and a_2 with real positive parts through the integrand. Later on, various extensions of classical gamma and beta functions were studied by renowned Mathematicians and proved to be significantly important in different areas of Applied Mathematics, Statistics, Physics and Engineering such as heat conduction, probability theory, Fourier, Laplace, K-transforms and so on [1-20].

Definition 1. [21] Oraby et al., proposed the following extended beta function:

$$B_{\zeta, \alpha_1}^{\alpha_2; m_1}(a_1, a_2) = \int_0^1 t^{a_1-1} (1-t)^{a_2-1} E_{\alpha_1, \alpha_2} \left(-\frac{\zeta}{t^{m_1(1-t)^{m_1}}}\right) dt, \quad (1)$$

$$(Re(a_1) > 0, Re(a_2) > 0, Re(\zeta) \geq 0, Re(\alpha_1) > 0, Re(\alpha_2) > 0, Re(m_1) > 0),$$

$E_{\alpha_1, \alpha_2}(\cdot)$ is two parameters Mittag-leffler function.

Definition 2. [22, 23] Wiman function or two parameters Mittag-Leffler function is defined by

$$E_{\alpha_1, \alpha_2}(z) = \sum_{\kappa=0}^{\infty} \frac{z^{\kappa}}{\Gamma(\kappa\alpha_1 + \alpha_2)}, \quad (\alpha_1, \alpha_2 \in \mathbb{C}, Re(\alpha_1) > 0, Re(\alpha_2) > 0). \quad (2)$$

Definition 3. [24 -26] Classical Mittag-Leffler or one parameter Mittag-Leffler function is defined by

$$E_{\alpha_1}(z) = \sum_{\kappa=0}^{\infty} \frac{z^{\kappa}}{\Gamma(\kappa\alpha_1 + 1)}, \quad (\alpha_1 \in \mathbb{C}, Re(\alpha_1) > 0). \quad (3)$$

*Corresponding author. e-mail address: umabubakar347@gmail.com

Definition 4. [27] Classical gamma function is defined using integral representation as

$$\Gamma(\alpha_1) = \int_0^\infty t^{\alpha_1-1} e^{-t} dt, \quad (Re(\alpha_1) > 0). \tag{4}$$

With the Euler reflection formula

$$\Gamma(\alpha_1) \Gamma(1 - \alpha_1) = \frac{\pi}{\sin\pi\alpha_1}, \quad (\alpha_1 > 0). \tag{5}$$

Definition 5. [27] Classical beta function is defined as

$$B(\alpha_1, \alpha_2) = \begin{cases} \int_0^1 t^{\alpha_1-1} (1-t)^{\alpha_2-1} dt, & (Re(\alpha_1) > 0, Re(\alpha_2) > 0), \\ \frac{\Gamma(\alpha_1) \Gamma(\alpha_2)}{\Gamma(\alpha_1+\alpha_2)}, & (\alpha_1, \alpha_2 \in \mathbb{C} \setminus \mathbb{Z}_0^-). \end{cases} \tag{6}$$

The relation also holds

$$B(\alpha_1, \alpha_2 - \alpha_1) = \frac{\alpha_2}{\alpha_1} B(\alpha_1 + 1, \alpha_2 - \alpha_1), \quad (Re(\alpha_2) > Re(\alpha_1) > 0). \tag{7}$$

Definition 6. [20, 28] Classical pochhammer symbol is defined as

$$(\alpha_1)_\kappa = \frac{\Gamma(\alpha_1+\kappa)}{\Gamma(\alpha_1)} = \begin{cases} \alpha_1(\alpha_1 + 1)(\alpha_1 + 2) \cdots (\alpha_1 + \kappa - 1), & (\kappa \geq 1), \\ 1, & (\kappa = 0, \alpha_1 \neq 0), \end{cases} \tag{8}$$

with the well-known binomial theorem

$$\sum_{\kappa=0}^\infty (\alpha_1)_\kappa \frac{(zt)^{\alpha_1}}{\kappa!} = (1 - zt)^{-\alpha_1}. \tag{9}$$

Definition 7. [29, 30] The Mellin transform of integrable function $f(z)$ with index l is defined by

$$f^*(l) = M\{f(\zeta); l\} = \int_0^\infty \zeta^{l-1} f(\zeta) d\zeta. \tag{10}$$

The inverse Mellin transform is defined by

$$f(\zeta) = M^{-1}\{f(\zeta); l\} = \frac{1}{2\pi i} \int_{BS} \zeta^{-l} f^*(l) dl. \tag{11}$$

Definition 8. [31] Classical Gauss hypergeometric function is defined

$$F(\alpha_1, \alpha_2; \alpha_3; z) = \sum_{\kappa=0}^\infty \frac{(\alpha_1)_\kappa (\alpha_2)_\kappa z^\kappa}{(\alpha_3)_\kappa \kappa!}, \tag{12}$$

$$(Re(\alpha_1) > 0, Re(\alpha_2) > 0, Re(\alpha_3) > 0, |z| < 1).$$

And

$$F(\alpha_1, \alpha_2; \alpha_3; z) = \frac{1}{B(\alpha_2, \alpha_3-\alpha_2)} \int_0^1 t^{\alpha_2-1} (1-t)^{\alpha_3-\alpha_2-1} (1-zt)^{-\alpha_1} dt, \tag{13}$$

$$(Re(\alpha_3) > Re(\alpha_2) > 0, |\arg(1-z)| < 1).$$

Definition 9. [31] Classical confluent hypergeometric function is defined as

$$\Phi(\alpha_2; \alpha_3; z) = \sum_{\kappa=0}^{\infty} \frac{(\alpha_2)_{\kappa} z^{\kappa}}{(\alpha_3)_{\kappa} \kappa!}, \quad (Re(\alpha_2) > 0, Re(\alpha_3) > 0, |z| < 1). \quad (14)$$

And

$$\Phi(\alpha_2; \alpha_3; z) = \frac{1}{B(\alpha_2, \alpha_3 - \alpha_2)} \int_0^1 t^{\alpha_2 - 1} (1 - t)^{\alpha_3 - \alpha_2 - 1} e^{zt} dt, \quad (15)$$

$$(Re(\alpha_3) > Re(\alpha_2) > 0, |\arg(1 - z)| < 1).$$

Definition 10. [32] The relations between Mittag-Leffler and gamma function is

$$\int_0^{\infty} u^{l-1} E_{\alpha_1, \alpha_2}^{\alpha_3}(-\mu u) du = \frac{\Gamma(l) \Gamma(\alpha_3 - l)}{\mu^l \Gamma(\alpha_3) \Gamma(\alpha_2 - l \alpha_3)}. \quad (16)$$

Setting $\alpha_3 = \mu = 1$ in equation (16), becomes

$$\int_0^{\infty} u^{l-1} E_{\alpha_1, \alpha_2}(-u) du = \frac{\Gamma(l) \Gamma(1-l)}{\Gamma(\alpha_2 - l)}. \quad (17)$$

Definition 11. The extended beta function is defined as

$$B_{\zeta, \alpha_1}^{\alpha_2; m_1, m_2}(a_1, a_2) = \int_0^1 t^{a_1 - 1} (1 - t)^{a_2 - 1} E_{\alpha_1, \alpha_2} \left(-\frac{\zeta}{t^{m_1} (1-t)^{m_2}} \right) dt, \quad (18)$$

$$(Re(a_1) > 0, Re(a_2) > 0, Re(\zeta) \geq 0, Re(\alpha_1) > 0, Re(\alpha_2) > 0, Re(m_1) > 0, Re(m_2) > 0),$$

$E_{\alpha_1, \alpha_2}(\cdot)$ is two parameters Mittag-Leffler function.

Definition 12. The extended Gauss hypergeometric function is defined as

$$F_{\zeta, \alpha_1}^{\alpha_2; m_1, m_2}(a_1, a_2; a_3; z) = \sum_{\kappa=0}^{\infty} (a_1)_{\kappa} \frac{B_{\zeta, \alpha_1}^{\alpha_2; m_1, m_2}(a_2 + \kappa, a_3 - a_2) z^{\kappa}}{B(a_2, a_3 - a_2) \kappa!}, \quad (19)$$

$$(Re(m_1) > 0, Re(m_2) > 0, Re(\alpha_1) > 0, Re(\alpha_2) > 0, Re(a_1) > 0, Re(a_3) > Re(a_2) > 0, Re(\zeta) \geq 0).$$

Definition 13. The extended Gauss hypergeometric function is defined as

$$\Phi_{\zeta, \alpha_1}^{\alpha_2; m_1, m_2}(a_2; a_3; z) = \sum_{\kappa=0}^{\infty} \frac{B_{\zeta, \alpha_1}^{\alpha_2; m_1, m_2}(a_2 + \kappa, a_3 - a_2) z^{\kappa}}{B(a_2, a_3 - a_2) \kappa!}. \quad (20)$$

$$(Re(m_1) > 0, Re(m_2) > 0, Re(\alpha_1) > 0, Re(\alpha_2) > 0, Re(a_3) > Re(a_2) > 0, Re(\zeta) \geq 0).$$

2. Special Cases

Some special cases of the new extended beta function are

Cases 1: When $m_1 = m_2$, then the new extended beta function reduces to the beta function [21]:

$$B_{\zeta, \alpha_1}^{\alpha_2; m_1, m_1}(a_1, a_2) = B_{\zeta, \alpha_1}^{\alpha_2; m_1}(a_1, a_2) = \int_0^1 t^{a_1-1} (1-t)^{a_2-1} E_{\alpha_1, \alpha_2} \left(-\frac{\zeta}{t^{m_1(1-t)^{m_1}}}\right) dt, \quad (21)$$

$$(Re(a_1) > 0, (Re(a_2) > 0, Re(\zeta) \geq 0, Re(\alpha_1) > 0, Re(\alpha_2) > 0, Re(m_1) > 0).$$

Cases 2: If $m_1 = m_2$ and $\alpha_2 = 1$, then the new extended beta function reduces to the beta function [33]:

$$B_{\zeta, \alpha_1}^{1; m_1, m_1}(a_1, a_2) = B_{\zeta, \alpha_1}^{\alpha_1; m_1}(a_1, a_2) = \int_0^1 t^{a_1-1} (1-t)^{a_2-1} E_{\alpha_1} \left(-\frac{\zeta}{t^{m_1(1-t)^{m_1}}}\right) dt, \quad (22)$$

$$(Re(a_1) > 0, (Re(a_2) > 0, Re(\zeta) \geq 0, Re(\alpha_1) > 0, Re(m_1) > 0).$$

Cases 3: If $m_1 = m_2 = 1$ and $\alpha_2 = 1$, then the new extended beta functions reduce to the beta function [34]:

$$B_{\zeta, \alpha_1}^{1; 1, 1}(a_1, a_2) = B_{\zeta, \alpha_1}^{\alpha_1}(a_1, a_2) = \int_0^1 t^{a_1-1} (1-t)^{a_2-1} E_{\alpha_1} \left(-\frac{\zeta}{t(1-t)}\right) dt, \quad (23)$$

$$(Re(a_1) > 0, (Re(a_2) > 0, Re(\zeta) \geq 0, Re(\alpha_1) > 0).$$

Cases 4: When $\alpha_1 = \alpha_2 = 1$, then the new extended beta function reduces to the beta function as in [35]:

$$B_{\zeta, 1}^{1; m_1, m_2}(a_1, a_2) = B_{\zeta}^{m_1}(a_1, a_2) = \int_0^1 t^{a_1-1} (1-t)^{a_2-1} \exp\left(-\frac{\zeta}{t^{m_1(1-t)^{m_2}}}\right) dt, \quad (24)$$

$$(Re(a_1) > 0, (Re(a_2) > 0, Re(\zeta) \geq 0, Re(m_1) > 0, Re(m_2) > 0).$$

Cases 5: When $m_1 = m_2$ and $\alpha_1 = \alpha_2 = 1$, then the new extended beta function reduces to the beta function as in [36]:

$$B_{\zeta, 1}^{1; m_1, m_1}(a_1, a_2) = B_{\zeta}^{m_1}(a_1, a_2) = \int_0^1 t^{a_1-1} (1-t)^{a_2-1} \exp\left(-\frac{\zeta}{t^{m_1(1-t)^{m_1}}}\right) dt, \quad (25)$$

$$(Re(a_1) > 0, (Re(a_2) > 0, Re(\zeta) \geq 0, Re(m_1) > 0).$$

Cases 6: If $m_1 = m_2 = \alpha_1 = \alpha_2 = 1$, then the new extended beta function reduces to the beta function as in [37]:

$$B_{\zeta, 1}^{1; 1, 1}(a_1, a_2) = B_{\zeta}(a_1, a_2) = \int_0^1 t^{a_1-1} (1-t)^{a_2-1} \exp\left(-\frac{\zeta}{t(1-t)}\right) dt, \quad (26)$$

$$(Re(a_1) > 0, (Re(a_2) > 0, Re(\zeta) \geq 0).$$

Cases 7: If $\xi = 0$ and $m_1 = m_2 = \alpha_1 = \alpha_2 = 1$, then the new extended beta function reduces to the classical beta function as in [27]:

$$B_{0, 1}^{1, 1, 1}(a_1, a_2) = B(a_1, a_2) = \int_0^1 t^{a_1-1}(1-t)^{a_2-1} dt, \tag{27}$$

$$(Re(a_1) > 0, (Re(a_2) > 0).$$

3. Generalized Beta Function

Theorem 1.

$$B_{\zeta, \alpha_1}^{\alpha_2; m_1, m_2}(a_1 + 1, a_2) + B_{\zeta, \alpha_1}^{\alpha_2; m_1, m_2}(a_1, a_2 + 1) = B_{\zeta, \alpha_1}^{\alpha_2; m_1, m_2}(a_1, a_2). \tag{28}$$

Proof. On setting left hand side of (28) to be L and direct calculation

$$L = \int_0^1 t^{a_1}(1-t)^{a_2} E_{\alpha_1, \alpha_2} \left(-\frac{\zeta}{t^{m_1(1-t)^{m_2}}}\right) \{(1-t)^{-1} + t^{-1}\} dt. \tag{29}$$

On simplification of the equation (29),

$$L = \int_0^1 t^{a_1}(1-t)^{a_2} E_{\alpha_1, \alpha_2} \left(-\frac{\zeta}{t^{m_1(1-t)^{m_2}}}\right) \{(1-t)^{-1}t^{-1}\} dt. \tag{30}$$

Applying equation (18) to (30), the desired result in (28) is obtained.

Theorem 2.

$$B_{\zeta, \alpha_1}^{\alpha_2; m_1, m_2}(a_1, 1 - a_2) = \sum_{\kappa=0}^{\infty} \frac{(a_2)_{\kappa}}{\kappa!} B_{\zeta, \alpha_1}^{\alpha_2; m_1, m_2}(a_1 + \kappa, 1). \tag{31}$$

Proof. By direct calculation

$$B_{\zeta, \alpha_1}^{\alpha_2; m_1, m_2}(a_1, 1 - a_2) = \int_0^1 t^{a_1-1}(1-t)^{a_2} E_{\alpha_1, \alpha_2} \left(-\frac{\zeta}{t^{m_1(1-t)^{m_2}}}\right) dt. \tag{32}$$

Applying equation (9) to (32), yield

$$B_{\zeta, \alpha_1}^{\alpha_2; m_1, m_2}(a_1, 1 - a_2) = \int_0^1 t^{a_1-1} \sum_{\kappa=0}^{\infty} (a_2)_{\kappa} \frac{t^{\kappa}}{\kappa!} E_{\alpha_1, \alpha_2} \left(-\frac{\zeta}{t^{m_1(1-t)^{m_2}}}\right) dt. \tag{33}$$

On interchanging the order of summation and integration in equation (33),

$$B_{\zeta, \alpha_1}^{\alpha_2; m_1, m_2}(a_1, 1 - a_2) = \sum_{\kappa=0}^{\infty} (a_2)_{\kappa} \frac{t^{\kappa}}{\kappa!} \int_0^1 t^{a_1-1} E_{\alpha_1, \alpha_2} \left(-\frac{\zeta}{t^{m_1(1-t)m_2}} \right) dt. \tag{34}$$

Applying equation (18) to (34), the desired result is obtained.

Theorem 3.

$$B_{\zeta, \alpha_1}^{\alpha_2; m_1, m_2}(a_1, a_2) = \sum_{\kappa=0}^{\infty} B_{\zeta, \alpha_1}^{\alpha_2; m_1, m_2}(a_1 + \kappa, a_2 + 1). \tag{35}$$

Proof. By direct calculation

$$B_{\zeta, \alpha_1}^{\alpha_2; m_1, m_2}(a_1, a_2) = \int_0^1 t^{a_1-1} (1-t)^{a_2} (1-t)^{-1} E_{\alpha_1, \alpha_2} \left(-\frac{\zeta}{t^{m_1(1-t)m_2}} \right) dt. \tag{36}$$

Applying equation (9) to (36), yield

$$B_{\zeta, \alpha_1}^{\alpha_2; m_1, m_2}(a_1, a_2) = \int_0^1 t^{a_1-1} (1-t)^{a_2} \sum_{n=0}^{\infty} t^n E_{\alpha_1, \alpha_2} \left(-\frac{\zeta}{t^{m_1(1-t)m_2}} \right) dt. \tag{37}$$

On interchanging the order of summation and integration in equation (37), we have

$$B_{\zeta, \alpha_1}^{\alpha_2; m_1, m_2}(a_1, a_2) = \sum_{\kappa=0}^{\infty} \int_0^1 t^{a_1+\kappa-1} (1-t)^{a_2} E_{\alpha_1, \alpha_2} \left(-\frac{\zeta}{t^{m_1(1-t)m_2}} \right) dt. \tag{38}$$

Applying equation (18) to (38), gives the desired result.

Theorem 4. For the new extended beta function,

$$B_{\zeta, \alpha_1}^{\alpha_2; m_1, m_2}(a_1, a_2) = B_{\zeta, \alpha_1}^{\alpha_2; m_2, m_1}(a_2, a_1). \tag{39}$$

Proof. Setting $t \rightarrow 1 - t$ in equation (18), gives the required result in (39).

4. Integral Representations

Theorem 5.

$$B_{\zeta, \alpha_1}^{\alpha_2; m_1, m_2}(a_1, a_2) = 2 \int_0^{\frac{\pi}{2}} \cos^{2a_1-1} \varphi \sin^{2a_2-1} \varphi E_{\alpha_1, \alpha_2} \left(-\frac{\zeta}{\sin^{2m_1} \varphi \cos^{2m_2} \varphi} \right) d\varphi, \tag{40}$$

$$B_{\zeta, \alpha_1}^{\alpha_2; m_1, m_2}(a_1, a_2) = \int_0^{\infty} \frac{t^{a_1-1}}{(1+t)^{a_1+a_2}} E_{\alpha_1, \alpha_2} \left(-\frac{\zeta(1+t)^{m_1+m_2}}{t^{m_1}} \right) dt, \tag{41}$$

$$B_{\zeta, \alpha_1}^{\alpha_2; m_1, m_2}(a_1, a_2) = 2^{1-(a_1+a_2)} \int_{-1}^1 (1+t)^{a_1-1} (1-t)^{a_2-1} E_{\alpha_1, \alpha_2} \left(-\frac{\zeta^{m_1+m_2}}{(1+t)^{m_1(1-t)m_2}} \right) dt, \tag{42}$$

$$B_{\zeta, \alpha_1}^{\alpha_2; m_1, m_2}(a_1, a_2) = \int_{a'}^{c'} \frac{(t-a')^{\alpha_1-1}(c'-t)^{\alpha_2-1}}{(c'-a')^{\alpha_1+\alpha_2-1}} E_{\alpha_1, \alpha_2} \left(-\frac{\zeta(c'-a')^{m_1+m_2}}{(t-a')^{m_1}(c'-t)^{m_2}} \right) dt. \quad (43)$$

Proof. Equations (40), (41), (42) and (43) can be obtained by putting $t = \cos^2 \varphi$, $t = u(1+u)^{-1}$, $t = 2^{-1}(1+u)$ and $t = (u-a')(c'-a')^{-1}$, respectively in equation (18) and by changing of variable.

Theorem 6.

$$B_{\zeta, \alpha_1}^{\alpha_2; m_1, m_2}(a_1, a_2) = n \int_0^1 t^{n\alpha_1-1}(1-t^n)^{\alpha_2-1} E_{\alpha_1, \alpha_2} \left(-\frac{\zeta}{t^{nm_1}(1-t^n)^{m_2}} \right) dt, \quad (44)$$

$$B_{\zeta, \alpha_1}^{\alpha_2; m_1, m_2}(a_1, a_2) = \int_0^{a'} t^{\alpha_1-1}(a'-t)^{\alpha_2-1} E_{\alpha_1, \alpha_2} \left(-\frac{\zeta a^{m_1+m_2}}{t^{m_1}(a'-t)^{m_2}} \right) dt. \quad (45)$$

Proof. Equations (44) and (45) can be obtained by putting $t = u^n$ and $t = ua^{r-1}$, respectively in equation (18) and change of variable.

5. Mellin Transform

Theorem 7.

$$M\{B_{\zeta, \alpha_1}^{\alpha_2; m_1, m_2}(a_1, a_2); l\} = \frac{\pi}{\Gamma(\alpha_2-l)\sin\pi l} B(a_1 + m_1 l, a_2 + m_2 l). \quad (46)$$

Proof. Using definition of Mellin transform in equation (10), we have

$$M\{B_{\zeta, \alpha_1}^{\alpha_2; m_1, m_2}(a_1, a_2); l\} = \int_0^\infty \zeta^{l-1} B_{\zeta, \alpha_1}^{\alpha_2; m_1, m_2}(a_1, a_2) d\zeta. \quad (47)$$

Substituting equation (18) into (47), we get

$$M\{B_{\zeta, \alpha_1}^{\alpha_2; m_1, m_2}(a_1, a_2); l\} = \int_0^\infty \zeta^{l-1} \left\{ \int_0^1 t^{\alpha_1-1}(1-t)^{\alpha_2-1} E_{\alpha_1, \alpha_2} \left(-\frac{\zeta}{t^{m_1}(1-t)^{m_2}} \right) dt \right\} d\zeta. \quad (48)$$

Interchanging the order of integrations in equation (48), yield

$$M\{B_{\zeta, \alpha_1}^{\alpha_2; m_1, m_2}(a_1, a_2); l\} = \int_0^1 t^{\alpha_1-1}(1-t)^{\alpha_2-1} \left\{ \int_0^\infty \zeta^{l-1} E_{\alpha_1, \alpha_2} \left(-\frac{\zeta}{t^{m_1}(1-t)^{m_2}} \right) d\zeta \right\} dt. \quad (49)$$

On setting $\zeta = ut^{m_1}(1-t)^{m_2}$ in equation (49), we obtain

$$M\{B_{\zeta, \alpha_1}^{\alpha_2; m_1, m_2}(a_1, a_2); l\} = \int_0^1 t^{\alpha_1+m_1l-1}(1-t)^{\alpha_2+m_2l-1} \left\{ \int_0^\infty u^{l-1} E_{\alpha_1, \alpha_2}(-u) du \right\} dt. \quad (50)$$

On applying equations (4), (5) and (17) to (50), the desired result can be obtained.

Corollary 8. The inverse Mellin transform:

$$B_{\zeta, \alpha_1}^{\alpha_2; m_1, m_2}(a_1, a_2) = \frac{1}{2\pi i} \int_{\gamma' - i\infty}^{\gamma' + i\infty} \frac{\Gamma(a_1 + m_1 l) \Gamma(a_2 + m_2 l)}{\Gamma(a_1 - \alpha_2 l) \Gamma(a_1 + a_2 + m_1 l + m_2 l)} \zeta^{-s} dl,$$

where

$$Re(m_1) > 0, Re(m_2) > 0, Re(a_1) > 0, Re(a_2) > 0, Re(\alpha_1 - s\alpha_2) > 0, Re(a_1 + m_1 l) > 0, Re(a_2 + m_2 l) > 0, Re(\zeta) \geq 0, \gamma' > 0$$

6. Beta Distribution

The beta distribution of the new extended beta function is

$$f(t) = \begin{cases} \frac{1}{B_{\zeta, \alpha_1}^{\alpha_2; m_1, m_2}(a_1, a_2)} t^{a_1-1} (1-t)^{a_2-1} E_{\alpha_1, \alpha_2} \left(-\frac{\zeta}{t^{m_1}(1-t)^{m_2}} \right), & 0 < t < 1, \\ 0, & \text{elsewhere,} \end{cases} \tag{51}$$

$$(a_1, a_2 \in \mathbb{R}, \zeta, \alpha_1, \alpha_2 \in \mathbb{R}^+).$$

The moment of X, is given by:

$$E(X^r) = \frac{B_{\zeta, \alpha_1}^{\alpha_2; m_1, m_2}(a_1+r, a_2)}{B_{\zeta, \alpha_1}^{\alpha_2; m_1, m_2}(a_1, a_2)}, \quad (a_1, a_2, r \in \mathbb{R}; \zeta, \alpha_1, \alpha_2 \in \mathbb{R}^+). \tag{52}$$

On setting $r = 1$ in (52), we obtained the mean of the distribution as

$$E(X) = \frac{B_{\zeta, \alpha_1}^{\alpha_2; m_1, m_2}(a_1+1, a_2)}{B_{\zeta, \alpha_1}^{\alpha_2; m_1, m_2}(a_1, a_2)}.$$

The variance of the distribution given in equation (51) is

$$\delta = E(X^2) - \{E(X)\}^2 = \frac{B_{\zeta, \alpha_1}^{\alpha_2; m_1, m_2}(a_1+2, a_2) - \{B_{\zeta, \alpha_1}^{\alpha_2; m_1, m_2}(a_1+1, a_2)\}^2}{\{B_{\zeta, \alpha_1}^{\alpha_2; m_1, m_2}(a_1, a_2)\}^2}.$$

Cumulative distribution is

$$F(x) = \frac{B_{\zeta, \alpha_1, x}^{\alpha_2; m_1, m_2}(a_1+1, a_2)}{B_{\zeta, \alpha_1}^{\alpha_2; m_1, m_2}(a_1, a_2)},$$

where $B_{\zeta, \alpha_1, x}^{\alpha_2; m_1, m_2}(a_1, a_2)$ is the new extended incomplete beta function defined by:

$$B_{\zeta, \alpha_1, x}^{\alpha_2; m_1, m_2}(a_1, a_2) = \int_0^x t^{a_1-1}(1-t)^{a_2-1} E_{\alpha_1, \alpha_2} \left(-\frac{\zeta}{t^{m_1(1-t)m_2}} \right) dt,$$

$$(a_1, a_2 \in \mathbb{R}; \zeta, \alpha_1, \alpha_2 \in \mathbb{R}^+).$$

7. Gauss and Confluent Hypergeometric Function

Theorem 9.

$$F_{\zeta, \alpha_1}^{\alpha_2; m_1, m_2}(a_1, a_2; a_3; z) = \frac{1}{B(a_2, a_3-a_2)} \int_0^1 t^{a_2-1}(1-t)^{a_3-a_2-1} \times (1-zt)^{-a_1} E_{\alpha_1, \alpha_2} \left(-\frac{\zeta}{t^{m_1(1-t)m_2}} \right) dt. \tag{53}$$

Proof. Applying equation (18) to (19), gives

$$F_{\zeta, \alpha_1}^{\alpha_2; m_1, m_2}(a_1, a_2; a_3; z) = \frac{1}{B(a_2, a_3-a_2)} \sum_{\kappa=0}^{\infty} (a_1)_{\kappa} \int_0^1 t^{a_2+\kappa-1}(1-t)^{a_3-a_2-1} \times E_{\alpha_1, \alpha_2} \left(-\frac{\zeta}{t^{m_1(1-t)m_2}} \right) dt \frac{z^{\kappa}}{\kappa!}. \tag{54}$$

Interchanging the order of summation and integration in equation (54), we have

$$F_{\zeta, \alpha_1}^{\alpha_2; m_1, m_2}(a_1, a_2; a_3; z) = \frac{1}{B(a_2, a_3-a_2)} \int_0^1 t^{a_2-1}(1-t)^{a_3-a_2-1} \times \sum_{\kappa=0}^{\infty} (a_1)_{\kappa} \frac{(zt)^{\kappa}}{\kappa!} E_{\alpha_1, \alpha_2} \left(-\frac{\zeta}{t^{m_1(1-t)m_2}} \right) dt. \tag{55}$$

Applying equation (9) to (55), give the desired result in (53).

Theorem 10.

$$F_{\zeta, \alpha_1}^{\alpha_2; m_1, m_2}(a_1, a_2; a_3; z) = \frac{1}{B(a_2, a_3-a_2)} \int_0^{\infty} \frac{t^{a_2-1}}{(1+t)^{a_3-a_1}} \{1+t(1-z)\}^{a_1} E_{\alpha_1, \alpha_2} \left(-\frac{\zeta(1+t)^{m_2+m_1}}{t^{m_1}} \right) dt, \tag{56}$$

$$F_{\zeta, \alpha_1}^{\alpha_2; m_1, m_2}(a_1, a_2; a_3; z) = \frac{2}{B(a_2, a_3-a_2)} \int_0^{\frac{\pi}{2}} \frac{\sin^{2a_2-1}\varphi \cos^{2a_2-2a_2-1}\varphi}{(1-z\sin^2\varphi)^{a_1}} \times E_{\alpha_1, \alpha_2}(-\zeta \sec^{2m_1}\varphi \csc^{2m_2}\varphi) d\varphi, \tag{57}$$

$$F_{\zeta, \alpha_1}^{\alpha_2; m_1, m_2}(a_1, a_2; a_3; z) = \frac{2}{B(a_2, a_3-a_2)} \int_0^{\infty} \frac{\sinh^{2a_2-1}\varphi \cosh^{2a_2-2a_2-1}\varphi}{(\cosh^2\varphi - z\sinh^2\varphi)^{a_1}} \times E_{\alpha_1, \alpha_2}(-\zeta \cosh^{2m_1}\varphi \coth^{2m_2}\varphi) d\varphi, \tag{58}$$

which are the new extended hypergeometric function integral representations.

Proof. Equations (56), (57) and (58) can be obtained by substituting $t = u(1 + u)^{-1}$, $t = \sin^2\varphi$ and $t = \tanh^2\varphi$, respectively in to (53).

Theorem 11.

$$\Phi_{\zeta, \alpha_1}^{\alpha_2; m_1, m_2}(a_2; a_3; z) = \frac{1}{B(a_2, a_3 - a_2)} \int_0^1 t^{a_2 - 1} (1 - t)^{a_3 - a_2 - 1} \exp(zt) E_{\alpha_1, \alpha_2} \left(-\frac{\zeta}{t^{m_1(1-t)^{m_2}}}\right) dt, \quad (59)$$

which is the new extended confluent hypergeometric function integral representation.

Proof. Applying equation (18) to (20), gives

$$\Phi_{\zeta, \alpha_1}^{\alpha_2; m_1, m_2}(a_2; a_3; z) = \frac{1}{B(a_2, a_3 - a_2)} \sum_{\kappa=0}^{\infty} \int_0^1 t^{a_2 + \kappa - 1} (1 - t)^{a_3 - a_2 - 1} E_{\alpha_1, \alpha_2} \left(-\frac{\zeta}{t^{m_1(1-t)^{m_2}}}\right) dt \frac{z^\kappa}{\kappa!}. \quad (60)$$

Interchanging the order of summation and integration in equation (60), we have

$$\begin{aligned} \Phi_{\zeta, \alpha_1}^{\alpha_2; m_1, m_2}(a_2; a_3; z) &= \frac{1}{B(a_2, a_3 - a_2)} \int_0^1 t^{a_2 - 1} (1 - t)^{a_3 - a_2 - 1} \\ &\quad \times \sum_{\kappa=0}^{\infty} \frac{(zt)^\kappa}{\kappa!} E_{\alpha_1, \alpha_2} \left(-\frac{\zeta}{t^{m_1(1-t)^{m_2}}}\right) dt. \end{aligned} \quad (61)$$

Corollary 12. For the new extended confluent hypergeometric function, the following formula hold.

$$\Phi_{\zeta, \alpha_1}^{\alpha_2; m_1, m_2}(a_2; a_3; z) = \frac{\exp(z)}{B(a_2, a_3 - a_2)} \int_0^1 t^{a_2 - 1} (1 - t)^{a_3 - a_2 - 1} \exp(-zt) E_{\alpha_1, \alpha_2} \left(-\frac{\zeta}{t^{m_1(1-t)^{m_2}}}\right) dt.$$

Theorem 13.

$$\frac{d}{dz} F_{\zeta, \alpha_1}^{\alpha_2; m_1, m_2}(a_1, a_2; a_3; z) = \frac{a_1 a_2}{a_3} F_{\zeta, \alpha_1}^{\alpha_2; m_1, m_2}(a_1 + 1, a_2 + 1; a_3 + 1; z), \quad (62)$$

$$\frac{d^\kappa}{dz^\kappa} F_{\zeta, \alpha_1}^{\alpha_2; m_1, m_2}(a_1, a_2; a_3; z) = \frac{(a_1)_\kappa (a_2)_\kappa}{(a_3)_\kappa} F_{\zeta, \alpha_1}^{\alpha_2; m_1, m_2}(a_1 + \kappa, a_2 + \kappa; a_3 + \kappa; z), \quad (63)$$

which are differential formulas.

Proof. Using equation (19), we have

$$\frac{d}{dz} F_{\zeta, \alpha_1}^{\alpha_2; m_1, m_2}(a_1, a_2; a_3; z) = \sum_{\kappa=1}^{\infty} \frac{B_{\zeta, \alpha_1}^{\alpha_2; m_1, m_2}(a_2 + \kappa, a_3 - a_2)}{B(a_2, a_3 - a_2)} (a)_\kappa \frac{z^{\kappa-1}}{(\kappa-1)!}. \quad (64)$$

Setting $\kappa \rightarrow \kappa + 1$ in equation (64), we get

$$\frac{d}{dz} F_{\zeta, \alpha_1}^{\alpha_2; m_1, m_2}(a_1, a_2; a_3; z) = a \sum_{\kappa=0}^{\infty} \frac{B_{\zeta, \alpha_1, \kappa}^{\alpha_2; m_1, m_2}(a_2 + \kappa + 1, a_3 - a_2)}{B(a_2, a_3 - a_2)} (a + 1)_{\kappa} \frac{z^{\kappa}}{\kappa!} \tag{65}$$

Applying equation (7) to (65), the desired result in equation (62) is obtained. On successive differentiation of equation (62), also the required result in (63) is obtained.

Corollary 14.

$$\frac{d}{dz} \Phi_{\zeta, \alpha_1}^{\alpha_2; m_1, m_2}(a_2; a_3; z) = \frac{a_2}{a_3} F_{\zeta, \alpha_1}^{\alpha_2; m_1, m_2}(a_2 + 1; a_3 + 1; z),$$

$$\frac{d^{\kappa}}{dz^{\kappa}} \Phi_{\zeta, \alpha_1}^{\alpha_2; m_1, m_2}(a_2; a_3; z) = \frac{(a_2)_{\kappa}}{(a_3)_{\kappa}} F_{\zeta, \alpha_1}^{\alpha_2; m_1, m_2}(a_2 + \kappa; a_3 + \kappa; z).$$

8. Mellin Transform

Theorem 15.

$$M\{F_{\zeta, \alpha_1}^{\alpha_2; m_1, m_2}(a_1, a_2; a_3; z); l\} = \frac{\pi B(a_2 + m_1 l, a_3 + m_1 l - a_2)}{\sin \pi l \Gamma(\alpha_1 - a_2) B(a_2, a_3 - a_2)} F(a_1, a_2 + m_1 l, a_3 + m_1 l + m_2 l; z). \tag{66}$$

Proof. Using definition of the Mellin transform in equation (10), we have

$$M\{F_{\zeta, \alpha_1}^{\alpha_2; m_1, m_2}(a_1, a_2; a_3; z); l\} = \int_0^{\infty} \zeta^{l-1} F_{\zeta, \alpha_1}^{\alpha_2; m_1, m_2}(a_1, a_2; a_3; z) d\zeta. \tag{67}$$

Substituting equation (19) into (67), we have

$$M\{F_{\zeta, \alpha_1}^{\alpha_2; m_1, m_2}(a_1, a_2; a_3; z); l\} = \int_0^{\infty} \zeta^{l-1} \left\{ \frac{1}{B(a_2, a_3 - a_2)} \int_0^1 t^{a_2-1} (1-t)^{a_3-a_2-1} \right. \\ \left. \times (1-zt)^{-a_1} E_{\alpha_1, \alpha_2} \left(-\frac{\zeta}{t^{m_1(1-t)^{m_2}}} \right) dt \right\} d\zeta. \tag{68}$$

Interchanging the order of integrations in equation (68), yields

$$M\{F_{\zeta, \alpha_1}^{\alpha_2; m_1, m_2}(a_1, a_2; a_3; z); l\} = \frac{1}{B(a_2, a_3 - a_2)} \int_0^1 t^{a_2-1} (1-t)^{a_3-a_2-1} (1-zt)^{-a_1} \\ \times \left\{ \int_0^{\infty} \zeta^{l-1} E_{\alpha_1, \alpha_2} \left(-\frac{\zeta}{t^{m_1(1-t)^{m_2}}} \right) d\zeta \right\} dt. \tag{69}$$

On setting $\zeta = ut^{m_1}(1-t)^{m_2}$ in (69), we obtain

$$M\{F_{\zeta, \alpha_1}^{\alpha_2; m_1, m_2}(a_1, a_2; a_3; z); l\} = \frac{1}{B(a_2, a_3 - a_2)} \int_0^1 t^{a_2-1} (1-t)^{a_3-a_2-1} (1-zt)^{-a_1} \\ \times \left\{ \int_0^{\infty} u^{l-1} E_{\alpha_1, \alpha_2}(-u) du \right\} dt. \tag{70}$$

On applying equations (4), (5) and (17) to (70), the desired result obtained.

Corollary 16.

$$F_{\zeta, \alpha_1}^{\alpha_2; m_1, m_2}(a_1, a_2; a_3; z) = \frac{1}{2iB(a_2, a_3 - a_2)} \int_{\gamma' - i\infty}^{\gamma' + i\infty} \frac{\Gamma(a_2 + m_1 l) \Gamma(a_3 + m_2 l - a_2)}{\Gamma(a_1 - \alpha_2 l) \Gamma(a_1 + a_2 + m_1 l + m_2 l)} \times F(a_1, a_2 + m_1 l, a_3 + m_1 l + m_2 l; z) \zeta^{-l} ds,$$

where

$$Re(m_1) > 0, Re(m_2) > 0, Re(a_1) > 0, Re(a_2) > 0, Re(\alpha_1 - sl) > 0, Re(a_1 + m_1 l) > 0, Re(a_2 + m_2 l) > 0, Re(\zeta) \geq 0, \gamma' > 0.$$

Corollary 17.

$$M\{\Phi_{\zeta, \alpha_1}^{\alpha_2; m_1, m_2}(a_1, a_2; a_3; z); l\} = \frac{\pi B(a_2 + m_1 l, a_3 + m_1 l - a_2)}{\sin \pi l \Gamma(\alpha_1 - \alpha_2) B(a_2, a_3 - a_2)} \times \Phi(a_2 + m_1 l, a_3 + m_1 l + m_2 l; z),$$

$$\Phi_{\zeta, \alpha_1}^{\alpha_2; m_1, m_2}(a_2; a_3; z) = \frac{1}{2i B(a_2, a_3 - a_2)} \int_{\gamma' - i\infty}^{\gamma' + i\infty} \frac{\Gamma(a_2 + m_1 s) \Gamma(a_3 + m_2 s - a_2)}{\Gamma(a_1 - \alpha_2 l) \Gamma(a_1 + a_2 + m_1 l + m_2 l)} \times \Phi(a_2 + m_1 l, a_3 + m_1 l + m_2 l; z) \zeta^{-l} dl,$$

Where

$$Re(m_1) > 0, Re(m_2) > 0, Re(a_1) > 0, Re(a_2) > 0, Re(\alpha_1 - l\alpha_2) > 0, Re(a_1 + m_1 l) > 0, Re(a_2 + m_2 l) > 0, Re(\zeta) \geq 0, \gamma' > 0$$

Theorem 18.

$$F_{\zeta, \alpha_1}^{\alpha_2; m_1, m_2}(a_1, a_2; a_3; z) = (1 - z)^{-a_1} F_{\zeta, \alpha_1}^{\alpha_2; m_1, m_2}\left(a_1, a_2; a_3; \frac{z}{z-1}\right), \tag{71}$$

$$\Phi_{\zeta, \alpha_1}^{\alpha_2; m_1, m_2}(a_2; a_3; z) = \exp(z) \Phi_{\zeta, \alpha_1}^{\alpha_2; m_1, m_2}(a_3 - a_2; a_3; z), \tag{72}$$

which are the transformation formulas for the extended Gauss hypergeometric and Kumar confluent hypergeometric functions.

Proof. Setting $t \rightarrow 1 - t$ in equations (53) and (59), we obtained the required results in (71) and (72), respectively.

Theorem 19.

$$F_{\zeta, \alpha_1}^{\alpha_2; m_1, m_2}(a_1, a_2; a_3; 1) = \frac{B_{\zeta, \alpha_1}^{\alpha_2; m_1, m_2}(a_2, a_3 - a_2)}{B(a_2, a_3 - a_2)}, \tag{73}$$

is the extended Gauss summation formula.

Proof. Taking $z = 1$, in equation (53), the required result in (73) is obtained.

9. Conclusions

The new extension of the extended beta function $B_{\zeta, \alpha_1}^{\alpha_2; m_1, m_2}(a_1, a_2)$, Gauss hypergeometric function $F_{\zeta, \alpha_1}^{\alpha_2; m_1, m_2}(a_1, a_2; a_3; z)$ and confluent hypergeometric function $\Phi_{\zeta, \alpha_1}^{\alpha_2; m_1, m_2}(a_2; a_3; z)$ were obtained and presented with their important properties. The extended beta, Gauss and confluent hypergeometric functions and their special cases proposed in [21, 33-37] can be regained from the newly proposed functions. It is hoped that it will be useful in Science and Technology [38-40].

Acknowledgement

The authors are thankful to the referees for their valuable remarks, comments and suggestions that led to the improvement of the presentation of the research work to this form.

Conflict of interest

The authors state that did not have conflict of interests.

References

[1] Chaudhry M.A., Zubair S.M., Generalized incomplete gamma functions with applications, *Journal of Computational and Applied Mathematics*, 55 (1994), 199-124.

[2] Chaudhry M.A., Zubair S.M., On decomposition of generalized incomplete gamma functions with applications to Fourier transform, *Journal of Computational and Applied Mathematics*, 59 (1995) 253-284.

[3] Chaudhry M.A., Zubair S.M., On extension of generalized incomplete gamma functions with applications, *Journal of Australian Mathematical Society Series B*, 37 (1996) 392-404.

[4] Chaudhry M.A., Transformation of extended gamma function $\Gamma_{0, 2}^{\alpha, 0}[(B, X)]$ with applications to astrophysical thermonuclear functions, *Astrophysics and Space Science*, 262 (1999) 263-270.

[5] Kulip M.A.H., Mohsen F.F., Barahmah S.S., Further extended gamma and beta functions in term of generalized Wright functions, *Electronic Journal of University of Aden for Basic and Applied Sciences*, 1 (2) (2020) 78-83.

[6] Ata E., Kiyamaz I.O., A study on certain properties of generalized special function defined by Fox –

- Wright function, *Applied Mathematics and Nonlinear Sciences*, 5 (1) (2020) 147-162.
- [7] He F., Bakhet A., Abdullah M. and Hidan M., On the extended hypergeometric functions and their applications for the derivatives of the extended Jacobi matrix polynomials, *Mathematical Problems in Engineering*, (2020) 4268361..
- [8] Sahin R., Yagci O., Fractional calculus of the extended hypergeometric function, *Applied Mathematics and Nonlinear Sciences*, 5 (1) (2020) 369-384.
- [9] Nisar K.S., Suthar D.I., Agarwal A. and Purohit S.D., Fractional calculus operators with Appell function kernels applied to Srivastava polynomials and extended Mittag-Leffler function, *Advance in Difference Equations*, 148 (2020) 1-14.
- [10] Kim T., kim D.S., Note on the degenerate gamma function, *Russian Journal of Mathematical Physics*, 27 (3) (2020) 352-358.
- [11] Tassaddiq A., An application of theory of distributions to the family of λ -generalized gamma function, *Mathematics*, 5 (6) (2020) 5839-5858.
- [12] Khan N., Usman T., Aman M., Extended beta, hypergeometric and confluent hypergeometric function, *Transactions of National Academy of Science of Azerbaijan. Series of Physical-Technical and Mathematical Sciences, Issue Mathematics*, 39 (1) (2019) 83-97.
- [13] Parmar R.K., Pogany T.K., On the Mathieu-type series for the unified Gauss hypergeometric functions, *Applicable Analysis and Discrete Mathematics*, 14 (2020) 138-149.
- [14] Tilahun K., Tadessee H., Suthar D.L., The extended Bessel-Maitland function and integral operators associated with fractional calculus, *Journal of Mathematics*, (2020) 7582063.
- [15] Suthar D.L., Baleanu D., Purohit S.D. and Ucar E., Certain k-fractional operators and images forms of k-struve function, *Mathematics*, 5 (3) (2020) 1706-1719.
- [16] Suthar D.L., Khan A.M., Alaria A., Puhohit S.D. and Singh J., Extended Bessel-Maitland function and its properties pertaining of integral transforms and fractional calculus, *Mathematics*, 5 (2) (2020) 1400-1414.
- [17] Abubakar U.M., Kabara S.R., A note on a new extended gamma and beta functions and their properties, *IOSR Journal of Mathematics*, 15 (5) (2019) 1-6.
- [18] Abubakar U.M., Kabara S.R., Some results on the extension of the extended beta function, *IOSR Journal of Mathematics*, 15 (5) (2019) 7-12.
- [19] Abubakar U.M., New generalized beta function associated with the Fox-Wright function, *Journal of Fractional Calculus and Application*, 12 (2) (2021), 204-227
- [20] Abubakar U.M., Kabara S.R., Lawan M.A. and Idris F.A., A new extension of modified gamma and beta functions, *Cankaya University Journal of Science and Engineering*, 18 (1), 9-23 (2021).
- [21] Oraby A., Ahmed M., Khaled M., Ahmed E. and Magdy M., Generalization of beta functions in term of Mittag-Leffler function, *Frontiers in Scientific Research and Tehnology*, 1 (2020) 81-88.
- [22] Wiman A., Uber den fundamenta satz under theorie de fonction $E_{\alpha_1}(x)$, *Acta Mathematica*, 29 (1950) 191-201.
- [23] Wiman A., Uber die nullstellum de funktionen $E_{\alpha_1}(x)$, *Acta Mathematica*, 29 (1950) 217-234.
- [24] Mittag-Leffler G.M., Sur la nouvelle function $E_{\alpha_1}(x)$, *Comptes Rendus de l'Academie des Sciences Paris Series II*, 11 (137) (1903) 537-539.
- [25] Mittag-Leffler G.M., Soprala funzione $E_{\alpha_1}(x)$, *Redicoti della Accademia dei Lincei*, V(13) (1904) 3-5.
- [26] Mittag-Leffler G.M., Sur larepresentation analytique d'une function monogone (inquieme note), *Acta Mathematica*, 29 (1905) 237-252.
- [27] Chaudhry M.A., Zubair S.M., On a class of incomplete gamma functions with application, Chapman & Hall / CRC, 2002.
- [28] Sahin R., Yagci, O., A new generalization of pochhammer symbol and its application, *Applied Mathematics and Nonlinear Science*, 5(1) (2020) 255-266.
- [29] Mardina F., Mura A., Pagnini G., The M-Wright function in Time-fractional diffusion processes: A tutorial survey, *International Journal of Differential Equations*, (2010) 104505.
- [30] Rahman G., Saboor A., Anjum Z., Nisar and Abdeljawad T.A., An extension of the Mittag-Leffler function and its associated properties, *Advances in Mathematical Physics*, (2020) 5792853.
- [31] Chaudhry M.A., Rathie A.K., Parmar R.K. and Kim Y.S., Generalization of extended beta function, hypergeometric and confluent hypergeometric functions, *Applied Mathematics and Computation* 159 (2004) 589-602.
- [32] Mathai A.M., Haubold H.J., Special functions for applied Scientists, Springer, 2008.
- [33] Rahman G., Mubeen S., Nisar K.S., A new generalization of extended beta and

- hypergeometric functions, *Journal of Fractional Calculus and Applications*, 11 (2) (2020) 32-44.
- [34] Shadab M., Jabee S., Choi J., An extended beta function and its applications, *Far East Journal of Mathematical Sciences*, 103 (1) (2018) 235-251.
- [35] Luo M-J., Milovanovic G.V., Agarwal P., Some results on the extended beta and extended hypergeometric functions, *Applied Mathematics and Computation*, 248 (2014) 631-651.
- [36] Lee D.M., Rathie A.K., Parmar R.K. and Kim Y.S, Generalization of extended beta function, hypergeometric and confluent hypergeometric functions, *Homam Mathematical Journal*, 33(2) (2011) 187-206.
- [37] Chaudhry M.A., Qadir A., Rafique M. and Zubair S.M., Extension of Euler's beta function, *Journal of Computational and Applied Mathematics*, 78 (1997) 19-32.
- [38] Abubakar U.M., A study of extended beta and associated functions connected to Fox-Wright function, *12th Symposium of the Fractional Calculus and Applications Group, 1st International (ONLINE) Conference in Mathematical Science and Fractional Calculus*, 16-18 February 2021, 1-23.
- [39] Abubakar, U.M., Patel, S., On a new generalized beta function defined by the generalized Wright function and its applications, *Malaysian Journal of Computing*, 6 (2) (2021) 851-870.
- [40] Abubakar U.M., A new generalization of Gengenbauer polynomials, *Journal of Informatics and Mathematical Sciences*, 13 (2) (2021) 119-128.



On the fine spectra of the Jacobi matrices on c_0, c, ℓ_p ($1 \leq p \leq \infty$) and bv_p ($1 \leq p < \infty$)

Nuh DURNA^{1,*} , Mustafa YILDIRIM¹ , Abbas KILIÇ¹ 

¹Sivas Cumhuriyet University, Department of Mathematics, Sivas/ TURKEY

Abstract

The spectrum and spectral divisions of band matrices are very new and popular topics of studies. In this paper, our aims are to investigate boundedness of Jacobi matrix which is a band matrix has important role in physics and give subdivisions of the spectra, which are approximate point spectrum, defect spectrum and compression spectrum, for a special type Jacobi matrix. Moreover, we will find the fine division of spectrum which is given by Goldberg with the help of it.

Article info

History:
Received: 22.02.2021
Accepted: 10.08.2021

Keywords:
Jacobi matrices,
Spectrum,
Fine spectrum.

1. Introduction

The band matrices are an interesting topic for researchers since they have important applications in applied mathematics. In the summability theory and functional analysis, there are applications of band matrices. Also, they are used in linear algebra, computation in classical and fractional situations and approximation theory. The spectrum and spectral divisions of band matrices are very new and popular topics of studies.

In recent years, some authors have investigated the spectral decomposition of generalized difference matrices on various sequence spaces. In 2011, Amirov, Durna and Yıldırım [1] calculated the approximate point spectrum, the defect spectrum, and the compression spectrum of the operators using the relationship between the spectral decompositions of the operators. Many researchers have benefited from this study and found the fine division of the operator. In the studies conducted so far, the approximate point spectrum, the defect spectrum and the compression spectrum were calculated using the fine spectrum of the operator. Generally, in order to examine the fine spectrum of operator, we investigate injectivity and surjectivity of its adjoint. Because it is well-known that " T has a dense range if and only if T^* is 1-1" and " T has a bounded inverse if and only if T^* is onto". But we can not always find adjoint operator. Even if we find it, we can not investigate the character of the

series obtained while examining the injectivity and surjectivity of the adjoint operator. For example, it is not possible to talk about the adjoint of operator in general on ℓ_∞ , because ℓ_∞ does not have the Schauder basis in the usual sense. And so, we will first calculate the approximate point spectrum, the defect spectrum and the compression spectrum of operator using the relationship between spectral division of operator and spectral division of its adjoint. Moreover, we will find the fine division of spectrum which is given by Goldberg with the help of it.

Firstly, we will recall basic definitions and properties of operator which are used by us.

Definition 1.1 Let $T: D(T) \rightarrow X$ be a linear operator, defined on $D(T) \subset X$, where $D(T)$ denote the domain of T and X is an infinite-dimensional complex normed space. Let $T_\lambda := \lambda I - T$ for $T \in B(X)$ and $\lambda \in \mathbb{C}$ where I is the identity operator, then different definitions and notations of spectra are defined as follows [2-3]:

- (1) The spectrum: $\sigma(T, X) := \{\lambda \in \mathbb{C}: T_\lambda \text{ is not invertible}\}$,
- (2) The resolvent set $\rho(T, X)$ is the complement of $\sigma(T, X)$ in \mathbb{C} ,
- (3) The point spectrum: $\sigma_p(T, X) := \{\lambda \in \mathbb{C}: T_\lambda \text{ is not injective}\}$,
- (4) The continuous spectrum: $\sigma_c(T, X) := \{\lambda \in \mathbb{C}: T_\lambda \text{ is injective and } \overline{R(T_\lambda)} = X \text{ but } R(T_\lambda) \neq X\}$, where $R(T_\lambda)$ denote the domain of T_λ ,

*Corresponding author. e-mail address: ndurna@cumhuriyet.edu.tr
<http://dergipark.gov.tr/csj> ©2021 Faculty of Science, Sivas Cumhuriyet University

- (5) The residual spectrum: $\sigma_r(T, X) := \{ \lambda \in \mathbb{C} : T_\lambda \text{ is injective but } \overline{R(T_\lambda)} \neq X \}$,
- (6) The defect spectrum: $\sigma_\delta(T, X) := \{ \lambda \in \sigma(T, X) : R(T_\lambda) \neq X \}$,
- (7) The compression spectrum: $\sigma_{co}(T, X) := \{ \lambda \in \mathbb{C} : \overline{R(T_\lambda)} \neq X \}$,
- (8) The approximate point spectrum: $\sigma_{ap}(T, X) := \{ \lambda \in \mathbb{C} : \text{there exists a sequence } (x_n) \text{ in } X \text{ such that } \|x_n\| = 1 \text{ for all } n \in \mathbb{N} \text{ and } \lim_{n \rightarrow \infty} \|T_\lambda(x_n)\| = 0 \}$.

In Banach spaces, Proposition 1.2 is frequently used for calculating the partition of the spectrum of the linear operator.

Proposition 1.2 [2] The spectra and subspectra of an operator $T \in B(X)$ and its adjoint $T^* \in B(X^*)$ are related by the following relations:

- (a) $\sigma(T^*, X^*) = \sigma(T, X)$,
- (b) $\sigma_c(T^*, X^*) \subseteq \sigma_{ap}(T, X)$,
- (c) $\sigma_{ap}(T^*, X^*) = \sigma_\delta(T, X)$,
- (d) $\sigma_\delta(T^*, X^*) = \sigma_{ap}(T, X)$,
- (e) $\sigma_p(T^*, X^*) = \sigma_{co}(T, X)$,
- (f) $\sigma_{co}(T^*, X^*) \supseteq \sigma_p(T, X)$,
- (g) $\sigma(T, X) = \sigma_{ap}(T, X) \cup \sigma_p(T^*, X^*) = \sigma_p(T, X) \cup \sigma_{ap}(T^*, X^*)$.

1.1. Goldberg's classification of spectrum

If X is a Banach space and $T \in B(X)$, then there are three possibilities for $R(T)$:

- (I) $R(T) = X$, (II) $\overline{R(T)} = X$, but $R(T) \neq X$,
- (III) $\overline{R(T)} \neq X$

and three possibilities for T^{-1} :

- (1) T^{-1} exists and continuous,

- (2) T^{-1} exists but discontinuous,
- (3) T^{-1} does not exist.

If these possibilities are combined in all possible ways, nine different states are created. These are labelled by: $I_1, I_2, I_3, II_1, II_2, II_3, III_1, III_2, III_3$. If an operator is in state III_2 for example, then $\overline{R(T)} \neq X$ and T^{-1} exist but is discontinuous (see [4]).

If λ is a complex number such that $T_\lambda \in I_1$ or $T_\lambda \in II_1$, then $\lambda \in \rho(T, X)$. All scalar values of λ not in $\rho(T, X)$ comprise the spectrum of T . The further classification of $\sigma(T, X)$ gives rise to the fine spectrum of T . That is, $\sigma(T, X)$ can be divided into the subsets $I_2\sigma(T, X) = \emptyset, I_3\sigma(T, X), II_2\sigma(T, X), II_3\sigma(T, X), III_1\sigma(T, X), III_2\sigma(T, X), III_3\sigma(T, X)$. For example, if T_λ is in a given state, III_2 (say), then we write $\lambda \in III_2\sigma(T, X)$.

Let us give a short survey concerning the spectrum and the fine spectrum and subdivision of the spectrum of the linear operators over certain sequence spaces.

First, the spectrum of the Cesàro operator of order one over the sequence space ℓ_2 has been examined by Brown, Halmos, and Shields [5] in 1965. In 1977, Cass and Rhoades [6], in 1978, Cardlidge [7] computed the spectrum of Weighted mean matrices.

Subdivisions of the spectrum for an operator on a sequence space were given by [8], [9] and [10] firstly.

Besides the above listed workers, the spectrum, fine spectrum and subdivision of the spectrum for various matrix operators have been investigated by many authors in the recent years, [11-25].

By the definitions given above, the following statements are obtained from the Table given by Durna and Yıldırım in [9]:

Table 1. Subdivisions of the spectrum of a linear operator

		1	2	3
		T_λ^{-1} exists and is bounded	T_λ^{-1} exists and is unbounded	T_λ^{-1} does not exists
<i>I</i>	$R(T_\lambda) = X$	$\lambda \in \rho(T, X)$ $\lambda \in \rho(T, X)$	–	$\lambda \in \sigma_p(T, X)$ $\lambda \in \sigma_{ap}(T, X)$
<i>II</i>	$\overline{R(T_\lambda)} = X$	$\lambda \in \rho(T, X)$	$\lambda \in \sigma_c(T, X)$ $\lambda \in \sigma_{ap}(T, X)$ $\lambda \in \sigma_\delta(T, X)$	$\lambda \in \sigma_p(T, X)$ $\lambda \in \sigma_{ap}(T, X)$ $\lambda \in \sigma_\delta(T, X)$
<i>III</i>	$\overline{R(T_\lambda)} \neq X$	$\lambda \in \sigma_r(T, X)$ $\lambda \in \sigma_\delta(T, X)$ $\lambda \in \sigma_{co}(T, X)$	$\lambda \in \sigma_r(T, X)$ $\lambda \in \sigma_{ap}(T, X)$ $\lambda \in \sigma_\delta(T, X)$ $\lambda \in \sigma_{co}(T, X)$	$\lambda \in \sigma_p(T, X)$ $\lambda \in \sigma_{ap}(T, X)$ $\lambda \in \sigma_\delta(T, X)$ $\lambda \in \sigma_{co}(T, X)$

In this paper, we computed subdivisions of the spectrum for constant Jacobi matrix.

2. Boundedness of Jacobi Matrix $J(s_n, r_n)$

A matrix of the form $J = (a_{ij})$ is called a Jacobi matrix, where $a_{ij} = 0$ unless $|j - i| < 1$. More specifically,

$$J(s_n, r_n) = \begin{pmatrix} s_0 & r_0 & 0 & 0 & \dots \\ r_0 & s_1 & r_1 & 0 & \dots \\ 0 & r_1 & s_2 & r_2 & \dots \\ 0 & 0 & r_2 & s_3 & \dots \\ \vdots & \vdots & \vdots & \vdots & \ddots \end{pmatrix} \tag{1}$$

where all s_n, r_n are real. If we get some constant sequences such as $(s_n) = (s)$ and $(r_n) = (r)$, this $J(s_n, r_n) = J(s, r)$ matrix is called constant Jacobi matrix. The spectral results are clear when $r = 0$, so for the sequel we will have $r \neq 0$.

Lemma 2.1 [25] Let T be an operator with the associated matrix $A = (a_{nk})$. Then the followings hold:

i. $T \in B(c)$ if and only if

$$\|A\| := \sup_n \sum_{k=1}^\infty |a_{nk}| < \infty, \tag{2}$$

$$a_k := \lim_{n \rightarrow \infty} a_{nk} \text{ exists for each } k, \tag{3}$$

$$a := \lim_{n \rightarrow \infty} \sum_{k=1}^\infty a_{nk} \text{ exists} \tag{4}$$

are valid.

ii. $T \in B(c_0)$ if and only if (2) and (3) with $a_k = 0$ for each k are valid.

iii. $T \in B(\ell_\infty)$ if and only if (2) is valid.

In these cases, the operator norm of T is

$$\|T\|_{(\ell_\infty:\ell_\infty)} = \|T\|_{(c:c)} = \|T\|_{(c_0:c_0)} = \|A\|. \tag{5}$$

iv. $T \in B(\ell_1)$ if and only if

$$\|A^t\| := \sup_k \sum_{n=1}^\infty |a_{nk}| < \infty \tag{6}$$

is valid.

In these cases, the operator norm of T is $\|T\|_{(\ell_1; \ell_1)} = \|A^\ell\|$.

Theorem 2.2 $\mu \in \{c_0, c, \ell_1, \ell_\infty\}$. $J(s, r) \in B(\mu)$ and $\|J(s, r)\|_{(\mu; \mu)} \leq 2|r| + |s|$.

Proof It is clear from Lemma 2.1.

Theorem 2.3 $J(s, r) \in B(\ell_p)$ ($1 < p < \infty$) and $\|J(s, r)\|_{(\ell_p; \ell_p)} \leq 2|r| + |s|$.

Proof Since

$$\begin{aligned} \|J(s, r)x\|_{\ell_p} &= \left(\sum_{n=1}^{\infty} |rx_{n-1} + sx_n + rx_{n+1}|^p \right)^{\frac{1}{p}} \\ &= \left(\sum_{n=1}^{\infty} |r(x_{n-1} + x_{n+1}) + sx_n|^p \right)^{\frac{1}{p}} \\ &\leq |r| \left(\sum_{n=1}^{\infty} |x_{n-1} + x_{n+1}|^p \right)^{\frac{1}{p}} + |s| \left(\sum_{n=1}^{\infty} |x_n|^p \right)^{\frac{1}{p}} \\ &\leq 2|r|\|x\|_{\ell_p} + |s|\|x\|_{\ell_p} \leq (2|r| + |s|)\|x\|_{\ell_p}, \end{aligned}$$

where $x_0 = 0$, we have $J(s, r) \in B(\ell_p)$ and $\|J(s, r)\|_{(\ell_p; \ell_p)} \leq 2|r| + |s|$.

Theorem 2.4 $J(s, r) \in B(bv_p)$ ($1 < p < \infty$) and $\|J(s, r)\|_{(bv_p; bv_p)} \leq |s - r| + 3|r|$.

Proof We have

$$\begin{aligned} \|J(s, r)x\|_{bv_p}^p &= |rx_1 + sx_2 + rx_3 - sx_1 - rx_2|^p + |rx_2 + sx_3 + rx_4 - rx_1 - sx_2 - rx_3|^p + \dots \\ &= |(r - s)x_1 + (s - r)x_2 + rx_3|^p + |(r - s)x_2 + (s - r)x_3 + rx_4 - rx_1|^p + \dots \\ &\leq \sum_{n=0}^{\infty} |(r - s)x_{n+1} + (s - r)x_{n+2} + r(x_{n+3} - x_{n+2} + x_{n+2} - x_{n+1} + x_{n+1} - x_n)|^p \\ &= \left[\left(\sum_{n=0}^{\infty} |(s - r)(x_{n+2} - x_{n+1}) + r(x_{n+3} - x_{n+2} + x_{n+2} - x_{n+1} + x_{n+1} - x_n)|^p \right)^{1/p} \right]^p \\ &\leq \left[\left(\sum_{n=0}^{\infty} |s - r|^p |x_{n+2} - x_{n+1}|^p \right)^{1/p} \right. \\ &\quad \left. + \left(\sum_{n=0}^{\infty} |r|^p |x_{n+3} - x_{n+2} + x_{n+2} - x_{n+1} + x_{n+1} - x_n|^p \right)^{1/p} \right]^p \\ &\leq \left[\left(|s - r| \sum_{n=0}^{\infty} |x_{n+2} - x_{n+1}|^p \right)^{1/p} \right. \\ &\quad \left. + \left(|r| \sum_{n=0}^{\infty} (|x_{n+3} - x_{n+2}| + |x_{n+2} - x_{n+1}| + |x_{n+1} - x_n|)^p \right)^{1/p} \right]^p \end{aligned}$$

$$\begin{aligned} &\leq \left[|s - r| \left(\sum_{n=0}^{\infty} |x_{n+2} - x_{n+1}|^p \right)^{1/p} \right. \\ &\quad \left. + |r| \left[\left(\sum_{n=0}^{\infty} |x_{n+3} - x_{n+2}|^p \right)^{1/p} + \left(\sum_{n=0}^{\infty} |x_{n+2} - x_{n+1}|^p \right)^{1/p} + \left(\sum_{n=0}^{\infty} |x_{n+1} - x_n|^p \right)^{1/p} \right] \right]^p \\ &\leq [|s - r| \|x\|_{bv_p} + |r| 3 \|x\|_{bv_p}]^p = [|s - r| + 3|r|]^p \|x\|_{bv_p}^p \end{aligned}$$

where $x_0 = 0$. Then

$$\|J(s, r)x\|_{bv_p} \leq (|s - r| + 3|r|) \|x\|_{bv_p}.$$

Hence we get $J(s, r) \in B(bv_p)$ and $\|J(s, r)\|_{(bv_p:bv_p)} \leq |s - r| + 3|r|$.

Theorem 2.5 $J(s_n, r_n) \in B(\mu)$ and $\|J(s_n, r_n)\|_{(\mu:\mu)} \leq 2\|r\|_{\infty} + \|s\|_{\infty}$ where $\mu \in \{c_0, c, \ell_1, \ell_{\infty}\}$, $(s_n), (r_n) \in \mu$.

Proof It is clear from Lemma 2.1.

Theorem 2.6 $J(s_n, r_n) \in B(\ell_p)$ ($1 < p < \infty$) and $\|J(s_n, r_n)\|_{(\ell_p:\ell_p)} \leq 2\|r\|_p + \|s\|_p$ where $(s_n), (r_n) \in \ell_p$.

Proof Since

$$\begin{aligned} \|J(s_n, r_n)x\|_p &= \left(\sum_{n=1}^{\infty} |r_{n-1}x_{n-1} + s_nx_n + r_nx_{n+1}|^p \right)^{\frac{1}{p}} \\ &\leq \left(\sum_{n=1}^{\infty} |r_{n-1}x_{n-1} + s_nx_n|^p \right)^{\frac{1}{p}} + \left(\sum_{n=1}^{\infty} |r_nx_{n+1}|^p \right)^{\frac{1}{p}} \\ &\leq \left(\sum_{n=1}^{\infty} |r_{n-1}x_{n-1}|^p \right)^{\frac{1}{p}} + \left(\sum_{n=1}^{\infty} |s_nx_n|^p \right)^{\frac{1}{p}} + \left(\sum_{n=1}^{\infty} |r_nx_{n+1}|^p \right)^{\frac{1}{p}} \\ &\leq (2\|r\|_p + \|s\|_p) \|x\|_p, \end{aligned}$$

we have $J(s_n, r_n) \in B(\ell_p)$ and $\|J(s_n, r_n)\|_{(\ell_p:\ell_p)} \leq 2\|r\|_p + \|s\|_p$.

3. Spectrum of Jacobi Matrix $J(s, r)$ with constant entries

In this section, we will give the spectral decomposition of Jacobi Matrix $J(s, r)$ with constant entries with the help of the spectrum and the fine spectrum, which were previously studied in [27] and [18].

3.1. Subdivision of the spectrum of $J(s, r)$ on c_0

Theorem 3.1 $\sigma_{ap}(J(s, r), c_0) = \sigma(J(s, r), c_0) = [s - 2r, s + 2r]$.

Proof From Table 1, we know

$$\sigma_{ap}(J(s, r), c_0) = \sigma(J(s, r), c_0) \setminus III_1 \sigma(J(s, r), c_0).$$

Since $\sigma_r(J(s, r), c_0) = \emptyset$ from [27, Theorem 3.3], we have $III_1\sigma(J(s, r), c_0) = \emptyset$ and we know $\sigma(J(s, r), c_0) = [s - 2r, s + 2r]$ from [27, Theorem 2.5]. Hence $\sigma_{ap}(J(s, r), c_0) = [s - 2r, s + 2r]$.

Theorem 3.2 $\sigma_\delta(J(s, r), c_0) = \sigma(J(s, r), c_0) = [s - 2r, s + 2r]$.

Proof We have

$$\sigma_\delta(J(s, r), c_0) = \sigma(J(s, r), c_0) \setminus I_3\sigma(J(s, r), c_0)$$

from Table 1. Since $\sigma_p(J(s, r), c_0) = \emptyset$ from [27, Theorem 2.1], we get $I_3\sigma(J(s, r), c_0) = \emptyset$ and we know $\sigma(J(s, r), c_0) = [s - 2r, s + 2r]$ from [27, Theorem 2.5]. Hence $\sigma_\delta(J(s, r), c_0) = [s - 2r, s + 2r]$.

Theorem 3.3 $\sigma_{co}(J(s, r), c_0) = \emptyset$.

Proof From Table 1, we get

$$\sigma_{co}(J(s, r), c_0) = III_1\sigma(J(s, r), c_0) \cup III_2\sigma(J(s, r), c_0) \cup III_3\sigma(J(s, r), c_0).$$

Since $\sigma_p(J(s, r), c_0) = \emptyset$ from [27, Theorem 2.1] and $\sigma_r(J(s, r), c_0) = \emptyset$ from [27, Theorem 3.3], we have

$$III_1\sigma(J(s, r), c_0) = III_2\sigma(J(s, r), c_0) = III_3\sigma(J(s, r), c_0) = \emptyset.$$

Therefore $\sigma_{co}(J(s, r), c_0) = \emptyset$.

3.2. The fine spectrum and subdivision of the spectrum of $J(s, r)$ on c

Theorem 3.4 $III_2\sigma(J(s, r), c) = \{s + 2r\}$.

Proof By [27, Theorem 3.5], $\sigma_r(J(s, r), c) = \{s + 2r\}$. So that $s + 2r \in III_1\sigma(J(s, r), c) \cup III_2\sigma(J(s, r), c)$. Now we investigate either $s + 2r \in III_1\sigma(J(s, r), c)$ or $s + 2r \in III_2\sigma(J(s, r), c)$. For this we must show that $((s + 2r)I - J(s, r))^{-1}$ is whether bounded or not.

$$\begin{aligned} (s + 2r)I - J(s, r) &= \begin{pmatrix} s + 2r & 0 & 0 & \dots \\ 0 & s + 2r & 0 & \dots \\ 0 & 0 & s + 2r & \dots \\ \vdots & \vdots & \vdots & \ddots \end{pmatrix} - \begin{pmatrix} s & r & 0 & 0 & \dots \\ r & s & r & 0 & \dots \\ 0 & r & s & r & \dots \\ \vdots & \vdots & \vdots & \vdots & \ddots \end{pmatrix} \\ &= r \begin{pmatrix} 2 & -1 & 0 & 0 & \dots \\ -1 & 2 & -1 & 0 & \dots \\ 0 & -1 & 2 & -1 & \dots \\ \vdots & \vdots & \vdots & \vdots & \ddots \end{pmatrix}. \end{aligned}$$

The inverse of above matrix is

$$\frac{1}{r} \begin{pmatrix} 1 & 1 & 1 & 1 & \dots \\ 1 & 2 & 2 & 2 & \dots \\ 1 & 2 & 3 & 3 & \dots \\ 1 & 2 & 3 & 4 & \dots \\ \vdots & \vdots & \vdots & \vdots & \ddots \end{pmatrix}$$

which is unbounded matrix. Therefore we get $s + 2r \in III_2\sigma(J(s, r), c)$. Hence $III_2\sigma(J(s, r), c) = \{s + 2r\}$, from $III_2\sigma(J(s, r), c) \subset \sigma_r(J(s, r), c)$.

Corollary 3.5 $III_1\sigma(J(s, r), c) = \emptyset$.

Proof By [27, Theorem 3.5], $\sigma_r(J(s, r), c) = \{s + 2r\}$ and $III_1\sigma(J(s, r), c) = \emptyset$ from Theorem 3.4

Corollary 3.6 $\sigma_{ap}(J(s, r), c) = [s - 2r, s + 2r]$.

Proof From Table 1, we get

$$\sigma_{ap}(J(s, r), c) = \sigma(J(s, r), c) \setminus III_1\sigma(J(s, r), c).$$

Since $III_1\sigma(J(s, r), c) = \emptyset$ from Corollary 3.5 and $\sigma(J(s, r), c) = [s - 2r, s + 2r]$ from [27, Theorem 2.5], we have $\sigma_{ap}(J(s, r), c) = [s - 2r, s + 2r]$.

Corollary 3.7 $\sigma_{\delta}(J(s, r), c) = [s - 2r, s + 2r]$.

Proof We know

$$\sigma_{\delta}(J(s, r), c) = \sigma(J(s, r), c) \setminus I_3\sigma(J(s, r), c)$$

from Table 1. Since $\sigma_p(J(s, r), c) = \emptyset$ from [27, Theorem 2.1] and $\sigma(J(s, r), c) = [s - 2r, s + 2r]$ from [27, Theorem 2.5], we get $\sigma_{\delta}(J(s, r), c) = [s - 2r, s + 2r]$.

Corollary 3.8 $\sigma_{co}(J(s, r), c) = \{s + 2r\}$.

Proof By Table 1, we get

$$\sigma_{co}(J(s, r), c) = III_1\sigma(J(s, r), c) \cup III_2\sigma(J(s, r), c) \cup III_3\sigma(J(s, r), c).$$

Using $\sigma_p(J(s, r), c) = \emptyset$ from [27, Theorem 2.1], we get $\sigma_{co}(J(s, r), c) = \{s + 2r\}$ from Theorem 3.4 and Corollary 3.5.

3.3. The fine spectrum and subdivision of the spectrum of $J(s, r)$ on ℓ_1

Theorem 3.9 $III_1\sigma(J(s, r), \ell_1) = \emptyset$.

Proof We know

$$\sigma_{ap}(J^*(s, r), c^* \equiv \ell_1) = \sigma(J^*(s, r), \ell_1) \setminus III_1\sigma(J^*(s, r), \ell_1)$$

by Table 1 and we have

$$\sigma_{ap}(J^*(s, r) = J(s, r), \ell_1) = \sigma_{\delta}(J(s, r), c_0)$$

by the Proposition 1.2. We get

$$\sigma_{\delta}(J(s, r), c_0) = \sigma(J(s, r), c_0) \setminus I_3\sigma(J(s, r), c_0)$$

by Table 1. Since $\sigma(J(s, r), c_0) = [s - 2r, s + 2r]$ from [27, Theorem 2.5], and $I_3\sigma(J(s, r), c_0) = \emptyset$, we have $\sigma_{\delta}(J(s, r), c_0) = [s - 2r, s + 2r]$. Therefore $\sigma_{ap}(J^*(s, r) = J(s, r), \ell_1) = [s - 2r, s + 2r]$ and since $\sigma(J^*(s, r), \ell_1) = \sigma(J(s, r), \ell_1) = [s - 2r, s + 2r]$ from Proposition 1.2, we get $III_1\sigma(J(s, r), \ell_1) = \emptyset$.

Corollary 3.10 $III_2\sigma(J(s, r), \ell_1) = (s - 2r, s + 2r)$.

Proof We know $\sigma_r(J(s, r), \ell_1) = (s - 2r, s + 2r)$ by [27, Theorem 3.4] and we have $III_2\sigma(J(s, r), \ell_1) = (s - 2r, s + 2r)$ by Theorem 3.9.

Corollary 3.11 $\sigma_{ap}(J(s, r), \ell_1) = [s - 2r, s + 2r]$.

Proof From Table 1, we know

$$\sigma_{ap}(J(s, r), \ell_1) = \sigma(J(s, r), \ell_1) \setminus III_1\sigma(J(s, r), \ell_1).$$

Since $\sigma(J(s, r), \ell_1) = [s - 2r, s + 2r]$ from [27, Theorem 2.5] and $III_1\sigma(J(s, r), \ell_1) = \emptyset$ from Theorem 3.9, we have $\sigma_{ap}(J(s, r), \ell_1) = [s - 2r, s + 2r]$.

Corollary 3.12 $\sigma_\delta(J(s, r), \ell_1) = [s - 2r, s + 2r]$.

Proof Since $\sigma_p(J(s, r), \ell_1) = \emptyset$ from [27, Theorem 2.1], we have $I_3\sigma(J(s, r), \ell_1) = \emptyset$. And since

$$\sigma_\delta(J(s, r), \ell_1) = \sigma(J(s, r), \ell_1) \setminus I_3\sigma(J(s, r), \ell_1)$$

by Table 1, we have $\sigma_\delta(J(s, r), \ell_1) = [s - 2r, s + 2r]$.

Corollary 3.13 $\sigma_{co}(J(s, r), \ell_1) = (s - 2r, s + 2r)$.

Proof From Table 1, we have

$$\sigma_{co}(J(s, r), \ell_1) = III_1\sigma(J(s, r), \ell_1) \cup III_2\sigma(J(s, r), \ell_1) \cup III_3\sigma(J(s, r), \ell_1).$$

Using $\sigma_r(J(s, r), \ell_1) = (s - 2r, s + 2r)$ from [27, Theorem 3.4] and $\sigma_p(J(s, r), \ell_1) = \emptyset$ from [27, Theorem 2.1], we have $\sigma_{co}(J(s, r), \ell_1) = (s - 2r, s + 2r)$ from Theorem 3.9 and Corollary 3.10.

3.4. Subdivision of the spectrum of $J(s, r)$ on ℓ_p

Theorem 3.14 $\sigma_{ap}(J(s, r), \ell_p) = \sigma(J(s, r), \ell_p) = [s - 2r, s + 2r]$.

Proof We know

$$\sigma_{ap}(J(s, r), \ell_p) = \sigma(J(s, r), \ell_p) \setminus III_1\sigma(J(s, r), \ell_p)$$

by the Table 1. Since $\sigma_r(J(s, r), \ell_p) = \emptyset$ from [18, Corollary 3.5], we find $III_1\sigma(J(s, r), \ell_p) = \emptyset$ and we have $\sigma(J(s, r), \ell_p) = [s - 2r, s + 2r]$ from [18, Theorem 3.2]. Therefore $\sigma_{ap}(J(s, r), \ell_p) = [s - 2r, s + 2r]$.

Theorem 3.15 $\sigma_\delta(J(s, r), \ell_p) = \sigma(J(s, r), \ell_p) = [s - 2r, s + 2r]$.

Proof From Table 1, we have

$$\sigma_\delta(J(s, r), \ell_p) = \sigma(J(s, r), \ell_p) \setminus I_3\sigma(J(s, r), \ell_p).$$

We have $I_3\sigma(J(s, r), \ell_p) = \emptyset$ and $\sigma(J(s, r), \ell_p) = [s - 2r, s + 2r]$ from [18, Theorem 3.2] since $\sigma_p(J(s, r), \ell_p) = \emptyset$ from [18, Theorem 3.3]. Hence $\sigma_\delta(J(s, r), \ell_p) = [s - 2r, s + 2r]$.

Theorem 3.16 $\sigma_{co}(J(s, r), \ell_p) = \emptyset$.

Proof We know

$$\sigma_{co}(J(s, r), \ell_p) = III_1\sigma(J(s, r), \ell_p) \cup III_2\sigma(J(s, r), \ell_p) \cup III_3\sigma(J(s, r), \ell_p)$$

by the Table 1. Since $\sigma_p(J(s, r), \ell_p) = \emptyset$ from [18, Theorem 3.3] and $\sigma_r(J(s, r), \ell_p) = \emptyset$ from [18, Corollary 3.5], we get $III_1\sigma(J(s, r), \ell_p) = III_2\sigma(J(s, r), \ell_p) = III_3\sigma(J(s, r), \ell_p) = \emptyset$. Hence $\sigma_{co}(J(s, r), \ell_p) = \emptyset$.

3.5. The fine spectrum and subdivision of the spectrum of $J(s, r)$ on ℓ_∞

Theorem 3.17 $I_3\sigma(J(s, r), \ell_\infty) = \emptyset$.

Proof From Table 1, we have

$$\sigma_\delta(J(s, r), \ell_\infty) = \sigma(J(s, r), \ell_\infty) \setminus I_3\sigma(J(s, r), \ell_\infty).$$

We get $\sigma_\delta(J(s, r), \ell_\infty) = \sigma_{ap}(J^*(s, r), \ell_1)$ from Proposition 1.2. Using Corollary 3.11, $\sigma_{ap}(J(s, r), \ell_1) = [s - 2r, s + 2r]$ and $\sigma(J(s, r), \ell_\infty) = [s - 2r, s + 2r]$ from [27, Theorem 2.5], we have $I_3\sigma(J(s, r), \ell_\infty) = \emptyset$.

Theorem 3.18 $III_1\sigma(J(s, r), \ell_\infty) = \emptyset$.

Proof We know

$$\sigma_{ap}(J(s, r), \ell_\infty) = \sigma(J(s, r), \ell_\infty) \setminus III_1\sigma(J(s, r), \ell_\infty)$$

by Table 1. $\sigma_{ap}(J^*(s, r), \ell_\infty) = \sigma_\delta(J(s, r), \ell_1)$ from Proposition 1.2. Since $\sigma_\delta(J(s, r), \ell_1) = [s - 2r, s + 2r]$ from Corollary 3.12 and $\sigma(J(s, r), \ell_\infty) = [s - 2r, s + 2r]$ from [27, Theorem 2.5], we have $III_1\sigma(J(s, r), \ell_\infty) = \emptyset$.

Corollary 3.19 $\sigma_{ap}(J(s, r), \ell_\infty) = [s - 2r, s + 2r]$.

Proof From Table 1, we get

$$\sigma_{ap}(J(s, r), \ell_\infty) = \sigma(J(s, r), \ell_\infty) \setminus III_1\sigma(J(s, r), \ell_\infty).$$

We have $\sigma_{ap}(J(s, r), \ell_\infty) = [s - 2r, s + 2r]$ since $\sigma(J(s, r), \ell_\infty) = [s - 2r, s + 2r]$ from [27 Theorem 2.5] and $III_1\sigma(J(s, r), \ell_\infty) = \emptyset$ from Theorem 3.18.

Corollary 3.20 $\sigma_\delta(J(s, r), \ell_\infty) = [s - 2r, s + 2r]$.

Proof We know

$$\sigma_\delta(J(s, r), \ell_\infty) = \sigma(J(s, r), \ell_\infty) \setminus I_3\sigma(J(s, r), \ell_\infty)$$

by the Table 1. Since $\sigma(J(s, r), \ell_\infty) = [s - 2r, s + 2r]$ from [27, Theorem 2.5] and $I_3\sigma(J(s, r), \ell_\infty) = \emptyset$ from Theorem 3.17, we have $\sigma_\delta(J(s, r), \ell_\infty) = [s - 2r, s + 2r]$.

3.6. Subdivision of the spectrum of $J(s, r)$ on bv_p

Theorem 3.21 $\sigma_{ap}(J(s, r), bv_p) = \sigma(J(s, r), bv_p) = [s - 2r, s + 2r]$.

Proof From Table 1, we get

$$\sigma_{ap}(J(s, r), bv_p) = \sigma(J(s, r), bv_p) \setminus III_1\sigma(J(s, r), bv_p).$$

Since $\sigma_r(J(s, r), bv_p) = \emptyset$ from [18, Theorem 4.3 (iii)], we have $III_1\sigma(J(s, r), bv_p) = \emptyset$ and $\sigma(J(s, r), bv_p) = [s - 2r, s + 2r]$ from [18, Theorem 4.2]. Therefore $\sigma_{ap}(J(s, r), bv_p) = [s - 2r, s + 2r]$.

Theorem 3.22 $\sigma_\delta(J(s, r), bv_p) = \sigma(J(s, r), bv_p) = [s - 2r, s + 2r]$.

Proof We know

$$\sigma_{\delta}(J(s, r), bv_p) = \sigma(J(s, r), bv_p) \setminus I_3\sigma(J(s, r), bv_p)$$

by the Table 1. Since $\sigma_p(J(s, r), bv_p) = \emptyset$ from [18, Theorem 4.3 (i)], we have $I_3\sigma(J(s, r), bv_p) = \emptyset$ and we have $\sigma(J(s, r), bv_p) = [s - 2r, s + 2r]$ from [18, Theorem 4.2]. Hence $\sigma_{\delta}(J(s, r), bv_p) = [s - 2r, s + 2r]$.

Theorem 3.16 $\sigma_{co}(J(s, r), bv_p) = \emptyset$.

Proof From Table 1, we get

$$\sigma_{co}(J(s, r), bv_p) = III_1\sigma(J(s, r), bv_p) \cup III_2\sigma(J(s, r), bv_p) \cup III_3\sigma(J(s, r), bv_p)$$

Since $\sigma_p(J(s, r), bv_p) = \emptyset$ from [18, Theorem 4.3 (i)] and $\sigma_r(J(s, r), bv_p) = \emptyset$ from [18, Theorem 4.3 (iii)], we have $III_1\sigma(J(s, r), bv_p) = III_2\sigma(J(s, r), bv_p) = III_3\sigma(J(s, r), bv_p) = \emptyset$. Hence $\sigma_{co}(J(s, r), bv_p) = \emptyset$.

Acknowledgment

This work is supported by the Scientific Research Project Fund of Sivas Cumhuriyet University under the project number F-449.

Conflicts of interest

The authors state that did not have a conflict of interests.

References

- [1] Amirov R. Kh., Durna N., Yildirim M., Subdivisions of the spectra for cesaro, rhyly and weighted mean operators on c_0, c and ℓ_p , *IJST*, A3 (2011) 175-183.
- [2] Appell J., Pascale E.D, Vignoli A., Nonlinear Spectral Theory, Berlin, New York: Walter de Gruyter, (2002).
- [3] Stone M.H., Linear transformations in Hilbert space and their applications to analysis, *New York (NY): American Mathematical Society*; 1932.
- [4] Goldberg S., Unbounded Linear Operators, *New York:McGraw Hill*, (1966).
- [5] Brown A., Halmos P.R., Shields A.L., Cesàro operators, *Acta Sci. Math. (Szeged)* 26(1-2) (1965) 125-137.
- [6] Cass, F.P.; Rhoades, B. E., Mercerian theorems via spectral theory, *Pacific J. Math.* 73(1) (1977) 63-71.
- [7] Cartlidge J.P., Weighted Mean Matrices as Operator on ℓ_p , *Ph.D. Dissertation*, Indiana University, 1978.
- [8] Başar F., Durna N., Yildirim M., Subdivisions of the Spectra for Generalized Difference Operator over Certain Sequence Spaces, *Thai J. Math.* 9(2) (2011), 285-295.
- [9] Durna N, Yildirim M., Subdivision of the spectra for factorable matrices on c_0 , *GUJ Sci*, 24(1) (2011) 45-49.
- [10] Durna N, Yildirim M., Subdivision of the spectra for factorable matrices on c and ℓ_p , *Math. Commun.*, 16 (2011) 519-530.
- [11] Durna, N. , Yildirim, M., Kılıç, R., Partition of the Spectra for the Generalized Difference Operator $B(r,s)$ on the Sequence Space cs ., *Cumhuriyet Sci. J.*, 39 (1) (2018), 7-15.
- [12] Akhmedov A.M., El-Shabrawy S.R., Spectra and Fine Spectra of Lower Triangular Double-Band Matrices as Operators on L_p ($1 \leq p < \infty$), *Mathematica Slovaca* 65(5) (2015) 1137-1152.
- [13] Bilgiç H., Furkan H., On the fine spectrum of the generalized difference operator $B(r, s)$ over the sequence spaces ℓ_p and bv_p ($1 < p < \infty$), *Nonlinear Anal.* 68(3) (2008) 499-506.
- [14] Coskun C., The spectra and fine spectra for p-Cesàro operators, *Turkish J. Math.*, 21 (1997) 207-212.
- [15] Das R., On the spectrum and fine spectrum of the lower triangular matrix $B(\pm r, \pm s)$ over the sequence space c_0 , *International Journal of Mathematical Archive* 6(1) (2015) 229-240.
- [16] Das R., On The fine spectra of the lower triangular matrix $\Delta(r, s)$ over the sequence space ℓ_1 ,

Internat. J. Functional Analysis, Operator Theory and Applications, 7(1) (2015) 1-18.

- [17] Fathi J., On the ne spectrum of generalized upper triangular double-band matrices uv over the sequence spaces c_0 and c , *Int. J. Nonlinear Anal. Appl.*, 7(1) (2015) 31-43.
- [18] Karakaya V., Manafov M., Şimşek N., On the fine spectrum of the second order difference operator over the sequence spaces ℓ_p and bv_p ($1 < p < \infty$), *Mathematical and Computer Modelling* 55(3-4) (2012) 426-431.
- [19] Rhoades B.E, Yıldırım M., Spectra and fine spectra for factorable matrices, *Integr.Equ. Oper. Theory*, 53 (2005) 127-144.
- [20] El-Shabrawy S.R., Spectra and fine spectra of certain lower triangular double-band matrices as operators on c_0 , *J. Inequal. Appl.*, 2014 (2014) 1-9.
- [21] Srivastava P.D., Kumar S., Fine spectrum of the generalized difference operator Δ_{uv} on sequence space ℓ_1 , *Appl. Math. Comput.*, 218(11) (2012) 6407-6414.
- [22] Tripathy B.C., Das R., Spectrum and fine spectrum of the upper triangular matrix $U(r, s)$ over the sequence space cs , *Proyecciones Journal of Mathematics* 34(2) (2015) 107-125.
- [23] Tripathy B.C., Das R., Spectrum and fine spectrum of the lower triangular matrix $B(r, 0, s)$ over the sequence space cs , *Appl. Math. Inf. Sci.* 9(4) (2015) 2139-2145.
- [24] Yıldırım M., On the spectrum and fine spectrum of the compact Rhally operators, *Indian J. Pure Appl. Math.*, 27(8) (1996) 779-784.
- [25] Yıldırım M.E., The spectrum and fine spectrum of q -Cesaro matrices with $0 < q < 1$ on c_0 , *Numerical functional analysis and optimization*, 41(3) (2020) 361-377.
- [26] Wilansky A., Summability through Functional Analysis, vol. 85 of *North-Holland Mathematics Studies*, North-Holland, The Netherlands, Amsterdam 1984.
- [27] Altun M., Fine Spectra of Tridiagonal Symmetric Matrices, *International Journal of Mathematics and Mathematical Sciences* (2011) 161209.



Measurement of out of field doses in brain proton therapy with GATE simulations

Melisa SÖNMEZ¹ , Sinan KUDAY² *

¹Istanbul Aydın University, Health Science Institute, Medical Physics, 34295, Istanbul / Turkey

²Ankara University, Physics Department, Tandogan, 06100, Ankara / Turkey

Abstract

Proton therapy as one of the radiotherapy applications, aims to treat the tumor by using the accelerated proton particle. High radiation dose distributions delivered to the tumor tissue, is characterized with Bragg curves, while the radiation in the tissues surrounding the tumor is expected to be as low as possible. In our study, proton treatment of the tumor volume placed in the brain created by GATE software was simulated. The absorbed doses in other organs created by GATE software during treatment were determined using DoseActor and TLEDoseActor algorithms. Nuclear interactions of the accelerated proton with the nucleus of the target atom make the target atom reactive and cause secondary radiation. Similar to the TLEDoseActor algorithm, NTLE algorithm was used to determine the doses caused by neutrons from these secondary radiations. With the algorithms used, out-of-field doses and secondary doses for proton beams at 250 MeV energy were determined. It is important to determine the secondary radiations caused by the interaction of the proton with the tissue and to determine the doses out of the field. These results may be helpful in determining and preventing secondary cancer formation in proton therapy in clinical applications.

Article info

History:

Received:10.05.2021

Accepted:22.06.2021

Keywords:

Geant4,
DoseActor,
TLE,
Radiotherapy.

1. Introduction

Proton therapy is the application of radiotherapy, which allows proton, one of the particles that make up the atom, to be used in the treatment of cancer. The basic principle of radiotherapy applications is to provide high doses to the tumor while minimizing the radiation dose that healthy tissues will receive. While the deep dose characteristics of protons increase tumor doses, the quality of life is improved by maintaining healthy tissues and providing local control of the tumor. [1] Considering the clinical advantages of proton therapy compared to traditional photon radiotherapy, their publications in the literature in this field are increasing. Although protons are considered to have clinical superiority in many types of cancers such as pediatric cancer, ocular melanoma, head and neck cancers, studies are limited to small research. [2] One of the most important reasons for this is that it is inadequate in number due to the cost and cost of proton therapy centers. When protons move through tissue, accelerated protons interact with atomic electrons, while high-energy protons can cause nuclear

interactions in atomic nuclei. The nucleus, which becomes reactive by nuclear interactions, allows secondary radiation in the form of smaller fragmentation and gamma release.[3] From these secondary radiations, neutrons in particular can cause extraterrestrial doses in healthy tissues located away from the treatment area. The likelihood of radiation-related tumor formation in organs other than the treatment area is less likely than tumor formation in organs close to the target volume. [4] Secondary radiation can cause cancer to recur in patients undergoing treatment. Therefore, it is important to calculate out-of-field doses caused by secondary radiation. [5]

The draft of the article is as follows: in the next section we describe the anthropomorphic phantom simulation installation, GATE software, algorithms used to calculate out-of-field doses and their calculations. In the findings section, we give the dose values obtained by GATE software, brain and out-of-field dose distributions and end our work with the result and interpretation part.

2. Materials and Methods

2.1. Anthropomorphic phantom preparation with GATE v.9.8

GATE is a simulation application that enables visualization using the Geant4 toolkit, which simulates interactions between particles and matter. [6] Shaping the simulation is done through simple macros to learn. It has a wide range of studies that can be used in many researches such as improving image quality in imaging and determining radiation doses taken in radiotherapy.

In the coordinate system, the World volume, which we have determined to be 2.1 m at the x, y and z coordinates, is created. It is created using MIRD female phantom data defined in skull, brain, tumor, thyroid, lungs, heart, breast, liver, spleen, kidneys, stomach and pancreatic GATE [7]. Excluding phantom as out-of-area doses are studied especially in the external environment where staff can be exposed calculation of doses has also been targeted. Global geometries are therefore placed outside the phantom. 4 spherical water-filled geometries are placed outside the MIRD phantom. 250 MeV proton energy has been selected as the typical upper energy limit for treatments in this area. The global tumor volume placed inside the brain is irradiated by a bundle of protons created by 100K accelerated protons in 250 MeV proton beam. Pen beam scanning method (PBS) was used for irradiation with proton. Different resource types can be defined in GATE. With the PBS source, the tumor is irradiated with ultra-narrow proton beams. With the PlanDescription file, parameters such as particle energy, patient position, and treatment head position are determined, while the SourceDescription file determines the source information for each pen beam source location and direction. Secondary radiation production in the treatment head is prevented by using the pencil beam scanning (PBS) method. Secondary radiation in irradiations using PBS method occurs as a result of nuclear interactions in patient tissues. DoseActor and TLEDoseActor are placed in all geometries for the calculation of out-of-field doses. DoseActor and TLEDoseActor algorithms will be mentioned in chapter 2.2.

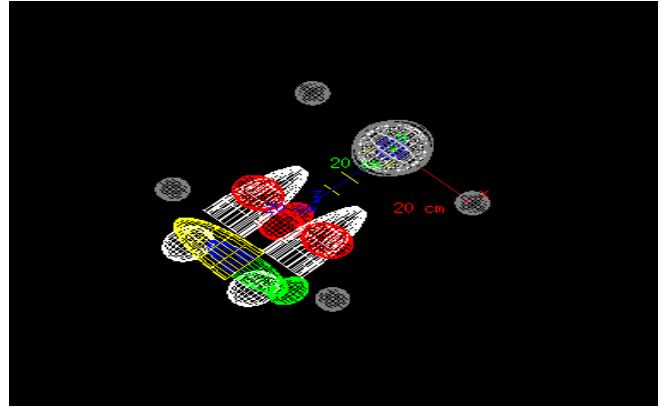


Figure 1. Image from phantom prepared in GATE

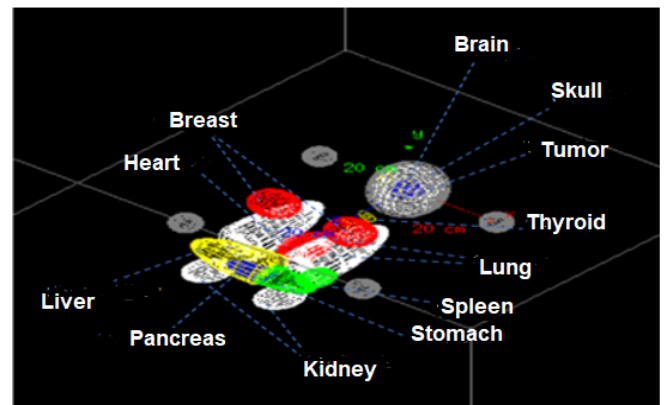


Figure 2. Representation of organs in phantom prepared in GATE

2.2 Description of DoseActor and TLEDoseActor algorithms

In the simulation, the source was selected as a proton particle with energy of 250 MeV and irradiation was performed by pencil beam scanning method (PBS). In GATE, actors are tools that record a lot of information, such as doses accumulated and particles accumulated as a result of interactions in simulation. In our study, we used two of these actors, DoseActor and TLEDoseActors. We placed these actors in all the organs we created and determined the doses and secondary doses accumulated in the organs. We filtered neutrons within both algorithms with the help of dose values we received from DoseActor and TLEDoseActor algorithms for each organ, as well as particle filters that we added to these algorithms. In algorithms, care should be taken that the step length is not too large compared to the voxel. Along this line, the position determined for the actor to hold the information can be chosen randomly. In our study, it was chosen as (post) because it is suitable for calculating out-of-area doses. We have received a total of 4 separate data from both algorithms in two ways,

total doses and neutron doses. We viewed and calculated the analysis of all data using ROOT. [8]

During the analysis phase, the dose absorbed in an area of GATE can be calculated by the DoseActor algorithm. The DoseActor algorithm is placed at the desired volume. The volume in which DoseActor is placed is divided into three-dimensional voxels and calculated by the energies left in the voxel by the particles passing through the voxels. This algorithm can calculate the absorbed dose volumetrically or massively. [9]

Volume-weighted algorithm is given in Equation 1.

$$D_{dose1} = \sum \frac{V_i}{V_{dose1}} \times D_i = \sum \frac{V_i}{V_{dose1}} \times \frac{E_i}{m_i} = \sum \frac{E_i}{V_{dose1} \cdot \rho_i} \quad (1)$$

The energy stored in the dosel volume is calculated by dividing the total energy in the region to which DoseActor is connected by E_i , Dosel volume (V_{dose1}) and density of the region (ρ_i).

Similarly, the mass-weighted algorithm is given in Equation 2.

$$D_{dose1} = \sum \frac{m_i}{m_{dose1}} \times D_i = \sum \frac{m_i}{m_{dose1}} \times \frac{E_i}{m_i} = \sum \frac{E_i}{m_{dose1}} = \frac{E_{dose1}}{m_{dose1}} \quad (2)$$

The energy stored in the dosel volume is calculated by dividing the dosel energy E_{dose1} by dosel mass m_{dose1} .

Similar to the DoseActor method, GATE uses the TLEDoseActor algorithm to determine photons with energies below approximately 1 MeV of energy. [10] With this algorithm, photon flux is shown in Equation 3 by determining the number of trace length (L) left by photons entering voxel volume (V):

$$\phi = \frac{L}{V} \quad (3)$$

The dose absorbed based on flux and trace length is shown in Equation 4:

$$D = \phi \cdot E \cdot \frac{\mu_{en}}{\rho} \quad (4)$$

Here ϕ is photon flux, E is the energy of photons, and $\frac{\mu_{en}}{\rho}$ is the mass energy absorption coefficient.

3. Results and Discussion

Total dose values absorbed for 11 different organ structures and 4 spherical geometries created and photon and neutron doses resulting from interaction of high-energy protons with target volume are given in Table 1. In addition to the absorbed doses in our study, the percentage of doses absorbed in organs and spherical geometries was determined and 77.26 % of the total dose was absorbed in the tumor as expected. %16.3 of the absorbed dose is absorbed by the brain and 6.33 % by the skull. Percentages of doses in non-field organs remain below %1. In our study, it is seen that bragg peak, which is defined as the characteristic dose curve of proton, indicates the highest doses to the tumor, while doses in out-of-field organs are quite low compared to traditional photon radiotherapy. [11] In addition to the total absorbed doses, doses resulting from photons and neutrons produced as a result of nuclear interactions during the irradiation of the brain tumor are given in Table 1.

Clinically, the treatment of a brain tumor is planned to be treated with approximately 1.8 Gy absorbed radiation daily, depending on the tumor size, only 5 days a week for approximately 6-7 weeks. In line with this planning, it is aimed to give approximately 60 Gy doses to the tumor at the end of the treatment. [12] In our simulation study, when the tumor dose of the patient is calculated to be 60 Gy at the end of the treatment based on the absorption dose values given in the DoseActor total dose column, the total doses that the brain and skull will absorb are 12.74 Gy and 4.94 Gy respectively, while the total doses absorbed in other organs range from 0.3 mGy to 38.4 mGy. In our study, neutron and photon doses that contributed to these total absorbed doses were calculated and it was observed that the doses of neutrons absorbed in the organs were formed in the kidneys with at least 0.07 μ Gy and in the skull with a maximum of 921.9 μ Gy. These values are seen to be very low in the formation of secondary cancer of proton therapy.

TLEDoseActor algorithm, it was possible to calculate the dose by absorption of low-energy photons in the tissue. At the end of the treatment process, photon doses of the skull, brain and tumor ranged from 65mGy to 397mGy, while in remote organs outside the treatment area, these doses were calculated to be as low as 7.62 μ Gy.

Table 1.DoseActor and TLEDoseActor algorithms for dose values absorbed in organs (250 MeV)

PROTON BEAM				
	DoseActor		TLE DoseActor	
	Total dose (Gy)	Neutron dose (Gy)	Total dose (Gy)	NTLE dose (Gy)
Skull	1,24511 e-05	2,58111 e-09	9,99404 e-07	1,39916 e-07
Brain	3,21134 e-05	1,94425 e-09	7,36327 e-07	1,0308578 e-07
Tumor	1,51157 e-04	4,2541 e-09	1,64756 e-07	2,306584 e-08
Thyroid	1,32034 e-08	6,98735 e-10	5,09889 e-10	7,138446 e-11
Lung	6,98735 e-09	8,2216 e-12	2,08297 e-11	2,916158 e-12
Liver	4,8393 e-09	4,44157 e-11	2,57861 e-09	3,610054 e-10
Breast	9,69003 e-07	1,96138 e-10	8,1 e-09	1,134 e-09
Stomach	1,04147 e-09	1,76101 e-11	4,97604 e-10	6,966456 e-11
Heart	2,12196 e-09	5,38965 e-11	3,6467 e-10	5,10538 e-11
Kidney	1,61768 e-09	2,2062 e-12	5,09065 e-10	7,12691 e-11
Pancreas	5,25745 e-09	3,44521 e-12	9,4511 e-10	8,41123 e-11
Sphere 1	5,16413 e-09	1,98501 e-11	1,48072 e-09	2,073008 e-10
Sphere 2	9,79271 e-09	3,28908 e-11	3,8489 e-10	5,38846 e-11
Sphere 3	1,07722 e-09	1,80002 e-11	4,01108 e-10	5,615512 e-11
Sphere 4	5,32978 e-09	3,52746 e-11	2,74903 e-09	3,848642 e-10
Total	1,96625 e-04	9,89946 e-09	1,918 e-06	2,67534 e-07

With this study, we calculated the total doses absorbed by tumor and other organs with DoseActor algorithm using accelerated proton beams in the irradiation of the brain tumor, neutron doses that contribute to the total dose absorbed in the organs using particle filter in the DoseActor algorithm. Using particle filtering in the TLE algorithm, we filtered neutrons defined as NTLE. NTLE was used to determine neutrons that are part of the secondary dose. [13] Figures 3 and 4 show particle and dose distributions in brain tissue and out off-field global dosimetry.

TLE and NTLE algorithms as in actual measurements does not depend on the absorbed dose. This is experimental algorithms are being developed. On the tumor, the protons sent directly The direct interaction with the absorption is the dominant interaction. On the other hand dose in the tumor, since off-field doses were taken into account is outside the scope of the study. As a result; TLE and NTLE algorithms in calculating the dose amount in the directly affected tissue alone unusable result.

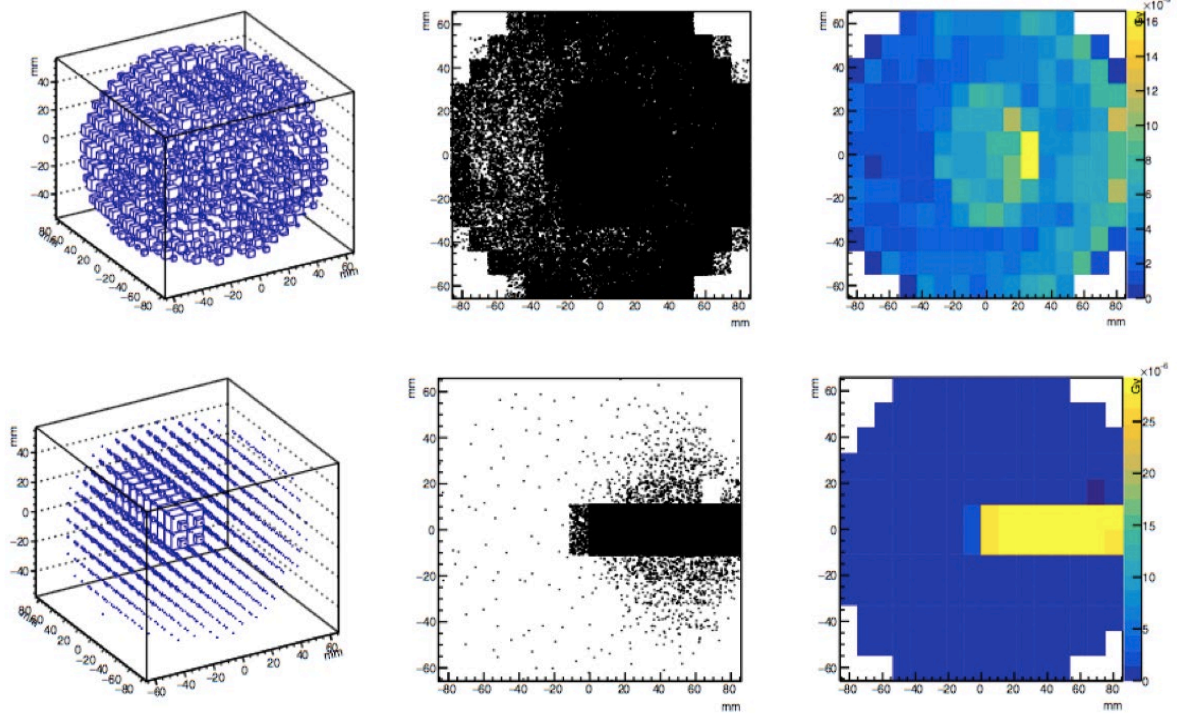


Figure 3. Measured by simulation in brain tissue; 3B particle distribution (left), 2B particle distribution (centre) dose distribution (right) TLE algorithm (top) and DoseActor algorithm (bottom) dose data

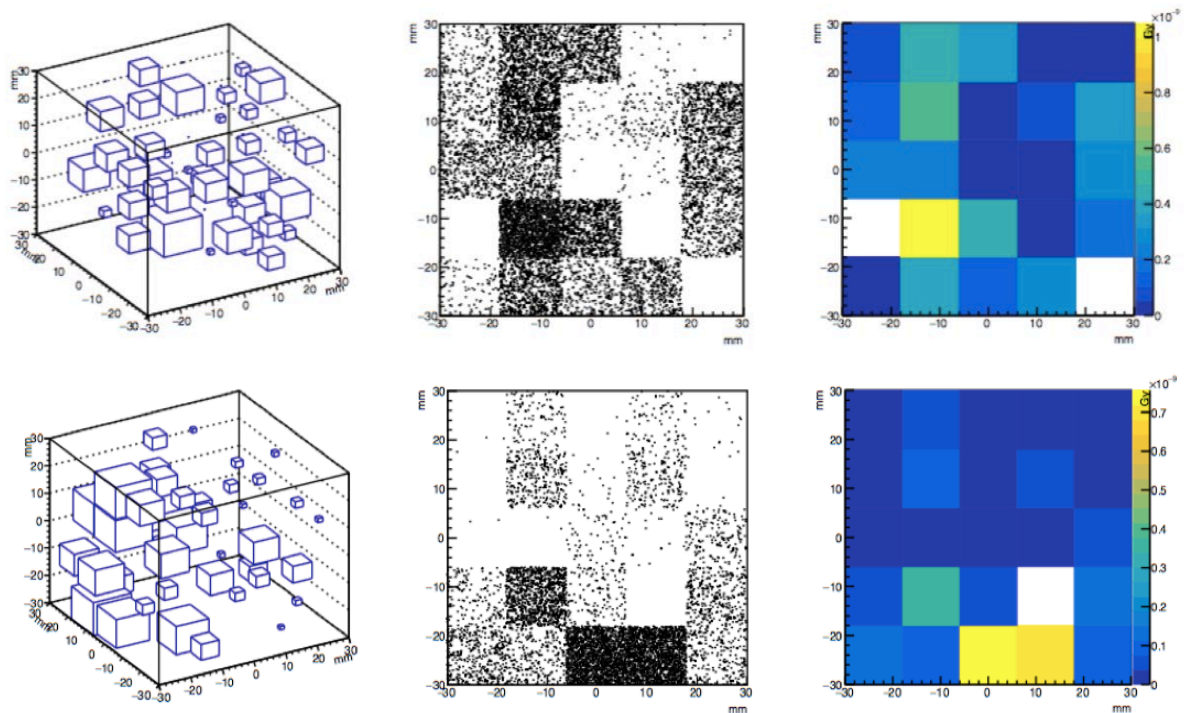


Figure 4. Measured by simulation in the out-of-field dosimeter (Sphere 4); 3B particle distribution (left), 2B particle distribution (centre) dose distribution (right) TLE algorithm (top) and DoseActor algorithm (bottom) dose data

4. Conclusion

As in this study, it is very important to determine the characteristic dose distributions and out-of-field doses

of proton in proton treatment applications in GATE software. The treatment of complex brain tumors becomes possible with protons after surgical procedure or without the need for surgical procedure. However, it

is very important to determine the out-of-field doses exposed to protect healthy tissues in the patient and to minimize the exposure of radiation-powered health workers to radiation. In general dose calculations, the proton therapy (N)TLE and DoseActor algorithms calculated doseactor chi-square value $13,6767.10^{-6}$, TLEDoseActor ki-squared value $18,6570.10^{-6}$ and no significant difference was seen according to the comparison of %5 alpha value. It has been observed that the TLE algorithm determines particle distributions and scattered secondary particles with higher precision. This result is however, statistically, (N)TLE and Doseactor algorithms are both applicable in dose calculations to issue similar results that justified by our simulation data. Note that it is critical to determine out-of-field doses so that doses taken in proton therapy do not lead to secondary cancers and other diseases in the long term.

Conflicts of interest

As the authors of this study, we have no conflict of interest.

References

- [1] Mohan R., Grosshans D., Proton therapy - Present and future, *Advanced Drug Delivery Reviews*, 109 (2017) 26-44.
- [2] Riley B., Peaking into the future with proton therapy, *Journal of Radiology Nursing*, 26(4) (2007) 115-120.
- [3] Didi A., Dekhissi H., Sebihi R., Krim M., & Mohamed R. M., Calculate primary and secondary dose in proton therapy using 200 and 250 MeV proton beam energy, *The Physics of the Atomic Nucleus and Elementary Particles*, 74 (2019) 364-368.
- [4] Ardenfors O., Dasu A., Lillhök J., Persson L., Gudowska I., Out-of-field doses from secondary radiation produced in proton therapy and the associated risk of radiation-induced cancer from a brain tumor treatment, *Physica Medica*, 53 (2018) 129-136.
- [5] Jia S. B., Hadizadeh M. H., Mowlavi A. A., Loushab M. E., Evaluation of energy deposition and secondary particle production in proton therapy of brain using a slab head phantom, *Reports of Practical Oncology & Radiotherapy*, 19(6) (2014) 376-384.
- [6] Slimani F. A. A., Hamdi M., Bentourkia M., G4DARI: Geant4/GATE based Monte Carlo simulation interface for dosimetry calculation in radiotherapy, *Computerized Medical Imaging and Graphics*, 67 (2018) 30-39.
- [7] Snyder W. S., Ford M. R., Warner G. G., MIRD Pamphlet No. 5 Revised, Estimates of absorbed fractions for monoenergetic photon sources uniformly distributed in various organs of a heterogeneous phantom, *Journal of Nuclear Medicine*, 3 (1969) 5-52.
- [8] Rene Brun and Fons Rademakers, ROOT-An Object Oriented Data Analysis Framework, Proceedings AIHENP'96 Workshop, Lausanne, Sep. 1996, Nucl. Inst.&Meth. In Phys. Res. A 389 (1997) 81-86. See also [root.cern.ch/] (<http://root.cern.ch/>).
- [9] Sarrut D., Bardies M., Bousson N., Freud N., Jan S., Letang J. M., Loudos G., Maigne L., Marcatili S., Mauxion T., Papadimitroulas P., Perrot Y., Pietrzyk U., Robert C., Schaart D. R., Visvikis D., Buvat I., A review of the use and potential of the GATE Monte Carlo simulation code for radiation therapy and dosimetry applications, *Medical Physics*, 41(6) (2014).
- [10] Baldacci F., Mittone A., Bravin A., Coan P., Delaire F., Ferrero C., Gasilov S., Letang J. M., Sarrut D., Smekens F., Freud N., A track length estimator method for dose calculations in low-energy X-ray irradiations: implementation, properties and performance, *Zeitschrift für Medizinische Physik*, 25(1) (2015) 36-47.
- [11] Riley B., Peaking Into the Future With Proton Therapy, *Journal of Radiology Nursing*, 26(4) (2007) 115-120.
- [12] Liu H., Chang J. Y., Proton therapy in clinical practice, *Chinese Journal of Cancer*, 30(5) (2011) 315-326.
- [13] Elazhar H., Deschler T., Letang J. M., Nourreddine A., Arbor N., Neutron track length estimator for GATE Monte Carlo dose calculation in radiotherapy, *Physics In Medicine and Biology*, 63(12) (2018).



Effect of size modulation and donor position on intersubbands refractive index changes of a donor within a spherical core/shell/shell semiconductor quantum dot

Emre Bahadır AL^{1,*}

¹Sivas Cumhuriyet University, Faculty of Science, Department of Physics, Sivas/TURKEY

Abstract

In the current study, linear, nonlinear and total relative refractive index changes of a single shallow hydrogenic donor atom confined in semiconductor core/shell/shell quantum dot heterostructure are investigated in detail by compact density matrix formalism. For this purpose, the energy eigenvalues and the corresponding wave functions are calculated by diagonalization method in the effective mass approximation. Then, intersubband $1s \rightarrow 1p$ and $1p \rightarrow 1d$ donor transition energies are calculated. In the study, the effects of core/shell sizes, donor position and depth of confinement potential are analyzed. The numerical results show that the linear and nonlinear refractive index changes undergo significant changes.

Article info

History:
Received:26.04.2021
Accepted:28.06.2021

Keywords:
Hydrogenic shallow donor impurity, Quantum dots, Optical transitions, Refractive index, Size effect.

1. Introduction

It is accepted that the progress of electronic and optoelectronic devices depends on understanding the basic chemical and physical properties of low-dimensional structures (LDSs). In these LDSs, the geometric confinement limits the movement of charge carriers in space and it causes major changes in electrical and optical properties due to the occurrence of discrete electronic energy distribution. Therefore, in recent years, intensive research activities have been conducted around the world on the behavior of matter at nanoscale. Although various devices have been devoted to nanoscale particles, the properties of controlled nanoscale materials such as light emitting diodes, photo detectors and quantum dot (QD) single photon source are still the biggest problem of scientists.

Due to the recent development of semiconductor nanoelectronics, it has become possible to reduce dimensionality from bulk semiconductors to zero-dimensional semiconductor nanostructures (QDs). These nanostructures are very important because their charge carrier motion is confined in three directions, and therefore efficient control of the physical properties of these structures becomes possible. Proper adjustment of the physical properties of QDs is

advantageous because of their potential applications in the development of semiconductor optoelectronic devices. For this reason, some optical properties of semiconductor QDs such as dipole transition [1,2], oscillator strength [3,4], photoionization cross-sections [5], optical absorption coefficients (OACs) [6,7] and refractive index changes (RICs) [3,8] have attracted the attention of researchers in experimental and theoretical studies in recent years.

Since the electronic and optical properties in a QD are affected by the impurity, the physical properties related to impurity have been investigated using different methods such as variational approximation [5], tight-binding model [9], perturbation theory [10] and diagonalization method [6]. Some studies have revealed that it is possible to realize a single dopant scheme in QDs [11-13]. This enables the production of various optoelectronic devices.

Moreover, it should be noted that in the presence of the donor atom, calculating energy levels and wave functions is a difficult task that requires theoretical effort. In this case, it is very difficult to find analytical solutions. To overcome this difficulty, the calculation of the electronic state in the presence of donor atom will be done by the diagonalization method. It is hoped that this will allow a more detailed description of the impurity states in the structures under study.

*Corresponding author. e-mail address: emrebahadir@hotmail.com
<http://dergipark.gov.tr/csj> ©2021 Faculty of Science, Sivas Cumhuriyet University

In theoretical studies, it is common to use spherical shaped QDs, and many researchers have focused on the optical properties of this type of structure [3,6,14-16]. Thanks to the rapid development of material growth techniques such as molecular beam epitaxy, metal-organic chemical vapor deposition and electron lithography and the advancement of chemical production processes, various dimensional new generation quantum nanostructures that allow electrons to be confined in these nanostructures have been produced, one of which is the coated spherical QDs called core/shell/shell QDs (CSSQDs) [17,18]. These structures consist of two semiconductors with different band gaps. They are spatially arranged in such a way that the larger bandwidth core acting as a substrate is covered by a smaller bandwidth spherical shells. The originality of these structures is that their physical properties can be adjusted in a controlled manner, leading to changes in energy levels. Therefore, it is important to study the electronic and optical properties of CSSQDs.

Previously, some studies on RICs of donor atom in spherical core/shell QDs have been published. The relative RICs as well as the OACs in the *GaAs/AlAs* core/shell QD were calculated by M'zerd et al [19], considering the effects of presence of the donor atom and the donor position, as well as the interaction with the LO-phonon. Taking into account the effects of structure parameters, magnetic field and dielectric mismatch, Feddi et al [20] investigated the OACs and relative RICs for the $1s - 1p$ transition of a single dopant confined in *AlAs/GaAs/SiO₂* core/shell QDs. Linear and nonlinear intersubband OACs and RICs in *GaAs/AlGaAs* core/shell spherical QDs were theoretically investigated by Zhang et al [21] for te cases with and without impurity at the center. The effect of pressure on the binding energy and the linear and nonlinear OACs and RICs associated with the intersubband transition of a dopant in an *AlAs/GaAs* spherical core/shell QD, were studied by El Haouari et al [22].

However, there is no study in the literature on RICs caused by $1s \rightarrow 1p$ and $1p \rightarrow 1d$ single dopant transitions in the CSSQDs. Therefore, in the current theoretical study, the effect of the impurity position and confinement potential on the linear, nonlinear and total RICs of a single impurity atom in a CSSQD is numerically analyzed and discussed using density matrix formalism. As a result of this research, it has been shown that the RICs in CSSQD are strictly dependent on its geometric parameters and donor position.

2. Materials and Methods

2.1. Electron-impurity Hamiltonian and wave function

Since the optical behavior of nanoscale semiconductors is related to the electronic properties of the structure, the energy behavior of the confined donor must first be examined.

Consider a hydrogen-like shallow donor impurity located anywhere in the core region of a CSSQD nanocrystal with a spherically symmetrical *GaAs(core)/Al_{x₁}Ga_{1-x₁}As(inner shell)/Al_{x₂}Ga_{1-x₂}As(outer shell)* design, where x_1 (x_2) is the aluminum concentration in the inner (outer) shell. *GaAs* core material with radius a_1 is covered with *Al_{x₁}Ga_{1-x₁}As* shell, which has a wider band gap. *Al_{x₁}Ga_{1-x₁}As* inner shell material with thickness $T_s = a_2 - a_1$ is covered with *Al_{x₂}Ga_{1-x₂}As* shell which has a wider band gap ($x_2 > x_1$). In order to protect the nanostructure from contamination of the external environment, it is assumed that the structure is covered with a glass matrix. In the effective mass approximation, the Hamiltonian which describes the energy behavior of a single electron bound to the donor confined in such a system with a finite depth potential in the region $0 < r \leq a_1$, can be expressed as,

$$H = -\frac{\hbar^2}{2m^*} \nabla^2 + V(r) + V_C, \tag{1}$$

where the first term is the kinetic energy operator of the electron, \hbar is the reduced Planck constant, m^* is the conduction band effective mass of the electron in the *GaAs*-core region, and ∇^2 is Laplacian in spherical coordinates.

The second term in Equation (1) represents the confinement potential. Due to the band gap difference between *GaAs* ($E_g = 1.424 \text{ eV}$) and *Al_xGa_{1-x}As* ($E_g = 1.424 + 1.247x \text{ eV}$) [23], it is thought that the probability density will mostly be limited within the core region and the charge carriers will be confined within *GaAs*. It is a good approximation that the dielectric material outside the structure is considered to have an infinite potential barrier, and in this case it is possible to write the confinement potential in the form

$$V(r) = \begin{cases} 0, & r < a_1 \\ V_1, & a_1 \leq r < a_2 \\ V_2, & a_2 \leq r < a_3 \\ \infty, & r \geq a_3 \end{cases} \tag{2}$$

where $V_{1,2} = 0.6 (1247x_{1,2}) \text{ meV}$ is the conduction band offset between *AlGaAs* and *GaAs*.

The third term in Equation (1) shows the Coulomb potential energy between donor impurity and electron and it has the form

$$V_C = -\frac{Ze^2}{\epsilon|\vec{r}-\vec{r}_d|}, \quad (3)$$

where $Z = 0$ ($Z = 1$) corresponds to the case without (with) a hydrogenic donor impurity in the system, e is the charge of electron, ϵ is the dielectric constant, $|\vec{r} - \vec{r}_d|$ is the electron-impurity distance, \vec{r} (\vec{r}_d) is the radial position of the electron (ionized donor) with respect to the center of the spherical QD. It is assumed that the ionized donor is placed along the z -axis. In terms of spherical harmonics $1/|\vec{r} - \vec{r}_d|$ term is given by [10]

$$\frac{1}{|\vec{r}-\vec{r}_d|} = \sum_{\mu} \frac{4\pi}{2\mu+1} f_{\mu}(r) \sum_{\nu=-\mu}^{\mu} Y_{\mu,\nu}^*(\theta, \phi) Y_{\mu,\nu}(\theta_d, \phi_d), \quad (4)$$

where $Y_{\mu,\nu}(\theta, \phi)$ are spherical harmonics, θ and ϕ (θ_d and ϕ_d) are the polar angles of the electron (impurity atom) and $f_{\mu}(r)$ is

$$f_{\mu}(r) = \begin{cases} \frac{1}{r_d} \left(\frac{r}{r_d}\right)^{\mu}, & r \leq r_d \\ \frac{1}{r} \left(\frac{r_d}{r}\right)^{\mu}, & r \geq r_d \end{cases}. \quad (5)$$

At this point, in order to simplify numerical calculations, reduced units are used, defining $Ryd^* = \frac{m^*e^4}{2\hbar^2\epsilon^2}$ as energy unit and $a_B^* = \frac{\epsilon\hbar^2}{m^*e^2}$ as length unit. With these units, the Hamiltonian becomes in the form

$$H = -\nabla^2 + V(r) - 2Z \sum_{\mu} \frac{4\pi}{2\mu+1} f_{\mu}(r) \sum_{\nu=-\mu}^{\mu} Y_{\mu,\nu}^*(\theta, \phi) Y_{\mu,\nu}(\theta_d, \phi_d). \quad (6)$$

The solution of the Schrödinger equation $H\psi_{nlm}(r, \theta, \phi) = E_{nlm}\psi_{nlm}(r, \theta, \phi)$ is sought to determine the allowed energy levels and wave functions of the system, where, E_{nlm} is the electron energy eigenvalue for certain quantum numbers (n is the principal quantum number, l is the orbital quantum number, and m is the magnetic quantum number) and $\psi_{nlm}(r, \theta, \phi)$ is the wavefunction corresponding to this energy. The orbital quantum number $l = 0, 1, 2, \dots$ is marked by the usual notation s, p, d, \dots . The diagonalization method will be used to solve this Schrödinger equation. For this purpose, the single electron wavefunctions of the infinite QD will be taken as the basis function:

$$\psi_{nlm}(r, \theta, \phi) = \sum_j c_{nj} \psi_{njlm}^{(0)}(r, \theta, \phi), \quad (7)$$

where c_{nj} are the expansion coefficients and $\psi_{njlm}^{(0)}(r, \theta, \phi)$ are the total wave functions describing the motion of the electron without the impurity atom.

It should be remembered that the exact solutions for an electron in an infinite radial potential are [6]

$$\psi_{njlm}^{(0)}(r, \theta, \phi) = R_{nl}^{(0)}(r) Y_{l,m}(\theta, \phi), \quad (8)$$

where the radial wavefunction- $R_{nl}^{(0)}(r)$ is given as

$$R_{nl}^{(0)}(r) = \begin{cases} N j_l(k_{nl}r), & r < a_3 \\ 0, & r \geq a_3 \end{cases}, \quad (9)$$

where N is the normalization constant, k_{nl} is the n th root of the spherical Bessel function- j_l and a_3 ($a_3 \gg a_2$) is the radius of the infinite spherical QD.

2.2. Linear, nonlinear and total RICs of the system

In a monochromatic electromagnetic field with a frequency ω , the probability of transition between states i and j is called as the oscillator strength- P_{ij} given by the Fermi golden rule and it is expressed in the form [22]

$$P_{ij} = \frac{2m^*}{\hbar^2} E_{ij} |M_{ij}|^2, \quad (10)$$

where, $E_{ij} = E_j - E_i$ is the energy difference, while M_{ij} is the dipole moment matrix element of the transition between the i and j states. The oscillator strength is highly dependent on the overlap of wave functions and the energy difference between states and thus it gives an idea of the dominant color of the emitted light.

Expressions of RICs can be obtained by density matrix approximation. Analytical expressions of linear and third order nonlinear sensitivities for a two-level quantum system are given in the forms

$$\chi_{\omega}^{(1)}(\omega) = \frac{\sigma_s |M_{ij}|^2}{\epsilon_0 (E_{ij} - \hbar\omega - i\hbar\Gamma_{ij})}, \quad (11)$$

and

$$\chi_{\omega}^{(3)}(\omega) = \frac{\sigma_s \hbar\omega |M_{ij}|^2 |\bar{E}|^2}{\epsilon_0 (E_{ij} - \hbar\omega - i\hbar\Gamma_{ij})} \left[\frac{4|M_{ij}|^4}{(E_{ij} - \hbar\omega)^2 + (\hbar\Gamma_{ij})^2} - \frac{|M_{jj} - M_{ii}|^2}{(E_{ij} - i\hbar\Gamma_{ij})(E_{ij} - \hbar\omega - i\hbar\Gamma_{ij})} \right], \quad (12)$$

where σ_s is the electron density in the system, ϵ_0 is the dielectric constant of the vacuum, ω is the angular frequency of light interacting with QD, $\hbar\omega$ is the incident photon energy, $\hbar\Gamma_{ij}$ is Lorentzian line width, $\Gamma_{ij} = 1/T_{ij}$ is the non-diagonal damping term known as the relaxation ratio between the final and initial states, and it is defined as the inverse of the relaxation time- T_{ij} .

The sensitivity $\chi(\omega)$ is associated with the RIC in the form

$$\frac{\Delta n(\omega)}{n_r} = Re \left[\frac{\chi(\omega)}{2n_r^2} \right]. \tag{13}$$

Using Equations (11) and (12), linear and third order nonlinear RICs are obtained analytically in the form

$$\frac{\Delta n^{(1)}(\omega)}{n_r} = \frac{1}{2n_r^2 \epsilon_0} \frac{\sigma_s(E_{ij}-\hbar\omega) |M_{ij}|^2}{(E_{ij}-\hbar\omega)^2 + (\hbar\Gamma_{ij})^2}, \tag{14}$$

and

$$\frac{\Delta n^{(3)}(\omega, I)}{n_r} = - \frac{\mu c I \sigma_s |M_{ij}|^4}{n_r^3 \epsilon_0} \frac{E_{ij}-\hbar\omega}{[(E_{ij}-\hbar\omega)^2 + (\hbar\Gamma_{ij})^2]^2} \left[1 - \frac{|M_{jj}-M_{ii}|^2 \left[E_{ij}^2 - E_{ij} \left(\hbar\omega + \frac{(\hbar\Gamma_{ij})^2}{E_{ij}-\hbar\omega} \right) - 2(\hbar\Gamma_{ij})^2 \right]}{4|M_{ij}|^2 [E_{ij}^2 + (\hbar\Gamma_{ij})^2]} \right], \tag{15}$$

respectively, where $I = 2\epsilon_0 n_r c |\vec{E}|^2$ is the intensity of the linearly polarized electromagnetic field and μ indicates the magnetic susceptibility of the material. Thus, the total RIC is given as

$$\frac{\Delta n(\omega, I)}{n_r} = \frac{\Delta n^{(1)}(\omega)}{n_r} + \frac{\Delta n^{(3)}(\omega, I)}{n_r}. \tag{16}$$

Assuming that electromagnetic radiation is linearly polarized along the z-axis, the dipole moment matrix element is defined in a single electron system by

$$M_{ij} = e \langle \psi_i | r \cos \theta | \psi_j \rangle, \tag{17}$$

where, ψ_i and ψ_j are wave functions of the initial and final states, respectively. In order for the dipole transition moment to be different from zero, the selection rules $\Delta l = \pm 1$ and $\Delta m = 0$ must be provided. Here, only the intersubband transitions between the $m = 0$ states of the CSSQD will be considered.

3. Results and Discussion

In this section, the effects of geometric confinement and change in donor position on RICs will be discussed

according to the spherical CSSQD nanostructure model outlined above. The values of the material input parameters taken into account are presented as follows: $\epsilon = 13.18$, $m^* = 0.067m_0$ ($m_0 = 9.10956 \times 10^{-31} \text{ kg}$ is the mass of the free electron), $I = 400 \text{ MW/m}^2$, $\sigma_s = 1 \times 10^{23} \text{ m}^3$, $T_{ij} = 0.14 \text{ ps}$, $n_r = 3.2$, $a_B^* = 10.42 \text{ nm}$, $Ryd^* = 5.23 \text{ meV}$.

In Figure 1, the variation of linear, nonlinear and total RICs associated with $1s \rightarrow 1p$ and $1p \rightarrow 1d$ transitions is plotted as a function of photon energy for different core/shell sizes. The single donor is assumed to be located at the center of QD. As can be seen from the figure, the linear RICs increase with the photon energy and they reach a maximum value. Also, as can be seen from Equations 14 and 15, RICs are zero when $\hbar\omega = E_{ij}$. When the core radius increases, the peaks of the RICs show a visible redshift (Figure 1 (a)). In addition, it is found that the increase in the peak amplitudes of the RICs is also associated with the increase in core size. Because the increase in the size of the core causes a decrease in the transition energy and an increase in the square of the non-diagonal electric dipole moment. It should also be noted that, due to the negative nonlinear term, the total RICs peaks get weaker compared to the linear response. The theoretical results reveal that the RICs associated with the $1p \rightarrow 1d$ transition have a significant decrease in the peak amplitudes with the increase in shell thickness, while the RICs associated with the $1s \rightarrow 1p$ transition are not affected by the shell thickness (Figure 1 (b)). Increasing shell thickness does not affect well-localized $1s$ and $1p$ electrons in the core region, while $1d$ -level electron with greater energy than confinement potential- V_1 is localized in a larger region. In addition, it can be said that the nonlinear RICs are almost too weak. On the other hand, it is found that the peak positions of the RICs associated with the $1p \rightarrow 1d$ transition shift to red by increasing the shell thickness, but that the peak positions of the RICs associated with the $1s \rightarrow 1p$ transition are not affected by this increase.

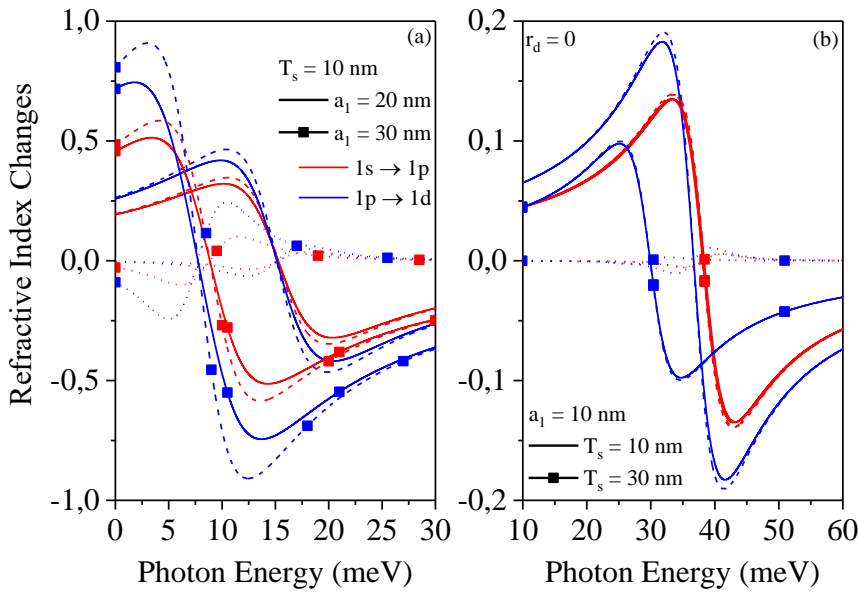


Figure 1. The variation of linear (dashed), third order nonlinear (dotted) and total (solid) RICs of $1s \rightarrow 1p$ and $1p \rightarrow 1d$ donor transitions for various core/shell sizes as a function of incident photon energy. The values are for $x_1 = 0.1$ and $x_2 = 0.4$.

In order to examine the effect of the intra-core position of the impurity atom on the on linear, nonlinear, and total RICs against the incident photon energy for the three important positions of the impurity are presented in Figure 2. For the $1s \rightarrow 1p$ transition, the peak amplitudes of the RICs increase as the impurity moves from the QD center to the core/shell boundary. The reason for this change is that as the impurity moves from the QD center to the core/shell boundary, the dipole matrix element increases as a result of better overlap of the wave functions of the respective states. However, due to the convergence of the $1s$ and $1p$ energy states, the peak positions of the RICs show a redshift as the impurity moves away from the QD

center. Moreover, since the peak amplitudes of nonlinear RICs are very small compared to linear ones, the peak amplitudes of total RICs show an equivalent variation to linear ones. The same is true for the $1p \rightarrow 1d$ transition. However, as the impurity moves away from the QD center, the peak positions of the RICs for the $1p \rightarrow 1d$ transition shifts slightly towards blue and then red. This is because as the donor atom moves away from the QD center, the energy difference between the $1p$ and $1d$ states first increases and then decreases. Also, the peak amplitudes of the RICs increase due to the larger dipole matrix element at the core/shell boundary.

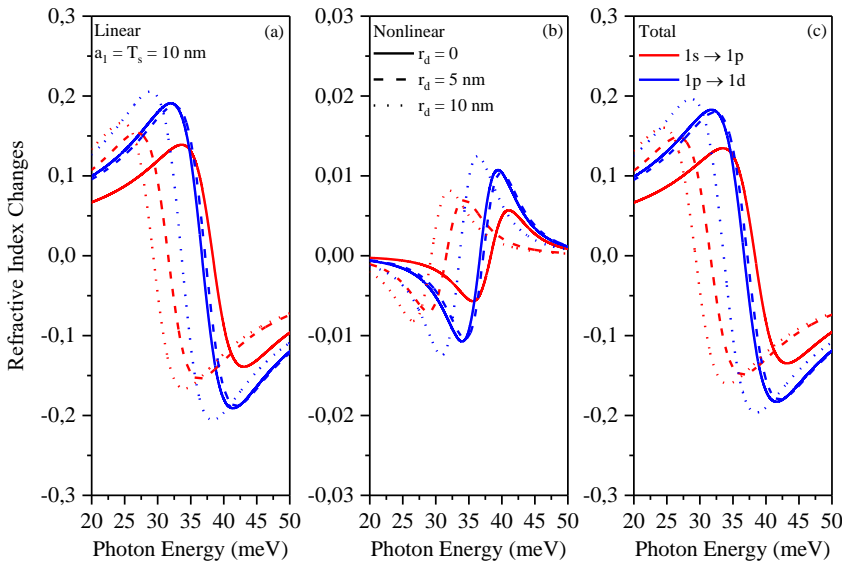


Figure 2. (a) Linear, (b) nonlinear and (c) total RICs related to $1s \rightarrow 1p$ and $1p \rightarrow 1d$ donor transitions against incident photon energy for $a_1 = T_s = 10 \text{ nm}$ and three impurity position values. The values are for $x_1 = 0.1$ and $x_2 = 0.4$.

Finally, RICs as a function of photon energy for different x_1 concentrations are presented in Figure 3. The figure shows that increasing x_1 concentration shifts the peak positions of RICs to blue. This is because the transition energy increases due to the quantum size effect with increasing x_1 concentration.

In addition, it is found that the peak amplitudes of RICs monotonously decrease with increasing x_1 concentration. This is because the coincidence of the wave functions of the states of interest decreases as the x_1 concentration increases.

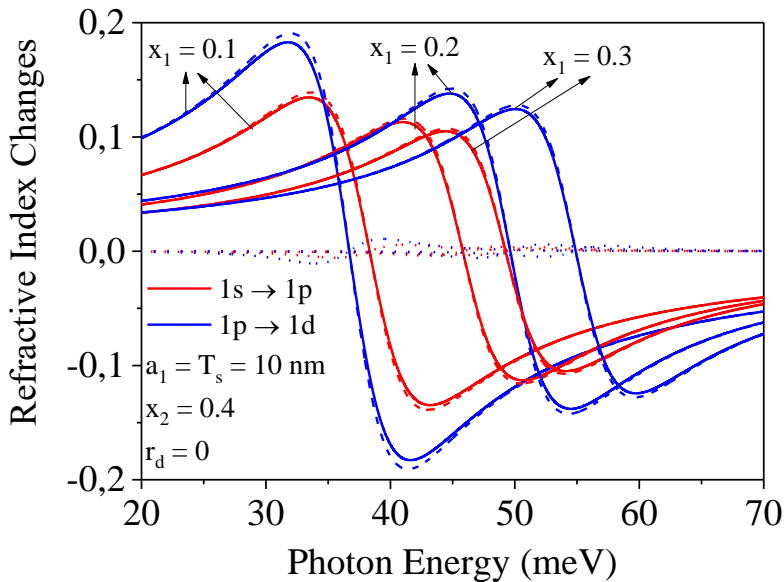


Figure 3. Linear (dotted), third-order nonlinear (dashed) and total (solid) RICs associated with $1s \rightarrow 1p$ and $1p \rightarrow 1d$ central donor transitions as a function of photon energy for various x_1 concentrations.

In conclusion, in the current theoretical study, the linear, nonlinear and total RICs of a single donor impurity atom confined within the spherical

$GaAs(\text{core})/Al_{x_1}Ga_{1-x_1}As(\text{inner shell})/Al_{x_2}Ga_{1-x_2}As(\text{outer shell})$ type CSSQD are extensively investigated, taking into account the

effects of core/shell sizes, donor position and depth of confinement potential. The results obtained show the following: The increase in core size increases the peak amplitudes of the RICs and shifts the peak positions to red. While the increase in shell thickness is not affect the peak amplitudes and peak positions of RICs related to the $1s \rightarrow 1p$ transition, it decreases the peak amplitudes of the RICs related to the $1p \rightarrow 1d$ transition and shifts the peak positions to red. As the impurity moves from the QD center towards the core/shell boundary, the peak amplitudes of the RICs of the $1s \rightarrow 1p$ transition increase and the peak positions shift to red. For the $1p \rightarrow 1d$ transition, as the impurity moves away from the QD center, the peak positions of the RICs shift to blue and then to red, and the peak amplitudes first decrease and then increase. Increasing x_1 concentration leads to a deeper confinement potential, and as a result, the peak amplitudes of the RICs decrease while the peak positions shift to blue. As a result, the theoretical results obtained here may contribute to experimental studies and offer a good model for practical applications such as optoelectronic devices and optical communication.

Acknowledgment

This work is supported by the Scientific Research Project Fund of Sivas Cumhuriyet University under the project number F-2021-641.

Conflicts of interest

The author state that did not have conflict of interests.

References

- [1] Hasanirokh K., Asgari A., Rokhi M. M., Theoretical study on nonlinear optical properties of CdS/ZnS spherical quantum dots, *Optik*, 188 (2019) 99-103.
- [2] Safeera T. A., Anila E. I., Synthesis and characterization of ZnGa₂O₄:Eu³⁺ nanophosphor by wet chemical method, *Scripta Mater.*, 143 (2018) 94-97.
- [3] Naimi Y., Comment on "Magnetic field effects on oscillator strength, dipole polarizability and refractive index changes in spherical quantum dot", *Chem. Phys. Lett.*, 767 (2021) 138380.
- [4] Sakr M. A. S., Gawad S. A. A., El-Daly S. A., Kana M. T. H. A., Ebeid El-Zeiny M., Photophysical and TDDFT investigation for (E, E)-2, 5-bis [2-(4-(dimethylamino)phenyl)ethenyl]pyrazine (BDPEP) laser dye in restricted matrices, *J. Mol. Struct.*, 1217 (2020) 128403.
- [5] Shi L., Yan Zu-Wei, Meng Mei-Wen, Binding energy and photoionization cross section of hydrogenic impurities in elliptic cylindrical core/shell quantum dots under a non-axial electric field, *Superlattice Microst.*, 150 (2021) 106818.
- [6] Al E. B., Kasapoglu E., Sari H., Sökmen I., Optical properties of spherical quantum dot in the presence of donor impurity under the magnetic field, *Physica B*, 613 (2021) 412874.
- [7] Mgidlana S., Şen P., Nyokong T., Direct nonlinear optical absorption measurements of asymmetrical zinc(II) phthalocyanine when covalently linked to semiconductor quantum dots, *J. Mol. Struct.*, 1220 (2020) 128729.
- [8] Yu D., Yu Z., Zhang Y., Chang Y., Yu D., Cation-exchange synthesis and measurement of PbS quantum dots with high nonlinear optical properties, *Optik*, 210 (2020) 164509.
- [9] Pérez-Conde J., Bhattacharjee A. K., Electronic structure and impurity states in GaN quantum dots, *Solid State Comm.*, 135 (2005) 496-499.
- [10] Yakar Y., Çakır B., Özmen A., Off-center hydrogenic impurity in spherical quantum dot with parabolic potential, *Superlattice Microst.*, 60 (2013) 389-397.
- [11] Mocatta D., Cohen G., Schattner J., Millo O., Rabani E., Banin U., Heavily doped semiconductor nanocrystal quantum dots, *Science*, 332 (2011) 77-81.
- [12] Koenraad P.M., Flatté M.E., Single dopants in semiconductors, *Nat. Mater.*, 10 (2011) 91-100.
- [13] Moraru D., Udhiarto A., Anwar M., Nowak R., Jablonski R., Hamid E., Tarido J.C., Mizuno T., Tabe M., Atom devices based on single dopants in silicon nanostructures, *Nanoscale Res. Lett.*, 6 (2011) 479-487.
- [14] Máthé L., Onyenegecha C. P., Farcaş A. -A., Pioraş-Ţimbolmaş L. -M., Solaimani M., Hassanabadi H., Linear and nonlinear optical properties in spherical quantum dots: Inversely quadratic Hellmann potential, *Phys. Lett.*, 397 (2021) 127262.
- [15] Naifar A., Zeiri N., Nasrallah S. Abdi-Ben, Said M., Linear and nonlinear optical properties of CdSe/ZnTe core/Shell spherical quantum dots embedded in different dielectric matrices, *Photonics and Nanostructures*, 40 (2020) 100789.
- [16] Al E. B., Kasapoglu E., Sakiroglu S., Sari H., Sökmen I. Duque C. A., Binding energies and optical absorption of donor impurities in spherical quantum dot under applied magnetic field, *Physica E*, 119 (2020) 114011.

- [17] Dorfs D., Hickey S., Eychmüller A., Type-I and Type-II core-shell quantum dots: Synthesis and characterization, *Kumar CSSR (Ed) Semiconductor Nanomaterials, Weinheim: Wiley-VCH*, (2010) 331-366.
- [18] Maximov M. V., Asryan L. V., Shernyakov Yu. M., Tsatsul'nikov A. F., Kaiander I. N., Nikolaev V. V., Kovsh A. R., Mikhrin S. S., Ustinov V. M., Zhukov A. E., Alferov Zh. I., Ledenstov N. N. Bimberg D., Gain and threshold characteristics of long wavelength lasers based on InAs/GaAs quantum dots formed by activated alloy phase separation, *IEEE J. Quant. Electron.*, 37 (2001) 676-683.
- [19] M'zerd S., El Haouari M., Talbi A., Feddi E., Mora-Ramos M. E., Impact of electron-LO-phonon correction and donor impurity localization on the linear and nonlinear optical properties in spherical core/shell semiconductor quantum dots, *J. Alloy. Comp.*, 753 (2018) 68-78.
- [20] Feddi E., Talbi A., Mora-Ramos M. E., Haouari M. El, Dujardin F., Duque C. A., Linear and nonlinear magneto-optical properties of an off-center single dopant in a spherical core/shell quantum dot, *Physica B*, 524 (2017) 64-70.
- [21] Zhang Zhi-Hai, Zhuang G., Guo Kang-Xian, Yuan Jian-Hui, Donor-impurity-related optical absorption and refractive index changes in GaAs/AlGaAs core/shell spherical quantum dots, *Superlattice Microst.*, 100 (2016) 440-447.
- [22] El Haouari M., Talbi A., Feddi E., El Ghazi H., Oukerroum A., Dujardin F., Linear and nonlinear optical properties of a single dopant in strained AlAs/GaAs spherical core/shell quantum dots, *Optic. Comm.*, 383 (2017) 231-237.
- [23] Adachi S., GaAs, AlAs, and $\text{Al}_x\text{Ga}_{1-x}\text{As}$: Material parameters for use in research and device applications, *J. Appl. Phys.*, 58 (1985) R1-R29.



Thermoluminescence characteristics and kinetic analysis of beta irradiated $\text{Ca}_4\text{LaO}(\text{BO}_3)_3$ phosphor

Ziyafer Gizem PORTAKAL UÇAR^{1,*}

¹ Çukurova University, Science and Arts Faculty, Physics Department, 01330, Adana/TURKEY

Abstract

Thermoluminescence (TL) properties of synthesized $\text{Ca}_4\text{LaO}(\text{BO}_3)_3$ exposed to beta radiation were analyzed and TL kinetic parameters of activation energy E (eV), the frequency factor s (s^{-1}), and order of kinetics b were determined in this study. TL glow curve recorded in 25–500 °C range presented two TL maxima around 70 and 200 °C and therefore, thermal cleaning was utilized for the further investigations on a single TL maximum. To investigate dosimetric characterizations of $\text{Ca}_4\text{LaO}(\text{BO}_3)_3$, additive dose and various heating rates, reusability, and storage time measurements were performed. $\text{Ca}_4\text{LaO}(\text{BO}_3)_3$ has a linear dose range between 10 to 100 Gy with a heating rate of 2 °C/s. An anomalous case of heating rate behavior was attained for the TL measurements carried out using variable heating rates between 0.1 and 10 °C/s which was considered through the semi-localized transition model. Reusability and storage time measurements indicated the results within the 5% standard deviation. The kinetic parameters were estimated by the initial rise (IR) and glow curve deconvolution (GCD) methods. Continuously distributed trapping levels were identified by T_M-T_{stop} with E ranging from 1.25 to 1.45 eV. GCD identified that the glow curve expressed general order kinetics and consist of three overlapping traps.

Article info

History:

Received:28.04.2021
Accepted:28.06.2021

Keywords:

$\text{Ca}_4\text{LaO}(\text{BO}_3)_3$,
Thermoluminescence,
Anomalous heating
rate,
 T_M-T_{stop} ,
GCD.

1. Introduction

The thermoluminescence (TL) process includes the excitation of electrons into the conduction band from the valance band due to an exposure by a radiation source and pursued by their capture by electron traps connected with defects or impurities in the crystal lattice. During the TL readout procedure, the trapped electrons are released by the heating usually through the conduction band and may execute radiative recombination with hole centers in the sample. Produced luminescence is detected as a function of the temperature [1]. TL method is widely used in various fields such as radiation and retrospective dosimetry for personal and environmental monitoring [2]. In general, TL is preferred in the field of radiation dosimetry and dosimetric properties such as reusability, linear dose response, negligible fading, heating rate behavior, i.e. are of great importance. Moreover, various models have been suggested to investigate the kinetic parameters of the traps within the phosphor. The single trap model, localized transition models, and semi-localized transition (SLT) model are the principally employed theoretical models of TL [3]. Mandowski

who developed the SLT model reported that the spatially related structure of traps and recombination centers are responsible for various anomalous TL phenomena in his further investigations [4-6]. The displacement peaks, the origination of very high frequency factors (s) connected with the cascade de-trapping mechanism, and the anomalous statement of the heating rate are argued by the SLT model [7]. Besides, the important points to understand the dosimetric characteristics of TL materials are the trap parameters of glow peaks providing main information on the TL emission mechanisms [8]. Since TL can provide information on the traps representing the recombination centers of a TL glow curve by the trap parameters of activation energy E , frequency factor s , and order of kinetics b .

Borate compounds have a great interest owing to their good thermal and chemical stability, low cost, convenient storage stability after the irradiation, high sensitivity, comparatively easy preparation, and the use of light-emitting diode lightening applications [9]. Detailed luminescence properties of various borate compounds have been studied for a long time. [9-13].

*Corresponding author. e-mail address: gportakal@cu.edu.tr

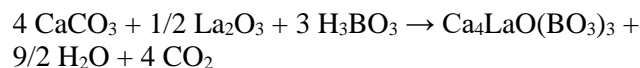
In addition to these investigations, TL studies are of great importance to evaluate the dosimetric characteristics and kinetic parameters of borate compounds. Especially, $\text{Li}_2\text{B}_4\text{O}_7$ is one of the most preferred borate phosphors by reason of its low effective atomic number ($Z_{\text{eff}} = 7.3$) to be used in radiation dosimetry [10-12]. However, the development of fresh phosphor materials for radiation detection is one of the primary works in TL dosimetry research. Recently, $\text{Ca}_4\text{LaO}(\text{BO}_3)_3$ (CLBO) phosphor has been searched in terms of its luminescence properties [14-16] and it is stated that CLBO has color-tunable luminescence after doping with rare-earth ions. In addition to these few luminescence studies, CLBO was investigated in terms of its other properties as well. Adams et al. stated the nonlinear optical characteristics of CLBO crystal [17]. Moreover, optical and thermal properties [18] electronic structure [19], magnetic properties [20], growth and spectroscopic properties [21-22], and detailed crystal structure [23] of CLBO were reported. Yet, the previous investigations about CLBO phosphor do not contain a TL study. This feature is the motivation for this work using TL.

The present work reports the TL characterization of beta-irradiated $\text{Ca}_4\text{LaO}(\text{BO}_3)_3$ prepared by a solid state method. First, the most suitable filter was selected by testing the available filter combinations in the TL reader and all measurements were utilized using the chosen filter. Second, preheating was applied to eliminate the unstable low-temperature TL peak(s) of CLBO phosphor. Dosimetric tests such as dose response, heating rate behaviors, storage time (short time fading), and reusability of CLBO exposed to beta radiation were evaluated after preheating. In addition, TL trapping parameters of a TL peak maximum were conducted using the initial rise (IR) method. The possible locations of the overlapping TL peaks were determined by T_M - T_{stop} analysis and the trapping parameters of each deconvolved peak were found by the glow curve deconvolution (GCD) method.

2. Experimental Details

2.1. Synthesis and XRD Analysis of $\text{Ca}_4\text{LaO}(\text{BO}_3)_3$ Phosphor

High-purity starting materials as CaCO_3 (99.99%, Merck), La_2O_3 (99.9%, Alfa Aesar), and H_3BO_3 (99.9%, Merck) were used to synthesize $\text{Ca}_4\text{LaO}(\text{BO}_3)_3$ phosphor by standard solid state reaction method. The oxide mixtures (weights on the strength of the stoichiometric ratio of the mixture according to the correct formula below) were ground in an agate mortar and mixed thoroughly.



The powder composition was transferred into a crucible and firstly heated at 900 °C in the air for 1 h to affect the decomposition of the boric acid. The powder sample was immediately cooled, reground, and reheated to 1200 °C for several hours (up to 6 h). Finally, the synthesized phosphor was cooled to room temperature (RT) to be used in further investigations. A small amount of the synthesized mixture was reserved for X-ray diffraction (XRD) analysis. The phase composition and crystallinity of synthesized $\text{Ca}_4\text{LaO}(\text{BO}_3)_3$ phosphor were identified by XRD using Rigaku Miniflex 600 at scanning steps of 0.1° in the range $10 \leq 2\theta$ (°) ≤ 80 with Cu K α (40 kV, 15 mA, $\lambda=0.15405$ nm) radiation.

2.2. Thermoluminescence (TL) Measurements

Lexsyg Smart TL/OSL reader having a $^{90}\text{Sr}/^{90}\text{Y}$ beta source with 0.10 Gy/s dose rate was used for all the TL measurements. Powder sample weighed as 30 mg was pressed to form the required pellet (diameter and thickness of 6 and 0.75 mm) by being held under a pressure of 2 ton-force/cm² for 10 minutes. A single aliquot (in 29.8 mg weight) in pellet form was employed in TL characterization and kinetic parameter calculation studies. TL glow curves were achieved from RT to 500 °C with a linear heating rate of 2 °C/s (apart from the heating rate analysis). Filter test of CLBO sample irradiated by 10 Gy beta dose was operated using the various filter combinations in the TL reader. Preheating was applied to eliminate the low temperature peak(s) by using the preheat (PH) plateau test to determine both PH temperature and duration. The preheated CLBO sample was exposed to beta irradiation at additive dose between 0.1 and 150 Gy for dose response evaluation. For investigations related to the impact of heating rate, the pellet sample was irradiated by 10 Gy beta dose and measured at variable heating rates (0.1–10 °C/s). Measurements conducted in an N₂ environment were made using the net TL intensity by subtracting the background from the first readout.

2.3. Kinetic analysis of TL glow curves

The kinetic analysis and the trap parameters of the CLBO phosphor were investigated from the obtained TL glow curve data by the T_M - T_{stop} , initial rise (IR), and glow curve deconvolution (GCD) methods.

2.3.1. T_M - T_{stop} method

One method to separate the overlapping TL peaks is based on preheating up to a stopping temperature (T_{stop}) before determining the TL glow curve. For this purpose, an irradiated phosphor is heated at a linear heating rate to T_{stop} related to a location on the low temperature tail of the first glow peak. Then, the sample rapidly cooled to RT is then reheated at the same heating rate to obtain the remaining TL glow curve, and the position of the first maximum temperature (T_M) is recorded. The process is repeated for newly irradiated sample using various T_{stop} which are increased by a small increment (i.e. between 2 and 5 °C). This method is generally used to estimate the numbers and possible locations of overlapped TL peaks and the so-called T_M - T_{stop} method. In general, T_M - T_{stop} plot represents two different manners as “staircase” structure or “continuous line” with a slope of 1.0 [24].

2.3.2. Initial rise (IR) method

This method defines that the initial part of the TL glow curves up to 15 % of its peak maximum (I_M) is an exponential function of the temperature and is reported to be pertinent in all the order of kinetics [25]. Thus, a plot of $\ln(I)$ versus $1/T$ produces a smooth line with a slope of $-E/k$ from which the activation energy E is determined where I is the TL intensity and k is the Boltzmann’s constant. Once E is found, the frequency factor s is thereafter computed using the intercept of the line equal to $\ln(s/\beta)$. Here β presents the heating rate in a unit of K. In the framework, the IR method was employed to three different glow curves obtained using additive dose, various heating rates, and T_M - T_{stop} measurements.

2.3.3. Glow curve deconvolution (GCD) method

GCD method is used to decompose the TL glow curve and achieve the kinetic parameters of the material. This method is applied in this study to determine the number of TL peaks in the glow curve and to extract the trap parameters E , s , and b . Figure of merit (FOM) defines the best GCD fitting of theoretical and experimental glow curve and FOM function is calculated using Eq. (1).

$$FOM = \left| \frac{\sum (TL_{exp} - TL_{fit})}{\sum TL_{fit}} \right| \times 100 \quad (1)$$

TL_{exp} defines the measured intensity at variable T in experimental data while TL_{fit} represents the best-fitted values of the intensity by the GCD method. FOM value states the goodness of fit and the values less than 2.5 % refer to a good fit [26]. The TL glow curve of CLBO

phosphor was decomposed by the `tgcd`: an R package [27] software.

3. Results and Discussion

3.1. Structural properties

The crystalline structure of CLBO phosphor was investigated by XRD. As presented in Fig.1, the observed reflection peaks are in good agreement and match well with the calcium lanthanum borate ($Ca_4LaO(BO_3)_3$) belonging to the $C1m1$ (No. 8) space group in the monoclinic crystal system (standard card: PDF#52-0621).

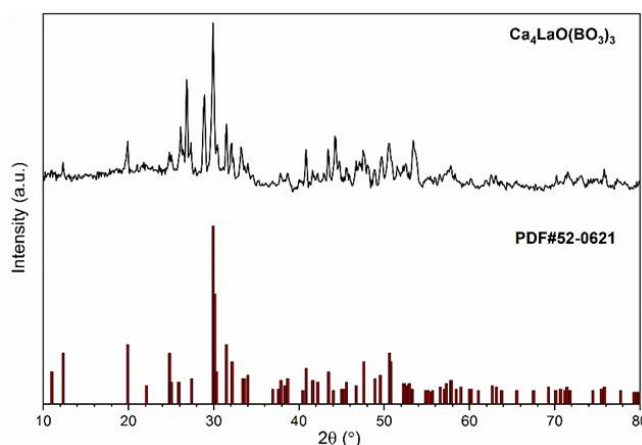


Figure 1. XRD pattern of $Ca_4LaO(BO_3)_3$ (CLBO) phosphor.

It was observed that the synthesized CLBO phosphor has the cell parameters of $a(\text{Å})$: 8.170, $b(\text{Å})$: 16.082, $c(\text{Å})$: 3.627 and $\alpha(^{\circ})$: 90, $\beta(^{\circ})$: 101.39, $\gamma(^{\circ})$: 90. However, three undefined peaks at $\sim 27^{\circ}$ (222), 29° (123), and 53° (622) attract attention. These diffraction peaks are from the starting material of La_2O_3 (PDF#03-065-3185). The possible explanation is due to the feature of La_2O_3 , namely, its aptitude to quickly absorb moisture from the atmosphere up to 20% of its weight [28]. Therefore, absorbed H_2O traces might be removed during the heating procedure at $1200^{\circ}C$ and so La_2O_3 may have remained. Nevertheless, the amount of La_2O_3 impurity was negligibly low and it is not thought to affect the TL characterization results.

3.2. TL characteristics

Fig. 2 presents the TL glow curves of CLBO phosphor after applying a filter test to decide on the most suitable optical filter. Different optical filter combinations including BSL-TL (365 nm) and IRSL-TL (wideband blue (wbb), 410 and 565 nm) filters were evaluated and IRSL-TL 565 nm filter giving the optimal TL glow curve having the highest TL intensity was chosen. Besides the TL intensity, another important point is the position and shape of the apparent peak maxima in the

TL glow curve of the CLBO phosphor. For this reason, it has been decided that IRSL-TL 565 nm is also the ideal filter for further TL analysis. As seen in Fig. 2, the glow curve of CLBO sample has two TL maxima at around 70 and 200 °C. As known, low temperature TL peaks, the trapping energies related to shorter lifetimes, are not resistant. These TL peaks can be erased using an appropriate thermal cleaning, namely preheating, the process performed before each TL readout to avoid the presence of an intense TL signal that may influence the shape and position of the respective peak(s) located at a higher temperature region. Thus, preheating was performed to CLBO phosphor by applying a plateau test to remove the TL signal at 70 °C.

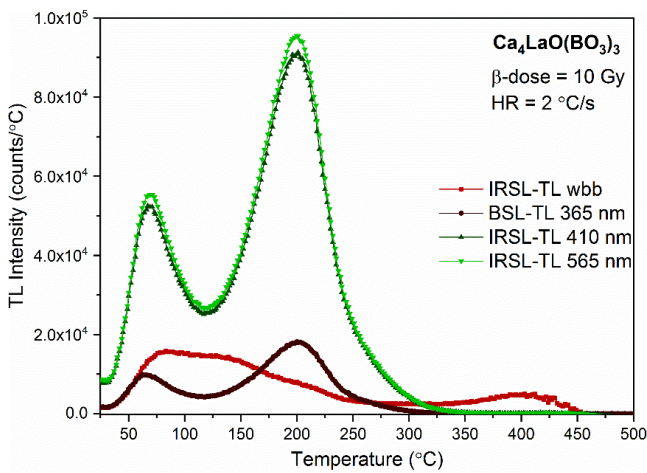


Figure 2. TL glow curves of CLBO phosphor obtained by the filter test

Preheating test was first applied to detect the PH temperature of the CLBO phosphor exposed to beta irradiation of 10 Gy before each readout. After the irradiation, the pellet sample was initially heated to a temperature (T_{stop}), then rapidly cooled to RT. Then the TL glow curve was utilized using a heating rate of 2 °C/s. For this purpose, the thermal cleaning process was reiterated for all T_{stop} values between 100 and 151 °C with 3 °C intervals. As presented in Fig. 3(a), the PH temperature of CLBO phosphor was selected as 125 °C connected with the plateau observed. Then, keeping the decided PH temperature constant, 125 °C PH temperature was applied to the 10 Gy irradiated CLBO sample for the periods between 0 and 40 s before each TL measurement (Fig. 3(b)). Subsequently, 25 s PH duration was chosen as an appropriate time corresponding to the plateau region as well. Defined PH temperature and time (125 °C, 25 s) were operated for the rest of the TL analysis.

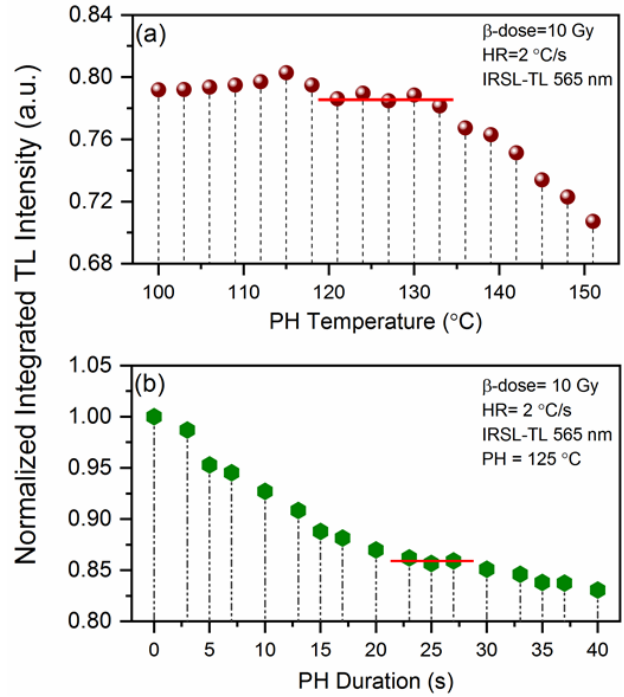


Figure 3. Normalized integrated TL intensities of CLBO phosphor vs (a) PH temperature and (b) PH time

As shown in Fig. 4, the glow curve of CLBO did not significantly change by the preheating procedure. If we draw the integral of the TL intensity versus temperature, we can get information about whether the apparent maximum at 200 °C consists of overlapped TL peaks (inset figure of Fig. 4). Hence, it has been seen that the apparent maximum actually consists of at least three peaks while the whole glow curve comprises at least four peaks where the first erased one corresponds to the low temperature peak.

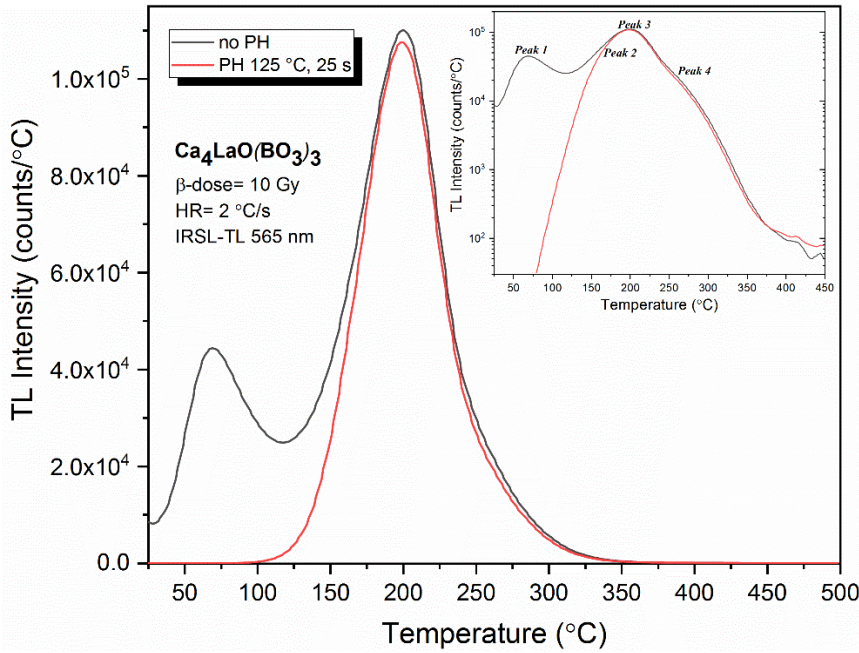
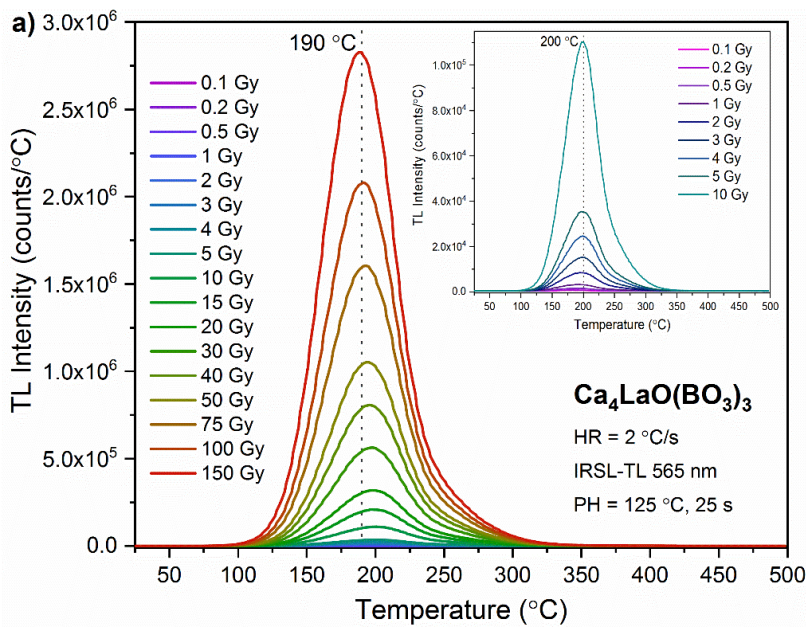


Figure 4. Preheated and non-preheated CLBO sample (inset: a logarithmic plot to evaluate overlapping TL peaks)

Fig. 5 shows the TL glow curves with changing exposure for the beta irradiations between 0.1–150 Gy and the linear behavior versus the given dose. The TL glow curves of CLBO phosphor were obtained after preheating (125 °C, 25 s) with a heating rate of 2 °C/s. TL emissions were increased with the increasing beta dose up to 150 Gy which was the highest dose that can be given since the photomultiplier tube (PMT) has reached the maximum detection limit it can detect. As

it is clear from Fig. 5(a), the TL peak intensity gradually increases but the shape of the TL glow peak expands by the increasing dose at the same time. Besides, the TL peak position is changed and shifts slightly to lower temperature sides when the given dose increases. The change in the T_M of the glow peak is observed as ~10 °C between the lowest (0.1 Gy) and highest (150 Gy) beta dose.



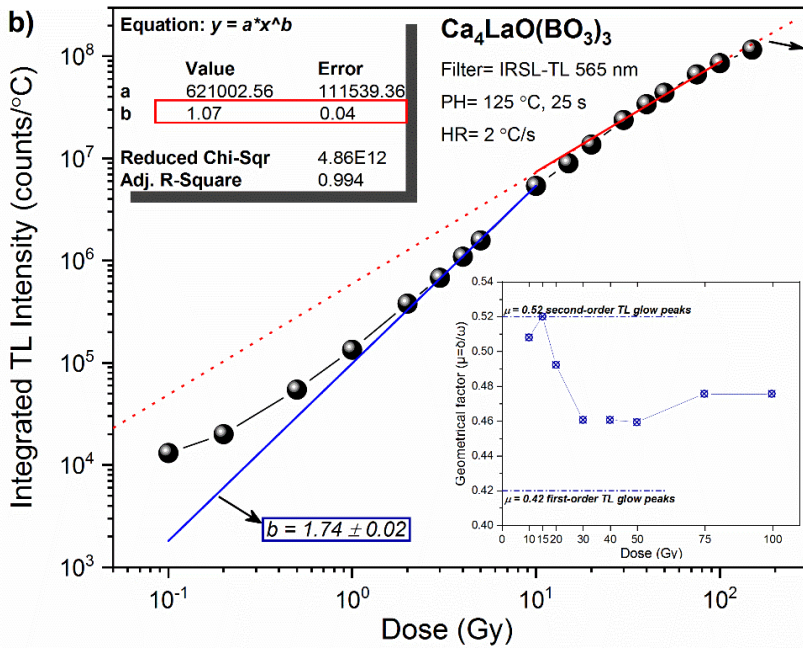


Figure 5. (a) Dose response of preheated CLBO in the range of 0.1–150 Gy (inset: 0.1–10 Gy), (b) Linearity plot (inset: symmetry factors of the glow curves obtained at the doses in the linear range)

The impact of the given dose on T_M is provided by one trap one recombination (OTOR) model which is the simplest phenomenological model for TL [29]. In the OTOR model, the radiation dose is represented by the ratio n_0/N , where n_0 (cm^{-3}) is the primary concentration of filled traps at first, N (cm^{-3}) is the total concentration of electron traps within the crystal. Here, the ratio describes the filling degree of the trap responsible for a TL peak. Although this model does not contain information about the kinetic order b , May and Partridge suggested a general order equation, and the dose is represented by the term $(n_0/N)^{b-1}$ [30]. For general order of kinetics, when the dose increases, the T_M shifts to lower temperatures since the re-trapping decreases and the recombination increases [31].

Furthermore, the obtained results of the TL glow curves for additive dose present that CLBO sample exhibits a linear behavior (e.g. the slope is nearly 1.0, $R^2 = 0.99$) in the range of 10–100 Gy as shown in Fig. 5(b). Superlinear behavior of the glow curve is also presented within the lower dose region between 0.1 and 10 Gy (in Fig. 5(b)). Although there was a decrease in the integrated intensity after 100 Gy, it could not be determined whether it was saturated since the higher

doses could not be applied. It has been observed that CLBO has a linearity at higher dose range compared to un-doped borate based phosphors evaluated previously by various researchers (especially, stated in the introduction section). Moreover, symmetry factor μ was obtained to argue the order of kinetics of the TL glow peak by taking its shape or geometrical characteristics into account. Symmetry factors correspond to 0.42 and 0.52 values for the occurrence of first and second order kinetics, individually. This method is based on the peak temperature T_M , the temperature at half of the maximum intensity (I_M) of the ascending part of the peak T_1 and the descending part T_2 . Thus, the symmetry factor ($\mu = \delta/\omega$) is calculated using the ratio of the half widths at high temperature side ($\delta = T_2 - T_M$) and the total one ($\omega = T_2 - T_1$) [32]. Thus, the symmetry factor μ was evaluated from the glow curves obtained by dose response analysis to evaluate the kinetic order. In Fig. 5(b), it is also noticed that the glow curves obey the general order of kinetics.

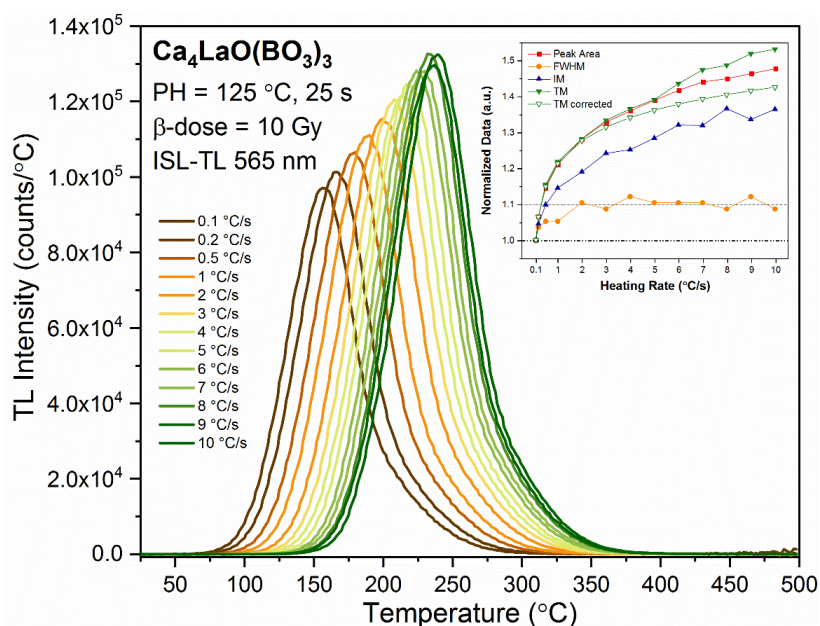


Figure 6. TL glow curves of CLBO obtained by using different heating rate values (0.1–10 °C/s) (inset: Normalized data)

In general, TL glow curves shift in the direction of the higher temperature side during the TL readout with faster heating rates [25,33]. Fig. 6 represents this outcome in the TL glow curves of CLBO phosphor using various heating rates. The inset figure contains the parameters obtained by the glow curves for various heating rates and each parameters were normalized according to the first data achieved by using the glow curve with the the lowest heating rate (0.1 °C/s). A slight shift is expected case since the traps within the band gap of the phosphor are emptied in a shorter time period at the faster heating rates and therefore, T_M increases. In addition, full width half maximum (FWHM) increases while maximum intensity (I_M) decreases according to the TL theory. However, the integrated peak intensity must be constant [34]. As seen in both Fig. 6 and the inset figure, both the peak integral and I_M increases with the increasing heating rate which is defined as an anomalous heating rate phenomenon contrary to the expected situation explained by the OTOR model. Pagonis et al. [3] reported this anomalous heating rate or “anti-quenching” effect by using the Mandowski model, namely semi-localized transitions (SLT), by introduced an accessional non-radiative transition through the recombination center from the directly excited state. The stimulated electrons by heating from the trap to an excited state are thermally delivered into the conduction band where they can be captured or reassembled with holes in the recombination centers. In the first scenario, this recombination mechanism is supposed to yield a TL signal. An electron in the excited state can directly recombine with a hole in the recombination center without a radiative transition in

either way. The relative ratio of radiative against non-radiative transition possibilities decreases when the heating rate decreases and vice versa. The two-stage process of stimulation of the charge carriers from the traps is the reason for such behavior. The whole amount of localized transitions is comparative to the entire time exhausted in an excited state by the trapped electrons. This time decreases resulting from the higher probability rates of thermally excited transitions into the conduction band at higher heating rates. Therefore, the physical base of the anomalous effect is a rivalry among the radiative and non-radiative mechanisms. This rivalry for current charges between the two mechanisms creates the integrated TL intensity to rise, whereas the comparable non-radiative one has to decrease with the identical quantity due to the charge conservation. Thus, the increase in the integrated TL intensity corresponds to the rise in the probability of radiative transitions over that of the non-radiative ones [3-7].

Moreover, T_M and FWHM values of the glow curve show an increasing tendency. If we look at the inset figure of Fig. 6, it is seen that two normalized T_M values are presented. This is due to the correction of T_M values for each heating rate value as a result of the temperature lag effect. The temperature of the heating element changes from the temperature of the sample during the TL readout and non-ideal thermal contact, namely temperature lag, may affect the calculated trapping parameters of the TL glow peak [35]. By accepting that the lowest two heating rates (0.1 and 0.2 °C/s) are not affected by the temperature lag, Eq. 2 is

used to correct T_M values for the glow curves obtained with the higher heating rates.

$$T_{M_j} = T_{M_i} - c \ln \left(\frac{\beta_i}{\beta_j} \right) \quad (2)$$

T_{M_j} and T_{M_i} represent the maximum temperatures for β_j and β_i heating rates, and c is a constant quantity that is computed utilizing the two lowest heating rates. Therefore, normalized values of both T_M data,

experimentally obtained (uncorrected) and corrected by utilizing temperature lag equation (Eq. 5) are presented in the inset figure of Fig. 6. After the temperature lag correction, it was seen that the increase in T_M is 10% less for the highest heating rate applied (10 °C/s) as the heating rate increased.

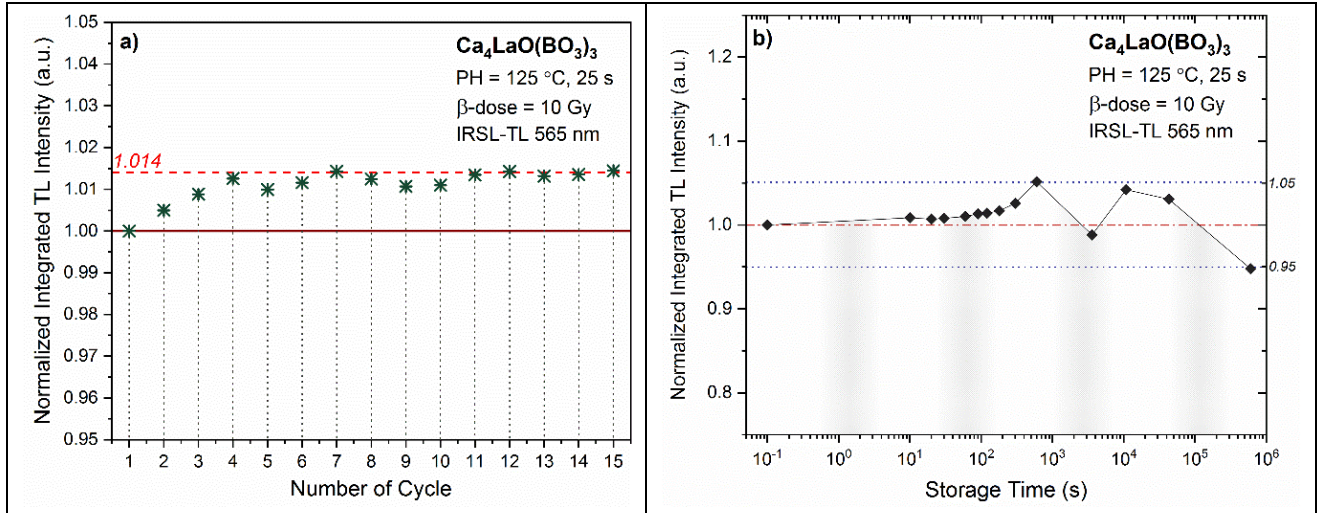


Figure 7. (a) Reusability plot achieved by 15 TL readout cycle and (b) storage time measurements up to a week

In dosimetric applications, reusability and storage time measurements are of great significance to search the usage of a prepared TL material. Since it is desirable that the material remains stable so as to give the same TL signal for each repetitive reading and during the elapsed time. As shown in Fig. 7(a), the obtained standard deviation of the integrated TL intensity is approximately 4 % which is in the tolerance ranges acceptable for dosimetric materials stated as less than 5 % [36]. Storage time characteristics of beta irradiated CLBO was checked to evaluate short time storage during a week in the dark at RT after 10 Gy beta exposure. For the visible peak maxima at ~200 °C, the fading rate was nearly 5 % after a week. Instead of fading, a fluctuation was observed within the 5 % confidence interval during the stored time period. A growth of peak height to 5 % over ten minutes and another increase to 3-4 % after three hours were observed however a forecastable fading was obtained

when the storage time was extended and a sort of recovery was observed after 3h storage time (Fig. 7(b)). An initial increase of the integrated TL intensity may have possibly occurred by a tunneling transfer among the traps as a non-thermal process due to the existence of intense spatial correlations between the traps and recombination centers [37]. Similar abnormal results were also highlighted in the literature by the various researchers for the different TL materials [38-39] as well.

3.3. TL kinetics

To estimate the kinetic parameters of $\text{Ca}_4\text{LaO}(\text{BO}_3)_3$ phosphor, T_M - T_{stop} , and IR methods have been operated on the strength of the presume that the TL glow curve consists of an isolated TL peak maximum. Further, the GCD method was performed to evaluate whether the experimental glow curve has overlapped TL peaks.

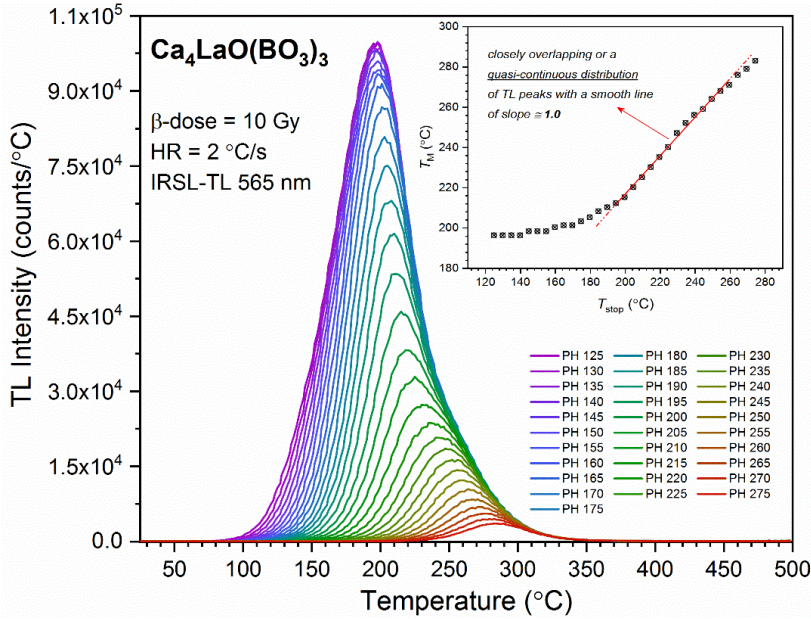


Figure 8. TL glow curves of CLBO sample obtained after preheating to various T_{stop} values (inset: T_M-T_{stop} dependency)

At first, 10 Gy beta dose was applied to the phosphor and then, it was heated up to a stopping temperature (T_{stop}). Afterward, the TL glow curve was obtained with a constant heating rate of 2 °C/s. This cycle was repeated under the same conditions using T_{stop} values between 125 and 275 °C with 5 °C intervals (Fig. 8). T_M-T_{stop} method is generally used to estimate the numbers and possible locations of overlapped TL peaks. Therefore, T_M versus T_{stop} plot was achieved for the preheated TL glow curve data of CLBO phosphor and presented in the inset figure of Fig. 8. If a TL glow curve contains various and clearly separated first order TL peaks, T_M-T_{stop} curve presents a characteristic “staircase” structure having individual flat regions. Considering a glow curve consisting of more closely overlapping peaks, the curve turns into a smoother shape and the T_M representing the flat regions can exclusively be utilized as an indicator of the locations of each individual peak. When the TL peaks overlap, even more, the case is disposed to the presence of a quasi-continuous distribution of the TL peaks (in other words, trapping centers). T_M-T_{stop} curve will transfer to a continuous line with a slope $f \approx 1.0$ at this stage. The limit of detection of flat regions within the T_M-T_{stop} curve gives a measure of the resolution of the technique [24]. According to the inset figure of Fig. 8, it is seen that the single TL maximum, obtained after a PH (125 °C, 25 s) procedure, consists of several closely located overlapping TL peaks rather than a single trapping level. Therefore, none of the overlapped TL peaks are subject to first order kinetics.

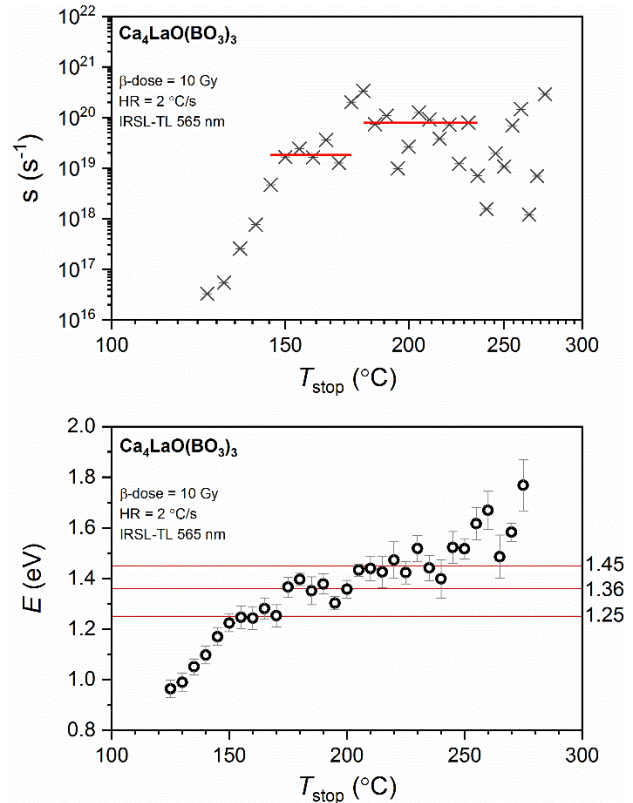


Figure 9. Trap parameters of s (top), E (bottom) against to T_{stop} for CLBO phosphor.

To examine the E and s values of CLBO phosphor by using T_M-T_{stop} analysis, the IR method which is a quite reliable technique to obtain trap parameters was also utilized. Therefore, this method was operated on to each glow curve obtained after the T_M-T_{stop} analysis. Mean activation energies and frequency factors of these energy levels were computed by utilizing the initial rise method to each TL peak at a different T_{stop} .

Calculated E and s values were plotted against the applied T_{stop} and presented in Fig. 9. As seen in Fig. 9, a variation of the activation energy and frequency factor present at least three possible trap levels of preheated CLBO phosphor. Supporting the result of the inset figure of Fig. 8, E and s values were obtained from 150 °C towards higher temperatures for the closely positioned TL peaks. Therefore, the results reveal that the preheated CLBO sample has a continuous trap distribution with activation energies of 1.25, 1.36, and 1.45 eV. Furthermore, frequency factors were found within the range of 10^{19} and 10^{20} s^{-1} . Since the transport phase includes several non-radiative routes of electron loss, the higher frequency factors pointed out that the trap and luminescence sites are closely linked [40]. Further, GCD analysis in Fig. 10 suggests that there are a variety of closely positioned component bands that all contribute to the TL glow peak.

Moreover, trap parameters E and s of the TL peak maximum at 200 °C were calculated by the IR method using the glow curves obtained from various heating rate and additive dose, respectively. Considering the fact that the use of the IR method may be more dependable than various heating rate (VHR) method to derive E , particularly for phosphors where there is a strong competition between radiative and non-radiative pathways stated by Pagonis et al. [3], the VHR method was not preferred for the calculation of trap parameters of the TL peak maximum in this study. Certain TL glow curves presented in Fig. 5(a) and 6 have been evaluated for this purpose. Therefore, the trap parameters were calculated by plotting the temperature-dependent graphs of the initial rise parts of the glow curves obtained using the heating rates between 0.1 and 5 °C/s (beta dose is fixed at 10 Gy) and doses between 10-100 Gy (a linear heating rate is fixed at 2 °C/s) in the linear dose range. Obtained parameters of E and s are shown in Table 1.

Table 1. Estimated kinetic parameters using IR method applied to the heating rate (HR) and dose response glow curves

HR (°C/s)	E (eV)	s (s ⁻¹)	Dose (Gy)	E (eV)	s (s ⁻¹)
0.1	1.035 ± 0.046	1.60 x 10 ¹⁸	10	1.210 ± 0.035	1.50 x 10 ¹⁹
0.2	1.026 ± 0.030	6.82 x 10 ¹⁷	15	1.187 ± 0.028	1.47 x 10 ¹⁹
0.5	1.067 ± 0.044	1.08 x 10 ¹⁸	20	1.162 ± 0.035	1.13 x 10 ¹⁹
1	1.152 ± 0.025	6.68 x 10 ¹⁸	30	1.184 ± 0.032	3.93 x 10 ¹⁹
2	1.171 ± 0.036	5.05 x 10 ¹⁸	40	1.164 ± 0.032	3.38 x 10 ¹⁹
3	1.237 ± 0.032	1.84 x 10 ¹⁹	50	1.170 ± 0.032	5.46 x 10 ¹⁹
4	1.182 ± 0.031	2.52 x 10 ¹⁸	75	1.173 ± 0.036	1.00 x 10 ²⁰
5	1.275 ± 0.047	2.14 x 10 ¹⁹	100	1.178 ± 0.037	1.62 x 10 ²⁰

According to the results presented in Table 1, E value of the TL peak maximum does not importantly vary with the increasing dose as a result of being dose-independent. However, a slight increase in E values from 1.04 to 1.28 eV is seen with the increasing heating rate. As seen in Table 1, the energy values obtained by the IR method using both ways are in concordance with each other. However, effective activation energies presented in Table 1 differ from the acquired IR results using T_M-T_{stop} analysis. This indicates that the TL glow curve of a preheated CLBO phosphor is a complex curve consisting of overlapped peaks, else the findings obtained using the three ways should match. In addition, similar and high frequency factors were found as also presented in those observed by T_M-T_{stop} analysis. Therefore, results supporting the interpretation that the trap and luminescence centers are located very close to each other have been obtained.

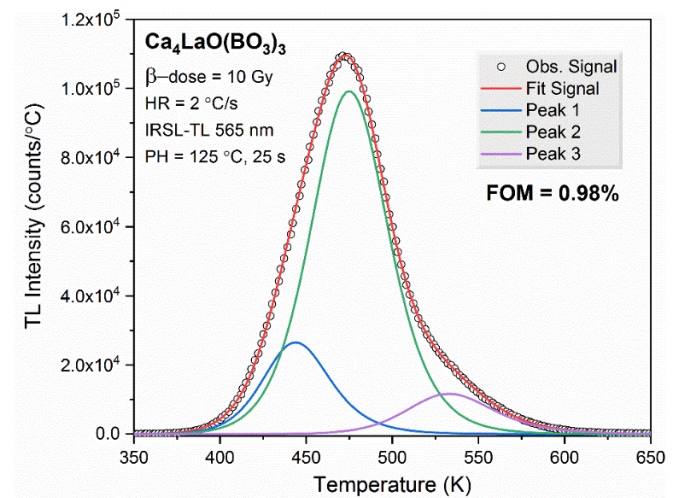


Figure 10. Deconvolution of the TL glow curve of preheated CLBO phosphor

The glow curve deconvolution (GCD) method is used to decompose the TL glow peak and achieve the kinetic parameters of the preheated CLBO phosphor. GCD method was operated using the general order kinetics in connection with the dose response evaluations of preheated CLBO phosphor. GCD plot and decomposed TL glow peaks in Fig. 10 presents that the experimental TL glow curve of the sample after 10 Gy beta exposure at a heating rate of 2 °C/s was decently fitted with three TL peaks. As presented in the figure, TL emission begins to increase after 350 K, arrives at maximum TL intensity at 474 K, and depletes entirely around 650 K. Thus, the remaining part of the recorded data from the total TL spectrum between 300 and 770 K is not included in the figure (Fig. 10). It is seen that the deconvolution results of CLBO phosphor give a reliable evaluation of the trap parameters with a FOM value of 0.98 %. In addition, lifetimes (τ) of the TL glow peaks are an important argument to investigate the TL materials about their effectiveness in either dosimetry or dating Eq. 3 was utilized to calculate the lifetimes of the decomposed TL peaks.

$$\tau = s^{-1} \exp\left(\frac{E}{kT}\right) \quad (3)$$

T is the storage temperature which was employed to be 298 K for the computation. All kinetic parameters of the deconvoluted TL peaks are shown in Table 2.

Table 2. Kinetic parameters of the deconvoluted TL glow curves of $\text{Ca}_4\text{LaO}(\text{BO}_3)_3$ using R-studio (FOM = 0.98%)

	$\text{Ca}_4\text{LaO}(\text{BO}_3)_3$				
	E (eV)	s (s^{-1})	b	T_M (°C)	σ (year)
Peak 1	1.233	1.40×10^{13}	2	171	1.60
Peak 2	1.146	1.61×10^{11}	1.79	201	4.54
Peak 3	1.375	1.07×10^{12}	2	259	5110.54

According to the results, when peak 1 at 171 °C and 3 at 259 °C are of second order of kinetics, peak 2 at 201 °C is of general order kinetics. GCD results represented similar results to those found by the IR method using T_M-T_{stop} analysis since the number of decomposed TL peaks and their maximum peak temperature are in good agreement. In addition, the average E values are also in concordance with the IR findings obtained by the results of T_M-T_{stop} analysis. The frequency factors of the continuously distributed overlapped peaks were found as 1.40×10^{13} , 1.61×10^{11} , and $1.07 \times 10^{12} \text{ s}^{-1}$, respectively. Moreover, the lifetimes of the TL peaks were obtained long enough for dosimetry applications.

4. Conclusion

$\text{Ca}_4\text{LaO}(\text{BO}_3)_3$ phosphor was produced by a solid state synthesis. XRD was conducted to evaluate the crystal structure and it was reported that the pattern of synthesized phosphor is in good agreement and matches well with the reference card. After applying adequate preheating, additive beta dose and various heating rates were applied to examine the behaviors of the TL glow curves. Consequently, 200 °C TL peak maximum presented a linear dose response behavior within 10 and 100 Gy. Anomalous behavior of the TL peak maximum of preheated $\text{Ca}_4\text{LaO}(\text{BO}_3)_3$ phosphor has been reported with increasing heating rate between 0.1 and 10 °C/s. This anti-quenching behavior may be interpreted by a semi-localized transition model presuming that radiative and non-radiative transitions compete. In addition, the material was reported as a reusable phosphor for dosimetric applications within the 5 % confidence interval. Storage time for a short period of up to a week was also found with an excellent 5 % standard deviation. Trapping parameters and the kinetic analysis of $\text{Ca}_4\text{LaO}(\text{BO}_3)_3$ phosphor were evaluated by using T_M-T_{stop} and IR methods and the results were compared with deconvoluted glow curve data, which was collected using tgcd: an R package software. The obtained results by GCD were found compatible with the other methods representing a continuous trap distribution. According to the findings, the main dosimetric peak of $\text{Ca}_4\text{LaO}(\text{BO}_3)_3$ follows the general order kinetics, as supported by dose response plot. Furthermore, the lifetimes of the decomposed TL peaks have been found to be long enough. The findings of this study present that the $\text{Ca}_4\text{LaO}(\text{BO}_3)_3$ phosphor may be a good candidate to be used in high dose monitoring for dosimetric applications considering its high effective atomic number, $Z_{\text{eff}} \approx 36.4$, (tissue equivalence is not an issue) and the linear dose range. However, further investigations are required such as higher dose effect, long-term storage time measurements and applications of different radiation sources.

Acknowledgment

The author would like to thank Assoc. Prof. Dr. Y. Z. Halefoğlu (Çukurova University) for the valuable support on the phosphor synthesis and A. Yücel (Inonu University) for the substantial evaluations on the XRD results. The author would also appreciate Prof. Dr. M. Topaksu and Assoc. Prof. Dr. S. Akça Özalp for the precious discussions on the TL results.

Conflicts of interest

The author declares that she has no known competing financial interests or personal relationships that could have appeared to influence the work reported in this paper.

References

- [1] Chen R. and Pagonis V., The role of simulations in the study of thermoluminescence (TL), *Radiat. Meas.*, 71 (2014) 8–14.
- [2] Dogan T., Thermoluminescence properties of quartz rock after β -irradiation, *Cumhuriyet Sci. J.*, 39-4 (2018) 1136-1143.
- [3] Pagonis V., Blohm L., Brengle M., Mayonado G., Woglam P., Anomalous heating rate effect in thermoluminescence intensity using a simplified semi-localized transition (SLT) model, *Radiat. Meas.*, 51 (2013) 40–47.
- [4] Mandowski A., Semi-localized transitions model for thermoluminescence, *J. Phys. D: Appl. Phys.* 38 (2005) 17–21.
- [5] Mandowski A., Topology-dependent thermoluminescence kinetics, *Radiat. Prot. Dosim.*, 119 (2006) 23–28.
- [6] Mandowski A., Semi-localized transitions model-General formulation and classical limits, *Radiat. Meas.*, 43 (2008) 199–202.
- [7] Mandowski A., Bos A.J.J., Explanation of anomalous heating rate dependence of thermoluminescence in $\text{YPO}_4:\text{Ce}^{3+}, \text{Sm}^{3+}$ based on the semi-localized transition (SLT) model, *Radiat. Meas.*, 46 (2011) 1376–1379.
- [8] Kitis G., Fureta C., Prokic M., Prokic V., Kinetic parameters of some tissue equivalent thermoluminescence materials, *J. Phys. D Appl. Phys.* 33 (2000) 1252–1262.
- [9] Peng M., Wondraczek L., Orange-to-red emission from Bi^{2+} and alkaline earth codoped strontium borate phosphors for white light emitting diodes, *J. Am. Ceram. Soc.* 93 (2010) 1437–1442.
- [10] Kelemen A., Mesterházy D., Ignatovych M., Holovey V., Thermoluminescence characterization of newly developed Cu-doped lithium tetraborate materials, *Radiat. Phys. Chem.*, 81 (2012) 1533–1535.
- [11] Fureta C., Prokic M., Salamon R., Prokic V., Kitis G., Dosimetric characteristics of tissue equivalent thermoluminescent solid TL detectors based on lithium borate, *Nucl. Instrum. Meth. A* 456 (2001) 411–417.
- [12] Kafadar V.E., Yildirim R.G., Zebari H., Zebari D., Investigation of thermoluminescence characteristics of $\text{Li}_2\text{B}_4\text{O}_7:\text{Mn}$ (TLD-800), *Thermochim. Acta*, 575 (2014) 300–304.
- [13] Oglakci M., Akça S., Halefogluy Y.Z., Dogan T., Ayvacikli M., Karabulut Y., Topaksu M., Can N., Characterization and thermoluminescence behavior of beta irradiated NaBaBO_3 phosphor synthesized by combustion method, *Ceram. Int.*, 45 (2019) 7011–7017.
- [14] Chen Z., Chen X., Huang S., Pan Y., A novel tunable green-to-red emitting phosphor $\text{Ca}_4\text{LaO}(\text{BO}_3)_3:\text{Tb}^{3+}, \text{Eu}^{3+}$ via energy transfer with high quantum yield, *Ceram. Int.*, 42 (2016) 13476–13484.
- [15] Chen Z., Pan Y., Xi L., Pang R., Huang S., Liu G., Tunable Yellow-Red Photoluminescence and Persistent Afterglow in Phosphors $\text{Ca}_4\text{LaO}(\text{BO}_3)_3:\text{Eu}^{3+}$ and $\text{Ca}_4\text{EuO}(\text{BO}_3)_3$, *Inorg. Chem.*, 55 (2016) 11249–11257.
- [16] Wu X., Yin B., Ren Q., Zheng J., Ren Y., Hai O., Structure, luminescence, properties and energy transfer of Dy^{3+} and Eu^{3+} codoped $\text{Ca}_4\text{LaO}(\text{BO}_3)_3$ phosphor, *J. Alloys Compd.* 822 (2020) 153562.
- [17] Adams J.J., Ebberts C.A., Schaffers K.I., Payne S.A., Nonlinear optical properties of $\text{LaCa}_4\text{O}(\text{BO}_3)_3$, *Opt. Lett.* 26 (2001) 217–219.
- [18] Jiang H.D., Li D.W., Zhang K.Q., Liu H., Wang J.Y., Optical and thermal properties of nonlinear optical crystal $\text{LaCa}_4\text{O}(\text{BO}_3)_3$, *Chem. Phys. Lett.* 372 (2003) 788–793.
- [19] Nelson A.J., van Buuren T., Willey T.M., Bostedt C., Adams J.J., Schaffers K.I., Terminello L., Callcott T.A., Electronic structure of lanthanum calcium oxoborate $\text{LaCa}_4\text{O}(\text{BO}_3)_3$, *J. Electron Spectrosc. Relat. Phenom.* 137–140 (2004) 541–546.
- [20] Kelly N.D. and Dutton S.E., Magnetic Properties of Quasi-One-Dimensional Lanthanide Calcium Oxyborates $\text{Ca}_4\text{LnO}(\text{BO}_3)_3$, *Inorg. Chem.*, 59 (2020) 9188–9195.
- [21] Lu Y. and Wang G.F., Growth and spectroscopic properties of $\text{Nd}^{3+}:\text{LaCa}_4\text{O}(\text{BO}_3)_3$ crystals, *J. Cryst. Growth*, 253 (2003) 270–273.
- [22] Lu Y., Hu Z.S., Lin Z.B., Wang G.F., Growth and spectroscopic properties of $\text{Er}^{3+}/\text{Yb}^{3+}:\text{LaCa}_4\text{O}(\text{BO}_3)_3$ crystals, *J. Cryst. Growth*, 249 (2003) 159–162.

- [23] Christoph R., Robert M., Margitta H., Jens G., Anke S., Horst S., Growth and structure of $\text{Ca}_4\text{La}[\text{O}(\text{BO}_3)_3]$, *J. Cryst. Growth*, 320 (2011) 90–94.
- [24] McKeever S.W.S., On the analysis of complex thermoluminescence glow-curves resolution into individual peaks, *Phys. Status Solidi*, 62 (1980) 331–340.
- [25] Chen R. and Kirsh Y., *The Analysis of Thermally Stimulated Processes*, Oxford: Pergamon Press, (1981).
- [26] Balian H.G., Eddy N.W., Figure of Merit (FOM), an improved Criterion over the normalised Chi-squared Test for assessing Goodness-of-fit of Gamma Ray Spectra Peaks, *Nucl. Instrum. Methods*, 145 (1977) 389–395.
- [27] Peng J., Dong Z.B., Han F.Q., Tgcd: an R package for analyzing thermoluminescence glow curves, *SoftwareX*, 5 (2016) 112–120.
- [28] Fan T.Y. and Kokta M.R., End-Pumped Nd:LaF₃ and Nd:LaMgA₁₁O₁₉ Lasers, *IEEE J. Quantum Electron*, 25 (1989) 1845–1849.
- [29] Halperin A. and Braner A.A., Evaluation of Thermal Activation Energies from Glow Curves, *Phys. Rev.*, 117 (1960) 408–415.
- [30] May C.E. and Partridge J.A., Thermoluminescent Kinetics of Alpha-Irradiated Alkali Halides, *J. Chem. Phys.*, 40 (1964) 1401–1409.
- [31] Kitis G., Mouza E., Polymeris G.S., The shift of the thermoluminescence peak maximum temperature versus heating rate, trap filling and trap emptying: Predictions, experimental verification and comparison, *Physica B Condens. Matter.*, 577 (2020) 411754.
- [32] Pagonis V., Kitis G., Furetta C., *Numerical and Practical Exercises in Thermoluminescence*. USA:Springer, (2006).
- [33] Bos A., High sensitivity thermoluminescence dosimetry, *Nucl. Instrum. Methods Phys. Res., B* 184 (2001) 3–28.
- [34] Kitis G., Spiropulu M., Papadopoulos J., Charalambous S., Heating rate effects on the TL glow-peaks of three thermoluminescent phosphors, *Nucl. Instrum. Meth. Phys. Resear.*, 73 (1993) 367–372.
- [35] Kitis G., Tuyn J.W.N., A Simple Method to Correct for Temperature Lag in TL Glow-Curve Measurements, *J. Phys.D: Appl. Phys.*, 31 (1998) 2065–2073.
- [36] Furetta C. *Handbook of Thermoluminescence.*, Singapore: Word Scientific, (2003).
- [37] Pagonis V., Truong P., Thermoluminescence due to tunneling in nanodosimetric materials: A Monte Carlo study, *Physica B: Condens. Matter.*, 531 (2018) 171–179.
- [38] Annalakshmi O., Jose M.T., Amarendra G., Dosimetric characteristics of manganese doped lithium tetraborate - an improved TL phosphor, *Radiat. Meas.*, 46 (2011) 669–675.
- [39] Furetta C., Pellegrini R., Some dosimetric properties of Li₂B₄O₇:Mn (TLD-800), *Radiat. Eff. Defect. S.*, 58 (1-2) (1981) 17–23.
- [40] Townsend P.D. Taylor G., Wintersgill M.C., A model for the activation Energies observed in TL of TLD 100, *Rad. Effects*, 41 (1979) 11–16.

Magnetic phase transitions due to compositional variation across amorphous thin-films

Mustafa TOKAÇ^{1,*} 

¹Alanya Alaaddin Keykubat University, Faculty of Engineering, Department of Fundamental Sciences, Antalya/TURKEY

Abstract

The structural and magnetic properties of amorphous thin-films with various CoFeTaB thicknesses were studied to observe magnetic phase transitions due to compositional variation through the CoFeTaB layer. The investigations of the structural properties of amorphous CoFeTaB thin-films were undertaken to confirm layer thickness, interface roughness, and their amorphous structure. Temperature dependent magnetic characterizations were performed to extract Curie temperatures of each thin-film structure, where there is evidence of more than one magnetic transition point. These transition points indicate magnetic phase transitions, which may be attributed to compositional variations across the amorphous CoFeTaB thin-films. Investigation of diffusion process in ferromagnetic thin-films is crucial for the development of spintronic applications.

Article info

History:

Received:19.05.2021

Accepted:03.07.2021

Keywords:

Fe-based amorphous alloys,
Magnetic properties,
Ferromagnetic thin-films,
Magnetic phase transitions.

1. Introduction

High-moment ferromagnetic CoFe alloys show excellent soft magnetic properties, including high saturation magnetization, high spin polarization, and low coercivity, and they have been considered to have considerable potential for use in many technological applications in the fields of spintronics [1–3]. CoFe alloy has a BCC crystal structure with a cubic magnetocrystalline anisotropy. The addition of B of composition greater than 20% in the CoFe alloy produces an amorphous metallic glass with a reduced Curie temperature (T_C) and reduced magnetization compared to CoFe alloy [4]. Amorphous ferromagnetic alloys represent an important class of materials, which have a unique disorder atomic arrangements and zero magnetocrystalline anisotropy energy, which makes amorphous metallic alloys functional for a broad range of applications. Amorphous CoFeB thin-films have been attracted extensive attention in recent years in giant and tunnelling magnetoresistance devices [5,6], current-induced magnetization switching [7], and are utilized in commercial applications such as HDD read-heads and magnetic random access memories. The amorphous CoFeB alloys have high spin polarization, which could lead to a high TMR value at room temperature [5,6]. The addition of a transition metal to an amorphous Fe-based alloy, reduces both the T_C and the magnetic moment per Co and Fe atoms [8], where

this reduction can be explained as a result of charge transfers from the transition metal atoms to the unfilled holes in the electronic d-states of the Fe.

The discovery of the perpendicularly magnetized Ta/CoFeB/MgO heterostructures, which exhibit perpendicular magnetic anisotropy (PMA) is attracting significant interest for potential applications in magnetic random access memory (MRAM) [6]. The underlayer to the CoFeB layer also plays a crucial role in the size of PMA, where Ta is widely used as an underlayer because the Ta/CoFeB interface can control the perpendicular magnetic anisotropy and the related magnetic responses [9]. Diffusion of Fe atoms towards oxide layer has been reported in CoFeB/MgO structures during the deposition of MgO, where a Fe-O rich interfacial region was formed with reduced magnetization [10]. Another study showed that T_C can be tuned from 200 K to below 100 K by increasing Ta composition from ~ 15% to ~30% in FeTa amorphous alloy [8]. In order to identify the influence of the Ta diffusion in the magnetic properties of the ferromagnetic layer, the relationship between the structural and magnetic properties of this structure needs to be clarified. The influence of the diffusion of Ta in the Ta/CoFeB/MgO system has often been discussed [11–13], however, there is no sufficient information that clearly shows the relationship between the Ta diffusion and the magnetic properties of a ferromagnetic layer at low temperatures.

*Corresponding author. e-mail address: mustafa.tokac@alanya.edu.tr.

<http://dergipark.gov.tr/csj> ©2021 Faculty of Science, Sivas Cumhuriyet University

Previously, Ta diffusion within the CoFeTaB layer has been observed during the thin-film deposition, which causes variation of magnetization and T_C through the thin-film [14]. As many spintronic devices work at elevated temperatures, understanding the Ta diffusion on the magnetic properties of CoFeTaB thin-film is important for the development of spintronic applications. The amorphous CoFeTaB alloy used in this study was designed to have a T_C below room temperature in order to observe the influence of Ta diffusion on the magnetic properties at low temperatures. In this manuscript, the structural and magnetic properties of the bilayered amorphous thin-film with various CoFeTaB thicknesses were studied to indicate magnetic phase transitions due to Ta diffusions at low temperatures because diffusion of Ta produces regions of different composition through the CoFeTaB layer, which causes variation of magnetization and T_C through thin-films.

2. Experimental Procedures

In this study, a series of amorphous ferromagnetic thin-films ($\text{Co}_{30}\text{Fe}_{30}\text{Ta}_{25}\text{B}_{15}$ – The subscript represents the nominal composition of CoFeTaB) with a thickness from 10 Å to 40 Å were deposited at room temperature onto Si (100) substrate using dc magnetron sputtering under ultra-high vacuum. The structure of the layer stacks was Si/SiO₂/CoFeTaB (t)/Ta(30 Å)/Ta₂O₅ with a CoFeTaB layer thickness ranging from 10 to 40 Å, as shown schematically inset of Figure 1a. The $\text{Co}_{30}\text{Fe}_{30}\text{Ta}_{25}\text{B}_{15}$ layers (CoFeTaB hereafter) were capped with a 30 Å Ta layer to prevent oxidation. Grazing incidence x-ray reflectivity (XRR) was performed using a Rigaku Smartlab laboratory reflectometer at room temperature in order to characterize the physical structure of each thin-film. X-ray reflectivity scans were performed by scanning $\theta - 2\theta$ from 0° to 6° with a step size of 0.02°. All reflectivity measurements were fitted using the GenX simulation code [15], which utilizes the Parratt recursive formalism for simulating specular reflectivity. It uses a model based on the sample structure including free structural parameters to determine the layer thickness and interface/surface roughness and densities of each layer. In order to validate the amorphous nature of the CoFeTaB films, x-ray diffraction (XRD) profiles were obtained. Magnetic characterization of amorphous CoFeTaB

thin-films was performed using a Quantum Design superconducting quantum interference device (SQUID) magnetometry in a temperature range between 5 K to 300 K with an external magnetic field of 100 Oe to extract T_C for each thin-films.

3. Results and Discussion

3.1. Structural characterization of thin-films

Measured grazing incidence XRR data and corresponding best fit simulations for 40 Å CoFeTaB thin-film are presented in Figure 1a. Here, the red solid line represents simulated fits of specular reflectivity data. Reflectivity simulations were performed by starting with nominal thicknesses of each layer of the as-deposited thin-films and adding a thin Ta₂O₅ layer to model oxide formation on the Ta cap, with a thickness up to a few nanometers. To improve the fitting quality of the XRR data, a thermally oxidized SiO₂ layer on top of the Si (100) substrate was added. The structural parameters including layer thicknesses, interface roughnesses, and layer densities were obtained from the best-fitting simulations of amorphous thin-films as a function of CoFeTaB thicknesses. Sample parameters from best fit XRR including layer thickness and interface roughness used in the simulation of specular reflectivity of amorphous thin-films with various CoFeTaB thickness are summarized in Table 1. It is well-known that surface/interface roughness affects the magnetic properties of thin-film structures, such as domain structure, and magnetic anisotropy [16], where it has been shown that an increase in interface roughness increases the exchange bias field and the coercivity [17]. The roughness parameters for each structure are around 3 Å, indicating thin-films are continuous in the direction normal to the scattering plane.

The structural characterization of thin-films was undertaken using an x-ray diffraction (XRD) pattern to derive information on the nature of the crystal structure. Figure 1b presents the XRD patterns of all thin-films with various CoFeTaB thicknesses studied here. As shown in the figure, all thin-films revealed an XRD peak at 2θ of 69° corresponding to the (400) diffraction peak of the Si (100) substrate. The Bragg peaks corresponding to all CoFeTaB thin-films are not observed in these patterns which confirm the amorphous nature of CoFeTaB layers.

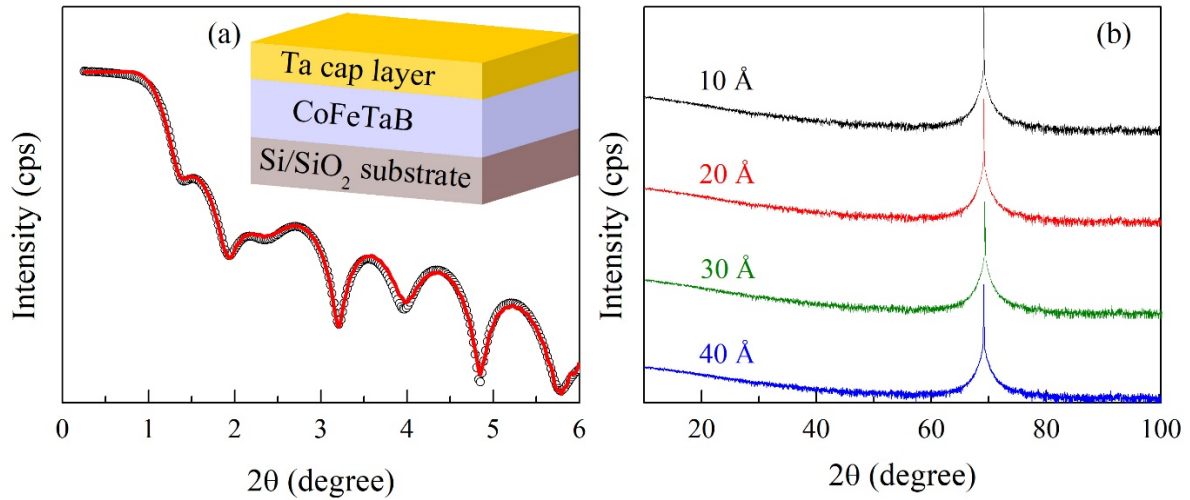


Figure 1: (a) Specular reflectivity data and corresponding simulated reflectivity for amorphous 40 Å CoFeTaB thin-film. The red solid line represents best-fit simulations. The inset shows the sample schematic. (b) X-ray diffraction pattern of the amorphous thin-films with various CoFeTaB thicknesses.

The structural scattering length density (SLD) profiles and their derivatives for all structures are given in Figure 2 for thin-films with various CoFeTaB thicknesses, as shown by shaded regions. Here, the width of the substrate/CoFeTaB interface appears relatively broad for all thin-films. This broad interface is attributed to the diffuse interface between the Si (100) substrate and the thin SiO₂ layer. Within the volume of the CoFeTaB films, the structural SLDs are roughly constant, which indicates the ferromagnetic CoFeTaB layers are uniform layers. However, the structural SLD profiles are varied from the bulk values in the interface of the CoFeTaB/Ta capping layer, which suggests that compositionally-graded layers are

formed in the region of CoFeTaB layers and the Ta capping layers. During the deposition of thin-films, the interdiffusion of Ta atoms into CoFeTaB layers is possible because highly energetic Ta atoms can penetrate into the CoFeTaB layer, resulting in a broad CoFeTaB/Ta structural interface. Interdiffusion of atoms has studied at CoFeB/Ta and CoFeB/Ru interfaces, where Ta atoms can penetrate more deeply into the CoFeB layer because Ta is heavier than Ru [18]. A similar study has shown that a 0.2 nm thick TaB layer is formed at CoFeB/Ta interface after annealing of CoFeB/Ta thin-films, which is due to out-diffusion of B atoms from the CoFeB layer to the Ta capping layer [19].

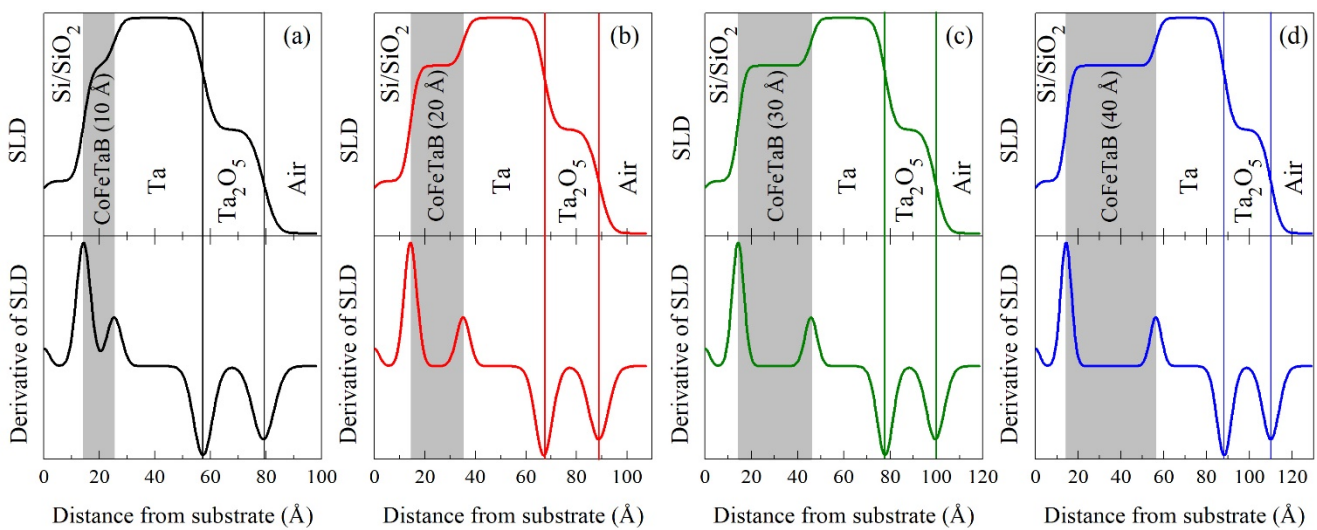


Figure 2: Structural scattering length density profiles and their derivatives for amorphous thin-films. The shaded regions show with various CoFeTaB layer thicknesses ranging from 10 to 40 Å. The vertical dashed lines correspond to the positions of the layer interfaces in the model structures.

The derivatives of the structural SLD profiles are plotted in Figure 2 to visualize positions of the structural interfaces more accurately in these structures with various CoFeTaB thicknesses. Here, the peaks and dips show each layer interfaces in the model structures, shown by vertical solid lines. In the derivative of SLDs, the first peaks correspond to the thickness of $\sim 15 \text{ \AA}$ for both structures which indicates the thickness of the SiO₂ layer, and beyond this thickness, the magnetic CoFeTaB layer starts to increase. The second peaks, indicating CoFeTaB/Ta interface, shift to the right as the thickness of the CoFeTaB layer increases. The shaded regions indicate the approximate thickness of CoFeTaB layers and the vertical solid lines correspond to the approximate positions of the layer interfaces in the model structures.

3.2. Magnetic characterization of thin-films

The main purpose of the present study is the investigation of the magnetic phase transitions for thin-films with various CoFeTaB thicknesses, as given in Figure 3. Here, the magnetic response of thin-films shows that the CoFeTaB layers do not act as a single homogeneous magnetic layer with a single T_C , as usual. Instead, the ferromagnetic layers comprise two or three magnetic sub-layers depending on layer thicknesses. These inhomogeneities are related to the Ta distribution within the CoFeTaB layer, as it varies the T_C , resulting in the asymmetry in magnetic properties at the CoFeTaB/Ta interface, and indicating the contribution of the different moments at the CoFeTaB/Ta interface and within the CoFeTaB layer. At low temperatures, the temperature dependent magnetization in a ferromagnetic material can be fitted using the spin-wave model and described by the Bloch $T^{3/2}$ power-law equation given as,

$$M(T) = M(0) \left[1 - \left(\frac{T}{T_C} \right)^{3/2} \right] \quad (1)$$

where $M(0)$ is the spontaneous magnetization at absolute zero. The spontaneous magnetization approaches zero when the temperature increases towards the T_C and phase transition from paramagnetic to ferromagnetic state is observed, which is identified as a point of abrupt change in magnetic behaviour. In order to understand the magnetic phase transitions due

to Ta diffusion within the CoFeTaB layer, there is evidence of more than one transition point, notated as T_C 's in the magnetic behavior of thin-films. Therefore, it is quite difficult to obtain T_C values from temperature dependent magnetization profiles using Equation (1).

The derivative of temperature dependent magnetization curves for all thin-film structures with various CoFeTaB thicknesses are calculated. The curves, where the derivative of magnetization reaches a minimum value, indicate more than one transition point in the magnetic response, as noted T_C 's for all thin-film structures. Two phase transitions are observed, indicating two different magnetic regions, denoted as T_{C1} and T_{C2} , across the thin-film with 10 \AA CoFeTaB thickness. For the rest of the thin-films, there are three transition temperatures, denoted as T_{C1} , T_{C2} , and T_{C3} , indicating three active magnetic regions. These transition points show magnetic phase transitions, which may be attributed to compositional variations across the CoFeTaB thin-films. These variations suggest non-uniformity in the magnetic profile due to the Ta distribution in the CoFeTaB layer, causing variations in the T_C 's.

Figure 3a shows temperature-dependent magnetization and its derivative for the thin-film with 10 \AA CoFeTaB thickness. The derivative of magnetization shows two sharp curves, which indicate magnetic phase transitions at temperatures as shown by T_{C1} and T_{C2} , where these transitions are at $\sim 220 \text{ K}$ and $\sim 50 \text{ K}$, respectively. The thinnest CoFeTaB film might have adopted the Volmer-Weber growth mode on SiO₂, where the vaporized atoms bond to each other more strongly than to the substrate surface. This strong bonding leads to the formation of islands that join to form continuous thin-film structures. The coverage of the CoFeTaB layer at 10 \AA may not be 100%, hence the Ta capping layer grown on top of CoFeTaB will have a lesser CoFeTaB neighbor. As a result of this low CoFeTaB thickness, Ta atoms may be in direct contact with the substrate surface, which may create compositional variations in the magnetic response of the CoFeTaB layer. This results in two magnetic phase transitions, where T_{C1} is the first transition temperature at 220 K , attributed to the magnetic region adjacent to the

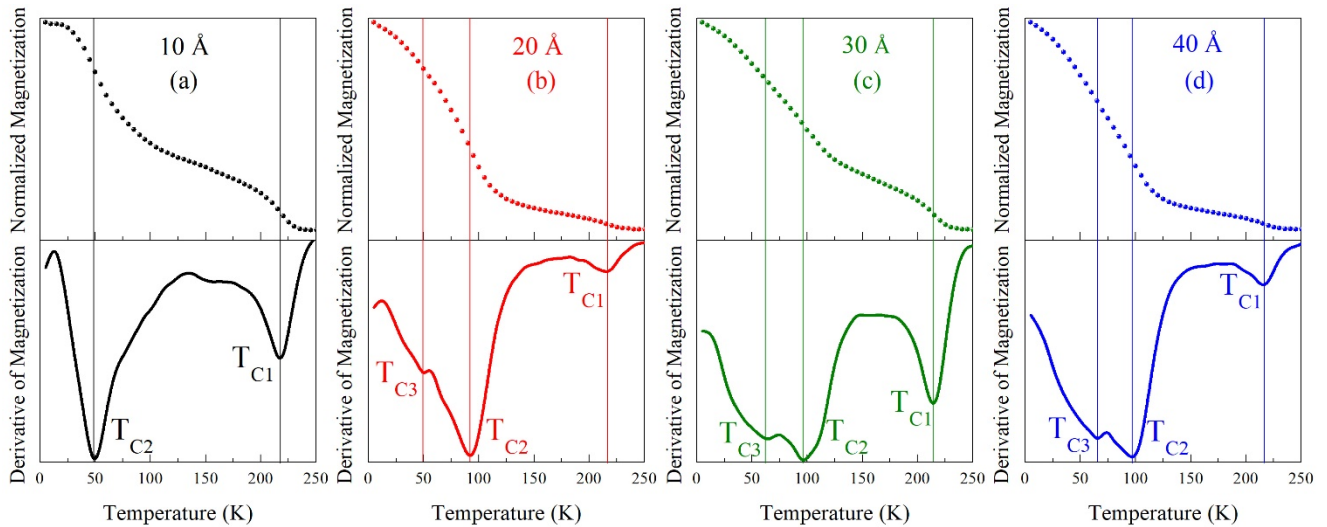


Figure 3: Temperature dependence of magnetization curves and their derivatives for amorphous thin-films with various CoFeTaB thicknesses measured under the magnetic field of 100 Oe.

buffer interface with less Ta concentration, and T_{C2} is the second transition temperature at 50 K, attributed to the magnetic region adjacent to the top interface with the maximum Ta concentration, the least magnetic moment and the lowest T_{C2} .

An increase in the thickness of the CoFeTaB layer leads to a better surface coverage due to the coalescence of grains, causing multiple phase transitions across CoFeTaB layers. As the thickness of the CoFeTaB layer increases to 20 Å, as shown in Figure 3b, the magnetization appears relatively broad at temperatures between 125 K to 225 K, and a magnetic phase transition is observed at $T_{C1} \sim 220$ K. This is attributed to the transition temperature of the sublayer with less Ta concentration, corresponding to a magnetic region adjacent to the buffer interface. A second transition point is observed more clear, as shown by the sharp curve on the derivative of magnetization at $T_{C2} \sim 90$ K. The T_{C2} may be the transition temperature of the magnetic thin-slab at the center of the CoFeTaB layer because heavy Ta atoms can penetrate within the center of the CoFeTaB layer during the deposition of the Ta capping layer. Also, a third transition point, which is not clear as others, emerges slightly indicated by $T_{C3} \sim 50$ K, which may be the transition temperature of a magnetic region adjacent to the top interface, with the lowest transition temperature and the highest Ta concentration.

Similar transition temperatures are obtained as $T_{C1} \sim 220$ K, $T_{C2} \sim 95$ K, and $T_{C3} \sim 65$ K for the rest of the

thin-films, as given in Figure 3c and 3d. Here, T_{C1} has the same transition temperature as for the films with 10 Å and 20 Å CoFeTaB thicknesses. This is attributed to the transition temperature of the magnetic region close to the bottom interface with less Ta concentration. The second transition temperature $T_{C2} \sim 95$ K, corresponds to the magnetic thin-slab at the center of the CoFeTaB layer with the higher Ta concentration compared to the magnetic region at the buffer interface. $T_{C3} \sim 65$ K, is the third transition temperature of the magnetic slab adjacent to the Ta capping layer, where the maximum Ta concentration at this thin-slab causes the reduction of T_C . All transition temperatures of each thin-film structures are summarized in Table 1.

10 nm thick CoFeTaB thin-film with 30% Ta concentration, sandwiched with 3 nm thick Pt layers was studied to understand the temperature dependent interfacial magnetization, where diffusion of Ta creates magnetic regions of different composition and resulting in three different transition temperatures. These transition temperatures were obtained as $T_{C1} \sim 215$ K, $T_{C2} \sim 120$ K, and $T_{C3} \sim 80$ K, where T_{C1} and T_{C2} correspond to the transition temperature of the region adjacent to the bottom/top interfaces, respectively. $T_{C3} \sim 80$ K indicates the transition point of the center of the CoFeTaB layer with the highest Ta concentration and least magnetic moment, which is attributed to the the transition temperature from paramagnetic to ferromagnetic state [20]. As it is known

Table 1: Sample parameters from best fit XRR including layer thickness and interface roughness used in the simulation of specular reflectivity of amorphous CoFeTaB thin-films, and transition temperatures, obtained from the minimum value of the derivative of magnetization.

Sample	Layer	Thickness (Å)	Roughness (Å)	Transition Temperatures (K)		
				T _{C1}	T _{C2}	T _{C3}
CoFeTaB (10 Å)	CoFeTaB	10.5 ± 0.8	2.4 ± 1.2	220	50	---
	Ta	31.5 ± 3.3	3.3 ± 1.3			
CoFeTaB (20 Å)	CoFeTaB	21.1 ± 1.4	2.1 ± 1.2	220	90	50
	Ta	32.3 ± 1.8	3.4 ± 1.7			
CoFeTaB (30 Å)	CoFeTaB	30.9 ± 1.6	2.3 ± 1.5	220	95	65
	Ta	31.8 ± 2.5	3.1 ± 1.8			
CoFeTaB (40 Å)	CoFeTaB	41.2 ± 2.3	2.4 ± 1.2	220	95	65
	Ta	30.9 ± 2.5	2.6 ± 1.5			

that higher Ta concentration decreases the T_C and the magnetic moment per Co and Fe atoms [8], it is also possible to comment about the location of transition temperatures for each magnetic region in this study. In the present work, similar behaviour of magnetic transition temperatures is obtained for CoFeTaB/Ta bilayered thin-films. Due to the compositional variation of Ta (30%) through the ferromagnetic layer, the T_C was estimated as ~ 80 K [20], which is 15 K lower than the T_C of 30 Å and 40 Å thick CoFeTaB thin-films studied here. The transition temperature of T_{C1} is obtained as ~ 220 K for all thin – film structures, which indicates the initial stage of the deposition for all thin-films show similar behaviour and resulting in the magnetic thin-slab adjacent to the buffer interface. These phase transitions confirm the expected compositional variations within the CoFeTaB layers.

4. Conclusion

In summary, the magnetic phase transitions due to compositional variation of the Ta capping layer were studied for amorphous thin-films with various CoFeTaB thicknesses. An investigation of the structural properties of amorphous thin-films was undertaken to confirm layer thickness, interface roughness, and the amorphous structure of thin-films. Temperature dependent magnetic characterizations were performed to extract Curie temperatures of each thin-film, where the CoFeTaB layer does not act as a homogenous magnetic layer with a single T_C. Instead, the data suggest more than one magnetic transition point, which indicates multiple magnetic phase transitions. These transitions may be attributed to

compositional variations through the amorphous CoFeTaB layer thickness.

Acknowledgement

The author acknowledges Dr. A. T. Hindmarch and Dr. C. J. Kinane for their assistance with film preparation and experimental work.

Conflicts of interest

The author states that there is no conflict of interests

References

- [1] Cooper E. I., Bonhote C., Heidmann J., Hsu Y., Kern P., Lam J. W., Ramasubramanian M., Robertson N., Romankiw L. T., Xu H., Recent developments in high-moment electroplated materials for recording heads, *IBM Journal of Research and Development*, 49 (1) (2005) 103-126.
- [2] Chen A. P., Burton J. D., Tsymbal E. Y., Feng Y. P., Chen J., Effects of B and C doping on tunneling magnetoresistance in CoFe/MgO magnetic tunnel junctions, *Physical Review B*, 98 (4) (2018) 045129.
- [3] Parkin S. S., Kaiser C., Panchula A., Rice P. M., Hughes B., Samant M., Yang S. H., Giant tunnelling magnetoresistance at room temperature

- with MgO (100) tunnel barriers, *Nature Materials*, 3 (12) (2004) 862-867.
- [4] Platt C. L., Minor N. K., Klemmer T. J., Magnetic and structural properties of FeCoB thin films, *IEEE Transactions on Magnetics*, 37 (4) (2001) 2302-2304.
- [5] Djayaprawira D. D., Tsunekawa K., Nagai M., Maehara H., Yamagata S., Watanabe N., Yuasa S., Suzuki Y., Ando K., 230% room-temperature magnetoresistance in CoFeB/MgO/CoFeB magnetic tunnel junctions, *Applied Physics Letters*, 86 (9) (2005) 092502.
- [6] Ikeda S., Miura K., Yamamoto H., Mizunuma K., Gan H. D., Endo M., Kanai S., Hayakawa J., Matsukura F., Ohno H., A perpendicular-anisotropy CoFeB-MgO magnetic tunnel junction, *Nature Materials*, 9 (9) (2010) 721-724.
- [7] Kubota H., Fukushima A., Yakushiji K., Nagahama T., Yuasa S., Ando K., Maehara H., Nagamine Y., Tsunekawa K., Djayaprawira D. D., Watanabe N., Suzuki Y., Quantitative measurement of voltage dependence of spin-transfer torque in MgO-based magnetic tunnel junctions, *Nature Physics*, 4 (1) (2008) 37-41.
- [8] Fukamichi K., Gambino R. J., The Curie temperature and magnetization of Fe-base amorphous binary alloys containing transition metal, *IEEE Transactions on Magnetics*, 17 (6) (1981) 3059-3061.
- [9] Cheng C.-W., Feng W., Chern G., Lee C. M., Wu T.-H., Effect of cap layer thickness on the perpendicular magnetic anisotropy in top MgO/CoFeB/Ta structures, *Journal of Applied Physics*, 110 (3) (2011) 033916.
- [10] Hindmarch A. T., Dempsey K. J., Ciudad D., Negusse E., Arena D. A., Marrows C. H., Fe diffusion, oxidation, and reduction at the CoFeB/MgO interface studied by soft x-ray absorption spectroscopy and magnetic circular dichroism, *Applied Physics Letters*, 96 (9) (2010) 092501.
- [11] Ikeda S., Hayakawa J., Ashizawa Y., Lee Y. M., Miura K., Hasegawa H., Tsunoda M., Matsukura F., Ohno H., Tunnel magnetoresistance of 604% at 300 K by suppression of Ta diffusion in CoFeB/MgO/CoFeB pseudo-spin-valves annealed at high temperature, *Applied Physics Letters*, 93 (8) (2008) 082508.
- [12] Wang W. X., Yang Y., Naganuma H., Ando Y., Yu R. C., Han X. F., The perpendicular anisotropy of Co₄₀Fe₄₀B₂₀ sandwiched between Ta and MgO layers and its application in CoFeB/MgO/CoFeB tunnel junction, *Applied Physics Letters*, 99 (1) (2011) 012502.
- [13] Worledge D. C., Hu G., Abraham D. W., Sun J. Z., Trouilloud P. L., Nowak J., Brown S., Gaidis M. C., O'Sullivan E. J., Robertazzi R. P., Spin torque switching of perpendicular Ta|CoFeB|MgO-based magnetic tunnel junctions, *Applied Physics Letters*, 98 (2) (2011) 022501.
- [14] Tokaç M., Kinane C. J., Atkinson D., Hindmarch A. T., Temperature dependence of magnetically dead layers in ferromagnetic thin-films, *AIP Advances*, 7 (11) (2017) 115022.
- [15] Björck M., Andersson G., GenX: an extensible X-ray reflectivity refinement program utilizing differential evolution, *J. Appl. Crystallogr.*, 40 (6) (2007) 1174-1178.
- [16] Zhang S., Levy P. M., Enhanced spin-dependent scattering at interfaces, *Physical Review Letters*, 77 (5) (1996) 916.
- [17] Fleischmann C., Almeida F., Demeter J., Paredis K., Teichert A., Steitz R., Brems S., Opperdoes B., Van Haesendonck C., Vantomme A., Temst K., The influence of interface roughness on the magnetic properties of exchange biased CoO/Fe thin films, *Journal of Applied Physics*, 107 (11) (2010) 113907.
- [18] Jang S. Y., Lim S. H., Lee S. R., Magnetic dead layer in amorphous CoFeB layers with various top and bottom structures, *Journal of Applied Physics*, 107 (9) (2010) 09C707.
- [19] Greer A. A., Gray A. X., Kanai S., Kaiser A. M., Ueda S., Yamashita Y., Bordel C., Palsson G., Maejima N., Yang S.-H., Conti G., Kobayashi K., Ikeda S., Matsukura F., Ohno H., Schneider C. M., Kortright J. B., Hellman F., Fadley C. S., Observation of boron diffusion in an annealed Ta/CoFeB/MgO magnetic tunnel junction with standing-wave hard x-ray photoemission, *Applied Physics Letters*, 101 (20) (2012) 202402.
- [20] Inyang O., Bouchenoire L., Nicholson B., Tokaç M., Rowan-Robinson R. M., Kinane C. J., Hindmarch A. T., Threshold interface magnetization required to induce magnetic proximity effect, *Physical Review B*, 100 (17) (2019) 174418.



e-ISSN: 2587-246X
ISSN: 2587-2680

Cumhuriyet Science Journal

Cumhuriyet Sci. J., 42(3) (2021) 722-727
<http://dx.doi.org/10.17776/csj.677410>



Projections for dual radioisotope applications in PET imaging

Yusuf ŞENGELEN¹ , Sinan KUDAY^{2,*}

¹Karabük Istanbul Aydın University, Health Science Institute, Medical Physics, 34295, Istanbul/TURKEY

²Ankara University, Physics Department, Tandoğan 06580, Ankara,/TURKEY

Abstract

Positron emission tomography (PET) are widely accepted and used as an effective medical imaging method. We have studied on the dual radioisotopes C11 and Cu60 together by modifying the isotopes used in Standard cylindrical PET through GATE imaging simulation. We scan the proper resolution intervals and the distances between the sources and present the differences in parameters such as full width at half maximum (FWHM), intensity and contrast. Applying statistical χ^2 method, we aim to show the significance limits of above parameteric differences in PET simulations. These results may help determine in which conditions the imaging devices can be used with dual isotope method in clinical applications.

Article info

History:

Received: 20.01.2020

Accepted: 06.07.2021

Keywords:

GATE, Geant4,
Simulations, PET,
Medical

1. Introduction

Molecular imaging technology used in nuclear medicine includes specific imaging methods such as optical imaging and scintigraphy. The main devices of scintigraphy are positron emission tomography (PET) and single photon emission computed tomography (SPECT). These imaging methods use images generated by radiation emitted in the body as a result of the application of radiopharmaceuticals to patients. This image provides useful information not only for diagnostic purposes such as detection of functional abnormalities or early imaging of tumors, but also for treatment planning and follow-up. Nuclear imaging is a diagnostic medical imaging method that uses radionuclides to study the physiology and metabolism of the body [1].

In parallel with the developing new techniques, the number of publications in the literature has been increasing recently in the field of medical imaging. The use of dual radioisotope, that is one of these techniques, is considered to be effective in imaging of complicated tumor structures and nested tissues in the field of SPECT as well as in PET imaging [2]. Myocardial perfusion and brain imaging have been reported to be highly conclusive if this technique is successfully implemented [3].

The dual isotope (DI) technique is based on the detection and visualization of two different gamma-

emitting radionuclides at one time, which are injected into the patient, via the different energy decay windows. Especially for the PET device, the fact that positron-electron annihilations occur at 511 KeV energy for each time does not create an energy difference and requires extra gamma radiation to be used by the radioisotope. Thus, the selection of dual radioisotopes and measuring triple coincidence of gammas in PET imaging becomes utmost important. Not that, dual and multi tracer techniques mostly offer similar solutions but different timings and algorithms. [4,5,6]

The outline of the paper as following: we explain the simulation setup and GATE software in the next section, the statistical methods and calculations of parameters that will shed on light of a feasible DI technique will be mentioned in section III, we give analysis results and additional comments in section IV and conclude our study in the section V.

2. PET Simulation Setup With GATEv.8

GATEv.8 is an advanced opensource software developed by the international OpenGATE collaboration and dedicated to numerical simulations in medical imaging and radiotherapy. Using an easy-to-learn macro mechanism to configurate simple or highly sophisticated experimental settings, GATE v.8 now plays a key role in the design of new medical imaging devices, in the optimization of acquisition

*Corresponding author. e-mail address: kuday@cern.ch

protocols and in the development and assessment of image reconstruction algorithms and correction techniques. It can also be used for dose calculation in radiotherapy experiments [7].

A cylindrical PET system that is a benchmark in GATEv.8 and composed of 4 rsectors (head), 64 cubic crystals (8 x 8) and 2 scintillation layers of BSO for inner and LSO for outer is implemented. Boxed world geometry with 0.4x0.4x0.4 m and water phantom with 20x20x20 cm is created. No CT system is added but the coincidences from standart read-outs are collected with rotating heads 30 deg/s for every 4 seconds (Total: 16 seconds). Most importantly two sources (C11 and Cu60) are implemented with their ion structures, half-lives, activities and decay energies at different placements. We have chosen those sources since they are commonly used radioisotopes in PET imaging and known as gamma emitters in addition to positron emissions. Figure 1 shows the visualization of the system before the irradiation step. For digitization of the data, with 10 ns. Coincidence window, 350 – 650 KeV threshold and upholder are used respectively. Not any of the PET systems has been referenced throughout the study. It is aimed to present the detectability parameters of the different radioisotopes. Standart physical interactions are implemented as Photoelectric, Compton, Rayleigh, Bremstrahlung scatterings and radioactive decays and positron annihilations are enabled.

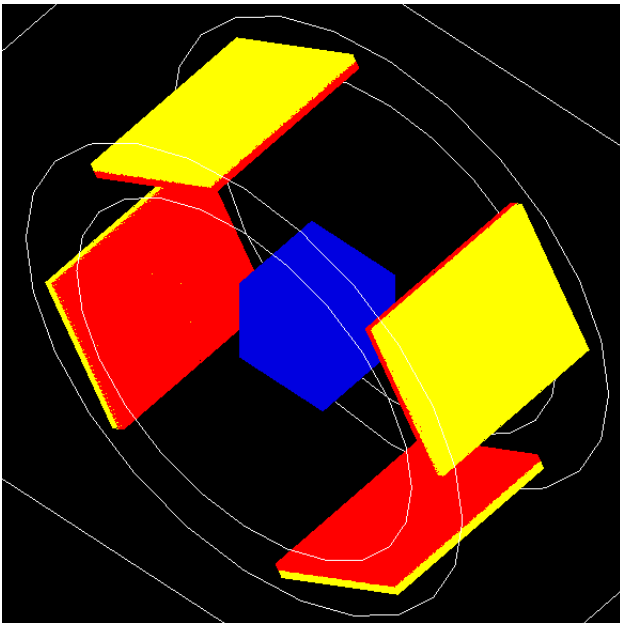


Figure 1. PET system design consisting of rotating BSO and LSO layers (red and yellow) and cubic water phantom (blue).

3. Material and Methods

In simulation, we scanned over different placements taking an interval between two sources starting from 0.4 cm to 4 cm. For each placements, we obtained two kind of outputs: Detector hits and coincidences (after digitization) with the histograms containing time lapse, energy, spatial distributions of gammas...etc. We also acquired data for blurred image resolutions 0.1, 0.26, 0.75 and 1 in digitization process respectively. All datas are analysed with a simple macro using ROOT [8].

In analysis step, we assume that the spatial distributions of sources are gauss curves with mean, standard deviations (σ) and total entries (hits). Thus, one can calculate that $FWHM = (2.35 \times \sigma)$ and take into account the Rayleigh criterion that says two point-like objects can be distinguished if the FWHM resolution of the optics is 0.82 times the distance of their images. As an example, two sources with 1 cm distance can be distinguished if the signal FWHM is no more than 0.82 cm. One can take this ratio for calculation optimal spatial resolution. Moreover an intensive analysis over σ distributions, as we present in this work, can give opportunity calculate optimal spatial resolutions with above mentioned blurring resolution set of PET device.

We also present contrast rates as a difference between two intensities as the following:

$$C = \frac{I_1 - I_2}{I_1 + I_2} \quad (1)$$

where the intensities I_1 for first source C11 and I_2 for the second source Cu60 can be calculated as follows;

$$I(r) = I_0 \exp\left(\frac{-2r^2}{w^2}\right) = \frac{2P}{\pi w^2} \exp\left(\frac{-2r^2}{w^2}\right) \quad (2)$$

where r is the spatial resolution, and w is the width taken as $(0.849 \times FWHM)$ in accordance with Rayleigh criterion. Moreover, as another feature of a PET device, we calculated digitization rate of the signal as digitized signal entries over detector entries. Lastly, we applied chi-square method to determine if FWHM differences in PET data is significant.

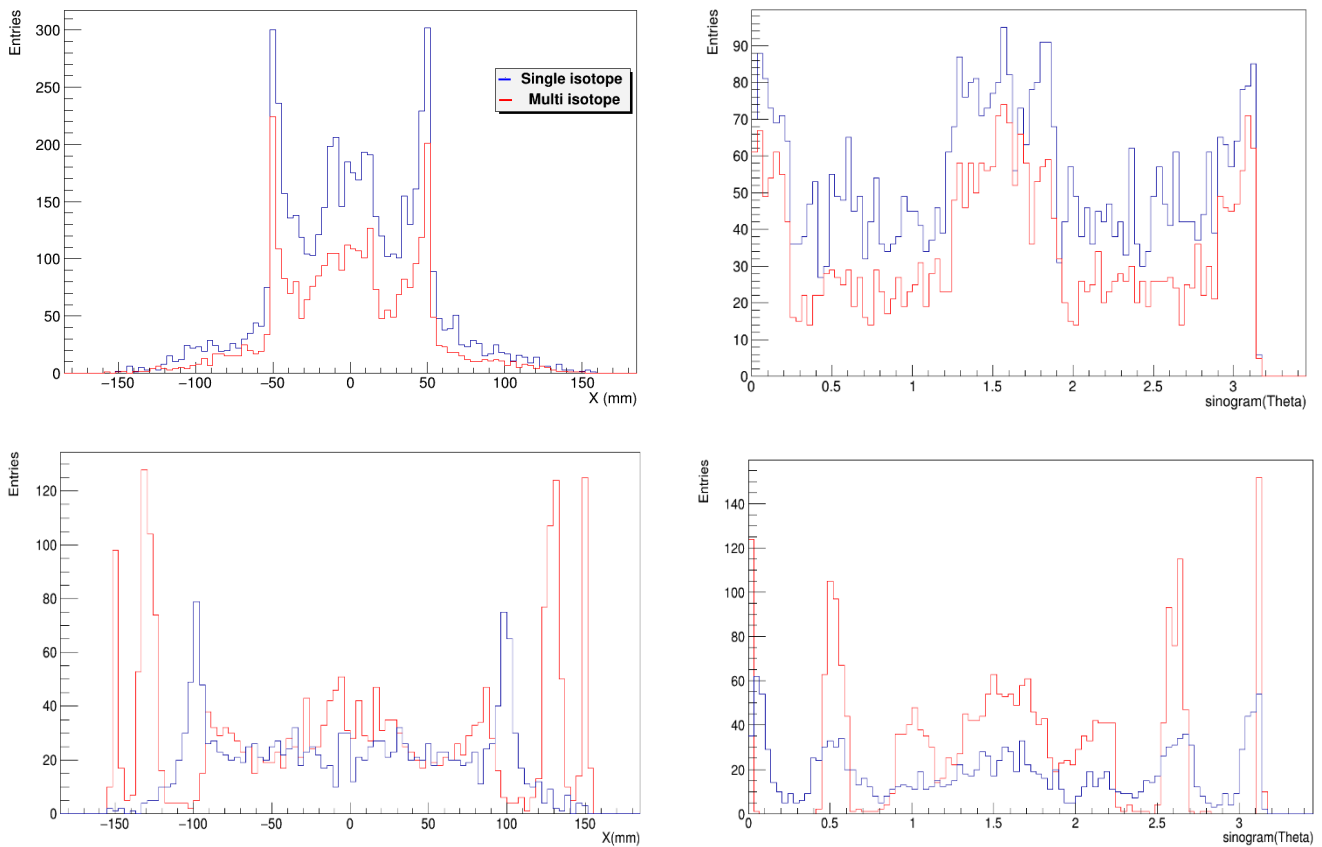


Figure 2. Sinograms for X axis (left) and scattering angle θ (right) in radians. Point-like C^{11} is implemented for single isotope (blue) at +50 and -50 mm distances (top row) and +100 and -100 mm distance (below row). Dual isotope histograms (red) for C^{11} and Cu^{60} are plotted in stacks with same distances.

4. Comparison and Analysis

A first observation from the comparison of sinograms that at small distances between dual sources (e.g.: 2 mm), annihilation of electron-positron pairs are dominant but at longer distances than 50 mm (in our setup) one can expect more entries individually from dual-pairs as seen in Fig. 2. The same situation is good for energy plots as seen in Fig. 3. This also indicates that one can get a stronger overall signal using of dual isotopes regardless of the distances. However, one can realise the huge data acquisition differences between detector hits and coincidences in Fig 4. Roughly, 1.5% of total data has been labelling as coincidence while the remaining data has not been processing at all.

An observation from the energy perspective shows that while two resources emits energies at 511 KeV and 1330 KeV, annihilation processes occurs with only energetic electrons at proper range. We have chosen semi free energy window between 510 – 1400 KeV to work on near signal strenghts. One can get higher amount of data by setting another energy references for additional isotopes. Surely, that corresponds to a modification on the detectors of PET device.

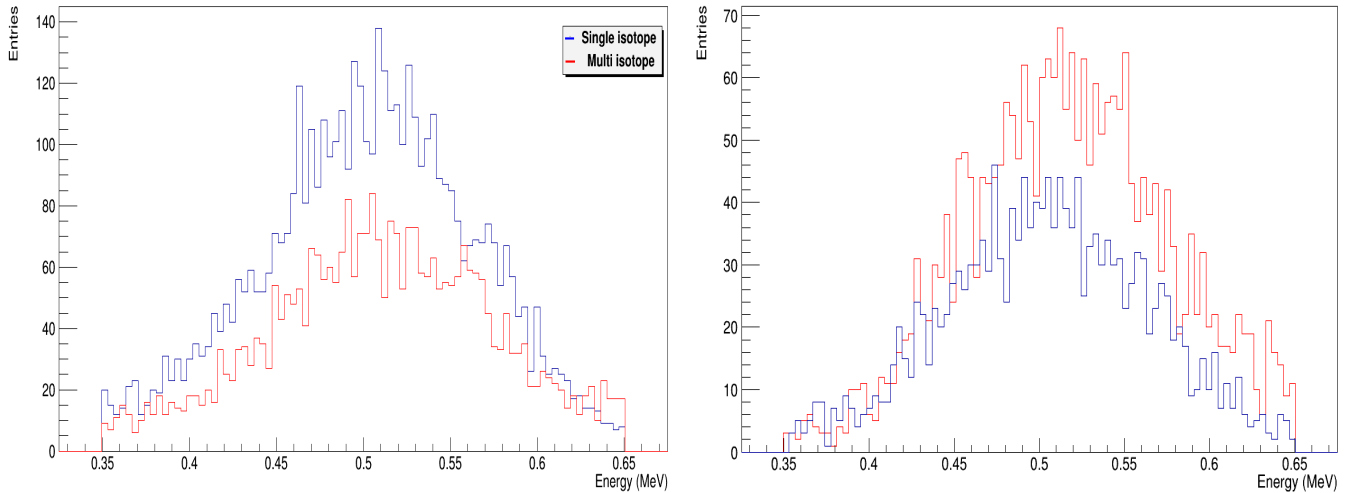


Figure 3. Total detected energy distributions in coincidences for +50 and -50 mm distances (left) and +100 and -100 mm distance (right). C^{11} has been placed for single isotope (blue), C^{11} and Cu^{60} together placed for dual isotope (red) measures.

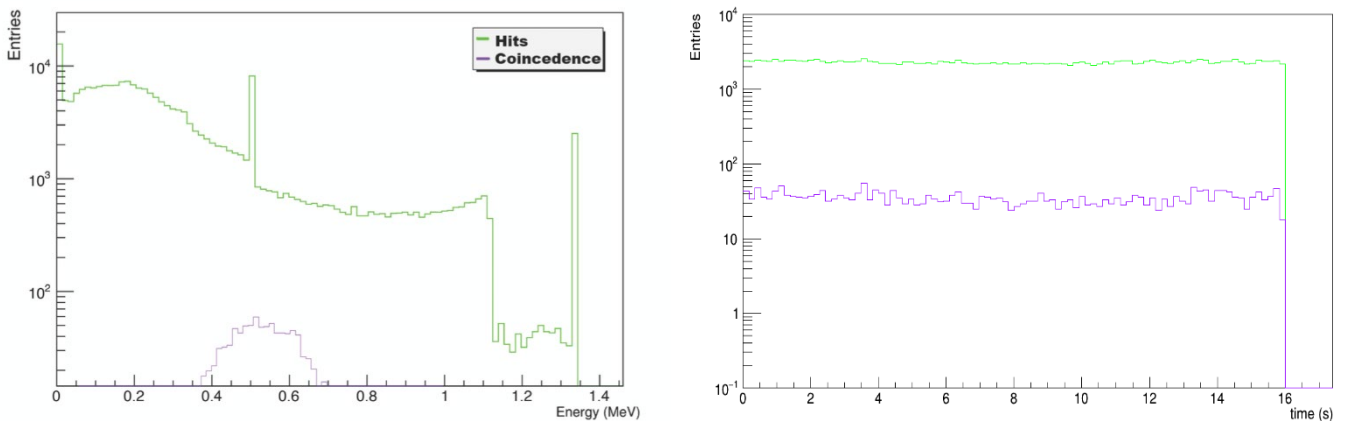


Figure 4 - For dual isotope resources of C^{11} and Cu^{60} energies that are considered at 511 KeV and 1330 KeV respectively, PET energy (left) and time (right) distributions in stacks with detected hits (green) and coincidences (purple).

It is analyzed the effects of dual isotope usage on PET device resolution as follows: We have placed C^{11} and Cu^{60} sources opposite to each other at several distances starting from (-2,+2) mm to (-20,+20) mm respectively as in Fig. 5 (left). Note that sources placed at (-2,+2) mm corresponds to 4 mm distance that is good for Rayleigh criterion since our smallest standart deviations is about 0.9. We mean that all distances are chosen in accordance with this criterion. We have repeated those similar runs changing the image resolutions of PET device as 0.1, 0.26, 0.75 and 1 mm. In profile histograms along (x,y,z), we have observed that the total entries are decreasing with the higher resolution for both single hits and coincidences. The same degradation is obtained also for enegy histograms as Fig. 5 (right). We have also observed that for the

coincidences that total entries are higher if the distance is small. However, we searched that if the resolution cut for entries are significant between dual isotope and single isotope usage. One can construct a null-hypothesis as “there is no difference from dual isotope and single isotope usage in any image resolutions” as well as “there is no difference bewtween C^{11} and Cu^{60} usage in any resolutions”. Chi-square analysis is selected to apply on standard deviations (σ) as they are related with Rayleigh criterion as mentioned above. In analysis, we have compared σ values of signals from all resolutions with the smallest possible resolution (0.1 mm). After collecting σ values, we have calculated the chi-square values as follows:

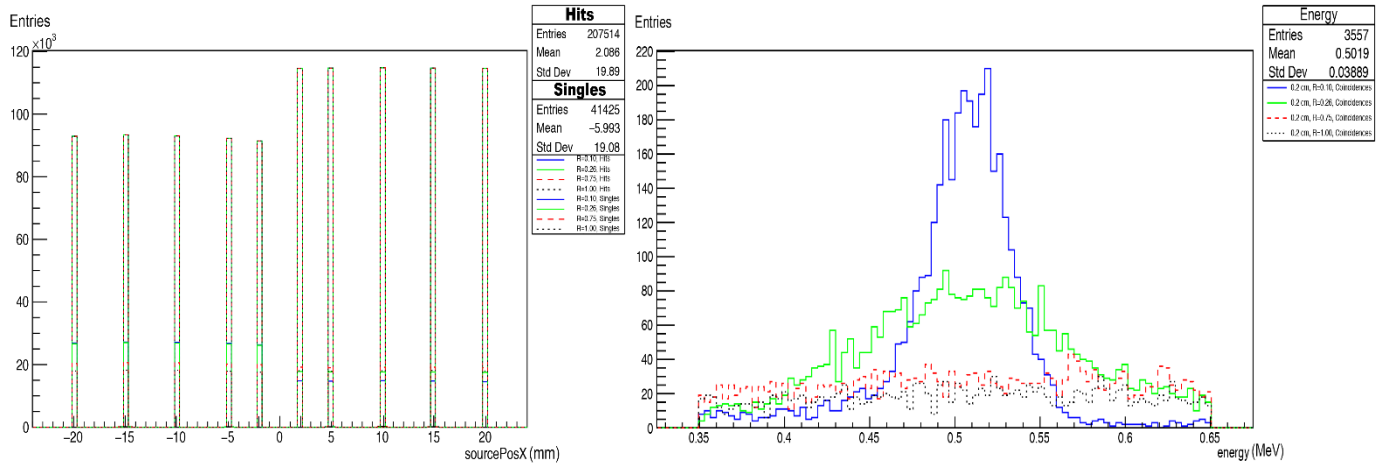


Figure 5 – (Left) Comparison of entries for dual isotopes placed at (-2,+2), (-5,+5), (-10,+10), (-15,+15), (-20,20) mm distances for hits and singles. (Right) Comparison of energy levels of entries from coincidences in different resolution as above. No major difference observed for singles and hits. Colors indicate different resolutions for both plots as 0.1 (blue), 0.2 (green), 0.5 (red dotted) and 1 (dashed) mm.

$$\chi^2 = \sum_{Distances} \frac{(\sigma_{0.1} - \sigma_{resolution})^2}{\sigma_{0.1}} \quad (3)$$

where $\sigma_{resolution}$ are collected values in 0.26, 0.75 and 1 mm image resolutions. We have summarized the results as in Table 1. According to chi-square values of single isotope simulations, one can see that resolution between 0.1 – 0.26 are low chi-square values indicate that the PET machine can distinguish two sources easily. It is also acceptable if the resolution is higher as 0.75 and 1 mm but significance level (α) drops about 0.975. For dual isotope simulations, low chi-square values show that the resolution is enough to distinguish two sources easily. For a comparison between dual isotope and single isotope simulations, PET device seems to be approx. 10 times (6 times) more precise at dual isotope usage for the worst case (best case).

We also calculated dual isotope image contrast values as in Table 2. Intensities are calculated normalising to highest intensity 1 and contrasts are obtained in percent in accordance with the equation (2). It can be seen directly that higher contrasts are obtained in small resolutions. Although all contrast values are good, 0.1 – 0.26 mm resolutions are give the best possible result. Note that the distances of sources are has no effect on contrast or intensities.

Table 1 – Chi-Square values over two different PET simulations: Single isotope and Dual isotope.

	PET Energy Single Isotopes		PET Energy Dual Isotopes
	C ¹¹	Cu ⁶⁰	C ¹¹ + Cu ⁶⁰
R=0.10-0.26	0.0808	0.0630	0.0116
R=0.10-0.75	0.2476	0.2114	0.0253
R=0.10-1.00	0.2554	0.3580	0.0262

Table 2 – Calculated contrast and intensity values over C¹¹ and Cu⁶⁰ source distances and resolutions.

PET SOURCE POSX2 COINCIDENCES				
Resolution (mm)	Distance (cm)	Intensity C ¹¹	Intensity CU ⁶⁰	Contrast (%)
R=0,10		0,018639911	0,000834623	0,914
R=0,26	0,2	0,010386333	0,001278318	0,781
R=0,75		0,002229608	0,000891843	0,431
R=1,00		0,001375709	0,000687855	0,330
R=0,10	0,5	0,003064223	0,000094284	0,940
R=0,26		0,001596620	0,000149683	0,830
R=0,75		0,000332145	0,000142348	0,400
R=1,00	1,0	0,000195623	0,000108679	0,286
R=0,10		0,000650233	0,000039408	0,886
R=0,26		0,000391067	0,000048131	0,781
R=0,75	1,5	0,000088933	0,000041502	0,364
R=1,00		0,000051728	0,000032671	0,226
R=0,10		0,000291441	0,000018215	0,882
R=0,26	2,0	0,000176340	0,000022392	0,775
R=0,75		0,000036463	0,000018231	0,333
R=1,00		0,000021637	0,000014425	0,200
R=0,10	2,0	0,000187356	0,000008922	0,910
R=0,26		0,000094633	0,000012411	0,769
R=0,75		0,000020771	0,000009644	0,367
R=1,00		0,000013141	0,000007608	0,267

5. Conclusion

As in this work, one can conclude that PET devices in GATE simulations can gain ability to distinguish dual isotope sources without extra modifications to virtual device. Although this kind of modifications are beyond the scope of this work, we have showed that there are quite amount of data that is excluded and expected to be processed simlutenously with the process of capturing annihilated particles and coincidences. Note that we have carried on an analysis upon two distinct sources and observed quite low total entries after processing. Therefore, a complex analysis over tissues and real PET images can be a future work.

Conflict of interest

The authors state that did not have conflict of interests.

References

- [1] Teksöz S., Müftüler FZB., Radioisotopes and Biomedical Applications in Nuclear Medicine, *Nucl Med Semin*, 5 (2019) 10-14.
- [2] Andreyev, A., Sitek, A., & Celler, A. (2014). EM reconstruction of dual isotope PET using staggered injections and prompt gamma positron emitters, *Medical Physics*, 41(2) (2014) 022501.
- [3] Andreyev, A., Celler, A., Dual-isotope PET using positron gamma emitters, *Phys. Med. Biol.* 56 (4539) (2011).
- [4] Figueiras, F. P., et al., Simultaneous dual-tracer PET imaging of the ratbrain and its application in the study of cerebral ischemia, *Mol. Imag. Biol.*, vol. 13(3) (2011) 500–510.
- [5] Black, N. F. , Mcjames, S. and Kadrmas, D.J., Rapid multi-tracer PET tumor imaging with [18F] FDG and secondary shorter-lived tracers, *IEEE Trans. Nucl. Sci.*, 56(5) (2009) 2750–2758.
- [6] El Fakhri, G., Sitek, A. and Guerin, B., Simultaneous dual tracer PET using generalized factor analysis of dynamic sequences, *Proc. Nucl.Sci. Symp. Conf. Rec.*, 15 (2006) 2128–2130.
- [7] Jan, S. et al. , GATE: a simulation toolkit for PET and SPECT, *Phys. Med. Biol.*, 49 (2004) 4543-4561.
- [8] Brun, R., & Rademakers, F., ROOT — A C++ framework for petabyte data storage, statistical analysis and visualization, *Computer Physics Communications; Anniversary Issue*; 180(12) (2009) 2499-2512.



Preheating in radiatively corrected ϕ^4 inflation with non-minimal coupling in Palatini formulation

Nilay BOSTAN^{1,*}

¹The University of Iowa, Department of Physics and Astronomy, Iowa City, IA 52242/U.S.A.

Abstract

We discuss the impact of the preheating stage due to the interaction of the inflaton to fermions in Palatini formulation. In Palatini inflation with large non-minimal coupling, the field is allowed to return to the plateau region during the reheating stage, therefore the average equation of state per oscillations is closer to -1 rather than $1/3$. The incursion in the plateau, however, leads to a highly efficient tachyonic instability, which is able to reheat the Universe in less than one e-fold. By taking prescription II into account, which is discussed in the literature, we calculate the spectral index n_s and the tensor-to-scalar ratio r in the wide range of $\kappa - \xi$. We will show the results which are compatible with the data given by the Keck Array/BICEP2 and Planck collaborations.

Article info

History:

Received:07.03.2021

Accepted:20.07.2021

Keywords:

Non-minimal inflation,
Palatini gravity,
Preheating,
Radiative corrections.

1. Introduction

Inflation [1-4] is an early period of nearly exponential expansion of the universe, and it has become a solution for several shortcomings such as the horizon, flatness, and unobserved magnetic monopoles since its proposal around 1980. The theory of cosmic inflation gives an acceptable explanation of the large-scale homogeneity of the universe, as well as the primordial density perturbations that grow into the cosmic structure. These primordial perturbations evolve in order to produce the observed large-scale structure and the cosmic microwave background (CMB) temperature anisotropy. In addition to this, several inflationary models have been suggested [5], and most of them are defined by the slow-rolling scalar field which is called the inflaton. Predictions of these models are currently being tested by polarization observations and CMB temperature anisotropies [6, 7]. In particular, the last results released by the Keck Array/BICEP2 and Planck collaborations [8] cast robust constraints on the tensor-to-scalar ratio (r), which explains the amplitude of primordial gravitational waves and the scale of inflation. As a result, the predictions of the simple monomial inflation models are ruled out at level, thus the models of non-minimally coupled to gravity become the most popular ones.

In this work, we take models of inflation with non-minimal coupling to gravity ($\xi\phi^2R$) into account, where ξ is the non-minimal coupling parameter, ϕ is

the scalar field (inflaton) and R is the Ricci scalar. $\xi\phi^2R$ term is necessary to provide the renormalizability of the scalar field theory in curved space-time [9]. In addition, the predictions of the inflationary models can change significantly according to the coefficient of this coupling term [5]. We show how the values of n_s and r change for the preheating stage due to the interactions of the inflaton to fermions in Palatini formulation by using prescription II, in the presence of the non-minimal coupling parameter ξ . In the literature, many articles have already studied inflation with non-minimal coupling in Metric formalism [10–12]. In particular, the most favorite one is the scenario where the Standard Model Higgs scalar [12] is the inflaton. Furthermore, in the Metric formulation, all model's asymptote to a universal attractor [13], which is called the Starobinsky model, for the large values of ξ independent of the original scalar potential. On the other hand, the attractor behavior of the Starobinsky model is lost in the Palatini formulation, and r can be much smaller in the Palatini formulation compared to the Metric one [14]. Also, consideration of the gravitational degrees of freedom is necessary for the presence of non-minimal coupling to gravity. In the metric formulation of gravity, the independent variables are the metric and its first derivatives [15], while in the Palatini formulation, the independent variables are the connection and the metric [16]. The predictions of these two formalisms correspond to the same equations of motion, therefore they describe equivalent physical theories. However,

*Corresponding author. e-mail address: nilay-bostan@uiowa.edu

in the case of non-minimal coupling between gravity and matter, such equivalence disappears, and the two formulations illustrate different gravity theories [14, 17–19]. In the literature, the Palatini formulation of inflation with non-minimal coupling was discussed in refs. [14, 19–21]. The Palatini self-interaction potential $V(\phi)$ was analyzed in ref. [14], and they figured out the observational parameters $n_s \simeq 0.968$ and $r \simeq 10^{-14}$ in the large-field limit. Also, Palatini Higgs inflation was examined in ref. [19], and they showed the range of the tensor-to-scalar ratio as $1 \times 10^{-13} < r < 2 \times 10^{-5}$. According to these papers, r takes very small values in Palatini formulation. In addition to this, it was showed that the radiative corrections to the inflationary potential can play a pivotal role [22–24], in the case of non-minimal coupling to gravity, generating the Planck scale dynamically [25].

In this paper, we study the impact of the preheating stage in Palatini radiatively corrected ϕ^4 inflation by using prescription II and the coupling of the inflaton to fermions. As compared to the metric formulation, the entropy production in Palatini Higgs inflation appears significantly more effective [20], decreasing the number of e-folds required to solve the flatness and horizon problems, producing a less spectral tilt for the primordial density perturbations. Furthermore, ref. [20] showed that after inflation, the slow decay of the Higgs oscillations allows the field to return to the plateau of the potential periodically during the reheating stage. In addition, in the large-field limit, the effective mass of the Higgs becomes negative, allowing for the exponential creation of Higgs excitations. Consequently, the preheating stage of the Palatini Higgs inflation is primarily instantaneous and this case decreases the value of N_* required to solve the Hot Big-Bang shortcomings [20]. The paper is organized as follows: the non-minimal inflation with Palatini formalism is presented in section 2. In section 3, we explain the radiatively corrected ϕ^4 potential with radiative corrections. In section 4, we numerically calculate the impact of the preheating stage in Palatini radiatively corrected ϕ^4 inflation for prescription II and the coupling of inflaton to fermions, and finally, we discuss our results in section 5.

2. Non-minimal inflation in Palatini formulation

Assuming the following Lagrangian density for a scalar-tensor theory in the Jordan frame with non-minimally coupled scalar field ϕ :

$$\frac{\mathcal{L}_J}{\sqrt{-g}} = \frac{1}{2}F(\phi)R - \frac{1}{2}g^{\mu\nu}\partial_\mu\phi\partial_\nu\phi - V_J(\phi), \quad (1)$$

where the subscript J indicates that the Lagrangian is described in a Jordan frame. In addition, $g^{\mu\nu}$ is a metric tensor, $F(\phi)$ is a non-minimal coupling function and $F(\phi) = 1 + \xi\phi^2$. The Lagrangian consists of a canonical kinetic term and a potential $V_J(\phi)$ in the Jordan frame. We consider the units where the reduced Planck scale, $m_p = 1/\sqrt{8\pi G} \approx 2.4 \times 10^{18}$ GeV, is fixed equal to unity, thus we require $F(\phi) \rightarrow 1$ after inflation. Here, G is a gravitational constant. Furthermore, to avoid repulsive gravity, we suppose $F(\phi) > 0$. This property of $F(\phi)$ is independent of the formulation of gravity, such as Metric and Palatini.

In the metric formulation, the connection is described as a function of a metric tensor called Levi-Civita connection $\bar{\Gamma} = \bar{\Gamma}(g^{\mu\nu})$:

$$\bar{\Gamma}_{\alpha\beta}^\lambda = \frac{1}{2}g^{\lambda\rho}(\partial_\alpha g_{\beta\rho} + \partial_\beta g_{\rho\alpha} - \partial_\rho g_{\alpha\beta}). \quad (2)$$

Unlike the metric formulation, $g_{\mu\nu}$ and Γ are independent variables in the Palatini formalism, and the only constraint is that the connection is torsion-free, $\Gamma_{\alpha\beta}^\lambda = \Gamma_{\beta\alpha}^\lambda$. By solving the EoM, we obtain [14]

$$\Gamma_{\alpha\beta}^\lambda = \bar{\Gamma}_{\alpha\beta}^\lambda + \delta_\alpha^\lambda \partial_\beta \omega(\phi) + \delta_\beta^\lambda \partial_\alpha \omega(\phi) - g_{\alpha\beta} \partial^\lambda \omega(\phi), \quad (3)$$

where

$$\omega(\phi) = \ln \sqrt{F(\phi)}. \quad (4)$$

Due to the fact that the connections (Eqs. (2) and (3)) are different, the metric and Palatini formalisms correspond to two different theories of gravity. On the one hand, we can explain the differences by taking into account the problem in the Einstein frame by means of the conformal transformation.

In order to calculate the observational parameters, it is more efficient to switch to the Einstein frame by using a Weyl rescaling $g_{E,\mu\nu} = g_{J,\mu\nu}/F(\phi)$. Then the Einstein frame Lagrangian density becomes [26]

$$\frac{\mathcal{L}_E}{\sqrt{-g_E}} = \frac{1}{2}R_E - \frac{1}{2Z(\phi)}g_E^{\mu\nu}\partial_\mu\phi\partial_\nu\phi - V_E(\phi), \quad (5)$$

where

$$Z^{-1}(\phi) = \frac{1}{F(\phi)}, \quad V_E(\phi) = \frac{V_J(\phi)}{F(\phi)^2}, \quad (6)$$

in the Palatini formalism. By making a field redefinition

$$d\sigma = \frac{d\phi}{\sqrt{Z(\phi)}}. \quad (7)$$

We find the Lagrangian density for a minimally coupled scalar field σ with a canonical kinetic term. Here, σ is a canonical scalar field. As a consequence,

for the Palatini formalism, the field redefinition is induced just by rescaling the inflaton kinetic term, and it does not include the Jordan frame Ricci scalar. On the other hand, in the Metric formalism, the field redefinition consists of the transformation of the Jordan frame Ricci scalar and the rescaling of the kinetic term of the Jordan frame scalar field [14]. Therefore, we can say that the difference between the metric and Palatini formalisms correspond to the different definitions of σ with the different non-minimal kinetic terms including ϕ .

In the large-field limit, for $F(\phi) = 1 + \xi\phi^2$, ($|\xi|\phi^2 \gg 1$), we can find

$$\phi \simeq \frac{1}{\sqrt{\xi}} \sinh(\sigma\sqrt{\xi}), \tag{8}$$

in the Palatini formalism. By using eq. (8), the inflationary potential can be described in terms of σ , so that we can obtain the slow-roll parameters in Palatini formalism for the $|\xi|\phi^2 \gg 1$ limit in terms of σ .

The observational parameters for the inflationary dynamics can be defined by the following slow-roll parameters [27],

$$\epsilon = \frac{1}{2} \left(\frac{V_{\sigma}}{V} \right)^2, \quad \eta = \frac{V_{\sigma\sigma}}{V}, \tag{9}$$

where σ 's in the subscript denote derivatives with respect to the canonical scalar field. Observational parameters, i.e. the spectral index n_s and the tensor-to-scalar ratio r can be expressed in terms of the slow-roll parameters as,

$$n_s = 1 - 6\epsilon + 2\eta, \quad r = 16\epsilon. \tag{10}$$

The number of e-folds in the slow-roll approximation is

$$N_* = \int_{\sigma_e}^{\sigma_*} \frac{V d\sigma}{V_{\sigma}}, \tag{11}$$

where the subscript “ $*$ ” indicates that the scale corresponding to k_* exited the horizon for that quantity, $k_* = 0.002 \text{ Mpc}^{-1}$ and σ_e is the inflaton value at the end of inflation, which we obtain by using $\epsilon(\sigma_e) = 1$.

The amplitude of the curvature power spectrum is given in the form

$$\Delta_{\mathcal{R}} = \frac{1}{2\sqrt{3}\pi} \frac{V^{3/2}}{|V_{\sigma}|}, \tag{12}$$

The best fit value for the pivot scale $k_* = 0.002 \text{ Mpc}^{-1}$ is $\Delta_{\mathcal{R}}^2 \approx 2.1 \times 10^{-9}$ [6] from the Planck results.

Furthermore, we reproduce the slow-roll parameters in terms of the original scalar field ϕ to use them in numerical calculations. By using them together with

the Eqs. (7) and (9), slow-roll parameters can be figured out in terms of ϕ [28]

$$\epsilon = Z\epsilon_{\phi}, \quad \eta = Z\eta_{\phi} + \text{sgn}(V')Z' \sqrt{\frac{\epsilon_{\phi}}{2}}, \tag{13}$$

where we defined

$$\epsilon_{\phi} = \frac{1}{2} \left(\frac{V'}{V} \right)^2, \quad \eta_{\phi} = \frac{V''}{V}. \tag{14}$$

Here, $V' \equiv dV/d\phi$. Similarly, Eqs. (11) and (12) can be found in terms of ϕ by using

$$N_* = \text{sgn}(V') \int_{\phi_e}^{\phi_*} \frac{d\phi}{Z(\phi)\sqrt{2\epsilon_{\phi}}}, \tag{15}$$

$$\Delta_{\mathcal{R}} = \frac{1}{2\sqrt{3}\pi} \frac{V^{3/2}}{\sqrt{|Z|}|V'|}. \tag{16}$$

These observable parameters that depend on the number of e-folds of inflation are required to solve such problems, i.e. the flatness and horizon. Following the standard method, we need

$$1 = a_0 = \frac{a_0}{a_{\text{RH}}} \frac{a_{\text{RH}}}{a_e} \frac{a_e}{a_*} a_* = \left(\frac{g_{*S \text{RH}}}{g_{*S \text{now}}} \right)^{1/3} \frac{T_{\text{RH}}}{T_0} \frac{k_*}{H_*} \exp(\Delta N + N_*), \tag{17}$$

where “0” denotes that the value of the corresponding quantity is the one at the present time (as used throughout this paper), and (“RH”) indicates that the value of the quantity is the one at the end of the reheating stage. In addition, (“e”) indicates at the end of inflation, and (“*”) illustrates the pivot scale corresponding to $k_* = 0.002 \text{ Mpc}^{-1}$ crosses the horizon. The quantity ΔN indicates the number of e-folds of reheating, g_{*S} is the effective number of entropy degrees of freedom with $g_{*S \text{RH}} = g_{* \text{RH}}$, as well as $g_{*S \text{now}} = 3.94$ [29] and $T_0 \simeq 2.7 \text{ K}$. T_{RH} is the reheating temperature [30]. In ref. [20], N_* is defined in the preheating stage of the Palatini Higgs inflation, which is necessarily instantaneous. Here, $g_{*S \text{now}}$ shows the current value of the effective number of entropy degrees of freedom. After the inflation, almost all of the background energy density is converted to the radiation, and by solving eq. (17) for the condition of $\Delta N \ll 1$, N_* can be found in the form [20]

$$N_* \simeq 54.9 - \frac{1}{4} \log \xi, \tag{18}$$

this result is precise to an integer order of N_* . In section 4, we numerically figure out the impact of the preheating stage in Palatini radiatively corrected ϕ^4 inflation for prescription II and inflaton to fermions coupling by using eq. (18).

3. Radiatively corrected ϕ^4 potential with radiative corrections

For the description of the couplings of the inflaton with other fields, it is necessary to produce radiative corrections in the inflationary potential for effective reheating. These corrections can be defined at the leading order in the form [31–33],

$$\Delta V(\phi) = \sum_i \frac{(-1)^v}{64\pi^2} M_i(\phi)^4 \ln\left(\frac{M_i(\phi)^2}{\mu^2}\right). \quad (19)$$

Here, v is +1 (–1) for bosons (fermions), μ is a renormalization scale and $M_i(\phi)$ corresponds to the field-dependent mass.

We consider the minimally coupled ϕ^4 potential interacting with another scalar χ and a Dirac fermion Ψ in the form,

$$V(\phi, \chi, \Psi) = \frac{\lambda}{4}\phi^4 + h\phi\bar{\Psi}\Psi + m_\psi\bar{\Psi}\Psi + \frac{1}{2}g^2\phi^2\chi^2 + \frac{1}{2}m_\chi^2\chi^2. \quad (20)$$

Here, λ is a self-coupling constant, g (h) are bosons (fermions) coupling constants, and m_ψ (m_χ) are the

mass terms for Dirac fermions (scalars). We assume that, with these approximations

$$g^2\phi^2 \gg m_\chi^2, \quad g^2 \gg \lambda, \quad h\phi \gg m_\psi, \quad h^2 \gg \lambda, \quad (21)$$

the inflationary potential consisting of the Coleman-Weinberg one-loop corrections given by eq. (19) can be found in the form

$$V(\phi) \simeq \frac{\lambda}{4}\phi^4 \pm \kappa\phi^4 \ln\left(\frac{\phi}{\mu}\right), \quad (22)$$

where + (–) sign indicates the inflaton coupling to bosons (fermions). We can describe the coupling parameter as follows

$$\kappa \equiv \frac{1}{32\pi^2} |(g^4 - 4h^4)|. \quad (23)$$

Here, the potential in eq. (22) is just an approximation of the one-loop RG improved effective actions [34].

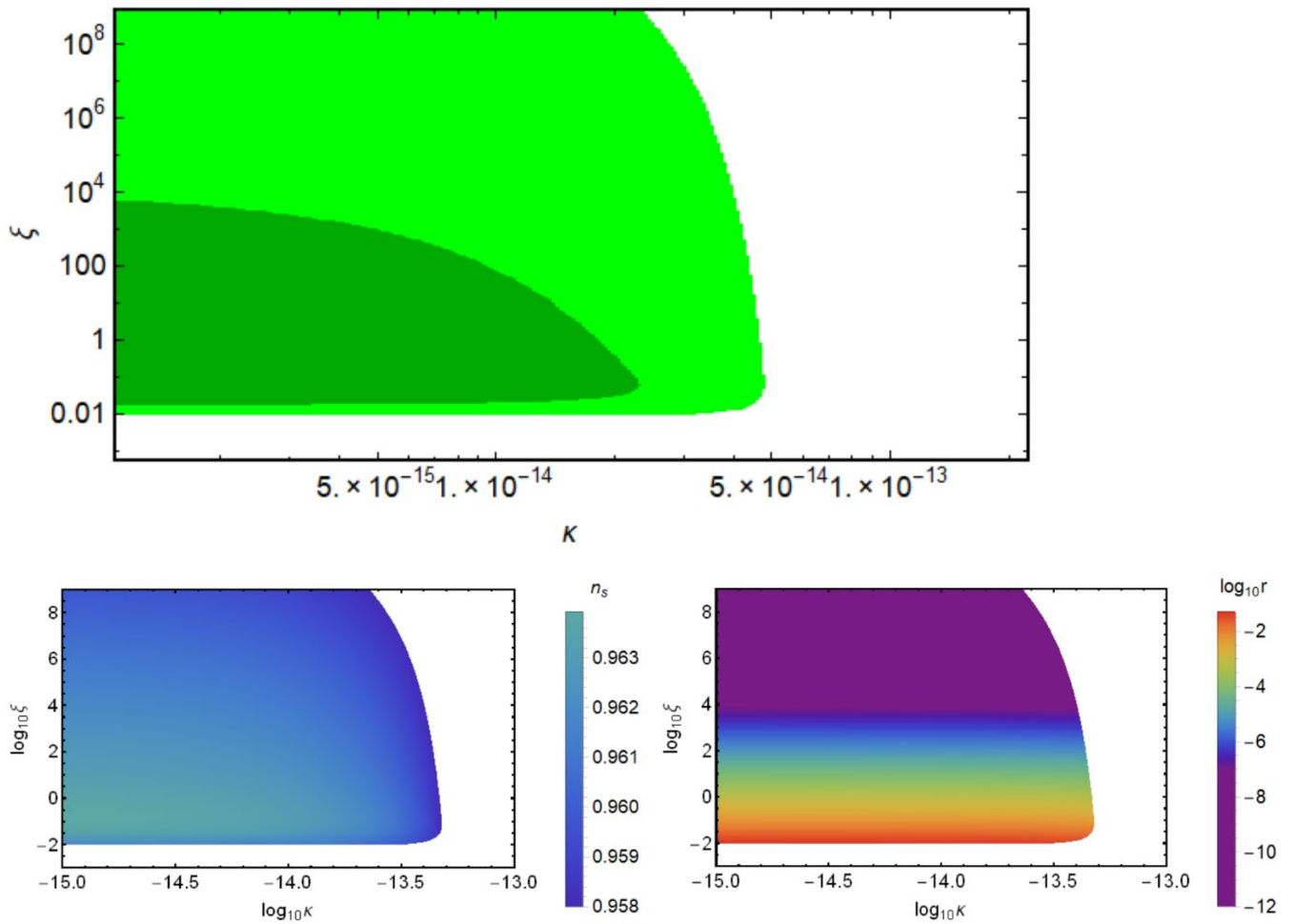


Figure 1. The top figure in light green (green) illustrates the regions in the $\kappa - \xi$ plane where the n_s and r values are inside the 95% (68%) CL contours based on data given by the Keck Array/BICEP2 and Planck collaborations [8]. Bottom figures display n_s and r values in these regions.

As discussed in the literature, one of the two different prescriptions is prescription II that is typically used for the calculation of radiative corrections [35–38]. In prescription II, the field-dependent masses in the one-loop Coleman-Weinberg potential are described in the Jordan frame, therefore eq. (22) corresponds to the one-loop Coleman-Weinberg potential in the Jordan frame. As a consequence, the Einstein frame potential for the interactions of the inflaton and fermions in prescription II is described by

$$V(\phi) = \frac{\frac{\lambda}{4}\phi^4 - \kappa\phi^4 \ln\left(\frac{\phi}{\mu}\right)}{(1+\xi\phi^2)^2}. \quad (24)$$

We can say that the variation of the value of the renormalization scale does not affect the form of the potential in eq. (24). The form of the potential only changes with a shift in λ . As a result, observational parameters do not change depending upon μ as well.

4. Inflationary results

In this section, we numerically investigate the effect of the preheating stage in Palatini radiatively corrected ϕ^4 inflation for prescription II and coupling of the inflaton to fermions. Figure 1 displays the regions in the κ - ξ plane where the n_s and r values are inside the 95% (68%) CL (confidence levels) contours based on data given by the Keck Array/BICEP2 and Planck collaborations. As it can be seen from Fig.1, for the values of $10^{-2} \lesssim \xi \lesssim 10^4$ and $10^{-15} \lesssim \kappa \lesssim 2.2 \times 10^{-14}$, observational parameters can be within the 68% CL contour based on the data given by the Keck Array/BICEP2 and Planck collaborations, and their values are $n_s \simeq 0.963$ and $10^{-7} \lesssim r \lesssim 10^{-2}$. On the other hand, as κ increases, it reaches a maximum value, κ_{\max} , for each ξ value. For $\kappa > \kappa_{\max}$, there are no solutions that provide the inflationary dynamics. Furthermore, in the range of $10^4 \lesssim \xi \lesssim 10^8$ and $10^{-15} \lesssim \kappa \lesssim 5 \times 10^{-14}$, we find $0.958 \lesssim n_s \lesssim 0.961$ and $10^{-12} \lesssim r \lesssim 10^{-7}$. These values are in the 95% CL contour based on the data given by the Keck Array/BICEP2 and Planck collaborations. As a result, for $10^4 \lesssim \xi \lesssim 10^8$ and $N_* \simeq 52$, we obtain $0.958 \lesssim n_s \lesssim 0.961$. Although still in 2σ confidence limits, these n_s values slightly disagreed with the observational results given by the Keck Array/BICEP2 and Planck collaborations, as well as the values of r are extremely tiny in the large ξ limits. Ref. [20] also showed that for the preheating stage of Higgs inflation in Palatini formulation, $n_s \simeq 0.961$ and r values are very tiny for large ξ values for the $N_* \simeq 51$ and finally, the behavior of Starobinsky attractor in metric formulation for large ξ values is lost for the potential we take into account.

5. Conclusion

In this paper, we described the non-minimal inflation in Palatini formulation in section 2, and then in section 3, we briefly presented the radiatively corrected ϕ^4 potential with radiative corrections. We numerically investigated the impact of the preheating stage on the observational parameters for this type of potential for fermions coupling in section 4.

In general, we found that r values are too small in the large-field limit, and the behavior of Starobinsky attractor in metric formulation for the large ξ values disappears for the potential which we considered. Furthermore, we found that for the cases of $\kappa > \kappa_{\max}$, there are no solutions that provide inflationary dynamics and for the values of $10^4 \lesssim \xi \lesssim 10^8$ and $N_* \simeq 52$, n_s values are in 2σ CL but marginally incompatible with the observational results.

In the large-field limit, for the Palatini formulation, the process of entropy production emerges very efficiently and leads to the complete reduction of the inflaton condensate in an e-fold expansion of smaller than one [20]. As a consequence, in the preheating stage, Palatini inflation with the radiative corrections to the coupling of fermions in prescription II is necessarily instantaneous, and after the inflation, almost all of the background energy density is converted to the radiation. This decreases the value of N_* required to solve the common Hot Big-Bang shortcomings, while an insignificantly smaller value for the spectral tilt produces.

Finally, by the consideration of $\mathcal{O}(10^{-3})$ accuracy of future precision measurements [38], the predictions of Palatini formulation could be distinguished from the metric ones within forthcoming results, and assuming larger values of r are obtained, the Palatini formulation can be ruled out.

Acknowledgements

The author thanks Javier Rubio and Ohannes Kamer Koseyan for their useful discussions.

Conflicts of interest

The author states that did not have conflict of interests.

References

- [1] Guth A. H., The Inflationary Universe: A Possible Solution to the Horizon and Flatness Problems, *Phys. Rev. D*, 23 (1981) 347-356.

- [2] Linde A. D., A New Inflationary Universe Scenario: A Possible Solution of the Horizon, Flatness, Homogeneity, Isotropy and Primordial Monopole Problems, *Phys. Lett.*, 108B (1982) 389-393.
- [3] Albrecht A., Steinhardt P. J., Cosmology for Grand Unified Theories with Radiatively Induced Symmetry Breaking, *Phys. Rev. Lett.*, 48 (1982) 1220-1223.
- [4] Linde A. D., Chaotic Inflation, *Phys. Lett.*, 129B (1983) 177-181.
- [5] Martin J., Ringeval C., Vennin V., Encyclopædia Inflationaris, *Phys. Dark Univ.*, 5-6 (2014) 75-235, arXiv:1303.3787.
- [6] Aghanim N. et al. [Planck Collaboration], Planck 2018 results. VI. Cosmological parameters, *Astron. Astrophys.*, 641 (2020) A6, arXiv:1807.06209.
- [7] Akrami Y. et al. [Planck Collaboration], Planck 2018 results. X. Constraints on inflation, *Astron. Astrophys.*, 641 (2020) A10, arXiv:1807.06211.
- [8] Ade P. A. R. et al. [BICEP2 and Keck Array Collaborations], BICEP2 / Keck Array x: Constraints on Primordial Gravitational Waves using Planck, WMAP, and New BICEP2/Keck Observations through the 2015 Season, *Phys. Rev. Lett.*, 121 (2018) 221301, arXiv:1810.05216.
- [9] Callan, Jr. C. G., Coleman S. R., Jackiw R., A New improved energy-momentum tensor, *Annals Phys.*, 59 (1970) 42-73.
- [10] Bezrukov F., Magnin A., Shaposhnikov M., Sibiryakov S., Higgs inflation: consistency and generalisations, *JHEP*, 1101 (2011) 016, arXiv:1008.5157.
- [11] Bostan N., Güleriyüz Ö., Şenoğuz V. N., Inflationary predictions of double-well, Coleman-Weinberg, and hilltop potentials with non-minimal coupling, *JCAP*, 1805 no. 05 (2018) 046, arXiv:1802.04160.
- [12] Bezrukov F. L., Shaposhnikov M., The Standard Model Higgs boson as the inflaton, *Phys. Lett. B*, 659 (2008) 703-706, arXiv:0710.3755.
- [13] Kallosh R., Linde A., Roest D., Universal Attractor for Inflation at Strong Coupling, *Phys. Rev. Lett.*, 112 no. 1 (2014) 011303, arXiv:1310.3950.
- [14] Bauer F., Demir D. A., Inflation with Non-Minimal Coupling: Metric versus Palatini Formulations, *Phys. Lett. B*, 665 (2008) 222-226, arXiv:0803.2664.
- [15] Padmanabhan T., Holographic gravity and the surface term in the Einstein-Hilbert action, *Braz. J. Phys.*, 35 (2005) 362-372, arXiv:gr-qc/0412068.
- [16] Palatini A., Deduzione invariante delle equazioni gravitazionali dal principio di Hamilton, *Rendiconti del Circolo Matematico di Palermo (1884-1940)*, 43(1) (1919) 203-212.
- [17] York, Jr J. W., Role of conformal three geometry in the dynamics of gravitation, *Phys. Rev. Lett.*, 28 (1972) 1082-1085.
- [18] Tenkanen T., Resurrecting Quadratic Inflation with a non-minimal coupling to gravity, *JCAP*, 1712 no. 12 (2017) 001, arXiv:1710.02758.
- [19] Rasanen S., Wahlman P., Higgs inflation with loop corrections in the Palatini formulation, *JCAP*, 1711 no. 11 (2017) 047, arXiv:1709.07853.
- [20] Rubio J., Tomberg E. S., Preheating in Palatini Higgs inflation, *JCAP*, 1904 (2019) 021.
- [21] Fu C., Wu P., Yu H., Inflationary dynamics and preheating of the nonminimally coupled inflaton field in the metric and Palatini formalisms, *Phys. Rev. D*, 96 no. 10 (2017) 103542, arXiv:1801.04089.
- [22] Marzola L., Racioppi A., Raidal M., Urban F. R., Veermäe H., Non-minimal CW inflation, electroweak symmetry breaking and the 750 GeV anomaly, *JHEP*, 1603 (2016) 190, arXiv:1512.09136.
- [23] Marzola L., Racioppi A., Minimal but non-minimal inflation and electroweak symmetry breaking, *JCAP*, 1610 no. 10 (2016) 010, arXiv:1606.06887.
- [24] Dimopoulos K., Owen C., Racioppi A., Loop inflection-point inflation, *Astropart. Phys.*, 103 (2018) 16-20, arXiv:1706.09735.
- [25] Kannike K., Racioppi A., Raidal M., Linear inflation from quartic potential, *JHEP*, 1601 (2016) 035, arXiv:1509.05423.
- [26] Fujii Y., Maeda K., The scalar-tensor theory of gravitation, Cambridge, UK: Cambridge University Press, (2007).
- [27] Lyth D. H., Liddle A. R., The primordial density perturbation: Cosmology, inflation and the origin of structure, Cambridge, UK: Cambridge Univ. Pr., (2009).
- [28] Linde A., Noorbala M., Westphal A., Observational consequences of chaotic inflation with nonminimal coupling to gravity, *JCAP*, 1103 (2011) 013, arXiv:1101.2652.

- [29] Husdal L., On Effective Degrees of Freedom in the Early Universe, *Galaxies*, 4 no. 4 (2016) 78, arXiv:1609.04979.
- [30] Gialamas I. D., Lahanas A. B., Reheating in R^2 Palatini inflationary models, *Phys. Rev. D*, 101 no. 8 (2020) 084007, arXiv:1911.11513.
- [31] Coleman S. R., Weinberg E. J., Radiative Corrections as the Origin of Spontaneous Symmetry Breaking, *Phys. Rev. D*, 7 (1973) 1888-1910.
- [32] Enqvist K., Karčiauskas M., Does Planck really rule out monomial inflation?, *JCAP*, 1402 (2014) 034, arXiv:1312.5944.
- [33] Weinberg E. J., Radiative corrections as the origin of spontaneous symmetry breaking, Ph.D. Thesis, Harvard University, Department of Physics, April 1973, arXiv: hep-th/0507214, arXiv:1005.5161.
- [34] Okada N., Rehman M. U., Shafi Q., Tensor to Scalar Ratio in Non-Minimal ϕ^4 Inflation, *Phys. Rev. D*, 82 (2010) 043502, arXiv:1005.5161.
- [35] De Simone A., Hertzberg M. P., Wilczek F., Running Inflation in the Standard Model, *Phys. Lett. B*, 678 (2009) 1-8, arXiv:0812.4946.
- [36] Barvinsky A. O., Kamenshchik A. Y., Kiefer C., Starobinsky A. A., Steinwachs C., Asymptotic freedom in inflationary cosmology with a non-minimally coupled Higgs field, *JCAP*, 0912 (2009) 003, arXiv:0904.1698.
- [37] Barvinsky A. O., Kamenshchik A. Y., Kiefer C., Starobinsky A. A., Steinwachs C. F., Higgs boson, renormalization group, and naturalness in cosmology, *Eur. Phys. J. C*, 72 (2012) 2219, arXiv:0910.1041.
- [38] M. Remazeilles et al. [CORE Collaboration], Exploring cosmic origins with CORE: B-mode component separation, *JCAP*, 1804 no. 04 (2018) 023, arXiv:1704.04501.

Effects of annealing on ZnS films produced by CBD method

Özlem YILMAZ¹ , Sevda İLDAN ÖZMEN^{2,*} , Hülya METİN GÜBÜR¹ 

¹Mersin University, Faculty of Science, Department of Physics, Mersin/TURKEY

²Mersin University, Advanced Technology Education Research and Application Center, Mersin/TURKEY

Abstract

The Zinc Sulfide (ZnS) thin films were produced at 60 °C on glass slides with the chemical bath deposition (CBD) method. The ZnS films were annealed for 1 hour at different temperatures in the air atmosphere. UV-visible spectrophotometer, X-ray diffraction (XRD), scanning electron microscope (SEM), energy dispersive X-ray spectroscopy (EDS), four-point probe technique and Hall-effect measurement techniques were used to examine the thermal annealing's effect on the films' optical, structural, and electrical properties. It was observed that with increased annealing temperature, the film thickness increased and thus the energy band gap decreased. It was seen that the particle size of the ZnS films grew depending on the annealing temperature, and the crystal structure turned into an amorphous structure. Finally, it was determined that with the impact of annealing the carrier type did not change, and the conductivity of the ZnS thin films increased.

Article info

History:

Received:03.05.2021

Accepted:24.08.2021

Keywords:

ZnS,
Chemical bath
deposition,
SEM,
Optical properties,
Hall Effect.

1. Introduction

Zinc sulfide with ZnS chemical formula is an important chalcogenide that belongs to the II-VI semiconductor family (e.g., CdSe, ZnSe, CdS, ZnS) [1–3]. Because of its wide fields of application such as optoelectronic devices, optical coatings, solar cells and light-emitting diodes, the ZnS thin films have been extensively studied. The thin film of zinc sulfide (ZnS), which has direct bandgap energies range from 3.50-3.70 eV at room temperature, is used for the semiconductor layers of solar cells and other technological devices [4–6]. ZnS is used as a buffer layer in CIGS, ZCTSSe, and CdTe cells since it has n-type conductivity due to a sulfur deficiency defect [7]. This material with a high refractive index (2.25-2.35) is found in cubic (zinc blende) and hexagonal (wurtzite) crystal structures [8, 9]. It is also an attractive material since it is environmentally friendly, inexpensive and flexible [10, 11].

Due to the importance of the functional properties of nanoscale materials, various techniques have been used to produce nanostructured ZnS semiconductors [12]. Synthesis techniques such as molecular beam epitaxy, thermal evaporation, RF sputtering, chemical bath deposition are used to deposit ZnS thin films [3, 6, 8, 10, 12]. Among these techniques CBD is the low

costly technique, it is easily deposited to wide areas and it is a simple technique that not need special equipment [3, 13, 14].

In this study, the ZnS nanocrystalline thin films were produced on glass slides with the CBD method at 60 ± 2 °C. The obtained ZnS films were annealed in the air atmosphere for 1 hour at temperatures of 150 °C, 250 °C and 350 °C. The optical, structural, and electrical properties of the nanocrystalline films were also examined.

2. Materials and Methods

2.1. Experimental details

0.050 M zinc sulphate (ZnSO₄), 25% ammonia (NH₃) / ammonium chloride (NH₄Cl), 1 M triethanolamine (C₆H₁₅NO₃), 0.050 M thioacetamide (C₂H₅NS) were prepared in an aqueous solution (pH = 10.8) at room temperature to obtain ZnS thin films. The solution was put into a water bath of 60 ± 2 °C which was placed on the hot plate. Glass slides for ZnS thin films were used as the substrate. Before coating, the glass substrates were cleaned with chromic acid, deionized pure water, propanol, and ethanol, respectively. Later, for a few minutes, an air dryer was used to dry them. The clean substrates were then positioned at a 45 °

*Corresponding author. e-mail address: sevdaildan@mersin.edu.tr
<http://dergipark.gov.tr/cs.j> ©2021 Faculty of Science, Sivas Cumhuriyet University

angle in a beaker containing 100 ml deposition mixture and held for 1h at 60°C without stirring. The bath temperature was controlled by a thermometer. The deposition of ZnS semiconductor thin films was repeated sixteen times for 1h duration time on the same substrate and each time the chemical bath solution was refreshed. The ZnS films were etched in 5% HF solution to remove the loosely adhered ZnS particles on the film surface, then washed with propanol and finally dried in air. At the end of the deposition, four identical 250 nm thick films were obtained and these nanocrystalline films were annealed at 150 °C, 250 °C, and 350 °C temperatures in an air atmosphere.

3. Results and Discussion

3.1. Optical properties

The transmission spectra in the wavelength range of 300-1100 nm of the ZnS films were used to record

using a UV-visible spectrophotometer. The thickness of the films was calculated from the transmission interference using the following equation,

$$t = \frac{1}{2n \left(\frac{1}{\lambda_2} - \frac{1}{\lambda_1} \right)} \quad (1)$$

where t is the film thickness, n is refractive index, and λ_1 and λ_2 are adjacent maxima or minima of the transmission spectra [15]. The absorption coefficients were calculated by Beer-Lambert law using the transmission spectrum.

$$\alpha = A(h\nu - E_g)^n / h\nu \quad (2)$$

where A is a constant, α is absorption coefficient, $h\nu$ is the photon energy and n is also a constant, equal to 1/2 for direct band gap semiconductor [16].

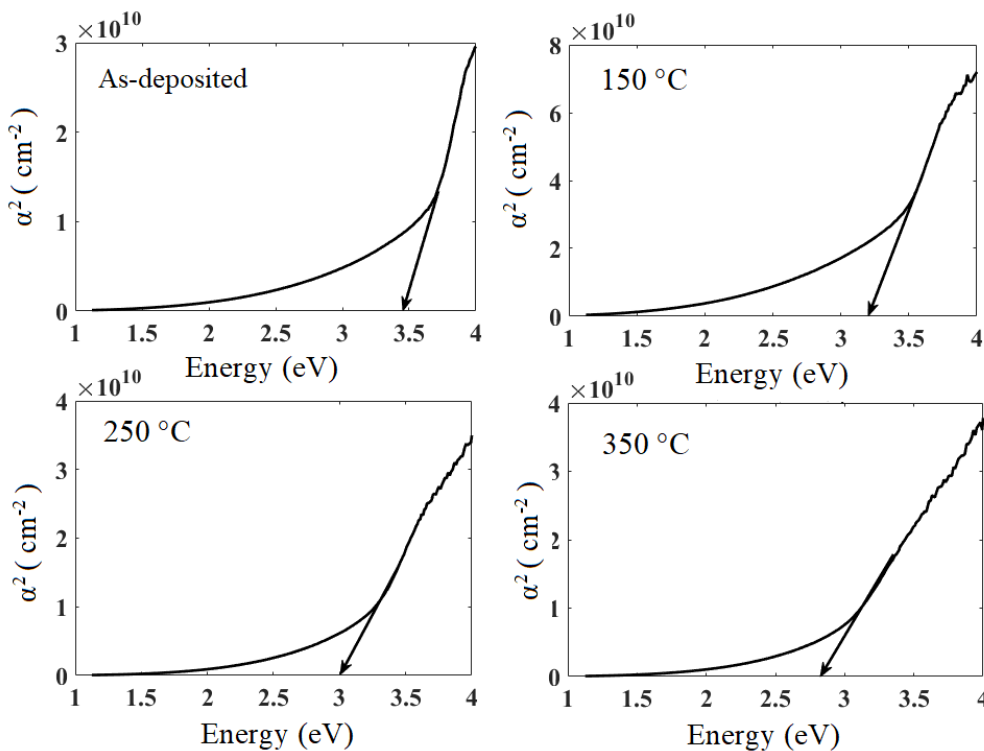


Figure 1. The α^2 versus photon energy of the ZnS films.

The band gap energy (E_g) is the energy value where $\alpha^2 = 0$ as shown in the energy versus absorption ($\alpha^2-h\nu$) graphs in Figure 1. The band gap energy and thickness changes of as-deposited and annealed ZnS films depending on annealing temperature are shown in Figure 2. It was seen that as the film annealing temperature was raised, the optical absorption in the forbidden zone decreased and the film thickness

increased. This property suggests that as the annealing temperature is raised, the film quality is improved. The optical absorption in the band-to-band region is also seen to decrease with the film annealing temperature. Since the size of the inter-granular empty space in the films increases as the annealing temperature increases, the density of the film decreases (lower α values). Optical scattering was also observed changes with

annealing temperature and this change was seen from the long-wavelength region in the absorption graph. The E_g of the as-deposited film (3.48 eV) is nearly identical to that of bulk ZnS (3.67 eV) [17, 18]. The optical absorption of films (at 150 °C, 250 °C and 350 °C) becomes sharper in the 300-400 nm wavelength region with annealing. Here, it is possible to identify the excitonic absorption. In the same region, the as-deposited film gives a broadened absorption spectrum. This observation can be explained as follows. In thinner films, the excitonic absorption/bulk absorption ratio is greater than thicker films, so the excitonic absorption can be observed much more easily. As the thicknesses of the films decrease, the ratio of surface to volume increases. A hole at the surface has a lower probability of catching an electron than a hole in the bulk. So, we expect that thinner films would show significant excitonic absorption than thicker films.

3.2. Morphological properties

The surface morphology of the ZnS nanocrystalline thin films was investigated in the SEM images, recorded with a Zeiss-Supra 55 SEM equipped with an energy dispersive X-ray (EDS) spectrometer. The SEM images in Figure 3 show that the samples are free of impurities and structural defects. The morphology, grain structure, and surface characteristics of the ZnS samples obtained at temperatures 150, 250 and 350 °C were almost similar. It can also be seen in Figure 3 that small spherical nanosized ZnS grains were well-deposited and homogeneous on the glass substrate. It was observed with increasing annealing temperature that the bigger particles are formed. This growth of particle size of the ZnS thin films is due to particle coalescence. The elemental ratio Zn : S was found to be more than three times higher (Zn : S elemental percentage ratio 77 : 23) in the quantitative analysis of the as-deposited ZnS thin film made with EDS and EDS graph is shown in Figure 4.

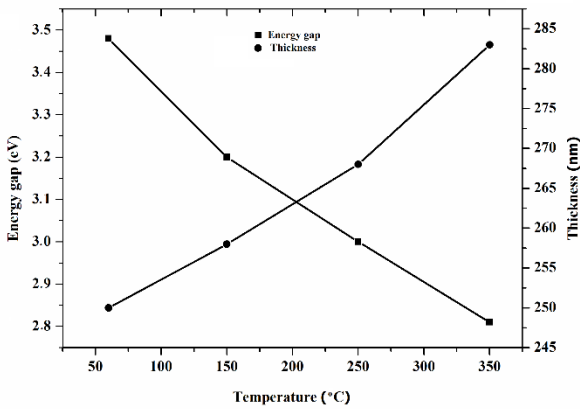


Figure 2. Temperature dependence of the thickness and energy gap of the ZnS films.

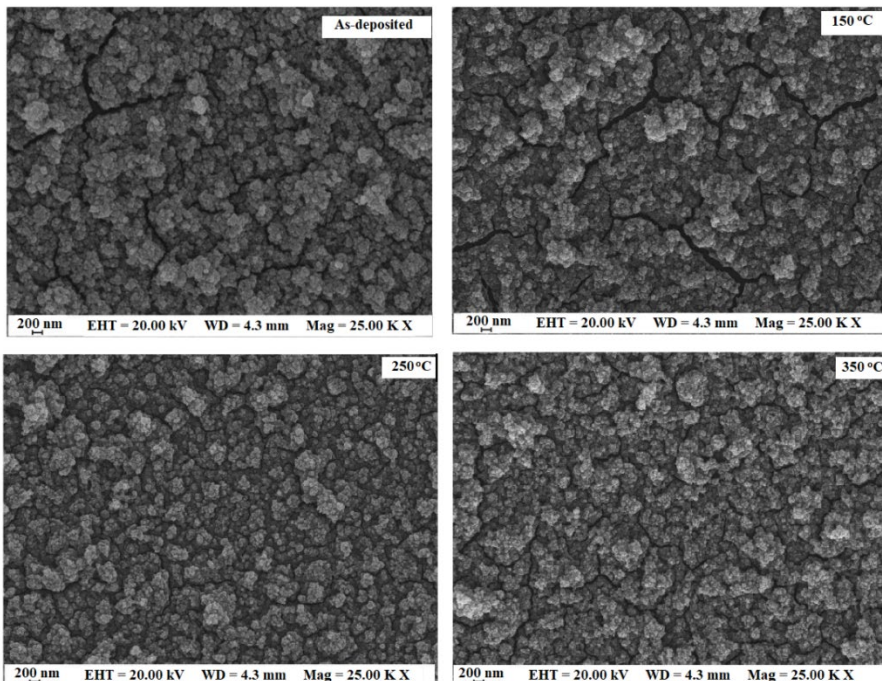


Figure 3. The SEM images of the ZnS films at different temperatures.

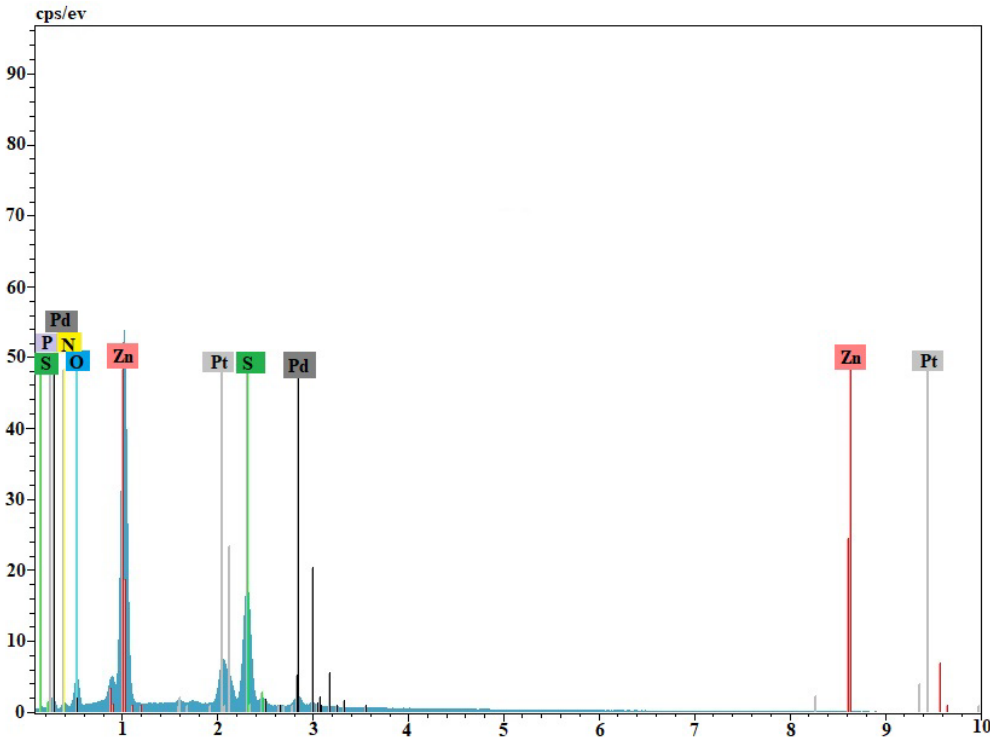


Figure 4. The EDS graph of the as-deposited ZnS films.

3.3. Structural properties

The structural properties of ZnS nanocrystalline thin films were investigated by Rigaku Smart Lab X-ray diffractometer using $\text{CuK}\alpha$ radiation ($\lambda = 1.54 \text{ \AA}$). The XRD graph of the as-deposited and annealed ZnS films is shown in Figure 5. Figure 5 shows that although there was a peak at the as-deposited film, this peak was lost at the annealed films. The plane indices of the observed “d” are obtained, by using the standard value of the “d” for the ZnS thin films, which are given by hexagonal (H) (JPSD Card No: 01-074-5002). The standard “d” values are in good agreement with the observed “d” values of the as-deposited ZnS. When the images of the annealed ZnS thin films were investigated, it was seen that broadening in the diffraction peaks of the films. This is due to the existence of nanosized materials. No peak was observed at annealed films because all films were amorphous, as seen in earlier studies [14, 19].

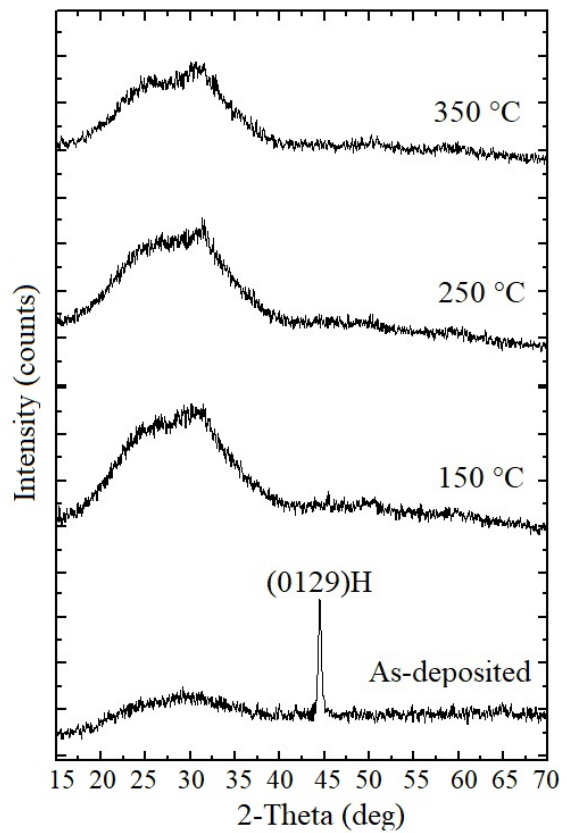


Figure 5. X-ray diffractograms of the as-deposited and the annealed ZnS films at different temperatures.

3.4. Electrical properties

The electrical conductivity of the ZnS nanocrystalline thin films was measured as a function of temperature in the range of 50-400 °C using the four-point probe technique. The resistivity and conductivity were determined as described in our previous publication [16].

Figure 6 shows the conductivity of the films as a function of temperature. The conductivity values are between 10^{-6} – 10^{-5} (Ω - cm)⁻¹ at the temperature range of 50-400 °C as seen in Figure 6. The conductivity of as-deposited and annealed (at 150 °C, 250 °C and 350 °C) films increases exponentially with the increasing

temperature, as is typical semiconductors. There are two distinct conductivity regions in Figure 6. Activation energies can be calculated using these regions. For this, the activation energy E_a of the ZnS films has been calculated by $\sigma = \sigma_o \exp(-E_a / k_B T)$ equation, where σ is the conductivity of the films, σ_o is the pre-exponential factor, E_a is activation energy, k_B is Boltzmann constant and T is temperature. The activation energy values of the films were calculated for two distinct temperature regions such as low temperature region (LT) ($40 \text{ }^\circ\text{C} \leq T \leq 250 \text{ }^\circ\text{C}$) and high temperature region (HT) ($250 \text{ }^\circ\text{C} \leq T \leq 400 \text{ }^\circ\text{C}$). Calculated values were shown in Table 1.

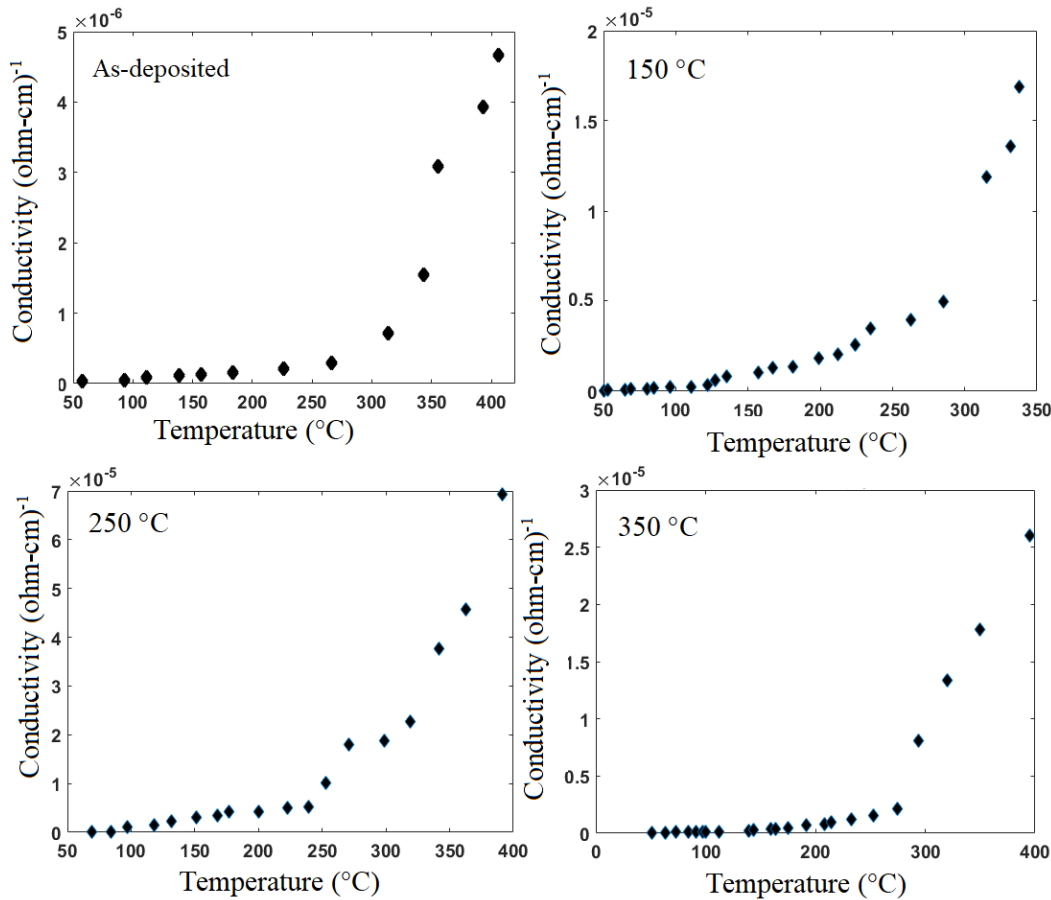


Figure 6. Temperature dependence of the electrical conductivity of the as-deposited and annealed ZnS films.

Table 1. The activation energies of the ZnS films.

Annealing temperature (°C)	LR (meV)	HR (meV)
As-deposited	10.00	29.00
150	20.00	23.00
250	15.00	25.00
350	14.00	30.00

LR: Low temperature region and HR: High temperature region

Except for the four-point probe technique, we used the Hall effect method to better understand the electrical properties. By this method, the electrical properties of the ZnS films were determined at room temperature using a Hall effect measurement generated by the Van der Pauw geometry. Hall effect measurements were performed by making ohmic contacts on four corners of the ZnS films. The magnitude of the magnetic field and current values were taken as 0.54 Tesla and 1 mA, respectively. Hall measurements for each sample were

repeated several times to ensure the reliability of the results.

The Hall effect measurements accomplished for as-deposited and annealed ZnS films are given in Table 2. All of the ZnS thin films that were as-deposited and annealed were n-type materials. With increasing annealing temperature, there was no significant change in carrier concentration and resistivity. It was observed

that the resistivity of the ZnS films were very low due to the excess of Zn in the structure. The higher mobility of the annealed ZnS films can be explained by the increasing grain size which was caused that annealing. Similar results have been given in previous work [20–24].

Table 2. The Hall Effect measurements of the ZnS films.

Annealing temperature (°C)	Carrier concentration (cm ⁻³)	Mobility (cm ² /Vs)	Resistivity (Ω - cm)	Carrier type
As-deposited	1.526 x 10 ¹²	4.768 x 10 ¹	8.576 x 10 ⁴	n
150	1.147 x 10 ¹³	6.551 x 10 ⁰	8.311 x 10 ⁴	n
250	1.835 x 10 ¹²	4.344 x 10 ¹	7.832 x 10 ⁴	n
350	1.351 x 10 ¹²	6.142 x 10 ¹	7.523 x 10 ⁴	n

4. Conclusions

The optical results of the ZnS films show that as the annealing temperature was increased, the film thickness increased, and the band gap energy (E_g) decreased from 3.36 to 2.82 eV. The grain structure and surface properties of as-deposited and annealed ZnS nanocrystalline films, which were coated well and homogeneously on the glass substrate and composed of small spherical nanoscale particles, were shown by SEM images of the films. It was also observed that the grain size increased for ZnS thin films and intergranular cavities increased with the increasing annealing temperature. XRD data showed that all of the annealed films were in the amorphous phase. The ZnS thin films were determined to be n-type using Hall measurements, and the carrier type did not change as the annealing temperature increased. In addition, it was observed in the four-point probe measurement data with increasing annealing temperature that the conductivity increased and the resistivity decreased, as seen in semiconductors. Considering all of these findings, it's possible to say that ZnS films might be used as buffer layers in CIGS solar cells.

Acknowledgment

This study was supported by the Scientific Research Project Fund of Mersin University with Project Numbers: 2017-2-TP3-2593 and 2017-2-TP2-2573. The authors would like to thank the Mersin

University Advanced Technology Education Research and Application Center (MEİTAM) for its technical support and Prof. Dr. Ramazan Esen for the Hall measurements.

Conflicts of interest

Sample sentences if there is no conflict of interest: The authors state that did not have conflict of interests.

References

- [1] Ojo A. A., Influence of electroplating temperature on the characteristic properties of zinc sulphide, *Mater. Res. Express*, 6 (2019).
- [2] Igweoko A. E., Augustine C., Idenyi N. E., Okorie B. A., Anyaegbunam F. N. C., Influence of processing conditions on the optical properties of chemically deposited zinc sulphide (ZnS) thin film, *Mater. Res. Express*, 5 (2018).
- [3] Nabiyouni G., Sahraei R., Toghiani M., Ara M. H. M., Hedayati K., Preparation and characterization of nanostructured ZnS thin films grown on glass and N-type Si substrates using a new chemical bath deposition technique, *Rev. Adv. Mater. Sci.*, 27 (2011) 52–57.
- [4] Metin H., Esen R., Changes on the Structural and Optical Properties of ZnS Films by Chemical Bath

Deposition Technique on Annealing in Air Atmosphere, *Cumhur. Univ. Fac. Arts Sci. - J. Sci.*, 28 (3) (2003) 82–91.

- [5] Xie Y. et al., Improving performance in CdTe/CdSe nanocrystals solar cells by using bulk nano-heterojunctions, *J. Mater. Chem. C*, 4 (2016) 6483–6491.
- [6] Zhou L., Tang N., Wu S., Hu X., Xue Y., Influence of deposition time on ZnS thin films performance with chemical bath deposition, *Phys. Procedia*, 22 (2011) 354–359.
- [7] Ortega-Cardenas J. A., Albor-Aguilera M. L., Hernabdez-Vasquez C., Impact of different thermal treatments on ZnS physical properties and their performance in CdTe solar cells, *Mater. Res. Express*, 6 (8) (2019).
- [8] Haddad H., Chelouche A., Talantikite D., Merzouk H., Boudjouan F., Djouadi D., Effects of deposition time in chemically deposited ZnS films in acidic solution, *Thin Solid Films*, 589 (2015) 451–456.
- [9] Arenas O. L., Nair M. T. S., Nair P. K., Chemical bath deposition of ZnS thin films and modification by air annealing, *Semicond. Sci. Technol.*, 12 (1997) 1323–1330.
- [10] Göde F., Güneri E., Kariper A., Ulutaş C., Kirmizigül F., Gümüş C., Influence of annealing temperature on the structural, optical and electrical properties of amorphous Zinc Sulfide thin films, 17th International Conference on Microscopy of Semiconducting Materials 2011- Journal of Physics: Conference Series, 2011.
- [11] Nwofe P. A., Robert B. J., Agbo P. E., Influence of processing parameters on the structural and optical properties of chemically deposited Zinc Sulphide thin films, *Mater. Res. Express*, 5 (10) (2018).
- [12] Talantikite-Touati D., Merzouk H., Haddad H., Tounsi A., Effect of dopant concentration on structural and optical properties Mn doped ZnS films prepared by CBD method, *Optik*, 136 (2017) 362–367.
- [13] Jobzari H. G., Iranmanesh P., Sabet M., Saeednia S., Effect of synthesis method and chemical reagents on the structural parameters, particle size, and optical and photoluminescence properties of ZnS nanostructures, *Luminescence*, (2019) 1-10.
- [14] Nikzad M., Khanlary M. R., Rafiee S., Structural , optical and morphological properties of Cu -doped ZnS thin films synthesized by sol – gel method, *Appl. Phys. A Mater. Sci. Process.*, 125 (507) (2019).
- [15] Pankove J. I., Optical Processes in Semiconductors. New York: Dover Publications, (1971).
- [16] Metin H., Erat S., Arı M., Bozoklu M., Characterization of CdSe films prepared by chemical bath deposition method, *Optoelectron. Adv. Mater. Rapid Commun.*, 2 (2) (2008) 92–98.
- [17] Yang K., Li B., Zeng G., Effects of temperature on properties of ZnS thin films deposited by pulsed laser deposition, *Superlattices Microstruct.*, 130 (2019) 409–415.
- [18] Liang G., Fan P., Chen C., Luo J., Zhao J., Zhang D., Improved microstructure and properties of CBD-ZnS thin films, *J. Mater. Sci. Mater. Electron.*, 26 (2015) 2230–2235.
- [19] Wei A., Liu J., Zhuang M., Zhao Y., Preparation and characterization of ZnS thin films prepared by chemical bath deposition, *Mater. Sci. Semicond. Process.*, 16, (6) (2013) 1478–1484.
- [20] Bakiyaraj G., Gopalakrishnan N., Dhanasekaran R., Influences of thermal annealing on the structural, optical and electrical properties of nanostructured cadmium sulphide thin films, *Chalcogenide Lett.*, 8 (7), (2011) 419–426.
- [21] Erdogan N. H., Kara K., Ozdamar H., Esen R., Kavak H., Effect of the oxidation temperature on microstructure and conductivity of Zn x N y thin films and their conversion into p-type ZnO:N films, *Appl. Surf. Sci.*, 271 (2013) 70–76.
- [22] Khallaf H., Oladeji I. O., Chow L., Optimization of chemical bath deposited CdS thin films using nitrilotriacetic acid as a complexing agent, *Thin Solid Films*, 516 (2008) 5967–5973.
- [23] Liu F. et al., Characterization of chemical bath deposited CdS thin films at different deposition temperature, *J. Alloys Compd.*, 493 (2010) 305–308.

- [24] Kose S., Atay F., Bilgin V., Akyuz I., Ketenci E.,
Optical characterization and determination of
carrier density of ultrasonically sprayed CdS:Cu
films, *Appl. Surf. Sci.*, 256 (2010) 4299–4303.



How to use adjusted degree of distinguishability and inter-rater reliability simultaneously?

Ayfer Ezgi YILMAZ^{1,*} 

¹Hacettepe University, Faculty of Science, Department of Statistics, Ankara/TURKEY

Abstract

When the categories of a square contingency table are ordinal, weighted kappa or Gwet's AC2 coefficients are used to summarize the degree of reliability between two raters. In addition, investigating the reliability among raters, the term category distinguishability should be considered. The study aims to assess the inter-rater reliability and category distinguishability in ordinal rating scales together. The weighted kappa, AC2, and adjusted degree of distinguishability coefficients are applied to pathology data. The results are discussed over the pathologist pairs.

Article info

History:

Received:16.03.2021
Accepted:06.08.2021

Keywords:

Ordinal rating scales,
Inter-rater reliability,
Adjusted degree of
distinguishability,
Weighted kappa,
AC2 coefficient.

1. Introduction

Square contingency tables are occurred with the same row and column classification [1] and are frequently used in many fields, such as medicine, sociology, and behavioral sciences [2]. When working on these kinds of tables, the inter-rater reliability of row and column variables is investigated. Inter-rater reliability shows the accuracy of the measurement of the data collected in the study, thus it has great importance [3]. It is expected to have reliable results when the severity of the disease is evaluated by several raters during a clinical trial when the radiographs are evaluated by trauma surgeons and radiologists, when two clinicians classified the patients in three categories according to their syndrome type, when the severity of depression is evaluated by two psychiatrists, or when a sample of interview protocols is examined by three evaluators.

The reliability of the raters is to be determined by measuring inter-rater agreement coefficients. Cohen's weighted kappa coefficient which is the most popular coefficient and AC2 coefficients are used to determine the level of agreement between the ordinal classifications of two raters [4,5].

It is also important to determine the distinguishability of the categories (or the severity of the disease). When the categories are not defined clearly or when the raters are not expert enough in their field, the distinguishability of the categories becomes lower. If

the reason is unclearly defined categories, then different raters may understand these categories differently or even the same rater may not distinguish the categories correctly. As a result of this indistinguishability, there occurs a low agreement.

In this study, it is purposed to assess the inter-rater agreement coefficients and category distinguishability in ordinal rating scales together. It is aimed to discuss how category distinguishability affects the level of reliability, and the possible solutions of low distinguishability are. Degree of distinguishability, weighted kappa, and AC2 coefficients are applied to a very well-known carcinoma in situ of the uterine cervix data. The results are discussed over the pairs of pathologists. The coefficients to measure inter-rater reliability and adjusted degree of distinguishability are introduced in Section 2. The pathology data is analyzed in Section 3, followed by the conclusions in Section 4.

2. Materials and Methods

2.1. Inter-rater agreement coefficients

Cohen's weighted kappa coefficient [4] is suggested for the analysis of reliability between the classifications of two raters. Suppose two raters rate n observations into R categories, independently. Let π_{ij} is the probability of cell (i, j) where π_i indicates the i th row total

*Corresponding author. e-mail address: ezgiyilmaz@hacettepe.edu.tr
<http://dergipark.gov.tr/csj> ©2021 Faculty of Science, Sivas Cumhuriyet University

probability and π_j indicates the j th column total probability. The weighted kappa coefficient (κ_w) is

$$\kappa_w = \frac{\sum_{i=1}^R \sum_{j=1}^R w_{ij} \pi_{ij} - \sum_{i=1}^R \sum_{j=1}^R w_{ij} \pi_i \pi_j}{1 - \sum_{i=1}^R \sum_{j=1}^R w_{ij} \pi_i \pi_j} \quad (1)$$

Gwet's AC2 coefficient [5] is suggested to overcome the prevalence and marginal probability problem of Cohen's kappa. AC2 coefficient is

$$AC2 = \frac{\sum_{i=1}^R \sum_{j=1}^R w_{ij} \pi_{ij} - \frac{w_T}{R(R-1)} \sum_{j=1}^R p_i (1 - p_i)}{1 - \frac{w_T}{R(R-1)} \sum_{j=1}^R p_i (1 - p_i)} \quad (2)$$

where

$$w_T = \sum_{i=1}^R \sum_{j=1}^R w_{ij} \quad (3)$$

and

$$p_i = (\pi_i + \pi_j)/2. \quad (4)$$

In Equations 1-3, w_{ij} are the weights range $0 < w_{ij} < 1$. Even there are many suggested weighting schemes, linear and quadratic weights are the well-known ones. For different weighting schemes in the literature, see [2].

- Linear weights [6]:

$$w_{ij} = 1 - \frac{|i - j|}{R - 1} \quad (5)$$

- Quadratic weights [7]:

$$w_{ij} = 1 - \frac{(i - j)^2}{(R - 1)^2} \quad (6)$$

In the literature, there are several interpretations of the kappa coefficient. The inference shown in Table 1 is the well-known one and can be assigned to the corresponding ranges of kappa [8].

Table 1. Interpretation of the kappa coefficient

Kappa	Strength of Agreement
0.81-1.00	Almost Perfect
0.61-0.80	Substantial
0.41-0.60	Moderate
0.00-0.20	Slight
<0.00	Poor

2.2. Category distinguishability

One of the assumptions of the kappa coefficient is the raters should rate the items independently. Even

though the raters rate the items independently, because of the ordinal structure of the table, there occurs a correlation between their decisions. There are two main components of agreement: (1) Marginal homogeneity which corresponds to the differences in the marginal distributions of raters and (2) category distinguishability which is the ability for raters to distinguish the categories [9].

In the agreement studies, it is necessary to determine if the categories of the table are distinguishable from one to another [10]. If the categories are indistinguishable, then there could occur some differences between raters' perceptions. The categories may not be distinguished because of two reasons. The first problem might be due to the definition of the categories. Different raters may understand the categories differently or the same rater may not distinguish the categories correctly. The second problem might be due to the nonexpert raters. The raters may not be experts in their fields and it may be difficult to distinguish the categories. The measure to calculate the distinguishability level of the categories is called the degree of distinguishability.

The degree of distinguishability is suggested to investigate the ability of the raters to distinguish between two categories [9]. The adjusted version of the degree of distinguishability (ADD) is suggested by Yilmaz and Saracbası [11]. ADD between i and $i + 1$ categories is calculated as

$$ADD_{i,i+1} = \begin{cases} 1 - \tau_{i,i+1}^{-1} & \text{if } \tau_{i,i+1} \geq 1, \\ 1 - \tau_{i,i+1} & \text{if } \tau_{i,i+1} < 1, \end{cases} \quad (7)$$

where $0 < ADD_{i,i+1} < 1$, $i = 1, 2, \dots, (R - 1)$. The odds ratio for square contingency tables is

$$\tau_{i,i+1} = \frac{\pi_{ii} \pi_{i+1,i+1}}{\pi_{i,i+1} \pi_{i+1,i}} \quad (8)$$

The interpretation levels of ADD are given in Table 2 [11].

Table 2. Interpretation of ADD

ADD	Strength of Distinguishability
>0.99	Perfect
0.94-0.99	Substantial
0.82-0.93	Moderate
0.57-0.81	Fair
0.00-0.56	Poor

3. The Pathology Data

The pathology data discussed by Holmquist, McMahon, and Williams [12] is used to illustrate the use of the adjusted degree of distinguishability and

inter-rater reliability. To investigate the variability in the classification of carcinoma in situ of the uterine cervix, seven pathologists are classifying 118 biopsy slides into five categories: (1) Negative, (2) Atypical Squamous Hyperplasia, (3) Carcinoma in Situ, (4) Squamous Carcinoma with Early Stromal Invasion, and (5) Invasive Carcinoma.

This data set has also been analyzed in the studies of Landis and Koch [13], Becker and Agresti [14], and Agresti [15]. In their studies, the categories are reclassified into three or four categories as (1), (2), (3)+(4)+(5) or (1), (2), (3), (4)+(5).

It is aimed to investigate carcinoma in situ of uterine cervix data from the point of inter-rater reliability, from the point of category distinguishability, and also from the point of inter-rater reliability and category distinguishability together.

3.1. From the point of inter-rater reliability

The estimated values of weighted kappa and AC2 coefficients with linear and quadratic weights, their standard errors are summarized in Figure 1 for each pair of pathologists. The levels of agreement are highlighted by Landis and Koch [8] intervals.

PAIR	Kw_L	Sdt.Error	PAIR	Kw_Q	Sdt.Error	PAIR	AC2_L	Sdt.Error	PAIR	AC2_Q	Sdt.Error
EF	0.266	0.052	EF	0.365	0.077	EF	0.440	0.049	EF	0.628	0.056
BF	0.320	0.055	BF	0.419	0.076	AF	0.463	0.051	AF	0.633	0.058
AF	0.334	0.052	AF	0.452	0.071	BF	0.518	0.045	BF	0.702	0.042
DE	0.343	0.054	DE	0.471	0.072	DE	0.550	0.042	AD	0.732	0.047
BD	0.406	0.054	CF	0.499	0.087	AD	0.579	0.045	DE	0.741	0.042
FG	0.406	0.055	FG	0.510	0.073	BD	0.604	0.040	AC	0.769	0.050
CF	0.408	0.060	BD	0.523	0.073	FG	0.610	0.041	FG	0.774	0.037
CE	0.429	0.056	CE	0.524	0.082	CF	0.623	0.043	CF	0.774	0.045
AD	0.440	0.052	BC	0.532	0.086	AC	0.630	0.044	BD	0.783	0.041
BC	0.454	0.059	AD	0.549	0.067	CE	0.633	0.042	CE	0.788	0.044
DF	0.462	0.055	CD	0.554	0.080	AE	0.655	0.040	BC	0.807	0.037
CD	0.477	0.058	AC	0.586	0.076	BC	0.663	0.041	AE	0.809	0.039
AC	0.494	0.053	DF	0.597	0.071	DF	0.679	0.038	CD	0.818	0.038
AE	0.509	0.053	CG	0.622	0.079	CD	0.684	0.040	DF	0.832	0.034
DG	0.545	0.052	AE	0.632	0.068	AG	0.700	0.039	AG	0.832	0.037
EG	0.550	0.053	EG	0.643	0.072	AB	0.713	0.039	AB	0.837	0.036
CG	0.557	0.056	DG	0.654	0.071	DG	0.713	0.035	CG	0.851	0.035
AG	0.563	0.050	AB	0.663	0.068	CG	0.735	0.037	DG	0.855	0.033
AB	0.572	0.054	AG	0.667	0.064	EG	0.736	0.038	EG	0.859	0.034
BE	0.586	0.054	BE	0.679	0.073	BE	0.764	0.036	BE	0.880	0.032
BG	0.651	0.055	BG	0.699	0.074	BG	0.814	0.034	BG	0.895	0.029

Fair

Moderate

Substantial

Almost perfect

Figure 1. The levels of inter-rater reliability that are highlighted by Landis and Koch's intervals

The results show that the values of quadratically weighted agreement coefficients are higher than the linearly weighted ones. Furthermore, the values of the AC2 coefficient are higher than the weighted kappa. The value of the inter-rater reliability is higher when the quadratically weighted AC2 coefficient is used and is lower when the linearly weighted kappa coefficient is used.

According to the linearly weighted kappa results, there are fair agreements between Pathologists E and F, B and F, A and F, D and E. According to the quadratically weighted kappa results, there is a fair agreement between Pathologists E and F. According to the AC2 coefficient results, there are more than fair agreements between all the pairs of pathologists. In general, Pathologist F has a low agreement with the other pathologists. The highest agreement is observed between Pathologists B and G, B and E.

As the overall agreement coefficient, Light's weighted kappa [16] is used. Linearly weighted Light's kappa is calculated as 0.465 and the quadratically weighted one is calculated as 0.564. There is a moderate agreement between the seven pathologists' decisions.

3.2. From the point of category distinguishability

The levels of ADD that are highlighted by Yilmaz and Saracbası [11] intervals are given in Figure 2 for the adjacent categories. The results show that six pairs of pathologists cannot classify (1) and (2) well. Three pairs of pathologists cannot classify (2) and (3) well. 14 pairs of pathologists cannot classify (3) and (4) well. 10 pairs of pathologists cannot classify (4) and (5) well. In general, pathologists have difficulties classifying the last three categories.

According to the results in Figure 2, when Pathologists C and E cannot distinguish (1) and (2) well, Pathologist G substantially distinguishes. When Pathologist F

cannot distinguish (2) and (3) well, Pathologist G substantially distinguishes. When Pathologist F cannot distinguish (3) and (4) well, Pathologist B substantially

distinguishes. When Pathologists D, G, and F cannot distinguish (4) and (5) well, Pathologist B substantially distinguishes.

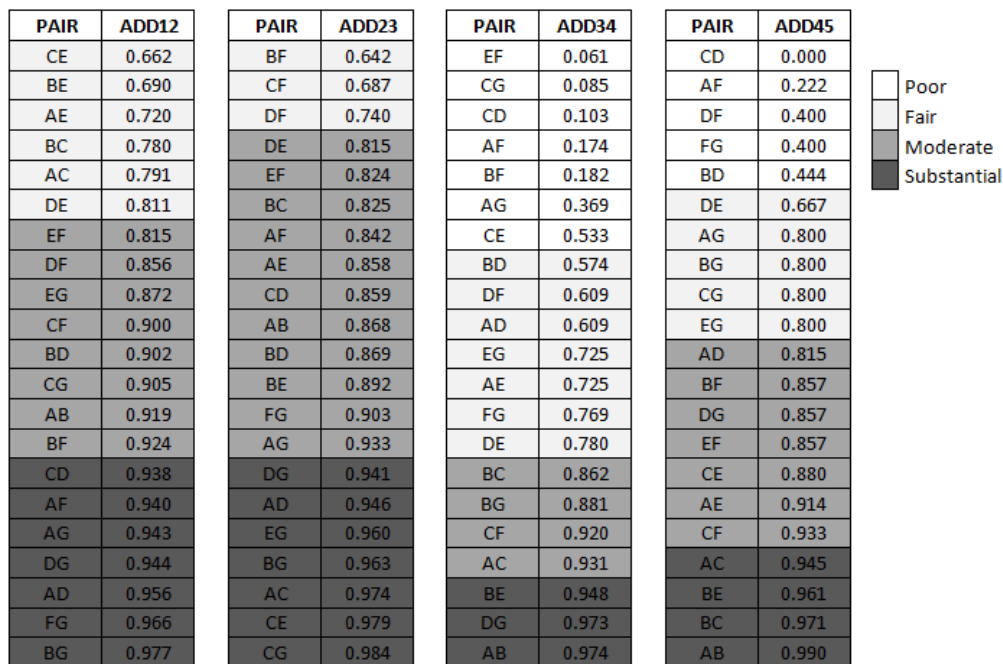


Figure 2. The levels of ADD that are highlighted by Yilmaz and Saracbası's intervals

3.3. From the point of reliability and category distinguishability

According to the inter-rater agreement coefficients, it is concluded that there are fair inter-rater reliabilities between Pathologists A and F, B and F, D and E, E and F. One of the reasons for the low agreement is a low ability of distinguishability. The unclearly defined

categories or non-expert pathologists may cause a low distinguishability. In this section, the sub-tables that low agreements occur are analyzed in more detail.

Pathologists A and F

The estimated values of linearly weighted inter-agreements and ADD coefficients of Pathologists A and F are summarized in Table 3.

Table 3. The summary of the linearly inter-agreements and ADD coefficients of Pathologists A and F

	ADD				Inter-Rater Agreement	
	12	23	34	45	κ_w (Std. Error)	AC2 (Std. Error)
Estimate	0.940	0.842	0.174	0.222	0.334 (0.052)	0.463 (0.051)
Level	Substantial	Moderate	Poor	Poor	Fair	Moderate

The results show that there is poor distinguishability between (3) and (4), and between (4) and (5). A poor distinguishability indicates that pathologists A and F cannot distinguish these categories well. Thus, the categories can be combined as (3+4), (4+5), or (3+4+5). Linearly inter-rater agreement and ADD

coefficients for adjacent categories are calculated for the reclassified tables. The results of the three alternatives are:

Alternative 1: 1, 2, (3+4), 5

	ADD			Inter-Rater Agreement	
	12	2(3+4)	(3+4)5	κ_w (Std. Error)	AC2 (Std. Error)
Estimate	0.940	0.908	0.968	0.366 (0.054)	0.479 (0.051)
Level	Substantial	Moderate	Substantial	Fair	Moderate

Alternative 2: 1, 2, 3, (4+5)

	ADD			Inter-Rater Agreement	
	12	23	3(4+5)	κ_w (Std. Error)	AC2 (Std. Error)
Estimate	0.940	0.842	0.890	0.329 (0.049)	0.331 (0.063)
Level	Substantial	Moderate	Moderate	Fair	Fair

Alternative 3: 1, 2, (3+4+5)

	ADD		Inter-Rater Agreement	
	12	2(3+4+5)	κ_w (Std. Error)	AC2 (Std. Error)
Estimate	0.940	0.924	0.364 (0.052)	0.272 (0.072)
Level	Substantial	Moderate	Fair	Fair

Alternative 1 is suggested to use because the highest values of inter-rater agreement coefficients are observed. The linearly weighted kappa increases to 0.366 and linearly weighted AC2 is increases to 0.479 after the reclassification 1. For the first alternative, the adjusted degree of distinguishability of (2) and (3+4) increases to moderate, the adjusted degree of

distinguishability of (3+4) and (5) increases to a substantial level.

Pathologists B and F

The estimated values of linearly weighted inter-agreements and ADD coefficients of Pathologists B and F are summarized in Table 4.

Table 4. The summary of the linearly inter-agreements and ADD coefficients of Pathologists B and F

	ADD				Inter-Rater Agreement	
	12	23	34	45	κ_w (Std. Error)	AC2 (Std. Error)
Estimate	0.924	0.642	0.182	0.857	0.320 (0.055)	0.518 (0.045)
Level	Moderate	Fair	Poor	Moderate	Fair	Moderate

The results show that there is poor distinguishability between (3) and (4). A poor distinguishability indicates that pathologists B and F cannot distinguish these categories well. Thus, the categories can be

combined as (2+3) or (3+4). Linearly inter-rater agreement and ADD coefficients for adjacent categories are calculated for the reclassified tables. The results of the two alternatives are:

Alternative 1: 1, (2+3), 4, 5

	ADD			Inter-Rater Agreement	
	1(2+3)	(2+3)4	45	κ_w (Std. Error)	AC2 (Std. Error)
Estimate	0.988	0.716	0.857	0.421 (0.070)	0.739 (0.037)
Level	Substantial	Fair	Moderate	Moderate	Substantial

Alternative 2: 1, 2, (3+4), 5

	ADD			Inter-Rater Agreement	
	12	2(3+4)	(3+4)5	κ_w (Std. Error)	AC2 (Std. Error)
Estimate	0.924	0.726	0.990	0.324 (0.053)	0.451 (0.051)
Level	Moderate	Fair	Substantial	Fair	Moderate

Alternative 1 is suggested to use because the highest values of inter-rater agreement coefficients are observed. The linearly weighted kappa increases to 0.421 and linearly weighted AC2 increases to 0.759 after the reclassification 1. For the first alternative, the adjusted degree of distinguishability of (1) and (2+3) is at a substantial level and the adjusted degree of distinguishability of (2+3) and (4) is at a fair level.

Pathologists D and E

The estimated values of linearly weighted inter-agreements and ADD coefficients of Pathologists D and E are summarized in Table 5.

Table 5. The summary of the linearly inter-agreements and ADD coefficients of Pathologists D and E

	ADD				Inter-Rater Agreement	
	12	23	34	45	κ_w (Std. Error)	AC2 (Std. Error)
Estimate	0.811	0.815	0.780	0.667	0.343 (0.054)	0.550 (0.042)
Level	Moderate	Moderate	Fair	Fair	Fair	Moderate

The results show that there is fair distinguishability between (3) and (4), and between (4) and (5). A poor distinguishability indicates that Pathologists D and E cannot distinguish these categories well. Thus, the categories can be combined as (3+4), (4+5), or

(3+4+5). Linearly inter-rater agreement and ADD coefficients for adjacent categories are calculated for the reclassified tables. The results of the three alternatives are:

Alternative 1: 1, 2, (3+4), 5

	ADD			Inter-Rater Agreement	
	12	2(3+4)	(3+4)5	κ_w (Std. Error)	AC2 (Std. Error)
Estimate	0.811	0.817	0.971	0.368 (0.054)	0.567 (0.041)
Level	Moderate	Moderate	Substantial	Fair	Moderate

Alternative 2: 1, 2, 3, (4+5)

	ADD			Inter-Rater Agreement	
	12	23	3(4+5)	κ_w (Std. Error)	AC2 (Std. Error)
Estimate	0.811	0.815	0.900	0.353 (0.053)	0.444 (0.050)
Level	Moderate	Moderate	Moderate	Fair	Moderate

Alternative 3: 1, 2, (3+4+5)

	ADD		Inter-Rater Agreement	
	12	2(3+4+5)	κ_w (Std. Error)	AC2 (Std. Error)
Estimate	0.811	0.823	0.384 (0.053)	0.389 (0.058)
Level	Moderate	Moderate	Fair	Fair

The highest value of linearly weighted kappa coefficient is observed when Alternative 3 is used and the highest value of linearly weighted AC2 coefficient is observed when Alternative 1 is used. The linearly weighted kappa increases to 0.364 after reclassification 3 and increases to 0.368 after reclassification 1. The linearly weighted AC2 increases to 0.567 after reclassification 1 and decreases to 0.389 after reclassification 3.

For the first alternative, the poor distinguishability increase to a substantial level after the reclassification as (3+4). For the third alternative, the adjusted degree

of distinguishability of (2) and (3+4+5) increases to a moderate level.

Even though the value of linearly weighted kappa in Alternative 1 is less than the value of kappa obtained from Alternative 3, the values of linearly weighted AC2 and ADD coefficients are higher. Thus, Alternative 1 is suggested to use the interpretation of Pathologists D and E's results.

Pathologists E and F

The estimated values of linearly weighted inter-agreements and ADD coefficients of Pathologists E and F are summarized in Table 6.

Table 6. The summary of the linearly inter-agreements and ADD coefficients of Pathologists E and F

	ADD				Inter-Rater Agreement	
	12	23	34	45	κ_w (Std. Error)	AC2 (Std. Error)
Estimate	0.815	0.824	0.061	0.857	0.266 (0.052)	0.440 (0.049)
Level	Moderate	Moderate	Poor	Moderate	Fair	Moderate

The results show that there is poor distinguishability between (3) and (4). A poor distinguishability indicates that Pathologists E and F cannot distinguish

these categories well. Thus, the categories can be combined as (2+3) or (3+4). Linearly inter-rater agreement and ADD coefficients for adjacent

categories are calculated for the reclassified tables. The results of the two alternatives are:

Alternative 1: 1, (2+3), 4, 5

	ADD			Inter-Rater Agreement	
	1(2+3)	(2+3)4	45	κ_w (Std. Error)	AC2 (Std. Error)
Estimate	0.972	0.414	0.857	0.272 (0.066)	0.638 (0.045)
Level	Substantial	Poor	Moderate	Fair	Substantial

Alternative 2: 1, 2, (3+4), 5

	ADD			Inter-Rater Agreement	
	12	2(3+4)	(3+4)5	κ_w (Std. Error)	AC2 (Std. Error)
Estimate	0.815	0.858	0.990	0.281 (0.050)	0.406 (0.049)
Level	Moderate	Moderate	Substantial	Fair	Moderate

The highest value of linearly weighted kappa coefficient is observed when Alternative 2 is used and the highest value of linearly weighted AC2 coefficient is observed when Alternative 1 is used. The linearly weighted kappa increases to 0.272 after reclassification 1 and increased to 0.281 after reclassification 2. The linearly weighted AC2 increases to 0.638 after reclassification 1 and decreases to 0.406 after reclassification 2.

For the first alternative, even though the adjusted degree of distinguishability of (1) and (2+3) increases to a substantial level, the adjusted degree of distinguishability of (2+3) and (4) is still at a poor level. For the second alternative, even though the adjusted degree of distinguishability of (1) and (2) is still at a moderate level, the adjusted degree of distinguishability of (2) and (3+4) increases to moderate and the adjusted degree of distinguishability of (3+4) and (5) increases to a substantial level.

Even though the value of AC2 decreases, because the values of linearly weighted kappa and ADD coefficients increase, Alternative 2 is suggested to use the interpretation of Pathologists E and F's results.

4. Conclusions

In recent studies, inter-rater reliability and category distinguishability have grown importances. It has been proposing to use agreement coefficients and degree of distinguishability simultaneously [11]. This study is aimed to illustrate how to use inter-rater reliability and degree of distinguishability, together. For this purpose, the carcinoma in situ of uterine cervix data is used. Seven pathologists classify 118 slides into five ordinal categories to investigate the variability in the classification of carcinoma in situ of the uterine cervix. Landis and Koch [13], Becker and Agresti [14], and Agresti [15] reclassify the data into three or four

categories, however, the reclassification procedures are made by considering the zero cells or the researcher's personal experience.

Adjusted degree of distinguishability, weighted kappa, and AC2 coefficients are applied to data for 21 pairs of the seven pathologists. The results are discussed together in terms of inter-rater reliability, category distinguishability, and inter-rater reliability and category distinguishability together.

The inter-rater reliability results showed that the value of the quadratically weighted kappa is higher than the value of the linearly weighted kappa. Besides, the value of the quadratically weighted AC2 is higher than the value of the linearly weighted AC2, as well. Pathologist F has the lowest, Pathologists B and G have the highest agreement with the others.

The adjusted degree of distinguishability results showed that Pathologist F cannot distinguish the categories except categories 1 and 2. The reason is Pathologist F may have less experience than the other pathologists. Pathologists C and E cannot distinguish the categories 1 and 2. In general, because Pathologist F has a lower agreement between the other pathologists, it may be excluded from the study.

The results showed that the pathologists have some problems distinguishing the categories (3) Carcinoma in Situ, (4) Squamous Carcinoma with Early Stromal Invasion, and (5) Invasive Carcinoma, and the incorrect classifications affect the level of the agreement in this respect. It is suggested to recollect the data or to combine the categories as considering the category distinguishability. According to the poor and fair inter-rater reliability between Pathologists A and F, B and F, D and E, E and F, the degrees of distinguishability of these sub-tables are analyzed in more detail. To get more reliable results for Pathologists A and F and Pathologists D and E, it is

suggested to combine (3) Carcinoma in Situ and (4) Squamous Carcinoma with Early Stromal Invasion. Besides, it is suggested to combine (2) Atypical Squamous Hyperplasia and (3) Carcinoma in Situ for Pathologists B and F and Pathologists E and F. As a result of reclassifications, an increase in the level of inter-rater reliability is observed.

Conflicts of interest

The authors state that did not have a conflict of interests.

References

- [1] Altun G., Aktaş, S., Karesel Olumsuzluk Tablolarında Asimetri ve Çarpık Simetri Modelleri, *Turkiye Klinikleri J Biostat*, 8 (2) (2016) 152–161.
- [2] Yilmaz, A.E., Saracbası, T., Assessing Agreement between Raters from the Point of Coefficients and Log-linear Models, *Journal of Data Science*, 14 (1) (2017) 1–24.
- [3] McHugh, M.L., Interrater Reliability: the Kappa Statistic, *Biochemia Medica*, 22 (3) (2012) 276–282.
- [4] Cohen, J., Weighted Kappa: Nominal Scale Agreement with Provision for Scaled Disagreement or Partial Credit, *Psychological Bulletin*, 70 (4) (1968) 213–220.
- [5] Gwet, K.L. Handbook of Inter-rater Reliability, The Definitive Guide to Measuring the Extent of Agreement among Raters. 3rd ed. Maryland: Advanced Analytics, LLC, (2002).
- [6] Cicchetti, D., Allison, T., A New Procedure for Assessing Reliability of Scoring EEG Sleep Recordings, *American Journal EEG Technology*, 11 (3) (1971) 101–109.
- [7] Fleiss, J.L., Cohen, J., The Equivalence of Weighted Kappa and the Intraclass Correlation Coefficient as Measure of Reliability, *Educational and Psychological Measurement*, 33 (3) (1973) 613–619.
- [8] Landis, J.R., Koch, G.G., The Measurement of Observer Agreement for Categorical Data, *Biometrics*, 33 (1) (1977a) 159–174.
- [9] Darroch, J.N., McCloud, P.I., Category Distinguishability and Observer Agreement, *Australian Journal of Statistics*, 28 (3) (1986) 371–388.
- [10] Perkins, S.M., Becker, M.P., Assessing Rater Agreement using Marginal Association Models, *Statistics in Medicine*, 21 (12) (2002) 1743–1760.
- [11] Yilmaz, A.E., Saracbası, T., Agreement and Adjusted Degree of Distinguishability for Square Contingency Tables, *Hacettepe Journal of Mathematics and Statistics*, 48 (2) (2019) 592–604.
- [12] Holmquist, N.D., McMahon, C.A., Williams, O.D., Variability in Classification of Carcinoma in Situ of the Uterine Cervix, *Archives of Pathology*, 84 (4) (1967) 334–345.
- [13] Landis, J.R., Koch, G.G., An Application of Hierarchical Kappa-type Statistics in the Assessment of Majority Agreement among Multiple Observers, *Biometrics*, 33 (2) (1977b) 363–374.
- [14] Becker, M.P., Agresti, A., Log-linear Modelling of Pairwise Interobserver Agreement on a Categorical Scale, *Statistics in Medicine*, 33 (1) (1992) 101–114.
- [15] Agresti, A., *Categorical Data Analysis*. New York: John Wiley and Sons, (2002).
- [16] Light, R.J., Measures of Response Agreement for Qualitative Data: Some Generalizations and Alternatives, *Psychological Bulletin*, 76 (5) (1971) 365-377.

AUTHOR GUIDELINES

Thank you for choosing to submit your paper to Cumhuriyet Science Journal. The following instructions will ensure we have everything required so your paper can move through pre-evaluating, peer review, production and publication smoothly. Please take the time to read and follow them as closely as possible, as doing so will ensure your paper matches the journal's requirements.

Submission

Cumhuriyet Science Journal is an international, peer-reviewed, free of charge journal covering the full scope of both natural and engineering sciences. Manuscripts should be submitted by one of the authors of the manuscript as online submission after registration to the Cumhuriyet Sciences Journal. Microsoft Word (.doc, .docx, .rtf), files can be submitted. There is no page limit. If there is a problem while uploading the files of manuscript, please try to reduce their file size, especially manuscripts including embedded figures. Submissions by anyone other than one of the authors will not be accepted. The submitting author takes responsibility for the paper during submission and peer review. If for some technical reason submission through the online submission system is not possible, the author can contact csj@cumhuriyet.edu.tr for support.

Submission or processing charges

Cumhuriyet Science Journal does not charge any article submission, processing charges, and printing charge from the authors.

Terms of Submission

Papers must be submitted on the understanding that they have not been published elsewhere (except in the form of an abstract or as part of a published lecture, review, or thesis) and are not currently under consideration by another journal. The submitting author is responsible for ensuring that the article's publication has been approved by all the other coauthors. It is also the authors' responsibility to ensure that the articles emanating from a particular institution are submitted with the approval of the necessary institution. Only an acknowledgment from the editorial office officially establishes the date of receipt. Further correspondence and proofs will be sent to the author(s) before publication unless otherwise indicated. It is a condition of submission of a paper that the corresponding author permit editing of the paper for readability. All enquiries concerning the publication of accepted papers should be addressed to csj@cumhuriyet.edu.tr. Please note that Cumhuriyet Science Journal uses iThenticate software to screen papers for unoriginal material. By submitting your paper to Cumhuriyet Science Journal are agreeing to any necessary originality checks your paper may have to undergo during the peer review and production processes. Upon receiving a new manuscript, the Editorial office conducts initial pre-refereeing checks to ensure the article is legible, complete, correctly formatted, original, within the scope of the journal in question, in the style of a scientific article and written in clear English. Any article that has problems with any of the journal criteria may be rejected at this stage.

Peer Review

This journal operates a single blind review process. All contributions will be initially assessed by the editor for suitability for the journal. Papers deemed suitable are then typically sent to a minimum of two independent expert reviewer to assess the scientific quality of the paper. The author is required to upload the revised article to the system within 15 days by making the corrections suggested by the referee. The article will be rejected if there are no fixes in it. The Editor is responsible for the final decision regarding acceptance or rejection of articles. The Editor's decision is final

Title and Authorship Information

The following information should be included

Paper title

Full author names

Full institutional mailing addresses

Corresponding address

Email address

Abstract

The manuscript should contain an abstract. The researchers who are native speakers of Turkish have to add Turkish title and abstract as well. The abstract should be self-contained and citation-free and should be 250-300 words.

Keywords

Keywords of the scientific articles should be selected from the web address of www.bilimadresleri.com

Introduction

This section should be succinct, with no subheadings.

Materials and Methods

This part should contain sufficient detail so that all procedures can be repeated. It can be divided into subsections if required.

Conflicts of interest

Sample sentence if there is no conflict of interest: The authors stated that did not have conflict of interests.

Acknowledgements

Sample sentences for acknowledgements: The work was supported by grants from CUBAP (T-1111). We would like to acknowledge Prof. Mehmet Sözer, MD, for his precious technical and editorial assistance. We would like to thank

References

References to cited literature should be identified by number in the text in square brackets and grouped at the end of the paper in numerical order of appearance. Each reference must be cited in the text. Always give inclusive page numbers for references to journal articles and a page range or chapter number for books. References should be styled and punctuated according to the following examples

- [1] Karaca E., Ulusoy S., Morgül Ü., Ulusoy H.I., Development of Analytical Method for Sensitive Determination of Streptozotocin based on Solid Phase Extraction, Cumhuriyet Sci. J., 41 (4) (2020) 826-831. (sample reference for journals)
- [2] Keskin B., Ozkan A.S., Inverse Spectral Problems for Dirac Operator with Eigenvalue Dependent Boundary and Jump Conditions, Acta Math. Hungar., 130 (2011) 150-159(sample reference for journals)
- [3] Mazur M.T., Kurman R.J., Dysfunctional Uterine Bleeding. In: Mazur M.T., Kurman R.J., (Eds). Diagnosis of endometrial biopsies and curettings, A practical approach. 2nd ed. Berlin: Springer, (2005) 100-120. (sample reference for book chapters)
- [4] Mazur M.T., Kurman R.J.,Diagnosis of endometrial biopsies and curettings, A practical approach. 2nd ed. Berlin, (2005) 100-120. (sample reference for book)
- [5] National Cancer Institute, Surveillance Epidemiology and End Results. Cancer of the Corpus and Uterus, NOS. Available at: http://seer.cancer.gov/statfacts/html/corp.html?statfacts_page=corp. Retrieved March 2, 2008. (sample reference for websites)
- [6] Surname N., Title of thesis, PD or master thesis, Name of university, name of institue, year. (sample reference for thesis)
- [7] Surname N., Title of fulltext conference paper, name of conference, city, year, pages. (sample reference for Abstratcs in conferences are not accepted as a valid reference except full text)

Preparation of Figures

Each figure can be integrated in the paper body or separately uploaded and should be cited in a consecutive order. Figure widths can be 4-6 inch as 300 dpi. The labels of the figures should be clear and informative. The name and the subtitles of the figures must be 9-point font.

Preparation of Tables

Tables should be cited consecutively in the text. Every table must have a descriptive title and if numerical measurements are given, the units should be included in the column heading. Tables should be simple with simple borders and text written as left text. The name and the subtitle of the tables must be 9-point font

Proofs

Corrected proofs must be returned to the publisher within 2 weeks of receipt. The publisher will do everything possible to ensure prompt publication. It will therefore be appreciated if the manuscripts and figures conform from the outset to the style of the journal.

Copyright

Open Access authors retain the copyrights of their papers, and all open access articles are distributed under the terms of the Creative Commons Attribution license, which permits unrestricted use, distribution and reproduction in any medium, provided that the original work is properly cited.

The use of general descriptive names, trade names, trademarks, and so forth in this publication, even if not specifically identified, does not imply that these names are not protected by the relevant laws and regulations.

While the advice and information in this journal are believed to be true and accurate on the date of its going to press, neither the authors, the editors, nor the publisher can accept any legal responsibility for any errors or omissions that may be made. The publisher makes no warranty, express or implied, with respect to the material contained herein.

Ethical Guidelines

New methods and ethically relevant aspects must be described in detail, bearing in mind the following:

Human Experiments. All work must be conducted in accordance with the Declaration of Helsinki (1964). Papers describing experimental work on human subjects who carry a risk of harm must include:

A statement that the experiment was conducted with the understanding and the consent of the human subject.

A statement that the responsible Ethical Committee has approved the experiments.

Animal Experiments. Papers describing experiments on living animals should provide:

A full description of any anaesthetic and surgical procedure used.

Evidence that all possible steps were taken to avoid animal suffering at each stage of the experiment. Papers describing experiments on isolated tissues must indicate precisely how the donor tissues were obtained.

Submission Preparation Checklist

As part of the submission process, authors are required to check off their submission's compliance with all of the following items, and submissions may be rejected that do not adhere to these guidelines.

The submission has not been previously published, nor is it before another journal for consideration (or an explanation has been provided in Comments to the Editor).

The submission file is in Microsoft Word document file (Times New Roman) format.

Where available, URLs for the references have been provided.

The text is single-spaced; uses a 11-point font; employs italics, rather than underlining (except with URL addresses); and all illustrations, figures, and tables are placed within the text at the appropriate points, rather than at the end.

The text adheres to the stylistic and bibliographic requirements outlined in the Author Guidelines, which is found in About the Journal.

If submitting to a peer-reviewed section of the journal, the instructions in Ensuring a Double-Blind Review have been followed.